CERTIFICATE OF RESEARCH

This is to certify that, except where specific reference is made, the work described in this thesis is the result of the candidate's research. Neither this thesis, nor any part of it, has been presented, or is currently submitted, in candidature for any degree at any other University.

.....
P. Davies
(Candidate)

10th June 2010
.....
(Date)

.....
Dr. D. B. Tann
(Director of Studies)

10 June 2010
.....
(Date)

DECLARATION

I declare that neither this thesis, nor any part of it, has been submitted in candidature for any degree at any other academic institution.

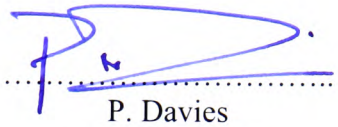

P. Davies
(Candidate)

10th June 2010
(Date)

DEDICATION

This work is dedicated to the memory of my father, whose hard work and sacrifice enabled me to achieve my position in life

ACKNOWLEDGEMENTS

The candidate would like to acknowledge the following:

- Dr. David Tann, my Director of Studies for his unfailing belief in my abilities and for convincing me to "stay on the tiger".

- Professor Ray Delpak whose continuing assistance and guidance have helped me to maintain direction and focus.

- The Engineering and Physical Sciences Research Council for the provision of funding for the research (Grant No. GR/R91397/01).

- Exchem Mining and Construction Ltd. for the provision of materials.

- The staff in the structural laboratories for their extensive assistance in the carrying out of the experimental programme; in particular, Mr. Daren Crocker, Mr. Tony Salmon, Mr Warren House and Mr Huw Williams.

- Special thanks must go to Mr. Paul Marshman, whose help with all aspects of the experimental programme has been invaluable.

- To my Mother, for her continuing and unwavering support in all my endeavours.

- Finally, to Suzanne, without whose invaluable help, counsel, support and guidance, the completion of this research would not have been possible.

ABSTRACT

There are many structures in need of strengthening and upgrading and the need for this is due to a number of factors:

- Structural deterioration over time
- Traffic volume increases
- Increases in allowable maximum vehicle weights
- Poor maintenance
- Poor construction quality
- Errors in initial design

Steel plate bonding has historically been used to enhance load-carrying capacity but there are inherent problems with such systems (e.g. section weight, corrosion susceptibility). Consequently, the use of advanced composites for strengthening has become more widespread in recent years, as such materials have high strength and stiffness but without the disadvantages encountered with steel plates. However, FRP composites do not possess the desired ductile characteristics and, hence, there is hesitance in their use, due to concerns of potentially sudden collapse.

In this research the investigation is based on Fibre Reinforced Polymer (FRP) strengthened reinforced concrete beams and slabs, with particular attention to the ductility of strengthened elements and their failure modes. A total of twenty beams and nine slabs were tested. The beams were 2.6m long, with a cross-section of 100mm x 200mm, and the slabs were 3m long, with a cross-section of 500mm x 100mm. All sets of elements consisted of a control member and strengthened members with varying amounts of CFRP sheet or plate.

The main conclusions drawn are:

- The inherent ductility of CFRP strengthened elements is not as low as has been previously thought. Some of the tested elements with lower

amounts of strengthening displayed acceptably ductile failure modes; i.e. the elements demonstrated levels of deflection/deformation prior to ultimate loads to ensure sufficient forewarning of impending failure.

- The crack patterns of strengthened elements vary considerably from un-strengthened ones, particularly with respect to beams. Cracks in strengthened members tend to be smaller and narrower, with an increased crack density. Additionally, cracks in strengthened elements tend to increase in number up to failure, unlike their un-strengthened counterparts.

- FRP strengthening is not suitable for elements already heavily-strengthened in flexure. Experiments have shown that there is insignificant improvement in performance, as the elements all fail due to crushing of the concrete in the compression zone, making any strengthening redundant.

- A non-linear numerical model has been created and verified using the data acquired from the experimental programme. This will enable the prediction of element deflection up to ultimate load and, hence, allow the ductility to be quantified during the design stage.

- A method of predicting the maximum deformation of fibre composites strengthened RC beam elements has been developed, enabling designers to effectively determine the deflection of such elements.

- A revised method has been developed for determining average crack widths under load, which builds on existing theory to include the effect of the CFRP strengthening on the element behaviour.

Keywords: Fibre Reinforced Polymers; Carbon Composites; Reinforced Concrete; Flexure; Strengthening; Retrofitting; Ductility; Deformability; Failure Modes; Over/Under Strengthening; Optimisation; Practical Considerations; Non-linear Modelling

TABLE OF CONTENTS

NOTATIONS

α	Concrete/steel modular ratio
β	Concrete FRP modular ratio
Δ_s	Mid-span deflection at serviceability load
Δ_u	Mid-span deflection at ultimate load
Δ_y	Mid-span deflection at yielding of internal steel reinforcement
$\Delta_{0.95u}$	Mid-span deflection at 95% of ultimate load
δ_E	Mid-span deflection at ultimate load after subtraction of estimated unloading curve from experimental results
δ_{max}	Maximum element deflection
δ_s	Mid-span deflection at ultimate load after subtraction of estimated unloading curve using Naaman *et al.*'s method
$\delta_{s'}$	Mid-span deflection at ultimate load after subtraction of estimated unloading curve using proposed 3-slope approach
δ_u	Mid-span deflection at ultimate load; used when calculating stored elastic energy
δ_1	Mid-span deflection at intersection of slopes S_1 and S_2; used when calculating stored elastic energy
δ_2	Mid-span deflection at intersection of slopes S_2 and S_3; used when calculating stored elastic energy
ε_b	Element strain at lowest DEMEC level
ε_c	Compressive strain at extreme top fibre
ε_{c1}	Concrete strain at peak stress
ε_{ci}	Concrete strain at level being assessed
ε_f	Tensile strain in bonded fibre composites
ε_m	Average strain at the level where cracking is being considered
$\varepsilon_{s'}$	Compressive steel reinforcement strain
ε_s	Tensile steel reinforcement strain

ε_t	Tensile strain at extreme bottom fibre
ε_{ult}	Ultimate strain
ε_l	Overall extension at a depth y below the neutral axis
κ	Curvature
κ_u	Curvature at ultimate limit state
λ	Ratio of ductility to deformability index
μ_Δ	Ductility index based on deflection at steel yield and ultimate load
$\mu\varepsilon$	Microstrain
μ_E	Ductility index based on stored energy at yielding of internal steel reinforcement and at ultimate loading
ρ_m	Density of machined steel sample
σ	Standard deviation
σ_c	Concrete compressive stress
σ_{ci}	Concrete compressive stress for slice 'i'
σ_{FRPT}	Tensile stress at centre of layer of bonded fibre composites
σ_{sc}	Steel compressive stress
σ_{steel}	Steel stress (up to yield)
σ_{st}	Tensile steel stress
σ_t	Concrete tensile stress
σ_{ti}	Concrete tensile stress at slice 'i'
φ_{df}	Deformability index
φ_E	Energy-based ductility index
φ_{3S}	Energy-based ductility index from proposed 3-slope approach
ψ	Cross-sectional area of bonded fibre composites as a percentage of the total element cross-sectional area
Ø	Diameter

$Ø_m$	Diameter of machined steel sample
a	Distance from support to nearest point load
a'	Depth from top of member to level at which cracking is being considered
a_{cr}	Distance from point where cracking is being considered to the nearest longitudinal steel bar
A_f, A_{FRP}	Area of bonded fibre composites
A_s	Area of tension steel reinforcement
A_s'	Area of compression steel reinforcement
b	Overall breadth of member
c_{min}	Minimum cover to tension steel
C_C	Compressive force in concrete
D_y	Depth of slice 'i'
d'	Depth to the centre of the compression steel
d	Effective depth of the member (to the centre of the tension steel reinforcement)
E	Elastic Modulus
E_c, E_0	Elastic modulus of concrete
E_{el}	Estimated stored elastic energy at ultimate load, using Naaman *et al.*'s method
E_{el}'	Estimated stored elastic energy at ultimate load using proposed 3-slope approach
E_{el}''	Estimated stored elastic energy at ultimate load from experimental Load deflection curve
E_{FRP}	Elastic modulus of fibre composites
E_s, E_{steel}	Elastic modulus of steel
E_u, E_{tot}	Area under Load deflection curve at ultimate load
E_y	Area under Load deflection curve at yielding of internal steel reinforcement

f	Stress
f_{ck}	Concrete cylinder strength
$f_{ck,\,cube}$	Concrete cube strength (EC2)
f_{ct}	Concrete tensile stress
f_{cu}	Concrete cube strength
f_s	Steel characteristic strength
f_y	Steel reinforcement yield strength
h	Overall depth of member
I	Second moment of area
I_0	Second moment of area of transformed, uncracked section
I_g	Second moment of area of strengthened section
K_0	Constant related to concrete aggregate
L, l	Effective span
L_m	Length of machined steel sample
L_s	Length of reinforcement specimen
m_m	Mass of machined steel sample
m_s	Mass of reinforcement specimen
M_s	Mid-span moment at serviceability load
M_u	Mid-span moment at ultimate limit state
M_x	Moment at distance 'x'
M_y	Mid-span moment at yielding of internal steel reinforcement
NA	Neutral axis
P	Applied load
P_{min}	Load at which concrete cracking occurs
P_1	Load at intersection of slopes S_1 and S_2
P_2	Load at intersection of slopes S_2 and S_3

P_s	Serviceability load
P_u	Ultimate load
R	Radius of curvature
S	Estimated unloading slope
S'	Estimated unloading curve using proposed 3-slope approach
S_C	Compressive force in steel
S_1	Initial slope of Load deflection curve
S_2	Second slope of Load deflection curve
S_3	Third slope of Load deflection curve
t_f	Thickness of the layer of the bonded FRP composites
T_C	Tensile force in concrete
T_S	Tensile force in steel
T_F	Tensile force in bonded fibre composites
x	Depth to the neutral axis
x_c	Calculated neutral axis depth, from strain readings, for control elements
x_s	Calculated neutral axis depth, from strain readings, for strengthened elements
v_m	Volume of machined steel sample
W_{av}	Design average surface crack width
W_{FRP}	Design average surface crack width for an element strengthened with bonded fibre composites
y	Depth from neutral axis to level at which cracking is being considered
y_i	Distance from neutral axis to slice 'i'

LIST OF FIGURES

LIST OF TABLES

CHAPTER 1 INTRODUCTION

1.1 Need for maintenance and strengthening of existing structures

1.1.1 Discussion of the problem

All engineering structures constructed from materials including reinforced concrete are designed for a finite life and this itself may be shortened further due to aggressive environments; for example, in car parks where de-icing salts are deposited on the surface of the deck slabs. Feedback from a Government commissioned survey of 200 highway concrete structures highlighted durability problems, even where materials, specification and construction practices were satisfactory (Tann, 2001).

Consequently, from a practical and commercial viewpoint, there are ample cases where it may become necessary to strengthen a reinforced concrete member. The need for strengthening is due to a number of factors:

- Deterioration of structures over time
- Increases in traffic volumes
- Increases in the allowable maximum vehicle weights
- Poor maintenance
- Poor construction quality
- Errors in the initial design
- Inadequate design codes in need of updating

1.1.2 Upgrading structural performance without fibre composites

Historically, strengthening would have been achieved using section enlargement or, more usually, by attaching steel plates to the tension surface, to help resist the tension forces in the degraded structure.

However, steel plate bonding has a number of disadvantages:

- Peeling-off of plates – this has been addressed in the past by the introduction of end anchors in the plates, where the plate has been bolted to the strengthened structural element;
- Heavy section weight – steel obviously has a high self-weight and this has implications when strengthening works are being carried out, with the need for extensive temporary support systems;
- Jointing – Due to the need to keep steel plates flat prior to application, to reduce induced stresses, the maximum practical transportation length is around 8 metres. This necessitates jointing of the plates, as most spans are greater than this, which is both time consuming and labour intensive;
- Corrosion – This is one of the more significant problems with steel plate bonding. Since such strengthening is on the external face of the structure, the steel is under constant attack from environmental conditions, even if protective coatings are used.

1.1.3 Strengthening techniques using fibre composites

In recent years, Fibre Reinforced Polymer (FRP) composites have increasingly been used instead of steel plates, see Table 1.1 and Figures 1.1(a) to (c), but there still remain technical issues to be resolved, for instance the potential for brittle failure modes of FRP composites strengthened structures. It is recognised that FRP composites strengthened, reinforced concrete (RC) elements behave differently from their steel reinforced counterparts, due to the primarily linear elastic stress/strain characteristics of composites up to failure. The main benefits of FRP composites are:

- resistance to corrosion and chemical attack
- lightness of material and, hence, ease of application.

Table 1.1 – Examples of strengthening works carried out in the UK in recent years using FRP composites

Structure	Year	Type of strengthening
Allders Department Store, Croyden	1997	Strengthening of 4 bays of floor slab to allow cut outs for escalators during night time working. CFRP laminates threaded over pipes, cables and ducts.
Bardirelli Square, Manchester	1997	Strengthening 2nd floor slab on office building subject to increased loading.
Abertillery Leisure Centre	1998	Flexural strengthening of swimming pool longitudinal RC beams with CFRP plate bonding.
Haversham Bridge, Milton Keynes	1998	Flexural strengthening of the longitudinal RC beams in hogging with CFRP plate bonding to the top of the deck, underneath the waterproofing membrane.
Hythe Bridge, Oxford	1999	Plate bonding of 125-year old cast iron beamed bridge, increasing the 7.5 tonne capacity to 40 tonnes. (See Figure 1.1(a))
Barnes Bridge, A34/M56 link over M60, Manchester	2000	Strengthening of bridge deck with CFRP plates to achieve higher flexural capacity due to increase in HGV loading to 40 tonnes. (See Figure 1.1(b))
Pioneer Centre, London	2000	Strengthening of floor slab in flexure with 100mm wide, 1.2mm thick CFRP strips
Sycamore Lane Footbridge, Warrington	2000	Strengthening of reinforced concrete column by wrapping with several layers of CFRP sheets
Covered Way 21 (CW21) Tunnel opening	2004	Strengthening of cast iron, roof support girders
Westfield London Retail and Leisure Development	2008	Strengthening of original slabs for increased loading. (See Figure 1.1(c))

Sources: Tann (2001); www.ngcc.org.uk; www.shef.ac.uk/uni/projects/tmrnet/index.html; http://www.structuralsystems.com.au; Proceedings of ACIC07.

Figure 1.1(a) – Hythe Bridge strengthening (www.ngcc.org.uk)

Figure 1.1(b) – Pioneer Centre, floor slab strengthening (www.ngcc.org.uk)

Figure 1.1(c) – Westfield London Retail and Leisure Development, floor slab strengthening (http://www.structuralsystems.com.au/SSL/Cases/SSUK-PDS-R009-WestfieldLondon.asp)

1.2 Mechanical Properties of FRP composites

There are three main types of FRP composites used in the construction industry; namely Glass Fibre (GFRP), Carbon Fibre (CFRP) and Aramid Fibre (AFRP). Table 1.2 shows the typical mechanical properties of the various composites.

Table 1.2 – Typical mechanical properties of composites*

Composite type	Fibre content (% by weight)	Density (kg/m^3)	Elastic modulus (kN/mm^2)	Tensile strength (N/mm^2)
GFRP	50-80	1600-2000	20-55	400-1800
CFRP	65-75	1600-1900	120-250	1200-2250
AFRP	60-70	1050-1250	40-125	1000-1800

It should be noted that the value ranges given in the table are only indicative and the properties of a particular product should be independently verified. Additionally, for FRP composites formed by wet lay-up techniques, it can be difficult to control the thickness and, hence, define precisely the elastic modulus and tensile strength. Consequently, two methods have been developed; the 'fibre sheet thickness' by Ahmed *et al.* (1999), and the nominal thickness, recommended by Teng *et al.* (2002).

All types of FRP composites display linear stress/strain behaviour up to failure, as can be seen in Figure 1.2. This is an important issue as the consideration of structural ductility is of predominant importance to all structural designers because all appropriately designed structures must attain sufficient ductility, under ultimate loads, to provide adequate warning of failure and prevent sudden and brittle collapse. This aspect is further explored in Section 1.3.

* Source: Teng *et al.*, (2002)

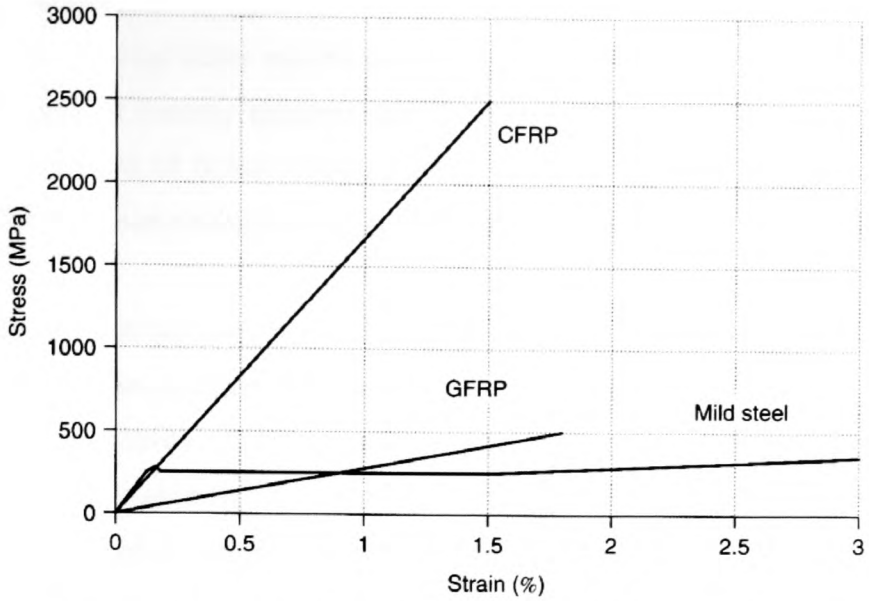

Figure 1.2 – Comparison of Steel and FRP composites Stress/strain plots (Teng *et al.*, 2002)

1.3 Ductility and its importance to FRP strengthening

The term 'ductility' derives from the Latin word *ductilis* and means the ability of materials, particularly metals, to retain strength while subjected to applied loading. This has more recently been extended to include the ability of any material to sustain inelastic deformation before fracture.

Ductility is of primary importance to structural design engineers, since all appropriately designed structures should be sufficiently ductile, at ultimate limit state, to:

- ensure that internal forces can be redistributed within the structure. This occurs when parts of the structure near ultimate limit state and allow plastic hinges to be formed.
- additionally, it is commonly agreed that ductile structures provide sufficient warning of impending failure, thereby removing the likelihood of sudden or "brittle" collapse.

The concept of 'designed-in' ductility is particularly applicable to RC beams and slabs. During many experiments in RC beam strengthening duc to steel plate bonding, it became apparent that sudden peeling of the plates was one of the main causes of failure (Tann, 2001). This characteristic has many similarities with RC beam strengthening using other materials such as FRP composites.

However, it has been noted from previous experimental work (Tann, 2001) that elements strengthened with an appropriate amount of FRP can exhibit a suitable level of ductility. This is significant because, as detailed earlier in this chapter, it is often mistaken by some that FRP composites strengthened RC structures show negligible or no ductility. The issues emerge as follows:

a) It is imperative when calculating the ductility of any strengthened element to first be able to determine the load/deflection behaviour. This needs to be developed via a numerical model that could be utilised during the design process.

b) Another unresolved technical issue is the determination of surface crack widths for FRP composites strengthened members (Tann, 2001). It has been noted that the crack width and density varies considerably from that of un-strengthened elements, particularly for RC beams.

c) Finally, the consideration of the effects of FRP composites strengthening on heavily-reinforced elements needs to be investigated, to confirm the influence of the internal steel reinforcement ratio on the strengthened element behaviour of FRP composites strengthened members.

1.4 Aims and objectives

Although guidance currently exists for the design of FRP composites strengthened structures, it is rather limited and, consequently, it is the main aim of the current research to develop a means of predicting the deformation

characteristics of FRP composites strengthened elements and, hence, determine their ductility and/or deformability. This will in turn lead to the formation of improved design guidelines.

The main objectives are as detailed below:

1) To carry out an experimental programme on both beam and slab elements, with parametrically varying cross-sectional areas of internal steel reinforcement, which have varying amounts of FRP composites sheets or plates bonded to the soffit, under strictly controlled laboratory conditions in order to:
   - Assess element behaviour by recording both displacements and strains up to ultimate limit state;
   - Characterise the mechanical properties of all the materials used; i.e. concrete, reinforcing steel and CFRP composites;
   - Evaluate the failure mechanisms of FRP-bonded under-, balanced- and over-strengthened RC elements (as defined in pre-FRP-bonding stage).

2) Use the data collected from the experimental programme to:
   - Assess the validity and reliability of the experimental data;
   - Develop a suitable means of processing the experimental results (e.g. the use of spread sheets);
   - Produce moment/curvature diagrams to assess the performance of the different experimental elements;
   - Investigate the influence of increasing amounts of CFRP strengthening on both beam and slab elements;
   - Identify typical failure modes for CFRP-strengthened elements.

3) Develop analytical models that will predict the load/deflection and moment/curvature behaviour of FRP composites strengthened elements.

The models will be validated using the data obtained from the experimental programme.

4) Determine ductility and deformability indices for the experimental elements and, together with a parametric study of elements tested elsewhere and published in peer-reviewed journals, define suitable ductility levels to ensure the prevention of brittle failure for FRP composites-strengthened RC elements.

5) Define a new method of calculating the ductility index for a CFRP-strengthened RC element.

6) Correlate the ductility and deformability levels of FRP composites-strengthened RC elements to ultimate load and failure mode.

1.5 Structure of the Thesis

This thesis is divided into nine chapters, which cover the following topics:

Chapter 1: This chapter begins with a general introduction to the need for structural repair, and then discusses more conventional methods for structural strengthening before discussing both the benefits and shortcomings of strengthening with fibre composites, with particular emphasis on the need for ductility. Finally, the aims and objectives of the current research are outlined.

Chapter 2: A comprehensive, critical literature review on the conventional methods of quantifying ductility in FRP composites strengthened RC elements, together with the classification of failure modes for such elements. A summary of the salient points of both aspects of the review is presented in tabular form at the end of the chapter and areas requiring further investigation are identified.

Chapter 3: An experimental investigation into elements, both in beam and slab form, with differing cross-sectional areas of internal steel reinforcement. These were later strengthened with varying levels of CFRP sheets or plates. Additionally, control RC elements were planned to be tested, in order that a comparison can be made with the FRP composites strengthened beams and slabs to determine not only changes in element behaviour but also differences in ductility indices.

Chapter 4: An analysis and examination of the results of the experimental programme, including presentation of data in graphs in the following forms:

- Load against deflection
- Deflection profiles
- Load against strain
- Element surface strains
- FRP composites surface strains
- Load against Neutral Axis depth
- Moment against curvature, derived from both strain and deflection data
- Total number of cracks against load
- Maximum crack length against load
- Average crack length against load
- Average crack width against load

Chapter 5: A new model for the prediction of deflections in fibre composites strengthened RC beam elements is presented, which utilises a novel method of determining the second moment of area of a strengthened element, based on the amount of bonded fibre composites. Subsequently, a method of deflection determination is presented and is tested by means of a study comprising not only

elements from the current research programme but also elements from published data.

Chapter 6: This chapter presents the analytical modelling developed, which includes a non-linear model created by the candidate utilising Visual Basic programming and presenting the program to the user via a Microsoft Excel interface. Analytical modelling is then carried out to simulate the flexural behaviour of both control and FRP composites-strengthened RC elements. The influence of varying levels of bonded FRP composites together with differing amounts of internal steel reinforcement is investigated and the results are compared with data obtained from the experimental programme.

Chapter 7: The determination of ductility and deformability is discussed, relating to fibre-composites strengthened elements and the appropriate level of both indices is considered. A comprehensive study is presented of both elements in the current research programme, together with numerous elements from published data.

Chapter 8: The development of cracks in FRP composites-strengthened RC elements is investigated and compared with that of normally-reinforced members to develop a better understanding of the behaviour of strengthened beams and slabs. A new method of determining the average crack width in strengthened elements is developed.

Chapter 9: A summary of the research project, together with the major conclusions from the study, is presented. Additionally, the limitations of the present work are identified and suggestions for further work included.

1.6 Concluding remarks

FRP composites have great potential for the strengthening of reinforced concrete structures but it is imperative that the issue of ductility, crack development and influence of internal reinforcement ratios be addressed, before guidelines can be developed to take account of any potential strengths as well as weaknesses.

If these parameters can be suitably quantified, the application of FRP composites in the structural strengthening field would be far more acceptable to structural design engineers.

The purpose of the current research is to suggest definitive approaches for more accurate performance evaluation of FRP composites strengthened elements, backed by empirical and analytical evidence.

CHAPTER 2 LITERATURE REVIEW

2.1 Introduction

To a structural designer, ductility is the ability of a structure to sustain deformation before its failure under ultimate load. Kemp (1998) described ductility as the "inelastic rotations through which critically stressed regions of a beam can deform in flexure, before a loss of moment capacity occurs". It has been generally accepted that ductility can be measured by a dimensionless factor, the "ductility factor" or "ductility index". This can be evaluated in several different forms from within two broad categories; namely deformation-based indices and energy-based indices.

Structural ductility is of particular concern to engineers when designing FRP-strengthened elements due to the linear-elastic behaviour of the FRP materials up to failure. Consequently, conventional methods for determining ductility indices are not appropriate for FRP-strengthened elements because insufficient inelastic deformation is achieved.

Additionally, the failure modes of strengthened elements are of particular concern, as it is desirable to design any structural element to fail in a mild or ductile manner and, thereby, remove the likelihood of a sudden, brittle failure.

2.2 Deformation-Based Methods

2.2.1 Spadea *et al*:

Spadea *et al.* (1998) (and, subsequently, Bencardino *et al.* (2002)) defined deflection-based ductility as being calculated using the mid-span deflection at

ultimate load, Δ_u, and the corresponding mid-span deflection at the load where the internal steel yields, Δ_y. This is presented in Equation 2.1.

$$\mu_\Delta = \frac{\Delta_u}{\Delta_y} \qquad 2.1$$

where Δ_u is the maximum mid-span deflection of a member at ultimate limit state and Δ_y is the corresponding value where the steel reinforcement reaches its yield strength.

The authors also presented an index based on the curvature of the element, which can be calculated using the curvature at ultimate limit state, Φ_u, and the corresponding curvature at the load where the internal steel yields, Φ_y. This is presented in Equation 2.2.

$$\mu_\Phi = \frac{\Phi_u}{\Phi_y} \qquad 2.2$$

where Φ_u is the curvature in the constant moment region at ultimate load and Φ_y is the curvature in the constant moment region at the steel reinforcement yield point.

2.2.2 Swamy *et al*:

Swamy *et al.* (1997) proposed a form of curvature based ductility index, based on the flexural rigidity of the element before and after the yielding of the internal steel-reinforcement has taken place:

$$\varphi = 1 + \frac{M_u - M_y}{\chi M_y} \qquad 2.3$$

Where M_u is the moment in the element at ultimate limit state, M_y is the corresponding moment at the point of yielding of the internal steel reinforcement and χ is the ratio of the element's flexural rigidity after and before yielding of the steel reinforcement, as derived using the following equation and with reference to Figure 2.1:

$$\chi = \frac{(EI)_2}{(EI)_1} \qquad 2.4$$

Where $(EI)_1$ is the flexural rigidity of the element before the yielding of the internal steel reinforcement and $(EI)_2$ is the flexural rigidity following the yielding of the steel.

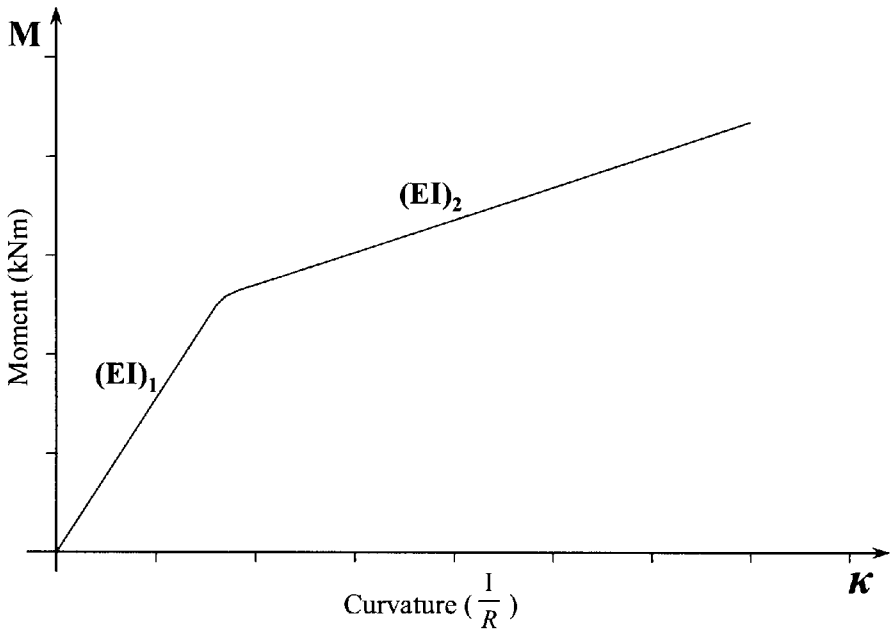

Figure 2.1 – Flexural rigidity from Moment curvature relationship

2.2.3 Tann:

In his PhD thesis, Tann (2001) proposed a new definition of the ductility of strengthened elements; namely, the "deformability index". Due to the primarily elastic nature of FRP composites, Tann identified that the more "traditional" methods of ductility determination could lead to a dangerous situation whereby an element could be classified as being sufficiently ductile to promote a mild failure mode, whereas, in reality, the element would be susceptible to "brittle" or catastrophic failure.

Subsequently, Tann suggested that a more appropriate approach would be to use the deformation at the serviceability load (Δ_s) in place of that at the steel

reinforcement yield point, together with the corresponding deformation at 95% of the ultimate load. This was termed the 'deformability index' and is shown in Equation 2.5:

$$\varphi_{df} = \frac{\Delta_{0.95P_u}}{\Delta_s} \qquad 2.5$$

The use of the 95% P_u was recommended as it had been shown that the load rate and general configuration of the testing system being used could affect the ductility index and result in a figure between four and five times higher than that of the same element at 95% of its failure loading. Consequently, Tann found that the element deformation at 95% was more representative.

In conclusion, Tann recommended that the traditional deformation-based methods of ductility calculation were not suited in the analysis of FRP strengthened sections and, consequently, only energy-based methods should be utilised when dealing with such elements. Energy-based index calculation is discussed in Section 2.3.

Tann (2005) further investigated the ductility and deformability of RC elements, in particular RC slabs, and determined that the ductility of such elements can be suitably determined by the use of an energy-based method of ductility determination. He recommended that for FRP strengthened slabs, a minimum ductility index of around 1.4 should be used for practical design purposes.

For all the above methods, an important deformation point to ascertain is the steel reinforcement yield point. Due to the primarily elastic manner in which FRP strengthened elements perform, this cannot easily be identified, as illustrated in Figure 2.2. Consequently, it is apparent that the above, conventional deformation-based methods of calculating ductility indices may be considered inappropriate for FRP strengthened elements.

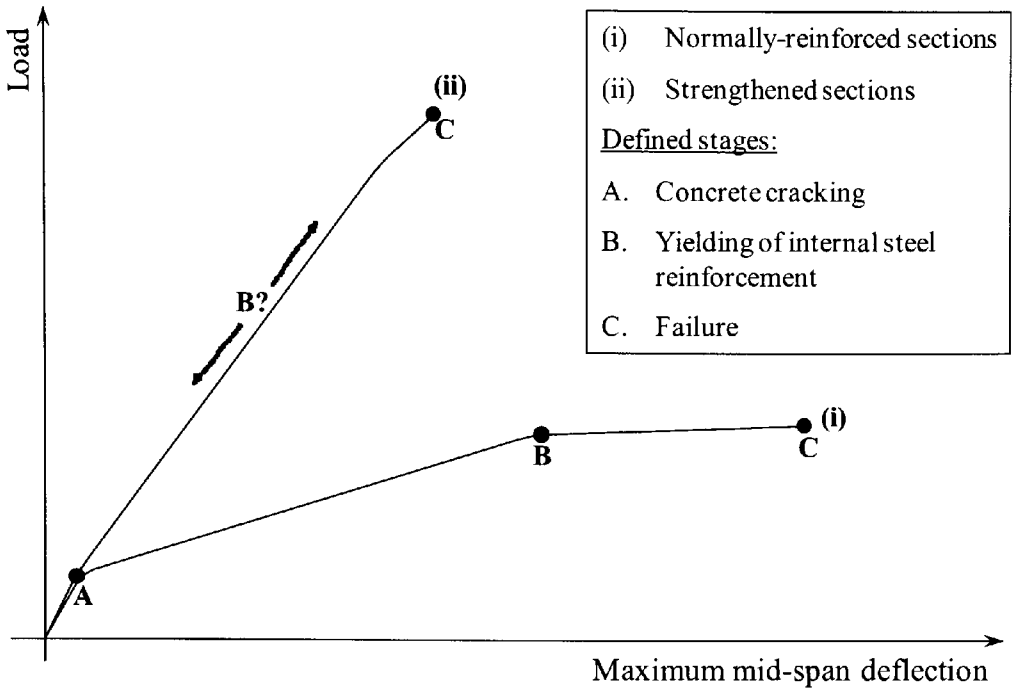

Figure 2.2 – Typical load deflection of Conventional and Strengthened RC beams

2.2.4 De Lorenzis *et al*:

De Lorenzis *et al.* (2004) promoted the use of a curvature-based ductility index, as shown in Equation 2.6

$$\mu = \frac{\chi_u}{\chi_y} \qquad 2.6$$

Where χ_y is the curvature of the element when the yielding of the internal steel reinforcement occurs, and χ_u is the curvature at ultimate loading.

This is the same form of ductility index as presented by Spadea *et al.* (1998), which was covered in Section 2.2.1.

2.3 Energy-Based Methods

2.3.1 Bencardino *et al*:

Bencardino *et al.* (2002) defined energy-based ductility as normally calculated using the element energy at ultimate load, E_u, and the corresponding element energy at the load where the internal steel yields, E_y. This is presented in equation 2.7.

$$\mu_E = \frac{E_u}{E_y} \qquad 2.7$$

where E_u is the area under the Load/Deflection curve at failure and E_y is the area under the Load/Deflection curve at the steel reinforcement yield point.

However, this approach has similar limitations to the deformation methods; namely, the difficulty in ascertaining the exact position of the point where the internal steel reinforcement yields.

2.3.2 Swamy *et al*:

Swamy *et al.* (1997) suggested an approach for an energy-based method, where the total energy under the load-deflection curve of an element is divided by the energy at 75% of the ultimate load:

$$\varphi = \frac{E_{total}}{E_{0.75Pu}} \qquad 2.8$$

To determine the amount of energy, one needs to integrate the area under the load-deflection curve at the respective points.

This approach, a variant of the deformation-based approaches, whilst a reasonable attempt to remove the sometimes misleading ductility indices generated when considering the element behaviour at ultimate limit state, does have certain problems in that the selection of $0.75P_u$ is a somewhat subjective choice.

2.3.3 Naaman *et al.*:

If we consider the idealised load-deflection relationship of a structural element, where the area under the curve at ultimate limit state is E_{tot}, the total energy, and the area under the unloading curve immediately prior to failure is E_{el}, the stored, elastic energy, shown in Figure 2.3.

From this, the following can be calculated:

$$E_{tot} = \frac{1}{2}(\Delta_y P_u) + [(\Delta_u - \Delta_y)(P_u)]$$

$$\Rightarrow E_{tot} = \frac{1}{2}(\Delta_y P_u) + \Delta_u P_u - \Delta_y P_u = \Delta_u P_u - \frac{1}{2}(\Delta_y P_u) \qquad 2.9$$

$$E_{el} = \frac{1}{2}(\Delta_y P_u) \qquad 2.10$$

Where Δ_y is the mid-span deflection at the point of yielding of the internal steel reinforcement, Δ_u is the mid-span deflection at ultimate limit state and P_u is the ultimate load.

If the total energy is now divided by the elastic stored energy the following ensues:

$$\frac{E_{tot}}{E_{el}} = \frac{\Delta_u P_u - \frac{1}{2}(\Delta_y P_u)}{\frac{1}{2}(\Delta_y P_u)} = \frac{2\Delta_u}{\Delta_y} - 1 \qquad 2.11$$

Substituting the traditional deformation-based ductility equation (Equation 2.1) into Eqn. 2.11:

$$\frac{E_{tot}}{E_{el}} = 2\varphi - 1$$

$$\Rightarrow \varphi = \frac{1}{2}\left(\frac{E_{tot}}{E_{el}} + 1\right) \qquad 2.12$$

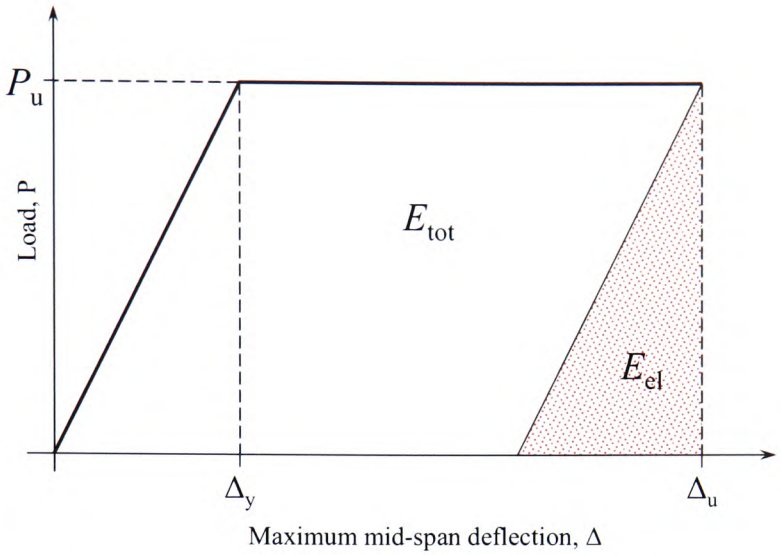

Figure 2.3 – Idealised load deflection behaviour

Naaman and Jeong first developed this energy-based method for determining the ductility index of a structural element that had been internally reinforced with FRP tendons (Naaman et al., 1995). The method was first published in 1995 but there are obvious practical difficulties in identifying the stored elastic energy in a structural element. Consequently, Naaman and Jeong suggested that the stored elastic energy could be estimated using an equivalent triangle area under the load-deflection curve. Once this has been calculated, the ductility index can be calculated using Equation 2.13, with the slope of the estimated unloading line determined using the Equation 2.14 (see also Figure 2.4):

$$\mu = \frac{1}{2}\left(\frac{E_{tot}}{E_{el}} + 1\right) \qquad 2.13$$

where E_{tot} is the total energy, calculated as the area under the load-deflection curve up to the failure load and E_{el} is the estimated, stored elastic energy.

$$S = \frac{P_1 S_1 + (P_2 - P_1) S_2}{P_2} \qquad 2.14$$

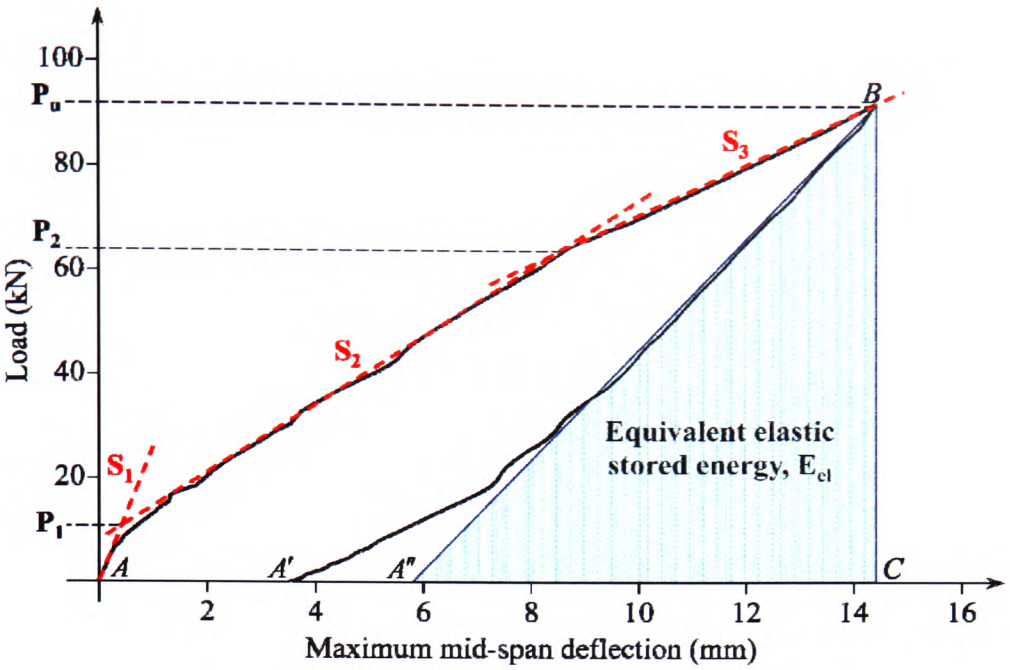

Figure 2.4 – Calculation of equivalent elastic stored energy

The method utilises the two initial loading slopes (S_1 and S_2) together with the corresponding values of load (P_1 and P_2) to define a weighted slope 'S', which characterises the equivalent unloading response at failure. Consequently, the area under this unloading line can be calculated to give the estimated, stored elastic energy in the region of the structural element being considered.

This empirical approach, although somewhat subjective, particularly in relation to the choice of slopes S_1 and S_2, is seen to produce reasonable results. It was primarily developed for elements where there is internally embedded FRP as reinforcement but, nevertheless, the principles can also be applied to members strengthened by externally-bonded FRP.

However, in cases of CFRP-strengthened elements, where the ultimate failure load is significantly higher than the load P_2, the use of Equation 2.14 underestimates the stored elastic energy. Consequently, it is the candidate's suggestion that a modification to the approach to take into account the inherent stored elastic energy present in strengthened elements up to and including failure would be advantageous. This would then provide a far more reliable indicator of

the inherent ductility of elements strengthened by fibre reinforced polymers. This consideration is explored further in Chapter 7.

2.3.4 Oehlers:

In 2006, Oehlers presented a paper discussing the problems of ensuring ductility in FRP plated RC beams, due to the nature of FRP plates to fracture and/or debond before the concrete in the compressive zone reaches its failure strain, ε_c, and crushes.

Oehlers concluded that, when compared with normally-reinforced RC members, the ductility of plated elements is far more complex and results in at least two further failure mechanisms; i.e. plate debonding and plate fracture. Other sources (Tann 2001; Andreou 2002) and also the candidate's MPhil research, have concurred that this is the case but moreover showed that there could be another failure mechanism where failure of the element is due to tearing-off of the concrete cover, i.e. where the cover to the internal steel reinforcement remains adhered to the FRP plate and, at failure, is ripped away from the soffit of the element.

2.3.5 Matthys *et al*:

Matthys *et al.* (2006) evaluated the current requirements for ductility in design guidelines for FRP strengthening and summarised that the design guidelines generally address ductility by means of a strain level criterion and do not consider energy dissipation requirements. Additionally, the authors suggested that the ductility index of elements strengthened in bending with FRP would decrease as the amount of applied FRP increases. Andreou (2002) confirmed this to be the case and also the candidate's MPhil Transfer Report concurred.

Finally, the authors also advised that a minimum curvature ductility index of 1.5 to 2.0 should be obtained, assuming that the design is not governed by bond failure.

2.4 Classification of failure identification in FRP-composites-strengthened elements

Failure modes in FRP-composites-strengthened RC elements tend to be one of four main types, namely FRP fracture, delamination of the FRP sheet/plate, tearing-off of the concrete cover or compressive failure of the concrete. The candidate's own research* confirms this, indicating that the higher the level of FRP strengthening (i.e. the higher the amount of FRP as a percentage of the element cross-sectional area) then the more sudden and brittle the failure of the element and can also be seen in the experimental results presented in Chapter 4.

2.4.1 Meier *et al*:

Meier *et al.* (1992) recommended that in order to ensure a more ductile failure mode in strengthened elements, the external FRP layer should fail in tension after the yielding of the internal steel-reinforcement but before the concrete fails in compression (which would obviously result in a sudden failure). This would not only concur with the candidate's previous research but also with other, published sources (Arduini *et al.*, 1997; Tann, 2001; Andreou, 2001).

2.4.2 Chajes *et al.*:

Chajes *et al.* (1995 & 1998) found that the failure mode of a strengthened element depended on the type of composite used – the elements strengthened with glass and carbon composites failed by rupture of the fibres, whereas the aramid-strengthened beam resulted in a debonding failure and so all subsequent layers of aramid were anchored using end-tabs. The authors felt that failure

* Davies *et al.*, 2007

occurred with a reasonable amount of ductility, although it was half that of the unstrengthened elements.

2.4.3 Hutchinson *et al.*:

Hutchinson *et al.* (1996) carried out an experimental programme on a series of RC beams with varying levels of internal steel reinforcement, which had been strengthened with either glass or carbon FRPs. They found that in beams with a low level of internal steel reinforcement, the flexural strength enhancement was considerable but resulted in a marked decrease in ductility. This is partially in agreement with the findings from the candidate's initial MPhil work; however, it has also been shown that there is a level of strengthening at which the increase in load-carrying capacity starts to decrease and the benefits of the FRP laminates are lost, due to over-strengthening of the element.

2.4.4 Shahawy *et al.*:

Shahawy *et al.* (1996) carried out an experimental programme on four RC beams, strengthening three of them with one, two and three layers of CFRP respectively. They summarised that all the strengthened beams failed due to crushing of the concrete but this is likely due to the higher level of internal steel reinforcement (2 x ∅13mm bars) resulting in over-strengthening of the elements. Additionally, the following points were made:

- Deflections for the strengthened beams were significantly lower than that for the control beam, which is to be expected due to the increased stiffness of strengthened elements;
- The strengthened beams exhibited closely spaced crack patterns, compared to the widely spaced cracking observed in the control beam, which is confirmed by the candidate's own research;
- Strains in the concrete and CFRP laminate reduce with increasing numbers of FRP laminates. This is to be expected due to the increase in element stiffness and corresponding reduction in deformations.

2.4.5 Takeda *et al.*:

Takeda *et al.* (1996) carried out an experimental investigation into the flexural behaviour of beams strengthened with CFRP sheets. They used varying amounts of FRP and also both three- and four-point loading. They concluded that the effect of the strengthening was considerable when considering the flexural rigidity of the element after crack initiation and that the reinforcing effect of the sheet was reduced as the number of sheets increased, due to sheet separation. The candidate's own work would agree with the statement that the benefit of the strengthening can be reduced as more FRP is added (which excessively increases the stiffness of the element) and that the reason would appear to be due to delamination but could also be due to tearing-off of the concrete cover.

2.4.6 Arduini *et al.*:

Arduini *et al.* (1997) suggested that the failure mode of any given element depends on whether it is effectively strengthened or not. The following failure modes have been reported:

- Concrete crushing long after yielding of the internal steel.
- Brittle concrete shear failure initiated by a crack starting at the end of the plates and propagating along the concrete cover parallel to the longitudinal steel reinforcing bars.
- FRP sheet rupture.
- Debonding of FRP sheet

2.4.7 Tegola *et al.*:

Tegola *et al.* (1998) suggested that any failure of FRP strengthened elements is heavily dependent on the interface properties; i.e. that the interfacial stress between the FRP and the concrete substrate results in shear failure of the adhesive layer and, consequently, a delamination of the FRP layer(s). The candidate's MPhil work suggested that, subject to correct preparation of the

concrete substrate and careful control of the adhesive being used, delamination failure could be avoided, particularly when using FRP sheets, unless unacceptably high deformations were present at the latter stages of loading.

2.4.8 Tumialan *et al.*:

Tumialan *et al.* (1999) carried out an experimental programme to further examine the tearing-off of concrete cover mode of failure. Various strengthening configurations were used, including varying the width and number of FRP layers, and using u-wrapping for anchorage. It was found that the primary mode of failure was due to tearing-off of the concrete cover and was of two forms; firstly, tearing-off of the concrete cover from the end of the sheet and, secondly, tearing-off initiating at an intermediate crack. This concurs with the candidate's own experience from his MPhil research, but concrete cover tearing-off mainly occurs where there is a large amount of FRP strengthening, which causes the element to become significantly stiffer, resulting in high stress concentrations at the ends of the FRP. The candidate also found that tearing-off failures that initiated at the ends of the FRP were due to the initiation of a shear crack at the end of the sheet/plate, which then enlarged and caused a horizontal crack to propagate along the level of the internal steel reinforcement, joining other shear cracks together.

2.4.9 Ramana *et al.*:

In an experimental and analytical study, Ramana *et al.* (2000) concluded that the first crack ultimate moment of strengthened elements were significantly higher than that of the control element indicating the "reinforcing effect of the CFRPC laminate". However, it is likely that it is the *stiffening* effect of the laminate, resulting in reduced deformations and, hence, reduced strains, that resulted in the higher values of moment when the first cracks were observed.

Additionally, they noted that as the amount of strengthening increased, the laminate and concrete strains reduced, which is to be expected due to the stiffer

nature of strengthened elements, resulting in reduced deformations and curvatures.

2.4.10 Andreou *et al.*:

Andreou *et al.* (2000) determined that externally strengthened beams have an increase in the ultimate load capacity, the number of FRP layers influence the overall performance of the system, including the failure mode of the specimen and the optimum amount of FRP reinforcement, which provides maximum strengthening effect, must be established for each FRP system, depending on its thickness and mechanical properties.

2.4.11 Tann *et al.*:

Tann *et al.* (2000) recommended that the failure modes of strengthened elements at the ultimate limit state should be ductile, thereby providing adequate warning of impending failure. They suggested that the ductility of an FRP-strengthened element be defined as the ability of the element to withstand further deformation between the serviceability and ultimate limit states.

2.4.12 Leung:

Leung (2002) carried out an experimental study on ten RC beams with varying amounts of GRFP strengthening and concluded that the application of external strengthening on structurally deficient beams may alter their failure mode, which agrees with the candidate's own findings.

2.4.13 Sheikh:

Sheikh (2002) considered the performance of concrete structures that had been retro-fitted with FRPs. He concluded that the procedure provided a feasible rehabilitation technique, not only for repair but also for strengthening,

particularly with reference to improving the flexural strength of RC slabs. Additionally, he stated that both carbon and glass composites provided significant strength enhancement of approximately 150%. However, the candidate's initial MPhil research into slab strengthening revealed a potential strength enhancement of 190% and Tann (2005) recorded an enhancement of 265%.

2.4.14 Arduini *et al*:

Arduini *et al.* (2004) conducted experimental research on 26 one-way spanning RC slabs and determined that the classical assumption of plane sections remaining plane after loading was valid for strengthened elements, which agrees with the candidate's own finding during his MPhil work.

2.4.15 De Lorenzis *et al*:

De Lorenzis *et al.* (2004) carried out a parametric study on RC elements that had been strengthened with FRPs and concluded not only that such strengthening systems provide significant strength enhancement but also that this enhancement is more significant as (a) the existing amount of internal reinforcing steel decreases, (b) the amount of FRP provided increases and (c) the stiffness of the FRP increases. This would concur with the findings of the experimental work carried out as part of the candidate's MPhil research.

2.4.16 Maalej *et al*:

Maalej *et al.* (2005) carried out an experimental programme on beams strengthened with CFRP sheets and concluded that the beam size does not significantly influence the deflection and energy ductility index of CFRP strengthened elements.

2.4.17 Tann:

In Tann's (2005) further investigations into strengthened RC slabs he stated that the level of strength enhancement increases until the total equivalent steel ratio reaches approximately 0.9%, where the full capacity of the concrete is reached and there was a five-fold increase in the load-carrying capacity of the slab. Where the total equivalent steel ratios exceeded 1%, Tann observed that premature debonding of the FRP plates occurred, although the reduced bonding area of plates, the plate thickness and defects on the bond layer could all have contributed to this. He concluded that all slabs with a total equivalent steel ratio of less than 0.9% resulted in a failure mode that could be considered acceptably ductile; i.e. there was no sudden or unexpected collapse at the ultimate limit state.

2.4.18 Oehlers *et al*:

Oehlers *et al.* (2006) identified the problems encountered in the last forty years of quantifying ductility in unplated, normally-reinforced structures, and that the issue of ductility in plated elements is that much more complex, with additional failure modes to consider. Nevertheless, it was found that plated beams can behave in a suitably ductile manner.

2.4.19 Esfahani *et al*:

Esfahani *et al.* (2007) made the observation that the flexural strength and stiffness of strengthened beams increased when compared to the control elements. This is as expected and has been confirmed by others as well as by the candidate in his MPhil experimental work.

2.4.20 Oehlers *et al*:

Oehlers *et al.* (2008) highlighted the need for sufficient rotational capacity in structural members. It was noted that this is a much more complex problem in FRP-plated elements but is nevertheless necessary, in order that a fundamental change in existing design procedures is not required.

2.5 Summary and overview

Summarised in Table 2.1 are the main published techniques by which the ductility and/or deformability index can be calculated, utilising both deformation- and energy-based methods. It can be seen from the review that:

1) The standard methods for determining ductility are unsuited to FRP-strengthened elements, as they rely heavily on the determination of the point at which the internal steel reinforcement yields, which can be problematic due to the primarily elastic way in which FRP-strengthened elements deform.

2) The energy-based indices have advantages over the more traditional methods but still rely on the determination of the stored elastic energy in any strengthened element at failure, which can be difficult to predict.

3) Any method of calculating the ductility index for an element that relies on reductions in the values of any variable can be somewhat subjective.

4) The method proposed by Naaman and Jeong (1995) provides a means of estimating the elastic stored energy and, hence, determining a ductility index for an element. However, the method was developed for use with beams that have been reinforced with pre-stressed FRP tendons and so

may not be wholly appropriate for use with externally strengthened beams and slabs.

In Table 2.2, a summary can be found of the main points and conclusions drawn by the authors reviewed in this chapter, which can be detailed further as shown below:

1) Many researchers have found that brittle or catastrophic failure modes can be a consequence from FRP strengthening of RC elements; e.g. plate/sheet debonding, tearing-off of concrete cover, etc. This results in under-utilization of the whole element. This can be addressed by the use of an optimum amount of FRP being used, resulting in a more ductile failure mode and, hence, full utilization of the mechanical properties of the structural system.

2) The problem of the reduction in deflections/curvatures and, hence, ductility of strengthened elements is directly linked to the premature failure modes detailed in Point (1) above.

3) There is general agreement that when properly designed, FRP strengthening systems can be controlled to produce the desirable pseudo-ductile failure modes but there is a need for universal agreement as to how best to determine structural ductility for FRP-strengthened elements.

Table 2.1 – Summary of ductility and deformability index determination techniques

Section ref.	Type of ductility/deformability determination	Equation(s)	Advantages	Limitations/disadvantages
2.2.1	Deformation ductility based on the mid-span deformation at ultimate and steel-yield loads	$\mu_{\Delta} = \frac{\Delta_u}{\Delta_y}$	Simplistic form of deformation-based index determination requiring limited calculation	Need to ascertain the point at which the internal steel reinforcement yields, which can be difficult in FRP strengthened elements
2.2.1	Curvature ductility based on the element curvature at steel-yield and ultimate loads	$\mu_{\Phi} = \frac{\Phi_u}{\Phi_y}$	Simplistic form of curvature-based index determination requiring limited calculation	Need to ascertain the point at which the internal steel reinforcement yields, which can be difficult in FRP strengthened elements
2.2.2	Curvature ductility based on the flexural rigidity of the element before and after the yielding of the internal steel	$\varphi = 1 + \frac{M_u - M_y}{\chi M_y}$	Reasonably simple form of curvature-based index calculation	Need to ascertain the point at which the internal steel reinforcement yields, which can be difficult in FRP strengthened elements
2.2.3	Deformability ductility, based on the mid-span deformation at serviceability and ultimate loads	$\varphi_{df} = \frac{\Delta_{0.95P_u}}{\Delta_s}$	Simplistic form of determining ductility index requiring limited calculation	Serviceability load for the element needs to be determined, otherwise a generic approach, of say $\frac{2}{3}$ ultimate load, may be misleading
2.3.1	Energy-based ductility, based on the stored elastic energy at internal-steel yield and ultimate loads	$\mu_E = \frac{E_u}{E_y}$	Simplistic form of energy-based index requiring limited calculation	As with the deformation-based methods, there is difficulty in ascertaining the exact point of steel yield
2.3.2	Energy-based ductility, based on the stored elastic energy at ultimate load and at 75% of ultimate load	$\varphi = \frac{E_{total}}{E_{0.75Pu}}$	Reasonably simple form of energy-based index calculation	Variant of deformation-based methods and only valid if materials exhibit elastic-plastic behaviour. Reference point of 75% somewhat subjective.
2.3.3	Energy-based ductility, Naaman and Jeong's method	$\mu_{E2} = \frac{1}{2}\left(\frac{E_{tot}}{E_{el}} + 1\right)$	More reliable form of determining energy-based ductility indices for strengthened elements	Method was developed for use with elements that have been internally reinforced with FRP bars and, hence, not entirely suitable for strengthened elements

Table 2.2 – Summary of findings from literature review

	Conclusion	**Reference(s)**	**Comments**
1.	Use of deformation-based indices for the determination of element ductility	Spadea *et al.* 1998; Bencardino *et al.* 2002; Swamy *et al.* 1997; Tann 2001 & 2005; Oehlers *et al.* 2006	Some researchers felt that deformation-based indices were unsuited to FRP-strengthened elements
2.	Use of energy-based indices for the determination of element ductility	Spadea *et al.* 1998; Swamy *et al.* 1997; Naaman *et al.* 1995; Oehlers 2006; Matthys *et al.* 2006	General agreement that energy-based methods generate more consistent indices but more investigation needed for strengthened elements
3.	Limiting of value in either numerator and/or denominator for more reliable calculation of ductility index	Tann 2001; Aburawi 1997; Naaman *et al.* 1995; Matthys *et al.* 2006	Agreement in principal that revised methods can be more consistent but more investigation needed for strengthened elements
4.	FRPs can increase both the load-carrying capacity and stiffness of RC elements	Meier *et al.* 1992; Chajes *et al.* 1994 & 1995; Hutchinson *et al.* 1996; Shahawy *et al.* 1996; Takeda *et al.* 1996; Tumialan *et al.* 1999; Ramana *et al.* 2000; Tann *et al.* 2000; Leung 2002; Maalej *et al.* 2005; Tann 2005; Oehlers *et al.* 2006; Esfahani *et al.* 2007; Oehlers *et al.* 2008	All references agree in principal

5.	Minimum ductility index of between 1.4 and 2.0 should be used to ensure acceptably mild failure	Tann 2005; Matthys *et al.* 2006	General agreement in principal.
6.	Low internal steel reinforcement ratio results in larger strength gains from bonded FRPs	Hutchinson *et al.* 1996; Arduini *et al.* 1997	Principles of under-reinforcement apply
7.	FRP rupture	Chajes *et al.* 1994 & 1995; Meier *et al.* 1992; Tann *et al.* 2000	Many cases when amount of FRP strengthening is low
8.	Tearing-off of concrete cover	Hutchinson *et al.* 1996; Meier *et al.* 1992; Tann *et al.* 2000, Andreou et al. 2000	Common failure mode due to high stress concentrations at FRP ends
9.	Delamination of FRP sheet/plate	Meier *et al.* 1992; Tann *et al.* 2000, Meier *et al.* 1992; Tegola *et al.* 1998	Indicates poor surface preparation and/or inadequate bonding
10.	Compressive concrete failure	Chajes *et al.* 1994 & 1995; Meier *et al.* 1992; Meier *et al.* 1992; Tann 2001	Indicative of full utilization of the concrete in the compression zone but results in unfavourable, brittle failure
11.	High stress concentrations at end of FRP	Tegola *et al.* 1998; Tann 2001	Further investigation required
12.	Effectiveness of FRP is dependent on the cross-sectional size of the element	Arduini *et al.* 1997; Tann 2001; Andreou *et al.* 2000	General agreement – there is an optimum amount of FRP over which the benefits of FRP strengthening start to be lost
13.	Need for control of ductility/deformability for optimisation of FRP strengthening	Andreou *et al.* 2000; Tann 2001; Oehlers *et al.* 2006	Very important to ensure mild failure modes

CHAPTER 3 EXPERIMENTAL PROGRAMME

3.1 Overview

In the experimental programme, twenty simply supported beams and nine simply supported slabs were cast and tested to failure, in the Structural Laboratory of the University of Glamorgan.

The various reinforcement and strengthening configurations are detailed in Table 3.1.

Table 3.1 – Element configuration for experimental programme

Element Ref.	Element type	Main tension reinf't ∅ (mm)	Internal tension steel reinf't area as %age of cross-sect. area	Effective Span (mm)	No of layers of CFRP sheet or plate
8CON	Singly-reinforced Beam	8	0.50	2400	0
8CF1		8	0.50	2400	1 sheet
8CF2		8	0.50	2400	2 sheets
8CF3		8	0.50	2400	3 sheets
10CON		10	0.79	2400	0
10CF1		10	0.79	2400	1 sheet
10CF2		10	0.79	2400	2 sheets
10CF3		10	0.79	2400	3 sheets
12CON		12	1.13	2400	0
12CF1		12	1.13	2400	1 sheet
12CF2		12	1.13	2400	2 sheets
12CF3		12	1.13	2400	3 sheets
16CON		16	2.01	2400	0
16CF1		16	2.01	2400	1 sheet
16CF2		16	2.01	2400	2 sheets
16CF3		16	2.01	2400	3 sheets
12DCON	Doubly-reinforced Beam	12	1.13	2400	0
12DCF1		12	1.13	2400	1 sheet
12DCF2		12	1.13	2400	2 sheets
12DCF3		12	1.13	2400	3 sheets
8SCON	Slab	8	0.40	2900	0
8SCF2		8	0.40	2900	2 sheets
8SCP2		8	0.40	2900	2x100mm plates
8SCP3		8	0.40	2900	3x100mm plates
12SCON		12	0.91	2900	0
12SCF2		12	0.91	2900	2 sheets
12SCF4		12	0.91	2900	4 sheets
12SCP2		12	0.91	2900	2x100mm plates
12SCP3		12	0.91	2900	3x100mm plates

3.2 Element layout and loading configuration

3.2.1 Beams

All tested beams were 2600mm long, with an effective span of 2400mm. The element cross section was 100 mm wide by 200 mm deep, see Figure 3.1. Two high-yield bars were used as tension reinforcement (f_y = 573 N/mm^2), providing four sets of beams with two 8mm, 12mm, 10mm or 16mm diameter bars as tension reinforcement, respectively. The shear links provided were 6 mm diameter at 100mm centres, placed in the shear spans. For four supplementary elements, two 12mm diameter bars were provided as compression reinforcement in addition to two 12mm diameter tension reinforcement bars.

Timber moulds were oiled and checked for width, cleanliness, etc., prior to the reinforcement cages being placed inside, with plastic spacers used to ensure a nominal cover of 15mm. The reinforcement configuration can be seen in Figure 3.1.

CFRP sheets were used to strengthen three of the beams in each set; one with 1 layer, one with 2 layers and one with 3 layers, referenced 10CF1, 10CF2 and 10CF3 respectively, with the control beam referenced 10CON. The sheets were 2.20m long, allowing a 100mm gap between the edge of the sheet and the support, and were 100mm wide.

A four-point loading configuration was used, with the two point loads situated at 625mm either side of the mid-span, resulting in a 'Constant Moment Zone' 1250mm wide. The load was applied at a rate of 0.125 kN/sec during all tests; the loading configuration can be seen in Figure 3.2.

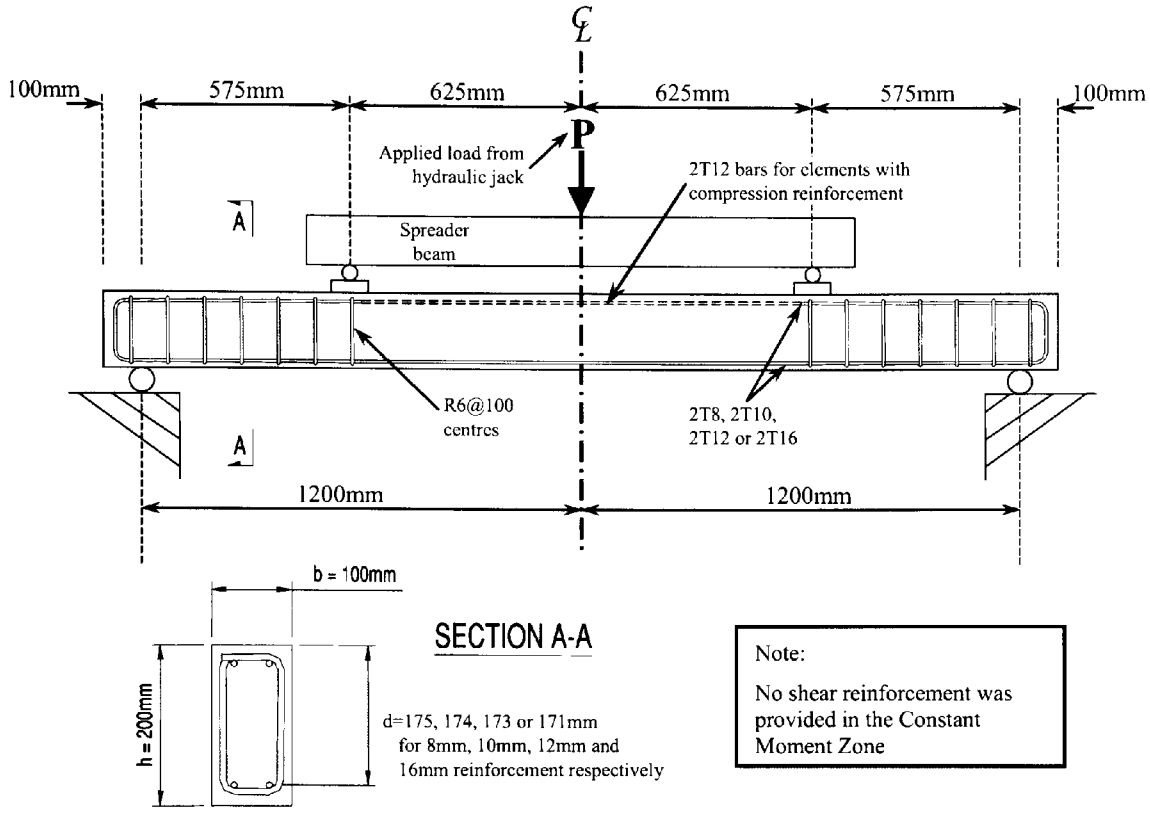

Figure 3.1 – Beam dimensions and internal reinforcement arrangement

3.2.2 Slabs

All slabs were 3000mm long with an effective span of 2900mm. The cross section was 500mm wide by 100mm deep, see Figure 3.3, and four high-yield (8mm or 12mm diameter) bars were used as tension reinforcement, while 8mm diameter high-yield bars at 150mm centres were used as distribution steel, in line with the requirements of BS 8110, Cl. 3.12.5.1 (a minimum percentage of steel in either direction of 0.13%).
Timber moulds were oiled and checked for width, cleanliness, etc., prior to the reinforcement cages being inserted, with plastic spacers used to ensure a nominal cover of 15mm. The reinforcement configuration can be seen in Figure 3.4.

Two Carbon Fibre Reinforced Polymer (CFRP) sheets were used to strengthen one of the slabs, referenced 8SCF2 or 12SCF2, with 2700mm long sheets being applied over the whole 500mm width of the slab; i.e. with the end of the sheet 150mm from the end of the slab and, as with the beams, 100mm from the support. For the remaining two

strengthened slabs in each set, referenced 8/12SCP2 or 8/12SCP3, one and two CFRP plates respectively, 120mm wide and 2700mm long, were applied to the tension faces of the slabs. Details of the strengthened slabs and CFRP sheet and plate dimensions can be seen in Figure 3.5. The control slab was referenced 8SCON.

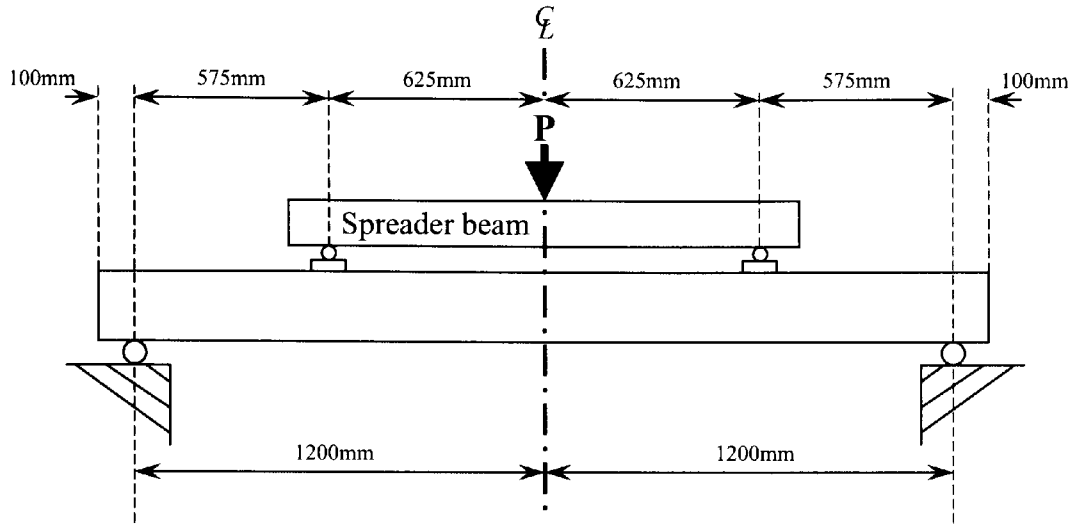

Figure 3.2 – Beam loading configuration

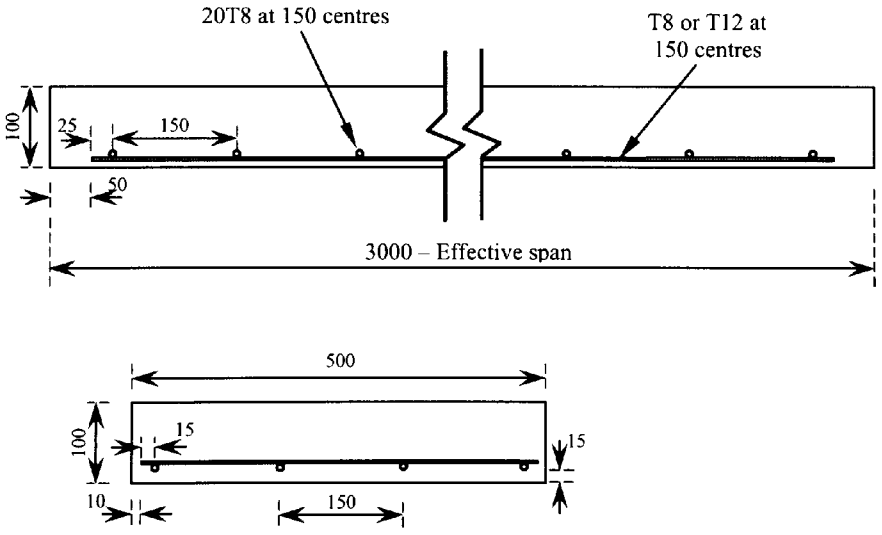

Figure 3.3 – Slab dimensions and steel reinforcement arrangement
(Dimensions in mm)

As with the beams, a four-point load configuration was used, with the two point loads situated at 500mm either side of the mid-span, giving a 1000mm wide 'Constant

Moment Zone'. Again, the load was applied at a rate of 0.125 kN/sec during all tests and the loading configuration can be seen in Figure 3.4.

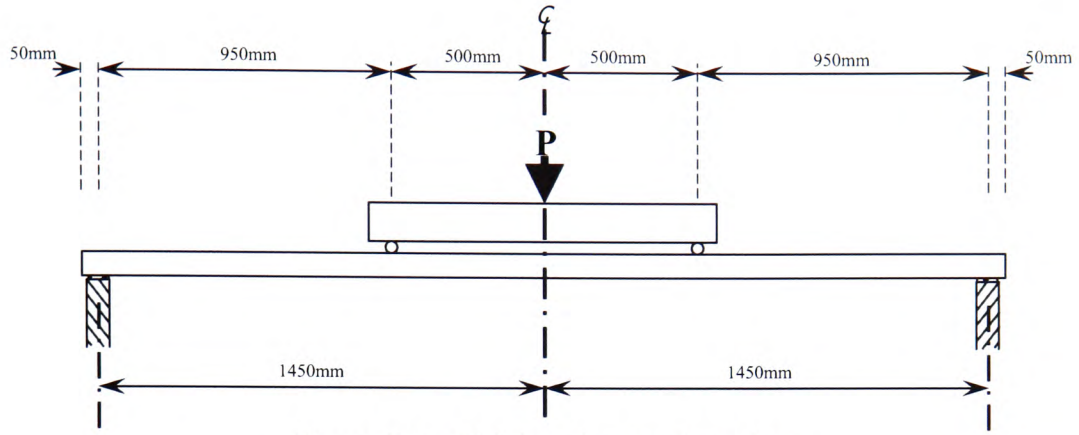

Figure 3.4 – Slab loading configuration

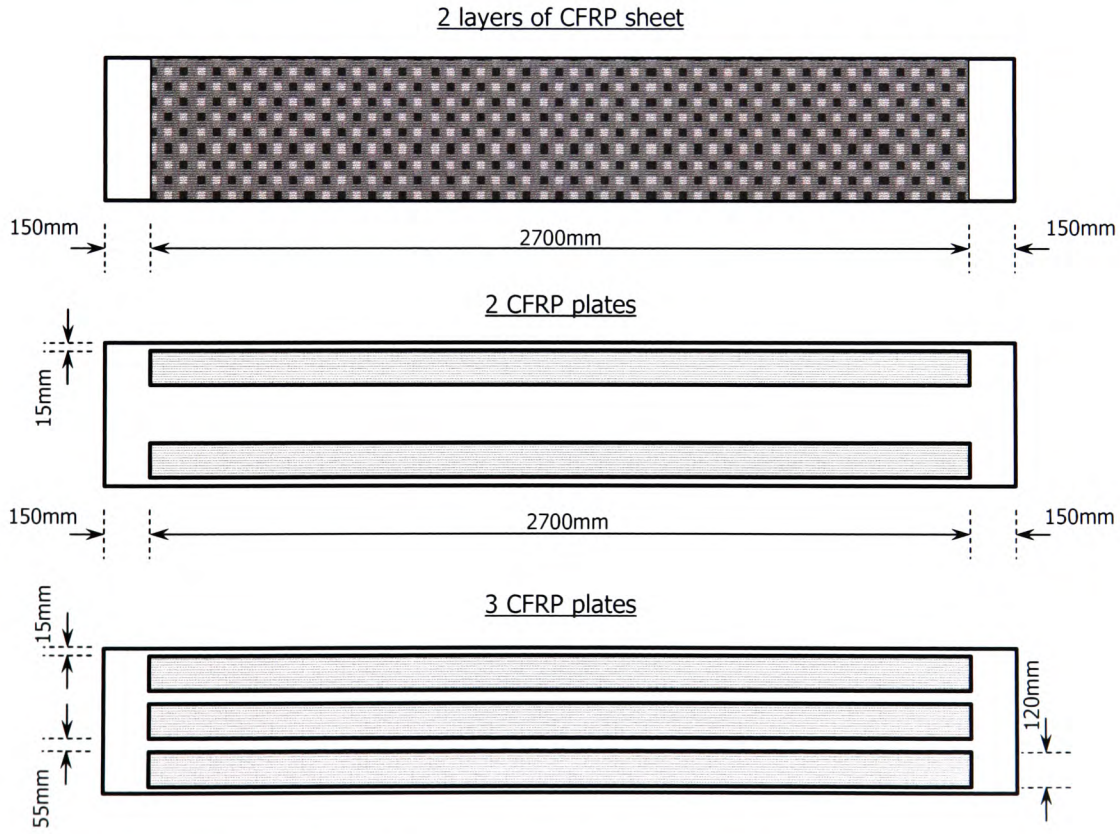

Figure 3.5 – CFRP sheet and plate configuration and dimensions for strengthened slabs with FRP at tension face (soffit)

3.3 Material Properties

3.3.1 Concrete

All concrete batches were produced using the same mix design; the proportions of water, cement, sand and aggregate were 0.5 : 1.0 : 2.0 : 3.0. The cement was Ordinary Portland Cement, with a minimum cement content of 350 kg/m^3. In addition, natural fine sand was used and the coarse aggregate had a nominal size of 10mm.

The beams were cast in pairs and during casting six 100mm cubes and two ∅150mm cylinders (300mm long) were made. The cube strengths and elastic moduli (calculated from cylinder tests) are shown in Table 3.2(a). The slabs were cast singly for each element cast, three 100mm cubes and one ∅150mm cylinder (300mm long) were made; the associated cube strengths and elastic moduli are presented in Table 3.2(b). The elastic modulus, E_c, was obtained using the procedure set out in BS 1881-121: 1983.

3.3.2 Steel reinforcement

The main tensile steel reinforcement used was high-yield bars with a characteristic strength stated by the supplier of 460 N/mm^2. Confirmatory tests were carried out in the Structural Laboratory of the University of Glamorgan, to determine the actual yield and ultimate strength value of the material.

Sample specimens of reinforcing bars were selected for testing and the specimens were cut into 250mm lengths and loaded to failure in a JJ Model M30-K universal tensile testing apparatus, at a rate of 1mm/min (see Figure 3.7).

As the bars were ribbed it was difficult to determine the cross-sectional area for the specimens. Hence, a method was developed in which a sample that had been machined to a known diameter (5.00mm) and length (27.5mm) was weighed in order to determine the density in g/mm^3. Accordingly, a specimen with a set length (100mm) could also be weighed and, using the calculated density, an average cross-sectional area could be established. The method is illustrated in Figure 3.6.

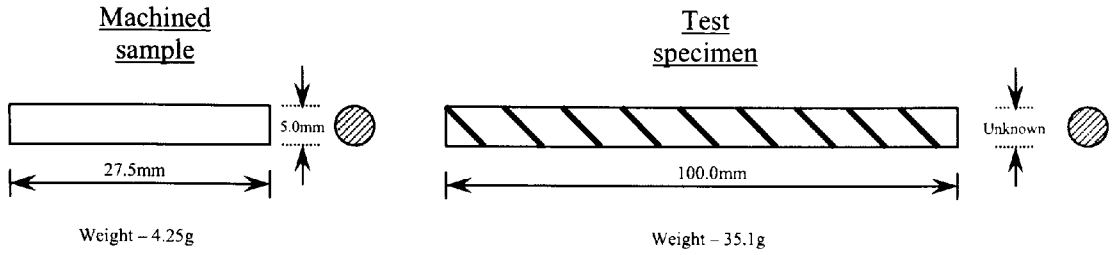

Figure 3.6 – Steel reinforcement specimens for cross-sectional determination

Machined sample:

Length, L_m = 27.5mm and Diameter, $\varnothing_m$ = 5.0mm

$\Rightarrow$ Volume, $v_m = 541.9mm^3$

Mass of sample, m_m = 4.25g

$\Rightarrow$ Density of sample, $\rho_m = m_m / v_m$

$\Rightarrow \rho_m = 4.25/541.9$

$= 7.84 \times 10^{-3}$ g/mm^3

Reinforcement specimen:

Length, L_s = 100.0 mm and mass, m_s = 35.1g

Calculated material density, $\rho = 7.84 \times 10^{-3}$ g/mm^3

$\Rightarrow \quad \frac{m_s}{L_s x(area)} = \rho$

$\Rightarrow \quad \frac{35.1}{100x(area)} = 7.84x10^{-3}$

$\Rightarrow$ **Average cross-sectional area = 44.8 mm^2**

$\Rightarrow$ **Equivalent diameter, Ø=7.6mm**

Consequently, as can be seen in Table 3.3, the resultant ultimate tensile strength of the reinforcement was 640.1 N/mm^2, with a corresponding yield stress of 573 N/mm^2. The stress/strain curves up to yield are presented in Figure 3.8.

Table 3.2(a) – Concrete cube strength and clastic modulus for beam tests

Beam Ref.	Cylinder Strength (N/mm^2)		Cube Strength (N/mm^2)		Average Cube Strength, f_{cu} (N/mm^2)	Elastic Modulus, E_c (kN/mm^2)
8CON & 8CF3	Cylinder 1 Cylinder 2	48.5	Cube 1 Cube 2 Cube 3 Cube 4 Cube 5 Cube 6	64.3 63.7 67.7 63.7 68.5 62.7	65.1 $\sigma = 2.39$	44.2
8CF1 & 8CF2	Cylinder 1 Cylinder 2	47.8	Cube 1 Cube 2 Cube 3 Cube 4 Cube 5 Cube 6	61.0 66.2 60.7 59.0 64.3 62.1	62.2 $\sigma = 2.62$	43.5
10CON & 10CF3	Cylinder 1 Cylinder 2	45.6 45.8	Cube 1 Cube 2 Cube 3 Cube 4 Cube 5 Cube 6	43.4* 51.5 52.5 37.6* 49.5 52.3	51.5 $\sigma = 1.37$	42.0
10CF1 & 10CF2	Cylinder 1 Cylinder 2	39.9 39.2	Cube 1 Cube 2 Cube 3 Cube 4 Cube 5 Cube 6	61.0 58.9 57.2 60.6 61.5 59.9	59.9 $\sigma = 1.58$	36.3
12CON & 12CF3	Cylinder 1 Cylinder 2	46.7 46.4	Cube 1 Cube 2 Cube 3 Cube 4 Cube 5 Cube 6	46.4 52.8 48.8 44.2 52.3 52.6	49.5 $\sigma = 3.65$	40.7
12CF1 & 12CF2	Cylinder 1 Cylinder 2	44.9 45.4	Cube 1 Cube 2 Cube 3 Cube 4 Cube 5 Cube 6	39.9 41.4 43.8 43.5 39.8 40.7	41.5 $\sigma = 1.75$	36.7
12DCON & 12DCF3	Cylinder 1 Cylinder 2	41.8 41.7	Cube 1 Cube 2 Cube 3 Cube 4 Cube 5 Cube 6	37.8 38.4 38.9 39.6 34.1 37.8	37.8 $\sigma = 1.9$	36.4
12DCF1 & 12DCF2	Cylinder 1 Cylinder 2	24.2 28.2	Cube 1 Cube 2 Cube 3 Cube 4 Cube 5 Cube 6	33.9 29.9 29.2 30.1 31.6 34.8	31.5 $\sigma = 2.30$	35.1
16CON & 16CF3	Cylinder 1 Cylinder 2	44.9 36.8	Cube 1 Cube 2 Cube 3 Cube 4 Cube 5 Cube 6	51.8 50.7 54.2 50.0 51.6 49.9	51.4 $\sigma = 1.60$	33.5
16CF1 & 16CF2	Cylinder 1 Cylinder 2	25.4 36.2	Cube 1 Cube 2 Cube 3 Cube 4 Cube 5 Cube 6	43.2 44.5 36.4* 45.9 46.6 36.6*	42.2 $\sigma = 1.51$	37.6

Note – Values marked * have been discounted due to observed poor compaction of the cube specimens

Table 3.2(b) – Concrete cube strength and elastic modulus for slab tests

Beam Ref.	Cylinder Strength (N/mm²)		Cube Strength (N/mm²)		Average Cube Strength f_{cu} (N/mm²)	Elastic Modulus E_c (kN/mm²)
8SCON	Cylinder 1	40.3	Cube 1 Cube 2 Cube 3	38.2 38.1 38.0	38.1 $\sigma = 0.10$	40.7
8SCF2	Cylinder 1	30.2	Cube 1 Cube 2 Cube 3	43.4 43.4 39.8	42.2 $\sigma = 2.08$	34.0
8SCP2	Cylinder 1	35.7	Cube 1 Cube 2 Cube 3	45.5 45.1 46.0	45.5 $\sigma = 0.45$	33.4
8SCP3	Cylinder 1	29.9	Cube 1 Cube 2 Cube 3	32.6 33.2 28.1	31.3 $\sigma = 2.79$	31.0
12SCON	Cylinder 1	40.3	Cube 1 Cube 2 Cube 3	38.2 38.1 38.0	38.1 $\sigma = 0.10$	40.7
12SCF2	Cylinder 1	30.2	Cube 1 Cube 2 Cube 3	43.4 43.4 39.8	42.2 $\sigma = 2.08$	34.0
12SCF4	Cylinder 1	30.2	Cube 1 Cube 2 Cube 3	43.4 43.4 39.8	42.2 $\sigma = 2.08$	34.0
12SCP2	Cylinder 1	35.7	Cube 1 Cube 2 Cube 3	45.5 45.1 46.0	45.5 $\sigma = 0.45$	33.4
12SCP3	Cylinder 1	29.9	Cube 1 Cube 2 Cube 3	32.6 33.2 28.1	31.3 $\sigma = 2.79$	31.0

Note – Values marked * have been discounted due to observed poor compaction of the cube specimens

Table 3.3 – Mechanical properties of steel reinforcement

Specimen No.	Area (mm²)	Load (kN)		Elongation (mm)		Stress (N/mm²)	
		Yield	Peak	Yield	Failure	Yield	UTS
1	44.8	25.5	28.2	12.5	43.0	567.0	629.5
2	44.8	25.5	28.6	11.5	40.5	567.0	638.4
3	44.8	25.7	28.7	12.5	47.0	573.7	640.6
4	44.8	26.2	29.2	12.5	43.5	584.8	651.8
Average	**44.8**	**25.7**	**28.7**	**12.3**	**43.5**	**573.1**	**640.1**

Figure 3.7 – JJ Model M30-K tensile testing apparatus for steel reinforcement

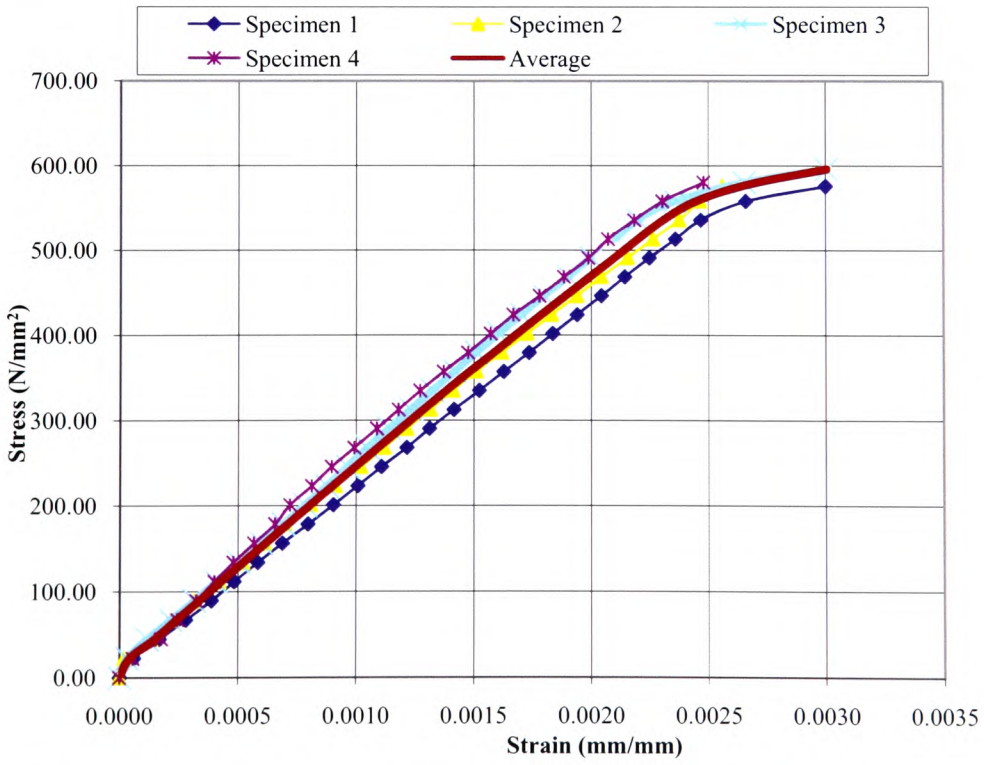

Figure 3.8 – Stress/strain graph for reinforcement specimens, up to yield

3.3.3 Carbon Fibre Reinforced Polymer (CFRP) Composites

Two types of CFRP composites were used. Firstly, the CFRP sheet was Selfix Carbofibe Wrapping System Type C, manufactured by Exchem Mining and Construction. The system is a carbon fibre, uni-directional sheet, specifically designed for structural strengthening.

Tests were carried out to determine the actual strength of the composite material used in the experimental programme. The composite sheet was cut into 250mm lengths, 15mm wide and of a single, 0.145mm thick layer, and laminated in accordance with the manufacturer's specifications using Selfix Carbofibe Laminating Resin. The cured samples were then loaded to failure in a tensile testing apparatus (see Figure 3.9).

The results of the tests are presented in Table 3.4 and the actual failed specimens are shown in Figure 3.10.

Secondly, Selfix Carbofibe Pultruded CFRP Plates were used. The plate cross-sectional dimensions were 120mm x 1.4mm. The system is a uni-directional, carbon fibre laminate with a minimum fibre content of 68%, and, as with the CFRP sheets, is specifically designed for strengthening of structural members by providing resistance against tensile forces.

Table 3.4 – Tensile test results for laminated CFRP sheet specimens

Specimen No.	**Failure Load (kN)**	**Tensile strength (N/mm^2)**	**Elastic modulus 'E' (kN/mm^2)**	**Ultimate strain ε_{ult} (%)**
1	4.4	1956	239.6	0.8
2	4.3	1911	217.0	0.9
3	4.3	1911	220.5	0.9
4	4.1	1822	212.7	0.9
Average	**4.3**	**1900**	**222.5**	**0.9**

Again, tests were carried out in the Structural Laboratory of the University of Glamorgan, to determine the actual strength value of the composite material used in the

experimental programme. Three samples, 250mm long and 15mm wide, were cut from the plate and then loaded to failure in an Instron 8502 tensile testing apparatus (Figure 3.9).

The results of the tests are presented in Table 3.5 and the actual failed specimens can be seen in Figure 3.11.

Figure 3.9 – Instron 8502 CFRP tensile test apparatus

Table 3.5 – Tensile test results for CFRP plate specimens

Specimen No.	Failure Load (kN)	Tensile strength (N/mm^2)	Elastic modulus 'E' (kN/mm^2)	Ultimate strain ε_{ult} (%)
1	40.8	1905	178.3	1.1
2	37.5	1787	174.1	1.0
3	42.9	2042	174.3	1.2
Average	**40.4**	**1911**	**175.6**	**1.1**

Figure 3.10 – Tested CFRP sheet specimens

Figure 3.11 – Tested CFRP plate specimens

3.3.4 Adhesive systems

(a) CFRP sheet primer and adhesive

The primer and adhesive used for bonding of the CRFP sheets were Selfix Carbofibe Primer and Selfix Carbofibe Laminating Resin respectively.

The primer is a solvent-free, two-part epoxy material, developed in conjunction with the laminating resin and CFRP sheet. The two-part system comprises a resin component and a hardener component, mixed in a ratio of 100:47 respectively. Once mixed, the material has a recommended pot-life of 60 minutes, although experience suggests that no more than can be used in a 20 minute period be mixed at any one time.

The laminating resin consists of a liquid epoxy resin and liquid hardener and has been formulated as a solvent-free, thixotropic to promote ease of mixing and maximum fibre impregnation. As with the primer, the system is two-part, with the resin:hardener mix ratio being 100:45. The recommended pot-life for the laminating resin is 20 minutes and use during experiments has shown this to be reasonable.

It is recommended by the manufacturer that, although the system would harden after an overnight cure, it is preferable to allow the adhesive to cure for several days (at 20 to 25°C), in order that adequate mechanical properties can develop. In this experimental programme, all samples were allowed to cure for a minimum of seven days at an ambient temperature of approximately 20° to 22° C.

(b) CFRP plate adhesive

The adhesive used for bonding of the CRFP plates was Resifix 31. The system is a two-part, thixotropic epoxy adhesive, formulated specifically for plate bonding in accordance with Advice Note BA 30/94. As with the sheet adhesive, the system is two-part, with the resin:hardener mix ratio being 1:1. The manufacturer's recommendations state a pot-life of 20 minutes, however, experience in the use of the material indicates that this is an absolute maximum and it is suggested that between 10 and 15 minutes would be a more appropriate time.

It is recommended by the manufacturer that, as with the sheet adhesive, although the system would harden after an overnight cure, it is preferable to allow the system to cure for several days (at 20 to 25°C), in order that the system can develop adequate mechanical properties. In this experimental programme, all samples were allowed to

cure for a minimum of seven days at an ambient temperature of approximately 20° to 22° C.

3.4 Instrumentation

A comprehensive instrumentation set-up was used during the experimental programme to monitor performance in various ways:

- Vertical deflection
- Concrete surface strains (using the DEMEC system)
- Fibre surface strains (using electronic strain gauges)
- Concrete compressive strain at mid-span (using electronic strain gauges)
- Crack development

3.4.1 Vertical deflection

Vertical deflections were recorded using Linear Variable Displacement Transducers (LVDT). The layout of the LVDTs is shown in Figures 3.12 and 3.13, for the beams and slabs respectively.

3.4.2 Concrete surface strains

Concrete surface strains were measured using the DEMEC (DEmountable MEChanical strain gauge) system; three columns of six rows of discs were mounted on each face of the beam, located centrally, with an initial spacing of 200mm as shown in Figure 3.14. A digital DEMEC gauge reader was used and the information downloaded and recorded directly into a laptop computer. The gauge constant was 0.403×10^{-6}.

For the slabs, three columns of four rows were mounted on each face, with an initial spacing of 200mm, as detailed in Figure 3.15.

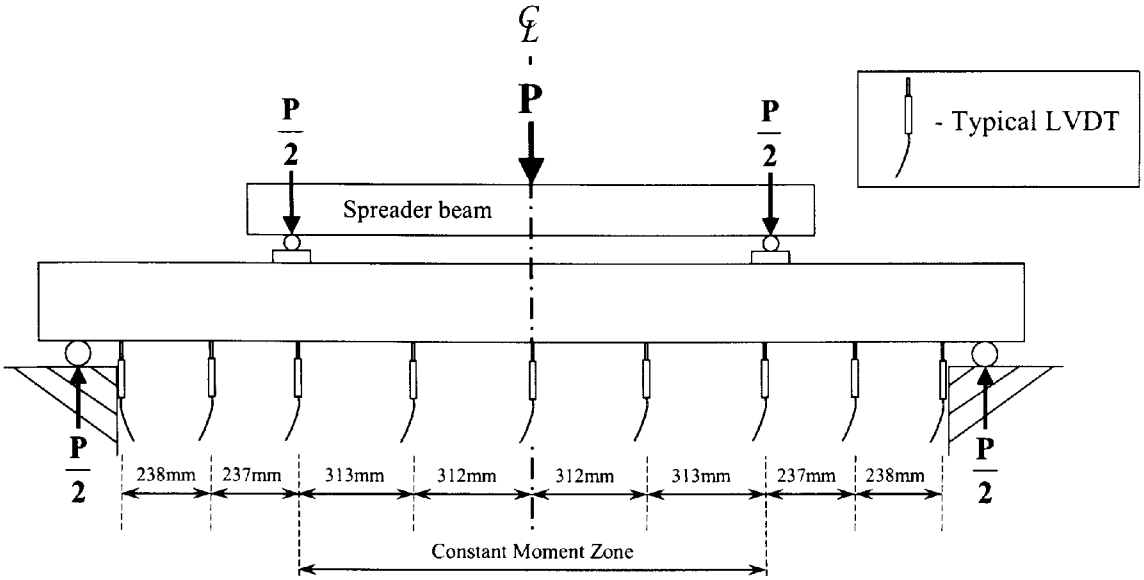

Note: Two LVDTs were placed at mid-span,

Figure 3.12 – Layout of Linear Variable Displacement Transducers (LVDTs) for beams

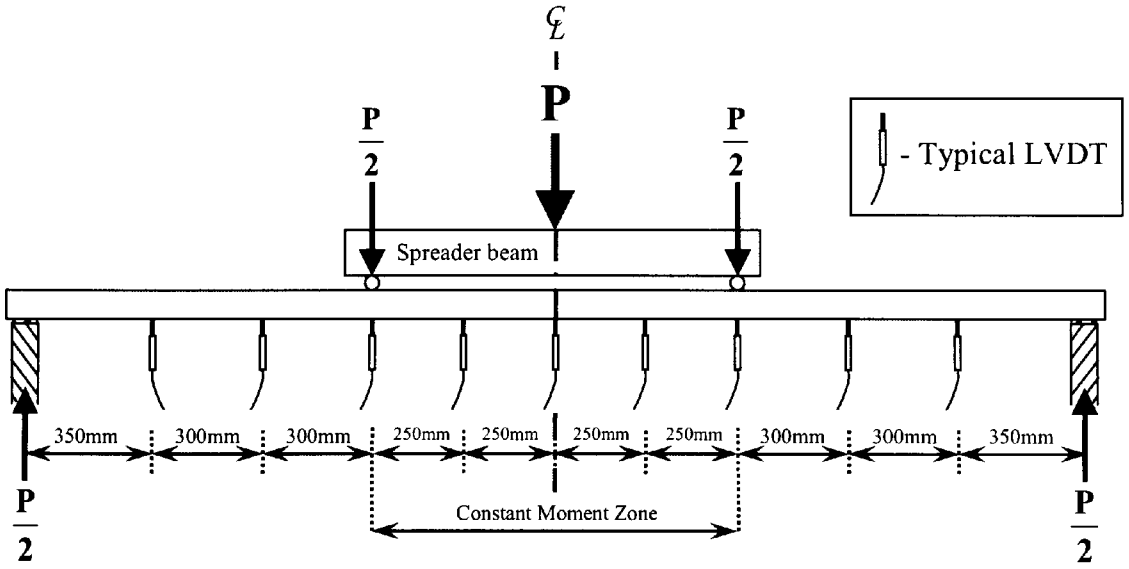

Note: Two LVDTs were placed at mid-span,

Figure 3.13 – Layout of Linear Variable Displacement Transducers (LVDTs) for slabs

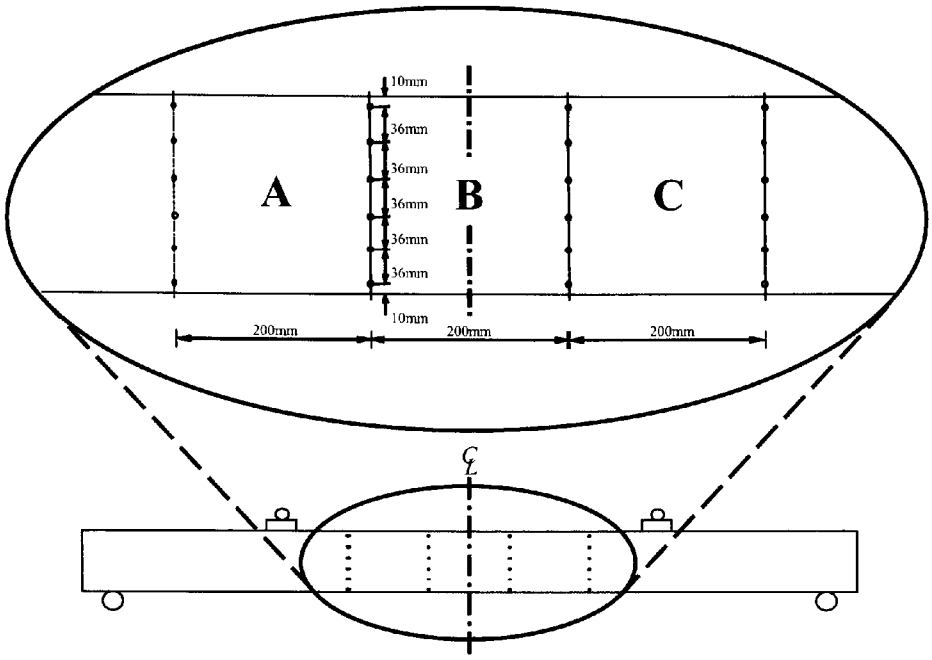

Note: Measurement zones on reverse side of beam were labelled A', B' and C', corresponding to A, B, and C.

Figure 3.14 – Layout of DEMEC strain gauges for beams (with magnified view showing measurements)

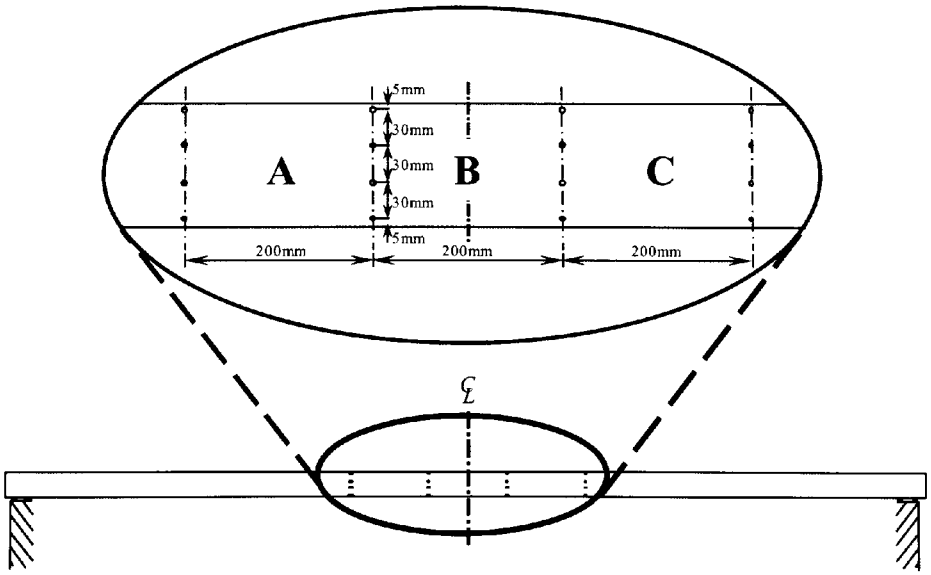

Note: Measurement zones on reverse side of slab were labelled A', B' and C', corresponding to A, B, and C.

Figure 3.15 – Layout of DEMEC strain gauges for slabs (with magnified view showing measurements)

3.5 Strengthening procedure

3.5.1 Beam strengthening

The beams to be strengthened were placed upside-down in order to facilitate easier placing of the CFRP sheets, and the surface was brushed with a mechanical wire brush to expose the aggregate and provide a sound bonding surface. The beam was then cleaned of debris and dust using an industrial vacuum-cleaner before the primer was applied. The primed beams were allowed to cure overnight, although it is important to laminate within 24 hours, in accordance with the manufacturers specifications, to negate the need for further preparation.

The CFRP sheets were then cut to length and width (1100mm long x 100 mm wide) and the laminating adhesive was mixed, by hand, and applied to the beam surface. The procedure for applying layers of CFRP sheets is as follows:

i. Apply laminating adhesive to beam surface
ii. Place CFRP sheet on beam surface
iii. Apply laminating resin to CFRP sheet
iv. Lift CFRP sheet off beam, turn through 180° and replace
v. Apply laminating resin to second side of CFRP sheet
vi. Repeat steps (ii) to (v) for further layers

Table 3.1 details the number of layers bonded to each beam. If applying two or three layers, when turning the sheets to apply adhesive to the second side it is essential to ensure that the previous sheet does not lift off, causing voids to occur, as this could significantly affect the performance of the system.

After no fewer than six days, when the adhesive was judged to have cured sufficiently, linear electronic strain gauges were applied to the surface of the CFRP, in the configuration shown in Figure 3.16, which also illustrates the length of the CFRP sheet.

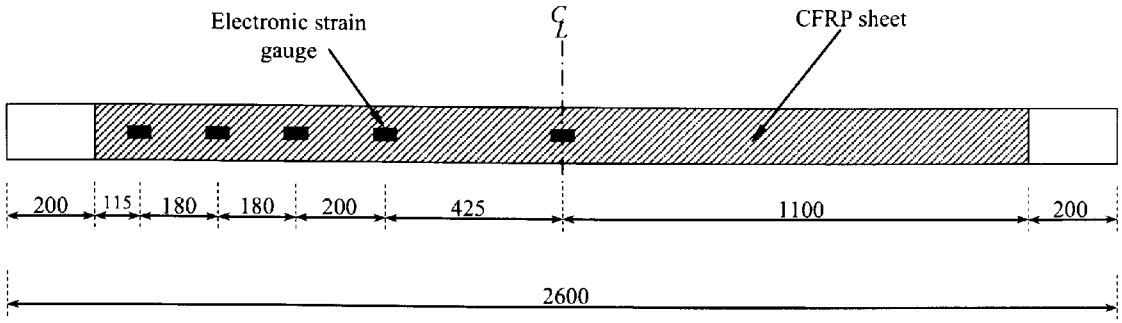

Figure 3.16 – Soffit view of strengthened beam showing CFRP layout and positions of linear electronic strain gauges (all dimensions in mm)

3.5.2 Slab strengthening

As with the beams, the slabs to be strengthened were placed upside-down in order to facilitate easier placement of the CFRP sheets and plates. The slab surface was roughened with a wire brush and was then cleaned of debris and dust using an industrial vacuum-cleaner.

The CFRP sheets or plates were then cut to length (2700mm). As the CFRP sheet was supplied in a roll 300mm wide, for each layer a full width length was cut together with a 200mm wide length to provide enough material to cover the slab surface of 500mm.

For the sheets, the laminating adhesive was then mixed, by hand, and applied to the slab surface. The procedure for applying layers of CFRP sheets is as detailed for the beams in Section 3.5.1.

For the plates, the adhesive was mixed, using a mechanical mixer, applied to the slab surface to a thickness of approximately 1mm and also to the surface of the plate, to a similar thickness. This ensured that when the plate was adhered to the slab, there would be an adhesive thickness of 2mm, in line with the manufacturer's guidelines and also this method aids in the prevention of trapped air voids being formed between the plate and concrete.

After no fewer than six days, when the adhesive had cured sufficiently, linear electronic strain gauges were applied to the surface of the CFRP sheets and plates, in the configuration shown in Figure 3.17.

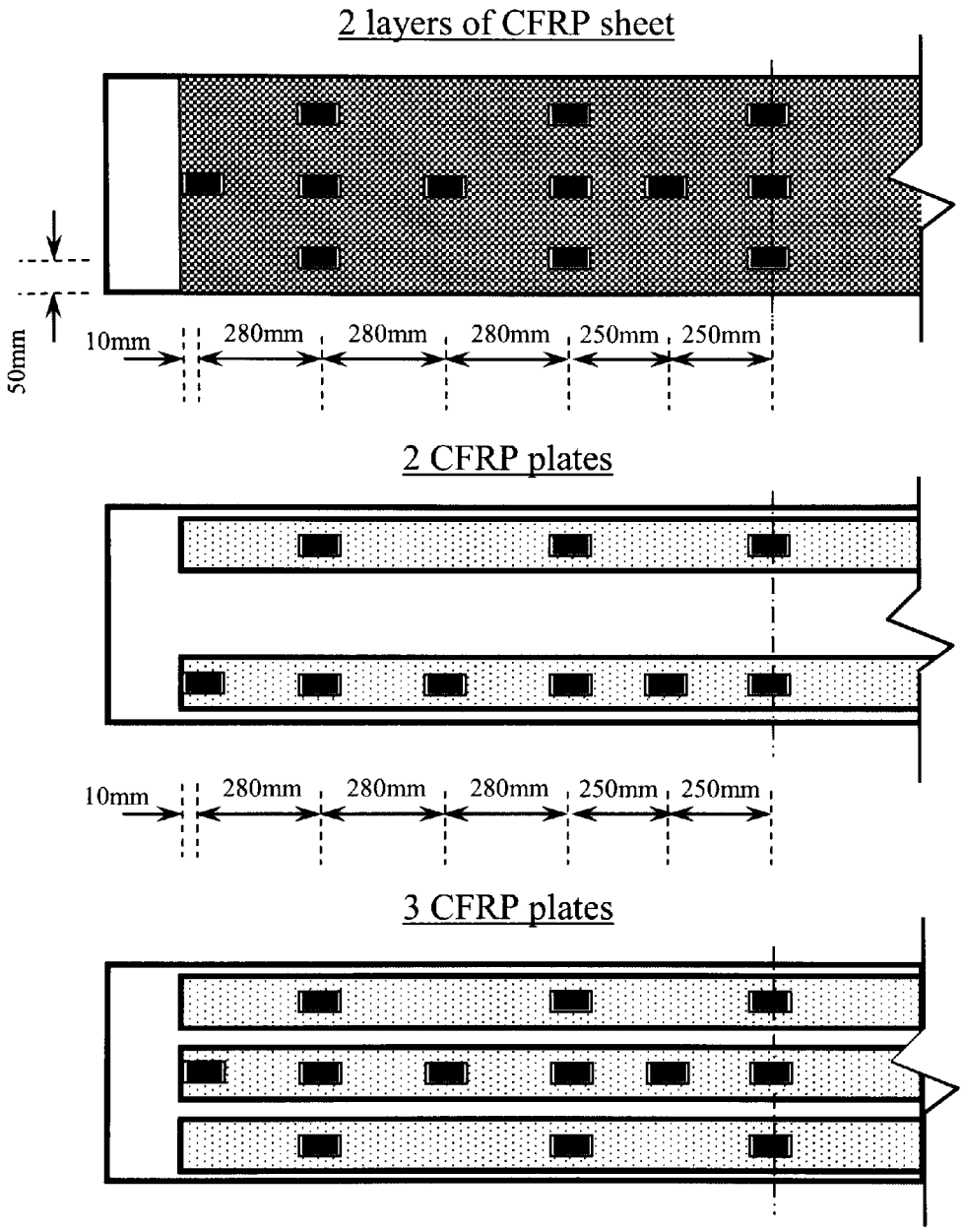

Note: All gauges on plates were located along the centreline of the plate.

Gauges on sheets were located along the centreline of the slab and along a line 50mm in from the edge.

Figure 3.17 – Soffit view of strengthened slabs showing positions of linear electronic strain gauges

3.6 Testing of elements

All tests were carried out under load-controlled conditions for two reasons; firstly, the loading apparatus used is calibrated for load but not deflection and secondly, because the aim of the research is to provide designers with guidance on the ductility and deformability of strengthened elements and, accordingly, post-peak behaviour is not as important as the element behaviour under realistic loading conditions. Consequently, any post-peak behaviour was not available. Additionally, all tests were carried out with simple support conditions; this was in order that a definitive method could be determined for the calculation of ductility indices before more complex structures, such as continuous elements, could be analysed. The testing apparatus for beams and slabs can be seen in Figures 3.18 and 3.19 respectively.

The loading increments for the tests were as follows:

- 0 to 10kN — Increments of 1kN in order that strains and deflections could be recorded accurately in the purely elastic stage
- 10 to 20kN — Increments of 2.5kN
- 20kN to failure — Increments of 5kN

However, for the control slab, 8SCON, which was expected to fail at a load of around 15 to 20kN, load increments of 1kN were used up to failure.

Additionally, if sufficient warning was given of impending failure, i.e. excessive strain readings or cracking, continuing deflection after attainment of loading step, etc., the load increments were reduced, sometimes to 1kN, in order that the element behaviour at the final stages of loading approaching failure could be recorded.

Also, for the beams, unloading curves were obtained at 20kN and 50kN for all beams, with additional unloading curves obtained as the element approached failure. This information is expected to be invaluable when, at a later stage of the research, a method of approximation of stored elastic energy at failure is intended to be developed.

At every load increment, the DEMEC readings were recorded, together with strain readings from the electronic gauges, and the beam was checked for cracking. Any visible cracks were highlighted with coloured markers, which made it easier, post-testing, to make a log of the crack numbers and lengths to enable an understanding of the development of cracking within any particular element. In Figure 3.19 is a picture of a typical section of marked cracks on a tested beam.

Figure 3.18 – Loading set-up for testing of beam specimens

Figure 3.19 – Loading set-up for testing of slab specimens

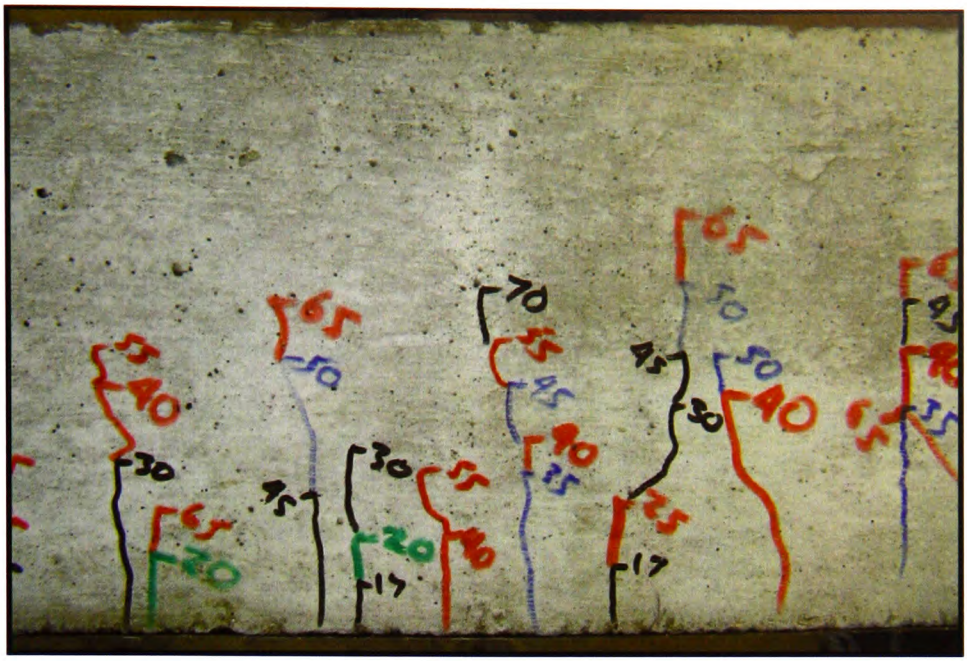

Figure 3.20 – Sample photograph of crack marking with coloured markers during testing

3.7 Failure Modes

3.7.1 Beam Failure Modes

A summary of the beam test results, which includes the failure mode, is presented in Table 3.6.

3.7.1.1 Ø 8mm reinforced beams

3.7.1.1.1 8CON

It can be seen in Figure 3.21 that the control beam, 8CON, failed as expected for a non-strengthened, under-reinforced element; i.e. yielding of the internal reinforcing steel followed by crushing of the concrete in the compression zone, in a relatively mild manner at a load of 35.1 kN, with adequate warning via the element deflection that was being monitored during the experiment.

3.7.1.1.2 8CF1

Element 8CF1 failed in a similar manner to the control beam (Figure 3.22), with a gradual but increasing displacement followed by a yielding of the internal steel reinforcement and a partial rupture of the CFRP (approximately 5% of the fibre width). Just prior to failure, which occurred at 58.0kN, the element emitted sounds that indicated the rupture of individual fibres (or small groups of fibres) was taking place.

Table - 3.6 Summary of beam and slab test results

Element ref.	Ultimate Load (kN)	Ultimate Moment (kNm)	Ultimate Deflection (mm)	Failure Mode
8CON	35.1	20.2	22.1	SY-CC
8CF1	58.0	33.4	29.8	FR
8CF2	62.5	35.9	31.4	DB-PTO
8CF3	55.0	31.6	16.5	PTO
10CON	56.5	16.3	30.0	SY-CC
10CF1	62.6	18.0	26.5	FR
10CF2	80.1	23.1	33.8	DB-PTO
10CF3	70.0	20.2	17.7	PTO
12CON	65.0	18.7	20.0	CC
12CF1	78.2	22.5	24.0	CC
12CF2	85.0	24.2	21.8	CC
12CF3	84.1	24.4	24.5	CC
16CON	98.0	28.2	22.7	CC
16CF1	96.0	27.6	20.7	ECC
16CF2	90.0	25.9	20.4	ECC
16CF3	101.2	29.1	24.9	CC
12DCON	70.0	20.1	33.4	SY-CC
12DCF1	90.0	23.6	38.5	DB-PTO
12DCF2	95.0	27.3	27.7	PTO
12DCF3	92.0	26.5	20.6	PTO
8SCON	17.1	8.1	51.0	SY-CC
8SCF2	55.0	26.1	69.0	FR-PTO
8SCP2	65.0	30.9	55.7	PPD
8SCP3	60.0	28.5	44.8	PPD
12SCON	32.0	15.2	53.0	SY-CC
12SCF2	68.0	32.3	93.5	FR
12SCF4	77.0	36.6	65.6	CC
12SCP2	75.0	35.6	54.6	PPD
12SCP3	92.5	44.0	66.7	PPD

Note: CC=Concrete crushing; SY-CC=Steel yield followed by concrete crushing; FR=Fibre rupture; DB=De-bonding of CFRP; PTO=Premature tearing-off of concrete cover; ECC=Explosive concrete crushing; PPD=Premature plate de-bonding.

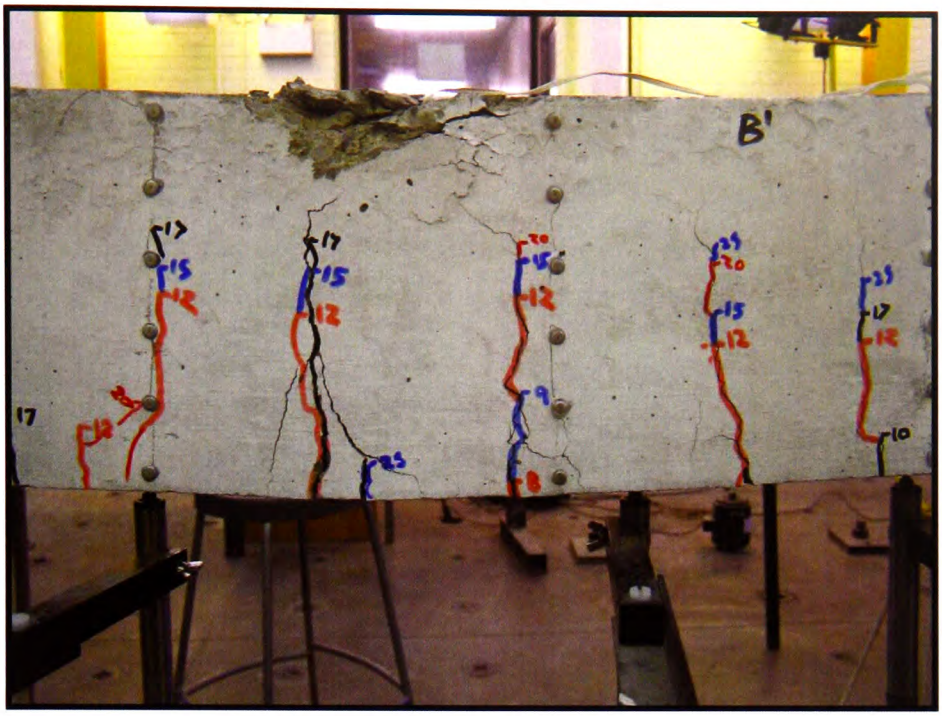

Figure 3.21 - Photograph of 8CON after failure

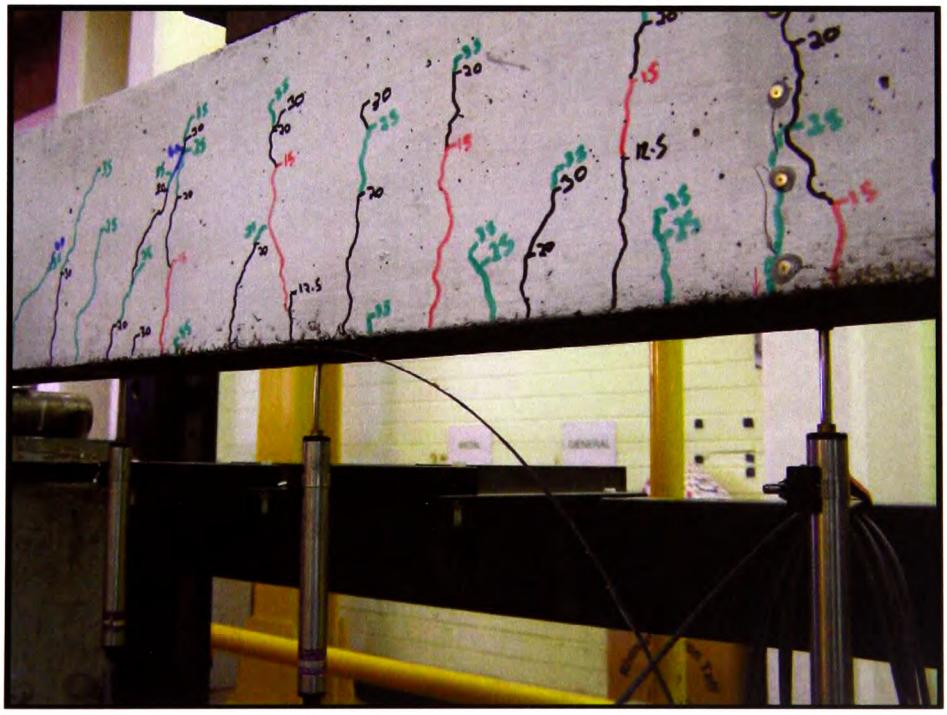

Figure 3.22 - Photograph of 8CF1 after failure

3.7.1.1.3 8CF2

As can be seen in Figure 3.23, beam 8CF2 failed due to debonding of the CFRP along half of the bonded length and a partial tearing-off of concrete cover where the debonding ended, at an ultimate load of 62.5 kN. The failure occurred with little obvious sign of impending collapse before the element failure took place.

3.7.1.1.4 8CF3

Beam 8CF3 failed at a load of 55.0 kN, due to partial debonding at the end of the CFRP, with a horizontal shear crack, originating close to the end of the FRP sheet, causing the initiation of a tearing-off of the concrete cover (Figure 3.24). The failure happened suddenly and without warning.

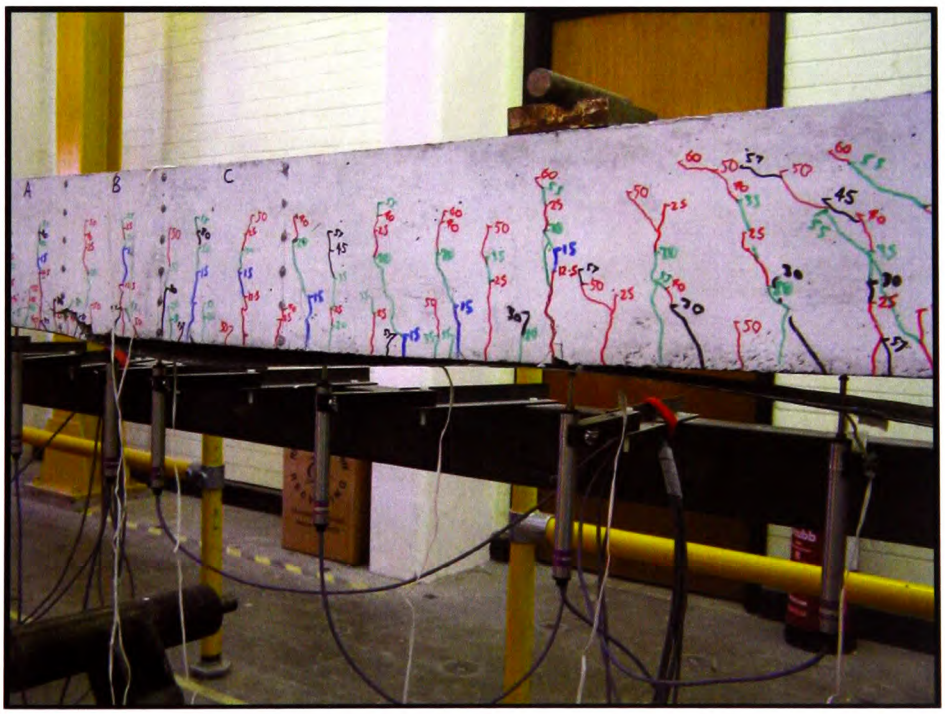

Figure 3.23 - Photograph of 8CF2 after failure

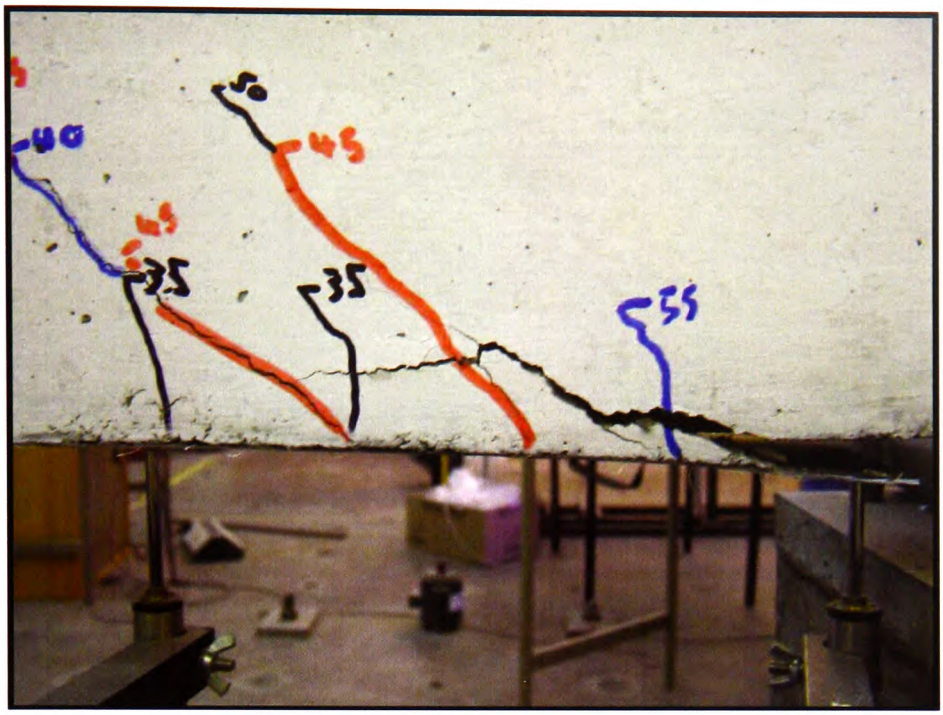

Figure 3.24 - Photograph of 8CF3 after failure

3.7.1.2 Ø 10mm reinforced beams

3.7.1.2.1 10CON

It can be seen in Figure 3.25 that the control beam, 10CON, failed normally at a load of 56.5 kN, as expected for an under-reinforced, un-strengthened element; i.e. a 'mild' failure with yielding of the internal reinforcing steel followed by crushing of the concrete in the compression zone, and adequate warning of impending collapse.

3.7.1.2.2 10CF1

The beam strengthened with one layer of CFRP sheet, 10CF1, failed in a similar manner to the control beam, 10CON, with yielding of the internal reinforcement followed by rupture of the CFRP and a little crushing of the concrete in the compressive zone (Figure 3.26(a)), at an ultimate load of 62.6 kN.

The failure was fairly mild, with the fibre rupture initially only occurring near mid-span, over about 15-20% of the fibre width, as can be seen in Figure 3.26(b), when the

loading apparatus 'trip-mechanism' was activated. The beam was reloaded but failed at 60kN, due to the reduced fibre section.

Figure 3.25 - Photograph of 10CON after failure
(Concrete crushing occurred just to the right of mid-span, circled)

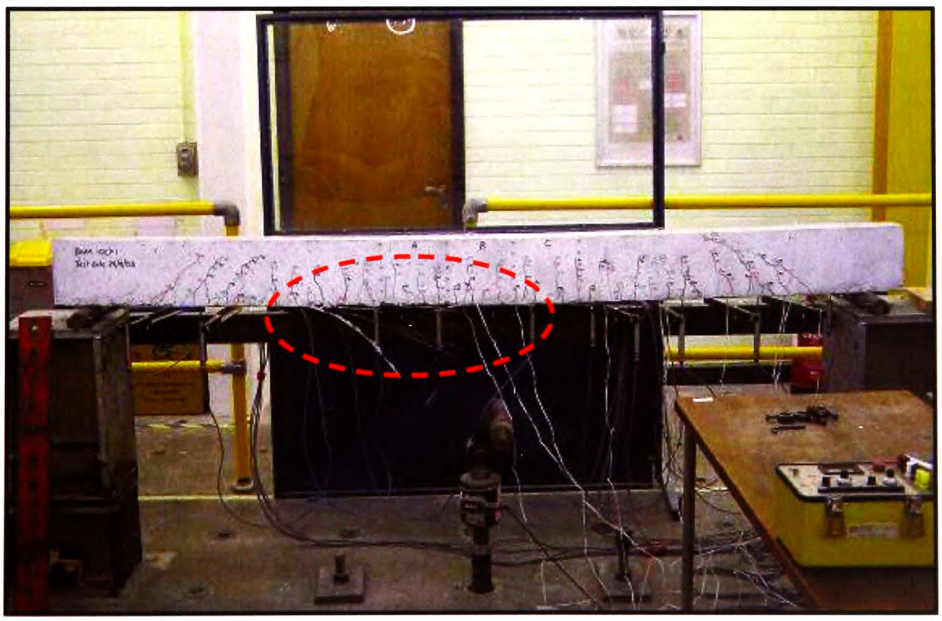

Figure 3.26(a) - Photograph of 10CF1 after failure
(Note the rupture CFRP hanging down near mid-span, circled)

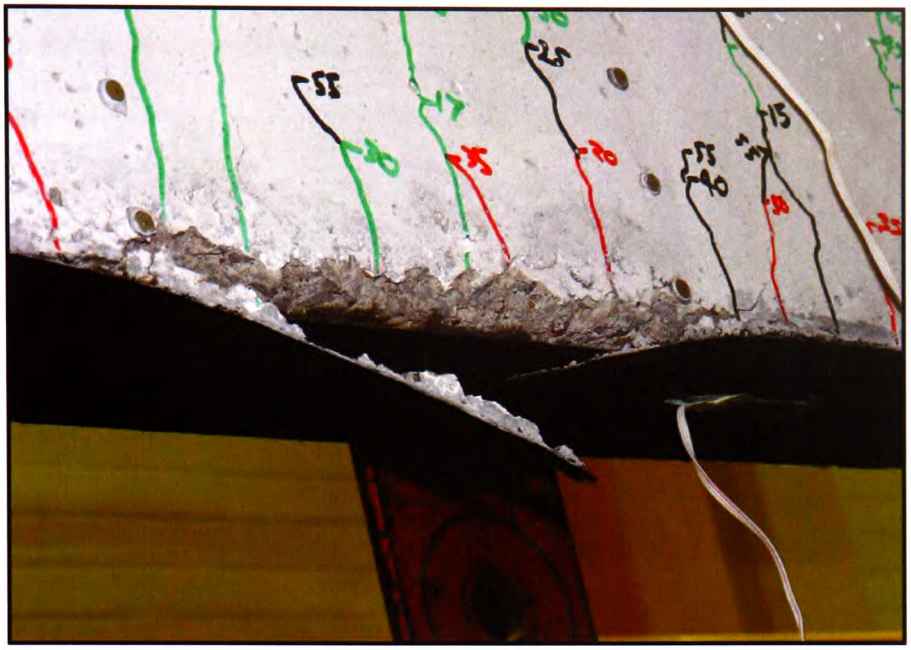

Figure 3.26(b) - Photograph of 10CF1 after initial failure, with 15 to 20% CFRP rupture

3.7.1.2.3 10CF2

10CF2, the beam strengthened with 2 layers of CFRP sheet, produced the highest gain in load-carrying capacity out of all those tested, failing at a load of 80.1 kN. However, the mode of failure was sudden, with partial de-bonding of the CFRP sheet and some tearing-off of concrete cover, illustrated in Figure 3.27. The only indication of imminent failure was a significant increase in the surface strains at 70kN. At 75kN, the beam started to emit sounds that suggested the rupture of individual (or small groups of) fibres or de-bonding of the CFRP. No further surface strains were taken but the deflections were consequently recorded every 1kN to failure. The load-deflection plot (which will be detailed in Chapter 4) showed no noticeable escalation in the rate of deflection under additional load.

3.7.1.2.4 10CF3

10CF3, the three-layer strengthened beam, failed at 70.0 kN. The failure was sudden, with no noticeable acceleration in the increasing strains or deflections. The element

failed with premature tearing-off of concrete cover, as can be seen in Figure 3.28. The tearing-off failure mode is discussed in more detail in 4.10.

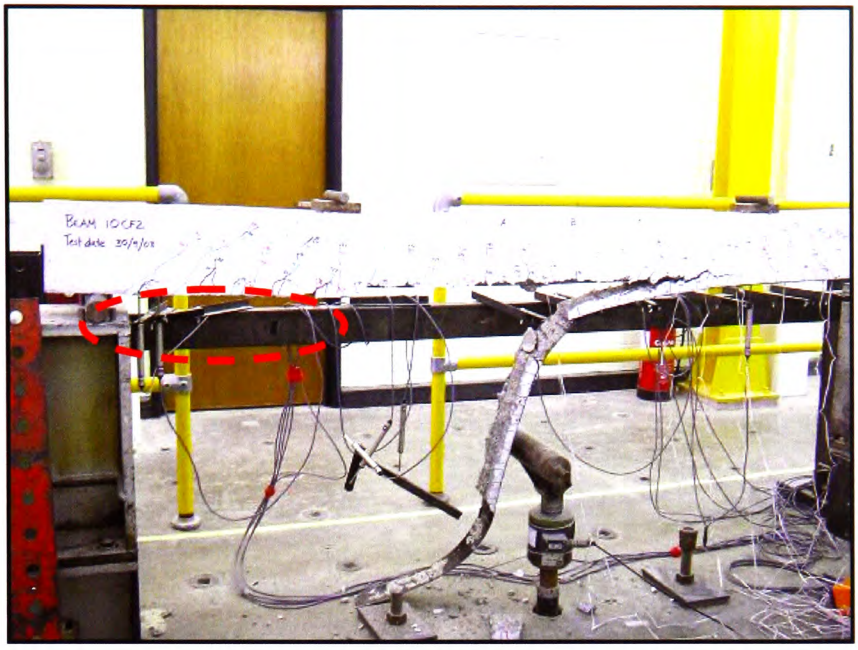

Figure 3.27 - Photograph of 10CF2 after failure
(Note the de-bonding of the first approximately 400mm of the CFRP sheet, circled on the beam, and the tearing-off of the concrete cover beyond mid-span)

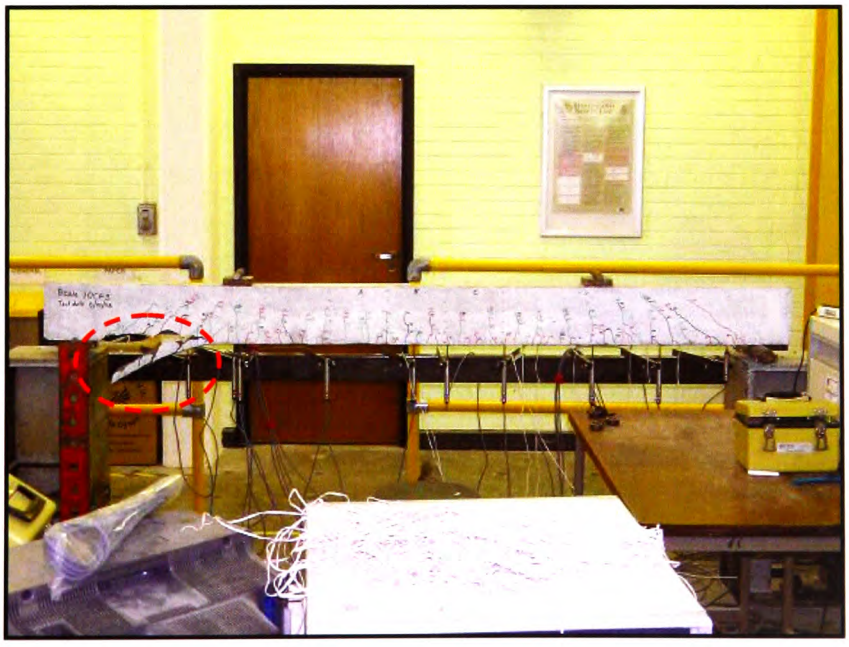

Figure 3.28 - Photograph of 10CF3 after failure
(Note the tearing-off of the concrete cover along the first approximately 350mm of the CFRP sheet, circled)

3.7.1.3 Ø 12mm reinforced beams

3.7.1.3.1 12CON

It can be seen in Figure 3.29 that 12CON, failed due to concrete crushing in the compression zone, which resulted in yielding of the internal steel reinforcement. Failure occurred at a load of 65.0 kN. The failure was mild and there was adequate warning of impending failure.

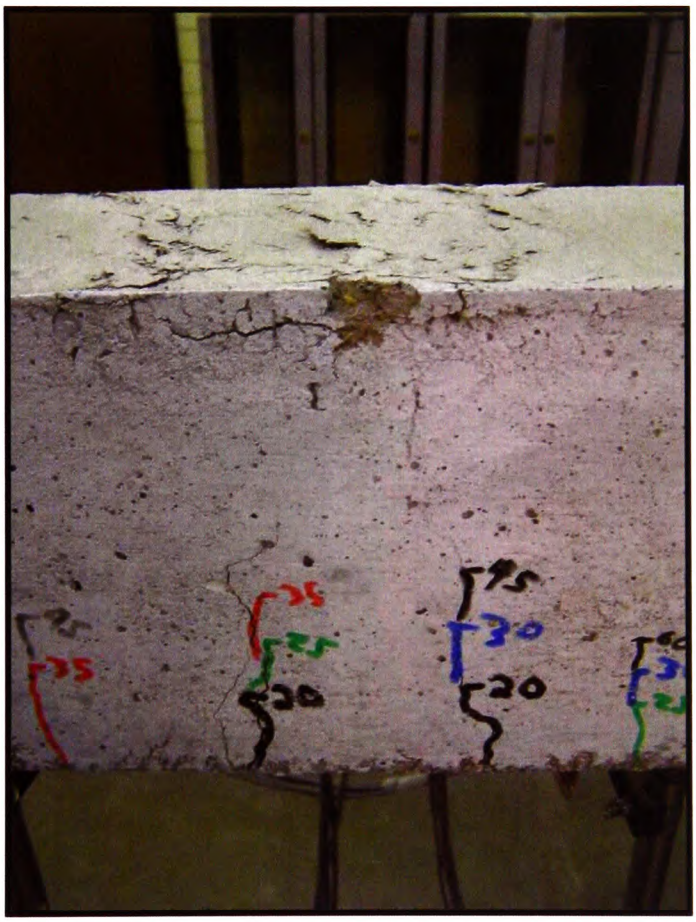

Figure 3.29 - Photograph of 12CON after failure

3.7.1.3.2 12CF1

Element 12CF1 failed at an ultimate load of 78.2 kN, due to compression of the concrete in the compression zone, which resulted in yielding of the internal steel

reinforcement, as can be seen in Figure 3.30. The failure was not as mild as for the unstrengthened element but could not be described as "sudden".

Figure 3.30 - Photograph of 12CF1 after compressive failure of the concrete

3.7.1.3.3 12CF2

Figure 3.31 illustrates the failure of element 12CF2, at a load of 85.0 kN, which was due to concrete crushing in the compression zone, followed by yielding of the internal steel reinforcement. The failure was more sudden than that for 12CF1, which is as to be expected for a higher-strengthened element.

3.7.1.3.4 12CF3

As with element 12CF2, failure of 12CF3 was caused by crushing of the concrete in the compressive zone (as can be seen in Figure 3.32) and then yielding of the internal steel reinforcement, at an ultimate load of 84.1 kN. The failure was relatively sudden and without warning.

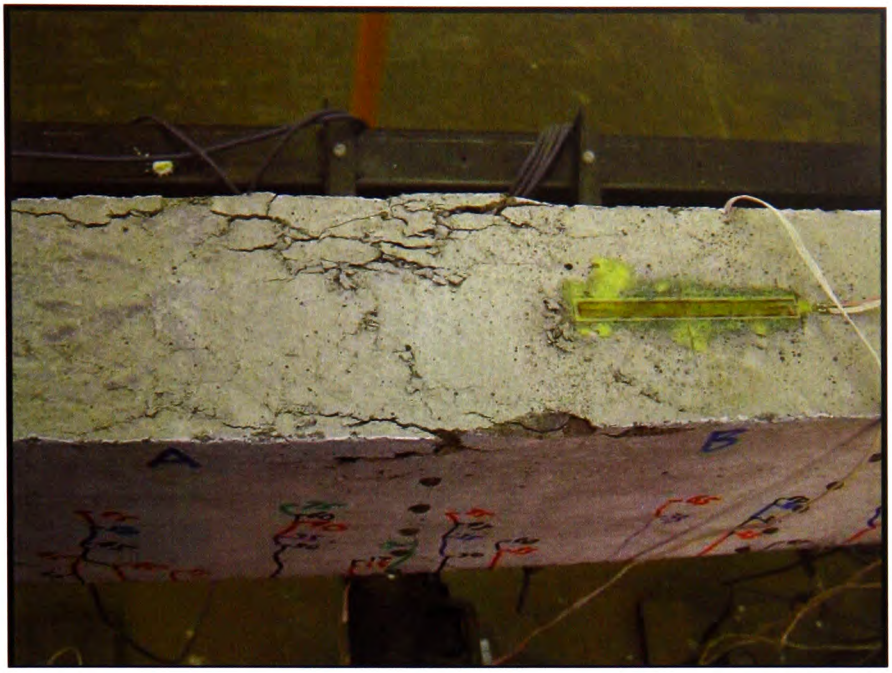

Figure 3.31 – Photograph of compressive concrete failure of 12CF2

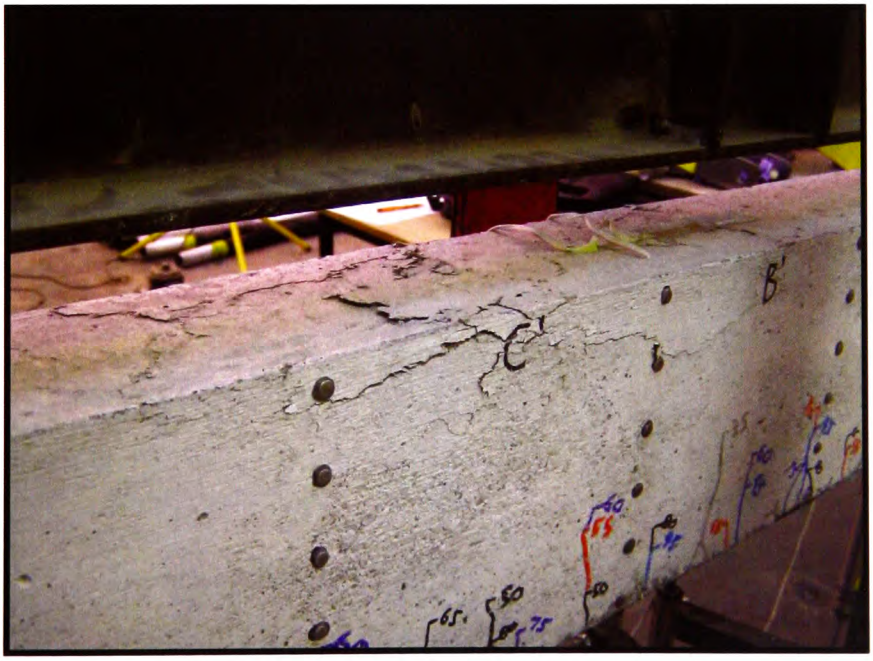

Figure 3.32 – Photograph of compressive concrete failure of 12CF3

3.7.1.4 Ø 16mm reinforced beams

3.7.1.4.1 16CON

The control beam, 16CON, failed due to a crushing failure of the concrete in the compressive zone near mid-span, as can be seen in Figure 3.33, at an ultimate load of 98.0 kN.

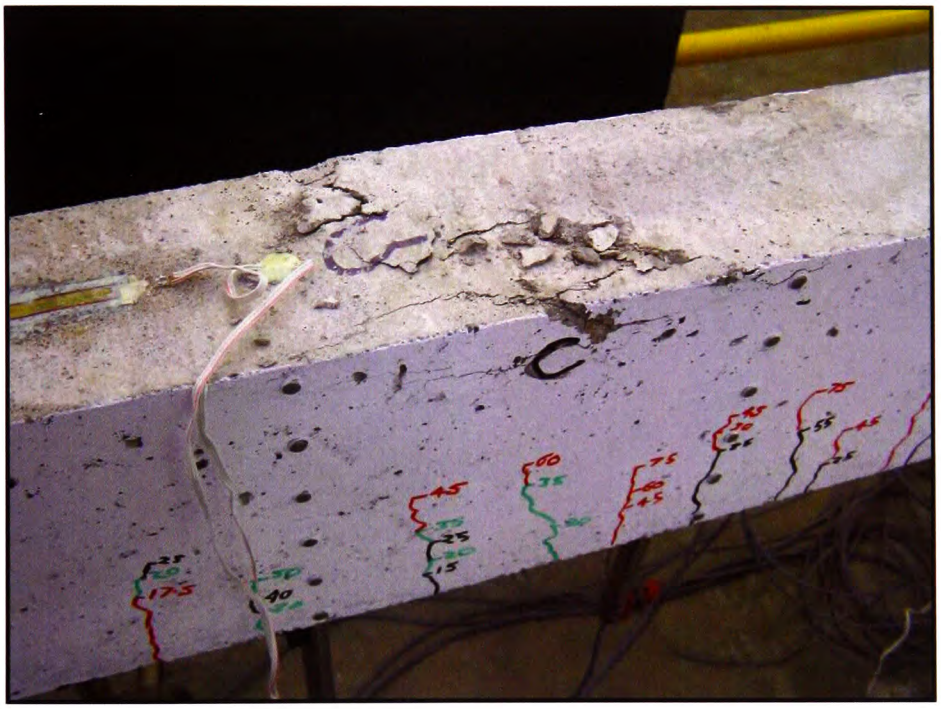

Figure 3.33 – Photograph of compressive concrete failure of 16CON

3.7.1.4.2 16CF1

As can be seen in Figure 3.34, the beam strengthened with 1-layer of CFRP sheet failed with a sudden crushing failure of the concrete in the compressive zone. The maximum load was 96.0 kN. The CFRP fabric remained intact and there was no indication that the element was about to fail; i.e. neither a sudden acceleration in the vertical deflection nor excessive cracking.

3.7.1.4.3 16CF2

The 2-layer beam also failed with a crushing failure of the concrete in the compressive zone, seen in Figure 3.35, at an ultimate load of 90.0 kN. Again the CFRP fabric remained intact and there was no indication that the element was about to fail from vertical deflection readings or excessive cracking.

Figure 3.34 – Photograph of concrete crushing failure of 16CF1

Figure 3.35 – Photograph of concrete crushing failure of 16CF2

3.7.1.4.4 16CF3

As with the previous 16mm strengthened elements, the 3-layer beam failed with a crushing failure of the concrete in the compressive zone; the ultimate load was 101.2kN. However, the failure was not as explosive and comprised a horizontal crushing/shear-failure near the top of the beam along the whole length between the loading points. Figure 3.36 shows a section of the failure near one of the loading points. Again the CFRP fabric remained intact and there was no indication that the element was about to fail from vertical deflection readings or excessive cracking.

The most probable reason for the 'milder' failure mode for this and the unstrengthened element, 16CON, is the higher concrete strength; 51.4 N/mm^2 for 16CON and 16CF3 compared with 42.2 N/mm^2 for 16CF1 and 16CF2.

Figure 3.36 – Photograph of horizontal crushing/shear failure of 16CF3 near loading point

3.7.1.5 Ø 12mm doubly-reinforced beams

3.7.1.5.1 12DCON

The control beam, 12DCON, for the elements internally reinforced with two 12mm diameter, high-yield bars in both tension and compression, failed at a load of 70.0 kN, due to crushing of the concrete in the compression zone together with yielding of the internal tension steel reinforcement. The failure type was mild and gradual and is illustrated in Figure 3.37.

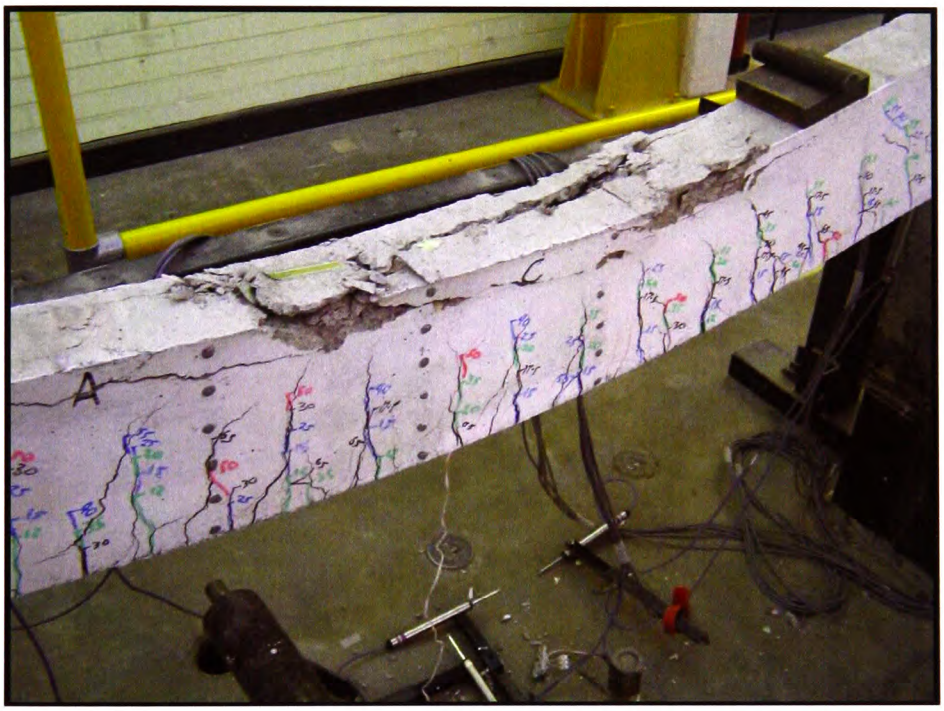

Figure 3.37 – Photograph of compressive concrete failure of 12DCON

3.7.1.5.2 12DCF1

Element 12DCF1, the beam strengthened with one layer of externally-bonded CFRP sheet failed, at a load of 90.0 kN, due to debonding of the CFRP sheet, together with some areas of partial tearing-off of concrete cover, as illustrated in Figure 3.38. The failure occurred quite suddenly and without a great deal of warning.

Figure 3.38 – Photograph of debonding and partial tearing-off of concrete cover failure of 12DCF1

3.7.1.5.3 12DCF2

Element 12DCF2, the beam strengthened with two layers of externally-bonded CFRP sheet, failed at an ultimate load of 95.0 kN, due to partial debonding of the CFRP sheet, which developed into a tearing-off of the concrete cover at a location approximately halfway between the support and the loading point, as can be seen in Figure 3.39.

Again, the failure occurred suddenly and there was no warning of impending failure from the deflections of cracking patterns.

3.7.1.5.4 12DCF3

The beam strengthened with three layers of CFRP sheet, 12DCF3, failed due to tearing-off of the concrete cover at one end of the bonded sheet. The tearing-off failure initiated at the end of the sheet, along a shear crack that had become visible at the surface at a load of 70kN, and then propagated horizontally at the level of the internal tension steel reinforcement, as can be seen in Figure 3.40.

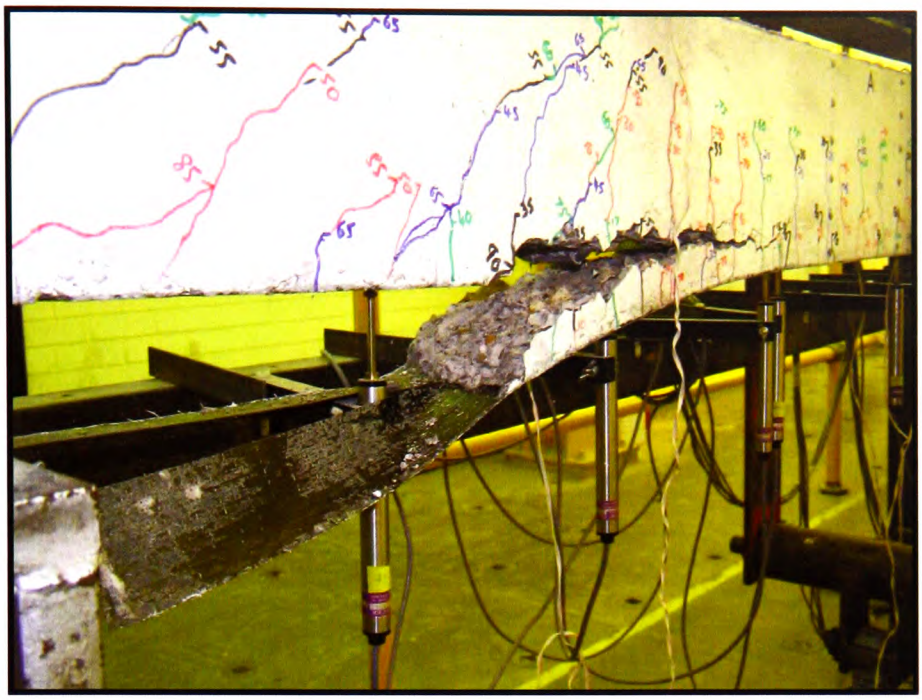

Figure 3.39 – Photograph of failure of 12DCF2 due to debonding of the CFRP sheet and tearing-off of the concrete cover

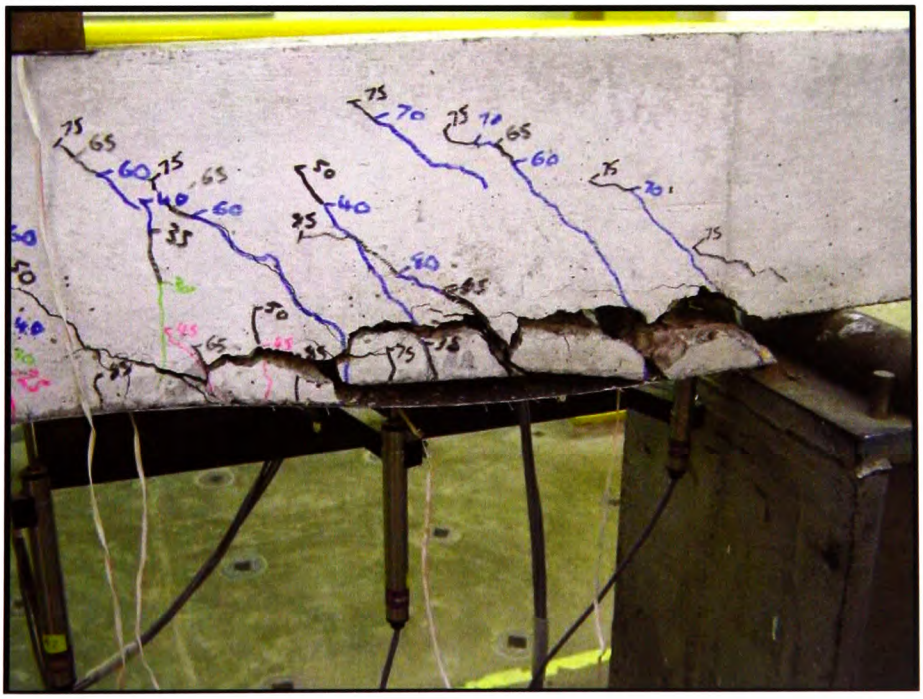

Figure 3.40 – Photograph of failure of 12DCF3 due to tearing-off of the concrete cover

3.7.2 Slab Failure Modes

A summary of the slab test results, which includes the failure mode, is presented in Table 3.6.

3.7.2.1 Ø 8mm reinforced slabs

3.7.2.1.1 8SCON

The failure mode for the control slab was as expected for a normally reinforced, un-strengthened section; i.e. the element failed with yielding of the internal steel reinforcement, followed by the formation of a large crack at the tension face and concrete crushing at the top of the slab. The failure occurred at a load of 16.0 kN. The failure can be seen in Figure 3.41.

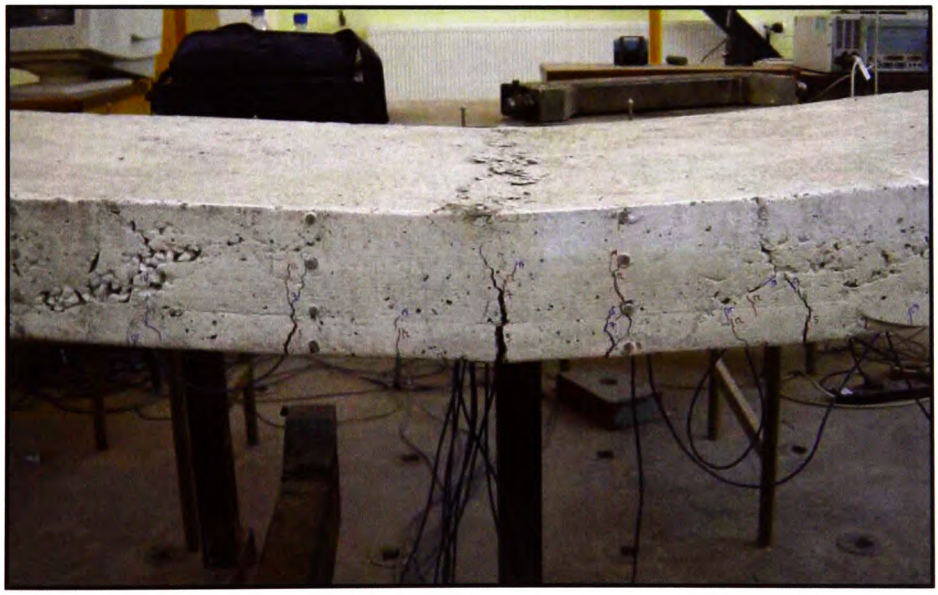

Figure 3.41 – Photograph of normal failure of 8SCON, with steel yielding and concrete crushing

3.7.2.1.2 8SCF2

It was noted, when loading 8SCF2, that the fabric started to emit sounds after 30kN had been applied. These noises, sounding like the failure of individual/groups of fibres,

became progressively louder as the load was increased and the decision was made at 40kN to reduce the load incrementally back to zero before reloading to failure. This was in order to obtain an unloading curve, as well as enabling the removal of the deflection transducers to minimise the risk of damage.

The slab was then reloaded up to 40kN and strain readings were taken together with a measurement of the height of the underside of the slab from the floor at the centre. This latter measurement could be compared with the reading taken at 40kN, which would tie-in with the transducer readings, to give a good indication of central deflection as the slab approached failure.

The slab was re-loaded at 5kN increments and it was noted that the noises were becoming more frequent, although not enough to suggest imminent failure. At 55kN the noises from the fabric became very noticeable and the slab failed at an applied load of 57.5kN, due to fabric rupture and tearing-off of the concrete cover on one side of the slab only, as can be seen in Figure 3.42.

Figure 3.42 – Photograph of 8SCF2 failure, with CFRP rupture and tearing-off of concrete cover

3.7.2.1.3 8SCP2

As with the two-layer CFRP sheet slab, 8SCF2, it was noted that the plates started to sound as though fibres were failing after about 40kN had been applied and the decision was made at 52.5 kN to reduce the load incrementally back to zero before reloading to failure.

Following unloading, the slab was then reloaded up to 55kN, before the loading was again incrementally applied, with the strains and deflections being taken as for 8SCF2, in 5kN increments. The sounds from the plates became very noticeable at 66kN and the slab failed at a slightly higher load of 68.5kN, due to sudden plate de-bonding, as can be seen in Figure 3.43.

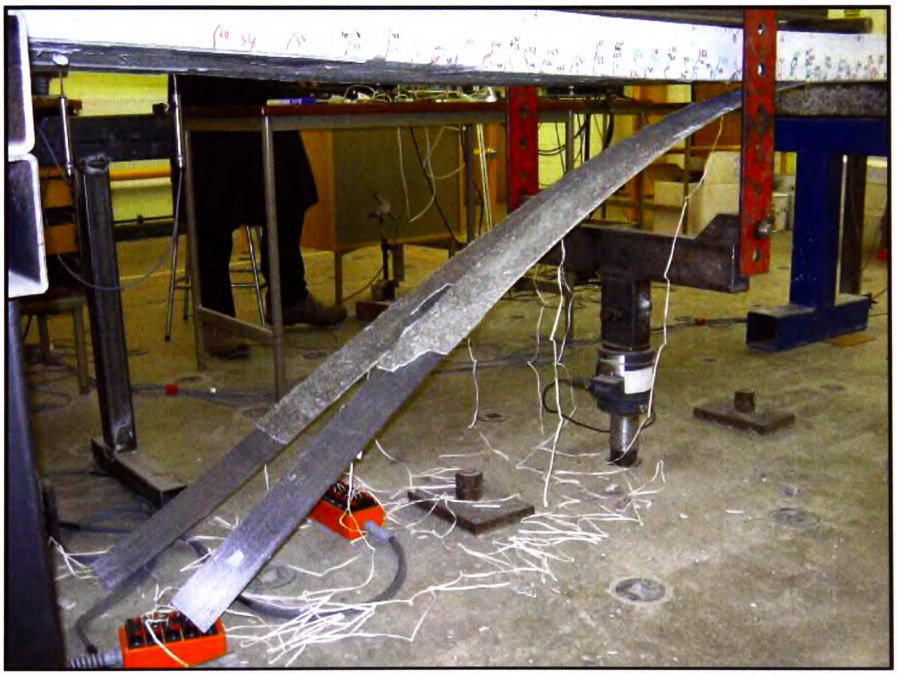

Figure 3.43 – Photograph of 8SCP2 failure, due to premature debonding of the CFRP plates

3.7.2.1.4 8SCP3

The plates on 8SCP3 started to emit sounds after about 30kN had been applied, which became progressively louder as the load increased to 60kN, when it was decided to reduce the load incrementally back to zero before reloading to failure.

Upon reloading past 60kN, the noises in the plates immediately became very noticeable. Once the slab reached an applied load of 65kN, it was allowed time to settle before any readings were taken or increases in load applied. However, the slab failed suddenly by adhesive failure/de-bonding in the central plate before further readings could be taken (Figure 3.44). The appearance of the de-bonded plate suggested that the premature failure was due to air voids in the adhesive, as can be seen in Figures 3.45 and 3.46, which shows the adhesive left on the plate following failure and the associated 'opposite side of the void' section on the slab.

Upon closer inspection of the surface of the failed plate, it appears that there was, to some degree, a shear failure along the interface between the adhesive applied to the slab and that applied to the plate. Any inherent weakness due to poor application would have been exacerbated by the presence, in the adhesive, of air voids, which is likely to have caused the observed failure.

Figure 3.44 – Photograph of 8SCP3 failure; premature debonding of the central CFRP plate

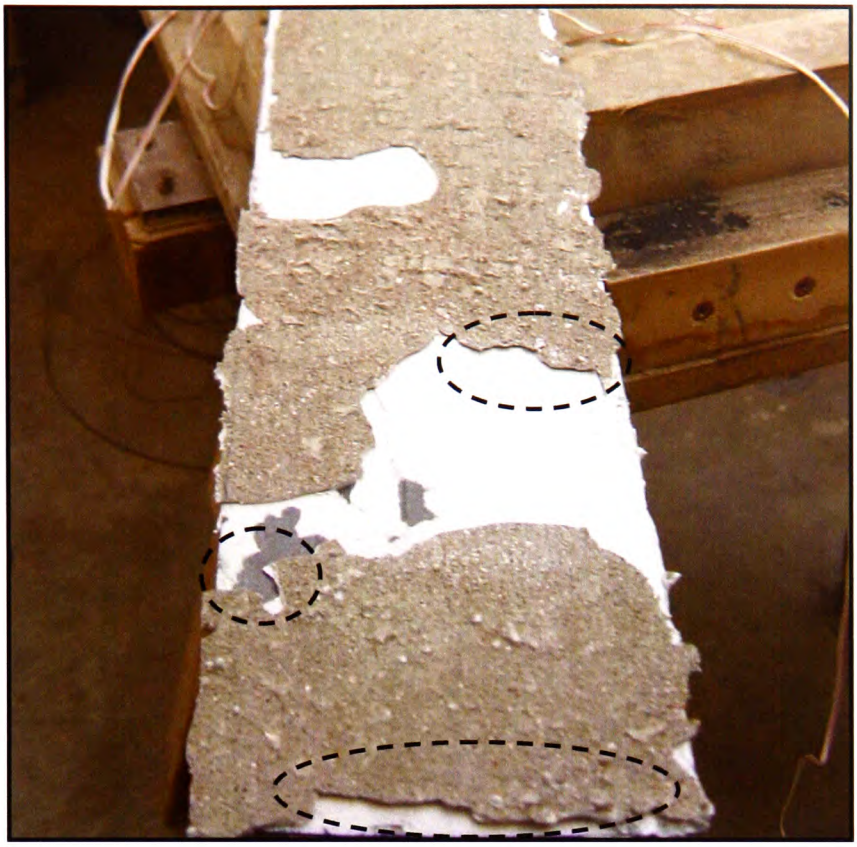

Figure 3.45 – View of de-bonded central plate from 8SCP3 showing air-voids in adhesive (Circled)

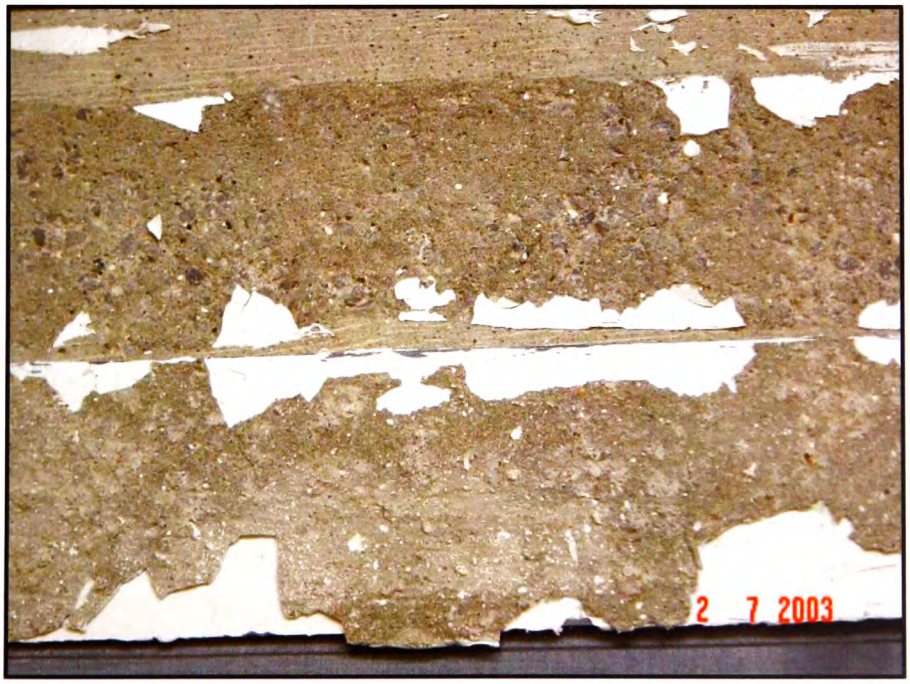

Figure 3.46 – View of central plate from 8SCP3 alongside failure surface of slab

3.7.2.2 Ø 12mm Reinforced slabs

3.7.2.2.1 12SCON

The failure mode for the control slab was as expected for a normally reinforced, un-strengthened section; i.e. the element failed with yielding of the internal steel reinforcement, followed by the formation of a large crack at the tension face and concrete crushing at the top of the slab, at an ultimate load of 32.0 kN. The failure can be seen in Figure 3.47.

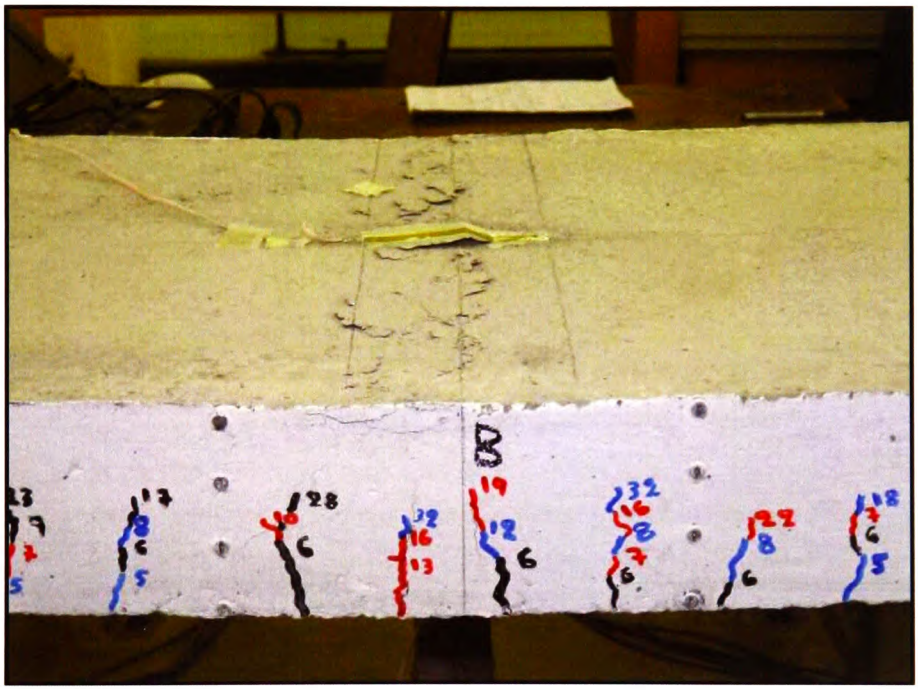

Figure 3.47 – View of concrete compression failure of 12SCON slab

3.7.2.2.2 12SCF2

The failure for the 12SCF2 was due to yielding of the internal steel reinforcement and rupture of the fibre, followed by crushing of the concrete in the compression zone, at a load of 68.0 kN. The failure mode is illustrated in Figure 3.48.

Figure 3.48 – View of fibre rupture failure of 12SCF2 slab

3.7.2.2.3 12SCF4

Element 12SCF4, which had four externally-bonded, full-width layers of CFRP, failed due to crushing of the concrete in the compression zone at mid-span, at a load of 77.0kN, and this can be seen in Figure 3.49.

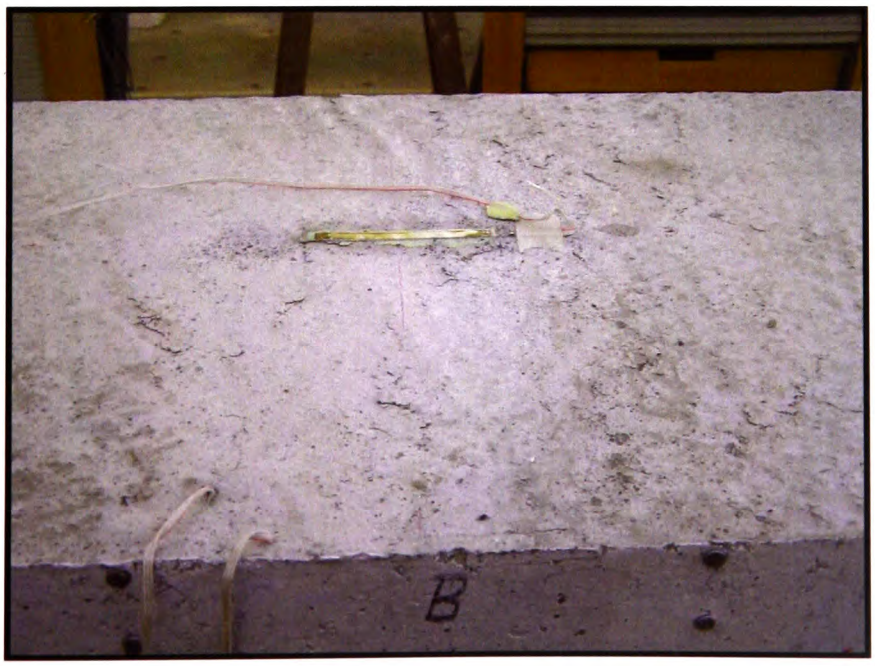

Figure 3.49 – View of compressive concrete failure of 12SCF4 slab

3.7.2.2.4 12SCP2

The failure of 12SCP2, the element with two CFRP plates bonded to the soffit, was due to unexpected and rapid delamination of one of the plates, which resulted in a small amount of tearing-off of the concrete surface, as can be seen in Figure 3.50. The failure occurred suddenly and without any warning, either audible or observed, at an ultimate load of 75.0 kN.

Figure 3.50 – View of debonding failure of 12SCP2 slab

3.7.2.2.5 12SCP3

Slab 12SCP3, which had three CFRP plates bonded to the soffit surface, failed due to sudden delamination of the central plate, which resulted in a small amount of tearing-off of the concrete surface, at a load of 92.5 kN. This is illustrated in Figure 3.51.

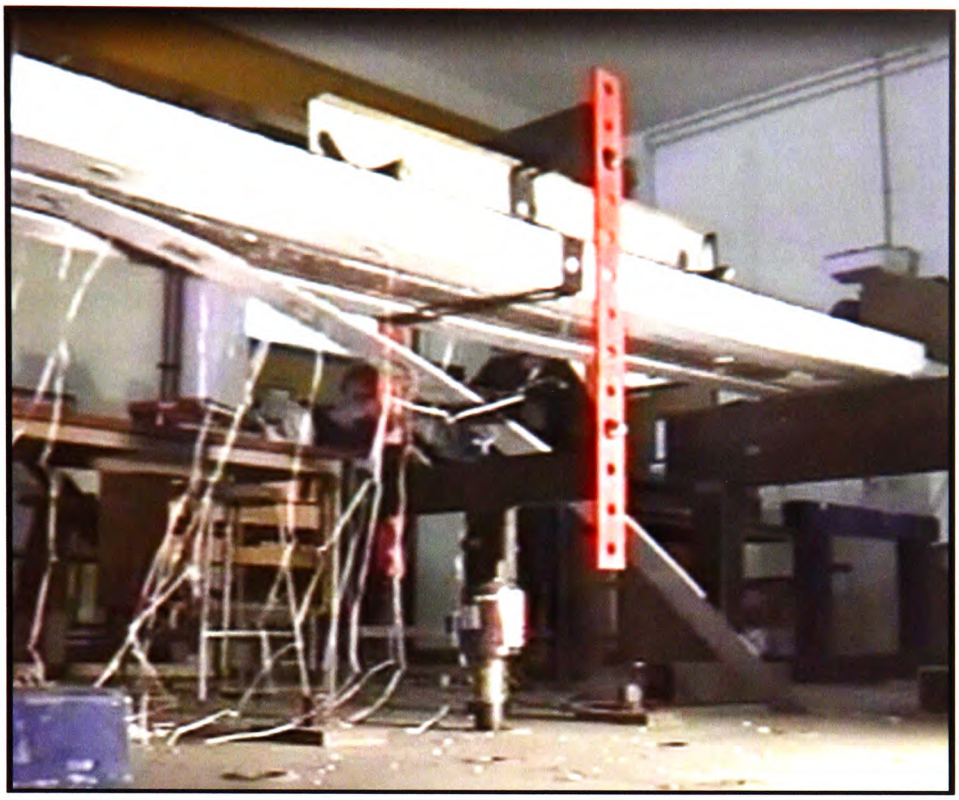

Figure 3.51 – View of debonding failure of central plate of 12SCP3 slab

CHAPTER 4 ANALYSIS OF EXPERIMENTAL RESULTS AND ELEMENT BEHAVIOUR

4.1 Introduction

All elements tested in the experimental programme were instrumented to ensure the accurate recording of average surface strains on both faces of the elements and deflections along the whole element length. This enabled the collated data to be analysed in a variety of ways to better understand the performance of the tested elements.

It should be noted that while reinforced concrete elements are all theoretically similar, being flexural elements, it is accepted that elements with lower levels of reinforcement (i.e. slabs) behave significantly differently to those with higher reinforcement levels (i.e. beams), due to a number of factors. Firstly, as stated, generally slab elements have lower levels of reinforcement but also there is an appreciably higher area of compressive resistance from the concrete. Additionally, the element stiffness of beams and slabs differs post-cracking. Consequently, all elements in this programme of research although being denoted by their percentage of internal reinforcement, ρ, have also been differentiated by being described as either beam or slab element.

4.2 Summary of test results

Extensive test data for each element, comprising deflections, strains, cracks and load, were collated during the experimental programme. The main details for all the twenty tested beams and nine tested slabs are presented in Table 4.1.

4.3 Load Deflection Analysis

4.3.1 ρ =0.50% - ∅ 8mm reinforced beams

Vertical deflections were recorded along the whole length of the element, between supports. The load to maximum mid-span deflection relationships, Figures 4.1 (a) to (c), show that there is an increase not only in the load-carrying capacity of the elements as the amount of externally-bonded CFRP increases, but also there is a noticeable increase in the element stiffness. However, once the element is strengthened with 3 layers of CFRP the element becomes increasingly stiff, which results in large stresses at the lower regions of the element and premature failure occurs. It is shown in Table 4.1 that the increases in applied load at serviceability deflection (taken for the purposes of this research as $\frac{L}{250}$) for 1, 2 and 3 layers of CFRP sheet, when compared to the non-strengthened control element, were 15%, 32% and 53% respectively, with the ultimate load carrying capacities increased by 65%, 78% and 57% respectively.

Also, shown in Table 4.1 are the element ultimate loads, moments, deflections and failure modes. It can be seen that the most heavily strengthened of the elements, namely 8CF3, failed at a load of 55.0 kN, an increase of 57% over the control element but significantly less than the 78% increase over control achieved by the element strengthened with 2 layers of CFRP. Additionally, it is observed that following cracking of the concrete, if the slopes of the load deflection curves for the strengthened elements were extrapolated back they would pass through the origin. This suggests that were strengthening to be introduced to a pre-cracked element, then the benefit would be comparable to the elements tested here.

4.3.2 ρ =0.79% - ∅ 10mm reinforced beams

As with the 8mm elements in 4.3.1, vertical deflections were recorded along the whole length of the element, between supports. As can be seen from Figures 4.2

(a) to (c), the load to maximum span deflection relationships show that an increase in load-carrying capacity is achieved with the strengthened elements but also an increase in the stiffness of the associated element.

It is shown that the load increases at serviceability deflection for 1, 2 and 3 layers of CFRP sheets, compared with the non-strengthened control element, were approximately 4%, 10% and 30% respectively, whilst the ultimate load increases are 11%, 42% and 24% respectively. These percentage gains are shown in Table 4.1, together with the ultimate loads, moments, deflections and failure modes.

It can be seen that the more heavily-strengthened elements, namely 10CF2 and 10CF3, failed with premature tearing-off of the concrete cover at the internal steel reinforcement level on the tension face. In the case of 10CF2, there was also a simultaneous localised crushing of the concrete in the compression zone. Again, it is observed that the element strengthened with 3 layers of CFRP failed with a lower percentage gain in load-carrying capacity over the control element than that of the element with 2 layers of CFRP; 24% compared to 42% respectively.

4.3.3 ρ =1.13% - ∅12mm reinforced beams

As with all tests, vertical deflections were recorded and, as can be seen from Figure 4.3 (a) to (c), the increases in load at serviceability deflection, when compared to the control element, were 15%, 28% and 22% for the beams with 1, 2 and 3 layers of CFRP respectively, with load-carrying capacity increases of 20%, 31% and 29%. The reduced stiffness of the element with three layers of CFRP sheet (when compared to the element with two layers) is likely due to minor behavioural differences in the elements. It can be seen, however, that both elements exhibit similar stiffness beyond serviceability deflection and it should be noted that as both elements are over-reinforced, the effect of the bonded CFRP sheets is mitigated.

It can be seen that, due to the higher percentage of internal steel reinforcement when compared to the ∅8mm and ∅10mm elements, the effect of the CFRP strengthening is diminished and in the case of the elements with 2 and 3 layers of CFRP sheets, the improvements in ultimate load between the two elements and the control are only 31% and 29% respectively.

Table 4.1 Summary of element test results, incl. %age gains in strength

Element ref.	Load at service. Defl. Limit (kN)	% Strength gain	Ultimate Load (kN)	% Strength gain	Ultimate Moment (kNm)	Ultimate Defl. (at peak load) (mm)	Failure Mode[1]
8CON	23.5	-	35.1	-	10.1	22.1	SY-CC
8CF1	27.0	+15%	58.0	+65%	16.7	29.8	FR
8CF2	31.0	+32%	62.5	+78%	18.0	31.4	DB-PTO
8CF3	36.0	+53%	55.0	+57%	15.8	16.5	PTO
10CON	34.5	-	56.5	-	16.3	30.0	SY-CC
10CF1	36.0	+4%	62.6	+11%	18.0	26.5	FR
10CF2	38.0	+10%	80.1	+42%	23.1	33.8	DB-PTO
10CF3	45.0	+30%	70.0	+24%	20.2	17.7	PTO
12CON	38.1	-	65.0	-	18.7	20.0	CC
12CF1	43.7	+15%	78.2	+20%	22.5	24.0	CC
12CF2	48.6	+28%	85.0	+31%	24.2	21.8	CC
12CF3	46.6	+22%	84.1	+29%	24.4	24.5	CC
16CON	50.0	-	98.0	-	28.2	22.7	CC
16CF1	55.0	+10%	96.0	-2%	27.6	20.7	ECC
16CF2	53.0	+6%	90.0	-8%	25.9	20.4	ECC
16CF3	55.0	+10%	101.2	3%	29.1	24.9	CC
12DCON	39.1	-	70.0	-	20.1	33.4	SY-CC
12DCF1	46.0	+18%	90.0	+29%	23.6	38.5	DB-PTO
12DCF2	47.0	+20%	95.0	+36%	27.3	27.7	PTO
12DCF3	50.0	+28%	92.0	+31%	26.5	20.6	PTO
8SCON	6.7	-	17.1	-	8.1	51.0	SY-CC
8SCF2	15.4	+130%	55.0	+68%	26.1	69.0	FR-PTO
8SCP2	19.0	+184%	65.0	+172%	30.9	55.7	DB
8SCP3	20.7	+209%	60.0	+130%	28.5	44.8	DB
12SCON	9.4	-	32.0	-	15.2	53	SY-CC
12SCF2	17.0	+81%	68.0	+113%	32.3	93.5	FR
12SCF4	20.9	+122%	77.0	+141%	36.6	65.6	CC
12SCP2	23.4	+149%	75.0	+134%	35.6	54.6	DB
12SCP3	24.6	+162%	92.5	+189%	44.0	66.7	DB

[1] CC=Concrete crushing; SY-CC=Steel yield followed by concrete crushing; FR=Fibre rupture; DB=De-bonding of CFRP; PTO=Premature tearing-off of concrete cover; ECC=Explosive concrete crushing

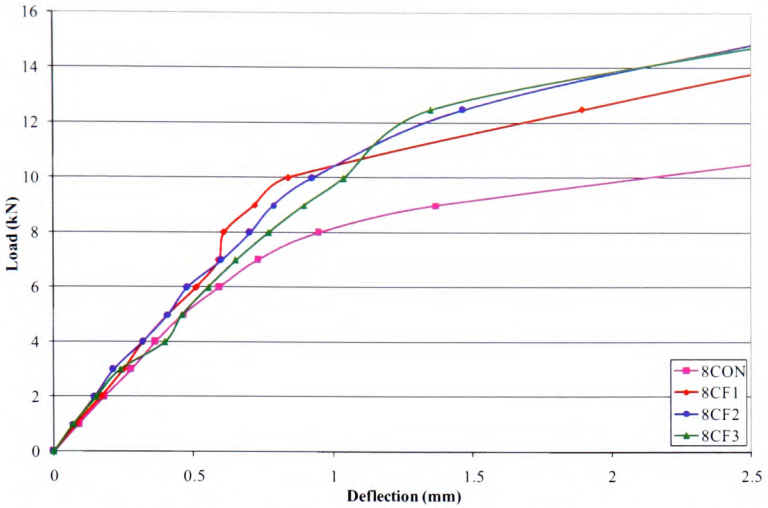

Figure 4.1(a) – Load deflection graph at initial loading stage for ρ =0.50% - ∅8mm reinforced beams {See Figure 4.1(b) for initial loading stage partition}

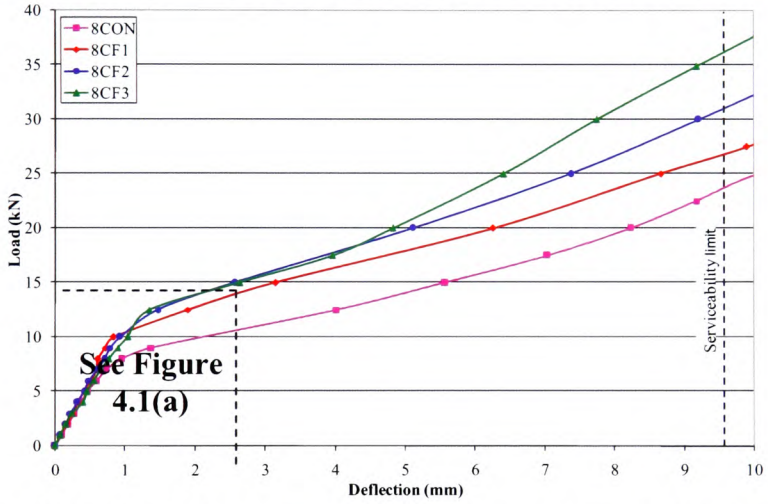

Figure 4.1(b) – Load deflection graph up to serviceability deflection for ρ =0.50% - ∅8mm reinforced beams

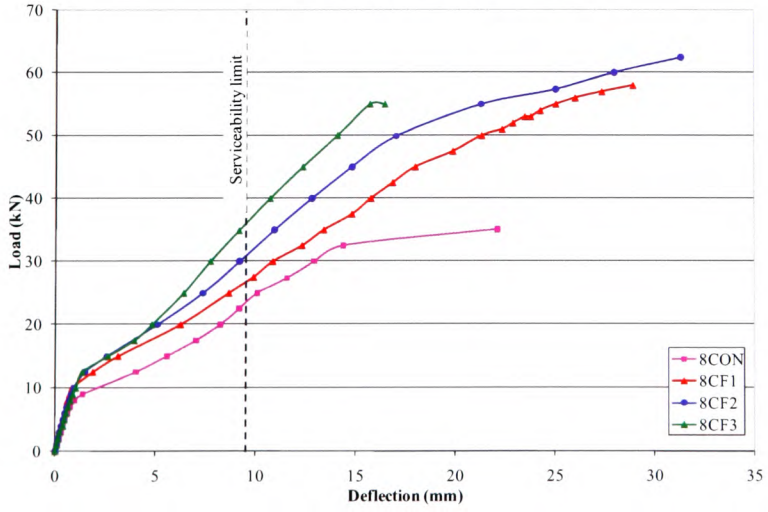

Figure 4.1(c) – Load deflection graph for ρ =0.50% - ∅8mm reinforced beams

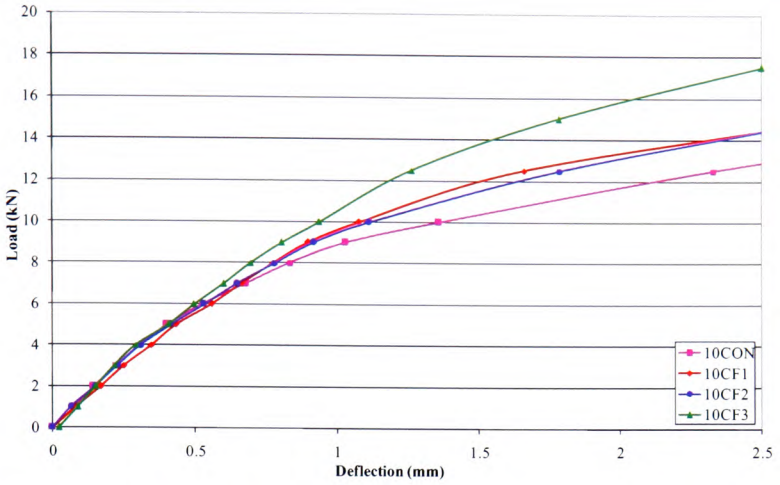

Figure 4.2(a) – Load deflection graph at initial loading stage for ρ =0.79% - ∅10mm reinforced beams {See Figure 4.2(b) for initial loading stage partition}

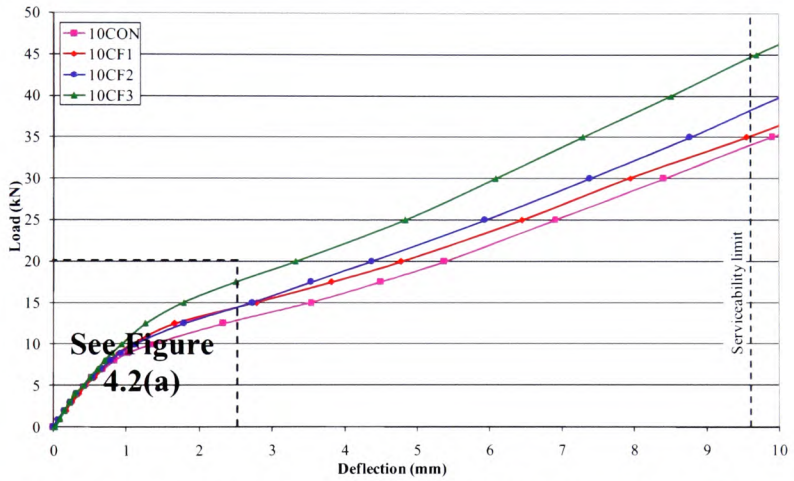

Figure 4.2(b) – Load deflection graph up to serviceability deflection for ρ =0.79% - ∅10mm reinforced beams

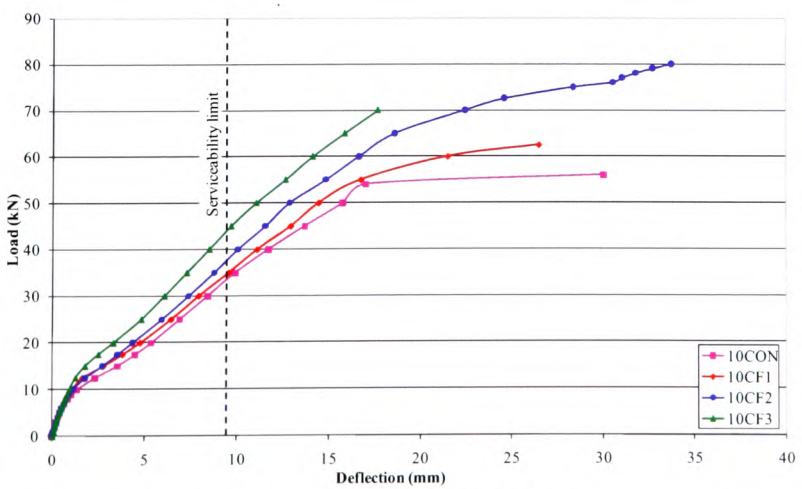

Figure 4.2(c) – Load deflection graph for ρ =0.79% - ∅10mm reinforced beams

4.3.4 ρ =2.01% - ∅16mm reinforced beams

As with the all other elements, vertical deflections were recorded along the whole length of the element. Figure 4.4 (a) to (c) shows that there is a minimal increase in load-carrying capacity and stiffness for the strengthened elements, due to their over-reinforced nature resulting in the CFRP strengthening becoming essentially redundant. There is also a noticeable decrease in deflection, all being in the range of 20.4mm to 24.9mm, far less than that for the other elements.

It can be seen from Table 4.1 that the increase in load at serviceability deflection never exceeds 10% and the ultimate load capacities actually show a decrease in two of the elements, 16CF1 and 16CF2, with only a 3% increase for 3 layers of CFRP. Additionally, due to the high percentage of tension reinforcement and strengthening, the element behaviour became highly unpredictable.

4.3.5 ρ =1.13% - ∅12mm doubly-reinforced beams

Vertical deflections and loads were recorded and are shown on Figures 4.5 (a) to (c). It can be seen that the increases in load at serviceability deflection were 18%, 20% and 28% for the elements with 1, 2 and 3 layers of CFRP respectively, when compared to the control element. The increases in load-carrying capacity were 29%, 36% and 31%, respectively, echoing the trend of the 8mm, 10mm and 12mm singly-reinforced elements, where the element with 2 layers of CFRP strengthening performs better then the element with 3 layers.

Also, as with the 12mm singly-reinforced elements, the higher percentage of internal steel reinforcement when compared to the 8mm and 10mm beams reduces the benefit of the CFRP strengthening. Additionally, the inclusion of two 12mm bars as compression reinforcement resulted in an increased load-carrying capacity for the elements, which one would expect as the singly-reinforced 12mm beams all failed due to compression failure of the concrete.

4.3.6 ρ =0.40% - ∅ 8mm reinforced slabs

As for the other tests, vertical deflections were recorded along the whole span of the element. Figures 4.6 (a) to (c) show a significant increase in load-carrying capacity and stiffness for the strengthened elements. It is also seen, from Table 4.1, that the load increases at serviceability deflection (11.6mm) were 130%, 184% and 209% for the 2 layers of CFRP sheet and the 2 & 3 CFRP plate strengthened elements respectively.

As noted in Chapter 3, 8SCP2 and 8SCP3 failed due to premature de-bonding of the CFRP plates. It is suggested that the failure loads for these two elements could have been considerably higher had the de-bonding not occurred, a viewpoint supported by the surface strains near the top fibre at failure, which were only approximately 2000με for both elements; only 60% of the compressive failure strain for concrete of 3500με.

4.3.7 ρ =0.91% - ∅12mm reinforced slabs

As in previous tests, vertical deflections were recorded along the entire span and the load deflection results are presented in Figure 4.7 (a) to (c).

As with the 8mm reinforced slab elements, the elements strengthened with CFRP plates failed prematurely due to debonding of one of the adhered plates.

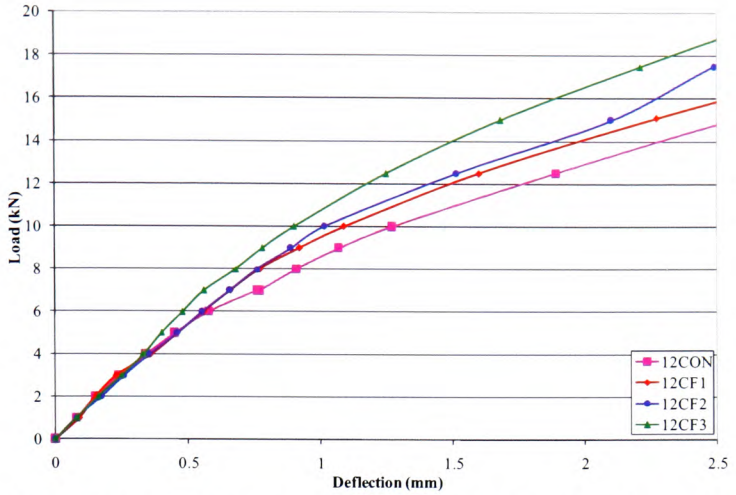

Figure 4.3(a) – Load deflection graph at initial loading stage for ρ =1.13% - ∅12mm reinforced beams {See Figure 4.3(b) for initial loading stage partition}

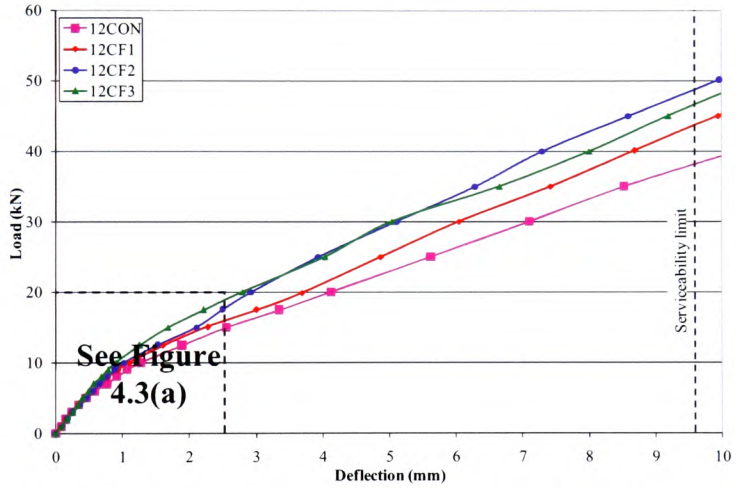

Figure 4.3(b) – Load deflection graph up to serviceability deflection for ρ =1.13% - ∅12mm reinforced beams

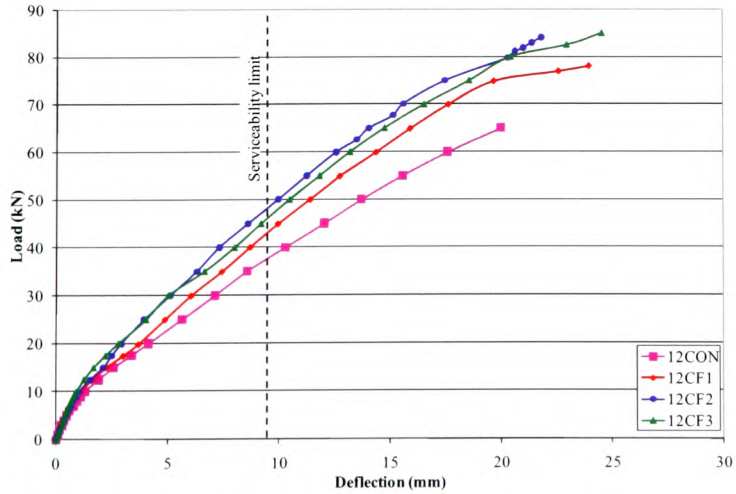

Figure 4.3(c) – Load deflection graph for ρ =1.13% - ∅12mm reinforced beams

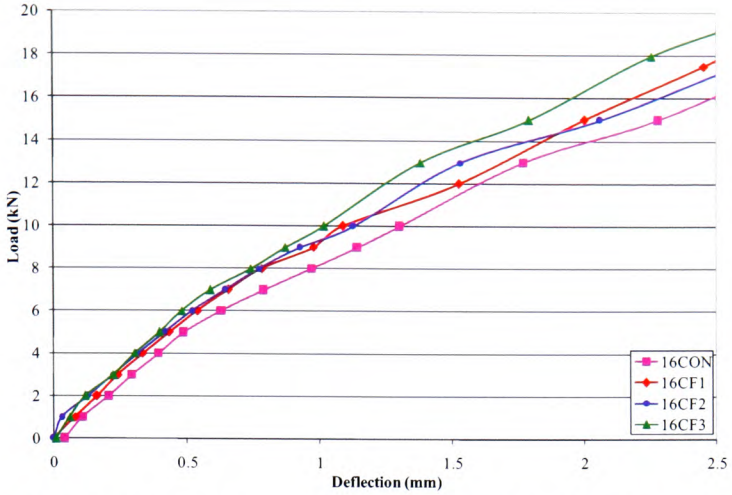

Figure 4.4(a) – Load deflection graph at initial loading stage for ρ =2.01% - ∅16mm reinforced beams {See Figure 4.4(b) for initial loading stage partition}

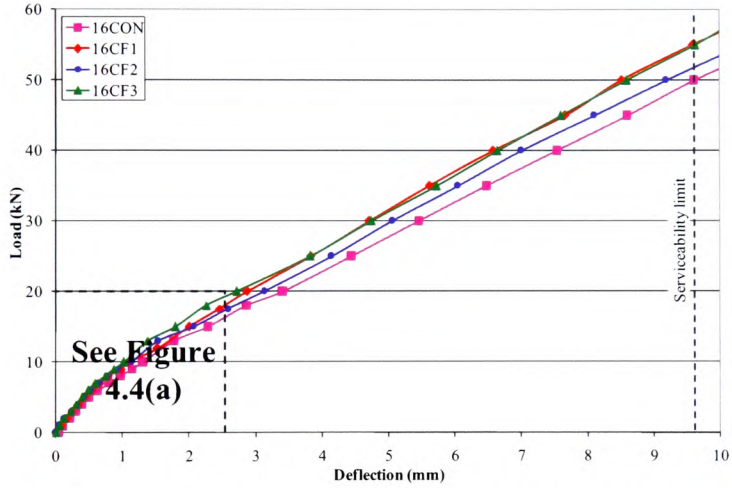

Figure 4.4(b) – Load deflection graph up to serviceability deflection for ρ =2.01% - ∅16mm reinforced beams

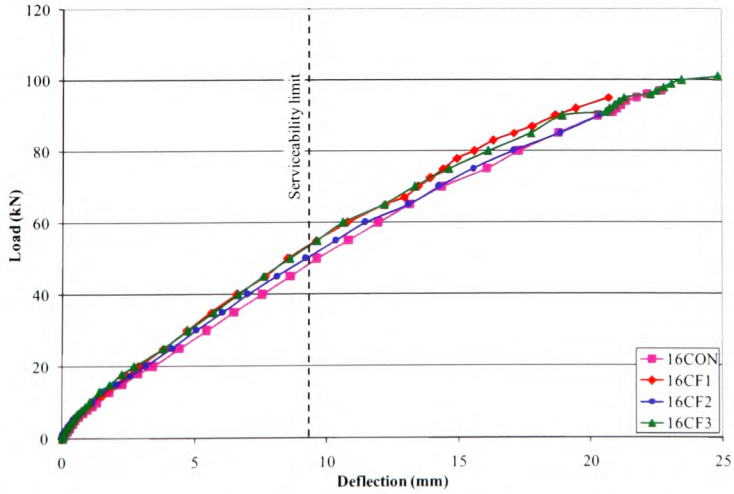

Figure 4.4(c) – Load deflection graph for ρ =2.01% - ∅16mm reinforced beams

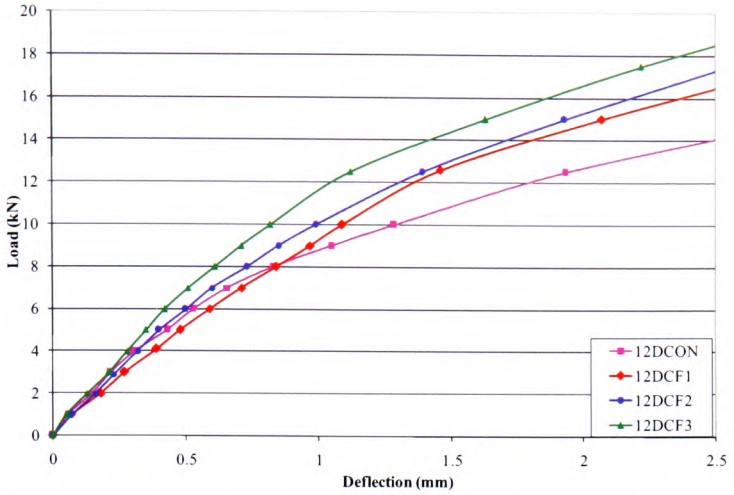

Figure 4.5(a) – Load deflection graph at initial loading stage for ρ =1.13% - ∅12mm doubly-reinforced beams {See Figure 4.5(b) for initial loading stage partition}

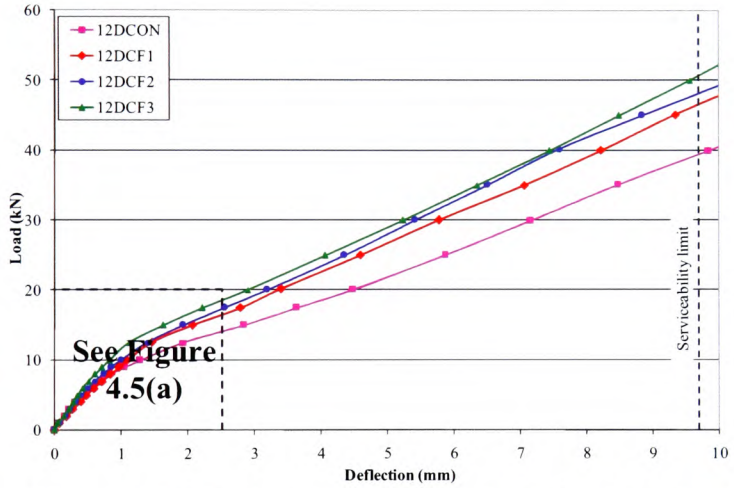

Figure 4.5(b) – Load deflection graph up to serviceability deflection for ρ =1.13% - ∅12mm doubly-reinforced beams

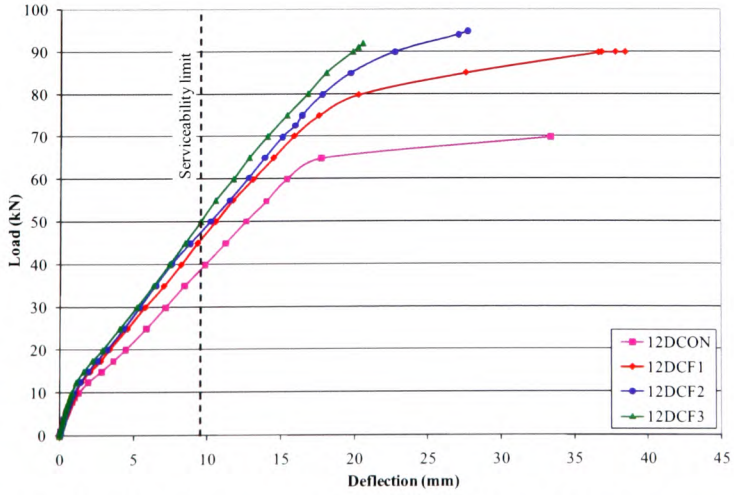

Figure 4.5(c) – Load deflection graph for ρ =1.13% - ∅12mm doubly-reinforced beams

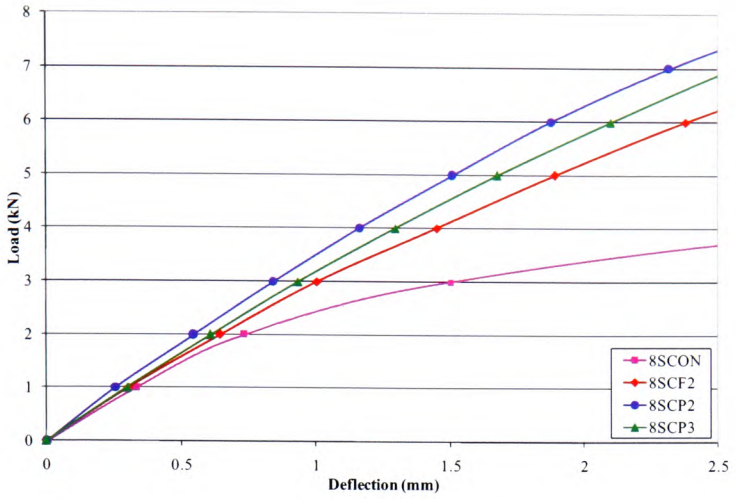

Figure 4.6(a) – Load deflection graph at initial loading stage for ρ =0.40% - ∅8mm reinforced slabs {See Figure 4.6(b) for initial loading stage partition}

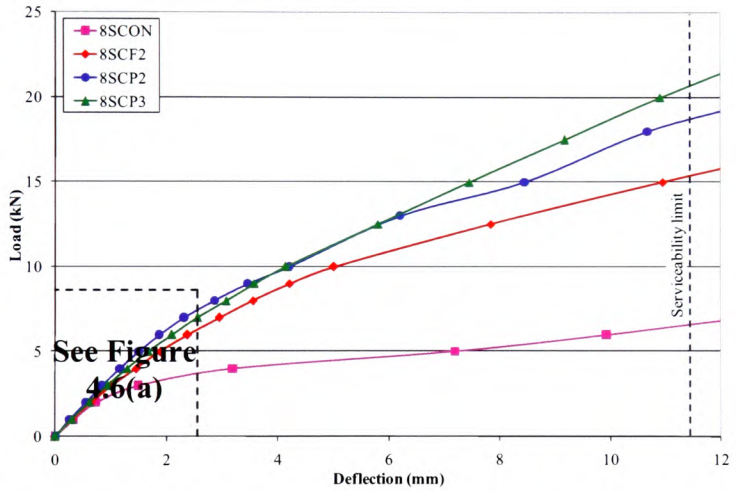

Figure 4.6(b) – Load deflection graph up to serviceability deflection for ρ =0.40% - ∅8mm reinforced slabs

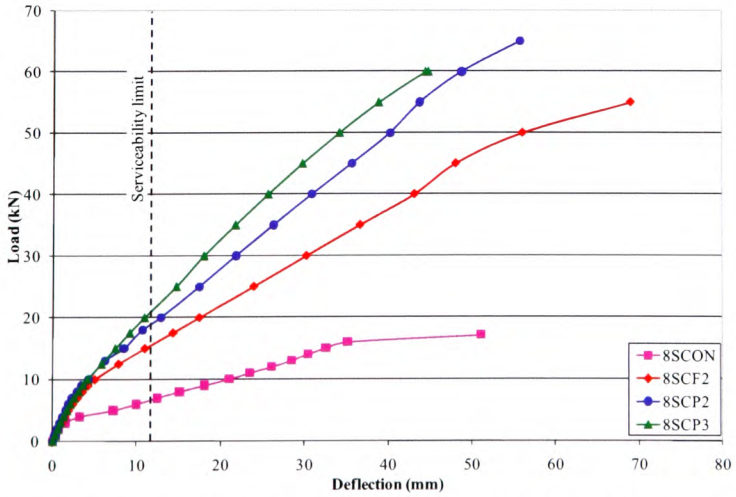

Figure 4.6(c) – Load deflection graph for ρ =0.40% - ∅8mm reinforced slabs

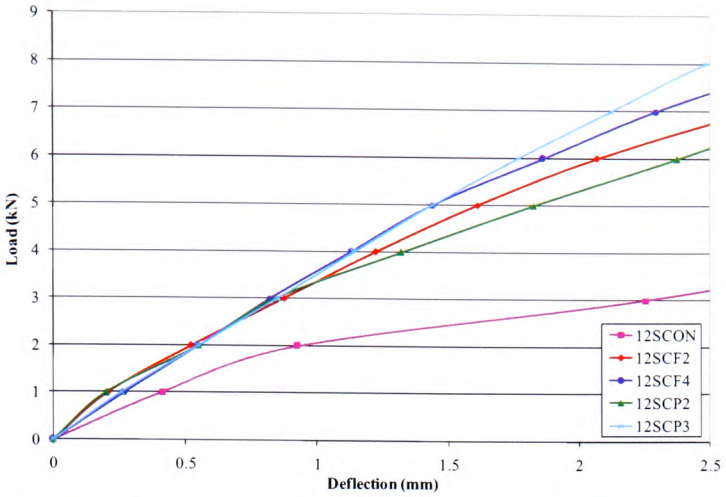

Figure 4.7(a) – Load deflection graph at initial loading stage for ρ =0.91% - ∅12mm reinforced slabs {See Figure 4.7(b) for initial loading stage partition}

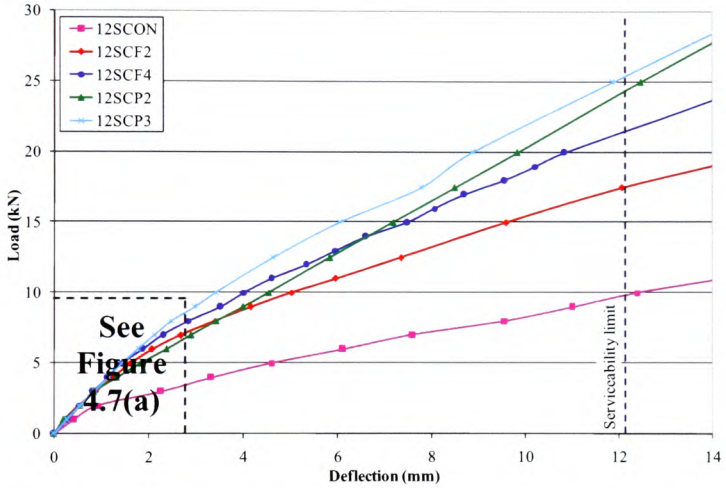

Figure 4.7(b) – Load deflection graph up to serviceability deflection for ρ =0.91% - ∅12mm reinforced slabs

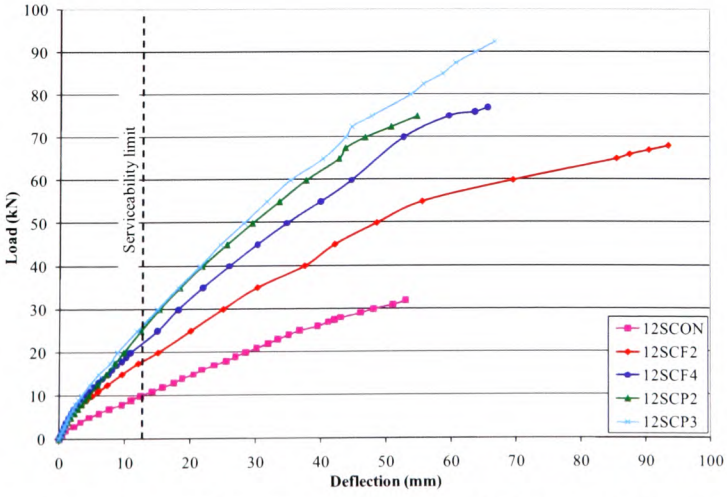

Figure 4.7(c) – Load deflection Graph for ρ =0.91% - ∅12mm reinforced slabs

4.4 Deflection profiles

Deflection profiles were created for all elements, utilising the section deformations recorded using the electronic linear variable displacement transducers (LVDTs). The positioning of the LVDTs can be seen in Figures 4.8(a) and (b). For all elements, a total of ten LVDTs were used and positioned symmetrically, with two gauges at mid-span to record the maximum mid-span element deflection. On pages 98 to 105, the deflection profiles for all elements are presented, in Figures 4.9(a) to 4.15(e).

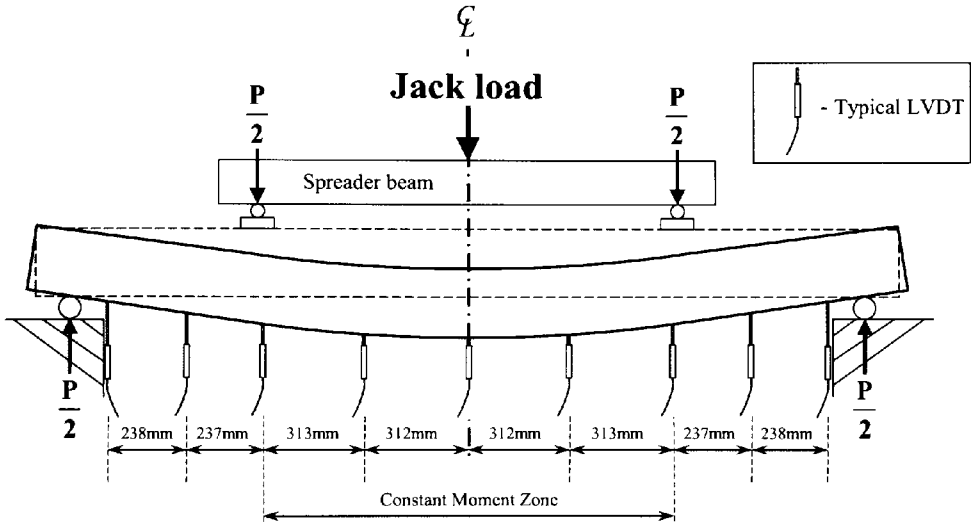

Figure 4.8(a) Location of Linear Variable Displacement Transducers for beam elements

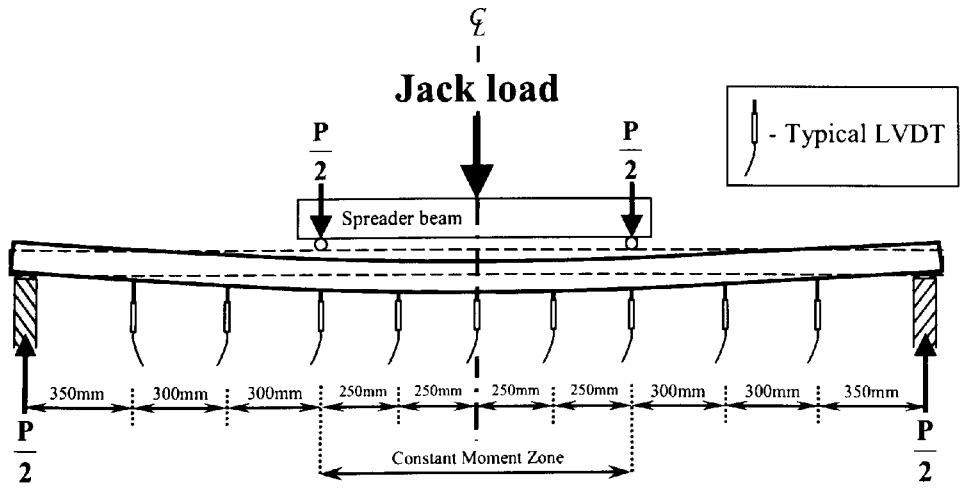

Figure 4.8(b) Location of Linear Variable Displacement Transducers for slab elements

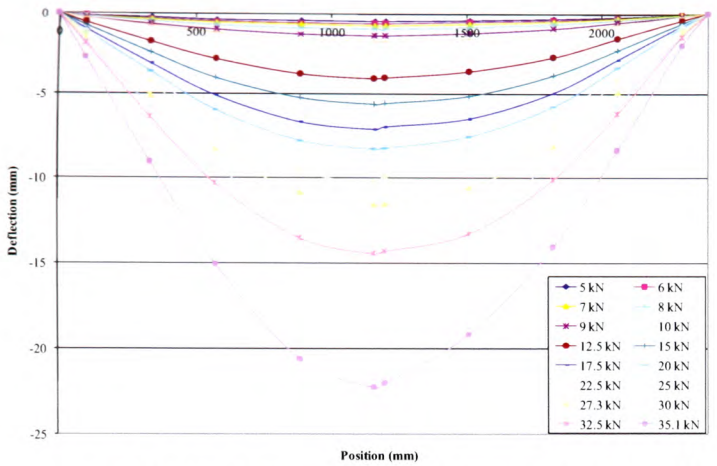

Figure 4.9(a) – Deflection profile for control element 8CON

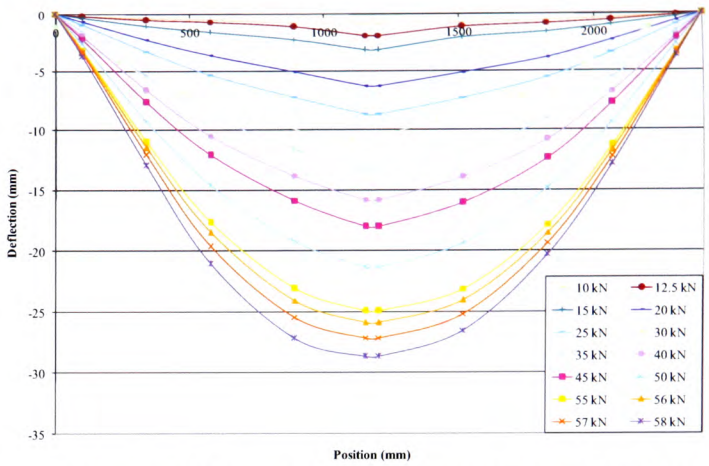

Figure 4.9(b) – Deflection profile for element 8CF1

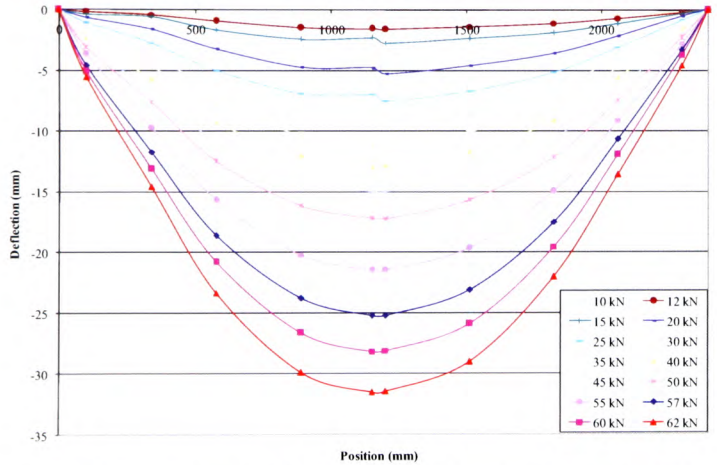

Figure 4.9(c) – Deflection profile for element 8CF2

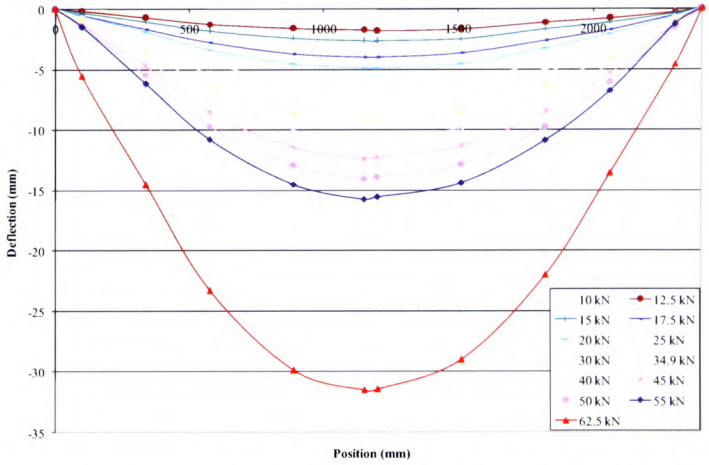

Figure 4.9(d) – Deflection profile for element 8CF3

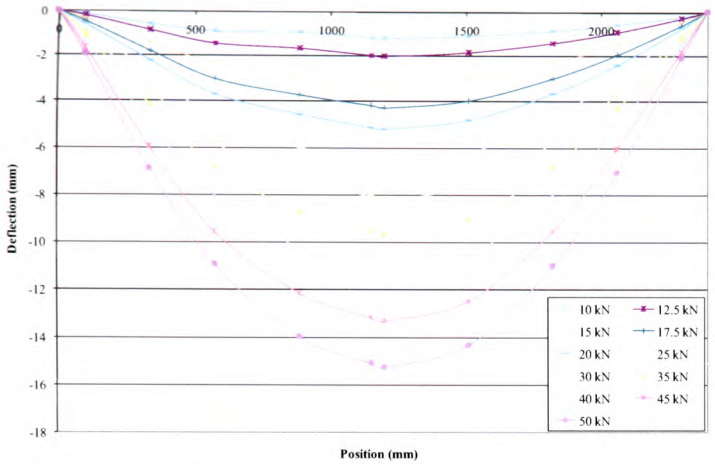

Figure 4.10(a) – Deflection profile for control element 10CON

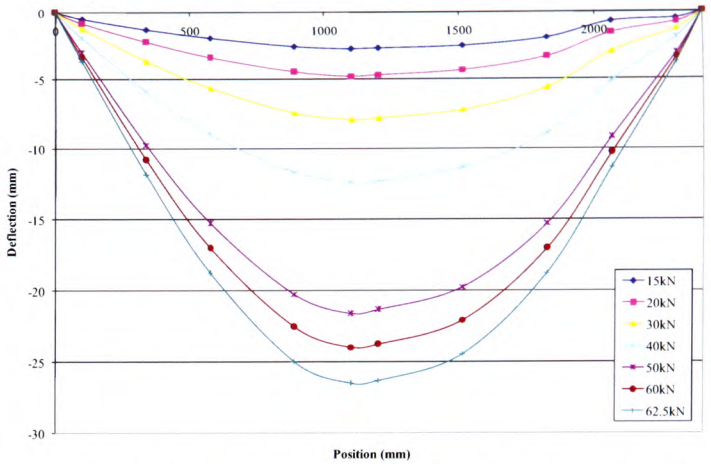

Figure 4.10(b) – Deflection profile for element 10CF1

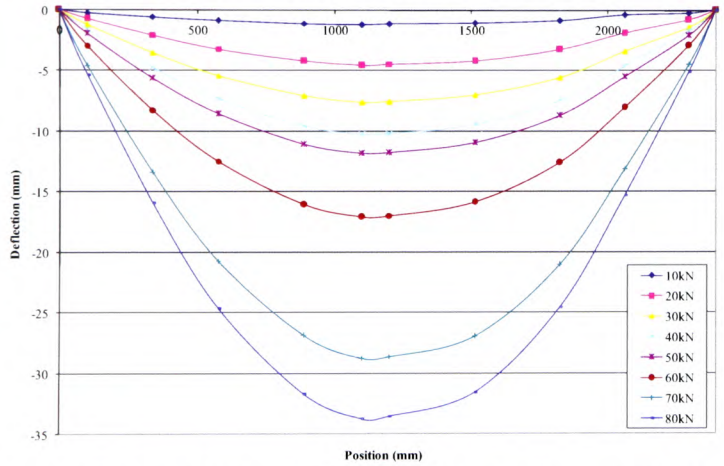

Figure 4.10(c) – Deflection profile for element 10CF2

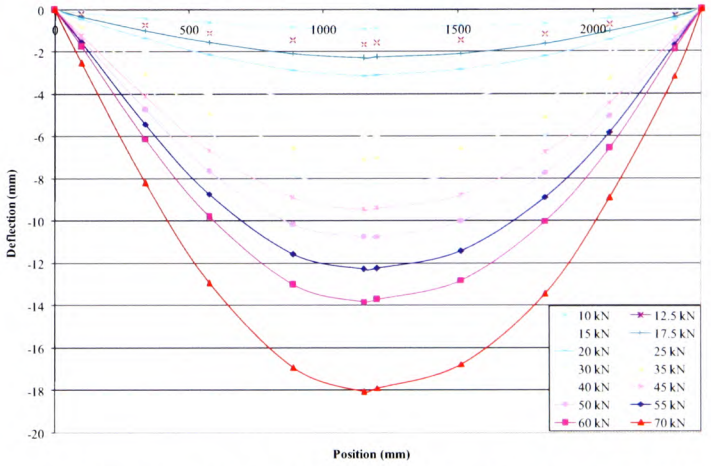

Figure 4.10(d) – Deflection profile for element 10CF3

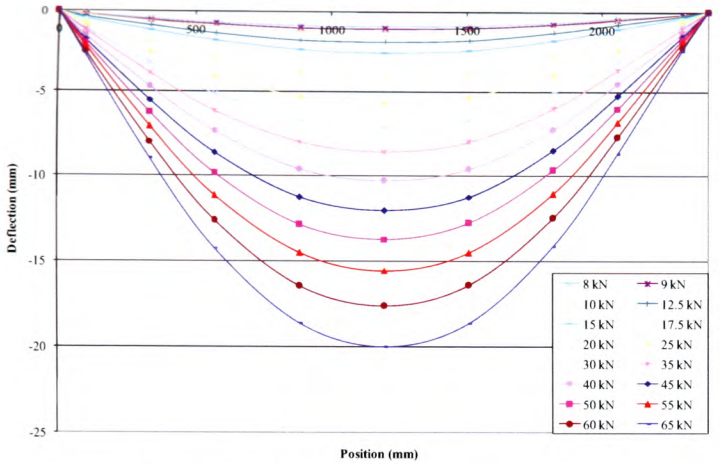

Figure 4.11(a) – Deflection profile for control element 12CON

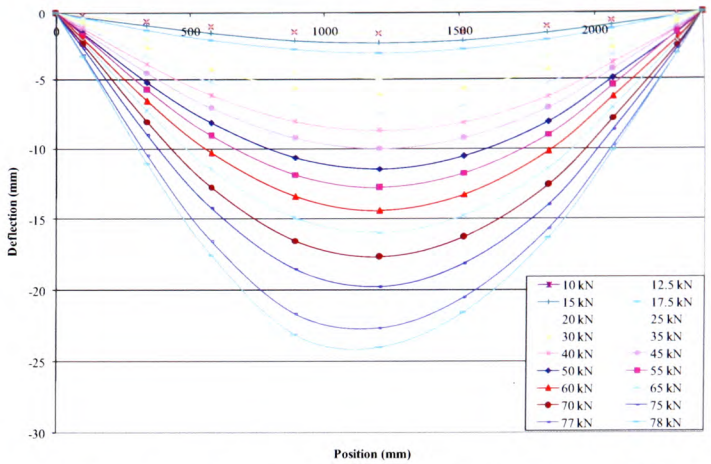

Figure 4.11(b) – Deflection profile for element 12CF1

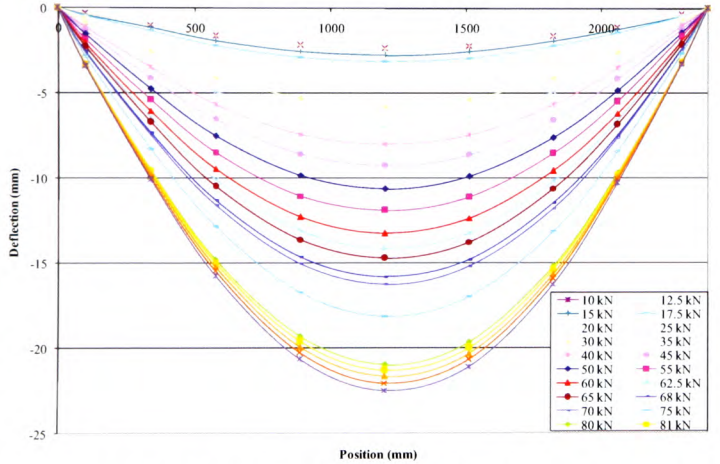

Figure 4.11(c) – Deflection profile for element 12CF2

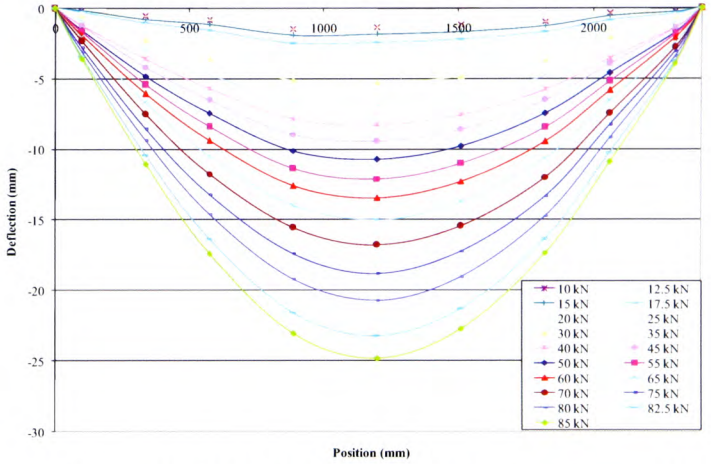

Figure 4.11(d) – Deflection profile for element 12CF3

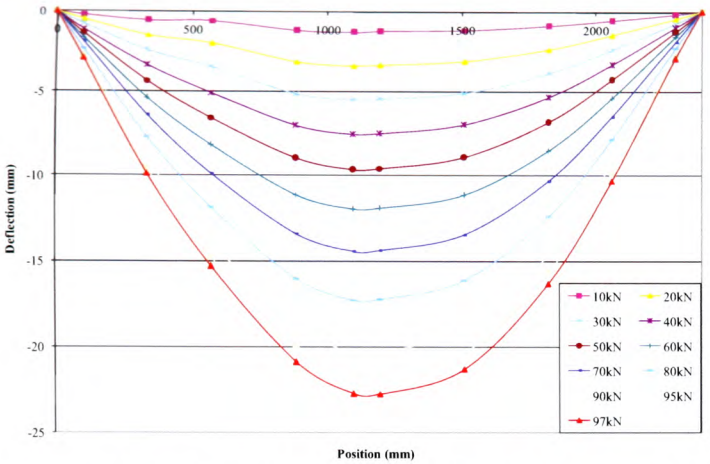

Figure 4.12(a) – Deflection profile for control element 16CON

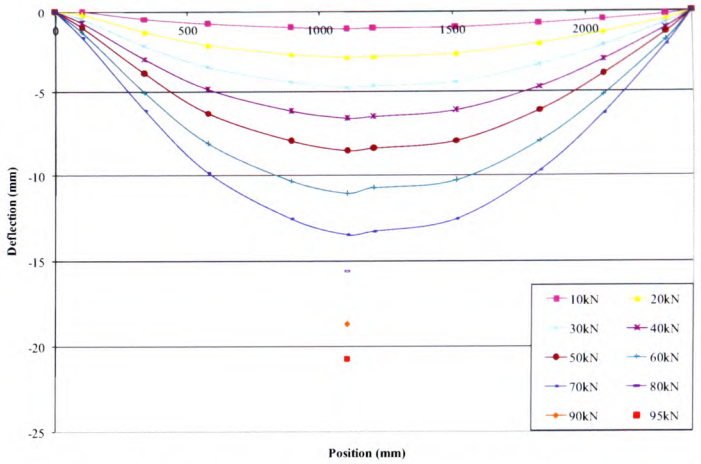

Figure 4.12(b) – Deflection profile for element 16CF1

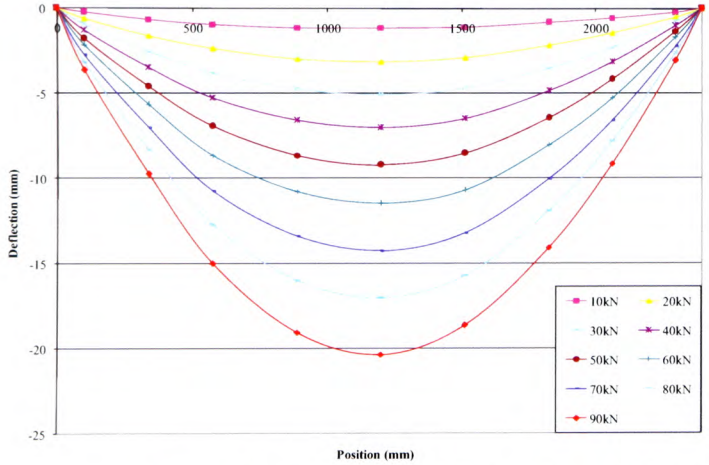

Figure 4.12(c) – Deflection profile for element 16CF2

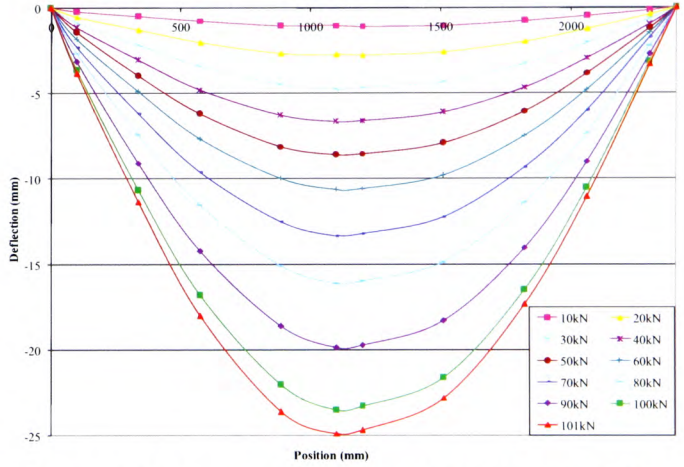

Figure 4.12(d) – Deflection profile for element 16CF3

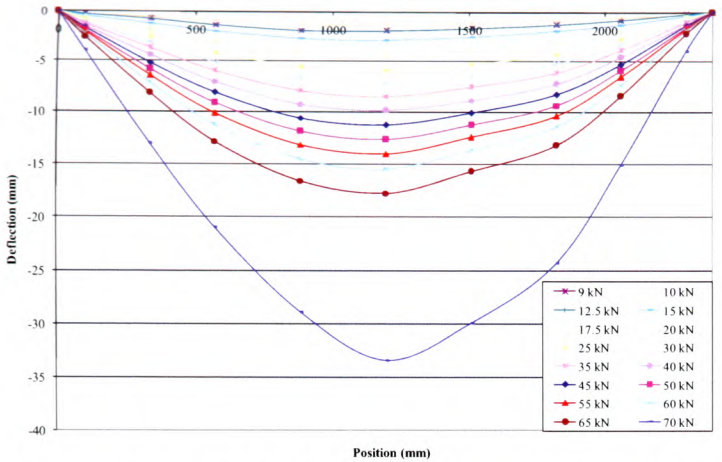

Figure 4.13(a) – Deflection profile for control element 12DCON

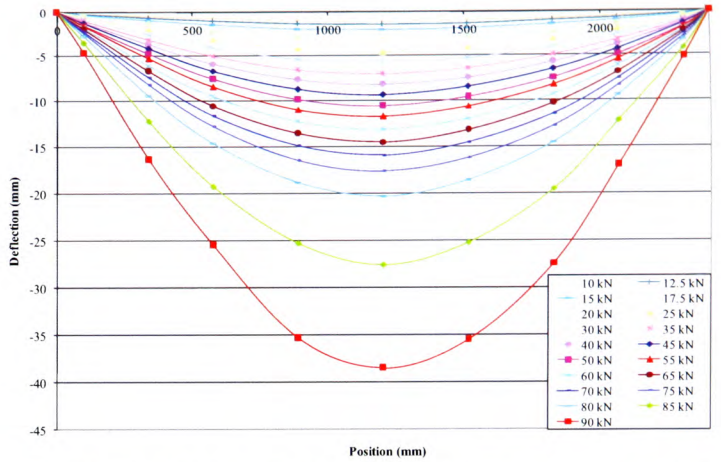

Figure 4.13(b) – Deflection profile for element 12DCF1

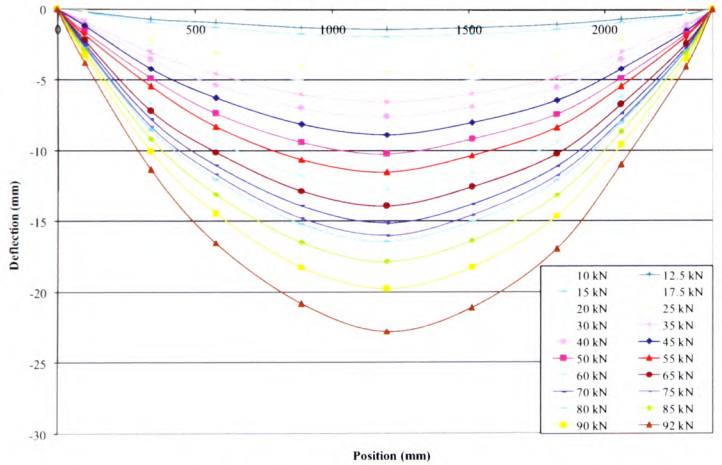

Figure 4.13(c) – Deflection profile for element 12DCF2

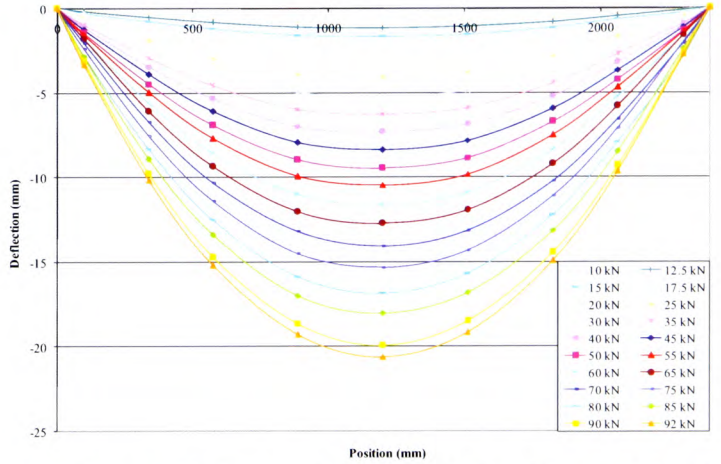

Figure 4.13(d) – Deflection profile for element 12DCF3

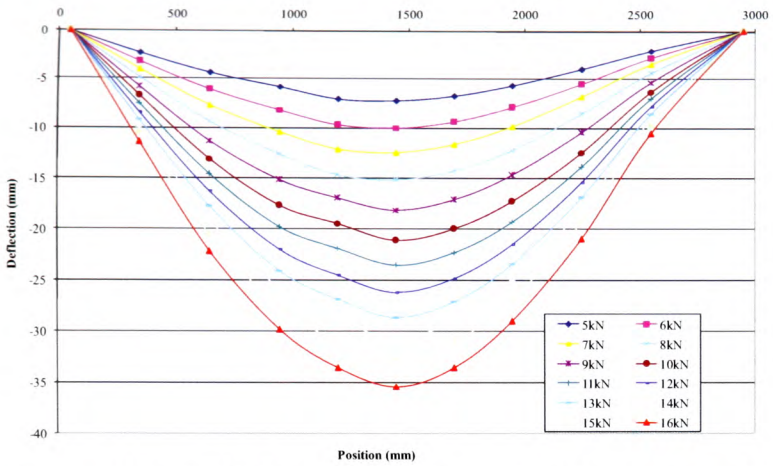

Figure 4.14(a) – Deflection profile for control element 8SCON

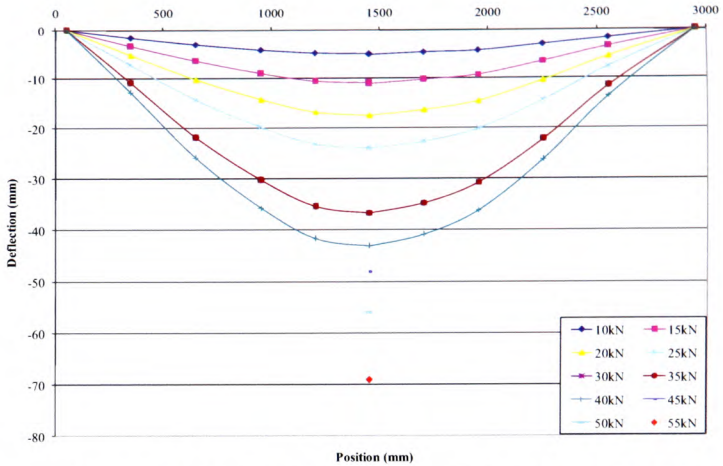

Figure 4.14(b) – Deflection profile for element 8SCF2

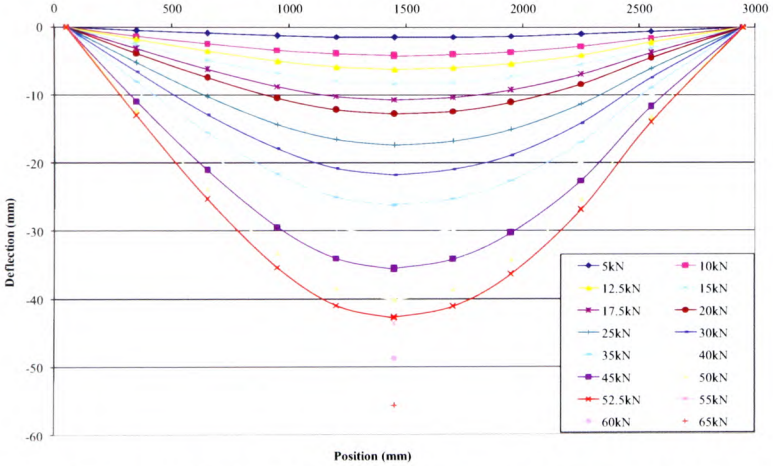

Figure 4.14(c) – Deflection profile for element 8SCP2

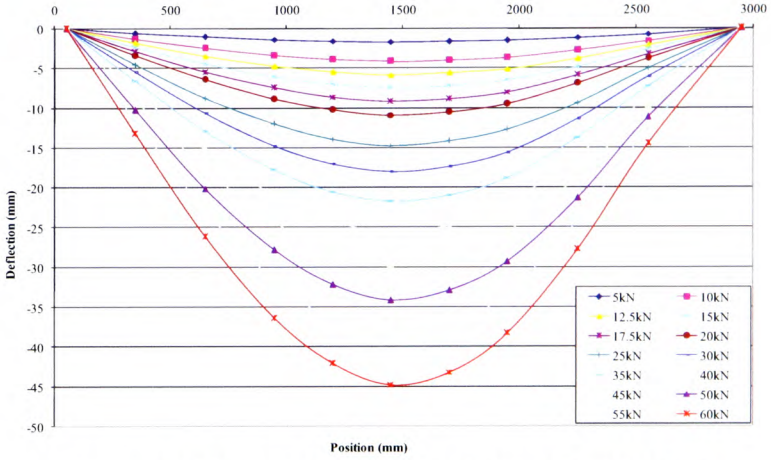

Figure 4.14(d) – Deflection profile for element 8SCP3

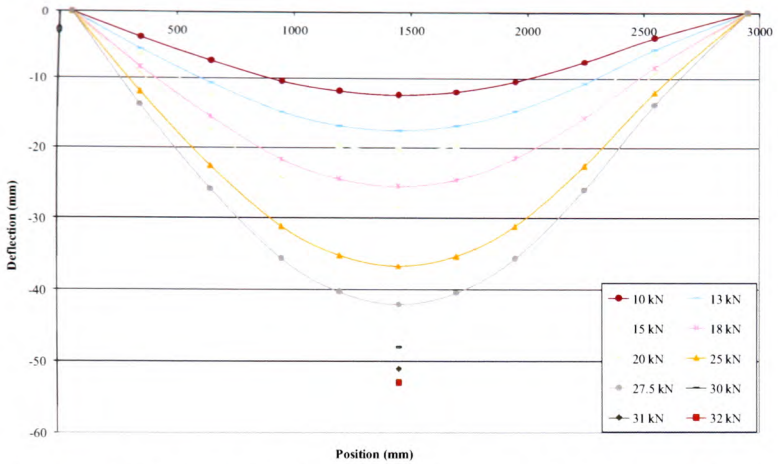

Figure 4.15(a) – Deflection profile for control element 12SCON

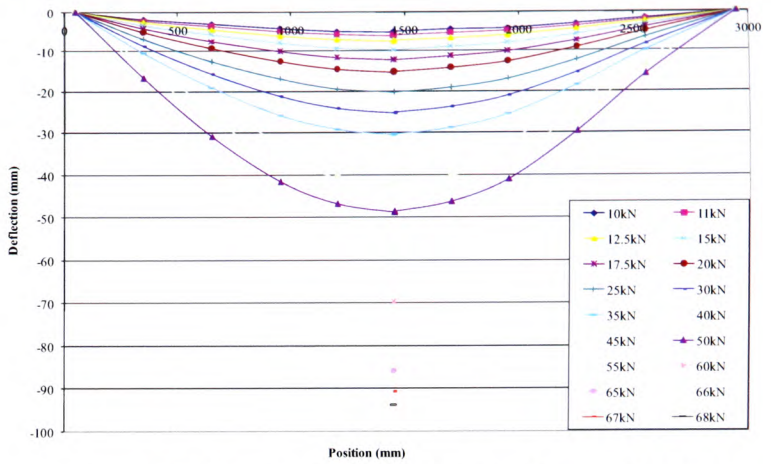

Figure 4.15(b) – Deflection profile for element 12SCF2

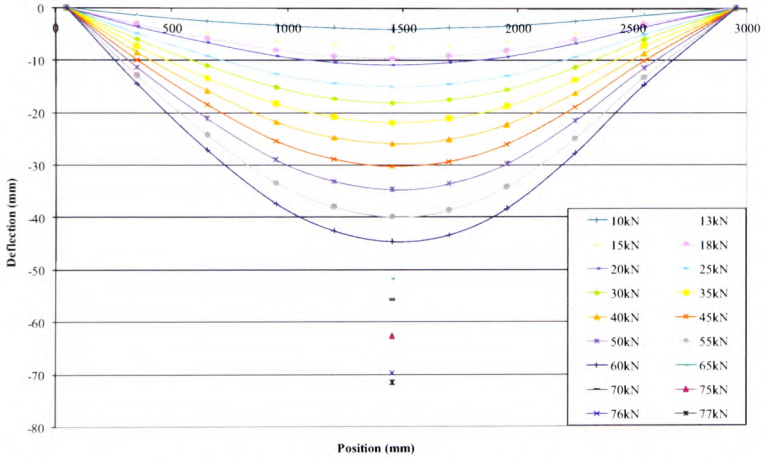

Figure 4.15(c) – Deflection profile for element 12SCF4

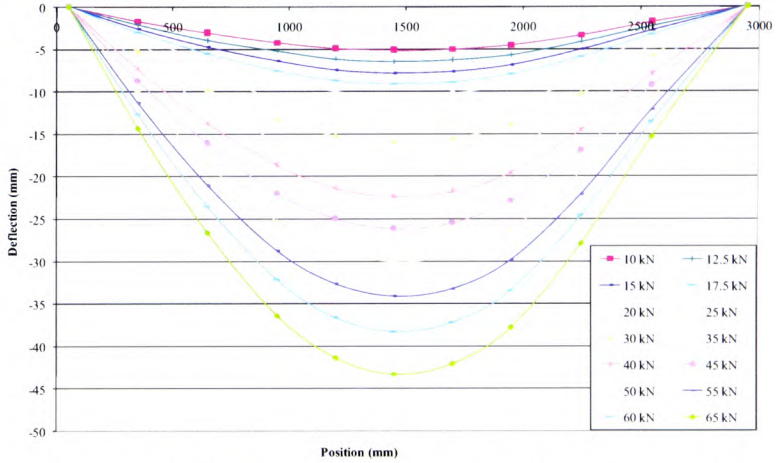

Figure 4.15(d) – Deflection profile for element 12SCP2

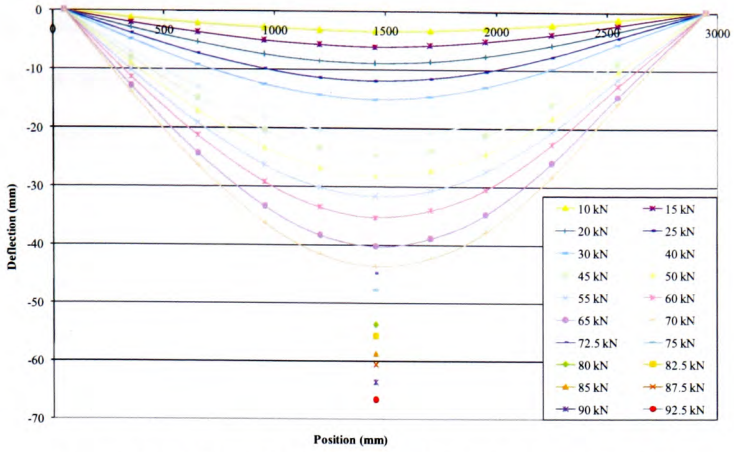

Figure 4.15(e) – Deflection profile for element 12SCP3

4.5 Load/strain relationship

The concrete surface strains in the Constant Moment Zone (CMZ) were recorded using the DEMEC system, as illustrated in Figures 3.14 and 3.15. The readings were subsequently input into Microsoft Excel and processed to produce a graphical representation of the Load/strain relationships, which are presented in the following sections.

4.5.1 ρ =0.50% - Ø 8mm reinforced beams

As can be seen from Figure 4.16(a), the tensile strain value near the bottom fibre of the control element, 8CON, was recorded at 3308 microstrain (με) at the failure load of 35kN, with the corresponding compressive strain at the top fibre recorded at -693 με.

For all the Ø8mm elements, the recorded tensile and compressive strains at failure were as shown in Table 4.2. The load/strain plots for the strengthened elements are presented in Figures 4.16(b), (c) and (d).

It can be seen from the results in Table 4.2 that the recorded compressive strain ranged between -693με and -2006με, even though the observed failure mode was steel-yielding followed by compressive failure of the concrete. It is likely that the internal steel yielded just after the strain values were recorded and the subsequent rotation resulted in localised crushing of the concrete in compression before the safety

trip switch engaged, which explains why concrete crushing was noted as part of the failure mechanism when compressive strains in the concrete were apparently lower than would be expected.

Table 4.2 – Compressive and tensile failure strains for ρ =0.50% - Ø8mm reinforced beams

Element	Failure strains ($\mu\varepsilon$)*		Failure load (kN)
	Compressive	Tensile	
8CON	-693	3308	35.0
8CF1	-893	3611	58.0
8CF2	-2006	5521	62.5
8CF3	-1177	3207	55.0

*Note that $1\mu\varepsilon = 1x10^{-6}\frac{mm}{mm}$ of strain

4.5.2 ρ =0.79% - Ø 10mm reinforced beams

The strengthened Ø10mm elements had recorded tensile and compressive strains at failure as shown in Table 4.3. Again, it is likely that the rotation in the element following yielding of the internal steel reinforcement, resulted in strains far exceeding those recorded before failure occurred, which resulted in localised concrete crushing.

In Figure 4.17(a) it is shown that, for the control element, the tensile strain value near the bottom fibre was recorded at 2990 microstrain (με) at a load of 50kN (approximately 90% of the failure load), with the corresponding compressive strain at the top fibre being recorded at -935 με.

Element 10CF1, with one layer of CFRP sheet, showed a significant increase in surface strain values from 55kN, approximately 90% of failure load, and, similarly, element 10CF2, with two layers of CFRP sheets, exhibited a dramatic increase in strains from 65kN, approximately 80% of failure load (see Figures 4.17 (b) and (c)).

This suggests a potential for ductile failure, which is not the case for more heavily strengthened elements, such as element 10CF3, which, as can be seen in Figure 4.17 (d), demonstrated a perfectly linear strain profile to failure.

The significantly higher strain values recorded at failure for element 10CF2 are because the element achieved higher ultimate loading than the other two strengthened elements. Element 10CF3 would have reached higher strain values at ultimate limit state had a premature tearing-off failure not occurred.

Table 4.3 – Compressive and tensile failure strains for ρ =0.79% - Ø10mm reinforced beams

Element	**Failure strains (με)**		**Failure load (kN)**
	Compressive	Tensile	
10CON	-935	2990	55.0
10CF1	-1603	4801	62.6
10CF2	-2194	5457	80.1
10CF3	-1484	3041	70.0

4.5.3 ρ =1.13% - Ø 12mm reinforced beams

As can be seen from Figures 4.18 (a) to (d), for the control element, the compressive strain value near the top fibre was -2424 microstrain (με) and the corresponding tensile strain near the bottom fibre was 3526 με at a load of 65kN. The strengthened 12mm reinforced elements had recorded tensile and compressive strains at failure as detailed in Table 4.4.

Even though the compressive concrete strains for all elements except 12CF3 are between -2125 με and -2325 με, the observed failure mode was concrete crushing; this can be seen in Figures 3.29 to 3.31. The reason for the low strain value at failure is likely due to the strain being recorded just prior to the initiation of element failure, which would have resulted in a rapid increase in compressive strain and, hence, compressive failure in the concrete.

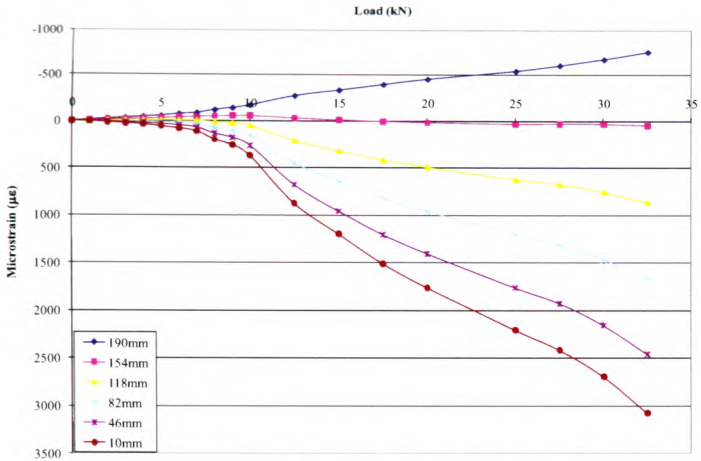

Figure 4.16(a) – Load/Strain graph for control element 8CON

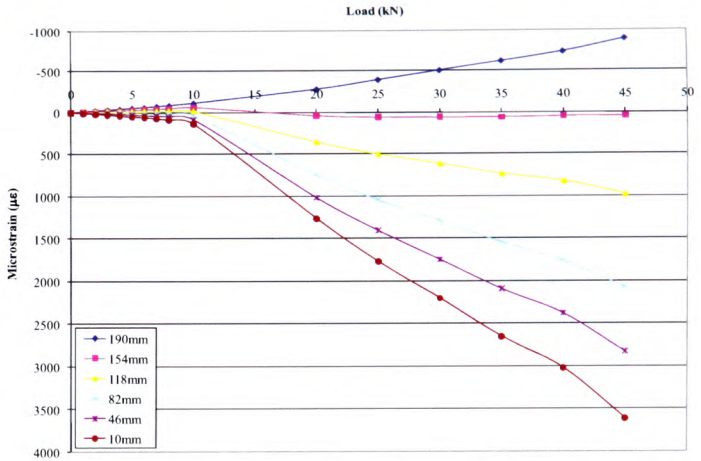

Figure 4.16(b) – Load/Strain graph for element 8CF1

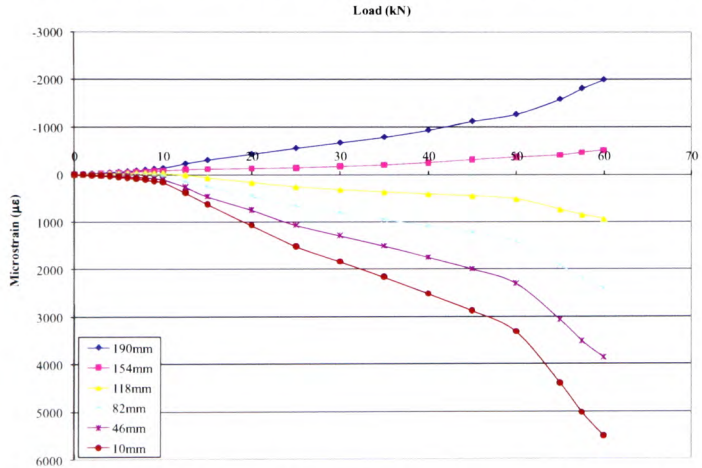

Figure 4.16(c) – Load/Strain graph for element 8CF2

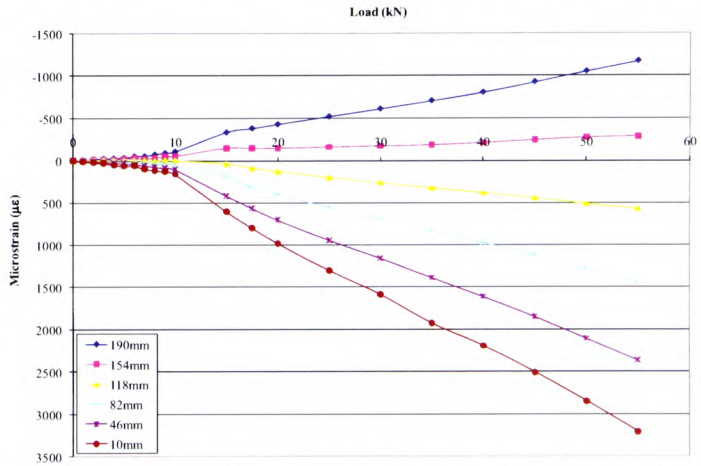

Figure 4.16(d) – Load/Strain graph for element 8CF3

Table 4.4 Compressive and tensile failure strains for ρ =1.13% - Ø12mm reinforced beams

Element	Failure strains (με)		Failure load (kN)
	Compressive	Tensile	
12CON	-2424	3526	65.0
12CF1	-2125	3134	78.2
12CF2	-2325	3147	85.0
12CF3	-3534	3498	84.1

4.5.4 ρ =2.01% - Ø 16mm reinforced beams

Problems with the recording equipment resulted in the surface strain data for the 16mm reinforced beams becoming corrupted and, consequently, it is not possible to produce strain against load plots for the elements in this set.

4.5.5 ρ =1.13% - Ø 12mm doubly-reinforced beams

For the doubly-reinforced control element, the compressive strain value near the top fibre was -2424 microstrain (με) and the corresponding tensile strain near the bottom fibre was 3526 με at a load of 65kN. Again, as with other elements in the experimental programme, it is likely that the rotation in the element following yielding of the internal steel reinforcement, resulted in strains far exceeding those recorded before failure occurred, which resulted in observed localised concrete crushing.

The strengthened 12mm reinforced elements had recorded tensile and compressive strains at failure as shown in Table 4.5.

The element strengthened with 3 layers of CFRP sheet displayed extremely linear strain behaviour up to failure, indicating a distinct lack of ductility in the structural system. All these points are illustrated in Figures 4.19 (a) to (d).

Table 4.5 Compressive and tensile failure strains for ρ =1.13% - Ø12mm doubly-reinforced beams

Element	Failure strains (με)		Failure load (kN)
	Compressive	Tensile	
12DCON	-2424	3526	65.0
12DCF1	-2153	6273	90.0
12DCF2	-1793	4288	95.0
12DCF3	-1595	2934	92.0

4.5.6 ρ =0.40% - Ø 8mm reinforced slabs

For the 8mm reinforced control element, the compressive strain value recorded near the top fibre was -713 microstrain (με) and the corresponding tensile strain near the bottom fibre was 2950 με at a load of 16kN.

The strengthened elements had recorded tensile and compressive strains at failure as shown in Table 4.6 and illustrated in Figures 4.20 (a) to (d):

Table 4.6 Compressive and tensile failure strains for ρ =0.40% - Ø8mm reinforced slabs

Element	Failure strains (με)		Failure load (kN)
	Compressive	Tensile	
8SCON	-713	2950	16.0
8SCF2	-1253	2775	55.0
8SCP2	-2248	3767	65.0
8SCP3	-1930	2462	60.0

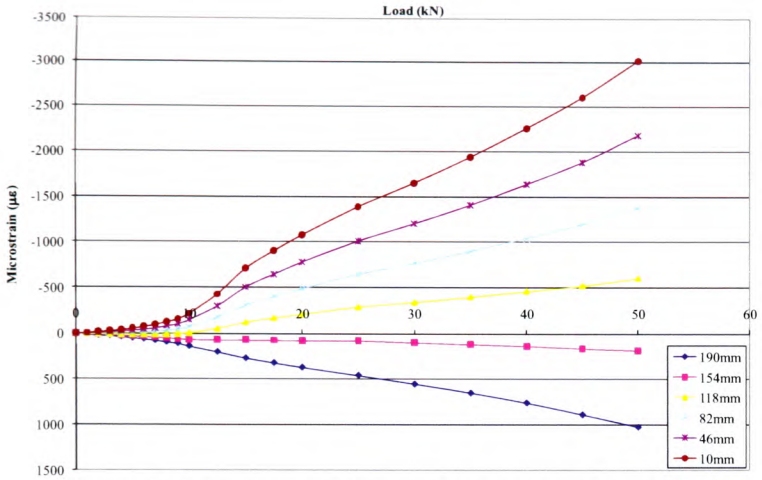

Figure 4.17(a) – Load/Strain graph for control element 10CON

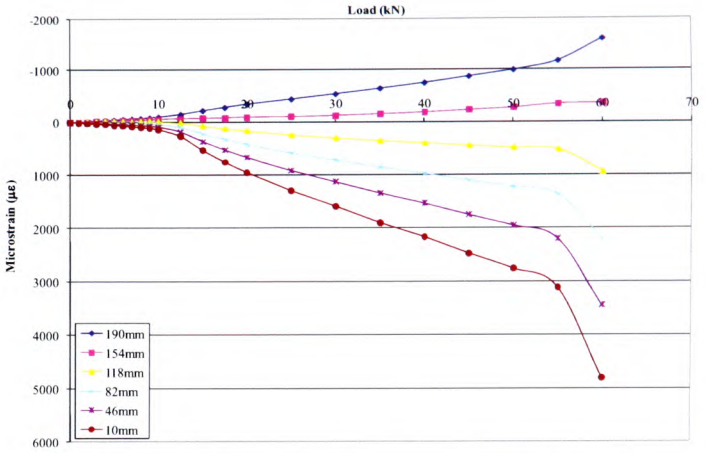

Figure 4.17(b) – Load/Strain graph for element 10CF1

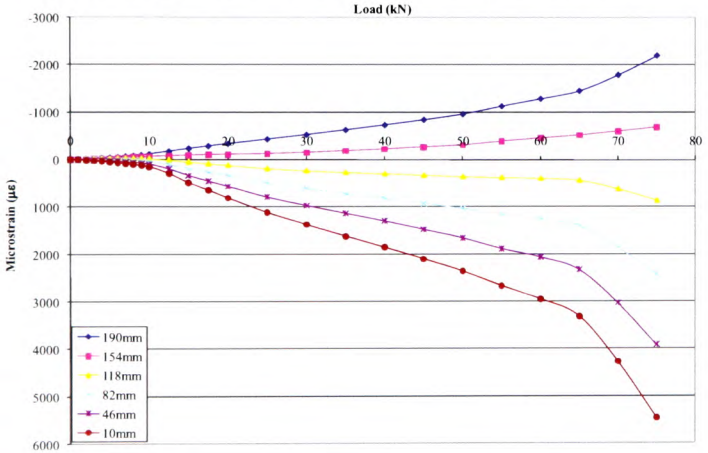

Figure 4.17(c) – Load/Strain graph for element 10CF2

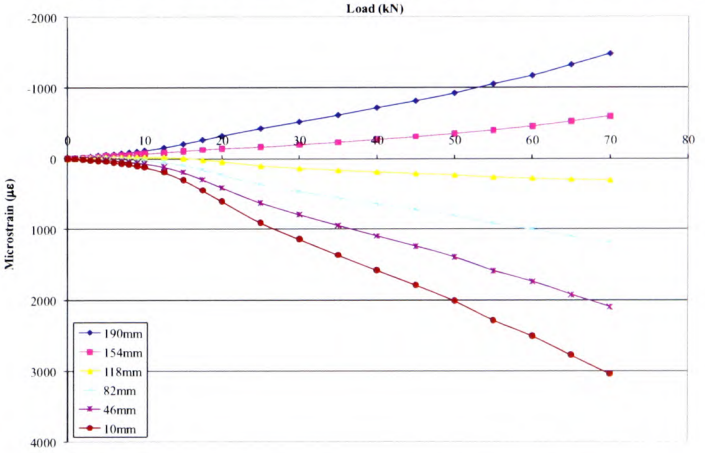

Figure 4.17(d) – Load/Strain graph for element 10CF3

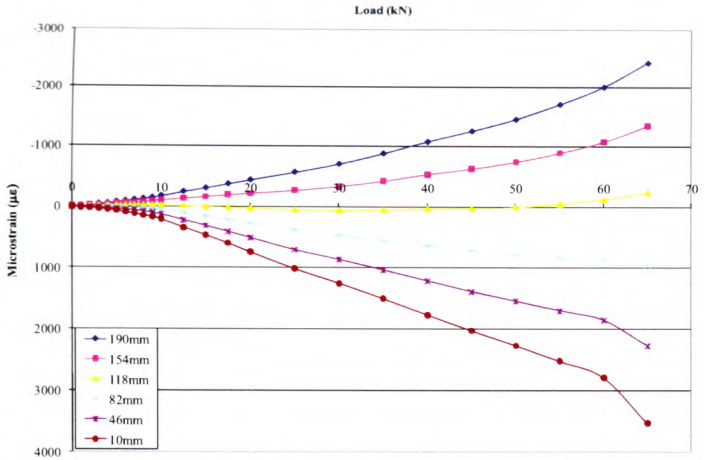

Figure 4.18(a) – Load/Strain graph for control element 12CON

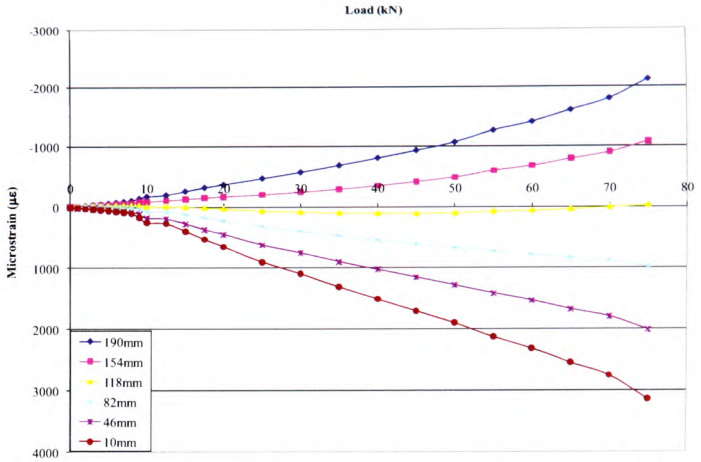

Figure 4.18(b) – Load/Strain graph for element 12CF1

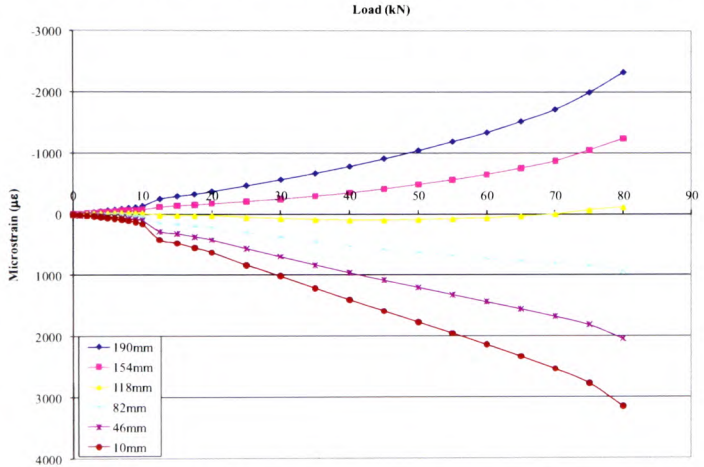

Figure 4.18(c) – Load/Strain graph for element 12CF2

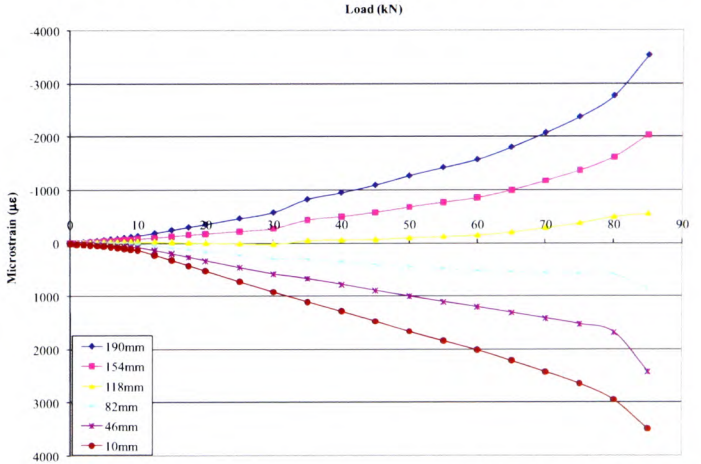

Figure 4.18(d) – Load/Strain graph for element 12CF3

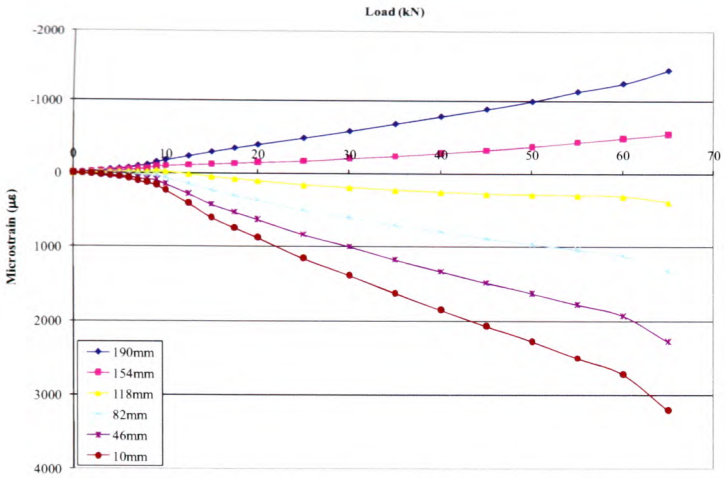

Figure 4.19(a) – Load/Strain graph for control element 12DCON

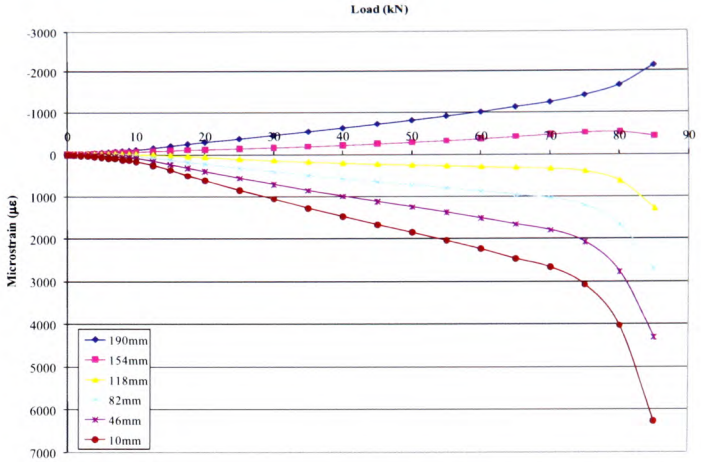

Figure 4.19(b) – Load/Strain graph for element 12DCF1

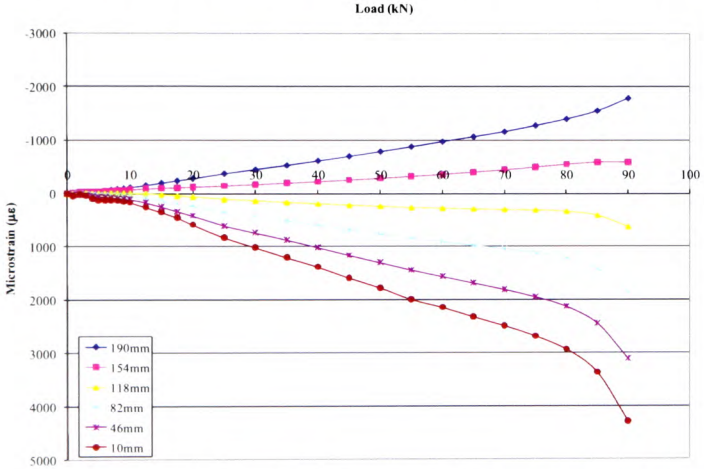

Figure 4.19(c) – Load/Strain graph for element 12DCF2

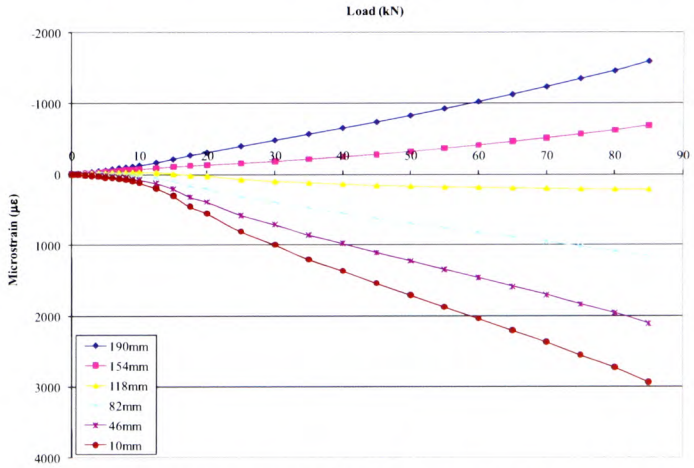

Figure 4.19(d) – Load/Strain graph for element 12DCF3

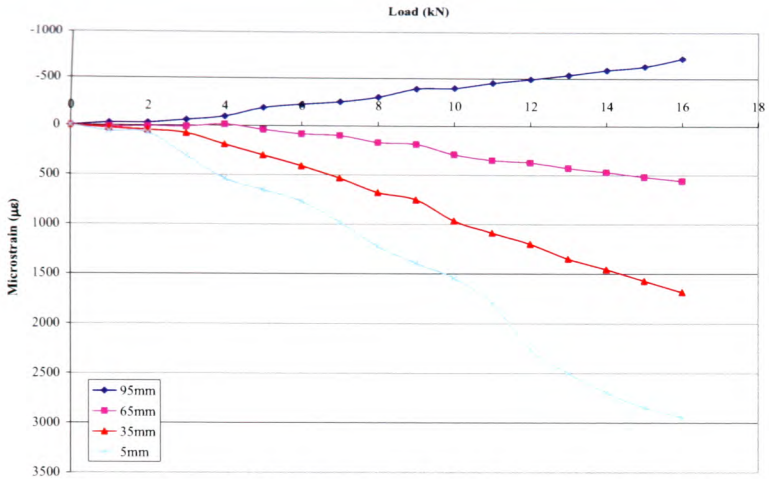

Figure 4.20(a) – Load/Strain graph for control element 8SCON

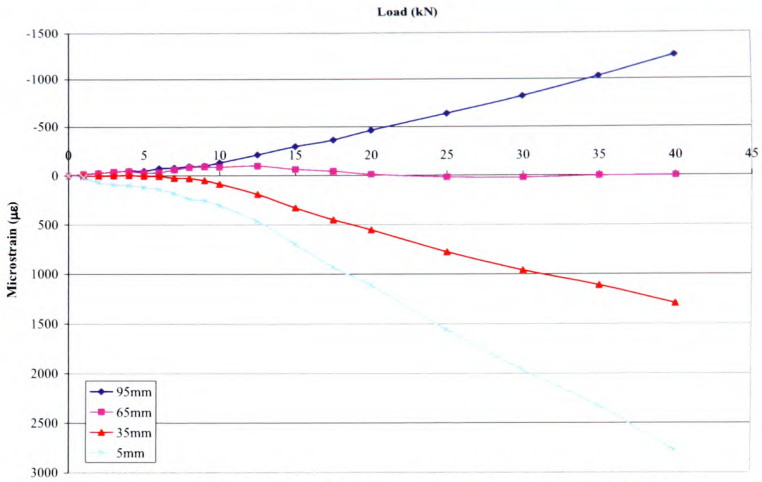

Figure 4.20(b) – Load/Strain graph for element 8SCF2

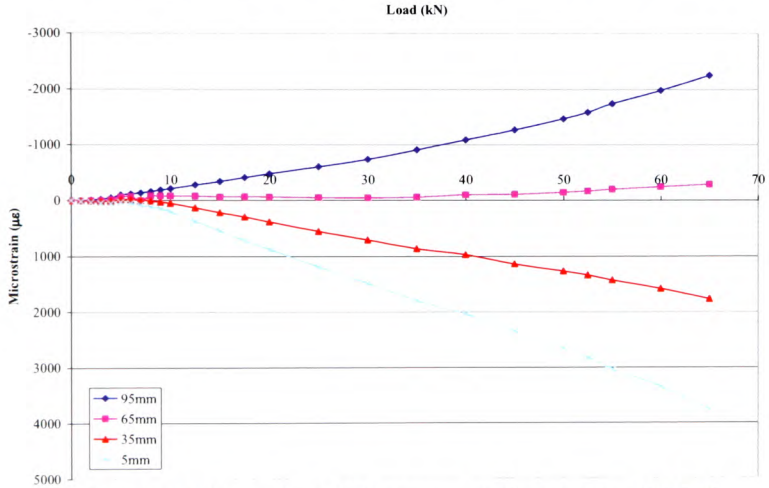

Figure 4.20(c) – Load/Strain graph for element 8SCP2

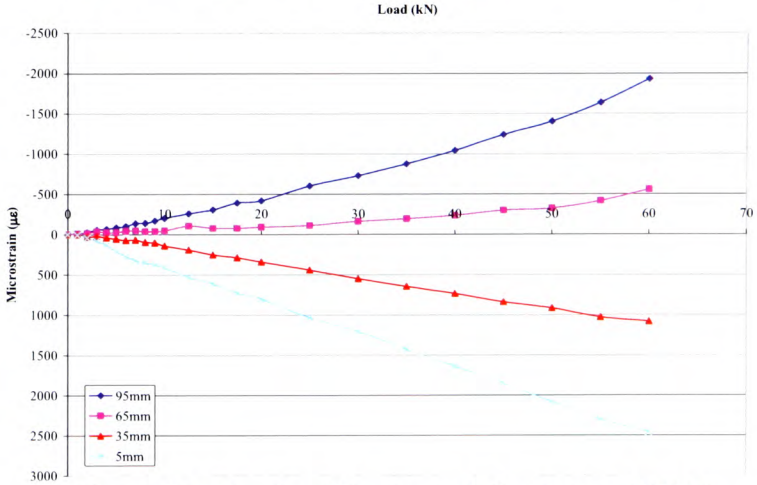

Figure 4.20(d) – Load/Strain graph for element 8SCP3

4.5.7 ρ =0.91% - Ø 12mm reinforced slabs

For the 12mm reinforced control element, the compressive strain value recorded near the top fibre was -1953 microstrain (με) and the corresponding strain near the bottom fibre was 3928 με at a load of 32 kN.

The strengthened elements had recorded tensile and compressive strains at failure as shown in Table 4.7 and illustrated in Figures 4.21 (a) to (e):

Table 4.7 Compressive and tensile failure strains for ρ =0.91% - Ø12mm reinforced slabs

Element	Failure strains (με)		Failure load (kN)
	Compressive	Tensile	
12SCON	-1953	3928	32.0
12SCF2	-3703	4707	68.0
12SCF4	-5038	3829	77.0
12SCP2	-2496	3429	75.0
12SCP3	-2999	2954	92.5

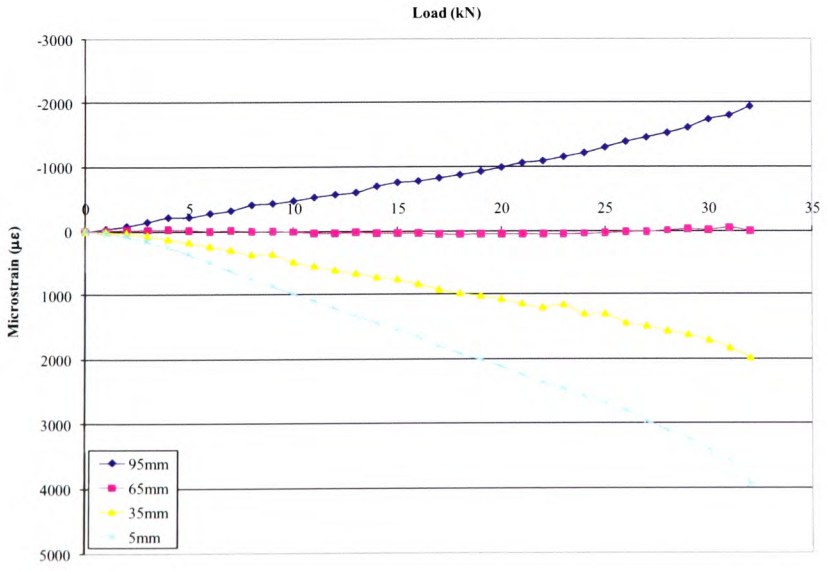

Figure 4.21(a) – Load/Strain graph for control element 12SCON

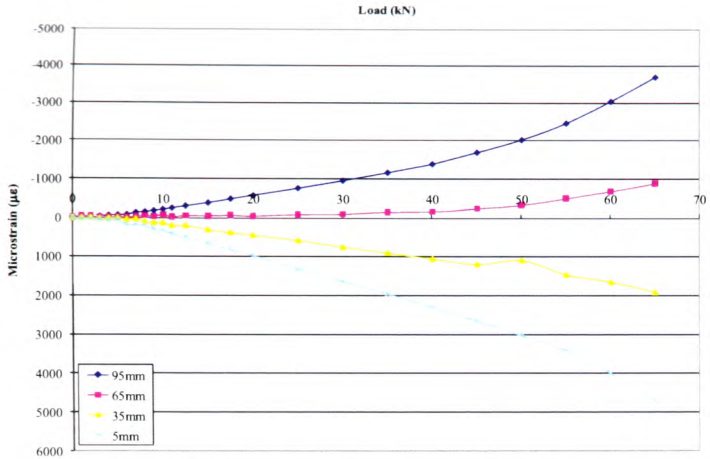

Figure 4.21(b) – Load/Strain graph for element 12SCF2

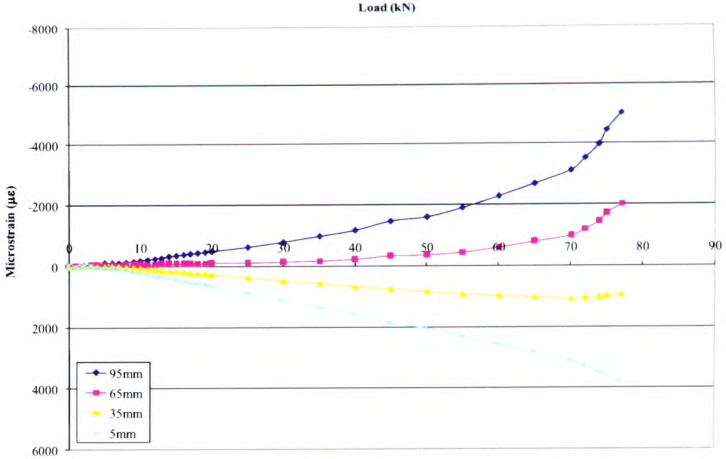

Figure 4.21(c) – Load/Strain graph for element 12SCF4

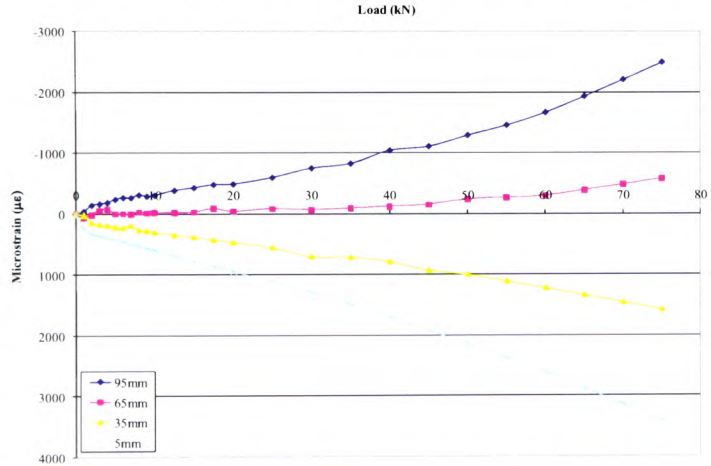

Figure 4.21(d) – Load/Strain graph for element 12SCP2

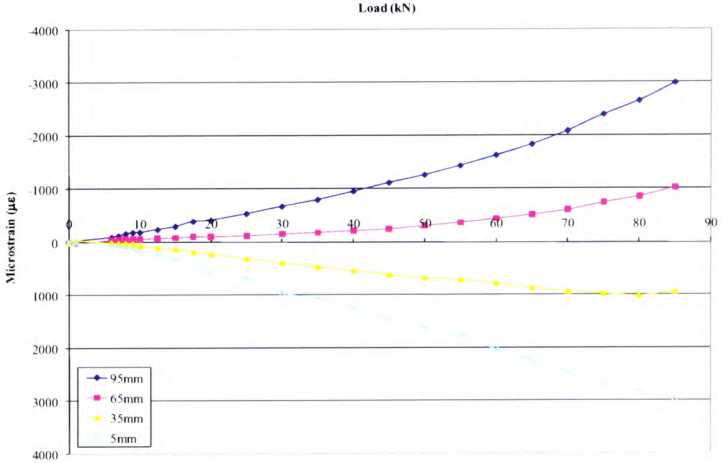

Figure 4.21(e) – Load/Strain graph for element 12SCP3

4.6 Strain Distribution

The concrete surface strains in the Constant Moment Zone (CMZ) were recorded using the DEMEC system, as detailed in Section 3.4.2 and illustrated in Figures 3.14 and 3.15. The readings were input into Microsoft Excel and processed to produce a graphical representation of the increase in strain with increased loading. As six zones were used for each element (three on either side), the strains presented are the averages for all zones.

Figure 4.22 displays the linear strain profile that was observed for all the elements across the element depth. This is demonstrated in the element strain profiles.

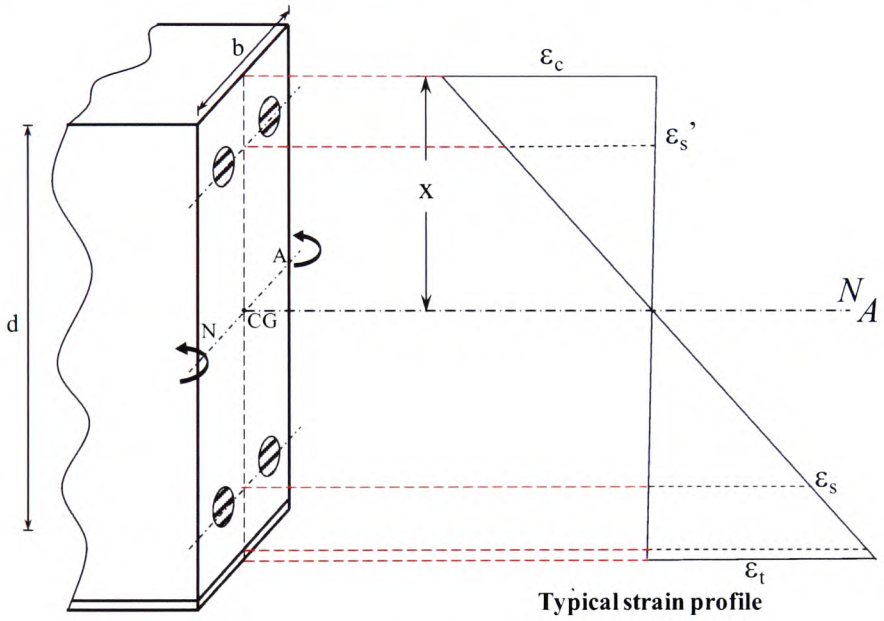

Figure 4.22 – Strain profile across element depth

4.6.1 ρ =0.50% - ∅ 8mm reinforced beams

As can be seen from 4.23(a), the readings fluctuated slightly at low loading levels (up to 10kN) but became perfectly linear as the loading increased past this level. This indicates that the plane section remained plane during the loading process for both the normally reinforced element, 8CON, and the strengthened elements, with each displaying linear strain variation up to failure. Figures 4.23(b) to (e) show the strain results for the 8mm reinforced elements, from 10kN to element failure.

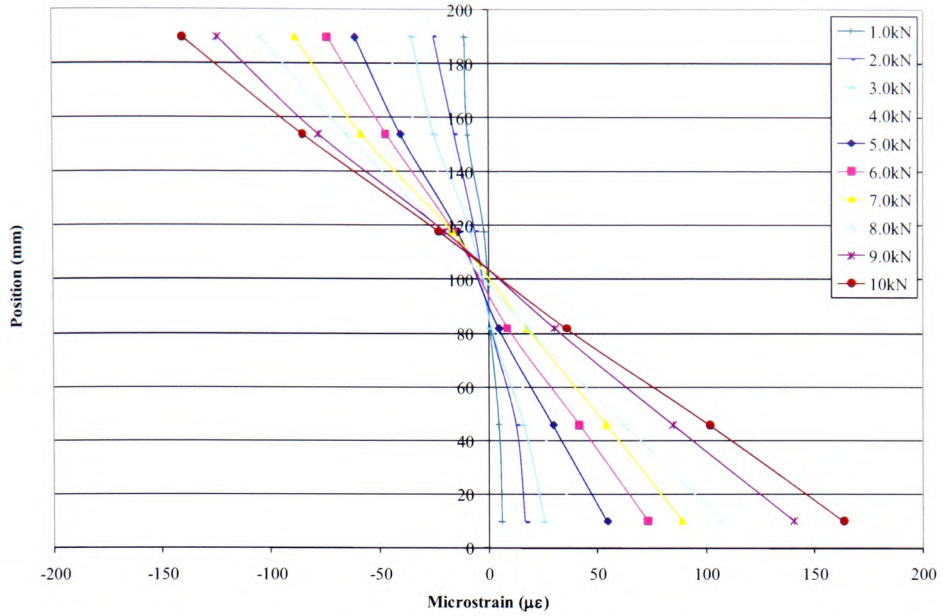

Figure 4.23(a) – Strain profile at mid-span for control element 8CON, up to 10kN

4.6.2 ρ =0.79% - ∅ 10mm reinforced beams

Figures 4.24 (a) to (e) show the strain data for the 10mm reinforced elements and, as can be seen, the readings fluctuated slightly at low loading levels in a similar manner to the 8mm reinforced elements but became linear as the loading increased, indicating that the plane section remained plane during the loading process for all elements.

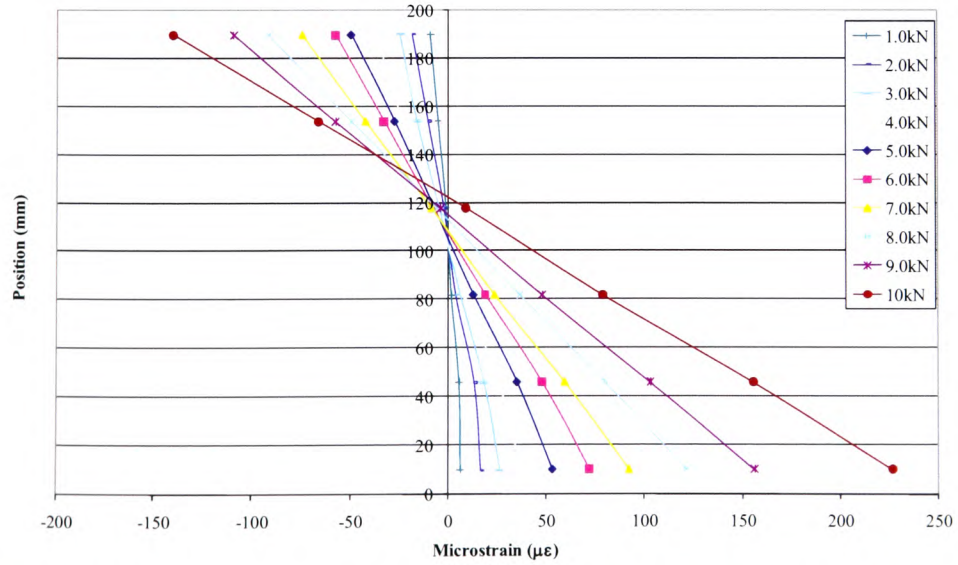

Figure 4.24(a) – Strain profile at mid-span for control element 10CON, up to 10kN

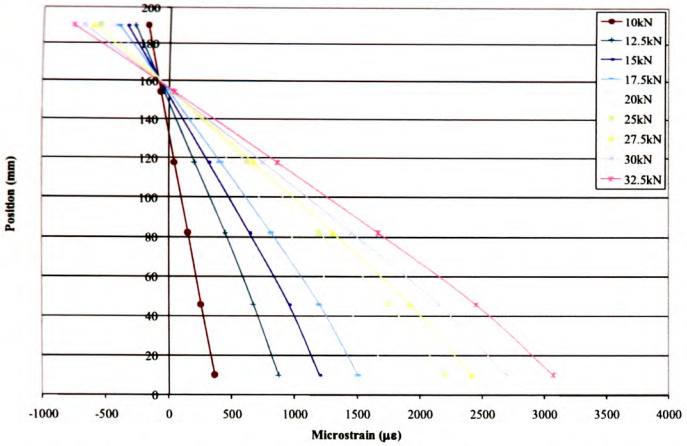

Figure 4.23(b) – Strain profile at mid-span for control element 8CON, 10kN to failure

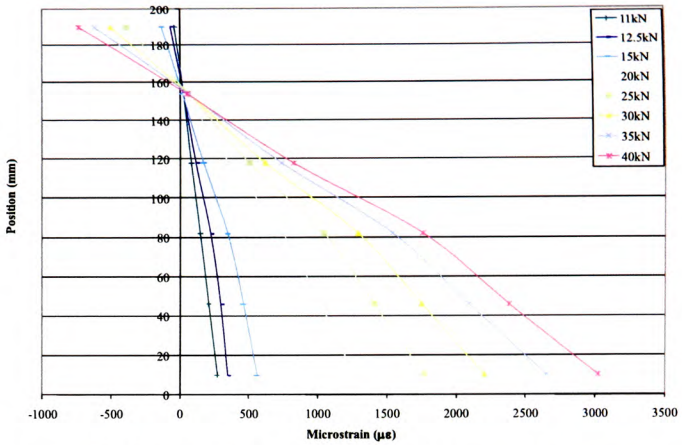

Figure 4.23(c) – Strain profile at mid-span for element 8CF1, 10kN to failure

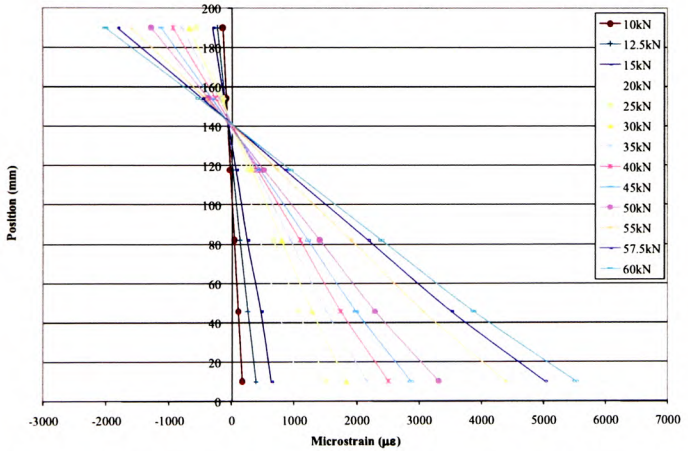

Figure 4.23(d) – Strain profile at mid-span for element 8CF2, 10kN to failure

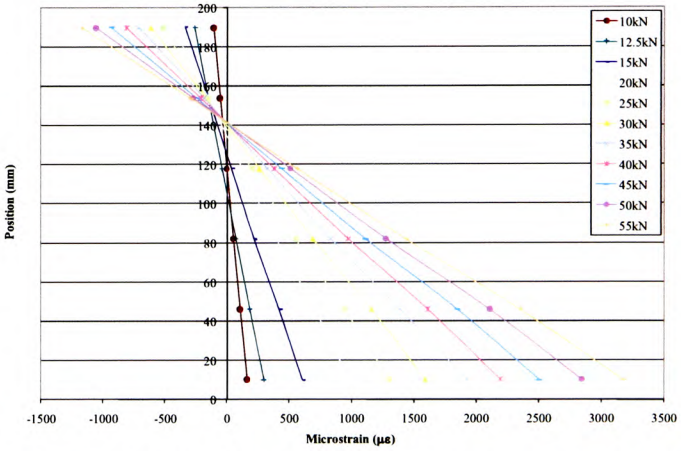

Figure 4.23(e) – Strain profile at mid-span for element 8CF3, 10kN to failure

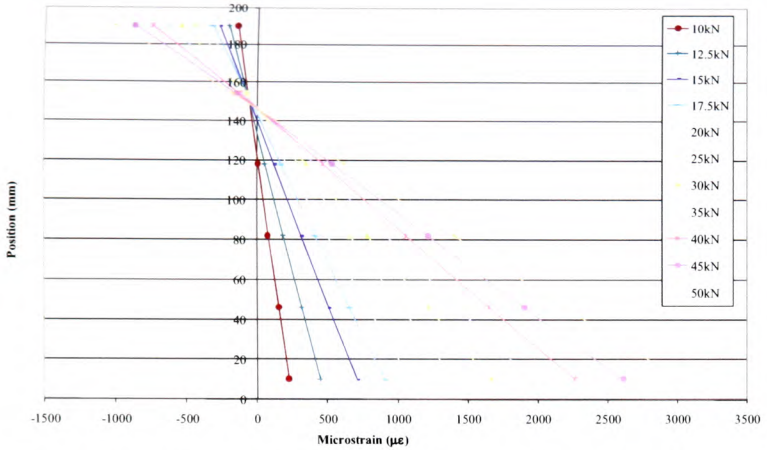

Figure 4.24(b) – Strain profile at mid-span for control element 10CON, 10kN to failure

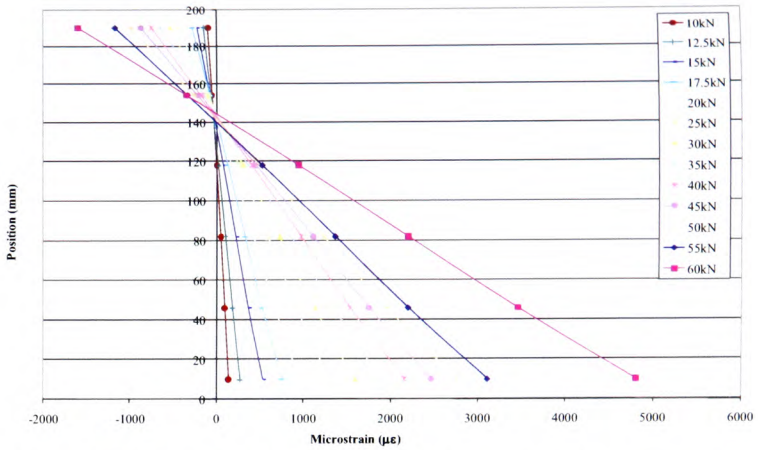

Figure 4.24(c) – Strain profile at mid-span for element 10CF1, 10kN to failure

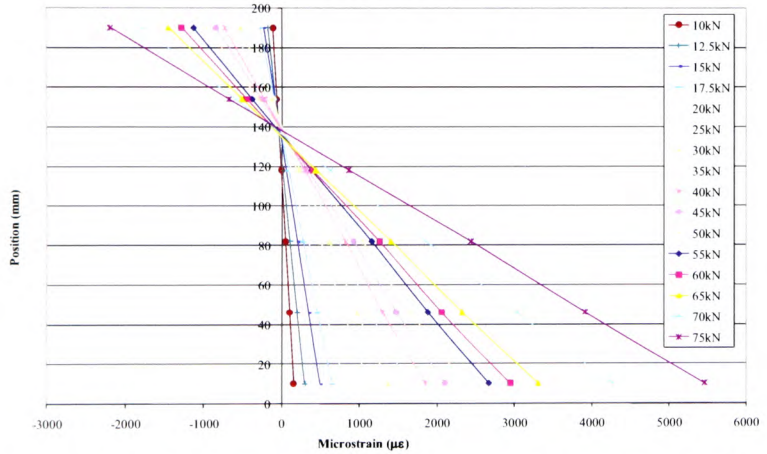

Figure 4.24(d) – Strain profile at mid-span for element 10CF2, 10kN to failure

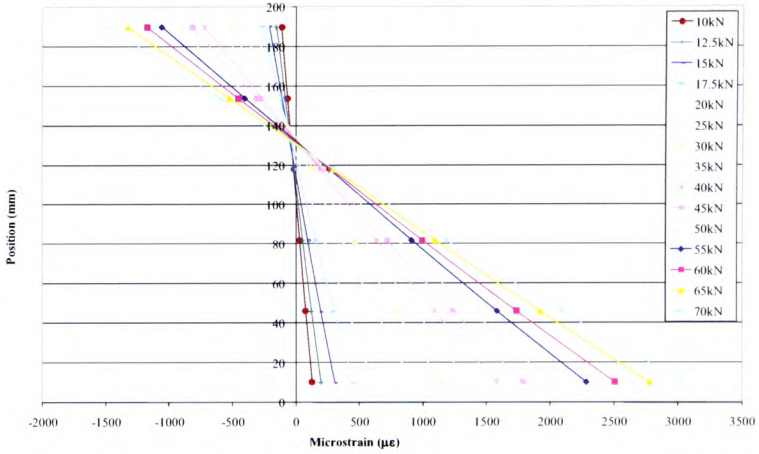

Figure 4.24(e) – Strain profile at mid-span for element 10CF3, 10kN to failure

4.6.3 ρ =1.13% - ∅ 12mm reinforced beams

The strain results for the ∅12mm reinforced elements are presented in Figures 4.25 (a) to (e). As has been mentioned previously, strain readings fluctuate slightly at low loading levels but became linear as loading progresses to failure, indicating that the plane section remained plane during the loading process for all elements.

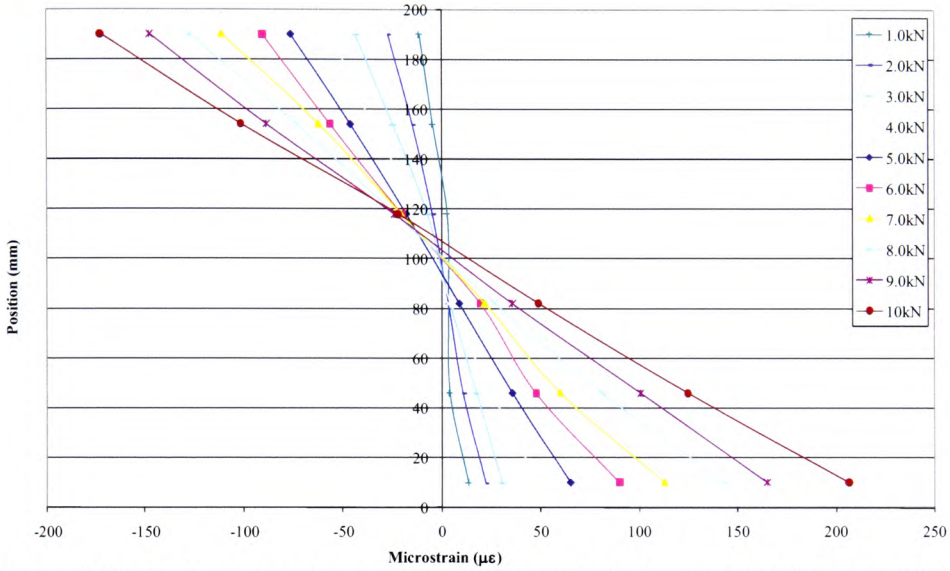

Figure 4.25(a) – Strain profile at mid-span for control element 12CON, up to 10kN

4.6.4 ρ =2.01% - ∅ 16mm reinforced beams

A fault with the recording equipment meant that the surface strains recorded for all the 16mm elements were corrupted and, therefore, unusable. Consequently, strain profiles were created from the electronic strain gauges fixed to the extreme fibre surfaces of the element, and these are presented in Figures 4.26(a) to (d).

4.6.5 ρ =1.13% - ∅ 12mm doubly-reinforced beams

The strain results for the 12mm doubly-reinforced elements are shown in Figures 4.27 (a) to (e). As before, strain readings fluctuated slightly at low loading levels but became linear as loading increased, indicating that the plane section remained plane during the loading process for all elements.

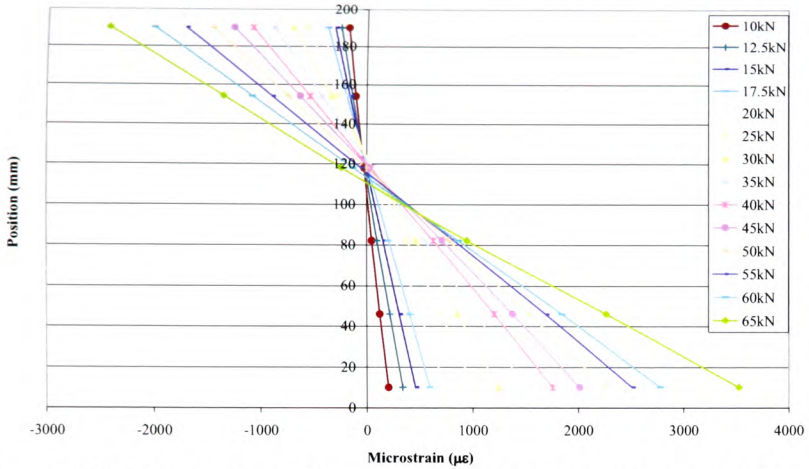

Figure 4.25(b) – Strain profile at mid-span for control element 12CON, 10kN to failure

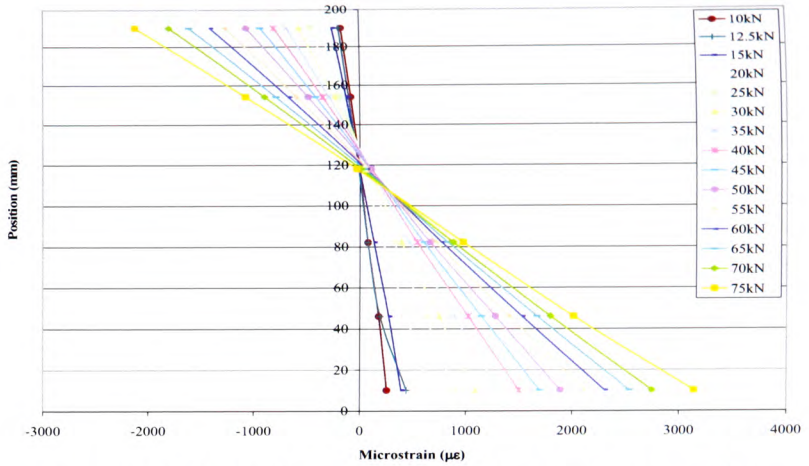

Figure 4.25(c) – Strain profile at mid-span for element 12CF1, 10kN to failure

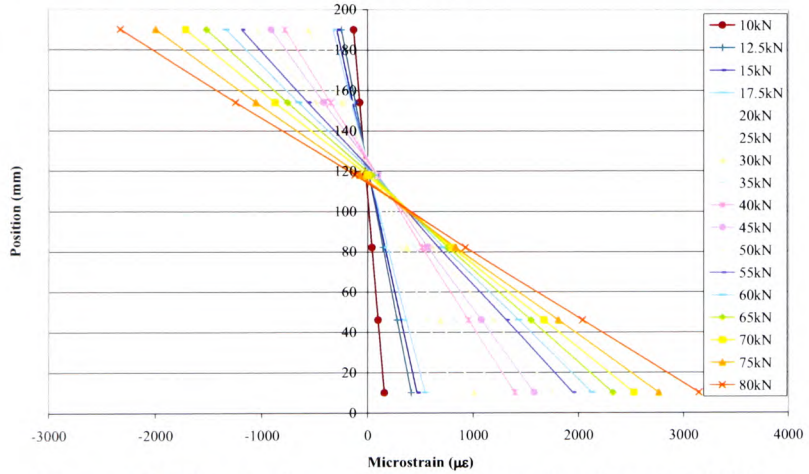

Figure 4.25(d) – Strain profile at mid-span for element 12CF2, 10kN to failure

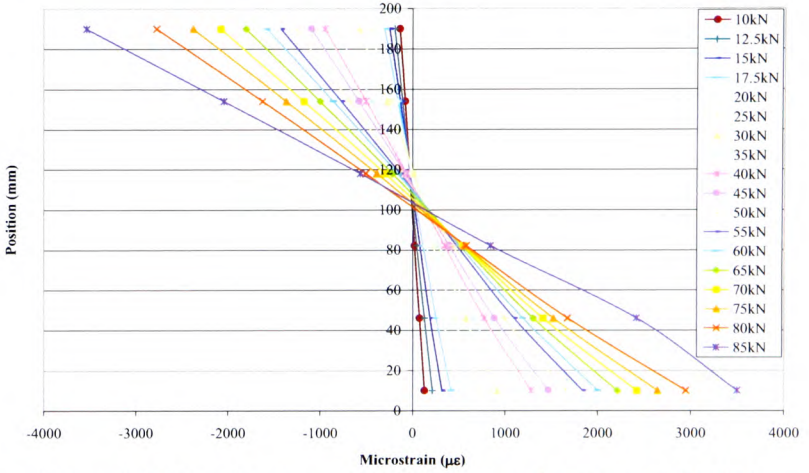

Figure 4.25(e) – Strain profile at mid-span for element 12CF3, 10kN to failure

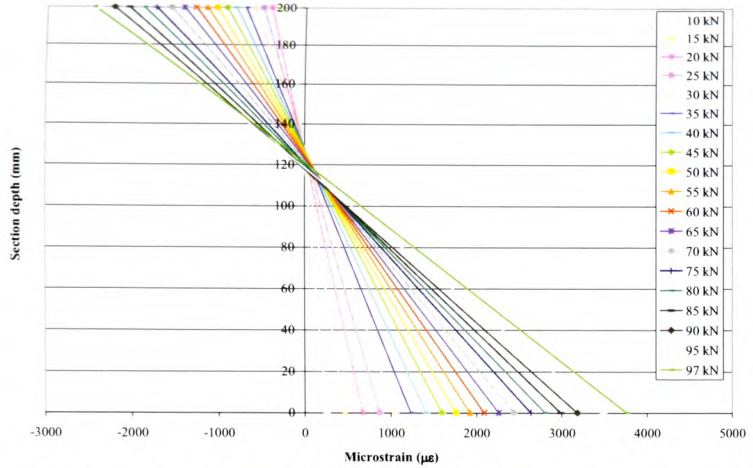

Figure 4.26(a) – Strain profile at mid-span for control element 16CON, 10kN to failure

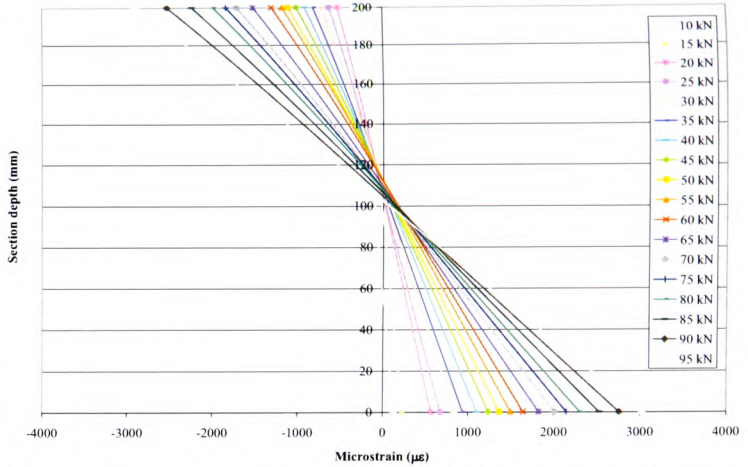

Figure 4.26(b) – Strain profile at mid-span for element 16CF1, 10kN to failure

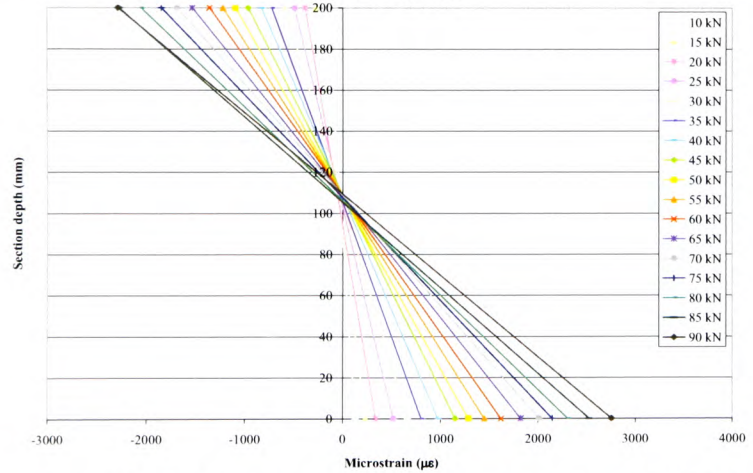

Figure 4.26(c) – Strain profile at mid-span for element 16CF2, 10kN to failure

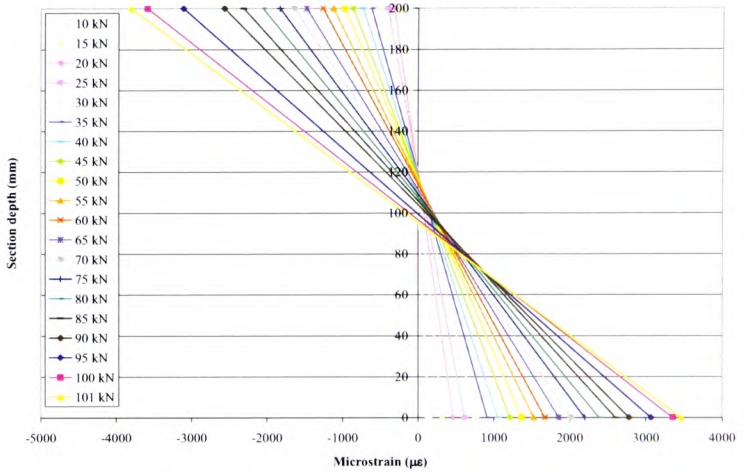

Figure 4.26(d) – Strain profile at mid-span for element 16CF3, 10kN to failure

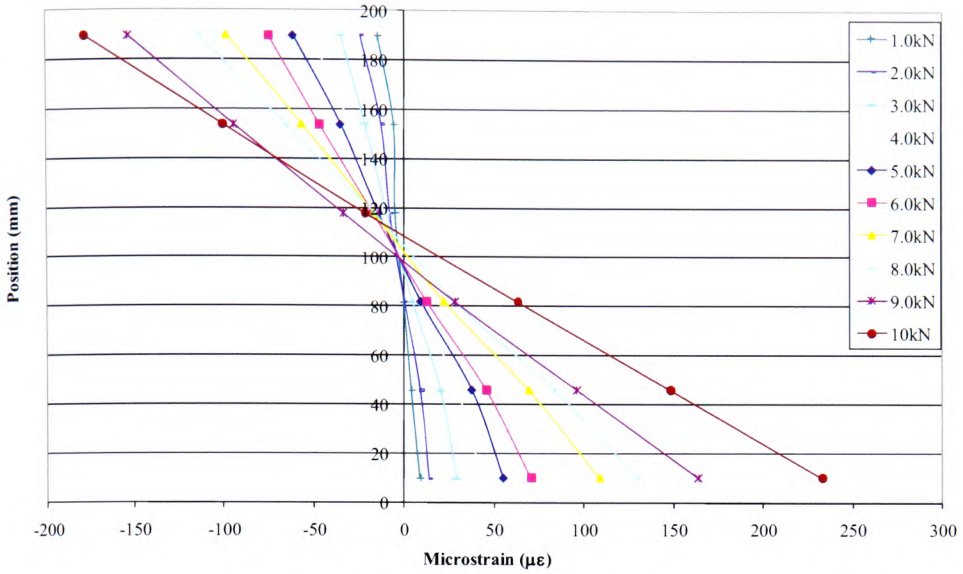

Figure 4.27(a) – Strain profile at mid-span for control element 12DCON, up to 10kN

4.6.6 ρ =0.40% - ∅ 8mm reinforced slabs

Figures 4.28(a) to (e) show the strain profiles for 8SCON, 8SCF2, 8SCP2 and 8SCP3 respectively. As with other elements in the experimental programme, it can be seen that the strain profiles remained linear throughout the loading cycle.

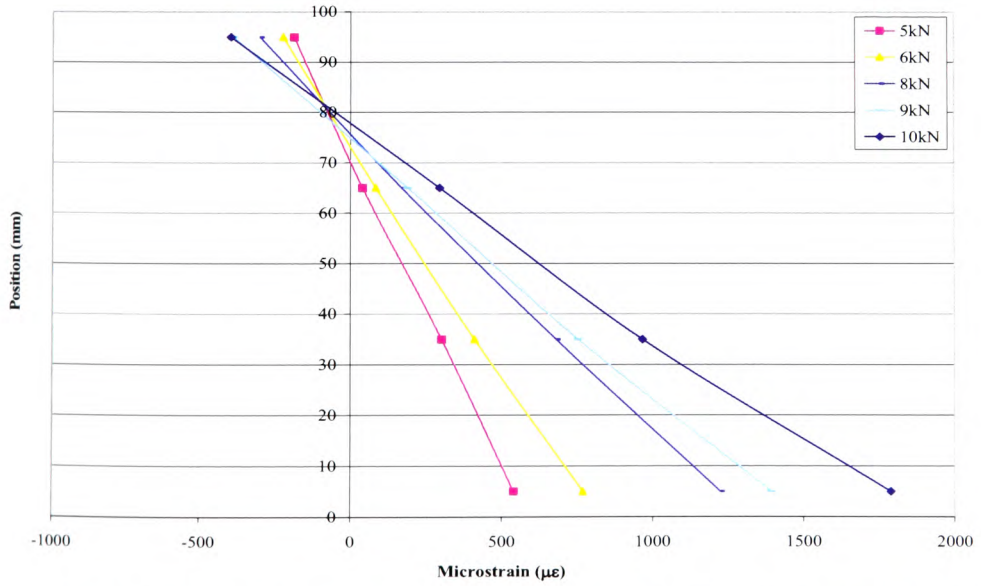

Figure 4.28(a) – Strain profile at mid-span for control element 8SCON, up to 10kN

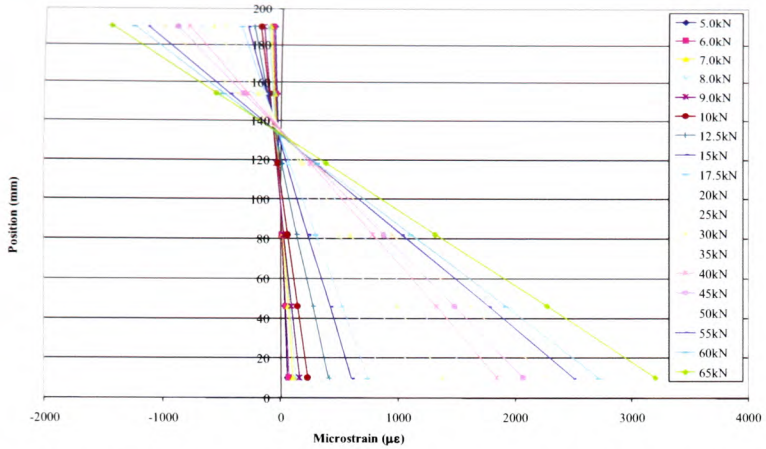

Figure 4.27(b) – Strain profile at mid-span for control element 12DCON, 5kN to failure

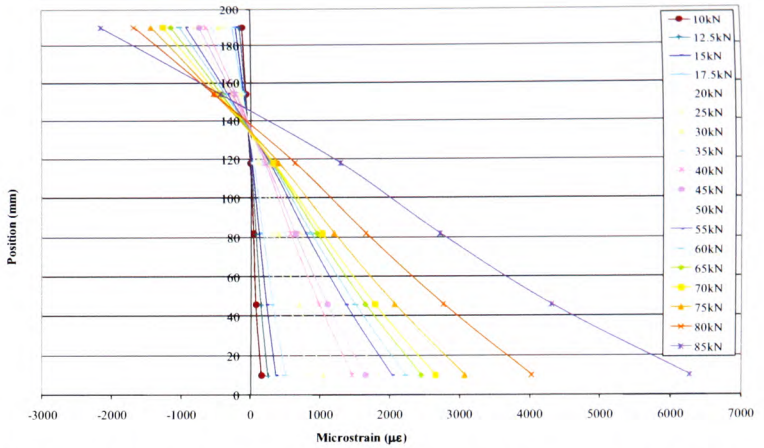

Figure 4.27(c) – Strain profile at mid-span for element 12DCF1, 10kN to failure

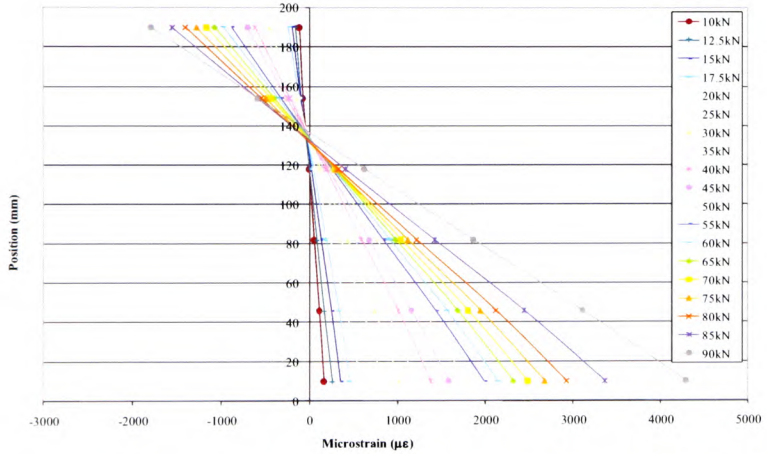

Figure 4.27(d) – Strain profile at mid-span for element 12DCF2, 10kN to failure

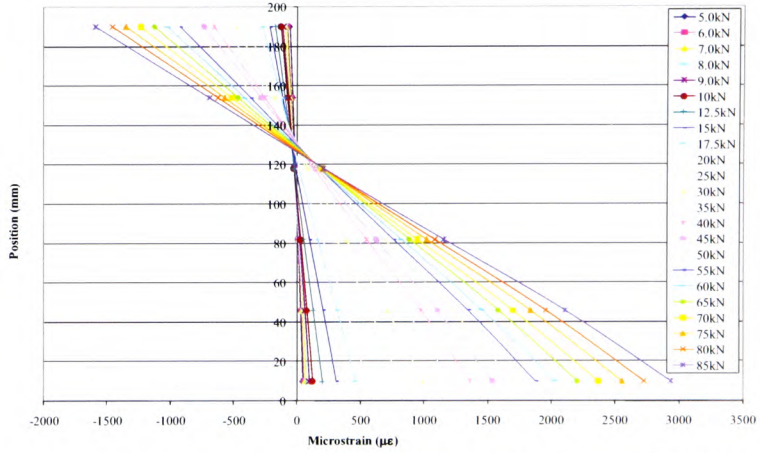

Figure 4.27(e) – Strain profile at mid-span for element 12DCF3, 5kN to failure

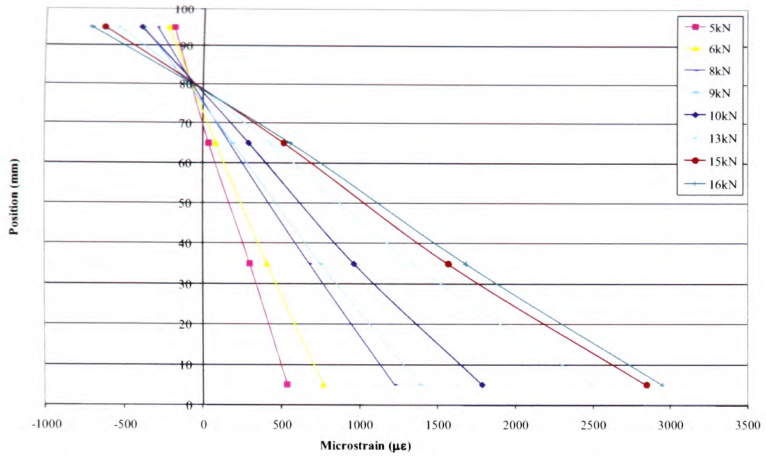

Figure 4.28(b) – Strain profile at mid-span for control element 8SCON, 5kN to failure

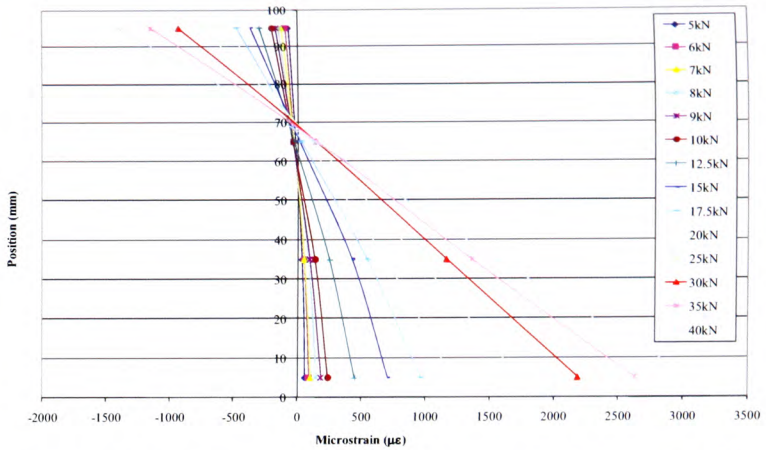

Figure 4.28(c) – Strain profile at mid-span for element 8SCF2, 5kN to failure

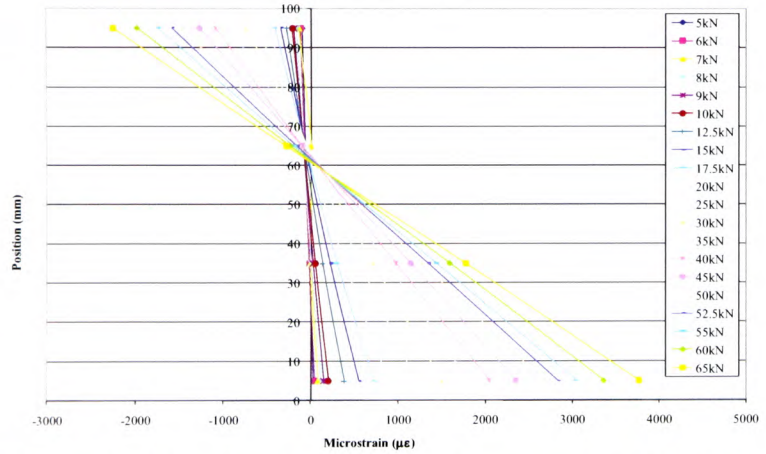

Figure 4.28(d) – Strain profile at mid-span for element 8SCP2, 5kN to failure

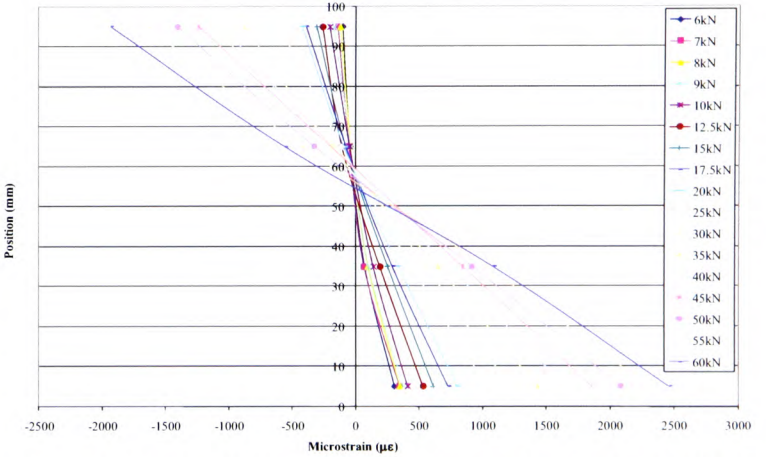

Figure 4.28(e) – Strain profile at mid-span for element 8SCP3, 6kN to failure

4.6.7 ρ =0.91% - ∅ 12mm reinforced slabs

Presented in Figures 4.29 (a) to (f) are the strain profiles for 12SCON, 12SCF2, 12SCF4, 12SCP2 and 12SCP3 respectively. As with all other tested elements, it can be seen that the strain profiles remained linear throughout the loading cycle to failure.

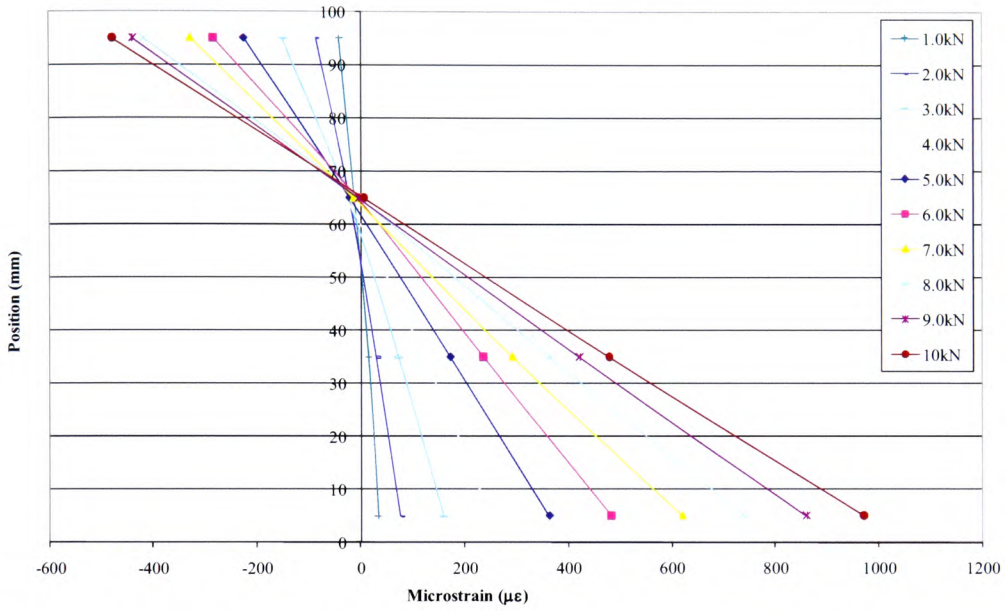

Figure 4.29(a) – Strain profile at mid-span for control element 12SCON, up to 10kN

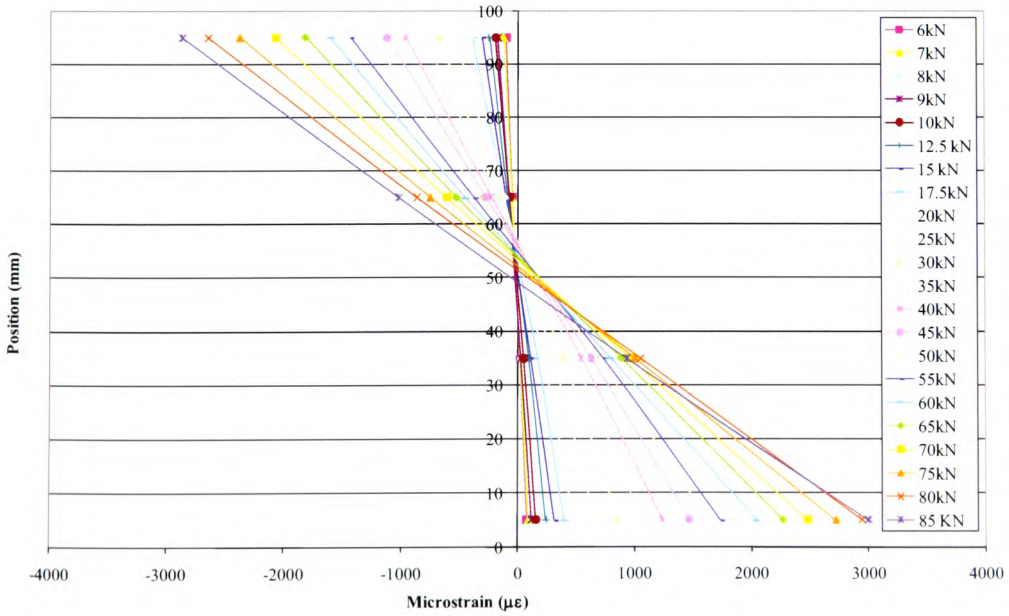

Figure 4.29 (b) – Strain profile at mid-span for element 12SCP3, 6kN to failure

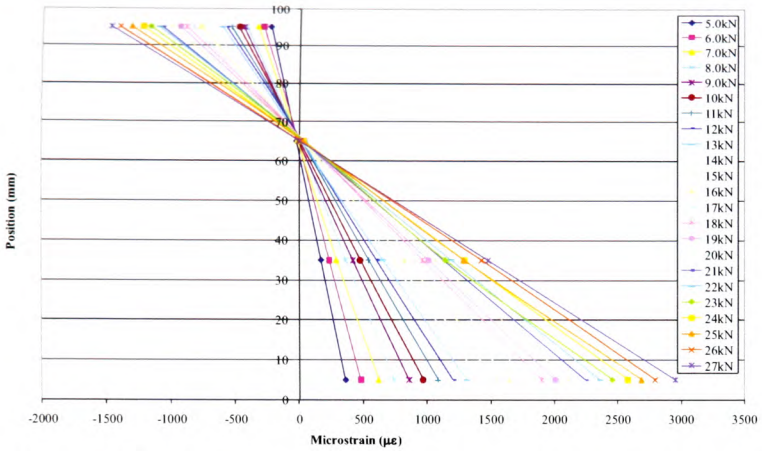

Figure 4.29(c) – Strain profile at mid-span for control element 12SCON, 5kN to failure

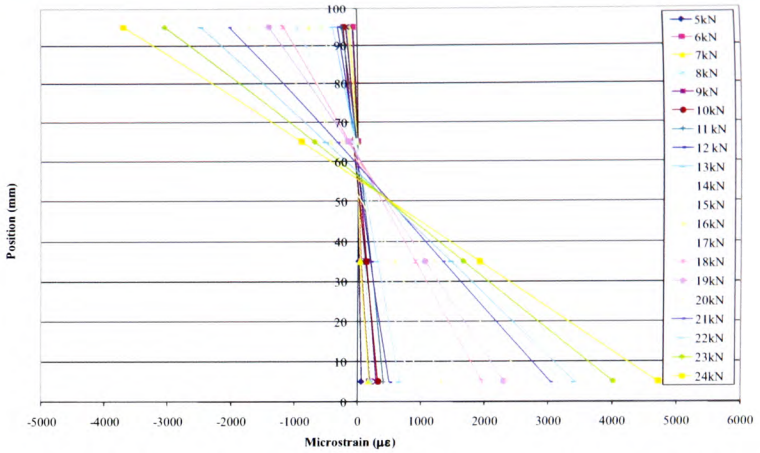

Figure 4.29(d) – Strain profile at mid-span for element 12SCF2, 5kN to failure

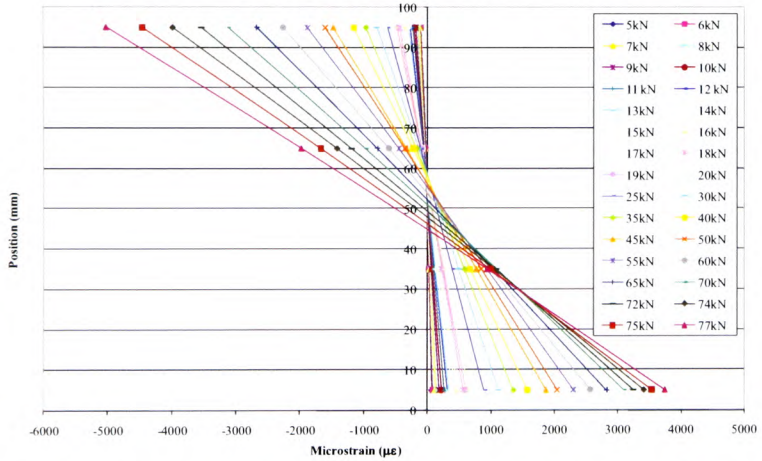

Figure 4.29(e) – Strain profile at mid-span for element 12SCF4, 5kN to failure

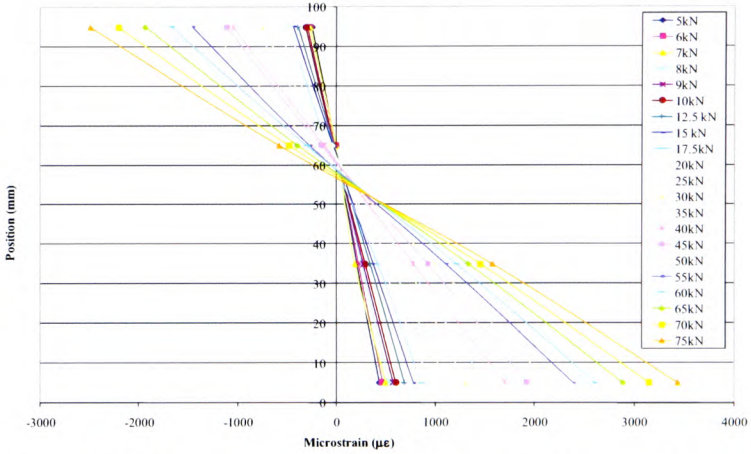

Figure 4.29(f) – Strain profile at mid-span for element 12SCP2, 5kN to failure

4.7 FRP surface strains

As detailed in Chapter 3, during the experimental programme, electronic strain gauges were bonded to the surface of the CFRP for all strengthened elements. Consequently, it has been possible to create strain profiles for the FRP in tension on the soffit of the tested, strengthened elements (a typical profile presented in Figure 4.30). The FRP surface strain profiles for all tested elements are presented in Figures 4.32(a) to 4.38(d).

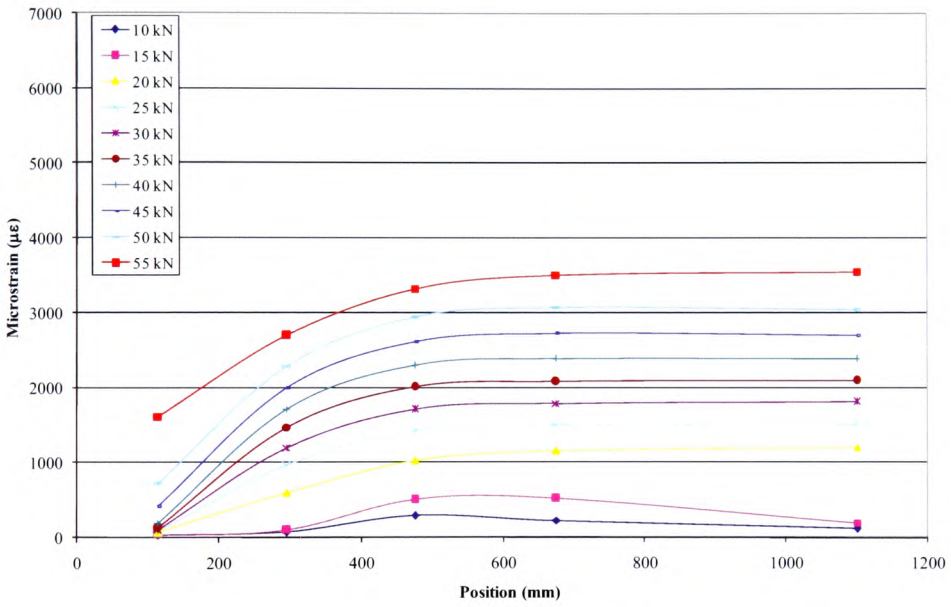

Figure 4.30 – Typical strain profile plot for FRP surface strains (8CF3 shown)

The positions of the electronic strain gauges adhered to the FRP surface were presented in Figures 3.16 and 3.17 in Chapter 3, but have been replicated here in Figure 4.31 for ease of reference. Where more than one strain gauge was present at any given position, an average value was used.

The DEMEC strain readings compare well with the electronic gauges on the surface of the FRP. For example, in the diagram shown below, the FRP surface strain at the soffit of the element at 55kN is seen to be 3550με. From Figure 4.23(e) the corresponding DEMEC strain reading is seen to be 3250με, which is

naturally a lower reading as the lowest DEMEC reading is taken at 10mm above the soffit. As the neutral axis depth is 65mm (Figure 4.40) simple linear extrapolation yields a value of 3510με, which is very comparable to the reading from the electronic strain gauge.

It should be noted that for all the elements where a debonding failure was observed, the maximum FRP surface strain never exceeded 7000 με, and in many cases was well below this value, as can be seen in Table 4.8. This is of particular interest as all values are significantly below the value of 8000 με, which is the current strain limit in the design guidelines to remove the possibility of debonding failure[§]. As the strain values presented are averages and were collected from more than one electronic gauge for each element, the possibility of erroneous gauge readings is removed and it must be considered that the debonding failures have occurred at the stated strain values. This matter calls into question the validity of the current guidance value of 8000με and merits further study, although such investigations are beyond the scope of this research programme.

Table 4.8 - Ultimate tensile FRP strains for elements with debonding failure modes

Element Ref.	**Tensile FRP strains at element failure(με)**
8CF2	6790
10CF2	6965
12DCF1	5197
8SCP3	3263**
12SCP2	4442
12SCP3	4445

§ Concrete Society, 2000

** It should be noted that, as detailed in Section 3.7.2.1.4, the presence of air voids in the adhesive layer for element 8SCP3 may have contributed to a very premature debonding failure mode, which would account for the very low tensile strain value in the FRP at failure.

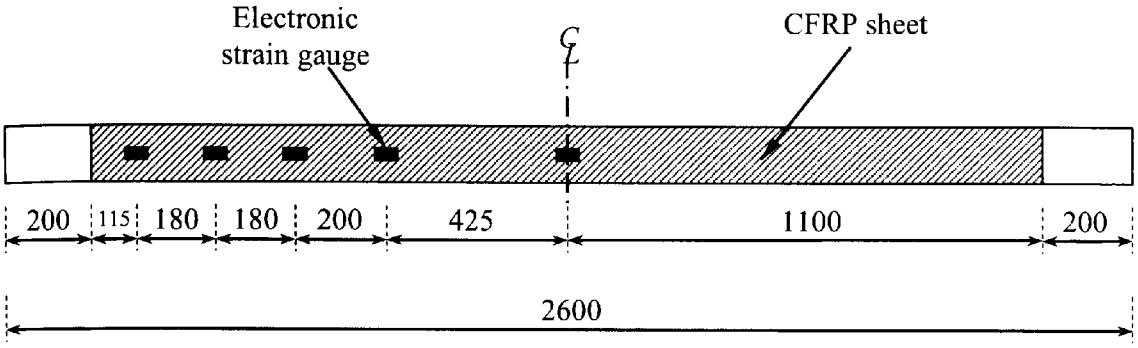

2 layers of CFRP sheet

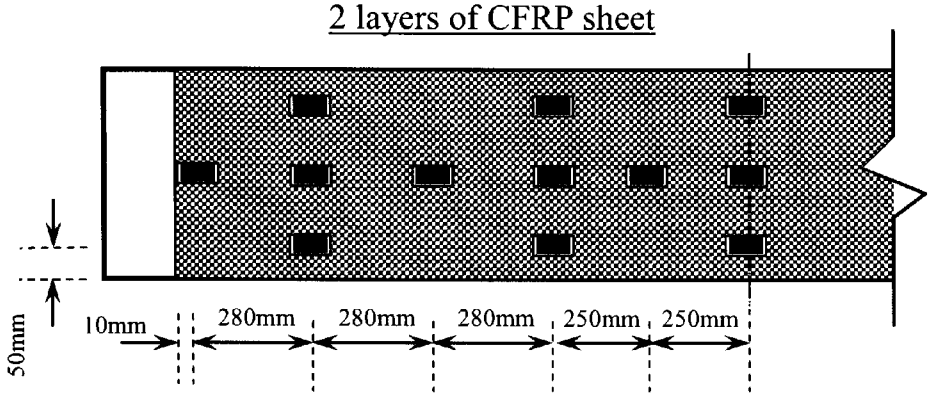

2 CFRP plates

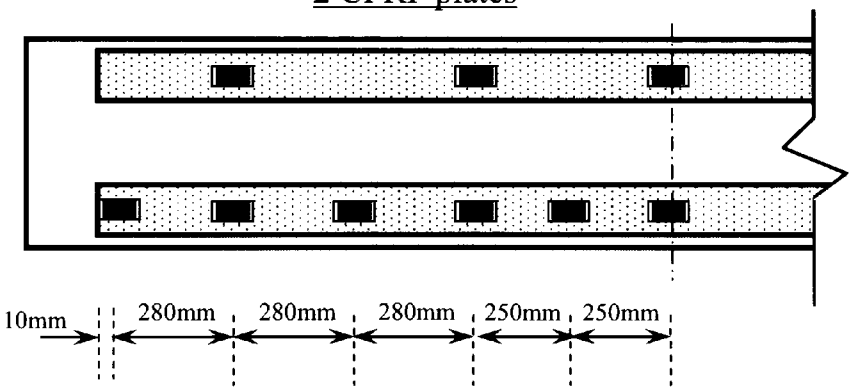

3 CFRP plates

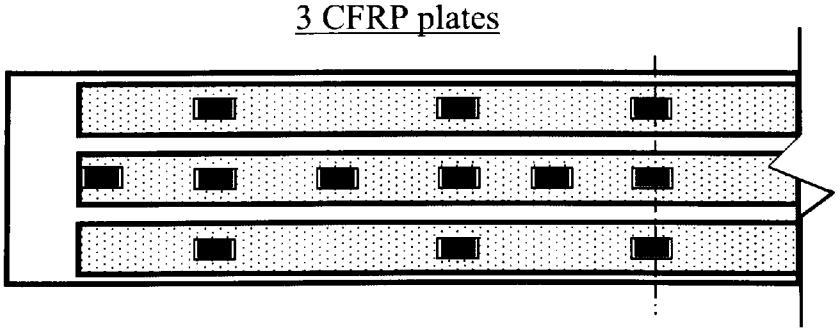

Figure 4.31 – Electronic strain gauge layouts for tested elements
(Replicated from Figures 3.16 and 3.17)

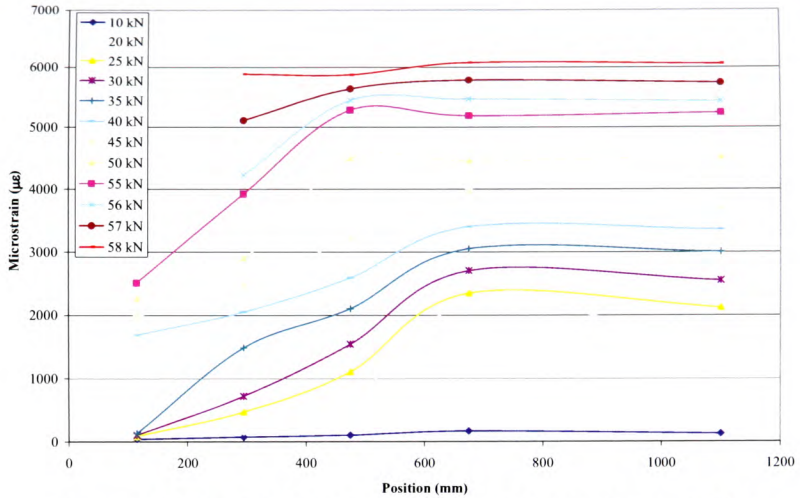

Figure 4.32(a) – FRP surface strain profile for element 8CF1

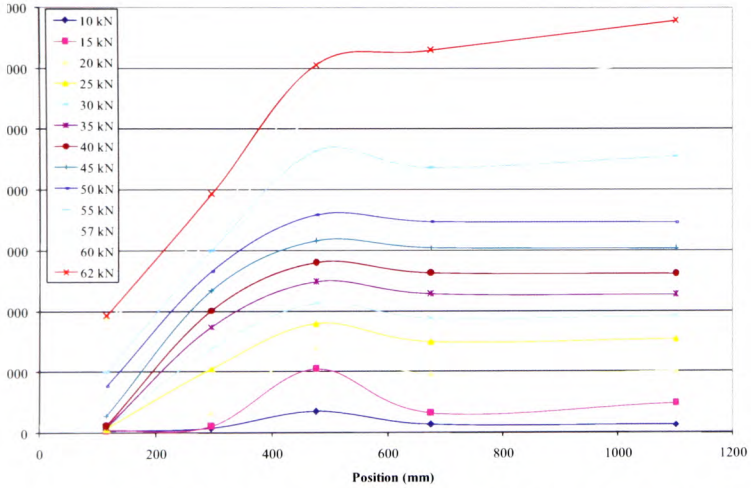

Figure 4.32(b) – FRP surface strain profile for element 8CF2

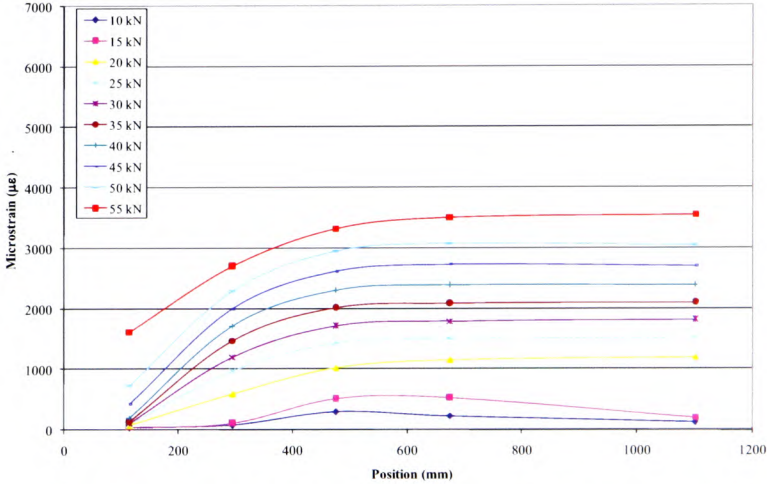

Figure 4.32(c) – FRP surface strain profile for element 8CF3

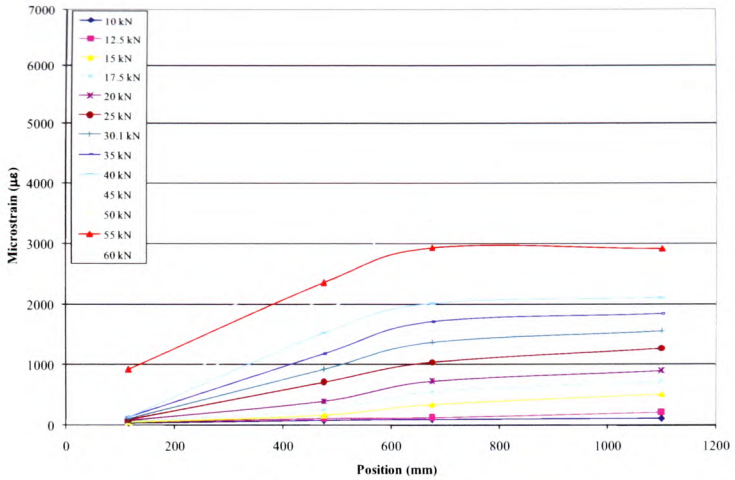

Figure 4.33(a) – FRP surface strain profile for element 10CF1

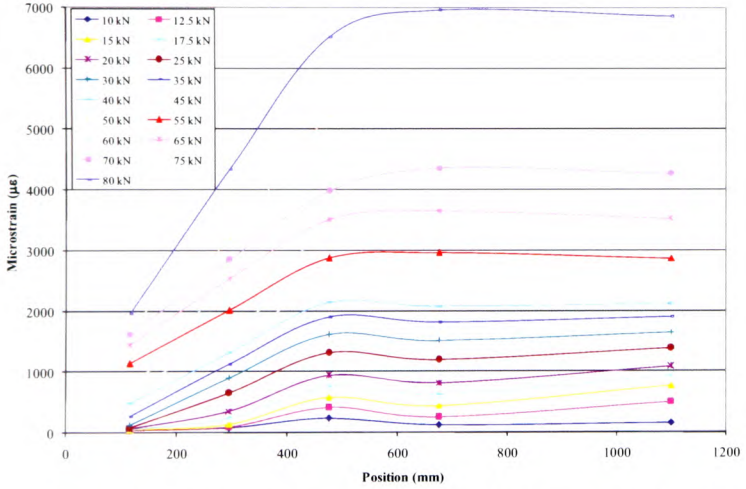

Figure 4.33(b) – FRP surface strain profile for element 10CF2

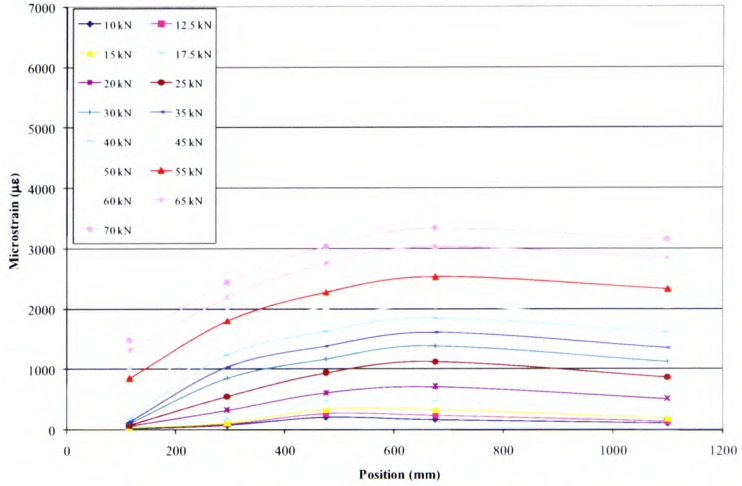

Figure 4.33(c) – FRP surface strain profile for element 10CF3

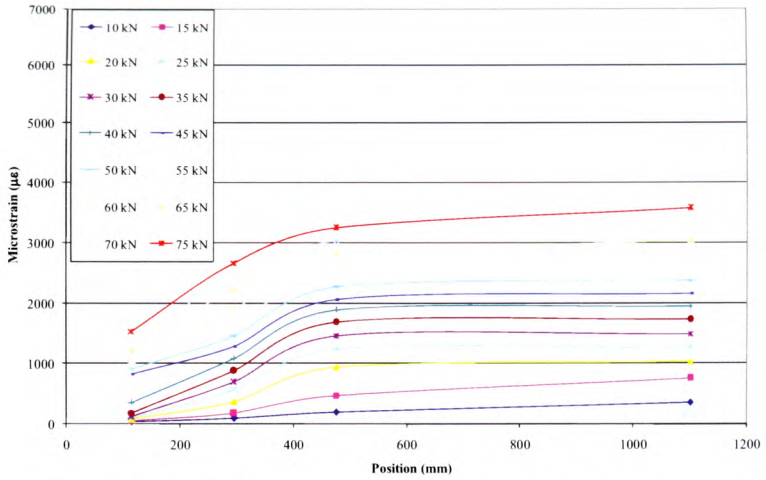

Figure 4.34(a) – FRP surface strain profile for element 12CF1

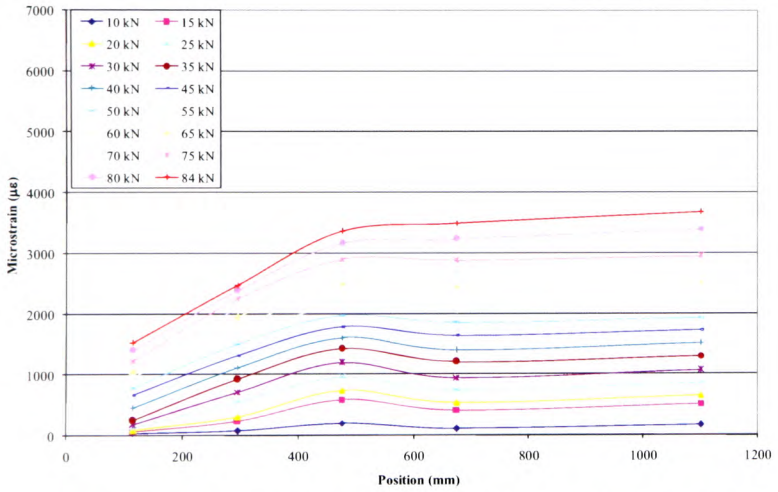

Figure 4.34(b) – FRP surface strain profile for element 12CF2

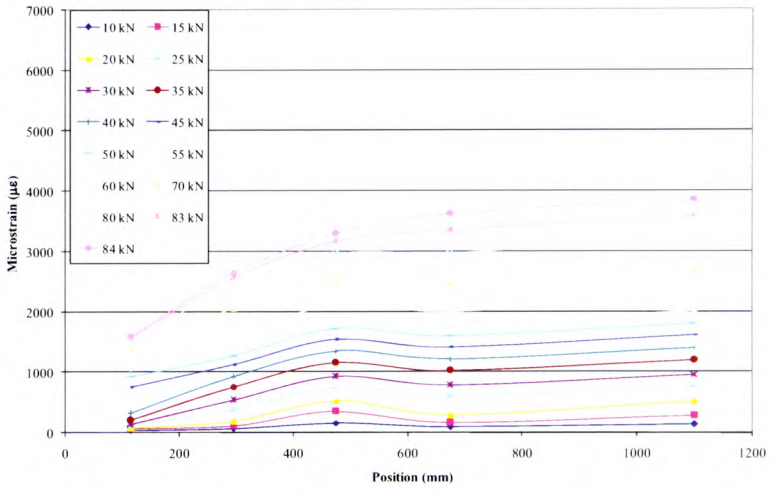

Figure 4.34(c) – FRP surface strain profile for element 12CF3

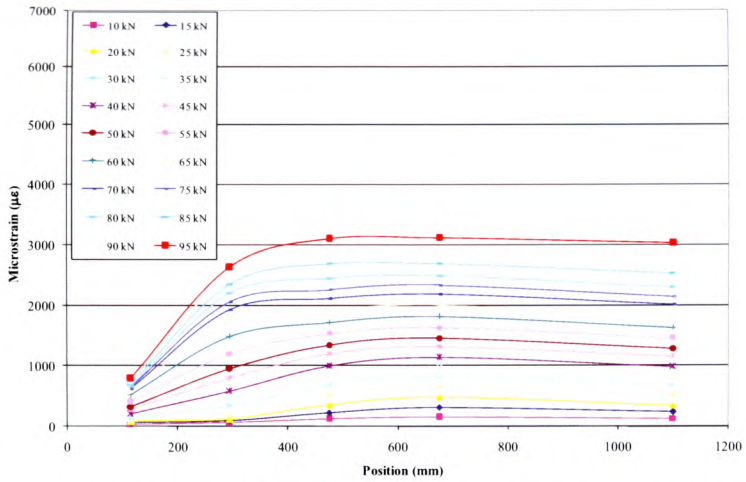

Figure 4.35(a) – FRP surface strain profile for element 16CF1

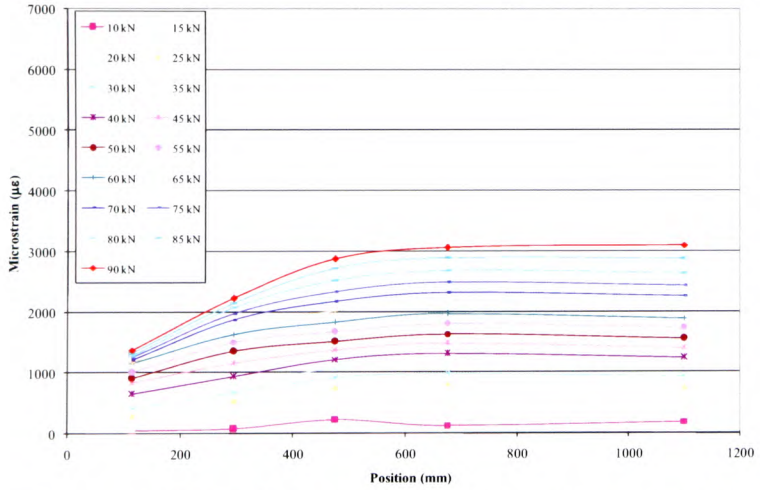

Figure 4.35(b) – FRP surface strain profile for element 16CF2

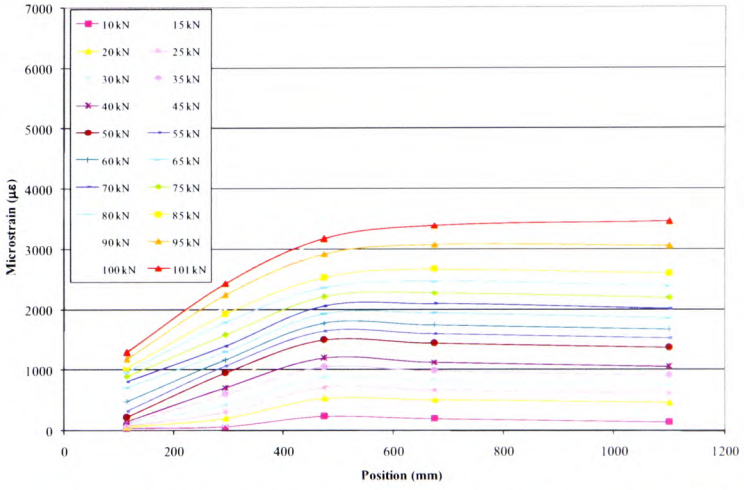

Figure 4.35(c) – FRP surface strain profile for element 16CF3

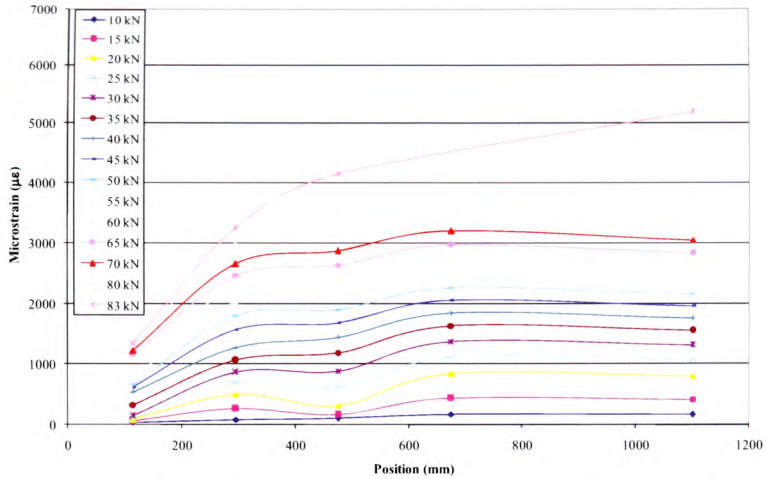

Figure 4.36(a) – FRP surface strain profile for element 12DCF1

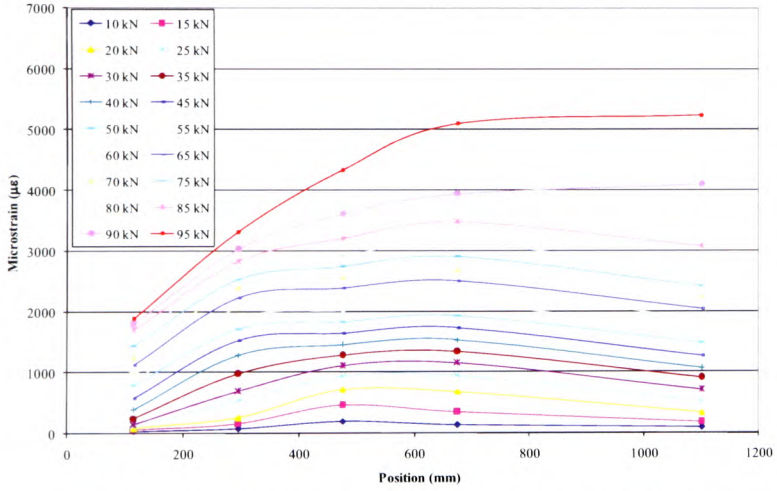

Figure 4.36(b) – FRP surface strain profile for element 12DCF2

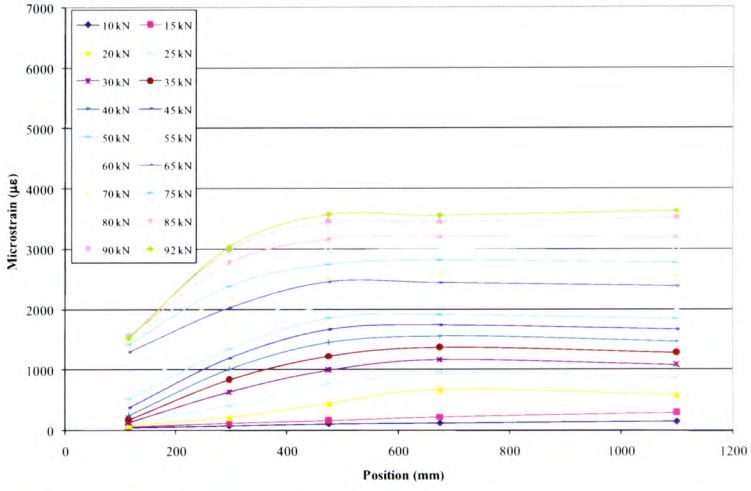

Figure 4.36(c) – FRP surface strain profile for element 12DCF3

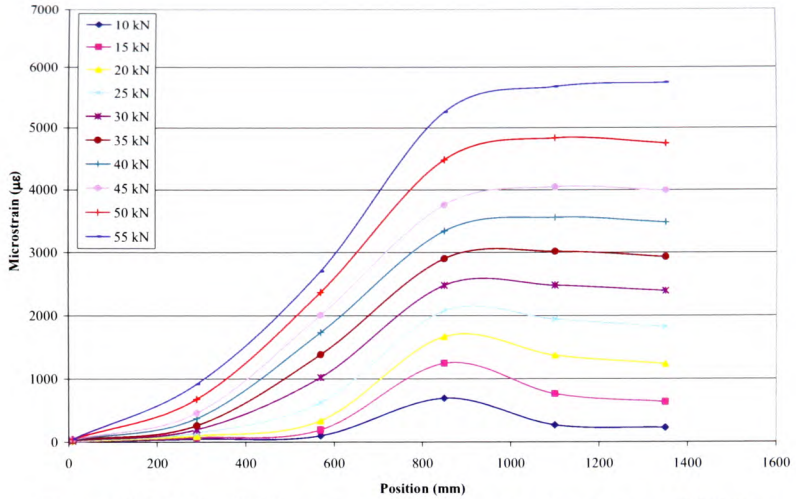

Figure 4.37(a) – FRP surface strain profile for element 8SCF2

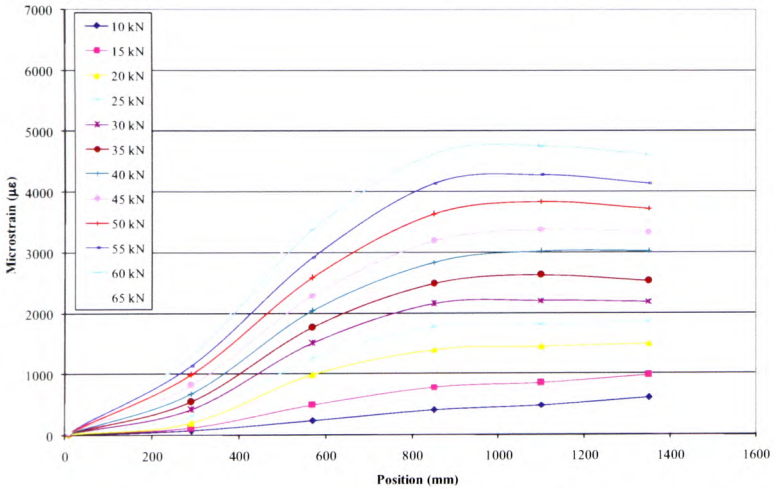

Figure 4.37(b) – FRP surface strain profile for element 8SCP2

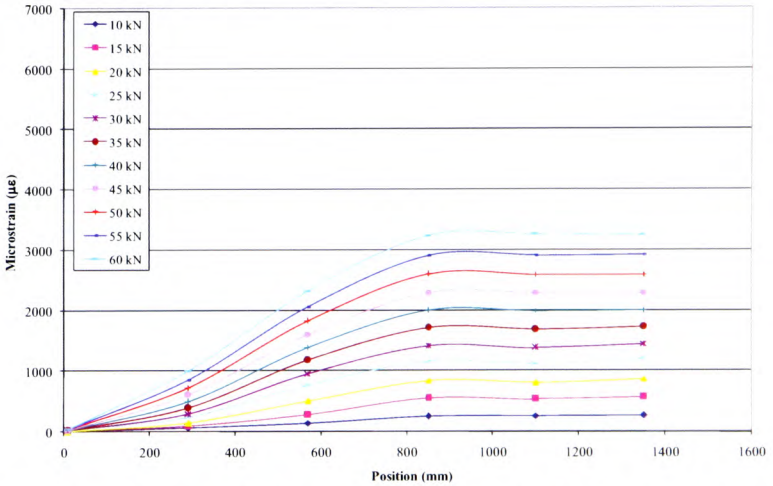

Figure 4.37(c) – FRP surface strain profile for element 8SCP3

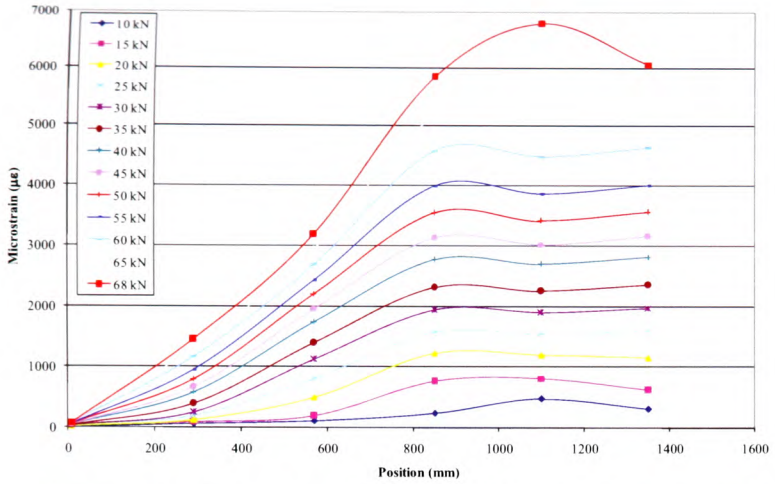

Figure 4.38(a) – FRP surface strain profile for element 12SCF2

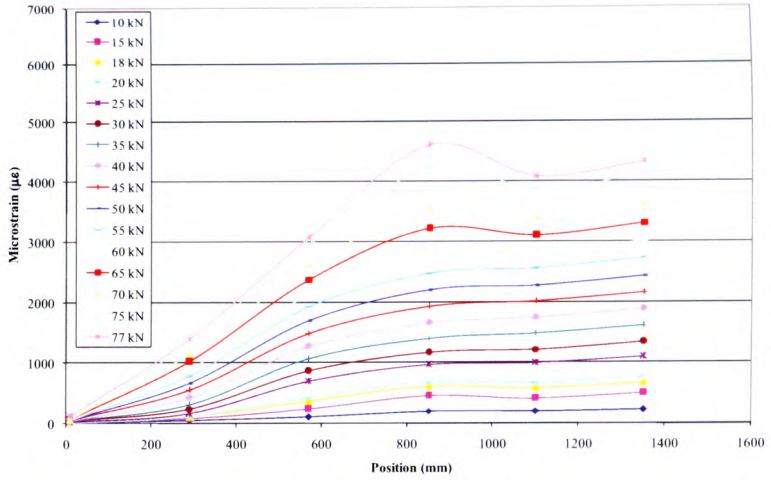

Figure 4.38(b) – FRP surface strain profile for element 12SCF4

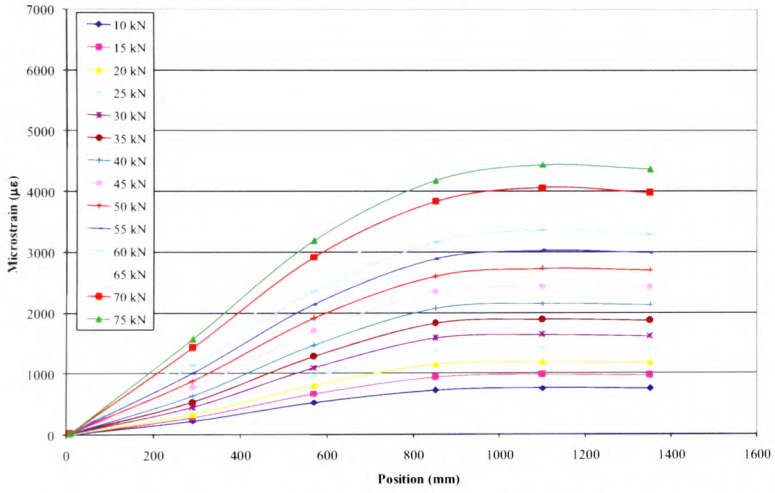

Figure 4.38(c) – FRP surface strain profile for element 12SCP2

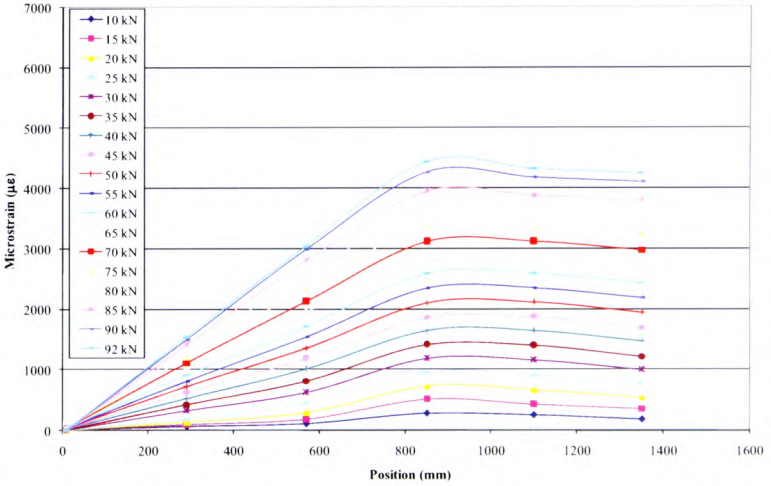

Figure 4.38(d) – FRP surface strain profile for element 12SCP3

4.8 Neutral axis depth

The neutral axis depth at mid-span was calculated, for all strengthened elements, using the readings from the electronic strain gauges on the top and bottom faces of the beams, ε_c and ε_t respectively. The neutral axis depth, x_s, can be expressed as:

$$x_s = \frac{(h + t_f)|\varepsilon_c|}{|\varepsilon_c| + |\varepsilon_t|} \qquad 4.8$$

Where; h is the total section depth

t_f is the thickness of the FRP layer

(Please also refer to Figure 4.39)

For a control element, where an electronic gauge was not placed on the tension face, ε_b represents the surface strain at the lowest DEMEC gauge point, i.e. 10mm above the bottom of the beam. This neutral axis depth, x_c, can be expressed as:

For beam elements: $$x_c = \frac{190|\varepsilon_c|}{|\varepsilon_c| + |\varepsilon_b|} \qquad 4.9(a)$$

For slab elements: $$x_c = \frac{95|\varepsilon_c|}{|\varepsilon_c| + |\varepsilon_b|} \qquad 4.9(b)$$

The benefit of using the electronic gauges was that it enabled the recording of strain values up to failure, whereas, for health and safety reasons, the manual recording of surface strains was ceased when it was considered the elements were approaching failure. Figures 4.40 to 4.46 display the load against neutral axis depth 'x' for all the elements contained within the experimental programme.

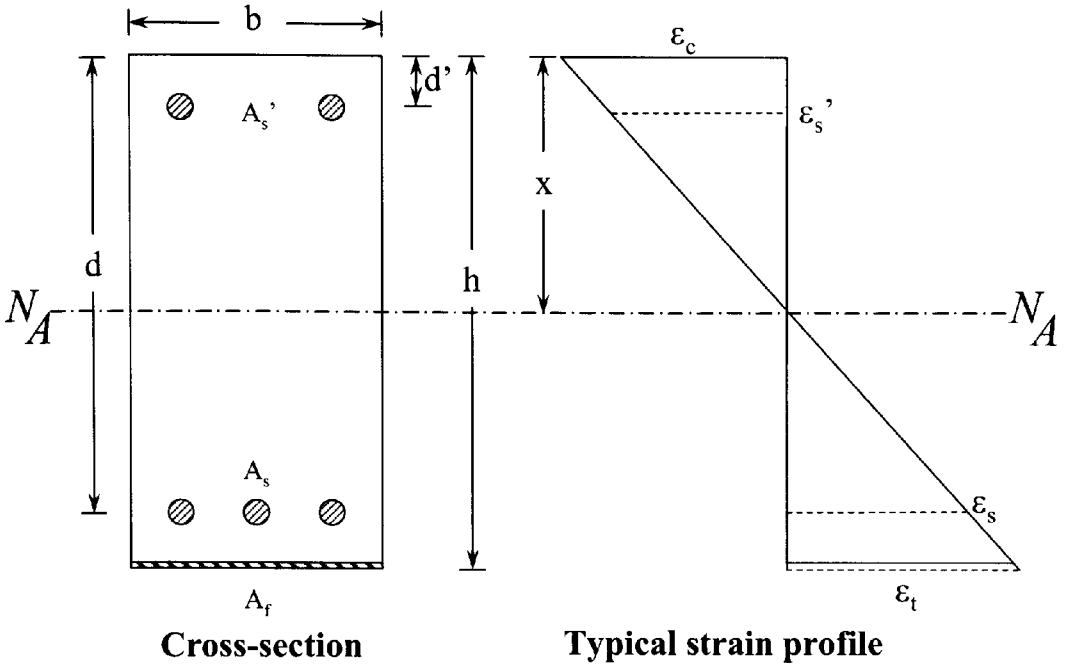

Figure 4.39 – Calculation of neutral axis depth from strains

It can be seen from the plots of neutral axis depth, 'x', against load, that at the early loading stages the depth of the neutral axis rapidly decreases, which indicates the point at which the initial concrete cracking has occurred.

It should also be noted that for strengthened elements with higher levels of internal steel reinforcement, the neutral axis depth increased as ultimate limit state was approached, indicating that some compressive resistance was being lost in the concrete, requiring a drop in the position of the neutral axis in order to maintain section equilibrium. This is particularly noticeable as the level of flexural reinforcement/strengthening increases significantly as with the Ø16mm elements. This hypothesis is further borne out if one looks at the plot for the Ø12mm doubly-reinforced elements. These elements display a much less pronounced increase in the depth of the neutral axis, due to the presence of compression steel reinforcement, which aids the concrete in providing compressive resistance in the element, particularly at latter loading stages.

4.8.1 ρ =0.50% - Ø 8mm reinforced beams

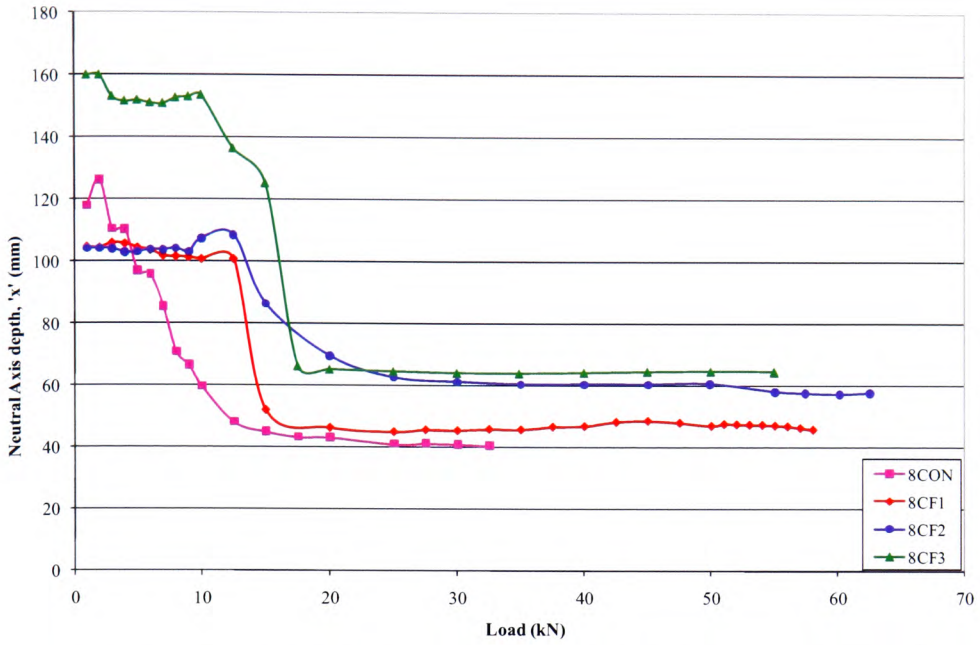

Figure 4.40 – Load/Neutral Axis depth 'x' at mid-span for ∅8mm reinforced elements

4.8.2 ρ =0.79% - Ø 10mm reinforced beams

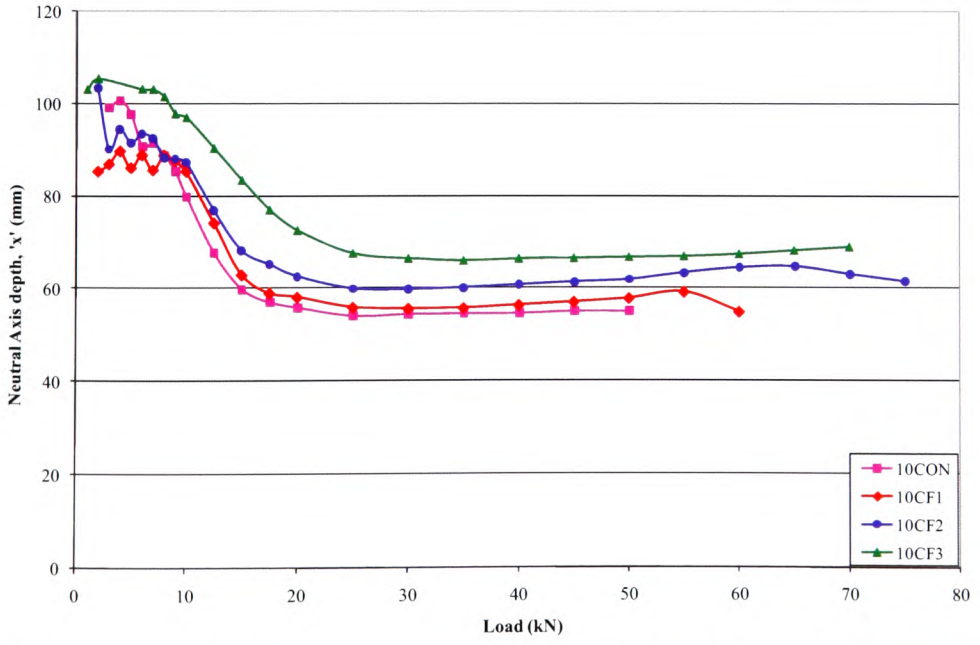

Figure 4.41 – Load/Neutral Axis depth 'x' at mid-span for ∅10mm reinforced elements

4.8.3 ρ =1.13% - Ø 12mm reinforced beams

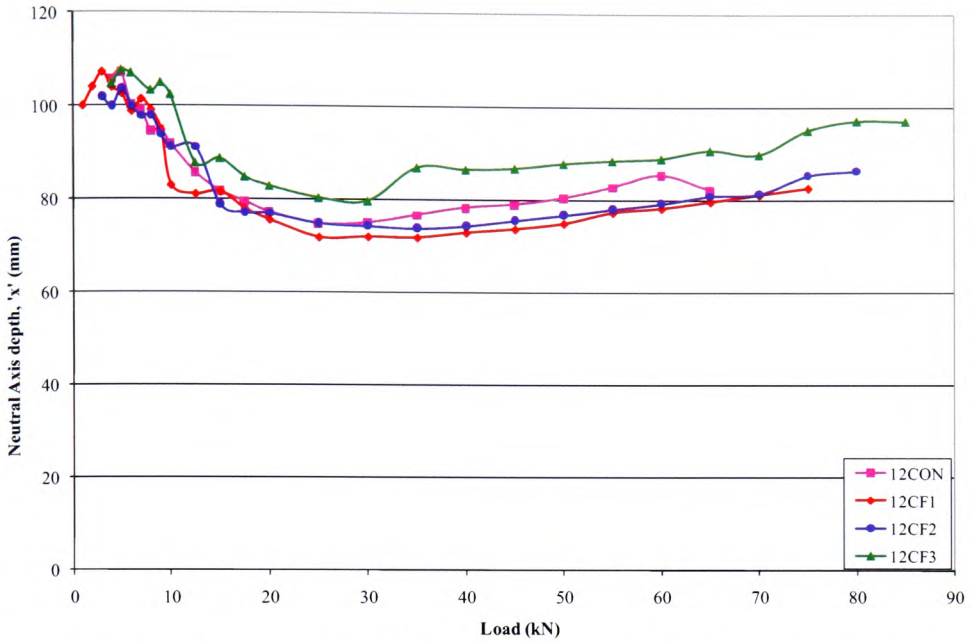

Figure 4.42 – Load/Neutral Axis depth 'x' at mid-span for ∅12mm reinforced elements

4.8.4 ρ =2.01% - Ø 16mm Reinforced beams

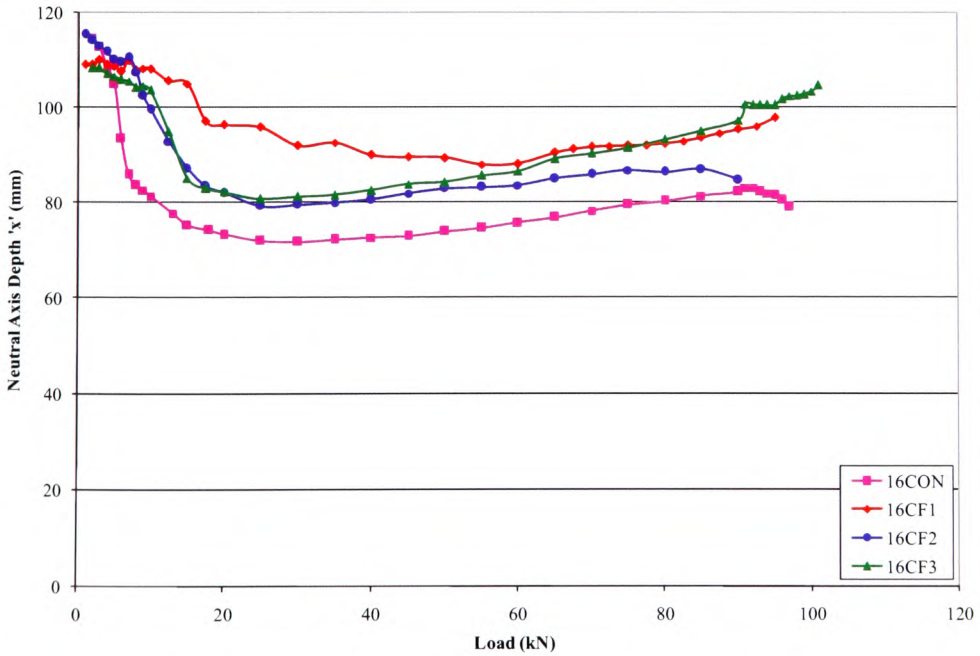

Figure 4.43 – Load/Neutral Axis depth 'x' at mid-span for ∅16mm reinforced elements

4.8.5 ρ =1.13% - Ø 12mm doubly-reinforced beams

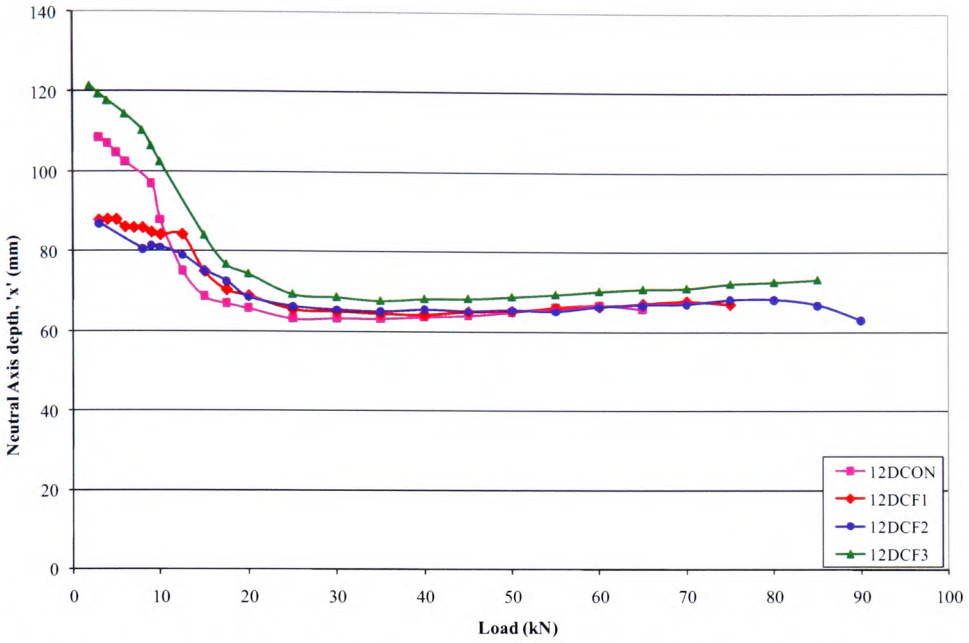

Figure 4.44 – Load/Neutral Axis depth 'x' at mid-span for ∅12mm doubly-reinforced elements

4.8.6 ρ =0.40% - Ø 8mm reinforced slabs

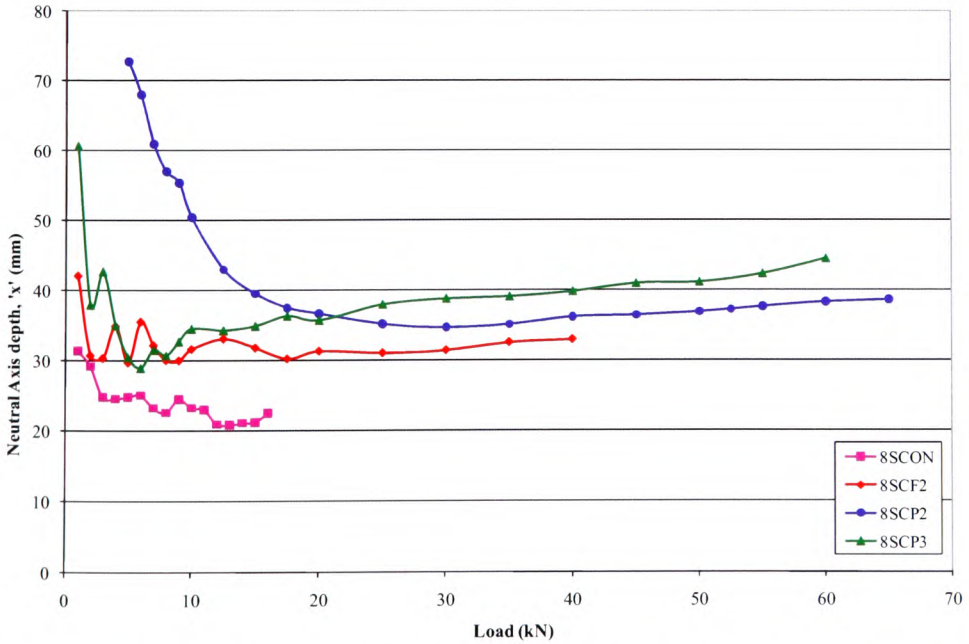

Figure 4.45 – Load/Neutral Axis depth 'x' at mid-span for ∅8mm reinforced elements

4.8.7 ρ =0.91% - Ø 12mm reinforced slabs

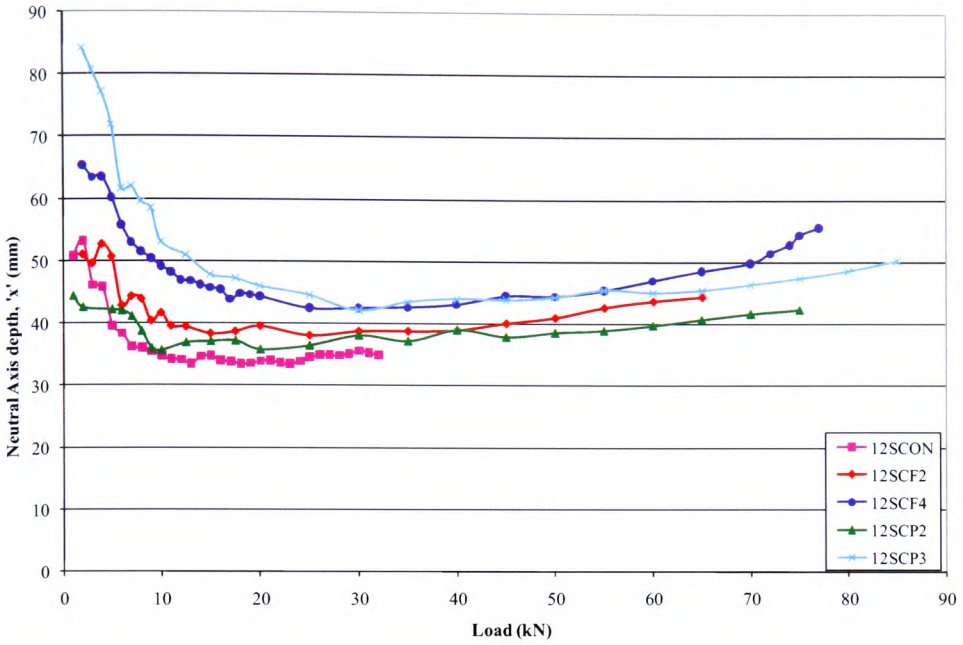

Figure 4.46 – Load/Neutral Axis depth 'x' at mid-span for ∅12mm reinforced elements

4.9 Moment Curvature

From the experimental results, it was possible to generate plots of moment against curvature for each tested element from two different data sources, namely deflections and DEMEC strains. This enabled the data to be compared and verified, which allowed both sets of experimental results to be corroborated.

It should be noted that due to the large deflections experienced when loading the slab elements, it was necessary to remove the LVDTs prior to element failure, in order to safeguard the recording equipment from damage. Consequently, the plots for the slab elements display a curtailed behaviour for the moment-curvature derived from deflections.

Presented in Figures 4.47(a) to 4.52(e) are the moment against curvature graphs for all elements.

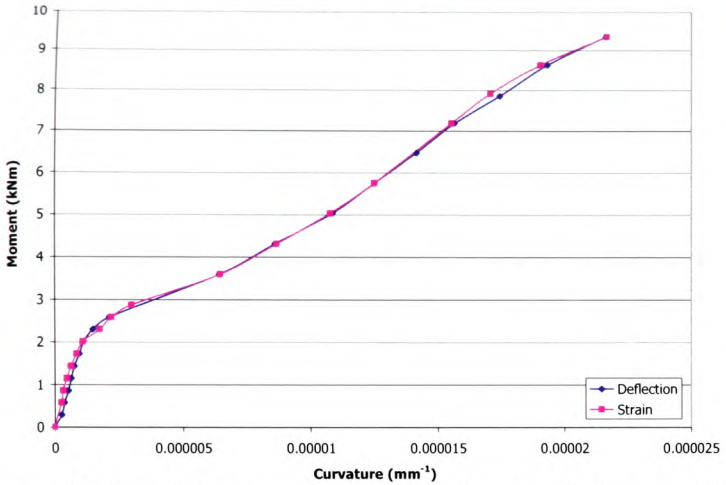

Figure 4.47(a) – Moment curvature plot for control element, 8CON

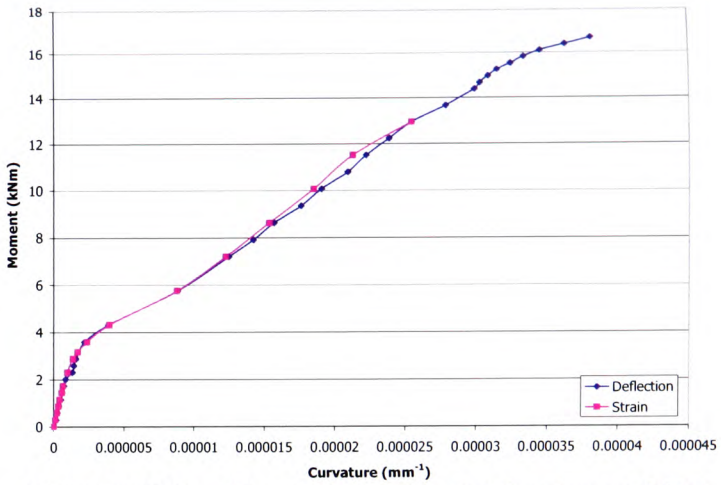

Figure 4.47(b) – Moment curvature plot for element 8CF1

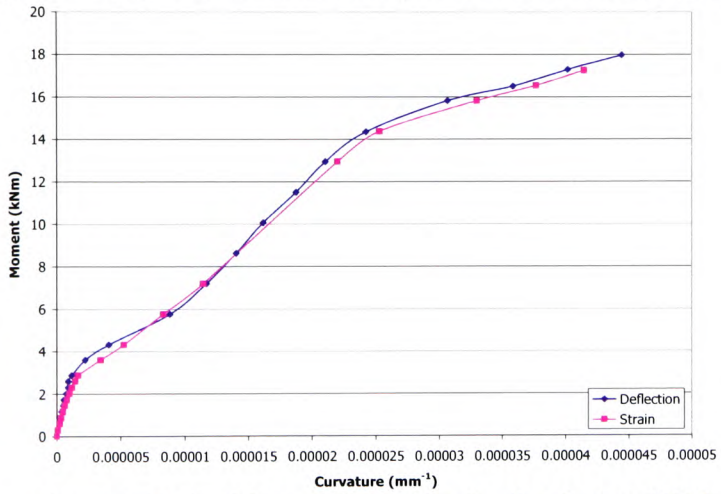

Figure 4.47(c) – Moment curvature plot for element 8CF2

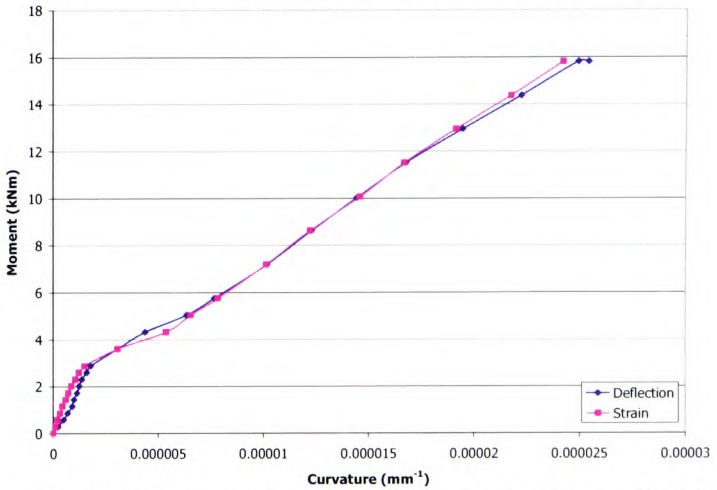

Figure 4.47(d) – Moment curvature plot for element 8CF3

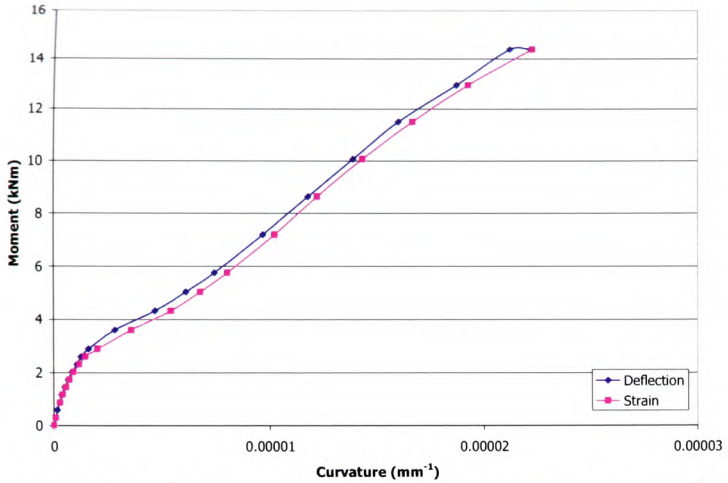

Figure 4.48(a) – Moment curvature plot for control element, 10CON

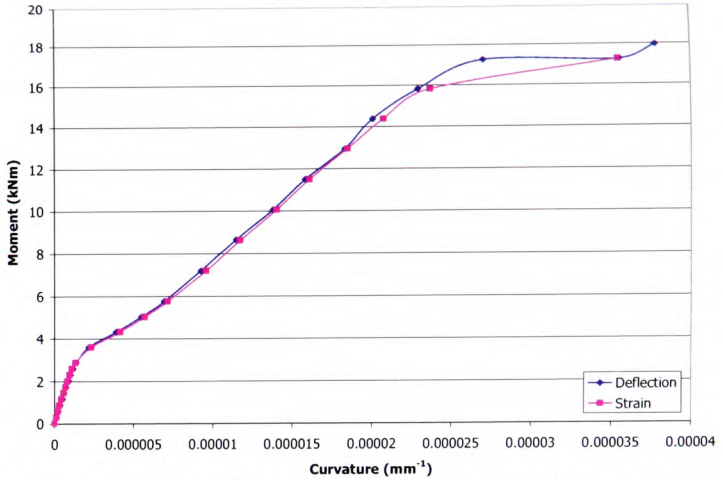

Figure 4.48(b) – Moment curvature plot for element 10CF1

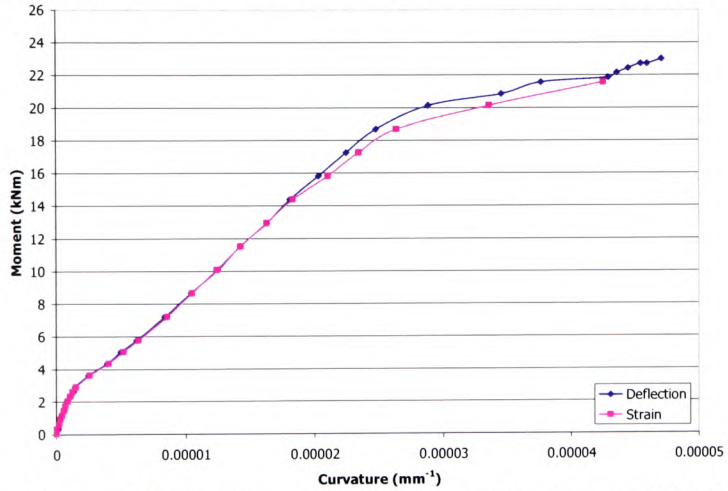

Figure 4.48(c) – Moment curvature plot for element 10CF2

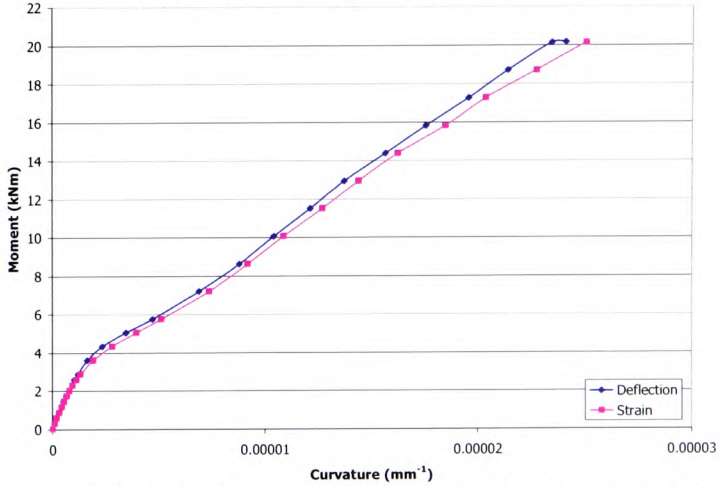

Figure 4.48(d) – Moment curvature plot for element 10CF3

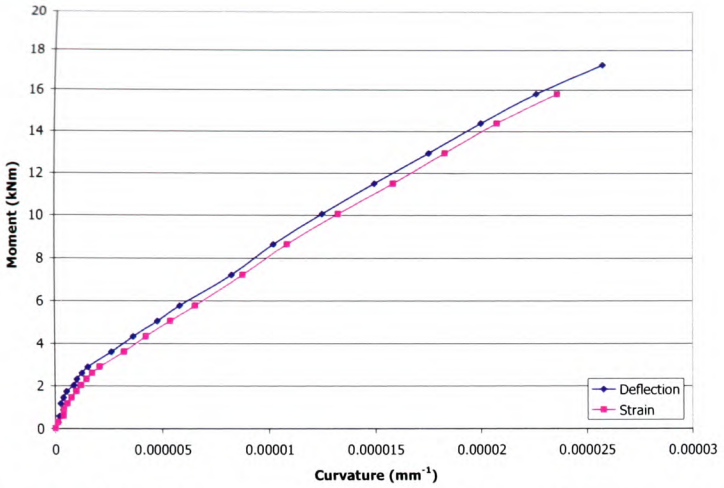

Figure 4.49(a) – Moment curvature plot for control element, 12CON

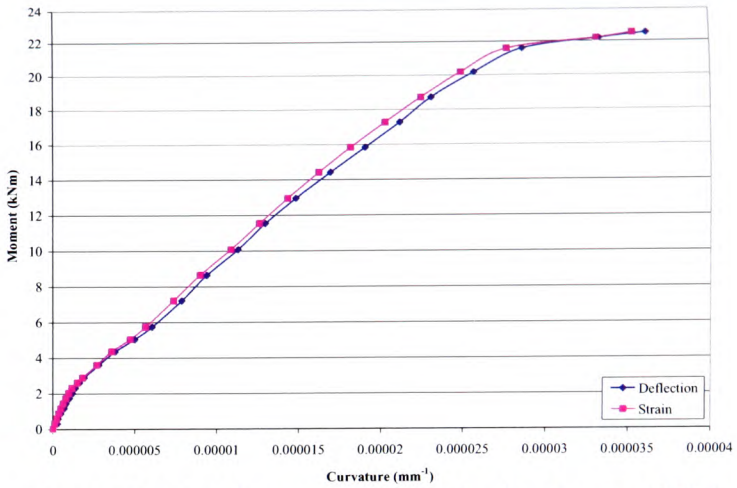

Figure 4.49(b) – Moment curvature plot for element 12CF1

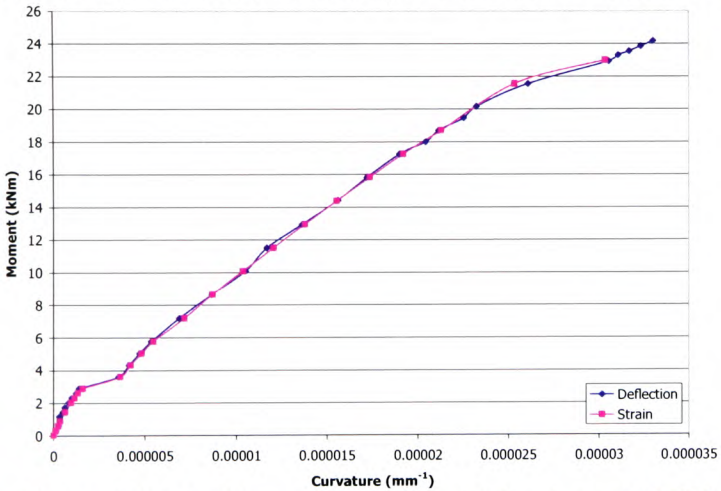

Figure 4.49(c) – Moment curvature plot for element 12CF2

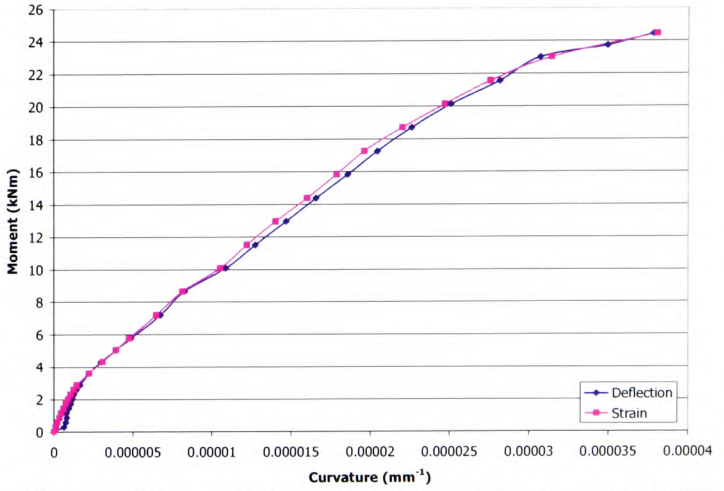

Figure 4.49(d) – Moment curvature plot for element 12CF3

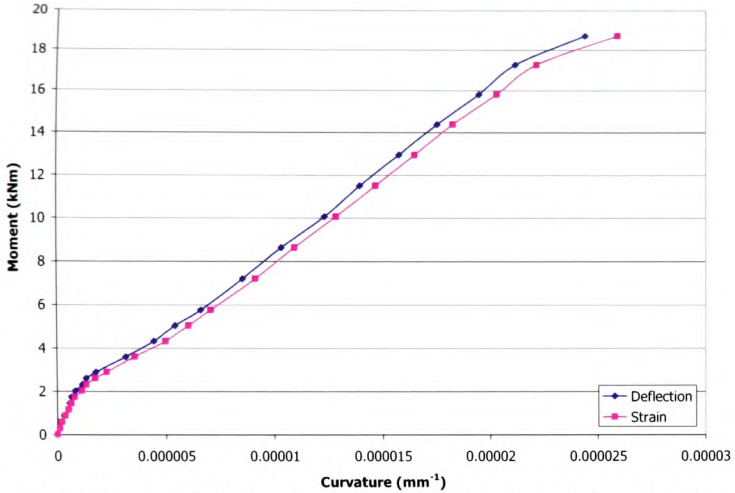

Figure 4.50(a) – Moment curvature plot for control element 12DCON

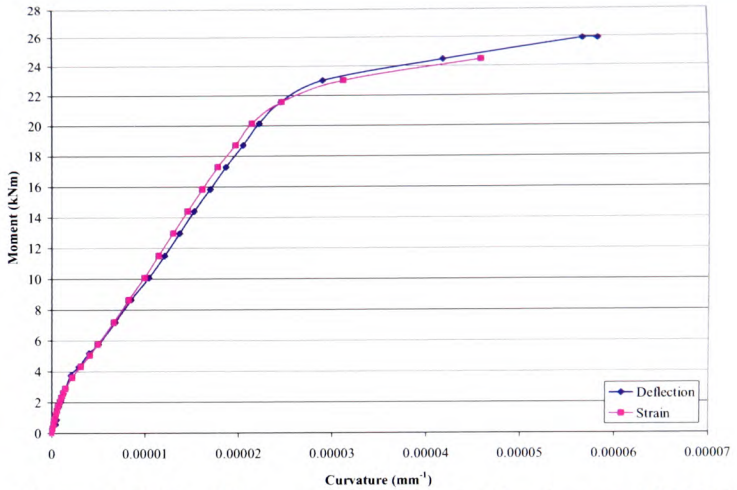

Figure 4.50(b) – Moment curvature plot for element 12DCF1

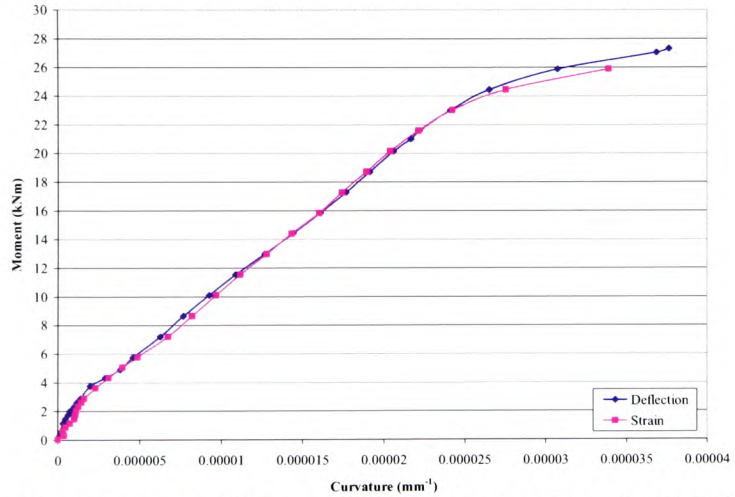

Figure 4.50(c) – Moment curvature plot for element 12DCF2

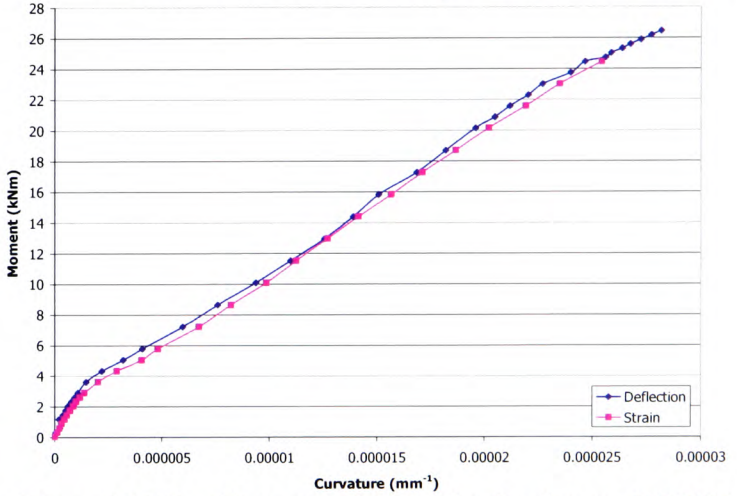

Figure 4.50(d) – Moment curvature plot for element 12DCF3

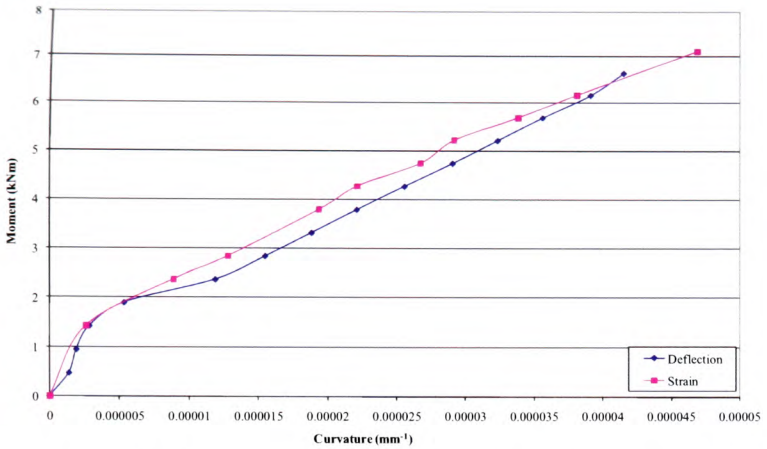

Figure 4.51(a) – Moment curvature plot for control element, 8SCON

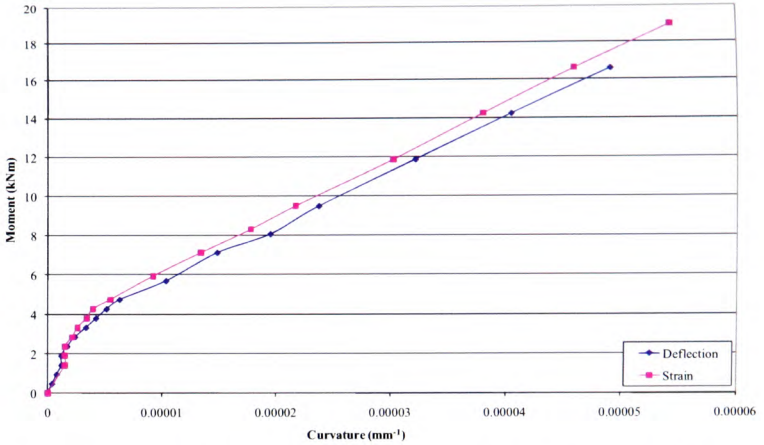

Figure 4.51(b) – Moment curvature plot for element 8SCF2

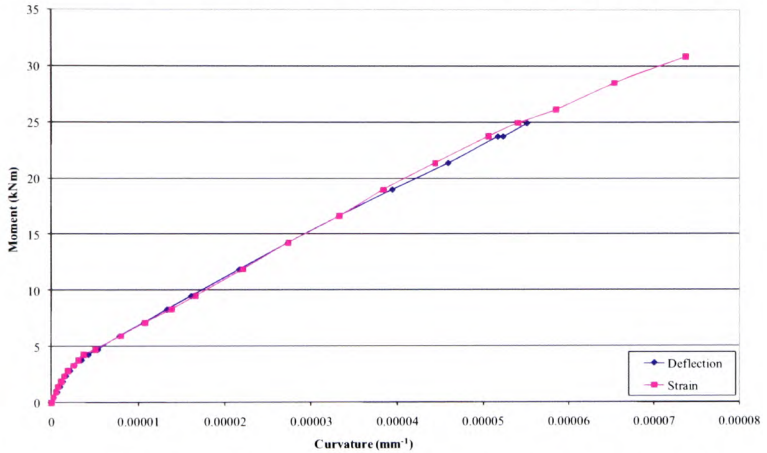

Figure 4.51(c) – Moment curvature plot for element 8SCP2

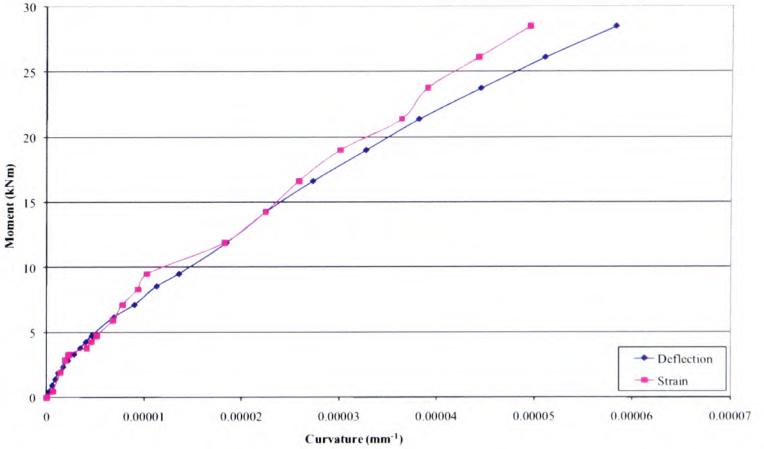

Figure 4.51(d) – Moment curvature plot for element 8SCP3

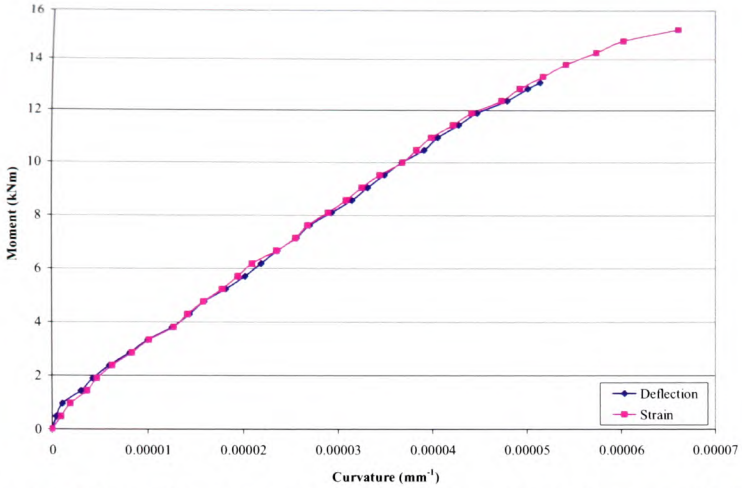

Figure 4.52(a) – Moment curvature plot for control element, 12SCON

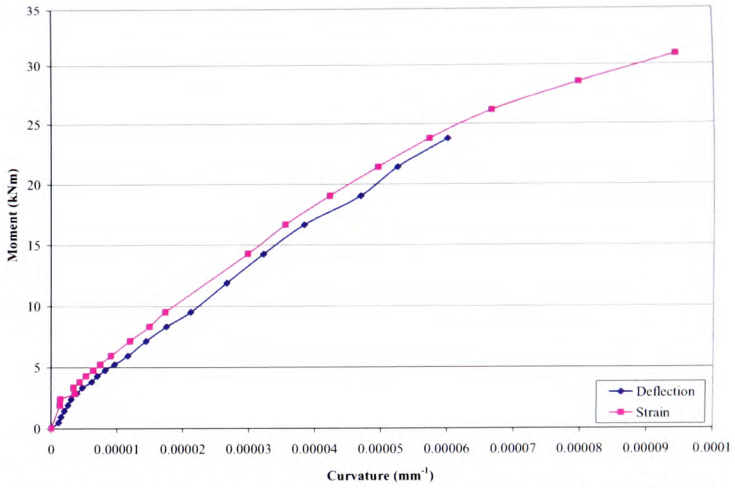

Figure 4.52(b) – Moment curvature plot for element 12SCF2

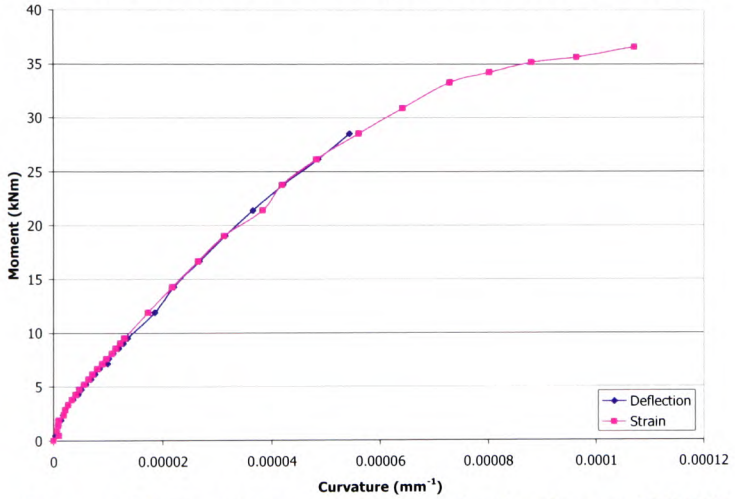

Figure 4.52(c) – Moment curvature plot for element 12SCF4

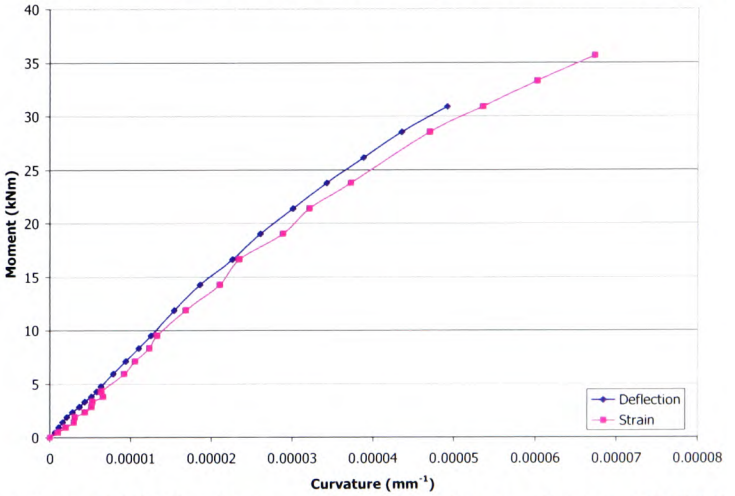

Figure 4.52(d) – Moment curvature plot for element 12SCP2

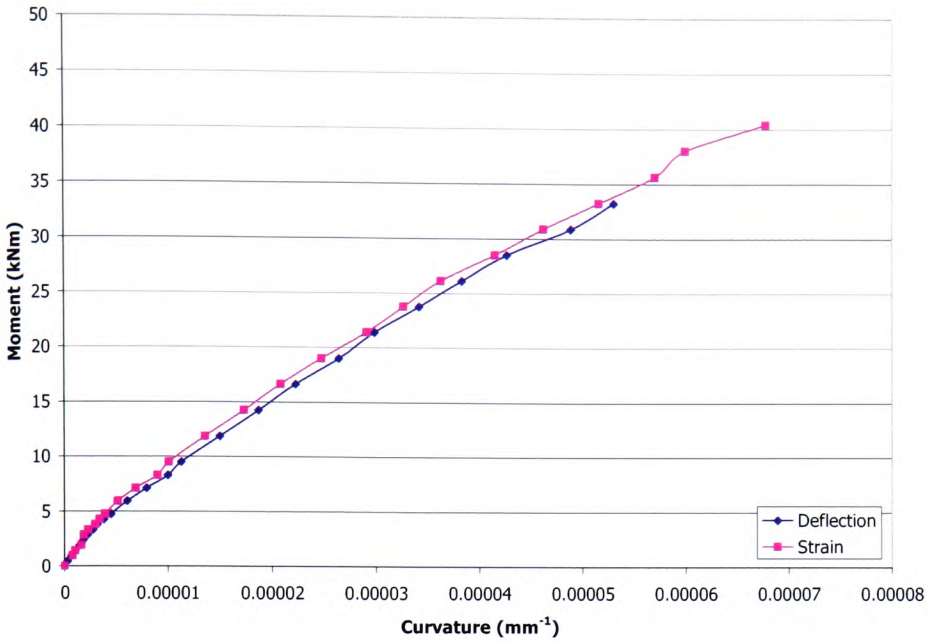

Figure 4.52(e) – Moment curvature plot for element 12SCP3

4.10 Crack propagation

It is evident from experimental observations, as well as the recorded information presented in Figures 4.53(a) to 4.59(d), that crack development in strengthened elements differs significantly from conventionally reinforced concrete elements. It is well known that in un-strengthened RC elements, the number of cracks will increase to a maximum before failure and subsequently the crack width and length increases to accommodate the additional deformation prior to the ultimate load stage.

It can also be seen, by comparing the maximum crack lengths with the neutral axis 'x' values (see Section 4.8) that there is excellent correlation between the two sets of data; i.e. the maximum crack length representing the depth of the beam in tension (below the neutral axis) when added to the corresponding value for 'x' should equal the total beam depth of 200mm. This is to say that for beam 10CF2, between the loads of 30kN and 60kN the maximum crack length, from Figure 4.53(b), is approximately 130mm and the corresponding calculated value for 'x' from Figure 4.41 (from strain readings) is 70mm.

4.10.1 ρ =0.50% - ∅ 8mm reinforced beams

The strengthened elements display an increase in the number of cracks up to failure. Additionally, as illustrated in Figure 4.53(d), the average crack width for strengthened elements is significantly smaller than for un-strengthened ones and remains stable until just before failure. This can be attributed to the perfect bond between the CFRP and the beam surface allowing the strengthening to distribute the load across the whole length of the element and also 'holding together' the tension face. Conversely, the 10CON displays an increase in crack width throughout the loading range.

4.10.2 ρ =0.79% - ∅ 10mm reinforced beams

The strengthened elements display an increase in the number of cracks up to failure. Additionally, as illustrated in Figure 4.54(d), the average crack width for strengthened elements is significantly smaller than for un-strengthened ones and remains stable until just before failure. This can be attributed to the perfect bond between the CFRP and the beam surface allowing the strengthening to distribute the load across the whole length of the element and also 'holding together' the tension face. Conversely, the 10CON displays an increase in crack width throughout the loading range.

Also, for the strengthened elements the maximum and average crack lengths remain stable for the majority of the loading range (Figures 4.54(b) and (c)). The corresponding average crack length for 10CON increases from the early loading stages through to failure and the maximum crack length increases dramatically during the last 10 to 15% of loading.

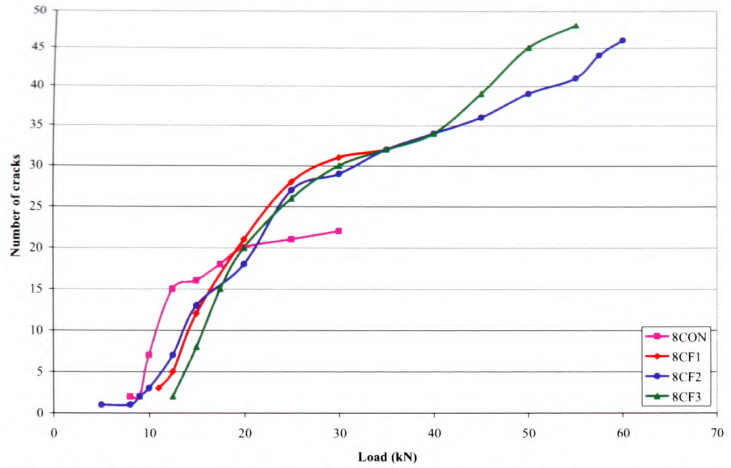

Figure 4.53(a) – Total number of cracks in constant moment zone against load for ∅8mm reinforced elements

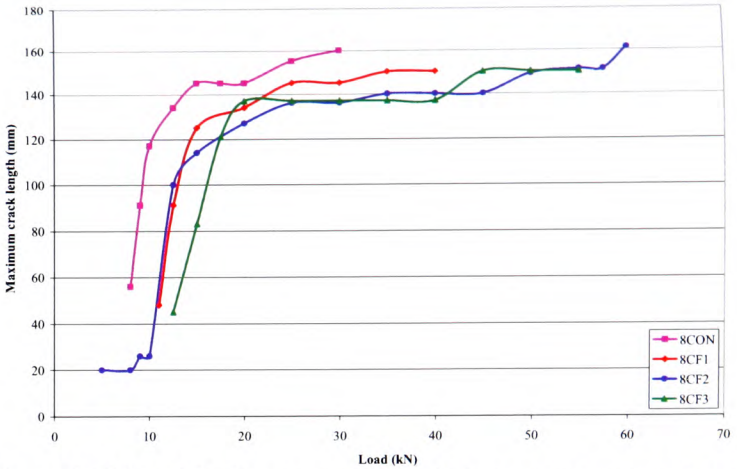

Figure 4.53(b) – Maximum crack length in constant moment zone against load for ∅8mm reinforced elements

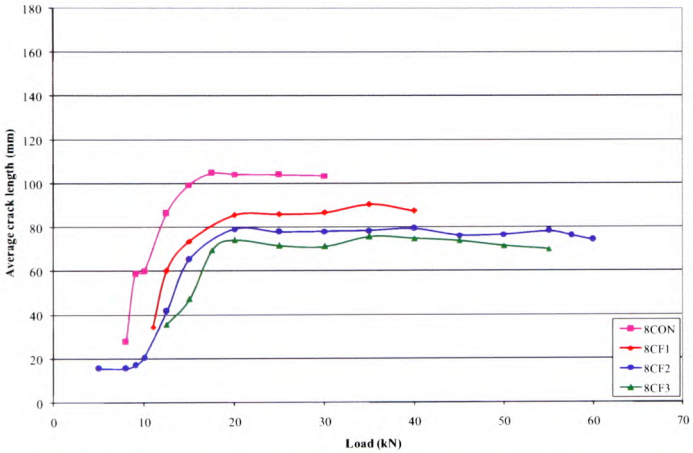

Figure 4.53(c) – Average crack length in constant moment zone against load for ∅8mm reinforced elements

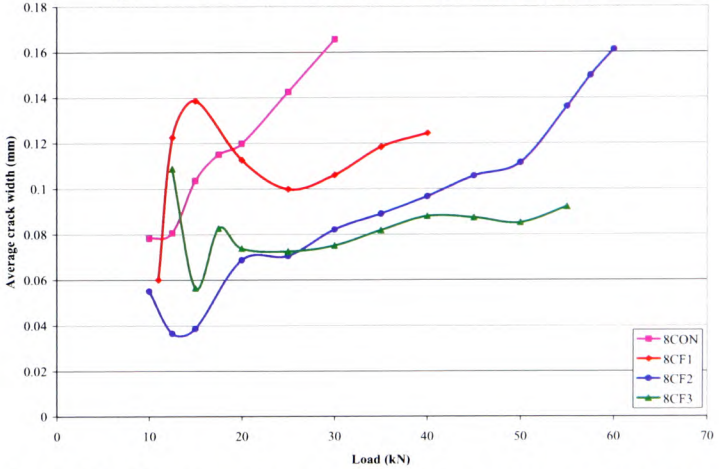

Figure 4.53(d) – Average crack width in constant moment zone against load for ∅8mm reinforced elements

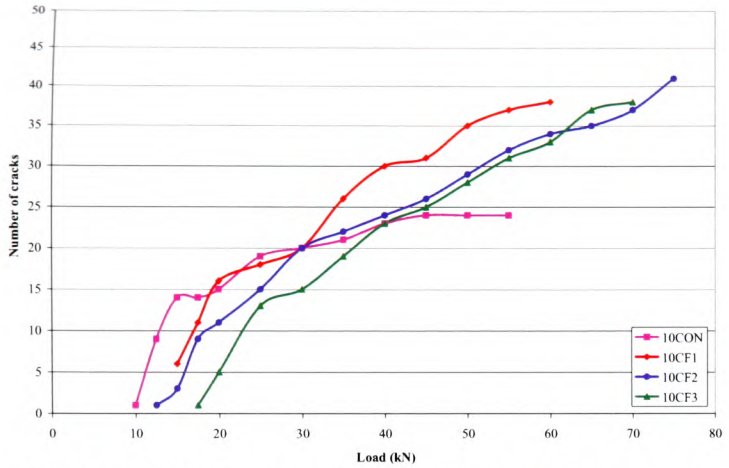

Figure 4.54(a) – Total number of cracks in constant moment zone against load for ∅10mm reinforced elements

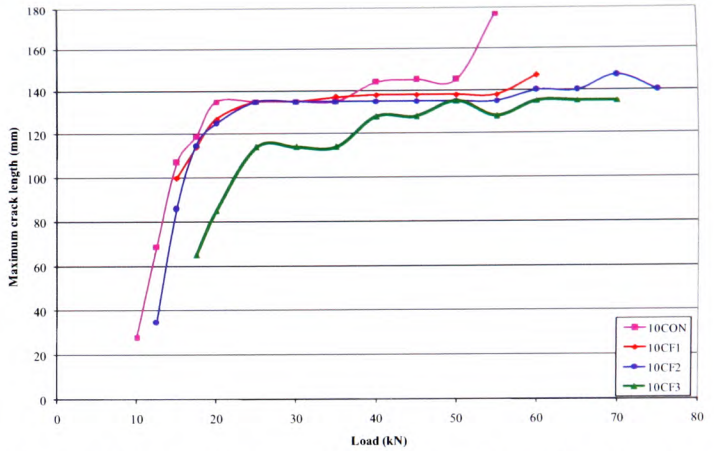

Figure 4.54(b) – Maximum crack length in constant moment zone against load for ∅10mm reinforced elements

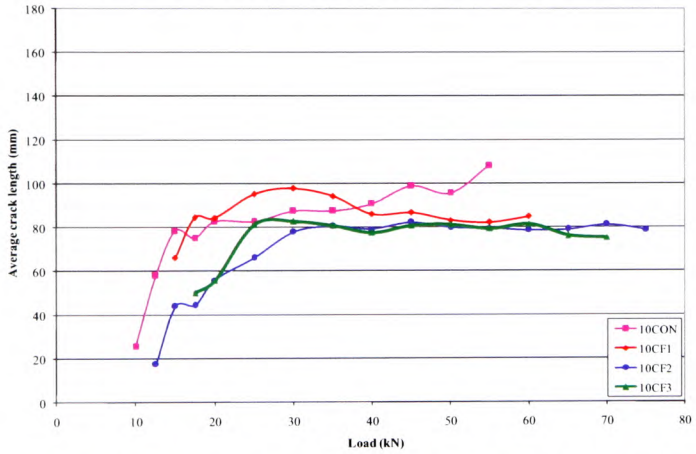

Figure 4.54(c) – Average crack length in constant moment zone against load for ∅10mm reinforced elements

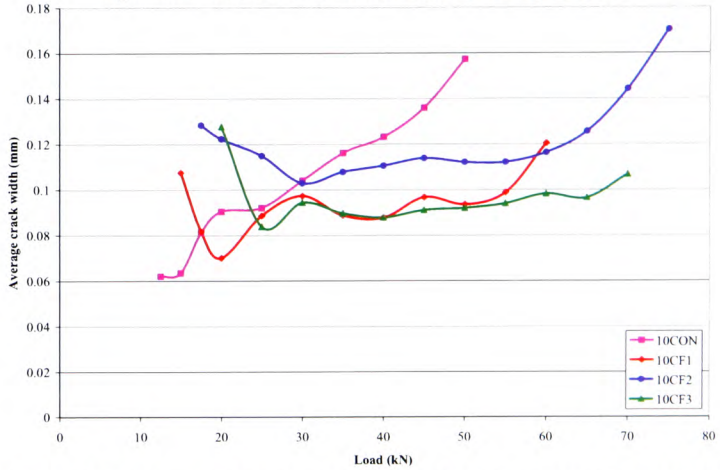

Figure 4.54(d) – Average crack width in constant moment zone against load for ∅10mm reinforced elements

4.10.3 ρ =1.13% - ∅ 12mm reinforced beams

The strengthened elements display an increase in the number of cracks up to failure. Additionally, as illustrated in Figure 4.55(d), the average crack width for strengthened elements is significantly smaller than for un-strengthened ones and remains stable until just before failure. This can be attributed to the perfect bond between the CFRP and the beam surface allowing the strengthening to distribute the load across the whole length of the element and also 'holding together' the tension face. Conversely, the 12CON displays an increase in crack width throughout the loading range.

4.10.4 ρ =2.01% - ∅ 16mm reinforced beams

It is apparent from Figure 4.56(a) that the increase in number of cracks between the control and strengthened elements varies only slightly, suggesting that the CFRP strengthening in these already heavily-reinforced members had little effect on performance.

This hypothesis of the lack of increase in performance for heavily-reinforced elements is further supported by the results shown in Figures 4.56(b), (c) and (d). The average crack width remains relatively constant for the majority of the loading range for all beams, as do the maximum and average crack lengths; this is in contrast to the results for the ∅10mm beams where the average crack width and crack lengths for the control beam varied noticeably from those of the strengthened elements.

4.10.5 ρ =1.13% - ∅ 12mm doubly-reinforced beams

It is apparent from Figure 4.57(a) that the increase in number of cracks between the control and strengthened elements varies only slightly, suggesting that the CFRP strengthening in these already heavily-reinforced members had little effect on performance.

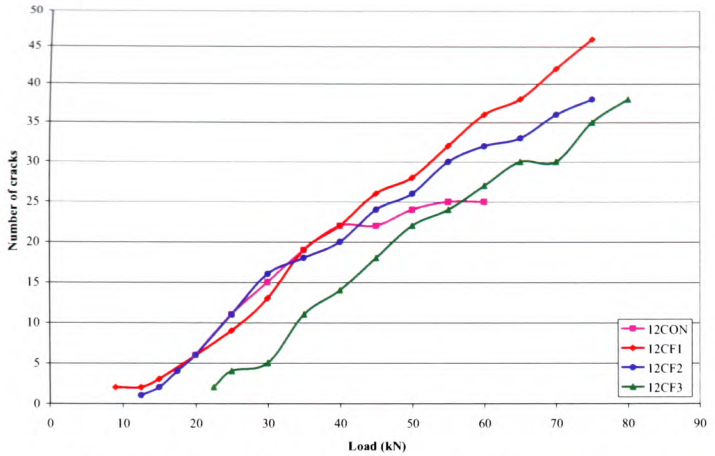

Figure 4.55(a) – Total number of cracks in constant moment zone against load for ∅12mm reinforced elements

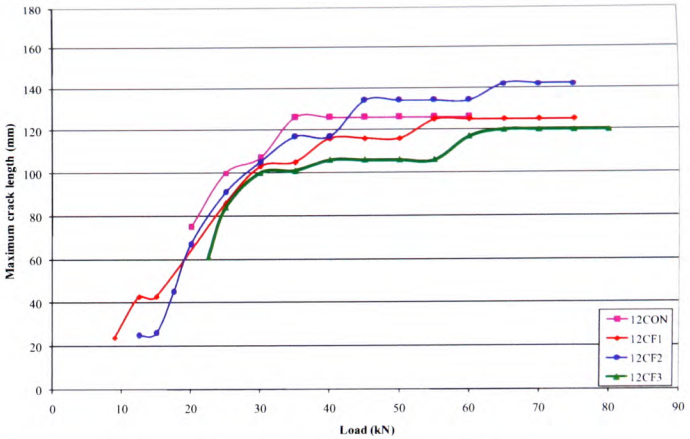

Figure 4.55(b) – Maximum crack length in constant moment zone against load for ∅12mm reinforced elements

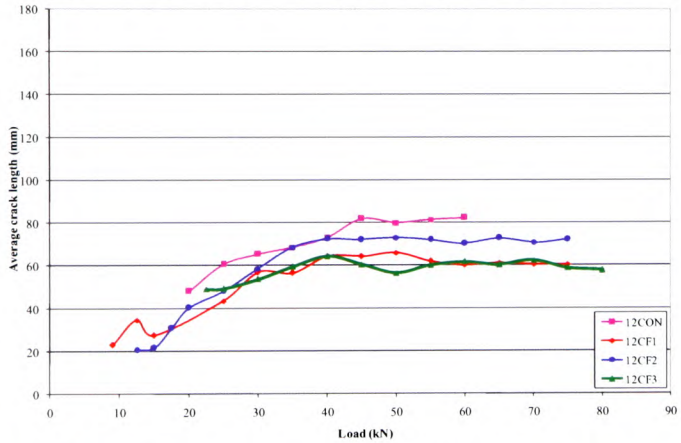

Figure 4.55(c) – Average crack length in constant moment zone against load for ∅12mm reinforced elements

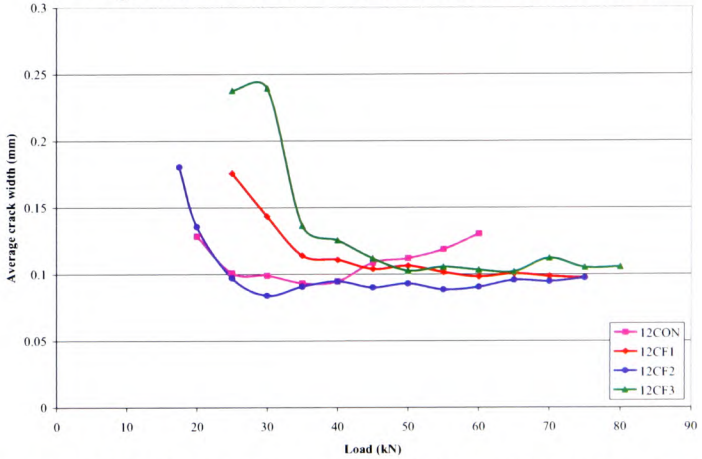

Figure 4.55(d) – Average crack width in constant moment zone against load for ∅12mm reinforced elements

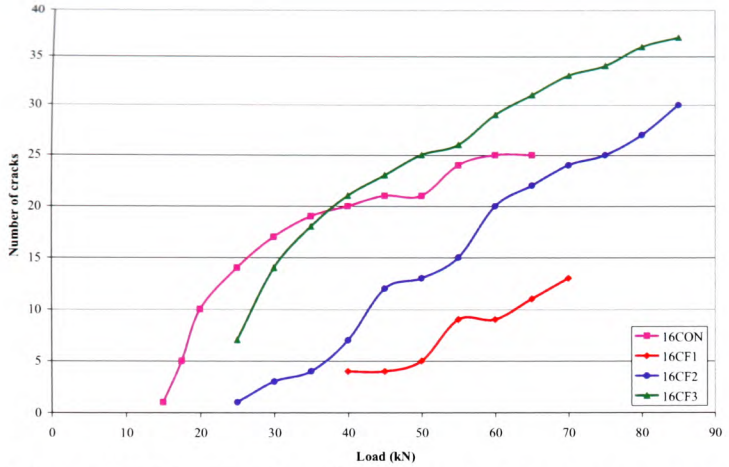

Figure 4.56(a) – Total number of cracks in constant moment zone against load for ∅16mm reinforced elements

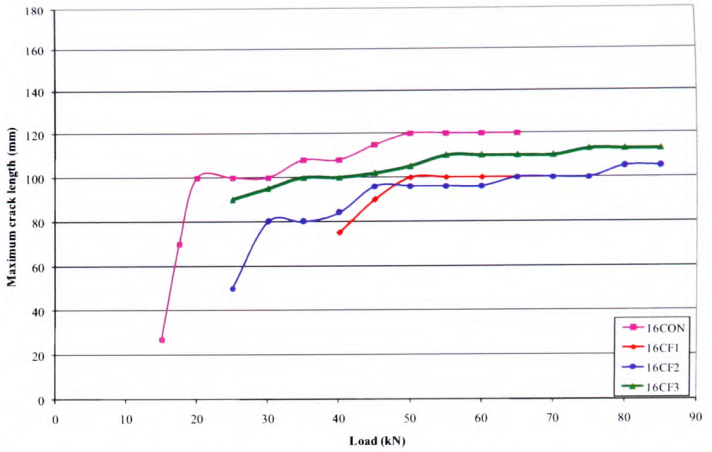

Figure 4.56(b) – Maximum crack length in constant moment zone against load for ∅16mm reinforced elements

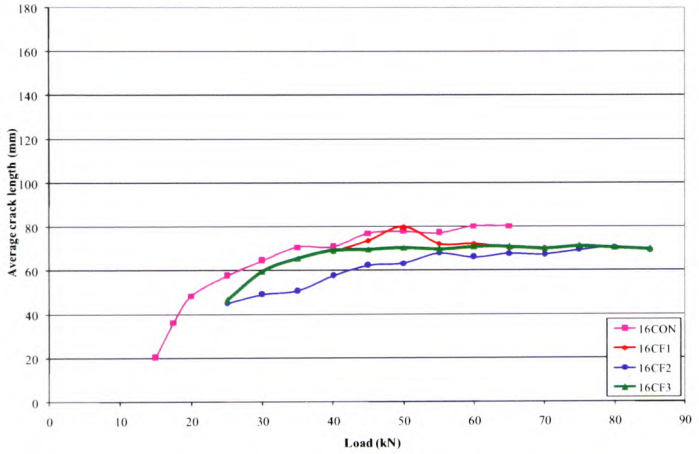

Figure 4.56(c) – Average crack length in constant moment zone against load for ∅16mm reinforced elements

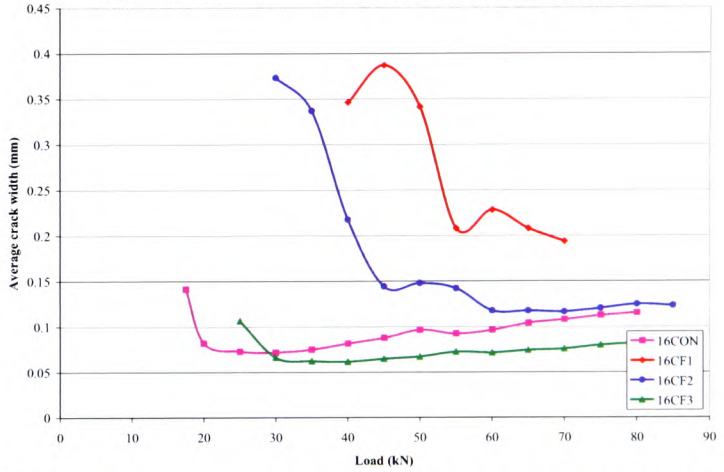

Figure 4.56(d) – Average crack width in constant moment zone against load for ∅16mm reinforced elements

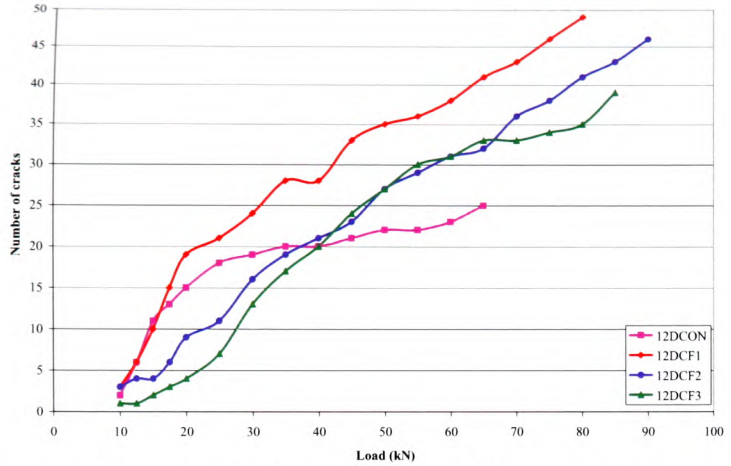

Figure 4.57(a) – Total number of cracks in constant moment zone against load for ∅12mm doubly-reinforced elements

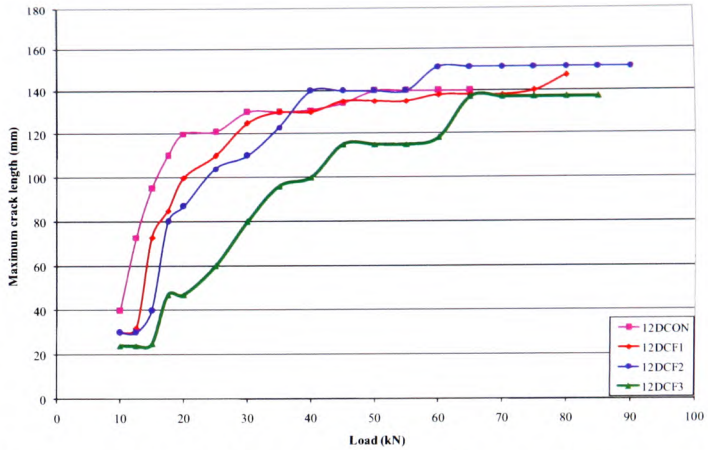

Figure 4.57(b) – Maximum crack length in constant moment zone against load for ∅12mm doubly-reinforced elements

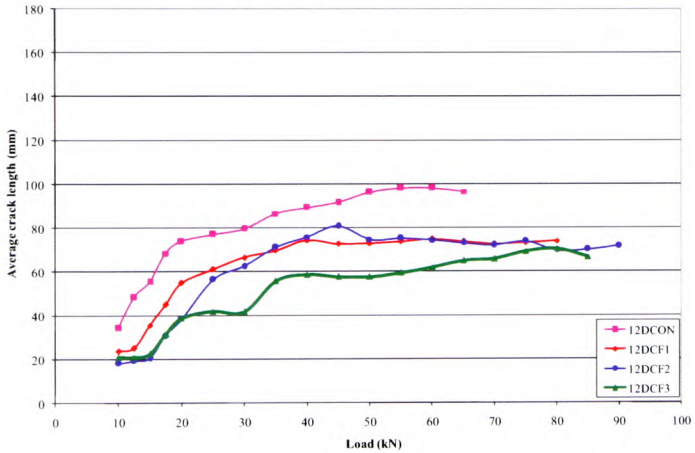

Figure 4.57(c) – Average crack length in constant moment zone against load for ∅12mm doubly-reinforced elements

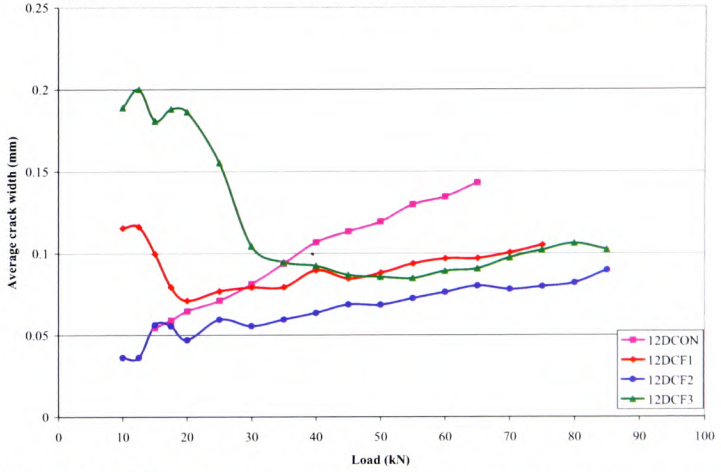

Figure 4.57(d) – Average crack width in constant moment zone against load for ∅12mm doubly-reinforced elements

4.10.6 ρ =0.40% - ∅ 8mm reinforced slabs

It can be seen from Figure 4.58(a) that the number of cracks for 8SCF2 increases more rapidly than for the other two strengthened slabs. This is most likely due to the nature of CFRP sheets adhered across the whole width of the element to better distribute the strain along the whole span at the edge of the element. As the plates were adhered in from the edge of the element, there was no strain redistribution where the cracks were being marked, which gave a suggestion of lower crack numbers along the whole span.

4.10.7 ρ =0.91% - ∅ 12mm reinforced slabs

It can be seen from Figure 4.59(a) that the number of cracks for 8SCF2 increases more rapidly than for the other two strengthened elements. This is most likely due to the nature of CFRP sheets adhered across the whole width of the slab to better distribute the strain along the whole span at the edge of the element. As the plates were adhered in from the edge of the element, there was no strain redistribution where the cracks were being marked, which gave a suggestion of lower crack numbers along the whole span.

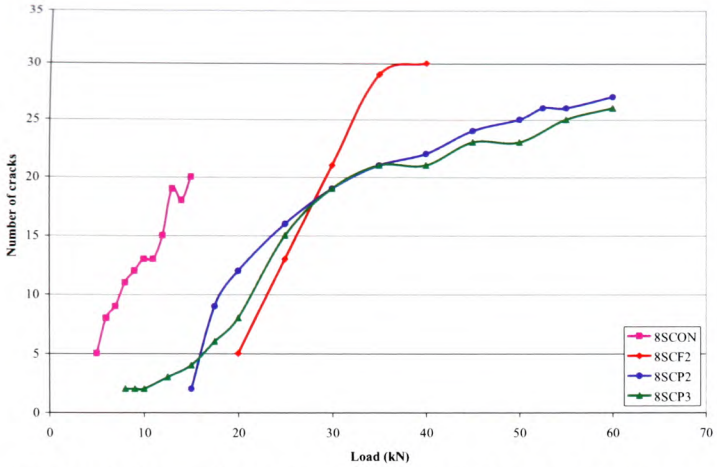

Figure 4.58(a) – Total number of cracks in constant moment zone against load for ∅8mm reinforced elements

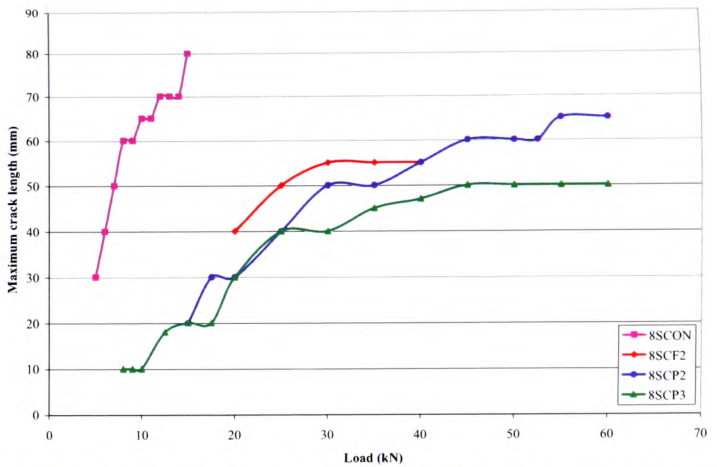

Figure 4.58(b) – Maximum crack length in constant moment zone against load for ∅8mm reinforced elements

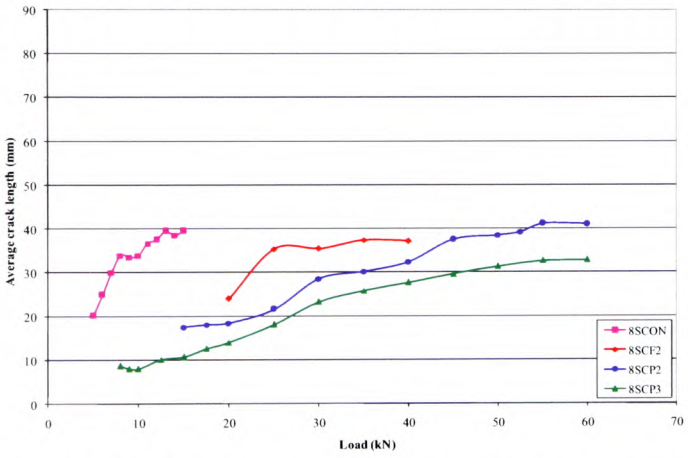

Figure 4.58(c) – Average crack length in constant moment zone against load for ∅8mm reinforced elements

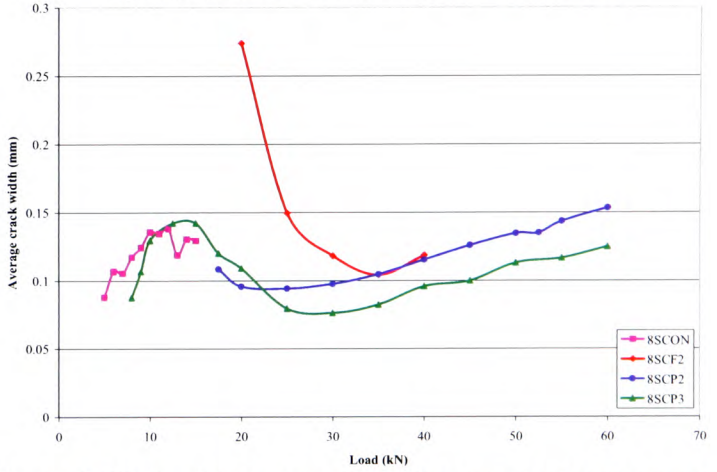

Figure 4.58(d) – Average crack width in constant moment zone against load for ∅8mm reinforced elements

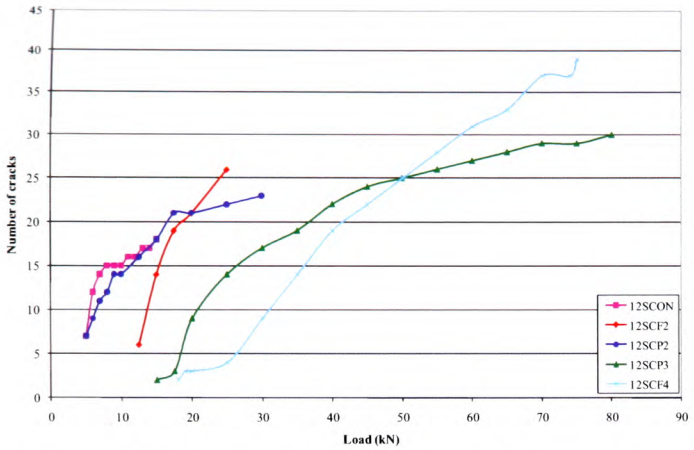

Figure 4.59(a) – Total number of cracks in constant moment zone against load for ∅12mm reinforced elements

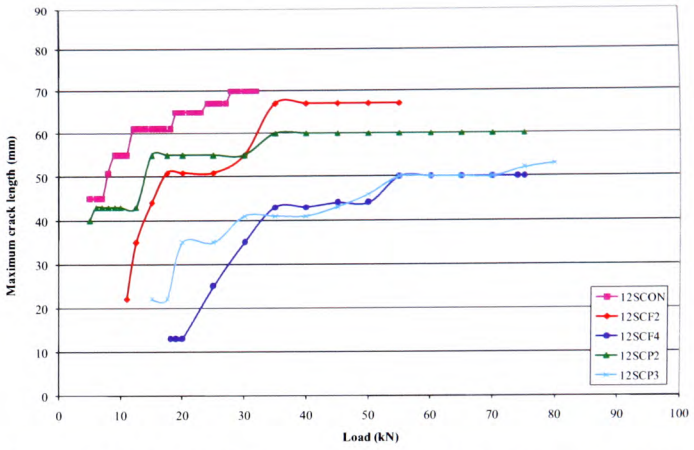

Figure 4.59(b) – Maximum crack length in constant moment zone against load for ∅12mm reinforced elements

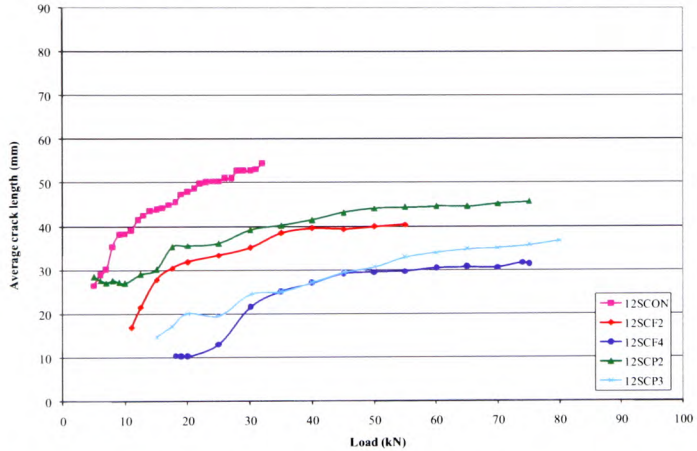

Figure 4.59(c) – Average crack length in constant moment zone against load for ∅12mm reinforced elements

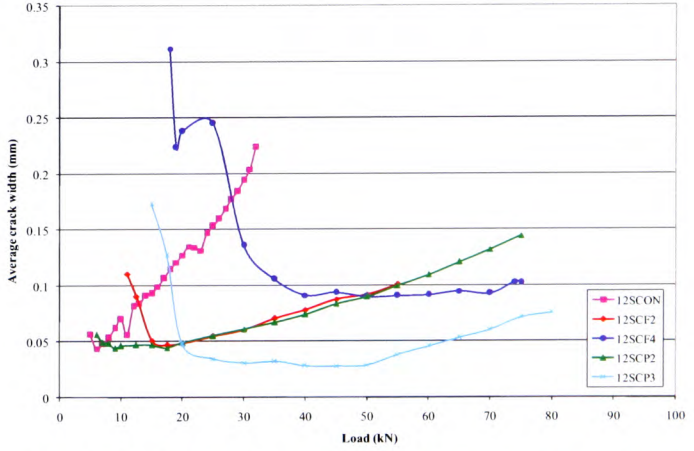

Figure 4.59(d) – Average crack width in constant moment zone against load for ∅12mm reinforced elements

4.11 Summary

A thorough experimental programme has been carried out and results have been processed for all tested elements. The results were initially presented in tabular form, detailing the salient loads, strength gains, moments, deflections and failure modes, before more detailed accounts were presented for each category.

Firstly, the load deflection analyses for all elements were presented and it was determined that as the amount of externally-bonded fibre composites increased, there was an increase not only in the load-carrying capacity of the element but also in the element stiffness; this can be seen from the load deflection plots for the tested elements. This concurs with published sources, covered in Chapter 2, which generally agreed that FRP composites can increase both the load-carrying capacity and stiffness of RC elements[§]. It can also be seen that the elements with the lower percentages of steel reinforcement display larger increases in load-carrying capacity when compared to their more heavily-reinforced counterparts, as discussed in Chapter 2[**]. Accordingly, the effect of the bonded composites for the elements reinforced with two ∅16mm bars was noticeably reduced, due to the high amount of reinforcing steel already present in the section.

The presented deflection profiles displayed that strengthened elements, in the same way as their non-strengthened counterparts, demonstrate a circular profile between the loading points (in the constant moment zone) and also that the deflection profiles remain symmetrical up to failure.

Next, the load strain relationship of each element set was presented and it was noted that for many of the elements that had observed steel-yield/concrete crushing failure modes, the recorded strain in the concrete in compression was

[§] Meier *et al.* 1992; Chajes *et al.* 1994 & 1995; Hutchison *et al.* 1996; Shahawy *et al.* 1996; Tumialan *et al.* 1999; Ramana *et al.* 2000; Tann *et al* . 2000; Leung 2002; Maalej *et al.* 2005; Tann 2005; Oehlers *et al.* 2006; Esfahani *et al.* 2007; Oehlers *et al.* 2008.

[**] Hutchison *et al.* 1996; Arduini *et al.* 1997

significantly lower than that expected for concrete crushing (≈3500με). However, it is likely that, following yielding of the internal steel reinforcement, the rotation in the element caused localised crushing of the concrete in compression after the last strain record was taken. In addition, the two Ø10mm elements with one and two layers of externally-bonded CFRP composite sheets respectively, displayed a dramatic increase in strains in the latter stages of loading. This demonstrates a potential for these strengthened elements to exhibit ductile failure characteristics, which is not present in more heavily strengthened elements.

The concrete surface strains, obtained using the DEMEC system, showed that the strain distribution across the element depth for strengthened elements, like un-strengthened ones remained linear from initial loading stages through to ultimate limit state.

It was shown that the FRP surface strain profiles displayed good correlation with the surface strains obtained from the DEMEC system. It was also noted that for all the elements where debonding was the failure mode, the recorded FRP surface strain was significantly below the 8000με recommended by published guidance to preclude debonding failure. Consequently, it is recommended that further study is needed in this area to verify the validity of the current strain limit, although such work is outside the scope of the current research.

The graphs of neutral axis depth against load displayed an increase in the neutral axis depth at the latter stages of loading, which demonstrated the initiation of failure in the concrete in compression, which resulted in a lowering of the neutral axis in the section. This was further corroborated by the elements doubly-reinforced with two Ø12mm reinforcing bars in compression and tension, as these elements displayed a much reduced increase in the neutral axis depth due to the presence of the steel in compression.

Moment curvature graphs were generated from two data sources; namely, deflections and strains. The resulting graphs demonstrated the lack of deviation between the curves, which in turn corroborated the quality of the acquired data.

Finally, the crack propagation for all elements was presented and it was noted that the strengthened elements displayed a number of behavioural differences with regard to cracking in the constant moment zone when compared with their non-strengthened counterparts. The strengthened elements showed:

- A higher overall number of surface cracks
- A shorter maximum crack length
- A shorter average crack length
- A smaller average crack width

These points are attributable to the ability of the FRP composites to better distribute the stress in the soffit of the element so that, for example, the extension is spread better over the whole element length, which results in a better, and more dense, crack distribution. Additionally, the increase in element stiffness causes a reduction in element deflection (as can be seen in the load deflection plots in Section 4.3), which in turn results in shorter cracks.

CHAPTER 5 DEFLECTION PREDICTION FOR FIBRE COMPOSITES STRENGTHENED RC ELEMENTS

5.1 Introduction

As discussed in Chapter 2, in order to define a deformation-based ductility index for a strengthened element, it is essential to determine the element deflection for a given load. However, it is recognized that once any loaded element progresses into its non-linear state, the prediction of deflection becomes significantly difficult, since the most important parameter, the flexural rigidity, EI, is no longer a constant value.

It is, nevertheless, viable to develop a semi-empirical method of deflection prediction by quantifying the flexural rigidity from the moment-curvature relationships obtained during the experimental programme. These EI values can then be analysed and a trend determined to quantify the flexural rigidity for any given section, under any loading greater than the service load, and, hence, the prediction of deflections in flexural members.

5.2 Background

The prediction of deflections in steel reinforced concrete flexural elements under service loading can be predicted with reasonable accuracy, utilising the equations found in BS 8110 and BS EN 1992-1-1:2004 (Eurocode 2). However, the prediction of deflections for fibre composites strengthened elements is not so well documented. In particular, no such predictions under ultimate load conditions have been investigated to any great detail. As discussed in 5.1, it is essential that the deflection of strengthened elements can be predicted not only at the service load level but also before they reach the ultimate limit state, so that appropriate ductility and deformability indices can be calculated.

The behaviour of fibre composites strengthened elements follows a pseudo-linear pattern in different stages up to failure and, consequently, it is possible to develop a numerical method of determining flexural rigidity, which would enable the establishment of element deflections up to ultimate limit state.

5.3 Semi-empirical equation for deflection determination

Consider the strengthened element 10CF2 from the experimental programme; i.e. a 200mm x 100mm concrete beam reinforced with two, 10mm diameter, high-yield steel bars and subsequently strengthened with two, full-width layers of CFRP fabric. The moment curvature relationship for this element, as detailed in Chapter 4, Section 4.9, is shown in Figure 5.1.

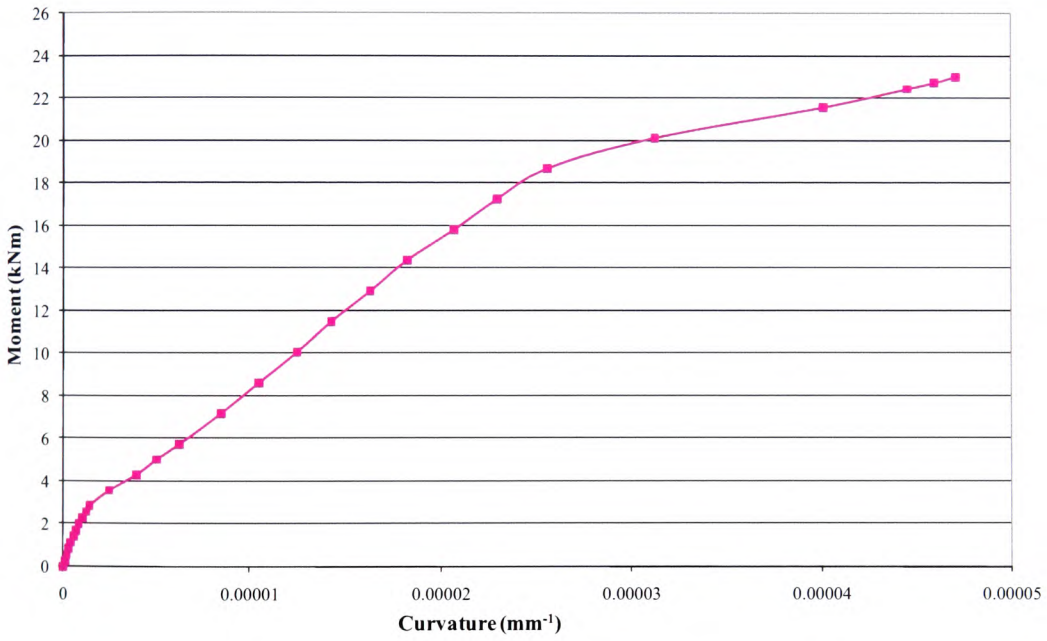

Figure 5.1 – Moment Curvature relationship for 10CF2

By using the equation for the mean value of the modulus of elasticity for normal weight concrete given in BS 8110 (Equation 5.1), it is possible to determine a value for the concrete used in the making of the element 10CF2:

$$E_c = K_0 + 0.2 f_{cu} \qquad 5.1$$

where K_0 is a constant closely related to the elastic modulus of the aggregate, taken as 20kN/mm^2 for normal weight concrete and f_{cu} is the concrete cube strength in N/mm^2. It should be noted that f_{cu} is input into the equation in N/mm^2, even though it yields a value in kN/mm^2.

This equation yields a value for 10CF2 of:

$$E_c = K_0 + 0.2f_{cu} = 20 + 0.2(59.9) = 32.0kN/mm^2$$

which is close to the experimental value of 36.3kN/mm^2.

The second moment of area of the beam can then be derived from the previously obtained, experimental, moment-curvature data. The following equation (5.2), defined by Tann (2003), defines the relationship between the applied load, P, and the calculated second moment of area of a CFRP strengthened slab section.

$$I_g = \left\{\left(\frac{0.01A_f}{\sqrt{P}}\right) + \left(\frac{P_{min}}{2P}\right)\right\} I_0 \qquad 5.2$$

Where:

I_g is the second moment of area of the CFRP strengthened section;

A_f is the area of the carbon fibre composite, in mm^2;

P is the applied load;

P_{min} is the load at which concrete cracking occurs, i.e. the stress at which the concrete reaches its tensile strength, taken for the purposes of this programme of work as 3.2N/mm^2;

I_0 is the second moment of area of the transformed, uncracked section.

The maximum deflection of an element subjected to four-point loading can be defined as follows, using the standard equation:

$$\delta_{max} = \frac{Pa}{24EI}(3l^2 - 4a^2) \qquad 5.3$$

Where:

a is the distance from the support to the nearest point load (in the case of 10CF2, this distance is 575mm)

l is the effective span of the element (in the case of 10CF2, 2.4 metres)

By substituting Equations 5.1 and 5.2 into Equation 5.3, it is possible to derive a semi-empirical equation for deflection prediction, as follows:

$$\delta_{max} = \frac{Pa}{24E_c I_0 \left\{\left(\frac{0.01A_f}{\sqrt{P}}\right) + \left(\frac{P_{min}}{2P}\right)\right\}}(3l^2 - 4a^2) \qquad 5.4$$

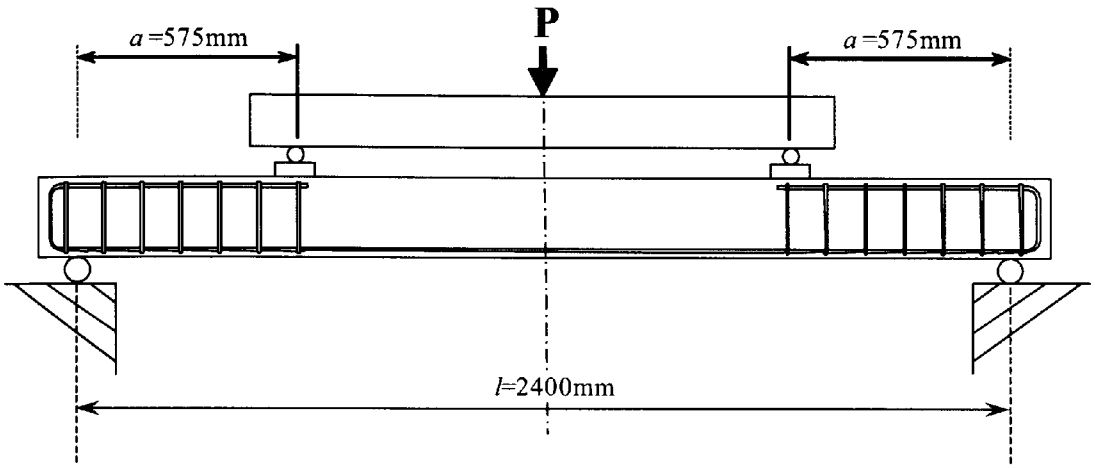

Figure 5.2 – Element dimensions for calculation of δ_{max}

This generic expression can be used to predict deflection for all slab elements in the experimental programme for the specific, four-point loading configuration used, and examples of the predicted deflections compared to actual, experimental values can be seen in Figures 5.3 (a) and (b).

However, as discussed, this method was originally designed for predicting the deflection in slab elements and, despite beam elements being theoretically identical to all such flexural elements for the purposes of analysis, it was found that when the above method was applied to beam elements from the experimental programme, the equation over-estimated the value for δ_{max}. Consequently, a revised equation has been developed that could predict the load deflection behaviour of beam elements. This variation is despite the slabs from the experimental programme with Ø12mm reinforcement having a higher reinforcement ratio than the beams reinforced with Ø8mm and Ø10mm bars and cannot therefore be connected to the reinforcement ratio of the flexural element being considered.

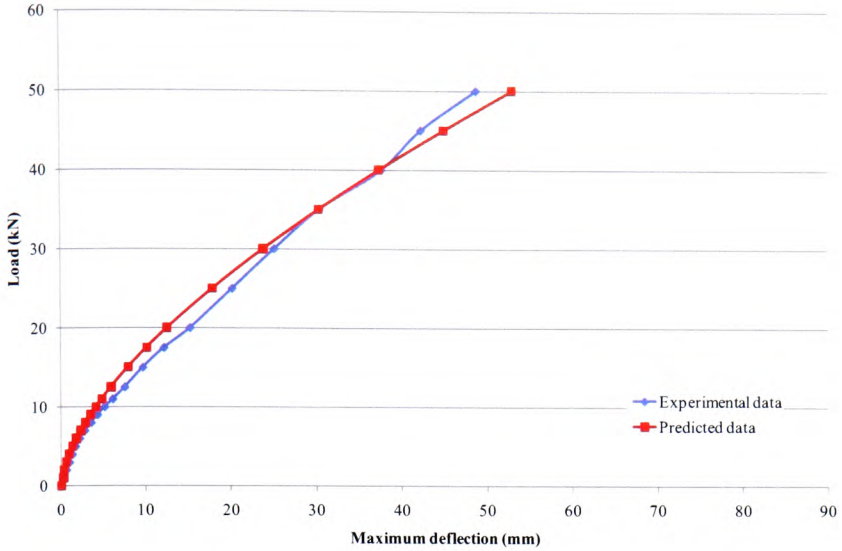

(a)

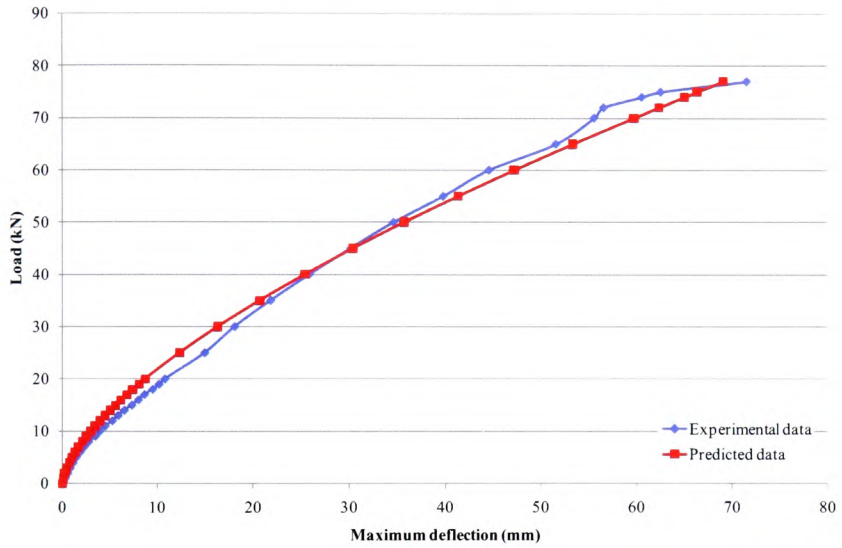

(b)

Figure 5.3 – Experimental and predicted load deflection behaviour for (a) 12SCF2 and (b) 12SCF4

Initially, a new form of Equation 5.2 was derived, utilising the moment curvature plots for various elements in the experimental programme, in order to determine a revised semi-empirical method that could estimate the second moment of area of a fibre-composites-strengthened beam element. This required the influence of the fibre composites to be reconsidered, which in turn enabled the value of the second moment of area to be better predicted. It was found that the factor of 0.01, applied to A_f, required altering to 0.05, shown in Equation 5.5. This resulted in a significantly improved method of prediction for the second moment of area throughout the loading of the beam elements; this is illustrated in Figures 5.4 (a), (b) and (c).

$$I_g = \left\{\left(\frac{0.05A_f}{\sqrt{P}}\right) + \left(\frac{P_{min}}{2P}\right)\right\} I_0 \qquad 5.5$$

Subsequently, a revised Equation 5.4 was developed, which predicted the load deflection behaviour for any beam element. The generic equation, derived from and calibrated against all beam elements in the experimental programme, is given in Equation 5.6.

Presented in Figures 5.4(a), (b) and (c), are the comparisons of predicted load deflection behaviour against actual experimental data for three of the experimental elements.

$$\delta_{max} = \frac{Pa}{48E_c I_0 \left\{\left(\frac{0.05A_f}{\sqrt{P}}\right) + \left(\frac{P_{min}}{2P}\right)\right\}} (3l^2 - 4a^2) \qquad 5.6$$

It should be noted that the expression has been amended to include a factor of $\frac{1}{2}$, which better represented the behaviour of fibre composite strengthened beam elements; this accounts for the '48', rather than '24', in the denominator.

The successful modelling of the load deflection behaviour of the elements in the experimental programme suggests that, in addition to the slab elements predicted by Tann (2003), the flexural rigidity of beam elements strengthened with fibre composites can also be acceptably estimated.

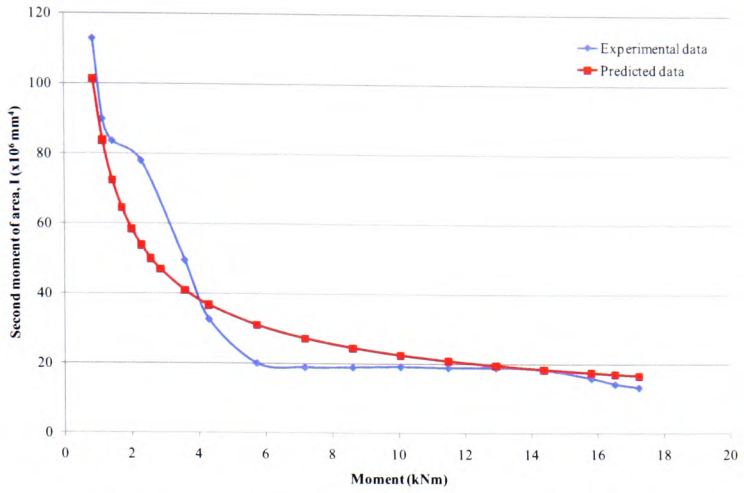

Figure 5.4(a) – Experimental and predicted values for second moment of area, I, using Equation 5.5 for element 8CF2

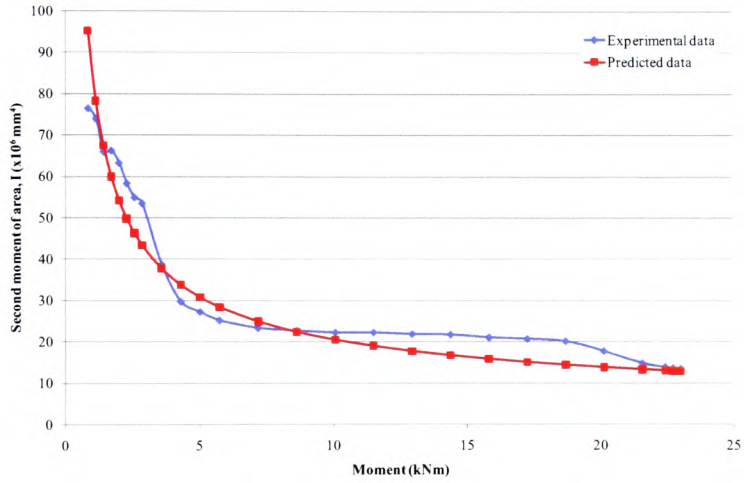

Figure 5.4(b) – Experimental and predicted values for second moment of area, I, using Equation 5.5 for element 10CF2

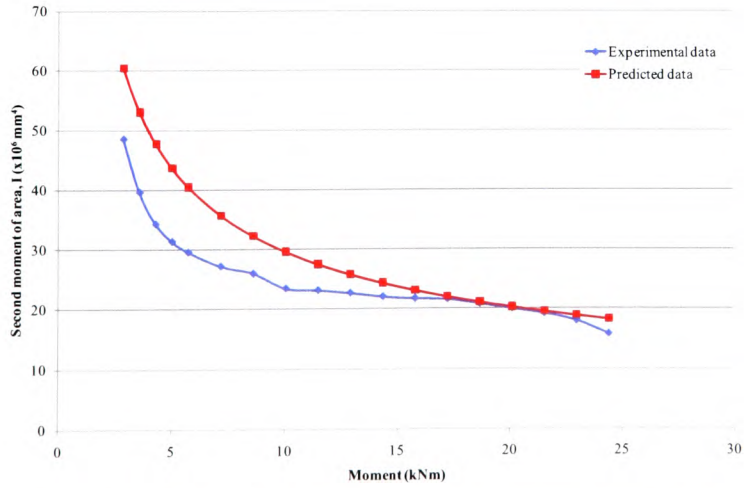

Figure 5.4(c) – Experimental and predicted values for second moment of area, I, using Equation 5.5 for element 12CF3

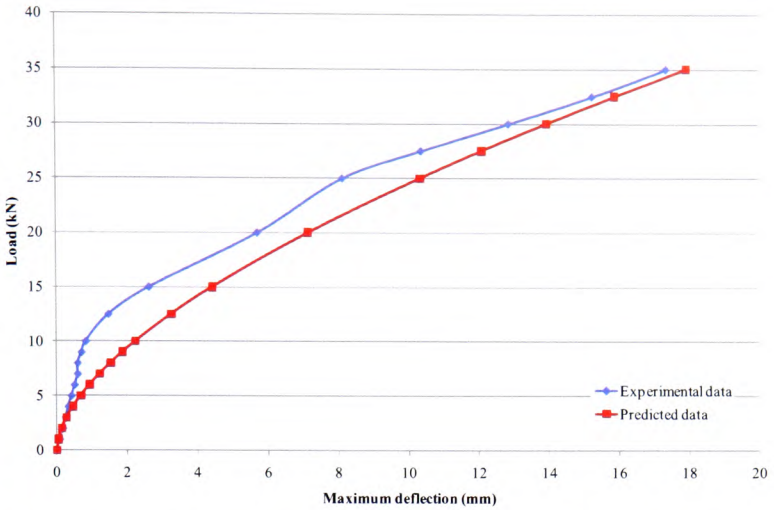

Figure 5.5(a) – Experimental and predicted load deflection behaviour for element 8CF1

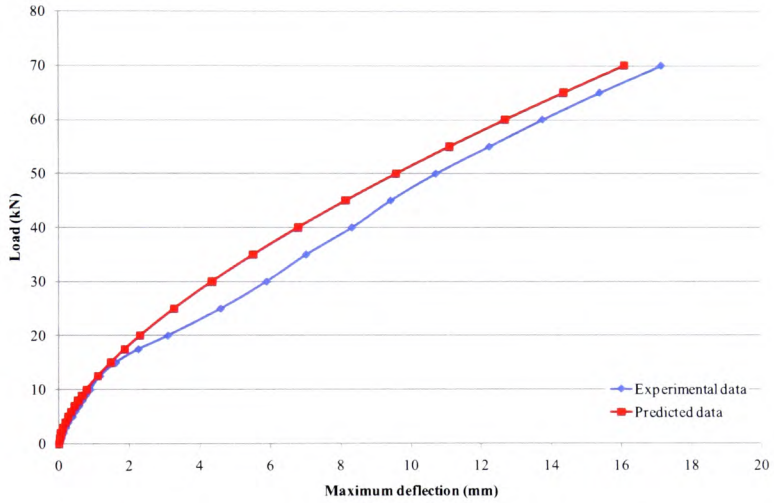

Figure 5.5(b) – Experimental and predicted load deflection behaviour for element 10CF3

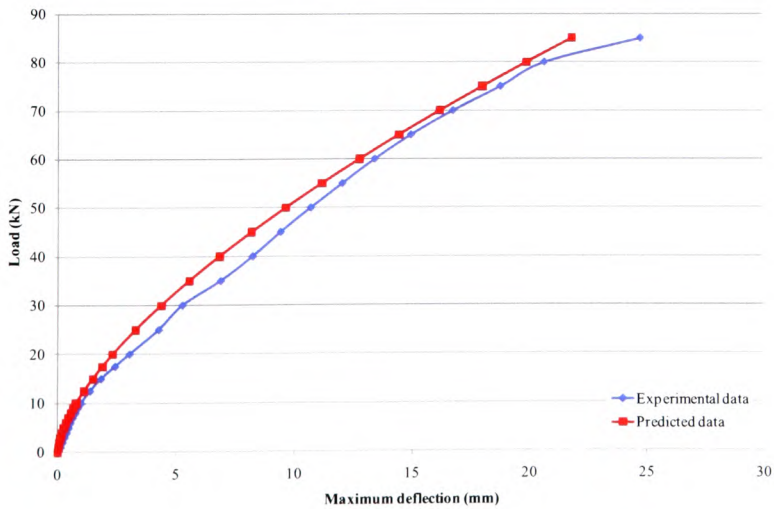

Figure 5.5(c) – Experimental and predicted load deflection behaviour for element 12CF3

5.4 Comparative study

In order to validate the accuracy of the deflection prediction method detailed in Section 5.3, it was necessary to carry out a further study on a number of strengthened elements from published data*. Consequently, the deflection prediction method was applied to additional elements with various geometry and amounts of strengthening. A comprehensive list of the element data is presented in Table 5.1.

Presented in Figures 5.6 (a) to (e) are comparisons of the predicted and actual, published load deflection behaviour for five strengthened elements from published data. Each Figure shows the predicted load deflection behaviour on the left hand side, on axes that are comparable to those in the published data, and on the right hand side is a reproduction of the published graph with the predicted curve superimposed on top. It can be seen there is very good correlation between the actual displayed load deflection behaviour for the compared elements, with that predicted by the proposed method.

5.5 Summary

It has been shown in Section 5.3 that the flexural rigidity of beam elements strengthened with fibre composites can now be modelled with acceptable accuracy. Consequently, the load deflection behaviour can also be acceptably predicted. This is possible primarily due to the fact that such elements display pseudo-elastic load-deflection behaviour even after the concrete and/or internal steel reinforcement have moved into their non-linear stages.

Using the method detailed in Section 5.3, in particular with Equations 5.5 and 5.6, one can determine the load deflection behaviour up to and including the predicted ultimate limit state. Consequently, the designer is able to determine the ductility characteristics of the element being considered and ensure that suitable ductility and/or deformability is achieved at the design stage.

* Tann (2001); Maalej *et al.* (2005); Wenwei *et al.* (2005); Esfahani *et al.* (2007)

Table 5.1 – Element data for comparative study

Elem. Ref.	Source	Size (mm)	Int'l flexural reinf't	FRP		Failure load (kN)
				Type[†]	*% of area*	
A8	Tann (2001)	100 x 200	2T10	C, P	0.64	68.8
B2			2T10	C, P	0.56	92.5
A5	Maalej *et al.* (2005)	115x146	3T10	C, F	0.23	87.4
CFC30	Wenwei *et al.* (2005)	150x200	3 x Ø14mm	C, F	0.09	140.0
B4	Esfahani *et al.* (2007)	150x200	2 x Ø12mm	C, F	0.264	74.4

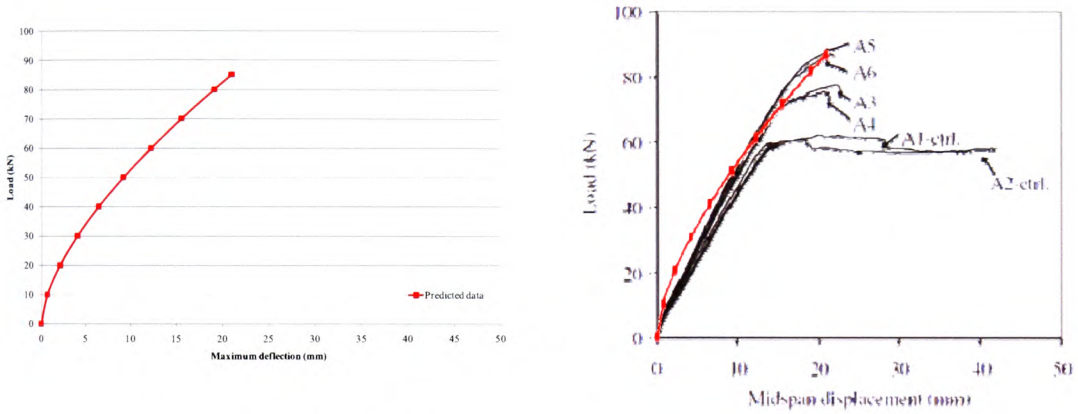

Figure 5.6 (a) – Predicted load deflection and overlayed graph for element A5 (Maalej *et al.* 2005)

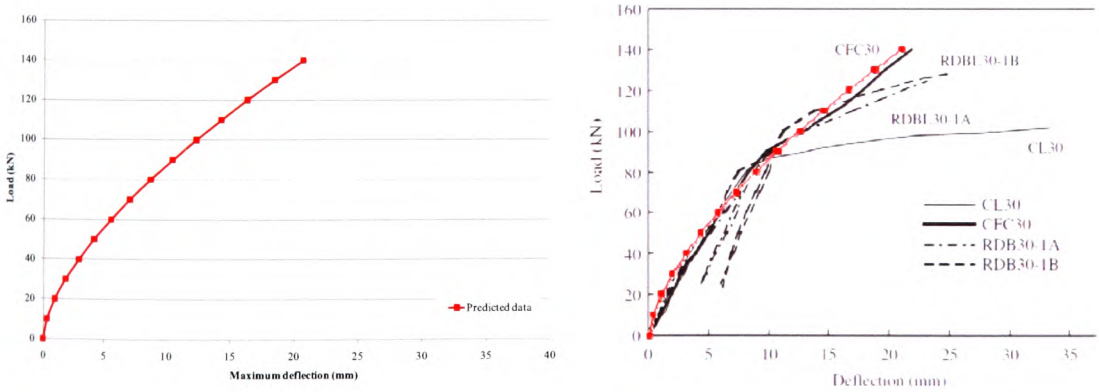

Figure 5.6 (b) – Predicted load deflection and overlayed graph for element CFC30 (Wenwei *et al.* 2005)

[†] C – Carbon fibre composites; F – Fabric; P - Plate

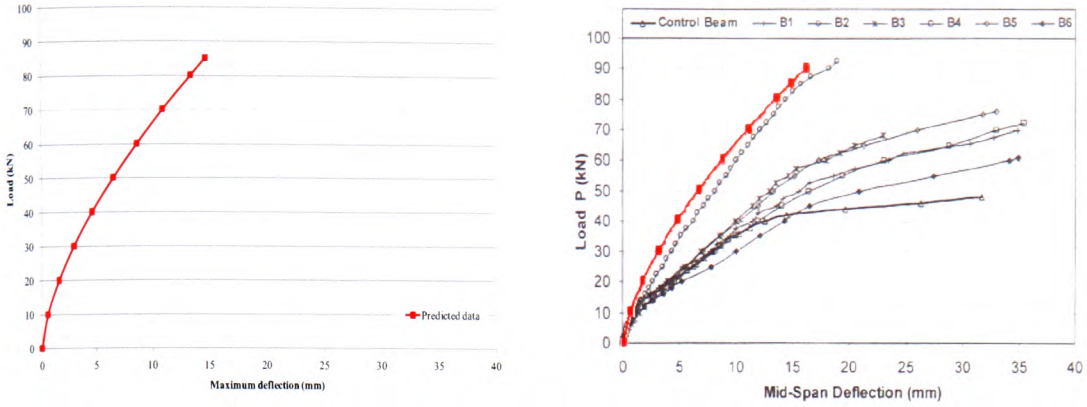

Figure 5.6 (c) – Predicted load deflection and overlayed graph for element B2 (Tann 2001)

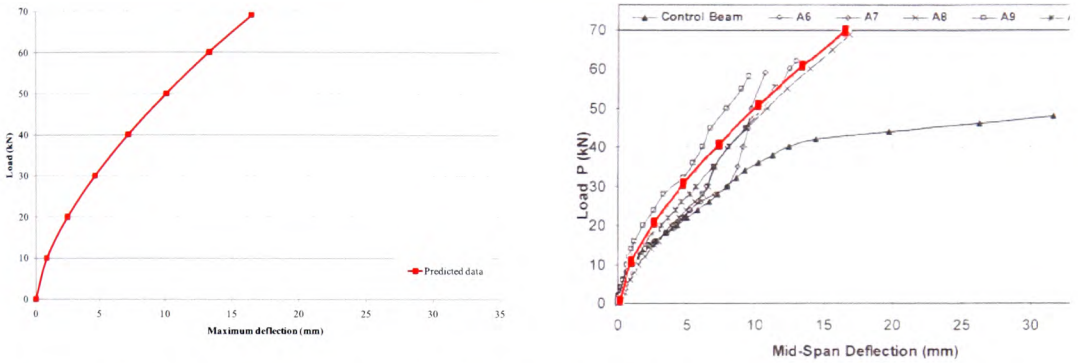

Figure 5.6 (d) – Predicted load deflection and overlayed graph for element A8 (Tann 2001)

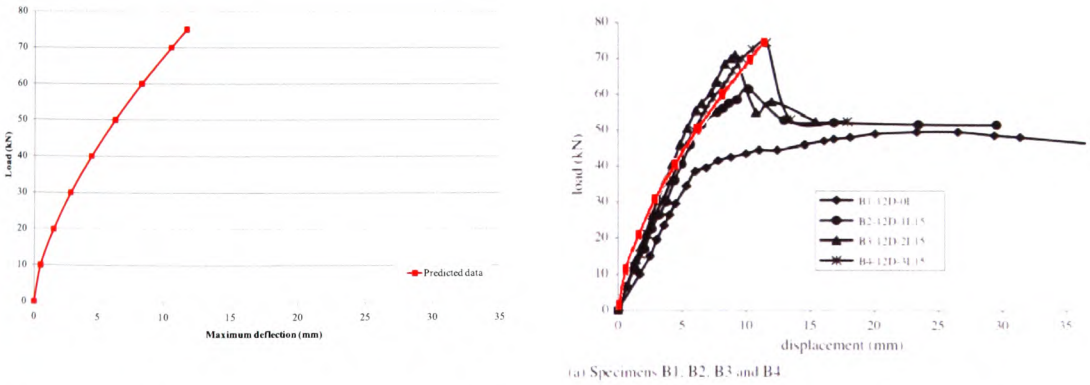

Figure 5.6 (e) – Predicted load deflection and overlayed graph for element B4 (Esfahani *et al.* 2007)

CHAPTER 6 ANALYTICAL MODELLING

6.1 Introduction

In Chapter 3, the flexural behaviour of reinforced concrete beams that had been strengthened with externally-bonded CFRP composites was investigated in the course of the experimental programme. It can be seen that there is scope to ensure sufficient ductility in a structural element to ensure a controllable, non-brittle mode of failure.

Additionally, a parametric study was needed, in order to corroborate the experimental data and represent the element behaviour and, subsequently, a non-linear, numerical model was developed, as detailed below.

6.2 Material Constitutive Laws

6.2.1 Flexural concrete in compression

The behaviour of concrete in compression is one of the primary concerns in any RC structural element. Both BS 8110 and BS EN 1992-1-1:2004 (Eurocode 2) provide stress/strain relationships for the analysis of reinforced concrete sections.

BS 8110 states the following as the stress-strain relationship for concrete in compression and this is also represented in Figure 6.1:

$$f = 0.8 f_{cu}\left[\frac{k\eta - \eta^2}{1 + (k-2)\eta}\right] \qquad 6.1$$

Where;

$$\eta = \frac{\varepsilon}{\varepsilon_{c,1}} = \frac{\varepsilon}{0.0022}\ ;\ k = \frac{1.4\varepsilon_{c,1}E_0}{f_{cu}} > 1\ ;\ E_0 = 5.5 f_{cu}$$

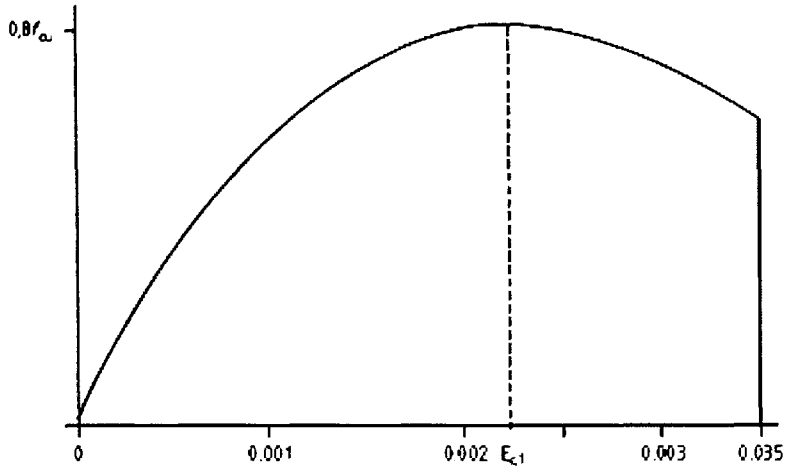

Figure 6.1 – Stress/strain curve for concrete in compression for rigorous analysis as per BS 8110-1:1997

Eurocode 2 gives the following as a stress/strain relationship for concrete in compression when conducting non-linear structural analysis (see also Figure 6.2):

$$\frac{\sigma_c}{f_{cm}} = \frac{k\eta - \eta^2}{1 + (k-2)\eta} \qquad 6.2$$

$$\Rightarrow \sigma_c = f_{cm}\left[\frac{k\eta - \eta^2}{1 + (k-2)\eta}\right] \qquad 6.3$$

Where;

$$\eta = \frac{\varepsilon_c}{\varepsilon_{c1}}$$

ε_{c1} *is the strain at peak stress*

$$k = 1.05(E_{cm})\frac{|\varepsilon_{c1}|}{f_{cm}}$$

Stress/strain curves for all values of f_{ck} are shown in Figure 6.3, calculated using the above equations and utilising the values shown in Table 6.1.

Table 6.1 – Strength and deformation characteristics for concrete (from Table 3.1 in Eurocode 2)

f_{ck} (N/mm^2)	12	16	20	25	30	35	40	45	50	55	60	70	80	90
$f_{ck,cube}$ (N/mm^2)	15	20	25	30	37	45	50	55	60	67	75	85	95	105
f_{cm} (N/mm^2)	20	24	28	33	38	43	48	53	58	63	68	78	88	98
E_{cm} (kN/mm^2)	27	29	30	31	33	34	35	36	37	38	39	41	42	44
ε_{c1} (‰)	1.8	1.9	2	2.1	2.2	2.25	2.3	2.4	2.45	2.5	2.6	2.7	2.8	2.8

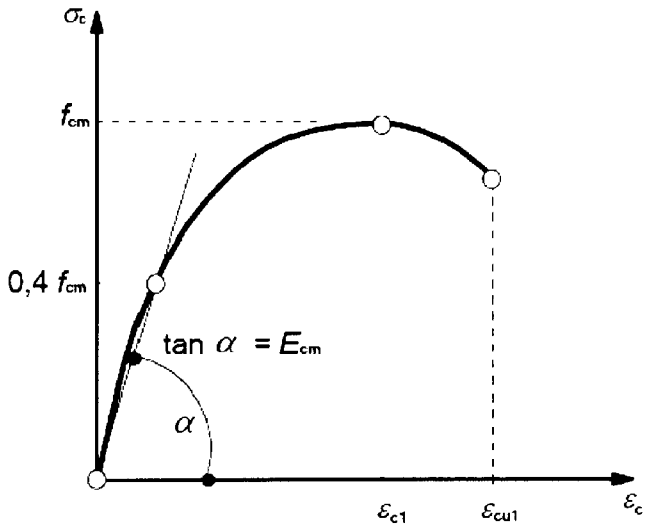

Figure 6.2 – Stress/strain curve for concrete in compression from BS EN 1992-1-1:2004 (Eurocode 2)

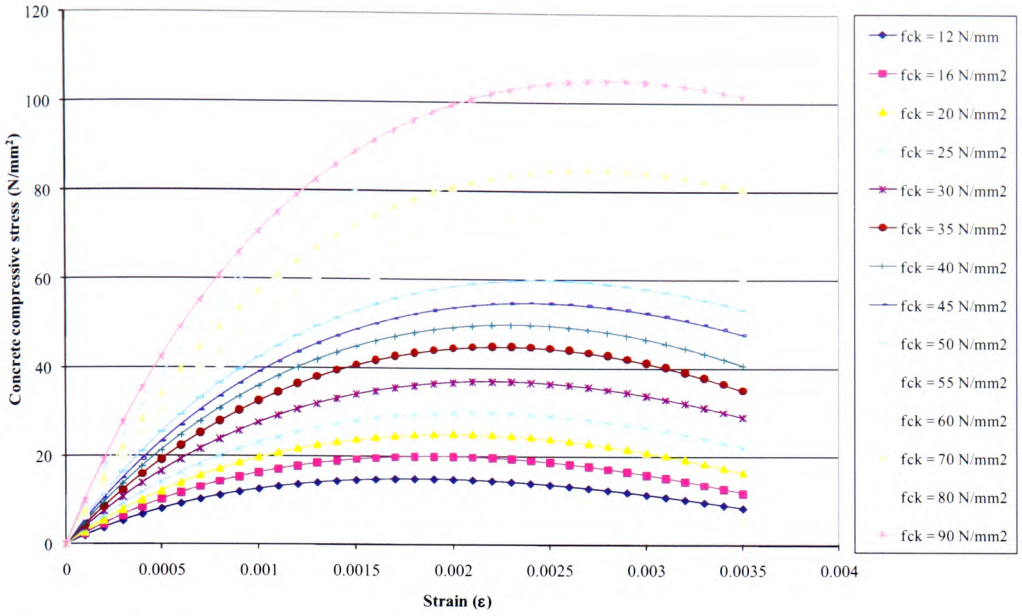

Figure 6.3 – Stress/strain curves for concrete in compression for values of f_{ck} from 12 to 90 N/mm^2, derived from Eurocode 2

6.2.2 Flexural concrete in tension

Both BS8110 and Eurocode 2 assume that the tensile strength of concrete is negligible and can therefore be taken to be zero for the purposes of design, thereby ensuring an over-designed and more conservative section. However, for the purposes of accurate structural analysis, some form of stress/strain relationship for flexural concrete in tension has to be assumed. To this end, the following relationship was assumed, when constructing the numerical model:

$$\sigma_t = f_{ct}\varepsilon_t \qquad \{\varepsilon_t < \varepsilon_{ct}\} \qquad 6.4$$

$$\sigma_t = f_{ct}\left(\frac{\varepsilon_{ct}}{\varepsilon_t}\right)^{0.4} \qquad \{\varepsilon_t > \varepsilon_{ct}\} \qquad 6.5$$

$$f_{ct} = 0.31\sqrt{f_{cu}}\,^{*} \qquad 6.6$$

* Belarbi *et al.* (1994)

Where ε_{ct} is the average concrete tensile strain when the first crack occurs and is assumed to be 80 $\mu\varepsilon$ or 0.000080 strains. The power of 0.4 is a coefficient that represents the bond that deformed steel reinforcing bars have with concrete (Sato *et al*, 1999). However, this material model is based on concrete cube strengths and, in order to maintain consistency with other concrete properties within the numerical model, it was considered necessary to determine the concrete tensile strength based on the cylinder strength. Hence, the value of $f_{ck,cube}$ corresponding to the chosen cylinder strength f_{ck}, as detailed in Table 3.1 of EN 1992-1-1:2004, was used to determine the tensile strength of the concrete.

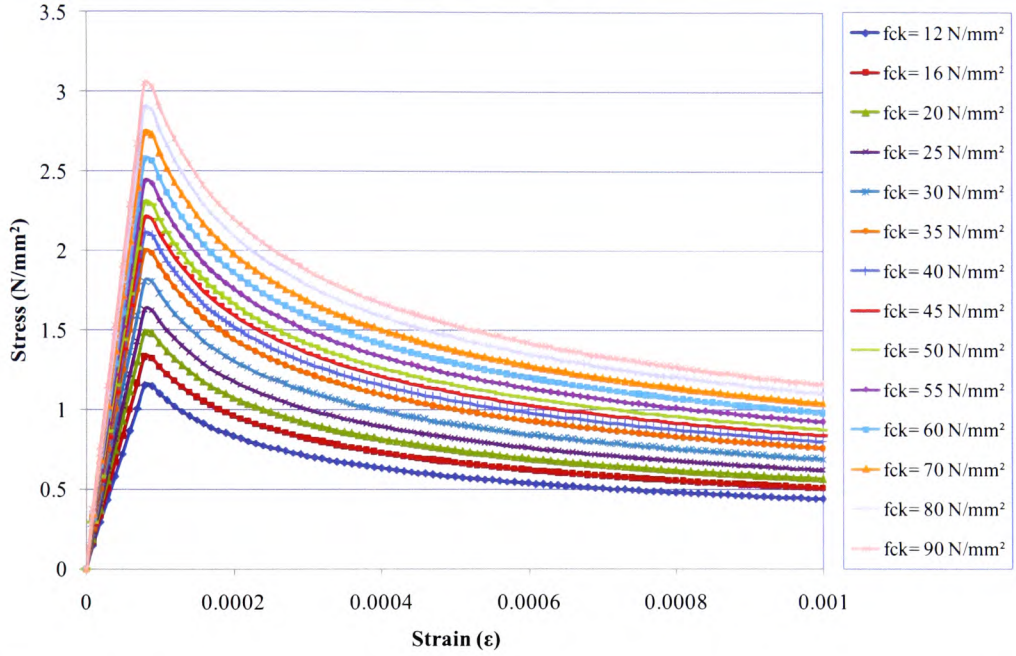

Figure 6.4 – Stress/strain curves for concrete in tension for values of f_{ck} from 12 to 90 N/mm^2, derived from Sato *et al*, 1999

6.2.3 Internal steel reinforcement in compression

A simplified bi-linear stress/strain relationship was used for the steel reinforcement as detailed in Figure 5.5. Up to the point where the steel yields, the corresponding stress is determined as the product of the strain multiplied by the elastic modulus:

$$\sigma_{steel} = E_{steel}\varepsilon \qquad 6.7$$

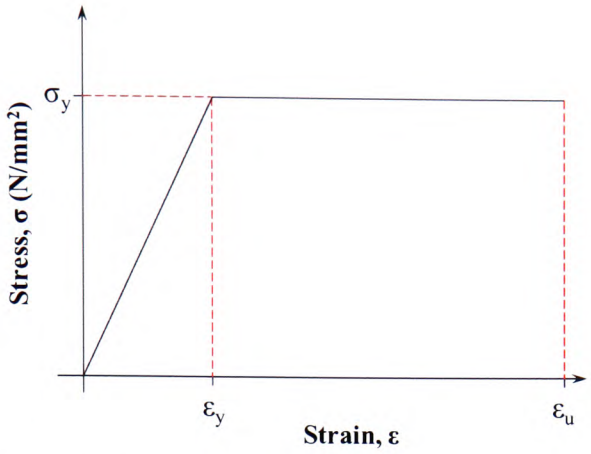

Figure 6.5 – Bi-linear stress/strain relationship for internal steel reinforcement in compression

6.2.4 Internal steel reinforcement in tension

The stress/strain relationship of steel reinforcement is normally assumed to be elastic-perfectly plastic, with a yield stress of f_y. However, a model suggested by Belarbi *et al.* (1994) takes into account the tension stiffening effects of steel bars which are embedded in concrete, which is different to that of bare bars in tension in that the yield stress lowers below, f_y. It was reported that the concrete tensile strength and the ratio of steel reinforcement were the primary influencing factors and the revised, apparent yield strength of the steel, f_y*, is given by Equation 6.8.

$$\frac{f_y^*}{f_y} = 1 - \frac{4}{\rho}\left(\frac{f_{ct}}{f_y}\right)^{1.5} \qquad 6.8$$

Where:
- ρ is the tension steel reinforcement ratio
- f_y* is the apparent yield strength of embedded bars
- f_y is the yield strength of the bare bar in tension
- f_{ct} is the concrete tensile strength (See 6.2.2)

In order to simplify the stress/strain relationship when determining the material behaviour for the analytical model, a tri-linear profile was used, as demonstrated in Figure 6.6.

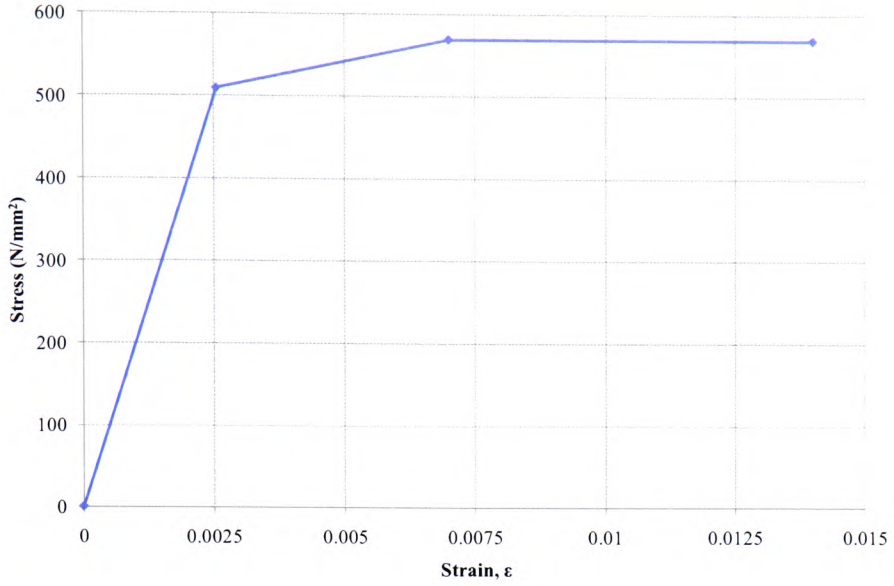

Figure 6.6 – Tri-linear stress/strain relationship for internal steel reinforcement in tension

6.2.5 Carbon Fibre Reinforced Polymer (CFRP) Composites

The CFRP composites used both in the experimental programme and during the development and execution of the numerical model, have a linear stress/strain relationship, up to failure. Therefore, it is appropriate to use the following relationship to define the material behaviour:

$$E_{FRP} = \frac{\sigma_{FRP}}{\varepsilon_{FRP}}$$

$$\Rightarrow \sigma_{FRP} = \varepsilon_{FRP} E_{FRP} \qquad 6.9$$

This is the standard 'Hooke's Law' and the "FRP" subscript in the above equations denotes their relation to the CFRP composites used in the research. For the CFRP sheet materials used in this study, the typical tensile failure strain for the sheets was in the region of 0.9%, which is contrary to that specified by the manufacturers, a stated tensile failure strain of 1.5%. The manufacturer's specifications also indicate an elastic modulus of 230kN/mm^2 and an ultimate tensile stress of 2400N/mm^2, compared to measured values of 222.5kN/mm^2 and 1900N/mm^2 respectively. For the CFRP plates used, the typical tensile failure

strain was 1.0%, with an associated elastic modulus of 175.6kN/mm^2; these values compare with those stated by the manufacturer of 1.5% and 150kN/mm^2. Figure 6.7 displays the stress-strain behaviour for the two types of FRP used in this study.

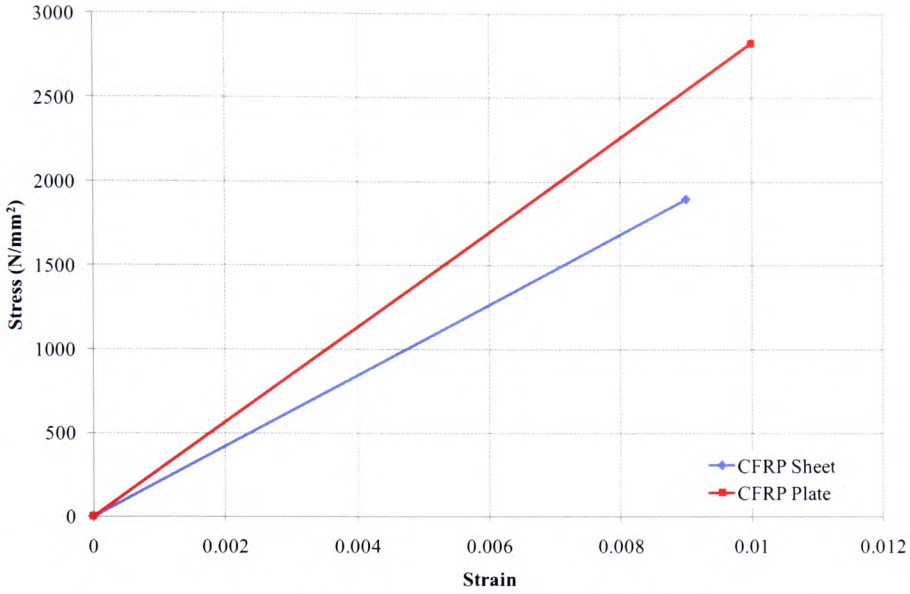

Figure 6.7 – Linear stress strain relationship of CFRP composites

6.3 Non-linear numerical model for flexural elements

Using the material constitutive properties discussed in 6.2, a non-linear, numerical model was developed that would be able to predict the behaviour of RC elements that were strengthened with externally-bonded polymer composites. A numerical integration method was used to determine the behaviour of the concrete in both compression and tension, and this is further discussed in Sections 6.3.1 and 6.3.3.

The code for the numerical model was written in Visual Basic for Applications (VBA) and utilised Microsoft Excel as a "front-end", where the user can input the relevant variables pertaining to his or her particular element.

The model was designed to replicate the behaviour of the element from the initial, uncracked, elastic stage, through the elasto-plastic stage and beyond the

point of steel-yielding (if appropriate) to ultimate failure, providing a variety of data on the element performance, including both data tables and graphical representations.

Based on the theory that plane sections remain plane (illustrated in Figure 6.8), the model has been designed to be "strain driven"; that is, the progression of element behaviour from an unloaded section up to failure is governed by the progressive increase of compressive strain at the extreme compressive concrete fibre at the top of the element. This approach is necessary due to the non-linear nature of the compressive concrete stress/strain profile, which results in two potential strain values for some corresponding values of stress. This is illustrated in Figure 6.9. Subsequently, all strains for other sections of the element, together with the neutral axis depth 'x', are calculated based on linear strain relationships, which in turn allows the calculation of stresses, forces and moments.

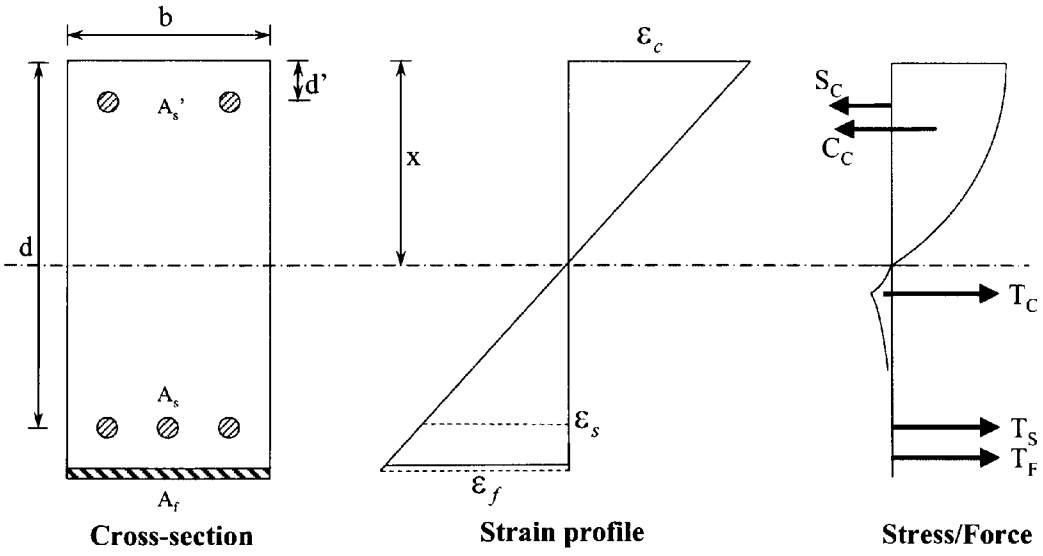

Figure 6.8 – Stress/strain configuration for reinforced concrete beams with externally-bonded FRP

For each increment of compressive strain, the model utilises a "balanced section" approach when determining the various parameters, enabling the neutral axis depth to be determined and, consequently, the strains and stresses at any depth in the section. This is achieved by setting the neutral axis depth to be equal to the

section depth at the start of each analytical step and reducing it until the section becomes "balanced" with the specific amount of compressive strain at the extreme fibre. The analytical process will be further discussed later in the chapter.

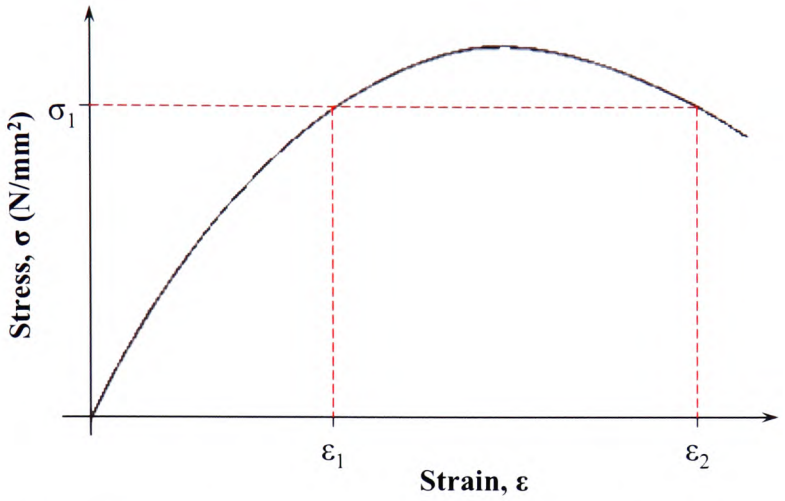

Figure 6.9 – Problem of two strain values for the same value of compressive concrete stress, necessitating strain-driven model

The initial strain value assigned to the extreme compressive fibre determines the first set of values for the loaded element. This initial value is assigned by the user, who specifies an increment value that is used to increase the compressive strain value from zero to the point of element failure.

The following sections will detail how the numerical model calculates the properties of the various components, namely:

- concrete in compression
- steel in compression
- concrete in tension
- steel in tension
- FRP in tension

6.3.1 Flexural concrete in compression

As stated above, the numerical model uses the principle of plane sections remaining plane and, consequently, once a neutral axis depth is found that results in a "balanced" section, strains at all other levels in the section can be calculated, by the use of simple similar triangle theory.

i.e
$$\varepsilon_{ci} = \frac{\varepsilon_c y_i}{x} \qquad 6.10$$

In order to determine the total force from the concrete in compression, a non-linear, numerical integration approach is adopted, which splits the compressive concrete strain into a number of "slices" (See Figure 6.10). For each of these slices the mean strain value can be calculated and then a stress value can be calculated, using equation 6.2 in Section 6.1.

Hence,
$$C_{CC} = \sum_{i=1}^{n} [(\sigma_{ci})(D_y)(b)] \qquad 6.11$$

where: σ_{ci} is the concrete compressive stress corresponding to the calculated strain for slice 'i';
D_y is the depth of slice 'i';
b is the breadth of the section.

In addition, for every slice, the distance from the neutral axis to the line of action can be calculated (y_i), which allows the moment for each slice to be calculated and stored, thereby resulting not only in a total compressive force but also a total moment for concrete in compression.

i.e.,
$$M_{CC} = \sum_{i=1}^{n} [(\sigma_{ci})(D_y)(b)(y_i)] \qquad 6.12$$

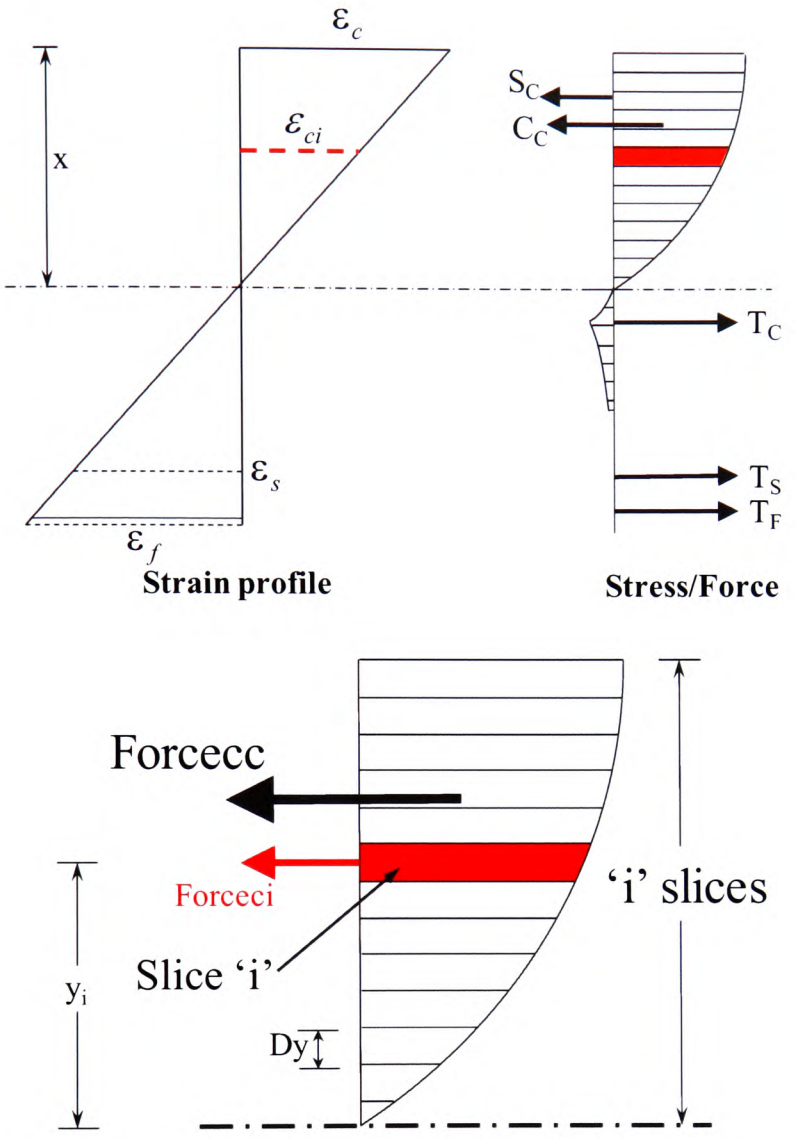

Figure 6.10 – Stress profile calculation for concrete in compression

6.3.2 Flexural steel in compression

To establish the total force from the reinforcing steel in compression, the strain profile determined previously is used to ascertain the compressive steel strain at the centre of the bars. Subsequently, the steel stress can be calculated and from this the compressive steel force is derived.

Hence, $$C_{SC} = [(\sigma_{SC})(A'_s)] \quad 6.13$$

where: σ_{SC} is the steel compressive stress corresponding to the calculated strain at the centre of the bars;

A_s' is the area of the compressive steel reinforcement.

The moment developed by the compressive steel force is calculated as follows:

$$M_{SC} = [(\sigma_{SC})(A'_s)(x - d')] \quad 6.14$$

where: x is the depth to the neutral axis from the top of the section;

d' is the depth to the centre of the compression steel reinforcement from the top of the section.

6.3.3 Flexural concrete in tension

Using equations 6.4, 6.5 and 6.6, together with the same principle employed when determining the compressive concrete force (i.e. using a number of 'slices' to form an equivalent area, see Figure 6.11), the total tensile force from the concrete is calculated.

Hence,

$$T_{CT} = \sum_{i=1}^{n} [(\sigma_{ti})(D_y)(b)] \quad 6.15$$

where: σ_{ti} is the concrete tensile stress corresponding to the calculated strain for slice 'i';

D_y is the depth of slice 'i'

b is the breadth of the section.

In addition, for every slice, the distance from the neutral axis to the line of action can be calculated (y_i), which allows the moment for each slice to be calculated and stored, thereby resulting not only in a total compressive force but also a total moment for concrete in compression.

i.e.,

$$M_{CT} = \sum_{i=1}^{n} [(\sigma_{ti})(D_y)(b)(y_i)] \quad 6.16$$

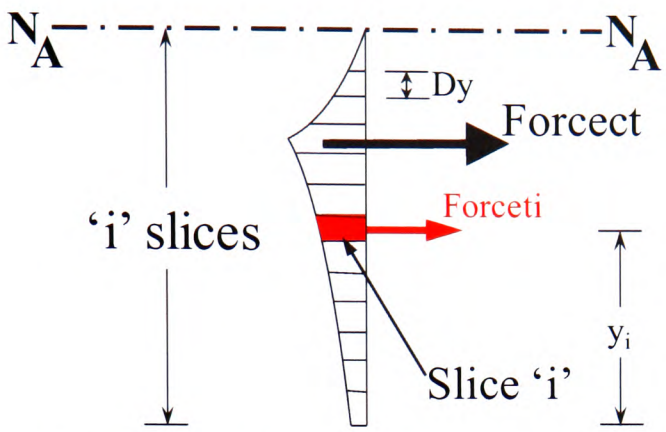

Figure 6.11 – Stress profile calculation for concrete in tension

6.3.4 Flexural steel in tension

To establish the total force from the reinforcing steel in tension, the determined strain profile is used to ascertain the tensile strain at the centre of the steel bars and then the steel stress can be calculated. Subsequently, the tensile steel force is calculated.

Hence, $$T_{ST} = [(\sigma_{ST})(A_S)] \quad 6.17$$

where: σ_{ST} is the tensile steel stress corresponding to the calculated strain at the centre of the bars

A_s is the cross-sectional area of the tensile steel reinforcement

The moment developed by the tensile steel force is calculated as follows:

Hence, $$M_{ST} = [(\sigma_{ST})(A_S)(d - x)] \quad 6.18$$

where: x is the depth to the neutral axis from the top of the section;

d is the depth to the centre of the tensile steel reinforcement from the top of the section.

6.3.5 Flexural FRP in tension

Again, the established strain profile is used to determine the tensile strain in the bonded FRP layer, in order that the total tensile FRP force can be calculated. Additionally, the calculation for the moment developed by the tensile FRP force is given in Equation 6.20.

Hence, $$T_{FRPT} = [(\sigma_{FRPT})(A_{FRP})] \quad 6.19$$

where: σ_{FRPT} is the tensile FRP stress corresponding to the calculated strain at the mid-depth of the FRP layer;

A_{FRP} is the cross-sectional area of the tensile FRP.

Hence, $$M_{FRPT} = \left[(\sigma_{FRPT})(A_{FRP}) \left\{(h - x) + \left(\frac{t}{2}\right)\right\}\right] \quad 6.20$$

where: x is the depth to the neutral axis from the top of the section;

h is the total depth of the section;

t is the thickness of the FRP layer .

6.3.6 Total section analysis

As can be seen from sections 6.3.1 to 6.3.5, by maintaining section equilibrium, the forces from the individual component materials can be calculated for each strain increment.

i.e. $$C_{CC} + C_{SC} = T_{CT} + T_{ST} + T_{FRPT} \quad 6.21$$

Subsequent to the calculation of strains, stresses, forces and moments for the section, it is possible to determine the curvature by the use of the following equality:

$$\frac{E}{R} = \frac{\sigma}{y} \quad 6.22$$

$$\Rightarrow \frac{1}{R} = \left(\frac{\sigma}{E}\right)\left(\frac{1}{y}\right)$$

As $$E = \frac{\sigma}{\varepsilon} \Rightarrow \varepsilon = \frac{\sigma}{E}$$

Then $$\frac{1}{R} = \kappa = \frac{\varepsilon}{y} \qquad 6.23$$

Where: R is the radius of curvature;

κ is the element curvature;

y is the distance from the neutral axis to the soffit of the section.

i.e. $y = (h - x)$

6.4 Section analysis

6.4.1 Control elements

The analytical model was run initially using the data pertaining to the control beams from each set of experimental tests. The model was able to calculate stresses, strains, neutral axis depth, compressive and tensile forces, moments and curvatures. The analytical failure moments for the control beams are contained in Table 6.2 below, together with the failure moments obtained from the experimental programme and the corresponding experimental and predicted failure modes.

In Figure 6.12, a comparison is shown between the profiles for the moment curvature data acquired from experimental data for 10CON against the data obtained for the same section from the numerical model. As can be seen, there is excellent parity between the two sets of data throughout the loading process. It should be noted that the failure moment from experimental data was actually 16.3kNm, not 14.4kNm as shown on the graph; this is due to curvature information being unavailable for the ultimate loading stages of the experiment.

In Figures 6.13(a) to (f) comparisons are shown for all of the control beams and slabs from the experimental programme, and it can be seen that there is excellent correlation between the actual elemental behaviour in the experimental programme and the results obtained from the numerical model. Additionally, there is very good correlation between the predicted failure mode and that observed in the experimental programme. Where the numerical model has predicted a steel-yielding failure, the observed failure mode is steel-yielding followed by concrete crushing; this is due to the situation during the experiments where when the reinforcing bars yielded the rotation caused the concrete to crush before the apparatus safety mode released the loading. However, the numerical model reports an element failure as soon as the steel yields.

Table 6.2 – Comparison of element failure moment and failure mode from numerical model and experimental programme for control elements

Element ref.	Experimental failure moment (kNm)	Numerical failure moment (kNm)	Experimental (observed) failure mode†	Predicted failure mode
8CON	9.3	9.6	SY-CC	SY
10CON	16.1	16.3	SY-CC	SY
12CON	18.7	18.9	CC	CC
12DCON	20.1	20.5	SY-CC	SY
16CON	28.2	32.5	CC	CC
8SCON	8.1	8.2	SY-CC	SY
12SCON	15.2	16.2	SY-CC	SY

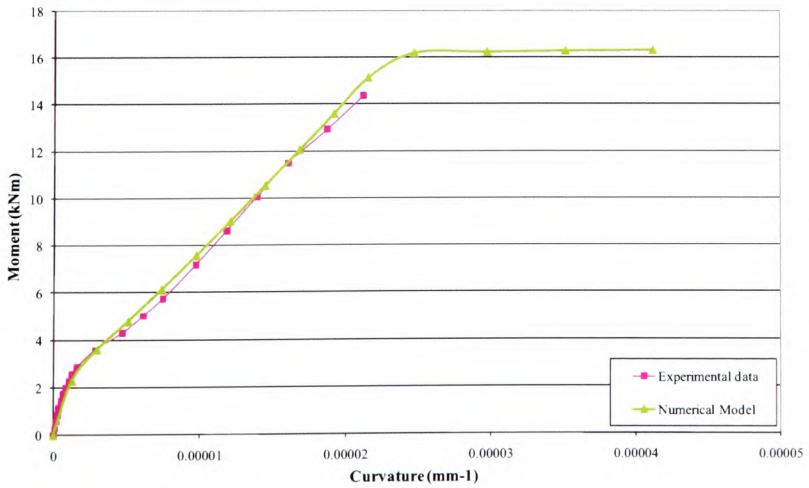

Figure 6.12 – Comparison of Moment curvature relationship for element 10CON

† SY=Steel yield; CC=Concrete crushing; SY-CC=Steel yield followed by concrete crushing

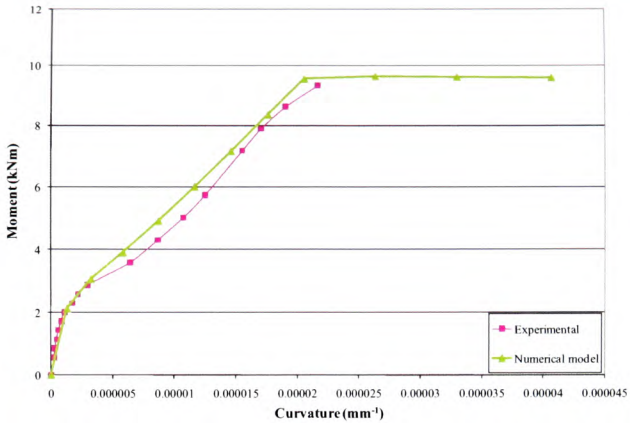

Figure 6.13(a) – Comparison of Moment curvature relationship for element 8CON

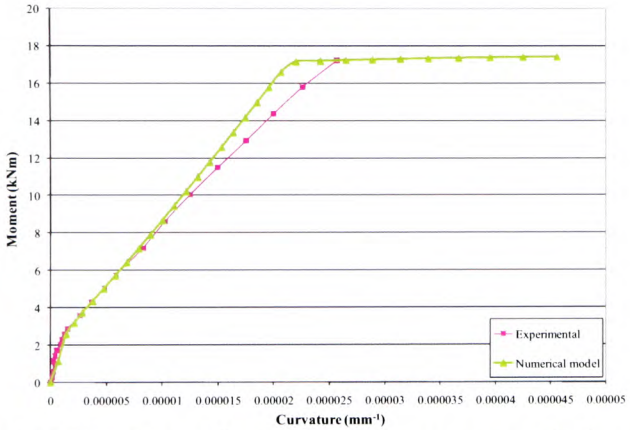

Figure 6.13(b) – Comparison of Moment curvature relationship for element 12CON

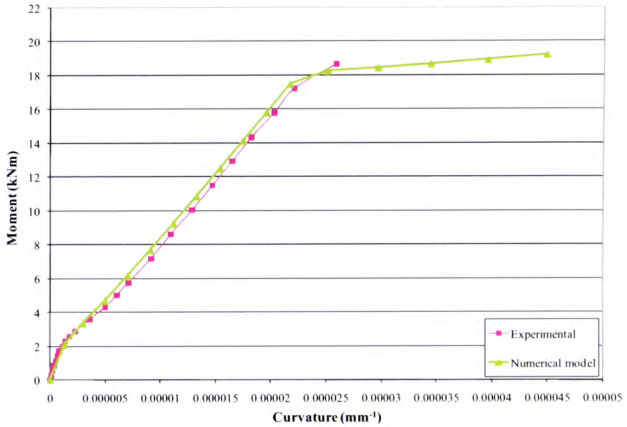

Figure 6.13(c) – Comparison of Moment curvature relationship for element 12DCON

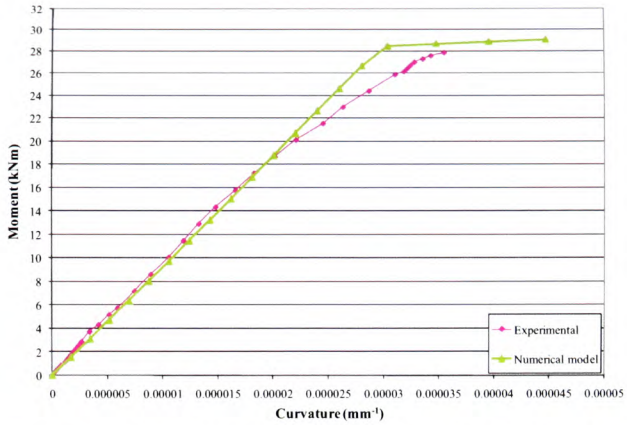

Figure 6.13(d) – Comparison of Moment curvature relationship for element 16CON

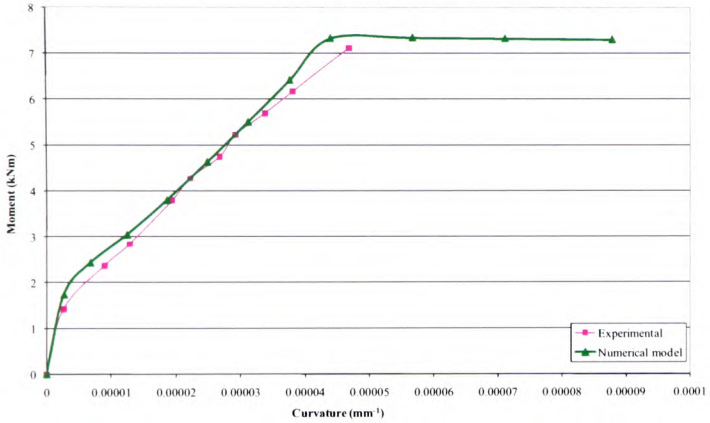

Figure 6.13(e) – Comparison of Moment curvature relationship for element 8SCON

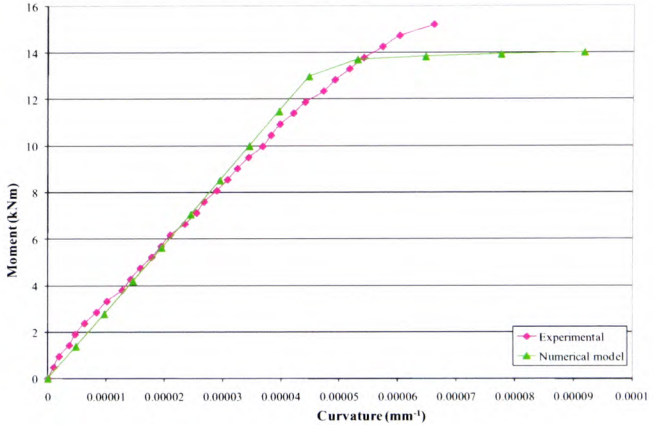

Figure 6.13(f) – Comparison of Moment curvature relationship for element 12SCON

6.4.2 Strengthened elements

Shown in Figures 6.14(a) to 6.20(d) are the moment curvature comparison graphs for all the strengthened elements; i.e. 8mm, 10mm, 12mm, 12mm doubly-reinforced and 16mm beams, together with the 8mm and 12mm reinforced slabs. Table 6.3 details the experimental and modelled ultimate moments and failure modes for the strengthened specimens.

As can be seen from the graphs, the moment curvature relationship obtained from the numerical model compares very favourably with the data obtained during the experimental programme. Some anomalies between the predicted and actual moment curvature relationship, where the two curves digress slightly (particularly as with 16CF1, 16CF2 and 16CF3) are due to the unpredictability of such elements that have been heavily over-reinforced with a combination of internal steel and bonded composites.

Additionally, as the model was not programmed to detect failure due to partial tearing-off of the concrete cover, for elements such as 12DCF1, 12DCF2 and 12DCF3, the predicted failure mode was concrete crushing for 12DCF1 and debonding of the fibre composites for 12DCF2 and 12DCF3. For the latter two instances, the predicted ultimate moment is higher than that observed in the associated experiment; this is due to the inability to predict the premature, tearing-off failure that occurred. Hence, the numerical model did not detect element failure (due to compressive failure of the concrete) until a slightly higher load/moment.

6.4.3 Neutral axis depth – Control elements

Consider the control beam element with two 10mm diameter steel reinforcing bars. The moment at which the first crack appears can be determined from simple bending theory, utilising the transformed, equivalent concrete section as shown in Figure 6.21, and assuming the modular ratio, α, to be 4.8. By taking

the first moment of area about the top of the beam, the depth to the neutral axis can be determined to be 102.4mm.

Table 6.3 – Comparison of element failure moment and failure mode from numerical model and experimental programme for strengthened elements

Element ref.	Experimental failure moment (kNm)	Numerical model failure moment (kNm)	Experimental (observed) failure mode‡	Predicted failure mode
8CF1	16.7	15.2	FR	FR
8CF2	17.9	18.4	DB-PTO	DB
8CF3	15.8	16.3	PTO	DB
10CF1	18.0	19.1	FR	FR
10CF2	23.1	23.1	DB-PTO	DB
10CF3	20.2	21.4	PTO	DB
12CF1	22.5	23.6	CC	CC
12CF2	24.2	25.4	CC	CC
12CF3	24.4	26.8	CC	CC
12DCF1	23.6	24.4	DB-PTO	DB
12DCF2	27.3	28.1	PTO	CC
12DCF3	26.5	27.2	PTO	CC
16CF1	27.6	28.6	CC	CC
16CF2	25.9	27.4	ECC	CC
16CF3	29.1	31.0	ECC	CC
8SCF2	26.1	28.3	FR-PTO	DB
8SCP2	30.9	31.3	DB	DB
8SCP3	28.5	32.5	DB	CC
12SCF2	32.3	33.3	FR	FR
12SCF4	36.6	37.4	CC	CC
12SCP2	35.6	37.7	DB	CC
12SCP3	44.0	45.3	DB	DB

‡ CC=Concrete crushing; SY-CC=Steel yield followed by concrete crushing; FR=Fibre rupture; DB=De-bonding of CFRP; PTO=Premature tearing-off of concrete cover; ECC=Explosive concrete crushing

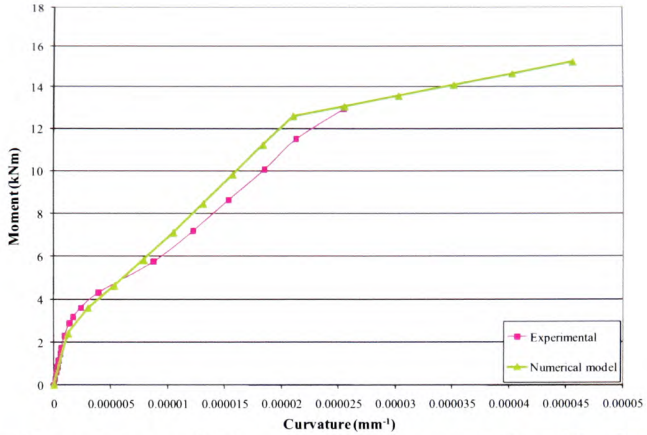

Figure 6.14(a) – Comparison of Moment curvature relationship for element 8CF1

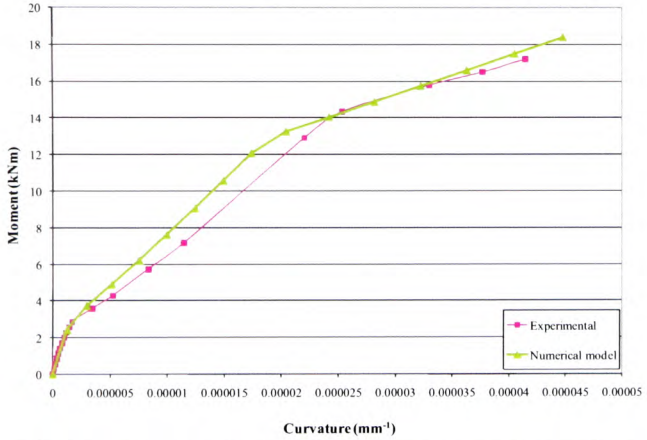

Figure 6.14(b) – Comparison of Moment curvature relationship for element 8CF2

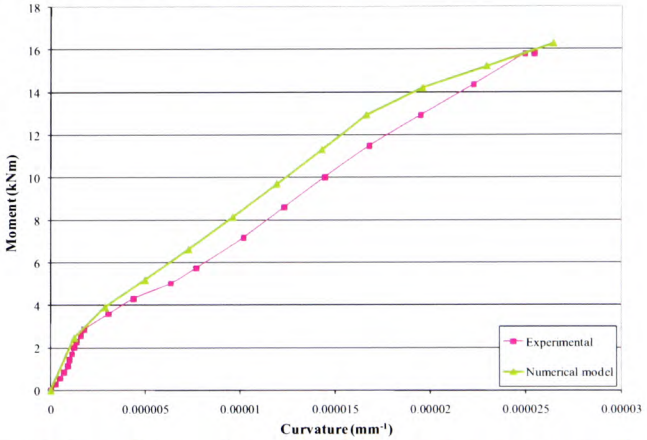

Figure 6.14(c) – Comparison of Moment curvature relationship for element 8CF3

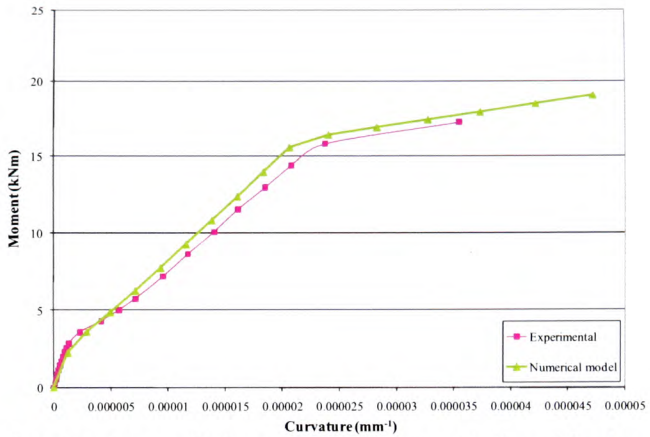

Figure 6.15(a) – Comparison of Moment curvature relationship for element 10CF1

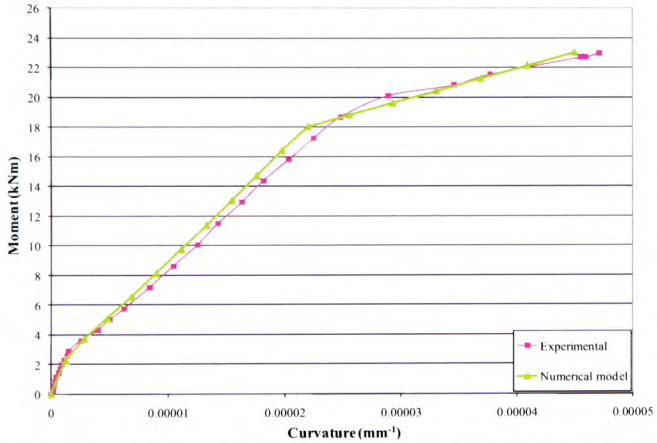

Figure 6.15(b) – Comparison of Moment curvature relationship for element 10CF2

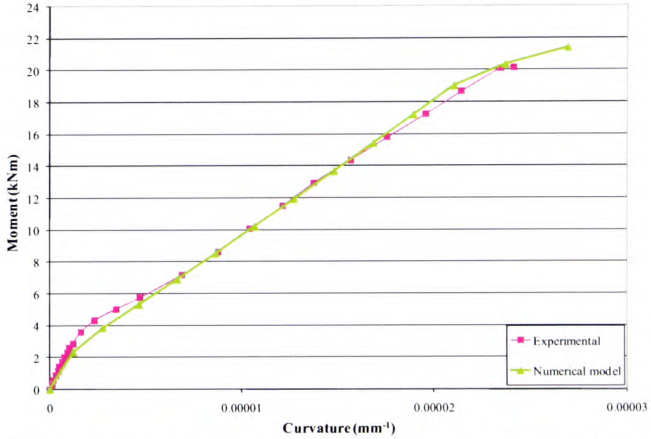

Figure 6.15(c) – Comparison of Moment curvature relationship for element 10CF3

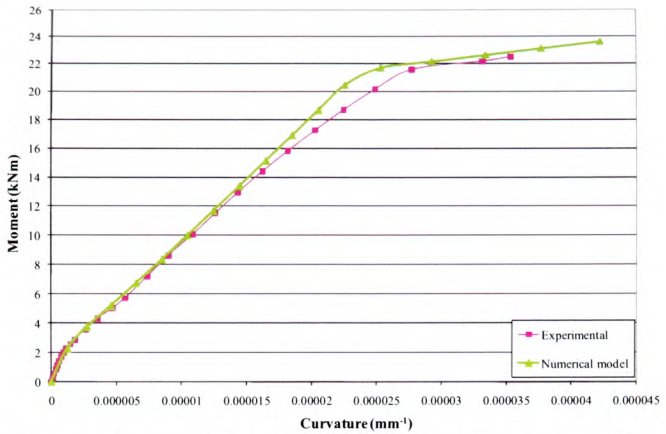

Figure 6.16(a) – Comparison of Moment curvature relationship for element 12CF1

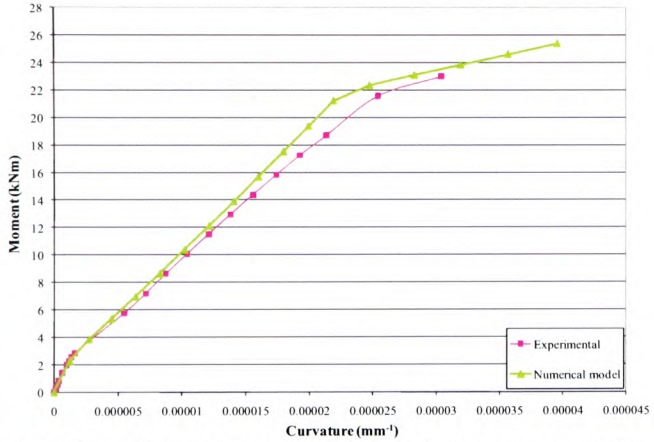

Figure 6.16(b) – Comparison of Moment curvature relationship for element 12CF2

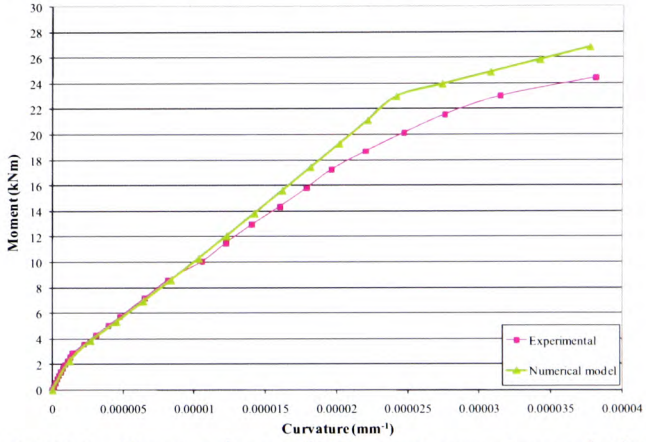

Figure 6.16(c) – Comparison of Moment curvature relationship for element 12CF3

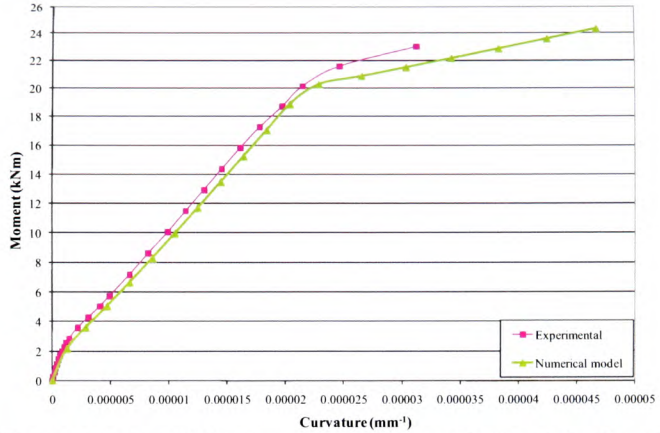

Figure 6.17(a) – Comparison of Moment curvature relationship for element 12DCF1

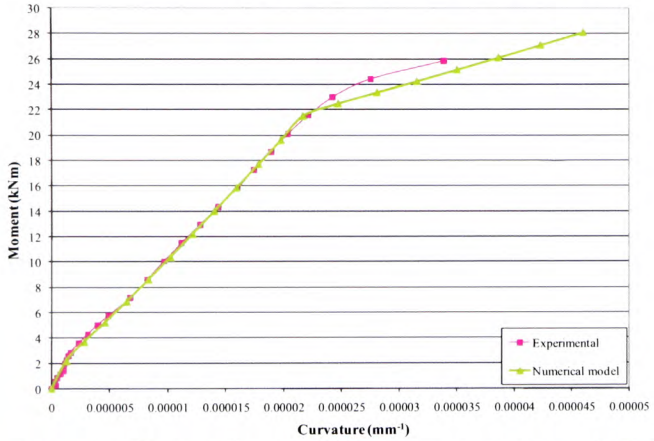

Figure 6.17(b) – Comparison of Moment curvature relationship for element 12DCF2

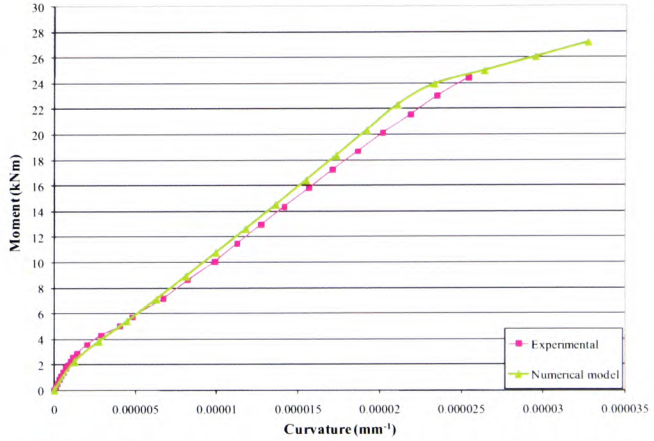

Figure 6.17(c) – Comparison of Moment curvature relationship for element 12DCF3

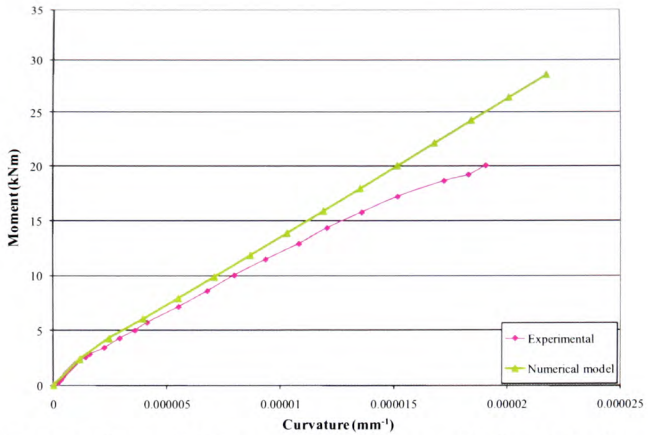

Figure 6.18(a) – Comparison of Moment curvature relationship for element 16CF1

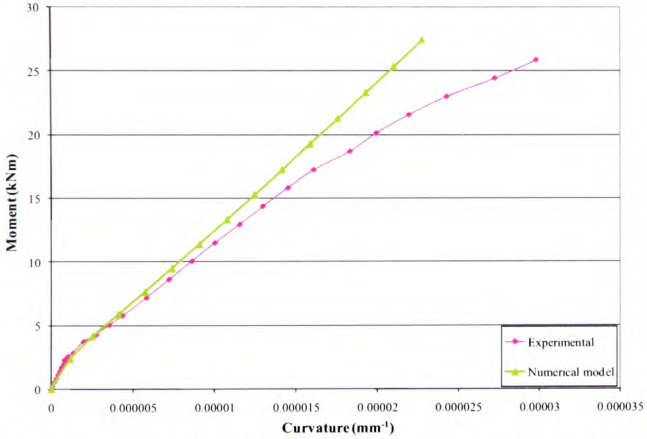

Figure 6.18(b) – Comparison of Moment curvature relationship for element 16CF2

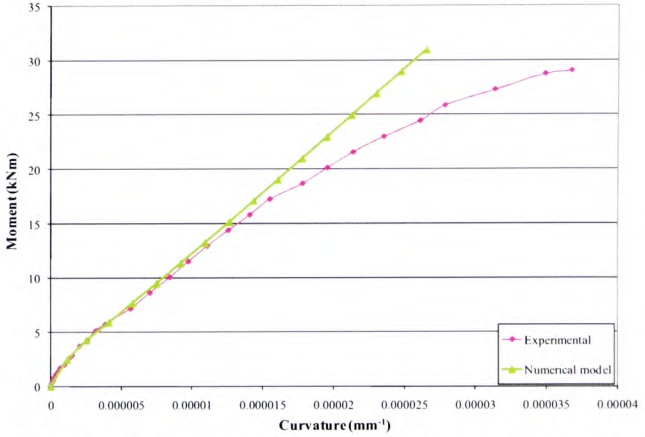

Figure 6.18(c) – Comparison of Moment curvature relationship for element 16CF3

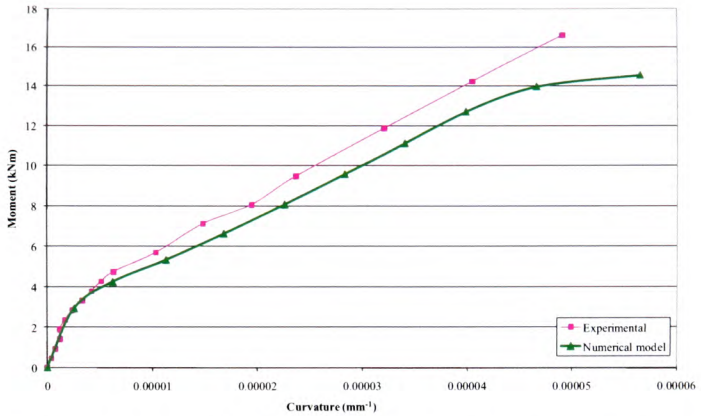

Figure 6.19(a) – Comparison of Moment curvature relationship for element 8SCF2

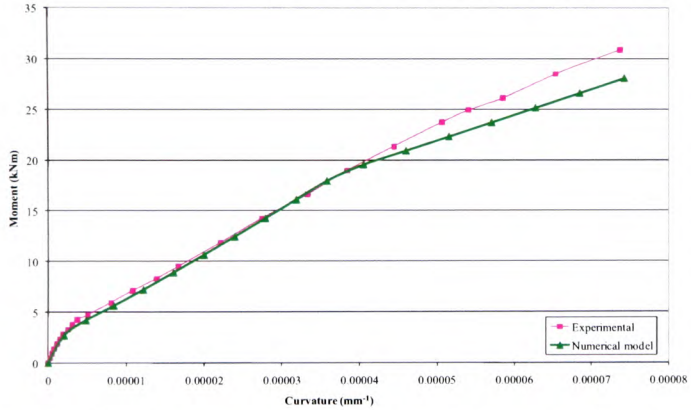

Figure 6.19(b) – Comparison of Moment curvature relationship for element 8SCP2

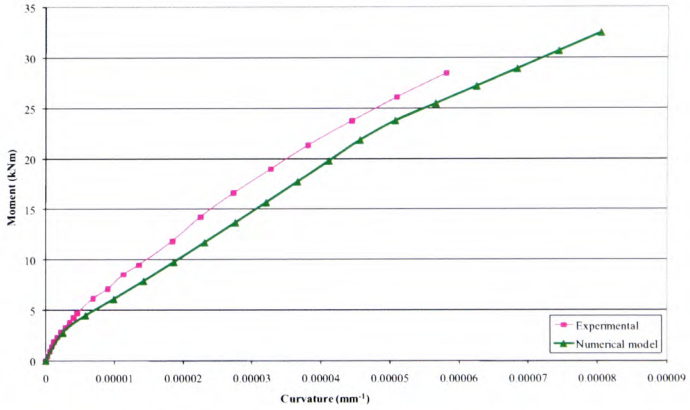

Figure 6.19(c) – Comparison of Moment curvature relationship for element 8SCP3

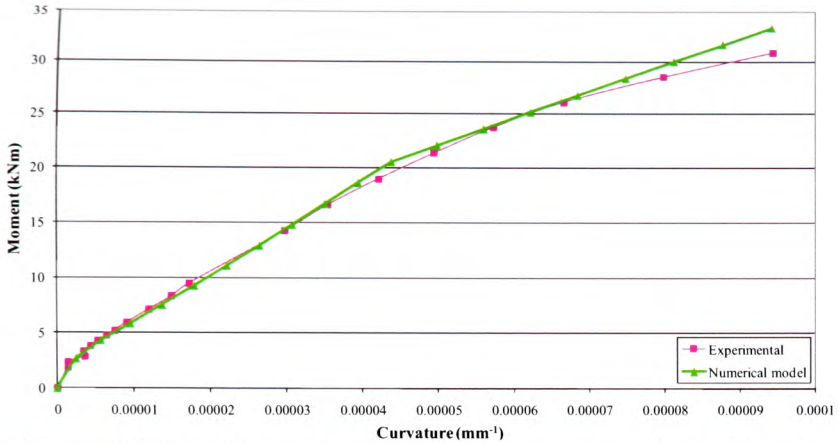

Figure 6.20(a) – Comparison of Moment curvature relationship for element 12SCF2

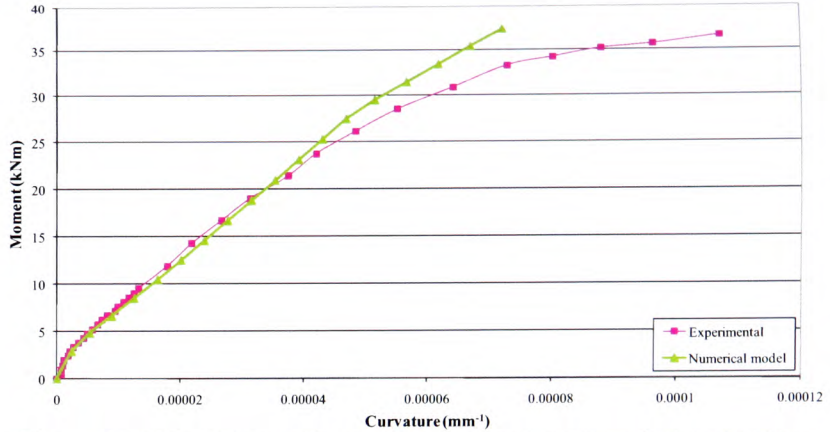

Figure 6.20(b) – Comparison of Moment curvature relationship for element 12SCF4

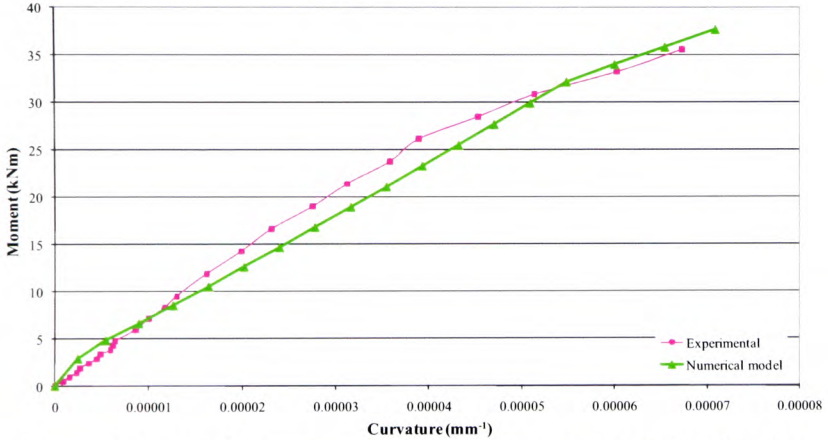

Figure 6.20(c) – Comparison of Moment curvature relationship for element 12SCP2

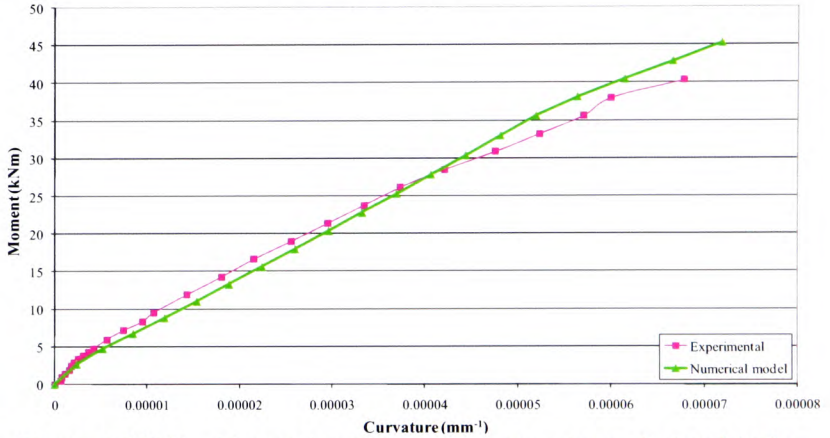

Figure 6.20(d) – Comparison of Moment curvature relationship for element 12SCP3

The second moment of area of the section can then be determined as follows:

$$I_{NA} = \frac{bx^3}{3} + \frac{b(h-x)^3}{3} + A_s(\alpha - 1)(d-x)^2 \qquad 6.24$$

$$I_{NA} = \frac{100(102.4^3)}{3} + \frac{100(97.6^3)}{3} + 157.1(4.8-1)(77.6^2)$$

$$I_{NA} = 70.8\ x\ 10^6 mm^4$$

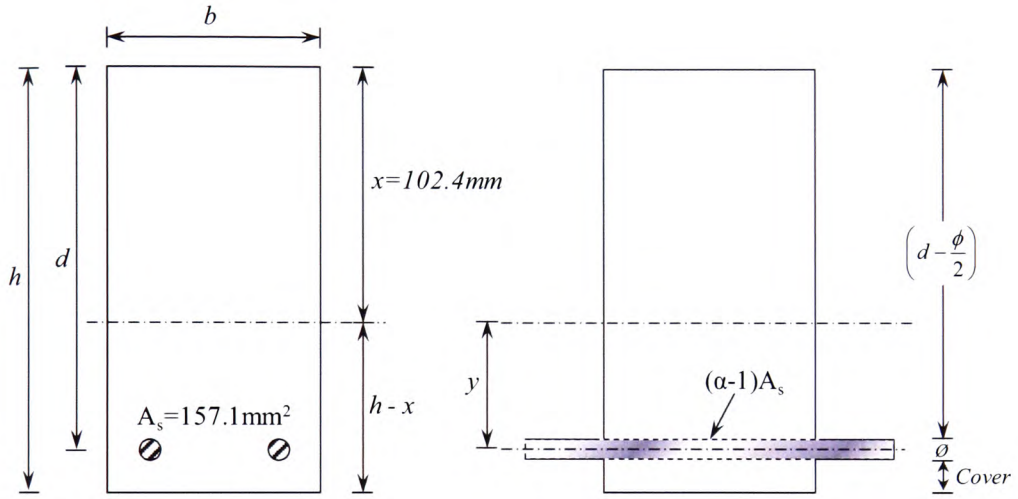

Figure 6.21 – Transformed section for Control element with two ∅10mm reinforcing bars

Subsequently, the moment at which cracking occurs can be calculated from:

$$\frac{M}{I} = \frac{\sigma}{y} \Rightarrow M = \frac{f_{ct} I}{y}$$

$$M = \frac{2.8(70.8\ x\ 10^6)}{97.6}$$

$$M = 2.03\ x\ 10^6 Nmm$$

$$\Longrightarrow M = 2.03\ kNm$$

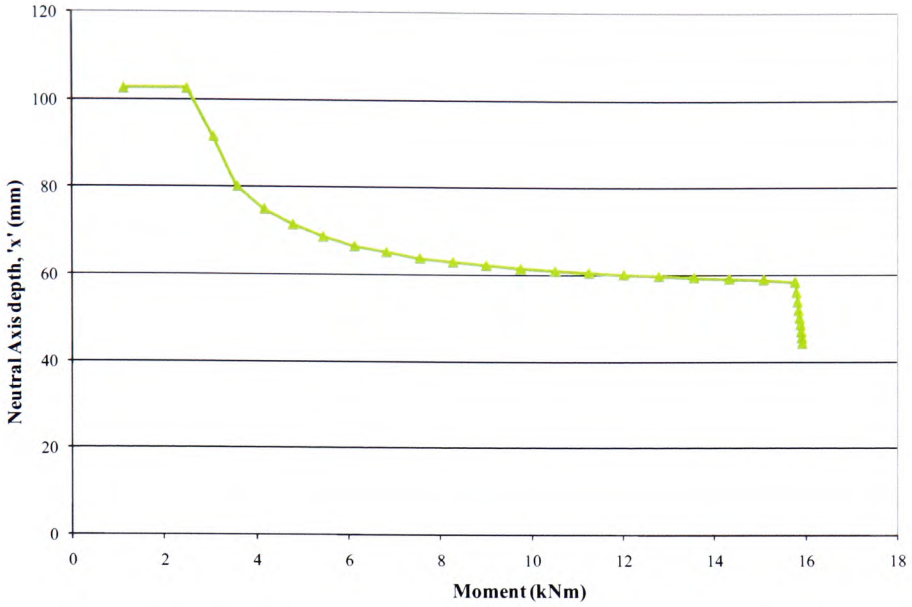

Figure 6.22 – Predicted neutral axis depth 'x' against moment for 10CON

As can be seen from the graph in Figure 6.22, the numerical model predicted a linear elastic behaviour up to approximately 2.5kNm, when initial concrete tensile cracking occurs. This is higher than the calculated moment of 2.03kNm, however the numerical model is considered to be a more accurate representation of the behaviour of the section.

Just after the cracking of the concrete in tension, it can be seen that the depth of the neutral axis decreases rapidly, which indicates that the tensile stresses have been transferred to the reinforcing steel bars.

The next notable point occurs at a moment of around 15.6kNm, when the steel achieves its yield stress and element failure commences. Subsequently, the trend continues until the steel reaches its failure strain of 7000με.

As can be seen, the results from the numerical model agree acceptably with those obtained during the experimental programme. In the laboratory, the first cracks were not visible until a load of 10kN had been achieved (equivalent to a moment

of 2.9kNm); however, this is likely due to the size of the micro-cracking at low loads/moments hinders viewing with the naked eye.

6.4.4 Neutral axis depth – strengthened elements

As with the control beam discussed in 5.4.3, a 100mm x 200mm deep reinforced concrete beam with two, full-width layers of CFRP sheet adhered to the soffit is considered, but with two 12mm steel reinforcing bars. A revised transformed section is shown in Figure 6.23, with the same concrete/steel modular ratio, α, of 4.8, but now also with a concrete/FRP modular ratio of β, given to be 6.1. Again, utilising simple bending theory and taking the first moment of area about the top of the section, the neutral axis depth is calculated to be 104.3mm.

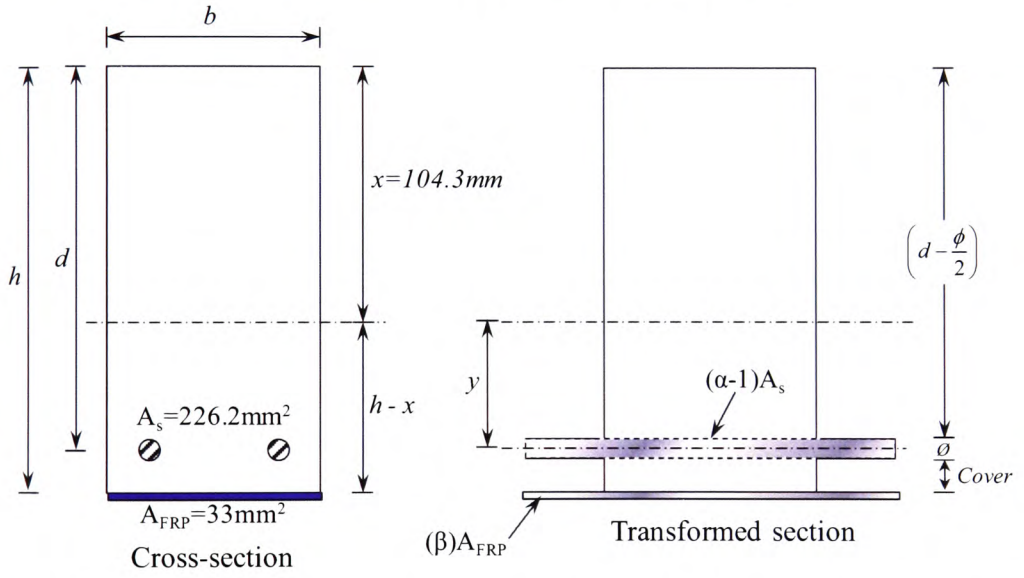

Figure 6.23 – Transformed section for element with two ∅12mm reinforcing bars and two, full-width layers of CFRP

The second moment of area of the section can then be determined as follows:

$$I_{NA} = \frac{bx^3}{3} + \frac{b(h-x)^3}{3} + A_s(\alpha - 1)(d-x)^2 + A_{FRP}(\beta)(h - x - \frac{t_f}{2})^2 \qquad 6.25$$

$$I_{NA} = \frac{100(104.3^3)}{3} + \frac{100(95.7^3)}{3} + 226.2(4.8-1)(75.7^2) + \left\{(33)(6.1)(200 - 104.3 - \frac{0.44}{2})\right\}$$

$$I_{NA} = 71.9\ x\ 10^6 mm^4$$

Subsequently, the moment at which cracking occurs can be calculated from:

$$\frac{M}{I} = \frac{\sigma}{y} \Rightarrow M = \frac{f_{ct} I}{y}$$

$$M = \frac{2.8(71.9\ x\ 10^6)}{95.7}$$

$$M = 2.10\ x\ 10^6 Nmm$$

$$\Rightarrow M = 2.10\ kNm$$

As can be seen from the graph in Figure 6.24, the numerical model predicted a linear elastic behaviour up to approximately 2.5kNm, when initial concrete tensile cracking occurs. This is higher than the calculated moment of 2.10kNm.

Just after the cracking of the concrete in tension, it can be seen that the depth of the neutral axis does not decrease as rapidly as with the previous, control example. This demonstrates the influence of the FRP strengthening in limiting the depth of the flexural cracking and, thereby, restricting the raising of the neutral axis as further loading is applied.

The next noteworthy point occurs at a moment of around 25kNm, when element failure commences.

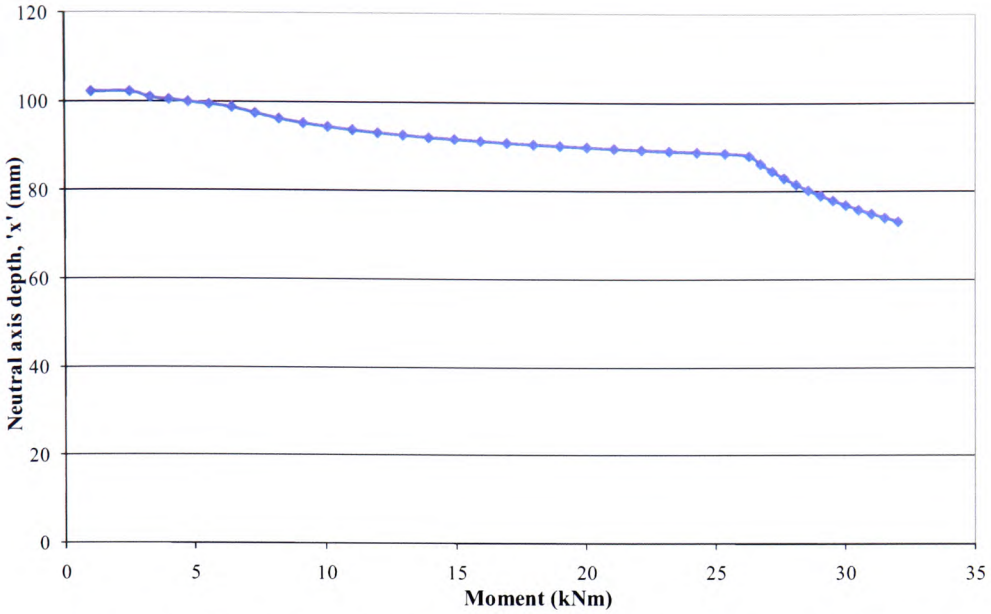

Figure 6.24 – Predicted neutral axis depth 'x' against moment for 12CF2

As with Section 6.4.3, the predicted results from the numerical model agree acceptably with those obtained during the experimental programme. In the laboratory, the first cracks were not visible until a load of 11kN had been achieved (equivalent to a moment of 3.2kNm); however, as with all elements in the experimental programme, this is likely due to the size of the micro-cracking at low loads/moments hinders viewing with the naked eye.

6.5 Flexural rigidity

An important factor of any structural element, either normally-reinforced or strengthened with fibre composites, is its flexural rigidity, 'EI'. The value of the flexural rigidity is easily available from the element moment curvature relationship behaviour, detailed in 6.4.

$$\frac{M}{I} = \frac{E}{R} \Rightarrow \frac{1}{R} = \frac{M}{EI}$$

$$\frac{1}{R} = \kappa \Rightarrow EI = \frac{M}{\kappa}$$

Consequently, the normalised non-dimensional stiffness can be determined as follows:

$$EI_{Norm} = \frac{\left(M/M_U\right)}{\left(\kappa/\kappa_U\right)}$$

where; M is the moment

M_u is the ultimate or failure moment

κ is the curvature

κ_U is the ultimate curvature

For strengthened elements, the value of EI obviously rises, for all loading stages, as the amount of bonded fibre composites is increased, due to the nature of the fibre composites to be stiffer than either their steel or concrete counterparts. This has been demonstrated in the results from the experimental programme, illustrated by the example shown in Figure 6.25, where it can be seen that as increasing amounts of CFRP are bonded to the soffit of the beams reinforced with two 10mm bars, the element flexural stiffness increases, creating a 'fan' effect.

6.6 Element strain

The load-strain relationship predicted by the numerical model follows the same trend as that observed in the experimental programme, with a "fanning" effect. Figure 6.26 presents the load against strain curves for element 10CF2 (two Ø10mm reinforcing bars and one layer of CFRP). It can be seen that there is very good agreement between the two sets of values.

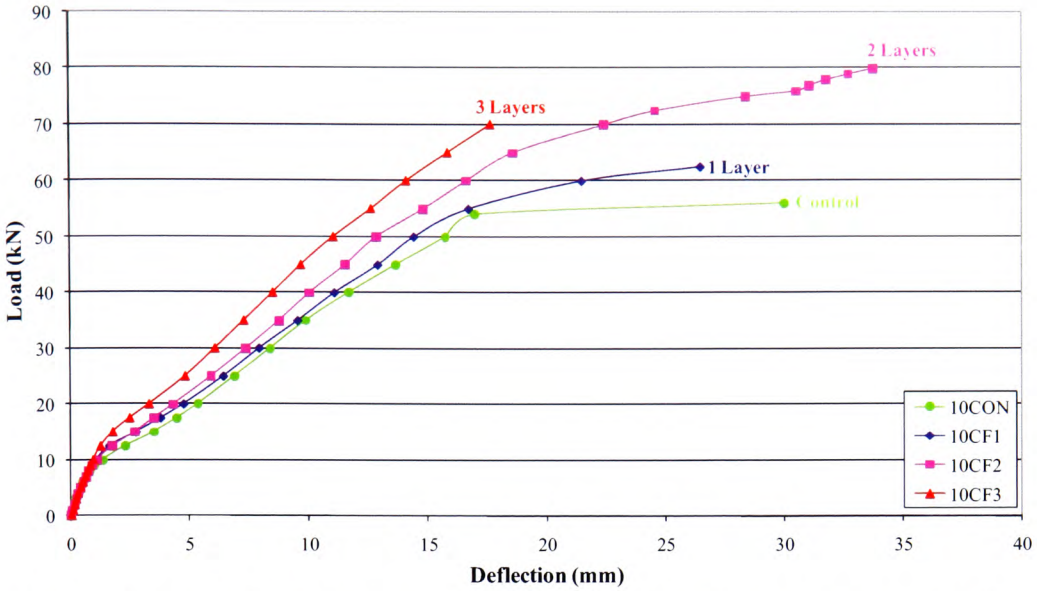

Figure 6.25 – 'Fan' effect of increasing flexural rigidity with increase in amount of bonded-CFRP (for elements internally-reinforced with two Ø10mm steel bars)

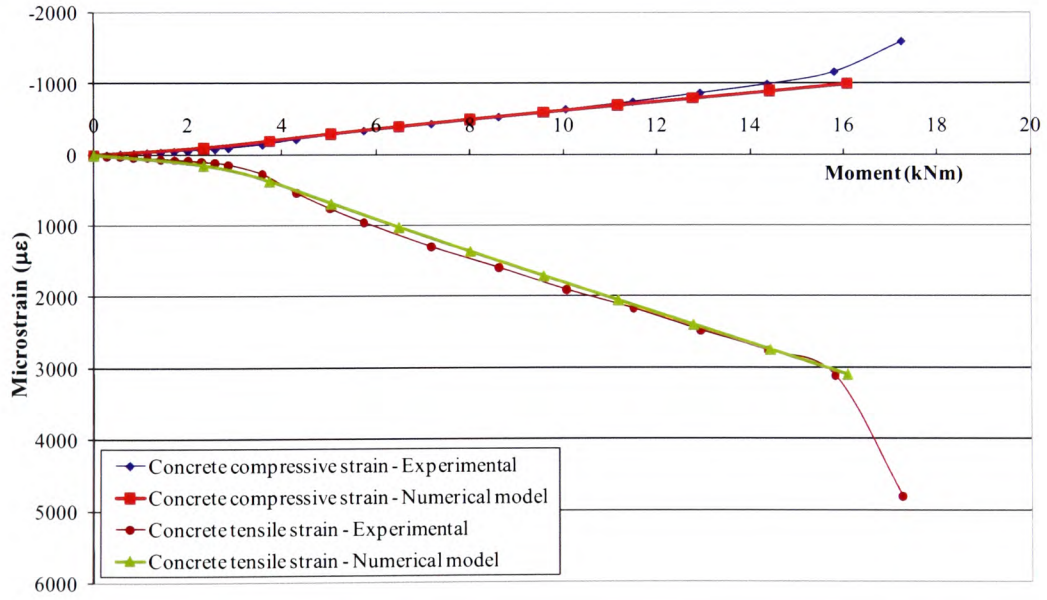

Figure 6.26 – Comparison of predicted and experimental element strains for 10CF1

6.7 Load deflection relationships

In order to determine any deformation-based ductility indices, it is necessary to obtain the load against deformation curve for the element in question. As the numerical model produces predicted moment and curvature values for each element, it is possible to (a) determine the loads using the value of the moment and element loading geometry, and (b) derive the deflection behaviour directly from the curvature values, utilising the following relationship.

6.7.1 Derivation of deflection based on predicted curvature values

The deflection of an element can be calculated from Equation 6.26, using elastic bending theory[**]:

$$M = EI\frac{d^2y}{dx^2} \qquad 6.26$$

Where M is the bending moment at a distance x.

For small deflections $\frac{d^2y}{dx^2}$ approximates to the curvature, which in turn is the inverse of the radius of curvature, R. If Equation 6.26 is doubly-integrated, as follows, we obtain a generic expression for deflection, Equation 6.27.

$$Mx + A = EI\frac{dy}{dx}$$

but if the slope is zero at mid-span, where $x = \frac{L}{2}$, then

$$A = -\frac{ML}{2}$$

$$\Rightarrow Mx - \frac{ML}{2} = EI\frac{dy}{dx}$$

[**] Mosely *et al.* 1996

Integrating for a second time gives:

$$\Rightarrow \frac{Mx^2}{2} - \frac{MLx}{2} + B = EIy$$

However, at the left-hand support, where x=0, then y=0, so B=0

$$y = \frac{M}{EI}\left(\frac{x^2}{2} - \frac{Lx}{2}\right) \qquad 6.27$$

As the maximum deflection will occur at mid-span, $x = \frac{L}{2}$, therefore:

$$y_{max} = \frac{M}{EI}\left(\frac{L^2}{8} - \frac{L^2}{4}\right) \qquad 6.28$$

$$\Rightarrow y_{max} = -\frac{M}{EI}\left(\frac{L^2}{8}\right) \qquad 6.29$$

However, since in an uncracked section $\frac{M}{I} = \frac{E}{R}$:

$$\Rightarrow \frac{1}{R} = \frac{M}{EI}$$

Substituting in Equation 6.29:

$$\Rightarrow y_{max} = -\frac{1}{8}\left(\frac{1}{R}\right)L^2 \qquad 6.30$$

Consequently, it is possible to estimate the load deflection behaviour of any element from the predicted moment-curvature values obtained from the numerical model.

6.7.2 Load deflection behaviour for flexural elements

Shown in Figure 6.27 are typical load deflection curves for the experimental and predicted behaviour of 10CF2. Subsequently, contained within Figures 6.28 (a) to 6.31 (d) are graphs illustrating the comparison between actual experimentally-measured deflection and that obtained from the numerical model data.

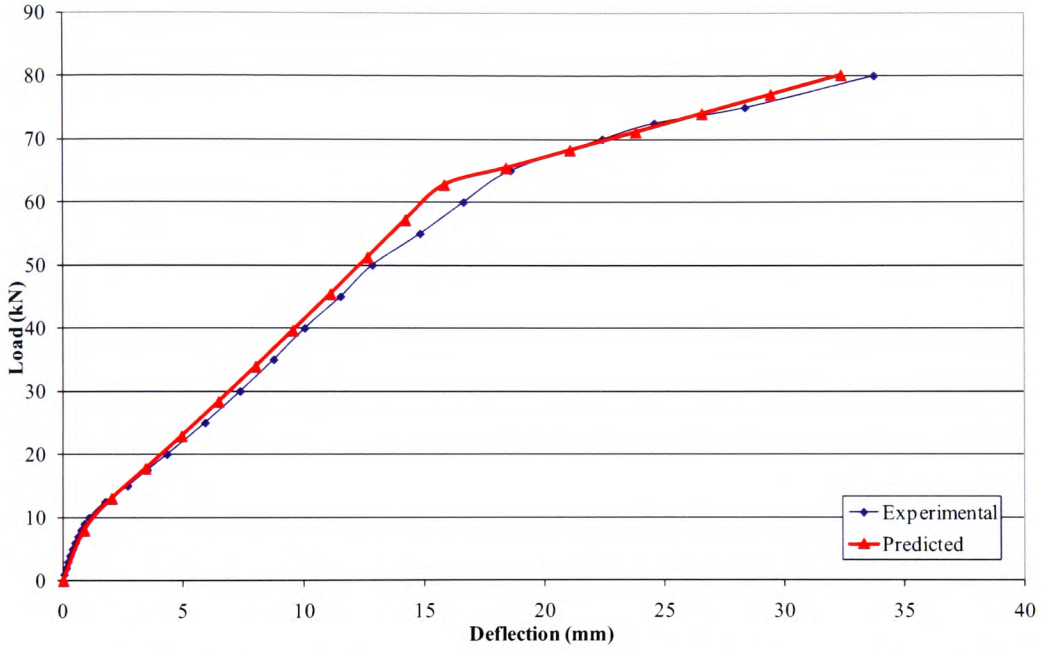

Figure 6.27 – Comparison of experimental and predicted load deflection behaviour for beam element 10CF2

6.7.3 Load deflection behaviour for slab elements

Equation 6.30 can be presented in a more generic form, as shown in Equation 6.31, where the constant of $-\frac{1}{8}$ is replaced with K, representing a constant specific to a particular type of element. As discussed in Section 4.1, all flexural elements are theoretically similar, despite the generic definitions of "beam" and "slab", which generally denote elements with differing amounts of steel reinforcement.

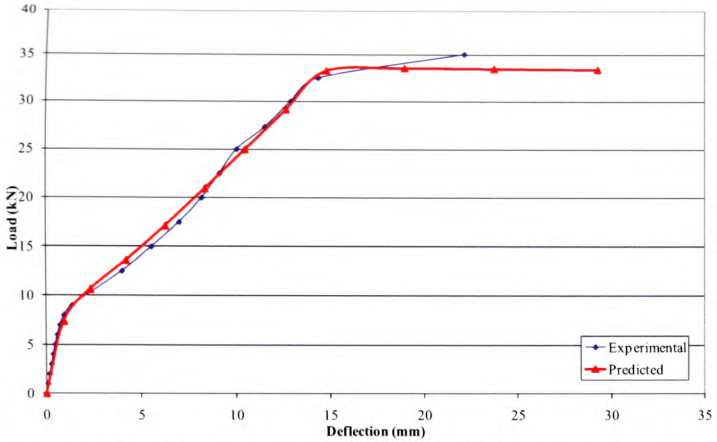

Figure 6.28(a) – Comparison of load deflection for 8CON

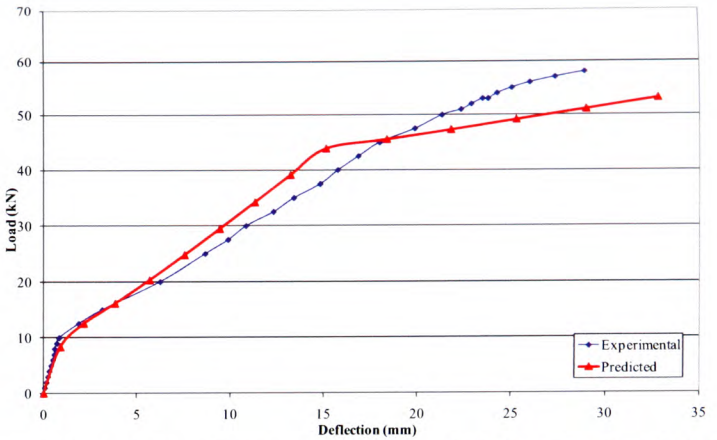

Figure 6.28(b) – Comparison of load deflection for 8CF1

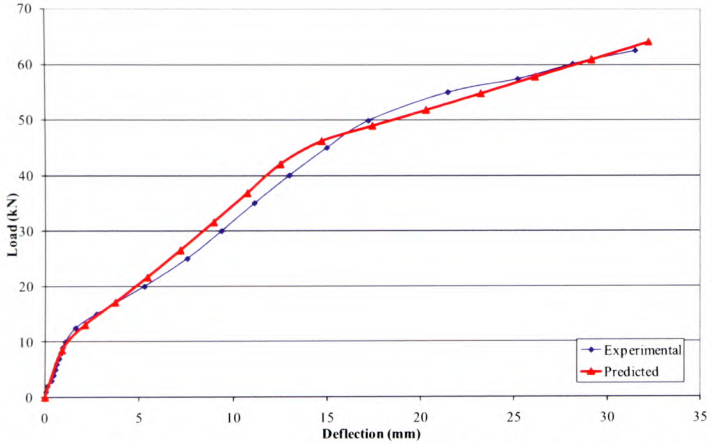

Figure 6.28(c) – Comparison of load deflection for 8CF2

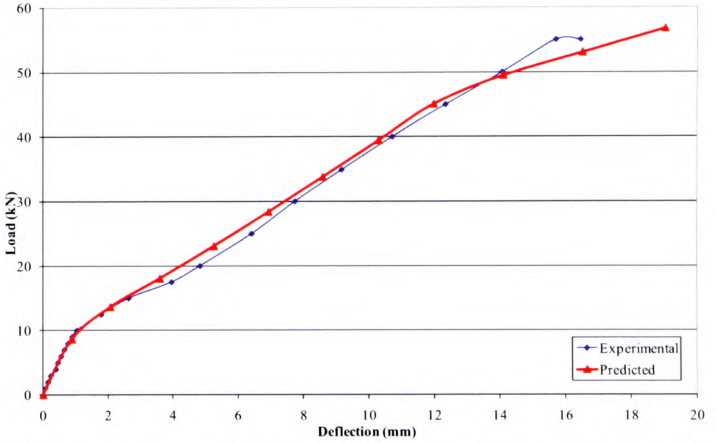

Figure 6.28(d) – Comparison of load deflection for 8CF3

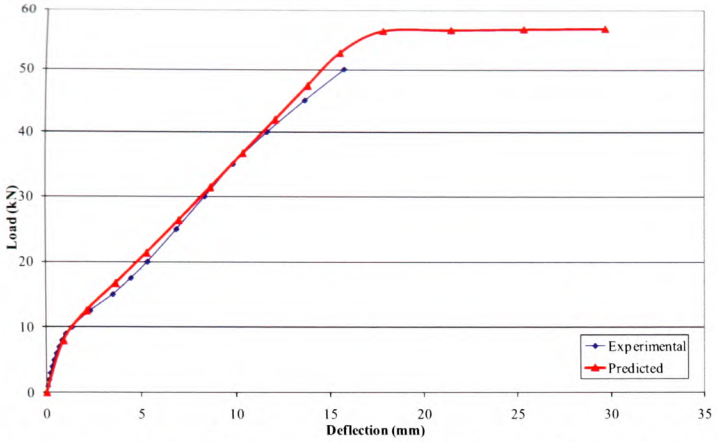

Figure 6.29(a) – Comparison of load deflection for 10CON

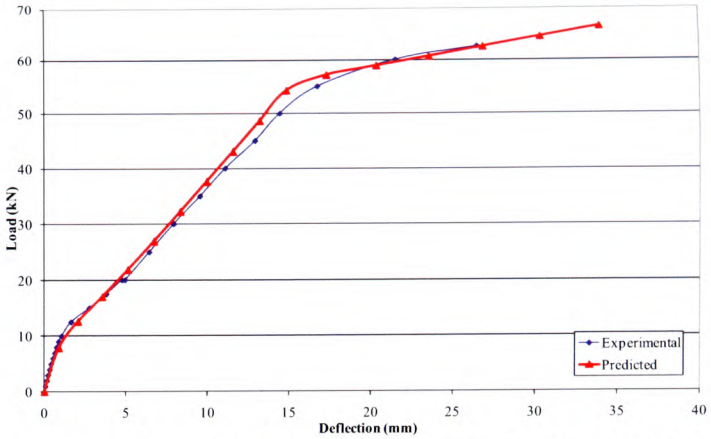

Figure 6.29(b) – Comparison of load deflection for 10CF1

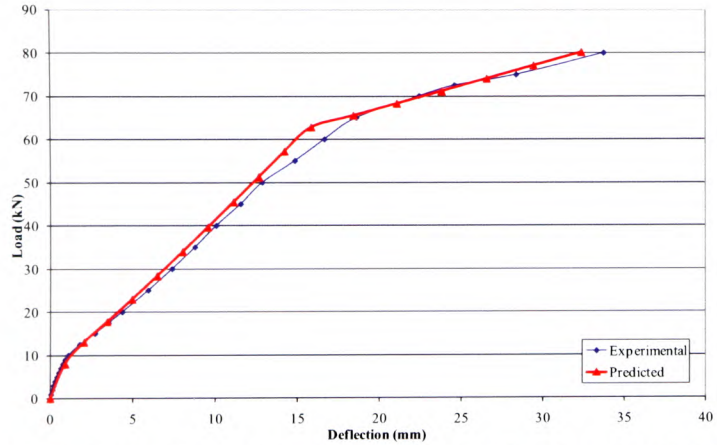

Figure 6.29(c) – Comparison of load deflection for 10CF2

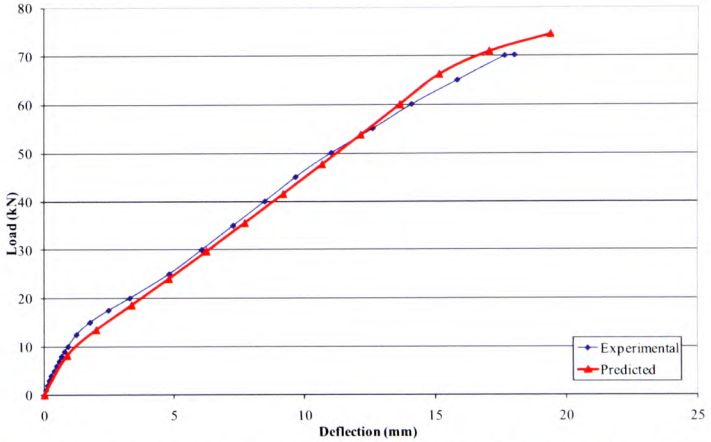

Figure 6.29(d) – Comparison of load deflection for 10CF3

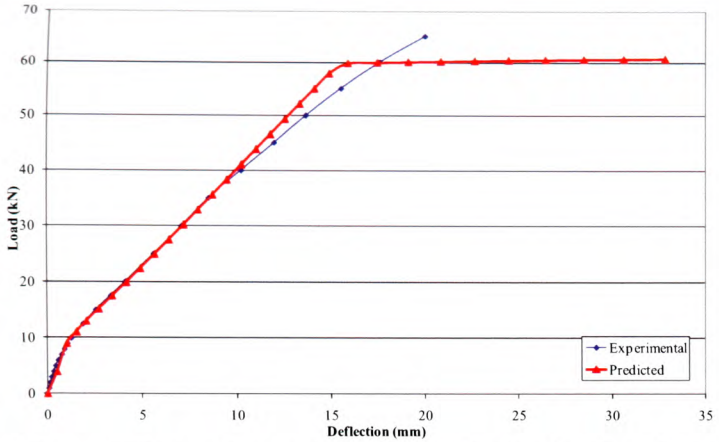

Figure 6.30(a) – Comparison of load deflection for 12CON

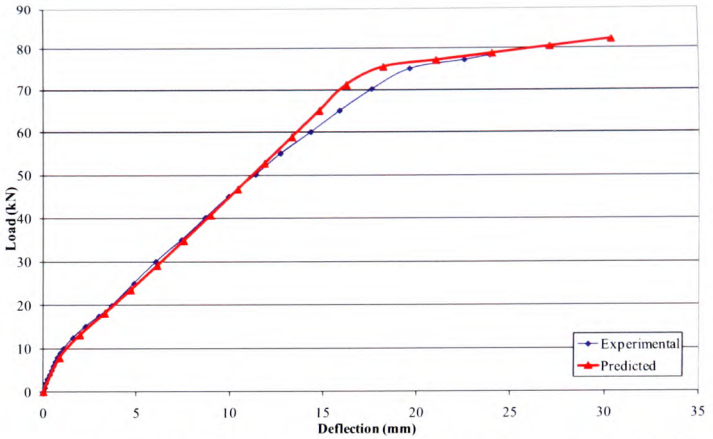

Figure 6.30(b) – Comparison of load deflection for 12CF1

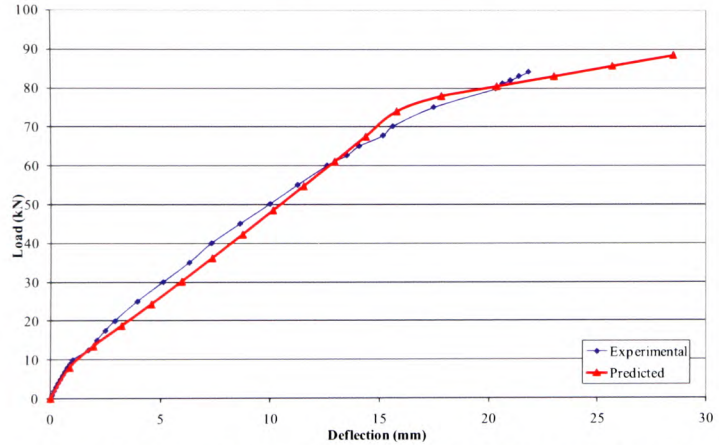

Figure 6.30(c) – Comparison of load deflection for 12CF2

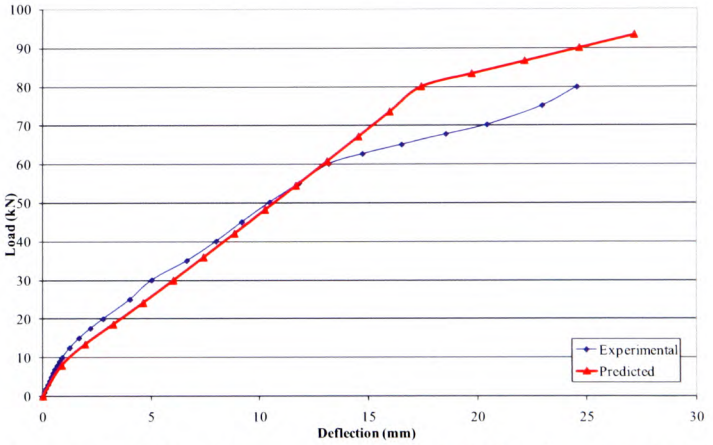

Figure 6.30(d) – Comparison of load deflection for 12CF3

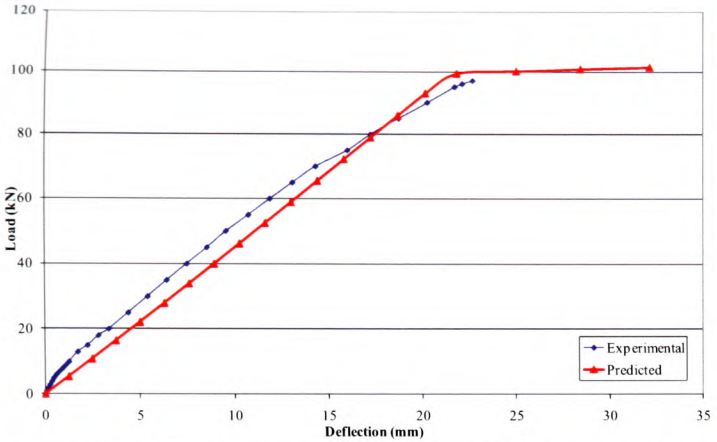

Figure 6.31(a) – Comparison of load deflection for 16CON

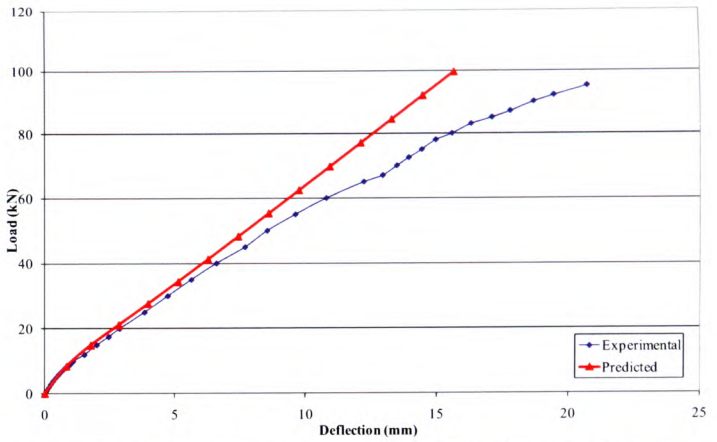

Figure 6.31(b) – Comparison of load deflection for 16CF1

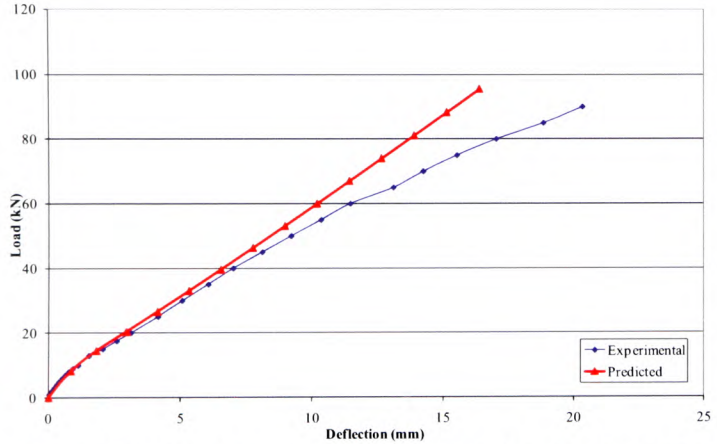

Figure 6.31(c) – Comparison of load deflection for 16CF2

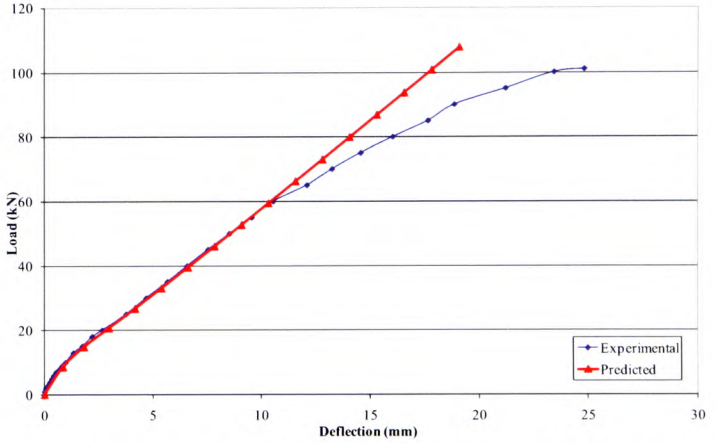

Figure 6.31(d) – Comparison of load deflection for 16CF3

$$\Rightarrow y_{max} = K\left(\frac{1}{R}\right)L^2 \qquad 6.31$$

However, it was also noted that such elements behave differently and, despite the slab elements with ∅12mm reinforcement having a reinforcement ratio higher than that of the beam elements reinforced with ∅8mm and ∅10mm bars, it was found that Equation 6.30 was unrepresentative of the load-deflection behaviour; specifically, the equation over-estimated the deflection for any given load by approximately 20%. Consequently, the value of K for all slab elements has been amended to $\frac{1}{10}$ (or 0.1), which gives very good correlation with the experimental data. A typical load deflection comparison (for element 12SCF2) is given in Figure 6.32.

Subsequently, graphs illustrating the comparison between actual experimentally-measured deflection and that obtained from the numerical model data for all slabs are presented in Figures 6.33 (a) to (d) and 6.34 (a) to (d).

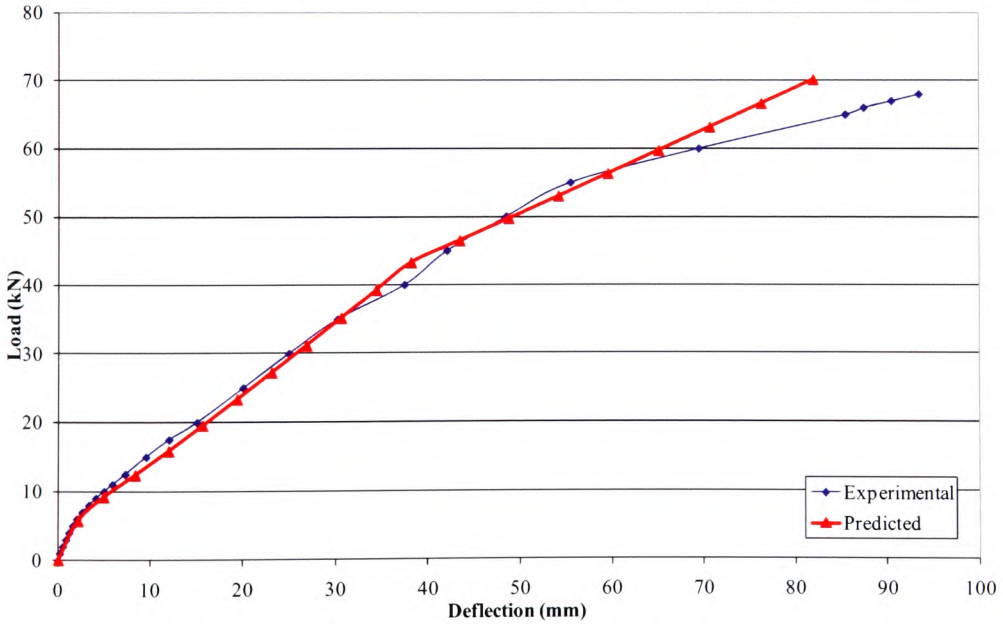

Figure 6.32 – Comparison of experimental and predicted load deflection behaviour for slab element 12SCF2

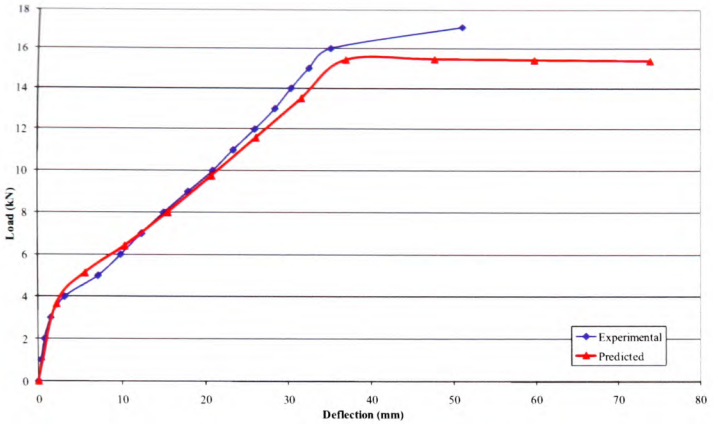

Figure 6.33(a) – Comparison of load deflection for 8SCON

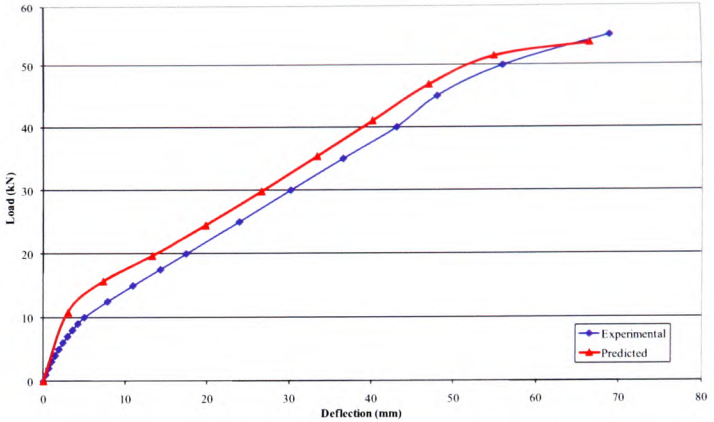

Figure 6.33(b) – Comparison of load deflection for 8SCF2

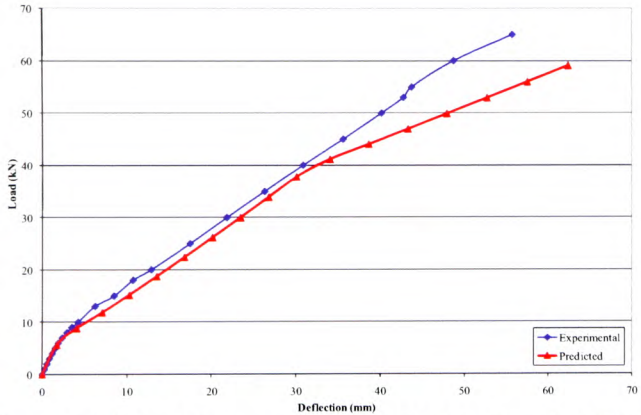

Figure 6.33(c) – Comparison of load deflection for 8SCP2

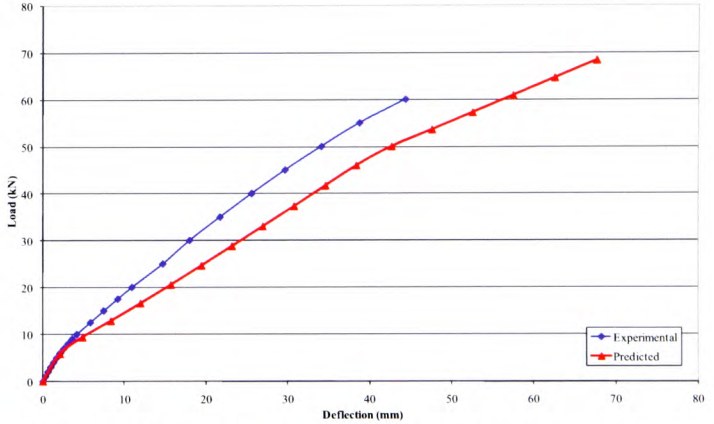

Figure 6.33(d) – Comparison of load deflection for 8SCP3

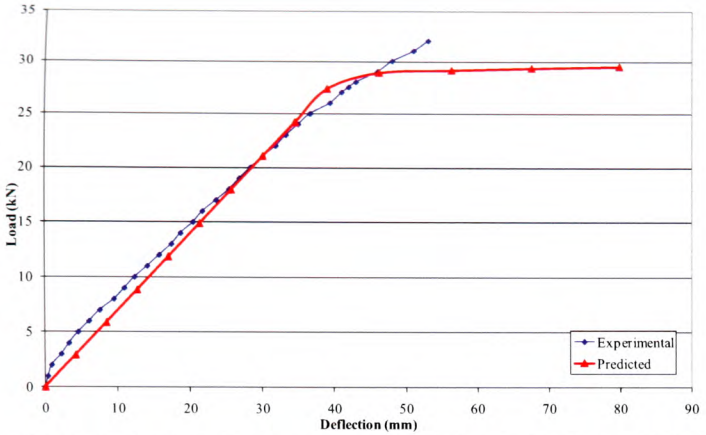

Figure 6.34(a) – Comparison of load deflection for 12SCON

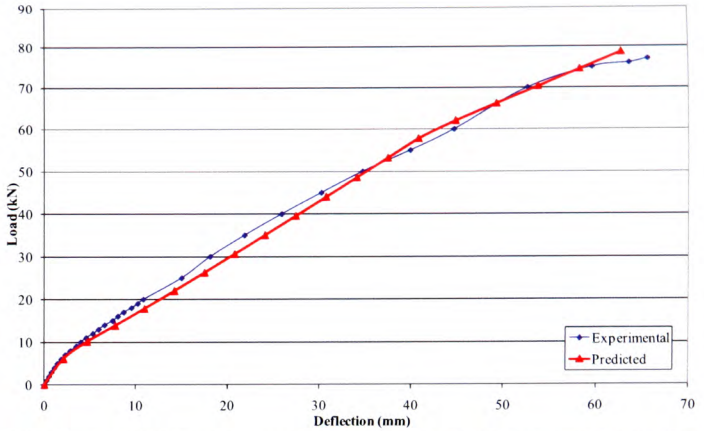

Figure 6.34(b) – Comparison of load deflection for 12SCF4

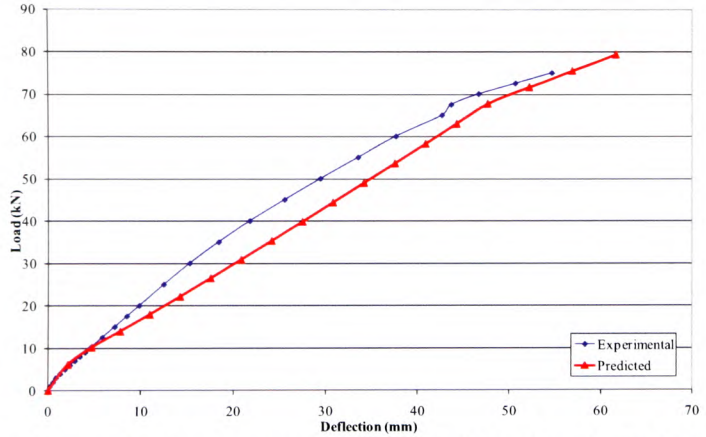

Figure 6.34(c) – Comparison of load deflection for 12SCP2

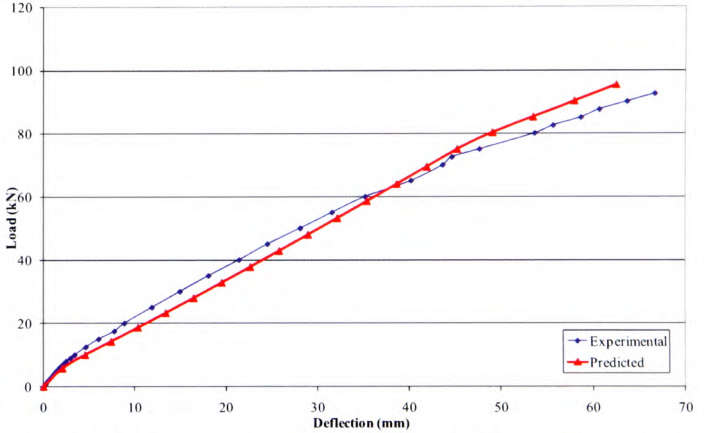

Figure 6.34(d) – Comparison of load deflection for 12SCP3

CHAPTER 7 DUCTILITY AND DEFORMABILITY DETERMINATION AND OPTIMISATION OF FIBRE COMPOSITES STRENGTHENED REINFORCED CONCRETE STRUCTURES

7.1 Introduction

As reviewed in Section 1.4 and Chapter 2, the consideration of structural ductility is of predominant importance to all structural designers, since all appropriately designed structures should contain sufficient reserves of ductility, under ultimate loads, in order to provide adequate warning of impending failure and, hence, resist sudden and brittle collapse.

The concept is particularly applicable to RC beams and slabs and to prestressed concrete elements. During many experiments in RC beams strengthened by steel plate bonding, it became apparent that sudden peeling-off of the plates was one of the main causes of failure. This characteristic has many similarities with RC beams strengthened using Fibre Reinforced Polymers (FRP) composites.

From a practical and commercial viewpoint, there are ample cases where it may become necessary to strengthen a reinforced concrete member. Historically, this has been achieved using section enlargement or by bonding of steel plates to the tension surface. Over the past decade, FRP composites have increasingly been used in place of steel plates for external strengthening systems but designers have been cautious in deploying this methodology, partly due to the uncertainty of sudden failure. It is believed that FRP composites-strengthened, reinforced concrete elements behave differently from their steel reinforced counterparts, due to the primarily linear elastic stress/strain characteristics of FRP composites up to failure.

The word ductility initiates from Latin *ductilis* and denotes the ability of metals and alloys to retain strength when their shape is altered due to applied stress. Today, the term is used to describe the ability of any material to sustain *inelastic* deformation before fracture. Concrete, in its natural form, is a brittle material but it is generally accepted that conventionally reinforced concrete members can attain suitable ductile behaviour by proper design and detailing of steel reinforcement. The yield point of steel is thus treated as an important datum beyond which inelastic deformation of the RC member takes place, thus enabling the full stress and strain capacity of concrete to be developed before ultimate failure.

Since the early 1990s, the feasibility of using FRP reinforcement instead of the conventional steel reinforcing bars has been widely researched, (Clarke *et al.*). The question of ductility for FRP reinforced concrete elements has been a topic of debate among many researchers; Saadatmanesh *et al.* (1998), Naaman *et al.* (1995) and Oehlers *et al.* (2008). Despite these attempts to address the issue of post-elastic behaviour, there is to date, still a distinctive lack of general agreement as to how the ductility characteristics of such elements may be quantified and analysed.

With regard to the ductility of FRP strengthened RC elements, there have been relatively fewer research activities focused on this important area. Yet, consideration of structural ductility is of predominant importance to any structural designer, as all appropriately designed structures should attain sufficiently ductile behaviour under ultimate load conditions. The reason for suitable ductility is threefold:

- Firstly, it is to ensure that there is a mechanism of redistribution of internal actions in a statically indeterminate structure. This is when parts of the element reach the ultimate capacity, and hence allow plastic hinges to be formed.

- Secondly, it is universally agreed that ductile structures can provide sufficient pre-warning to final state of collapse, so as to prevent the structure from sudden and brittle failure at ultimate limit state (ULS).
- Finally, the ability to absorb energy; e.g. seismic loading conditions.

7.2 Outline of chapter

In this chapter, the brief review of the current popular methods for ductility calculation will be carried out, followed by an initial comparative study, in which the suitability of these methods when applied to FRP composites strengthened RC elements will be evaluated.

Subsequently, a modification is proposed to the energy-based ductility calculation method, suggested by Naaman *et al.*, which results in more accurate approximations of the stored elastic energy at failure in FRP composites strengthened RC elements, and this is supported by an evaluation of both methods utilising data available from the candidate's experimental programme.

Following this, ductility and deformability indices are calculated and evaluated, first for the elements in the experimental programme and, subsequently, for all elements contained within the comparative study, together with additional elements from published data. This enables a comparison to be made of the effectiveness of the various methods in predicting possible non-ductile element failure.

Finally, the results of the study are summarised and a suitable minimum value for the ductility index is proposed that will ensure ductile behaviour from an element externally strengthened with FRP composites.

7.3 Current methods for ductility calculation

As discussed in Chapter 2, there are currently a number of different methods for calculating the ductility of fibre composites strengthened, reinforced concrete structures. These methods primarily centre around two distinct methodologies – either using deformation-based data or energy-based data.

7.3.1 Deformation-based methods

As previously presented in Section 2.2, the following is a summary of the most widely used methods for calculating ductility from deformation-based data:

Deflection-based ductility (Spadea *et al.* 1998), μ_Δ:

$$\mu_\Delta = \frac{\Delta_u}{\Delta_y} \qquad 7.1$$

where; Δ_u is the maximum mid-span deflection at ultimate limit state

Δ_y is the maximum mid-span deflection at the point where the internal steel reinforcement yields

Also, there is the method proposed by Tann (2001), where the deformation at the serviceability load (Δ_s) is used in place of that at the steel reinforcement yield point, together with the corresponding deformation at 95% of the ultimate load. This was termed the 'deformability index', φ_{df}:

$$\varphi_{df} = \frac{\Delta_{0.95u}}{\Delta_s} \qquad 7.2$$

where; $\Delta_{0.95u}$ is the maximum mid-span deflection at 95% of the ultimate load

Δ_s is the maximum mid-span deflection at serviceability loading (Tann, 2001)

7.3.2 Energy-based methods

Energy-based ductility (Bencardino *et al.* 2002), μ_E:

$$\mu_E = \frac{E_u}{E_y} \tag{7.3}$$

where; E_u is the energy under the load-deflection curve at ultimate limit state

E_y is the energy under the load-deflection curve up to the point of yielding of internal steel reinforcement

Energy-based ductility (Naaman *et al.*, 1995), φ_E:

$$\varphi_E = \frac{1}{2}\left(\frac{E_{tot}}{E_{el}} + 1\right) \tag{7.4}$$

where; E_{tot} is the energy under the load-deflection curve at ultimate limit state

E_{el} is the elastic stored energy

7.4 Initial comparative study

In order to determine the suitability of the existing ductility evaluation methods, when applied to reinforced concrete elements strengthened with FRP composites, an initial comparative study was undertaken. The study involved the consideration of a number of criteria including consistency of prediction, volatility of data, ease of application in practice, and accuracy.

Experimental results from a number of published sources* were used to evaluate the effectiveness of the various methods for determining the ductility indices. A comprehensive list of the element data is presented in Table 7.2, with the corresponding calculated indices and failure modes detailed in Table 7.3.

* Chajes *et al.*(1995); Quantrill *et al.*(1995); Chajes *et al.*(1998); Grace *et al.*(1999); Tumialan *et al.*(1999); Ahmed *et al.*(2001); Almusallam *et al.*(2001); Spadea *et al.*(2001); Tann(2001); Bencardino *et al.*(2002)

The values of indices for μ_Δ, φ_{df}, μ_E and φ_E (Equations 7.1, 7.2, 7.3 and 7.4 respectively) for members that had exhibited a 'brittle' failure mode, were analysed to determine whether there was an apparent trend in the calculated values.

As can be seen in Table 7.3, the various methods produce markedly different results for the ductility index for any given element; e.g. element 4, where the index value varies from 2.75 to 7.81, and element 34, where the indices vary from 2.45 to 10.14. Further analysis shows that the method utilising the serviceability load, φ_{df}, has a significantly lower standard deviation, therefore demonstrating a more consistent set of results. The mean, high and low values for the calculated indices, together with the standard deviation, are detailed in Table 7.1.

Both deformation-based methods displayed good correlation between data (see Figure 7.1), with slightly better congruence between the deformation methods (87% correlation) than the energy methods (81% correlation).

Table 7.1 - Comparison of various methods of calculating ductility/deformability index

Equation No.	Method	Low	Mean	High	Standard deviation, σ
7.1	$\mu_\Delta = \frac{\Delta_u}{\Delta_y}$	1.42	2.63	4.45	0.79
7.2	$\varphi_{df} = \frac{\Delta_{0.95u}}{\Delta_s}$	1.84	2.61	4.24	0.52
7.3	$\mu_E = \frac{E_u}{E_y}$	1.83	4.76	10.14	2.00
7.4	$\varphi_E = \frac{1}{2}\left(\frac{E_{tot}}{E_{el}} + 1\right)$	0.85	2.15	4.43	0.80

Of the two energy based methods, the first (μ_E) produced a much larger variance in the ductility index values. This particular method appears especially sensitive to sections that are over-reinforced with FRP, as the energy at yield can be

relatively small compared to the total energy and, hence, generate a large (and probably misleading) value for the ductility index.

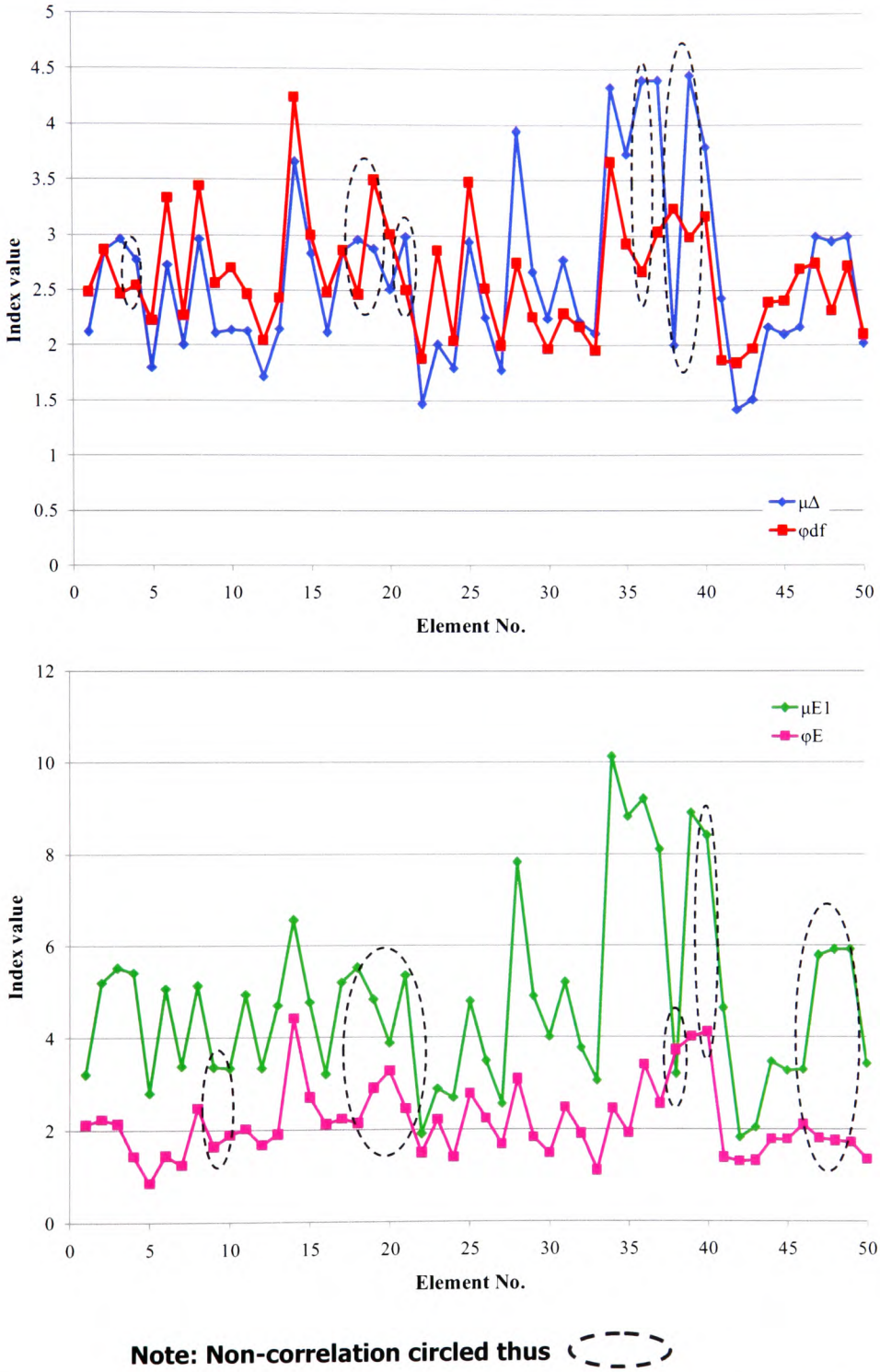

Figure 7.1 – Correlation of results between various ductility determination methods

Table 7.2 – Element data used in comparative study

Ref. No.	Elem. Ref.	Source	Size (mm)	Int'l flexural reinf't	FRP		Failure load (kN)
					Type[†]	*% of area*	
1	1A	Chajes *et al.* (1995)	127x76	1 x No.3	C, P	0.14	21.8
2	1B				C, P	0.46	21.8
3	1C				C, P	0.61	34.4
4	2A	Quantrill *et al.* (1995)	100x100	3 x No.R6	G, P	1.76	47.2
5	2B				G, P	1.76	36.7
6	2C				G, P	2.56	24.6
7	2D				G, P	2.56	35.0
8	3A	Chajes *et al.* (1998)	127x76	1 x No.3	A, F	1.37	16.9
9	3B				G, F	1.86	15.4
10	3C				C, F	1.60	14.5
11	4A	Grace *et al.* (1999)	152x292	2 x Ø16mm	C, P	0.45	110.3
12	4B				C, P	0.81	105.9
13	4C				C, P	1.30	113.9
14	5A	Tumialan *et al.* 1999	152x305	4 x No.5	C, P	0.05	146.35
15	5B				C, P	0.11	169.03
16	5C				C, P	0.16	171.70
17	5D				C, P	0.79	195.72
18	5E				C, P	0.79	211.29
19	5F				C, P	0.03	143.2
20	5G				C, P	0.06	170.3
21	5H				C, P	0.16	196.0
22	5I				C, P	0.06	74.8
23	5J				C, P	0.05	154.4
24	5K				C, P	0.11	153.9
25	6A	Ahmed *et al.* (2001)	125x225	3 x Ø8mm	C, F	0.05	121.1
26	6B				C, F	0.09	121.7
27	6C				C, F	0.18	126.7
28	7A	Almusallam *et al.* (2001)	150x200	3 x Ø10mm	G, P	1.52	70.4
29	7B				G, P	3.03	82.4
30	7C				G, P	6.07	105.9
31	7D				C, P	1.17	81.90
32	7E				C, P	2.33	103.10
33	8A	Spadea *et al.* (2001)	140x300	2 x Ø16mm	C, P	0.23	86.8
34	8B				C, P	0.23	98.0
35	8C				C, P	0.23	96.7
36	8D				C, P	0.23	75.00
37	8E				C, P	0.23	77.70
38	8F				C, P	0.23	74.80
39	8G				C, P	0.23	98.80
40	8H				C, P	0.23	98.30
41	9A	Tann (2001)	100x200	2T10	C, P	0.80	76.2
42	9B				C, P	0.80	90.0
43	9C				C, P	0.70	68.3
44	9D				C, F	0.70	76.0
45	9E				C, F	0.70	61.2
46	9F				G, P	0.70	67.3
47	10A	Bencardino *et al.* (2002)	140x300	2 x Ø16mm	C, F	0.41	101.3
48	10B				C, F	0.82	133.1
49	10C				C, F	0.41	90.0
50	10D				C, F	0.82	102.3

[†] C – Carbon fibre composites; G – Glass fibre composites; A – Aramid fibre composites; F – Fabric; P - Plate

Table 7.3 – Calculated indices and modes of failure for comparative study

Ref. No.	Ref.	μ_Δ[‡]	φ_{df}	μ_E	φ_E	Failure mode[§]
1	1A	2.12 *(1.9)*	2.48	3.20	2.12	PTO
2	1B	2.86 *(2.2)*	2.86	5.20	2.24	PTO
3	1C	2.96 *(2.6)*	2.46	5.52	2.14	PTO
4	2A	2.77	2.54	5.42	1.44	DB
5	2B	1.80	2.22	2.80	0.85	PTO
6	2C	2.73	3.33	5.07	1.45	PTO
7	2D	2.00	2.27	3.38	1.24	PTO
8	3A	2.96	3.44	5.13	2.48	CC
9	3B	2.11	2.56	3.35	1.64	FR
10	3C	2.14	2.70	3.33	1.89	FR
11	4A	2.13	2.46	4.94	2.02	PTO
12	4B	1.72	2.04	3.34	1.68	PTO
13	4C	2.15	2.43	4.71	1.90	PTO
14	5A	3.66 *(3.4)*	4.24	6.56	4.43	PTO
15	5B	2.83 *(2.1)*	3.00	4.77	2.70	PTO
16	5C	2.12 *(1.9)*	2.48	3.20	2.12	PTO
17	5D	2.86 *(2.2)*	2.86	5.20	2.24	PTO
18	5E	2.96 *(2.6)*	2.46	5.52	2.14	PTO
19	5F	2.88	3.50	4.83	2.90	PTO
20	5G	2.51	3.01	3.89	3.27	PTO
21	5H	2.99	2.50	5.36	2.46	PTO
22	5I	1.47	1.88	1.90	1.49	CC
23	5J	2.01	2.86	2.89	2.22	PTO
24	5K	1.80	2.04	2.69	1.39	PTO
25	6A	2.94	3.48	4.79	2.78	SY-FR
26	6B	2.26	2.52	3.48	2.24	PTO
27	6C	1.78	2.00	2.56	1.68	DB
28	7A	3.94	2.75	7.81	3.09	SY-CC
29	7B	2.67	2.26	4.90	1.83	SY-CC
30	7C	2.25	1.97	4.02	1.48	SY-CC
31	7D	2.78	2.29	5.19	2.48	SY/CC
32	7E	2.22	2.17	3.78	1.90	SY/CC
33	8A	2.11 *(1.5)*	1.95	3.06 *(1.9)*	1.10	DB
34	8B	4.34 *(4.3)*	3.66	10.14 *(9.5)*	2.45	DB
35	8C	3.74 *(3.5)*	2.92	8.82 *(7.6)*	1.91	DB
36	8D	4.40	2.67	9.20	3.40	DB
37	8E	4.40	3.03	8.10	2.55	DB
38	8F	2.00	3.24	3.20	3.72	DB
39	8G	4.45	2.98	8.90	4.01	DB
40	8H	3.80	3.17	8.40	4.12	DB
41	9A	2.43	1.86	4.63	1.38	PTO
42	9B	1.42	1.84	1.83	1.31	PTO
43	9C	1.51	1.97	2.04	1.32	CC
44	9D	2.17	2.39	3.47	1.79	FR-CC
45	9E	2.10	2.40	3.28	1.79	CC
46	9F	2.17	2.69	3.30	2.10	DB
47	10A	2.99 *(2.93)*	2.74	5.78 *(5.84)*	1.80	SY-CC
48	10B	2.94 *(2.87)*	2.31	5.91 *(6.00)*	1.75	FR
49	10C	2.99 *(3.02)*	2.72	5.92 *(6.42)*	1.72	SY-CC
50	10D	2.02 *(1.99)*	2.10	3.43 *(3.42)*	1.35	DB

[‡] *Note that figures in parentheses and italics are from the published paper, all other values are calculated*
[§] *SY-Steel yield; FR-Fibre rupture; PTO-Partial tearing-off of concrete cover; DB- Fibre debonding; CC-Concrete crushing*

7.5 Modification to Naaman *et al.*'s approach

The method for the determination of stored elastic energy at failure developed by Naaman *et al.* and discussed in 2.3.3, has limitations in that it is designed to be applied to sections that have been internally reinforced with FRP reinforcement, rather than to elements already internally reinforced with steel bars but also strengthened with externally-bonded fibre reinforced polymer sheets or plates. Consequently, the existing approach does not take into account the additional stored elastic energy that is inherent in strengthened elements in the latter stages of loading.

During the execution of the experimental programme, it was possible to unload numerous elements to near zero loading just prior to failure, thereby enabling an accurate representation of the unloading curve to be obtained. This, in turn, allowed the stored elastic energy in the element to be closely estimated, as it is determined by calculating the area underneath the unloading curve.

A modification could then be made to Naaman *et al.*'s approach that takes into consideration the additional stored elastic energy developed in any FRP strengthened element during the latter stages of loading.

The first aspect of this modified approach involves the incorporation of a third slope, S_3, when calculating the slope of the estimated unloading curve, as shown in Equation (7.5) and Figure 7.2:

$$S = \frac{P_1 S_1 + (P_2 - P_1)S_2 + (P_U - P_2)S_3}{P_U} \qquad 7.5$$

All strengthened elements display an approximately tri-linear behavioural pattern when presented as either load deflection or moment curvature graphs, in a similar way to normally-reinforced concrete elements. However, whereas normal RC sections tend to display a very flattened behaviour following yielding of the

internal steel, sections strengthened with externally-bonded FRP composites exhibit a far steeper (and therefore stiffer) behaviour after the internal steel reinforcement has yielded, up to failure.

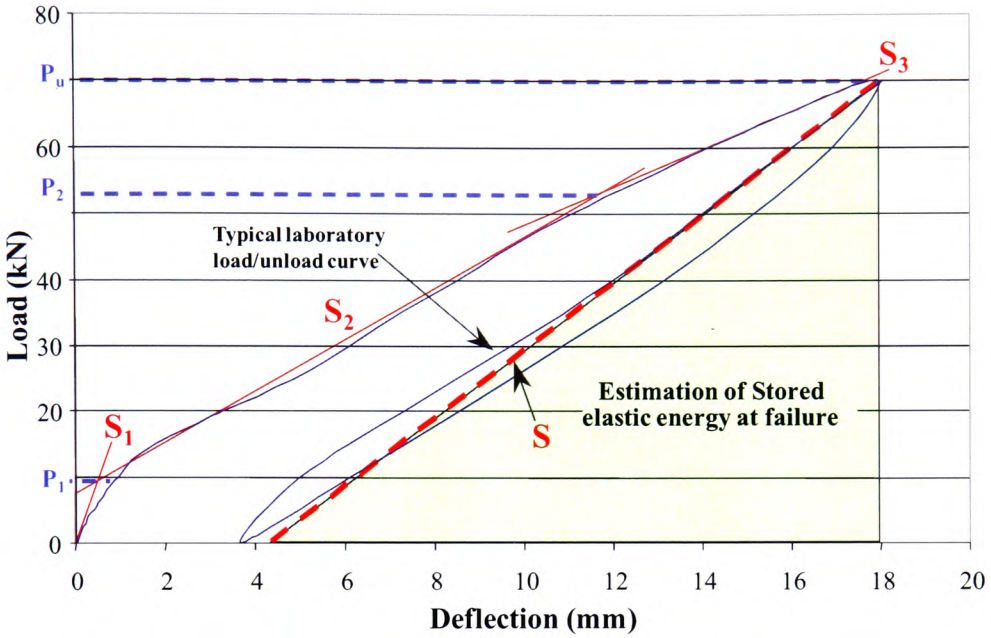

Figure 7.2 – Modification of Naaman *et al.* approach utilising a third slope, S_3

This revised, empirical approach will yield an adjusted value for the estimated stored elastic energy, E'_{el}, which can then be used to calculate the modified ductility index φ_{3S} as follows:

$$\varphi_{3S} = \frac{1}{2}\left(\frac{E_{tot}}{E'_{el}} + 1\right) \qquad 7.6$$

As stated previously, it is proposed that the third slope, S_3, be considered when approximating $E_{elastic}$, to take into account the additional elastic energy being stored in the element during the latter stages of loading and this method has been shown to yield accurate results for the estimation of stored elastic energy, which is further discussed in the following sections.

In order to test the method, an analysis has been carried out using the data obtained for 10CF2, the element with two 10mm internal reinforcing bars and strengthened with two-layers of externally-bonded CFRP sheets.

7.5.1 Analysis of 10CF2 using Naaman *et al.*'s approach

From analysis of the load deflection graph (Figure 7.3) the following can be calculated:

$$S_1 = \frac{P_1}{\delta_1} = \frac{9.2}{0.5} = 18.4 \qquad S_2 = \frac{(P_2 - P_1)}{(\delta_2 - \delta_1)} = \frac{(67.2 - 9.2)}{(12.1 - 0.5)} = 5.0$$

$$\Rightarrow S = \frac{(P_1)(S_1) + (P_2 - P_1)(S_2)}{P_2} = \frac{(9.2)(18.4) + (67.2 - 9.2)(5.0)}{67.2} = 6.83$$

$$\Rightarrow \delta_s = \delta_u - \left\{\frac{P_u}{S}\right\} = 21.7 - \left\{\frac{80.0}{6.83}\right\} = 10.0$$

$$\Rightarrow E_{el} = \frac{1}{2}(\delta_u - \delta_s)(P_u) = \frac{1}{2}(21.7 - 10.0)(80.0) = 468$$

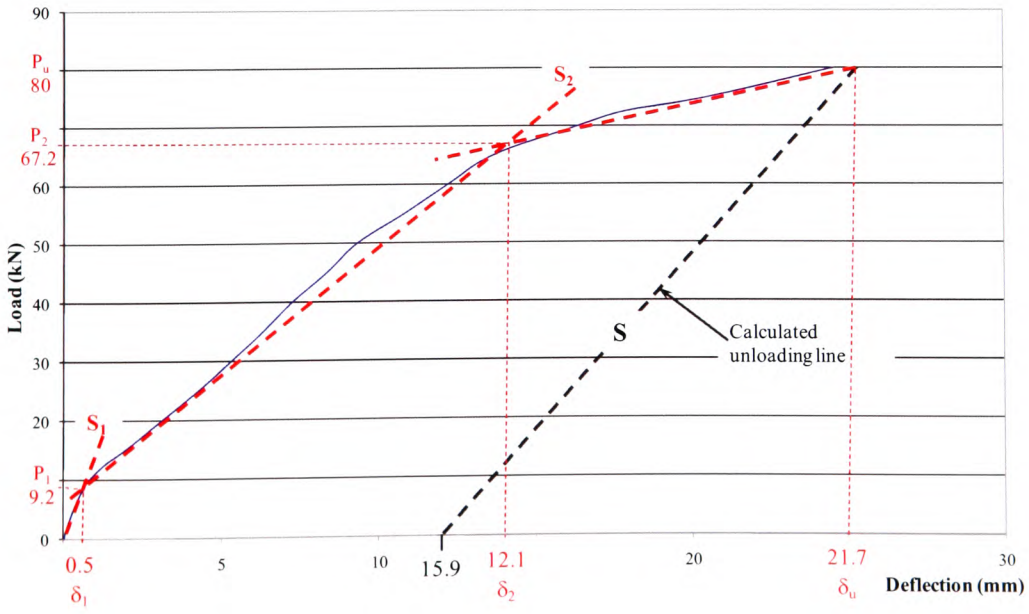

Figure 7.3 – Load deflection plot for 10CF2 detailing calculation of slope S

7.5.2 Analysis of 10CF2 using proposed modified approach

From analysis of the load deflection graph (Figure 7.4) the following can be calculated:

$$S_1 = 18.4,\ S_2 = 5.0 \quad \text{(Previously calculated)}$$

$$S_3 = \frac{(P_u - P_2)}{\delta_u - \delta_2} = \frac{80.0 - 67.2}{21.7 - 12.1} = 1.33$$

$$\Rightarrow S' = \frac{P_1 S_1 + (P_2 - P_1)S_2 + (P_u - P_2)S_3}{P_u}$$

$$\Rightarrow S' = \frac{(9.2)(18.4) + (67.2 - 9.2)(5.0) + (80.0 - 67.2)(1.33)}{80.0} = 5.95$$

$$\Rightarrow \delta_{s'} = \delta_u - \left\{\frac{P_u}{S'}\right\} = 21.7 - \left\{\frac{80.0}{5.95}\right\} = 8.14$$

$$\Rightarrow E_{el} = \frac{1}{2}(\delta_u - \delta_s)(P_u) = \frac{1}{2}(21.7 - 8.14)(80.0) = 543$$

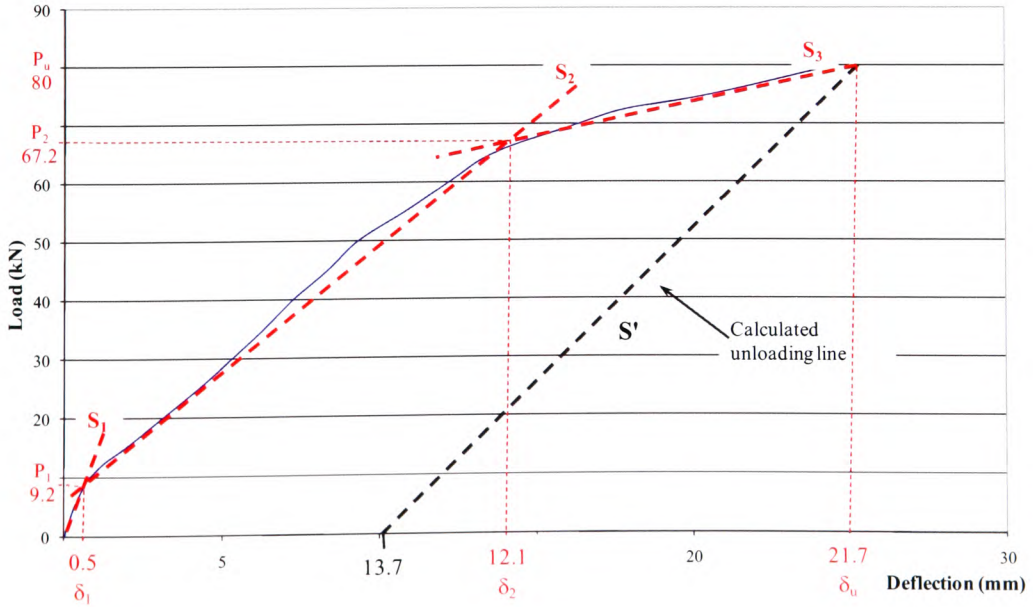

Figure 7.4 – Load deflection plot for 10CF2 detailing calculation of slope S'

7.5.3 Analysis using unloading curve obtained during experiment

It can be seen from the load deflection plot in Figure 7.5 that the beam was unloaded at 75kN, just prior to failure at the ultimate load of 80.0kN. The slope of this unloading curve can be duplicated onto the failure point and gives a value for δ of approximately 8.4mm.

$$\Rightarrow E_{el}'' = \frac{1}{2}(\delta_u - \delta_E)(P_u) = \frac{1}{2}(21.7 - 8.4)(80.0) = 532$$

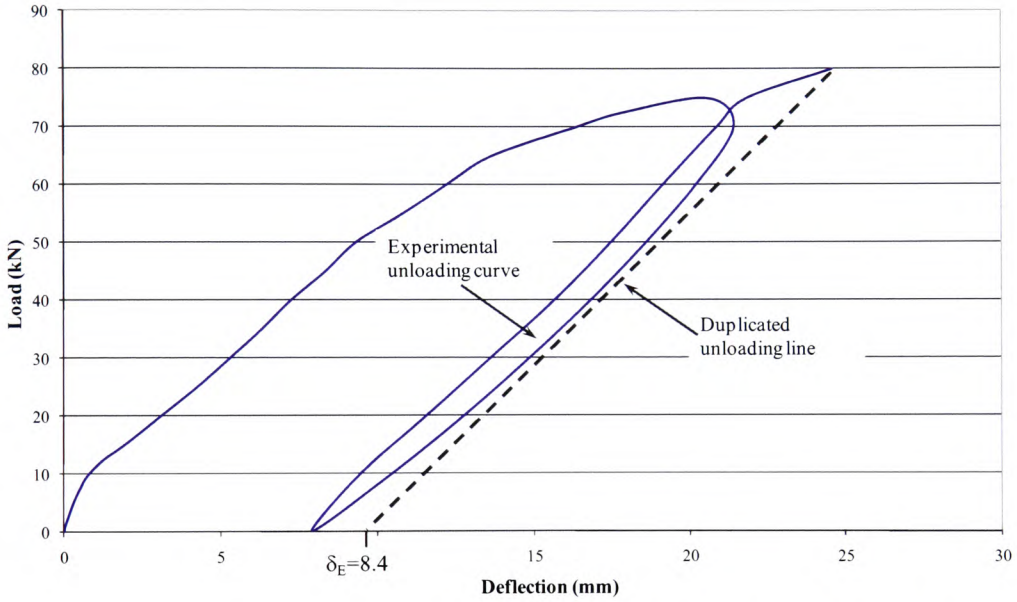

Figure 7.5 – Experimental load deflection plot for 10CF2 showing unloading curve

It is evident that the proposed method for estimating the stored elastic energy at failure compares far more favourably to the actual, experimental value. The magnitude of the value obtained through the modified approach is within 2.1% of that derived from experimental data, whilst the value obtained from the original Naaman *et al.* method differs by more than 13%. Additionally, the modified approach, as well as giving a closer approximation, also gives a slightly larger value for E_{el}, which allows for a more conservative estimate if utilising this approach during a design approach.

7.5.4 Substantiation of modified 3-slope approach for estimation of stored elastic energy

Following the initial study, as detailed in 7.3.1 to 7.3.3, further investigations were carried out on additional element data from the experimental programme, where an actual unloading curve was available close to or at the point of failure. This was possible for a further nine beams and the results from the analysis are shown in Table 7.4. It can be seen that for all the elements analysed, the modified method yields far more accurate results for the stored elastic energy at failure. An increased accuracy in the prediction of stored elastic energy will then, obviously, also result in a more reliable calculation of the associated energy-based ductility index, be it the method put forward by Naaman *et al.* or the modified 3-slope approach.

Figure 7.6 presents a graphical representation of the results, showing the better correlation with actual experimental values for stored elastic energy prediction for the modified 3-slope method.

Table 7.4 – Comparison of actual stored elastic energy with predicted stored elastic energy from both Naaman *et al.*, and Modified 3-slope methods

Element ref.	Actual stored elastic energy at failure	Estimated stored elastic energy using Naaman *et al.* method		Estimated stored elastic energy using modified 3-slope method	
		Result	% error	Result	% error
8CF1	398	324	-18.6%	361	-9.3%
8CF2	432	333	-22.9%	389	-10.0%
8CF3	245	297	+21.2%	281	+14.9%
10CF1	341	302	-11.4%	324	-5.0%
10CF2	532	460	-13.5%	542	+2.1%
10CF3	337	282	-16.3%	326	-3.3%
12CF1	354	338	-4.5%	353	-0.3%
12CF2	343	308	-10.2%	358	+4.4%
12CF3	376	331	-12.0%	363	-3.5%
16CF3	877	664	-24.3%	865	-1.4%

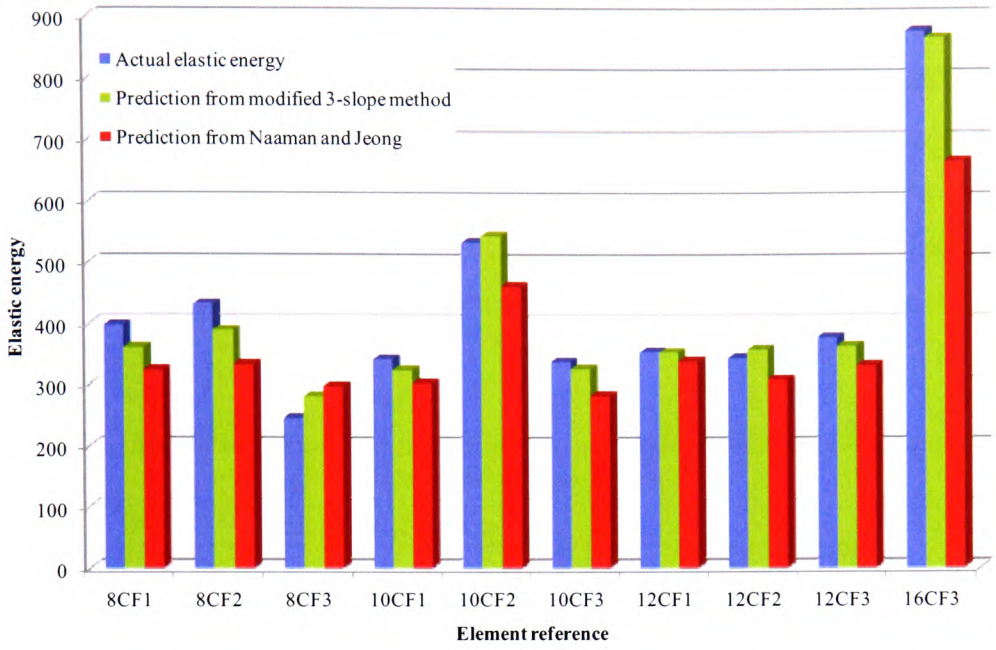

Figure 7.6 – Comparison of Modified 3-slope method and Naaman *et al.* method with actual stored elastic energy from experimental programme

7.6 Ductility and deformability indices from current research programme

Contained in Table 7.5 are the calculated ductility indices for all the elements, both beams and slabs, tested during the experimental programme, together with the ultimate moment and observed failure mode.

In Figures 7.7 to 7.10 are presented the plots of index value against failure mode for the four preferred ductility index calculation methods described earlier in this chapter, for all the beams tested in the experimental programme; the energy-based method detailed in Equation 7.3 has been discounted, due to the inappropriateness of this method when applied to fibre-composites-strengthened, as discussed in Section 7.2. On each graph is shown the minimum, maximum and average index value for the particular method in question. Presented in Figure 7.11 is a comparison of the average ductility index value against failure mode for all four methods.

From Figure 7.11, it can be seen that the modified three-slope method gives a much clearer numerical difference between what is considered a preferable failure mode (i.e. one where there is a suitable level of ductility) and those "non-preferable" failure modes, where sudden or brittle failure occurs, with no warning of impending failure. It is clear that the modified method is far more reliable at predicting a ductile failure mode and, additionally, it can be seen that there is far better consistency with the index values for undesirable failure modes.

Table 7.5 – Calculated indices, ultimate moments and modes of failure of elements from current research programme

	Element reference	Ductility/Deformability index				Ultimate Moment M_u (kNm)	Failure mode**
		μ_Δ $\left(\frac{\Delta_u}{\Delta_y}\right)$	φ_E $\frac{1}{2}\left(\frac{E_{tot}}{E_{el}}+1\right)$	φ_{df} $\frac{\Delta_{0.95u}}{\Delta_s}$	φ_{3S} $\frac{1}{2}\left(\frac{E_{tot}}{E'_{el}}+1\right)$		
Beams	8CON	1.53	1.97	1.78	1.89	10.1	SY-CC
	8CF1	1.36	1.70	1.68	1.55	16.7	FR
	8CF2	1.83	1.75	2.00	1.58	18.0	DB-PTO
	8CF3	1.06	1.21	1.49	1.20	15.8	PTO
	10CON	1.80	2.07	1.50	2.03	16.3	SY-CC
	10CF1	1.53	1.79	1.69	1.73	18.0	FR
	10CF2	1.77	1.78	1.98	1.61	23.1	DB-PTO
	10CF3	1.45	1.38	1.63	1.28	20.2	PTO
	12CON	1.28	1.19	1.54	1.14	18.7	CC
	12CF1	1.22	1.26	1.47	1.25	22.5	CC
	12CF2	1.25	1.20	1.55	1.13	24.2	CC
	12CF3	1.20	1.29	1.49	1.24	24.4	CC
	16CON	1.82	1.18	1.68	1.14	28.2	CC
	16CF1	1.73	1.26	1.58	1.21	27.6	ECC
	16CF2	1.77	1.48	1.65	1.35	25.9	ECC
	16CF3	1.99	1.41	1.79	1.28	29.1	CC
Slabs	8SCON	2.83	1.64	4.73	4.51	8.1	SY-CC
	8SCF2	1.57	1.66	1.48	1.38	26.1	FR-PTO
	8SCP2	1.49	1.49	1.24	1.19	30.9	DB
	8SCP3	1.68	1.37	1.25	1.14	28.5	DB
	12SCON	1.72	1.28	1.59	1.96	15.2	SY-CC
	12SCF2	2.17	1.59	1.93	1.45	32.3	FR
	12SCF4	1.77	1.27	1.53	1.25	36.6	CC
	12SCP2	1.82	1.22	1.63	1.15	35.6	DB
	12SCP3	1.83	1.28	1.69	1.18	44.0	DB

** Note: CC=Concrete crushing; SY-CC=Steel yield followed by concrete crushing; FR=Fibre rupture; DB=De-bonding of CFRP; PTO=Premature tearing-off of concrete cover; ECC=Explosive concrete crushing

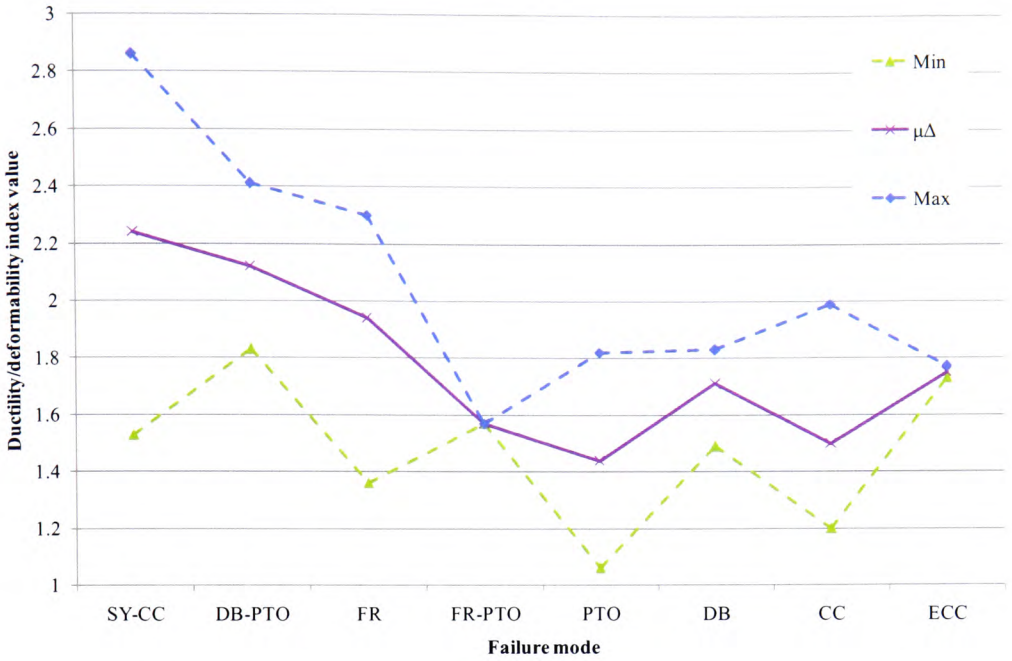

Figure 7.7 – Plot of ductility index against failure mode for μ_{Δ} (Equation 7.1) for elements from current research programme

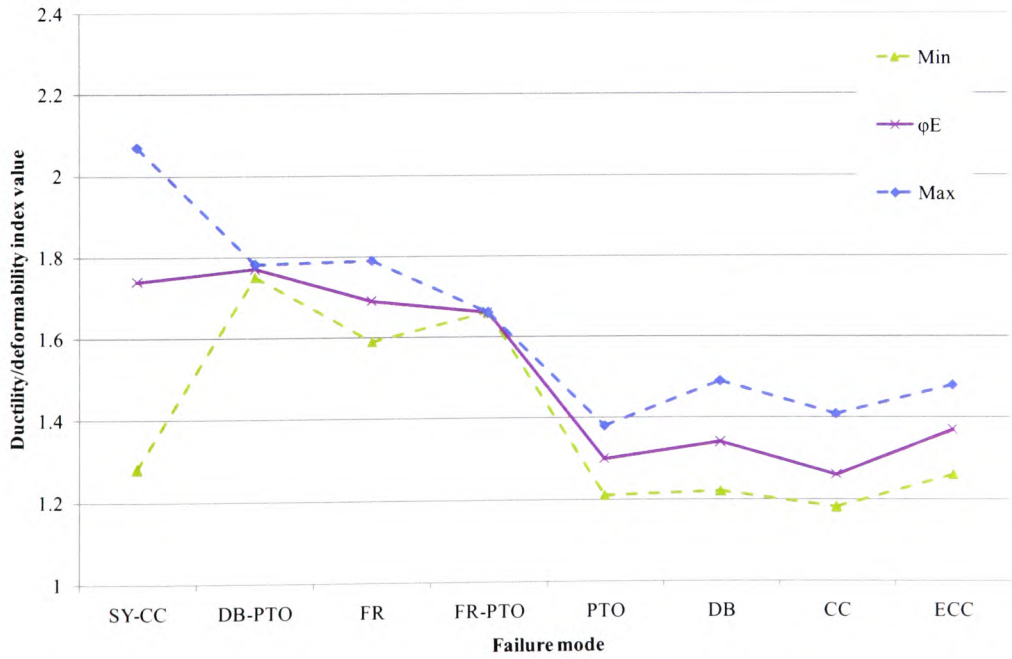

Figure 7.8 – Plot of ductility index against failure mode for φ_E (Equation 7.4) for elements from current research programme

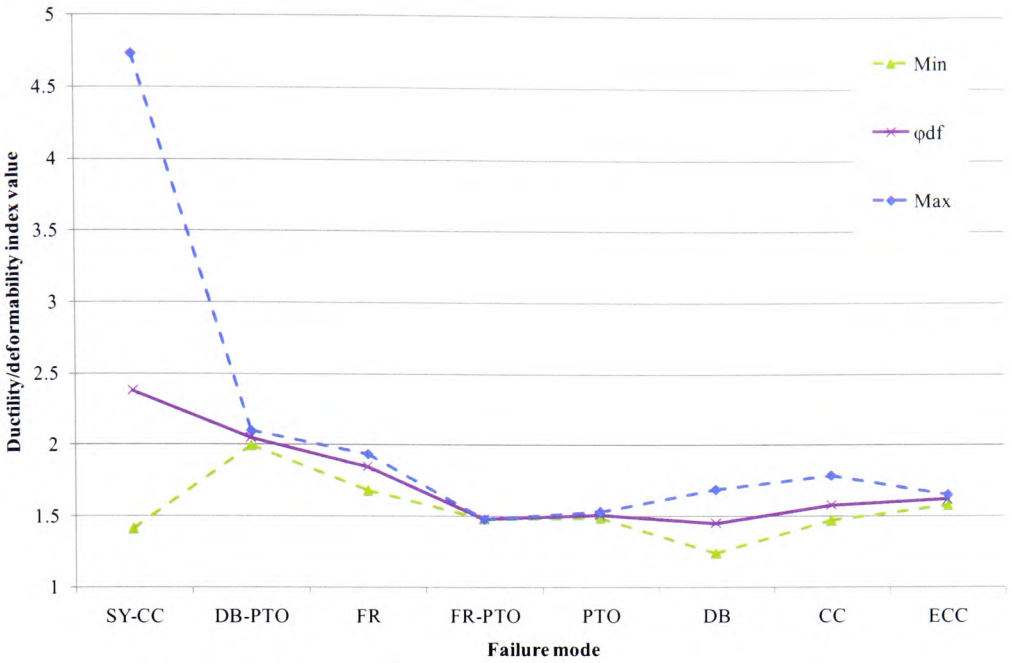

Figure 7.9 – Plot of deformability index against failure mode for φ_{df} (Equation 7.2) for elements from current research programme

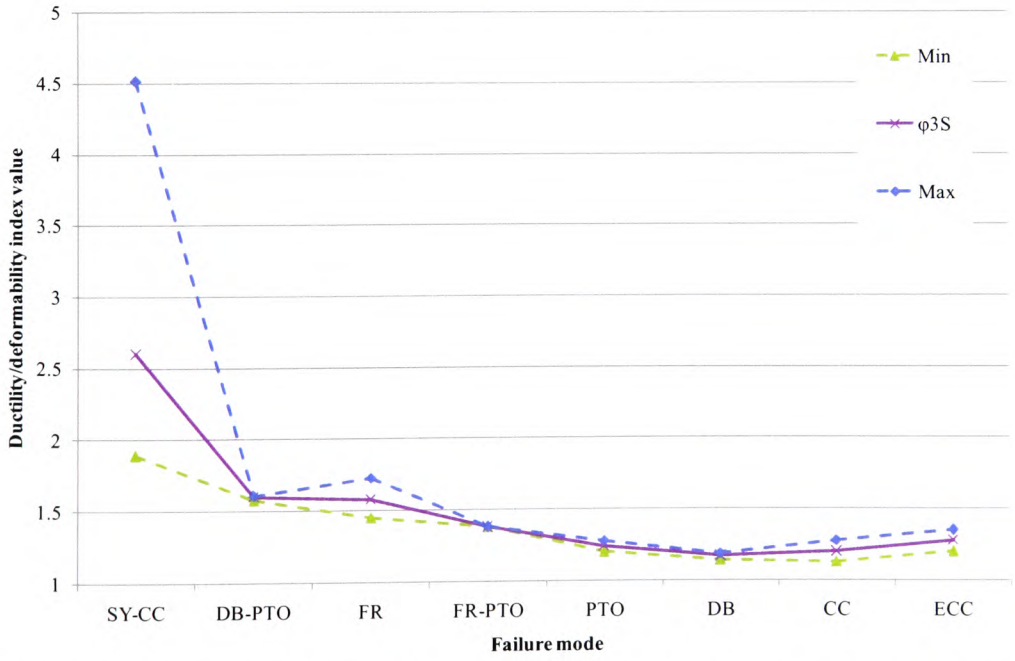

Figure 7.10 – Plot of ductility index against failure mode for φ_{3S} (Equation 7.6) for elements from current research programme

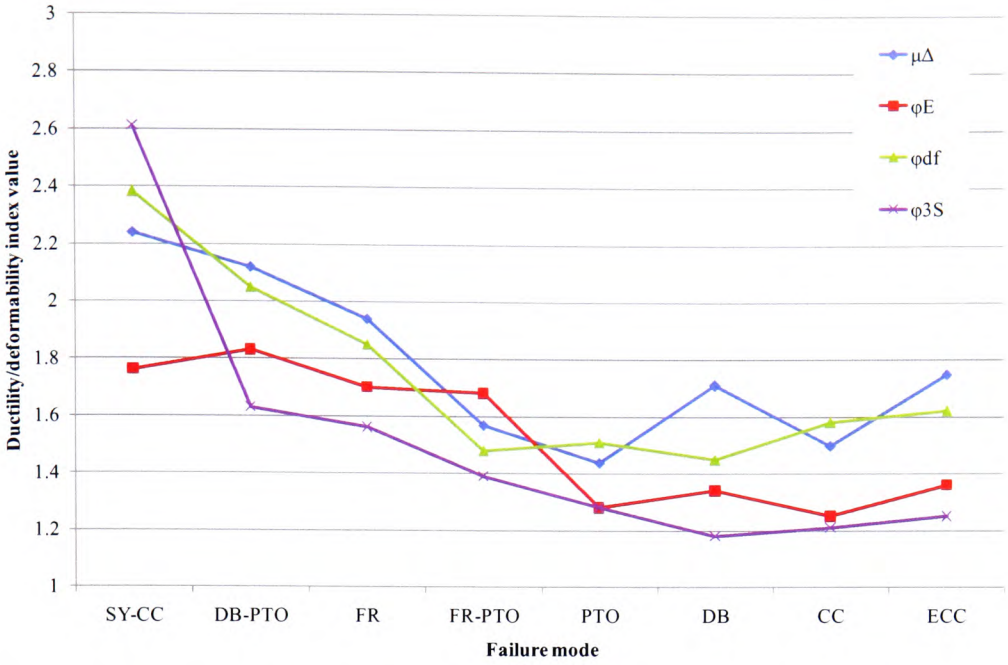

Figure 7.11 – Plot of ductility/deformability index against failure mode for all four methods for elements from current research programme

7.7 Ductility and deformability indices from study of published data

If the four methods are now applied to all the elements contained within the comparative study of published data discussed in Section 7.2, it can be seen that there is a definite difference between the index value for ductile and non-ductile failure modes for all methods. Presented in Figures 7.12 to 7.15 are the maximum, minimum and average indices for all four methods. Figure 7.16 displays a comparison of the average index values for the different failure modes for all four methods.

In addition to the elements contained within the original comparative study (detailed in Section 7.4), additional elements from further published data[††] have been included, which include a number of normally-reinforced, un-strengthened, "control" elements, in order that a more comprehensive approach to the

[††] Maalej *et al.* (2005); Wenwei *et al.* (2005); Esfahani *et al.* (2006); Oehlers *et al.* (2008)

optimisation of the various methods can be adopted. The details for these additional elements are presented in Tables 7.6 and 7.7.

It is apparent that there is a far larger difference between the ductile and non-ductile indices for the modified 3-slope method than for any of the alternatives. Additionally, there is far greater consistency for those indices representing non-ductile failure modes for the modified approach.

Table 7.6 – Additional element data used in comparative study

Ref. No.	Elem. Ref.	Source	Size (mm)	Int'l flexural reinf't	FRP		Failure load (kN)
					Type[‡‡]	*% of area*	
51	11A	Maalej *et al.* (2005)	115x146	3T10	-	-	60.4
52	11B				-	-	60.7
53	11C				C, F	0.11	77.5
54	11D				C, F	0.11	75.5
55	11E				C, F	0.23	87.4
56	11F				C, F	0.23	85.8
57	11G		230x292	3T20	-	-	203.9
58	11H				-	-	200.3
59	11I				C, F	0.11	263.5
60	11J				C, F	0.11	260.3
61	11K				C, F	0.23	294.7
62	11L				C, F	0.23	284.3
63	11M		368x467.2	3T32	-	-	520.0
64	11N				-	-	519.1
65	11O				C, F	0.11	652.9
66	11P				C, F	0.11	669.3
67	11Q				C, F	0.21	650.1
68	12A	Wenwei *et al.* (2005)	150x200	3 x Ø14mm	-	-	102.0
69	12B				C, F	0.09	140.0
70	13A	Esfahani *et al.* (2006)	150 X 200	3 x Ø12mm	-	-	49.5
71	13B				C, F	0.09	61.5
72	13C				C, F	0.18	70.9
73	13D				C, F	0.26	74.4
74	13E			3 x Ø16mm	-	-	75.9
75	13F				C, F	0.09	84.9
76	13G				C, F	0.09	94.9
77	13H				C, F	0.18	105.9
78	13I			3 x Ø20mm	-	-	96.4
79	13J				C, F	0.09	106.3
80	14A	Oehlers *et al.* (2008)	150x300	3 x Ø14mm	-	-	42.9
81	14B				C, P	0.17	101.5

[‡‡] C – Carbon fibre composites; F – Fabric; P - Plate

Table 7.7 – Calculated indices and modes of failure from additional elements in comparative study

Ref. No.	Elem. Ref.	μ_Δ	φ_E	φ_{df}	φ_{3S}	Failure mode[§§]
51	11A	2.80	2.91	1.45	2.91	SY-CC
52	11B	3.03	3.15	1.45	3.15	SY-CC
53	11C	1.53	1.46	1.69	1.40	DB
54	11D	1.43	1.40	1.54	1.36	DB
55	11E	1.31	1.30	1.57	1.25	DB
56	11F	1.26	1.26	1.52	1.23	DB
57	11G	2.48	2.56	1.44	2.56	SY-CC
58	11H	1.96	2.02	1.44	2.02	SY-CC
59	11I	1.60	1.48	1.72	1.41	DB
60	11J	1.65	1.52	1.74	1.45	DB
61	11K	1.50	1.26	1.70	1.18	DB
62	11L	1.4	1.22	1.65	1.16	DB
63	11M	2.20	2.21	1.44	2.15	SY-CC
64	11N	2.03	2.04	1.45	1.98	SY-CC
65	11O	1.39	1.41	1.46	1.37	DB
66	11P	1.48	1.47	1.62	1.41	DB
67	11Q	1.23	1.10	1.49	1.08	DB
68	12A	1.90	2.28	2.58	2.07	SY-CC
69	12B	2.31	1.52	2.16	1.31	FR
70	13A	2.13	4.34	2.29	4.34	SY-CC
71	13B	1.63	1.35	1.81	1.25	FR
72	13C	1.18	1.13	1.54	1.10	PTO
73	13D	1.34	1.25	1.64	1.20	PTO
74	13E	4.50	4.34	1.45	4.22	SY-CC
75	13F	1.36	1.20	1.66	1.15	FR
76	13G	1.23	1.25	1.57	1.21	FR
77	13H	1.23	1.21	1.66	1.17	FR
78	13I	2.71	2.70	1.48	2.65	SY-CC
79	13J	1.27	1.35	1.60	1.33	FR
80	14A	3.40	3.52	1.74	3.40	SY-CC
81	14B	2.41	2.13	2.88	1.86	DB

[§§] *SY-Steel yield; FR-Fibre rupture; PTO-Partial tearing-off of concrete cover; DB–Fibre debonding; CC–Concrete crushing*

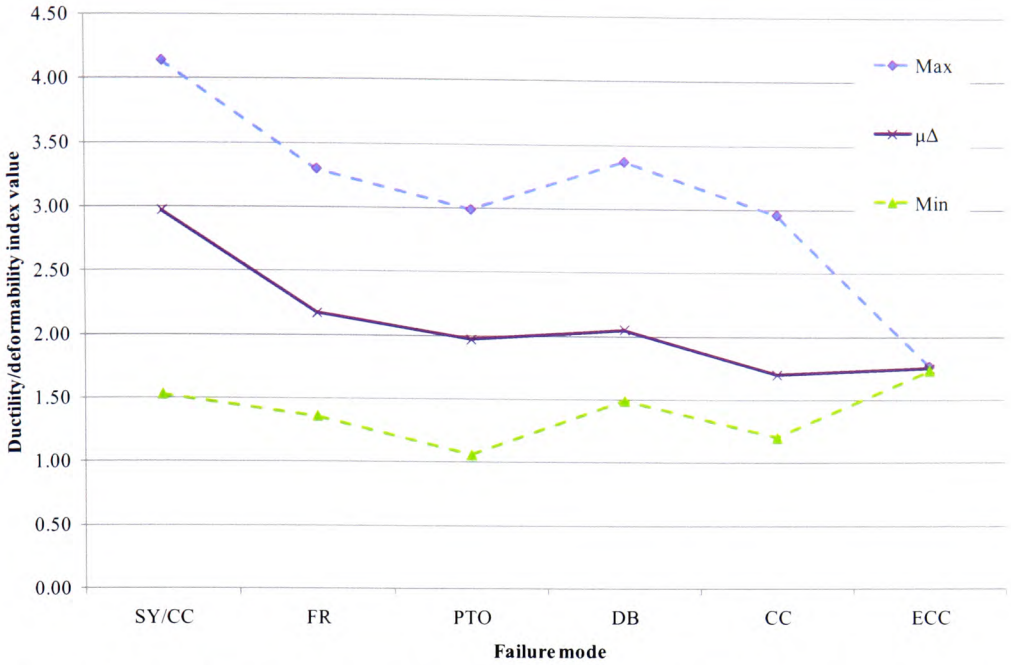

Figure 7.12 – Plot of ductility index against failure mode for μ_{Δ} (Equation 7.1) for elements from parametric study

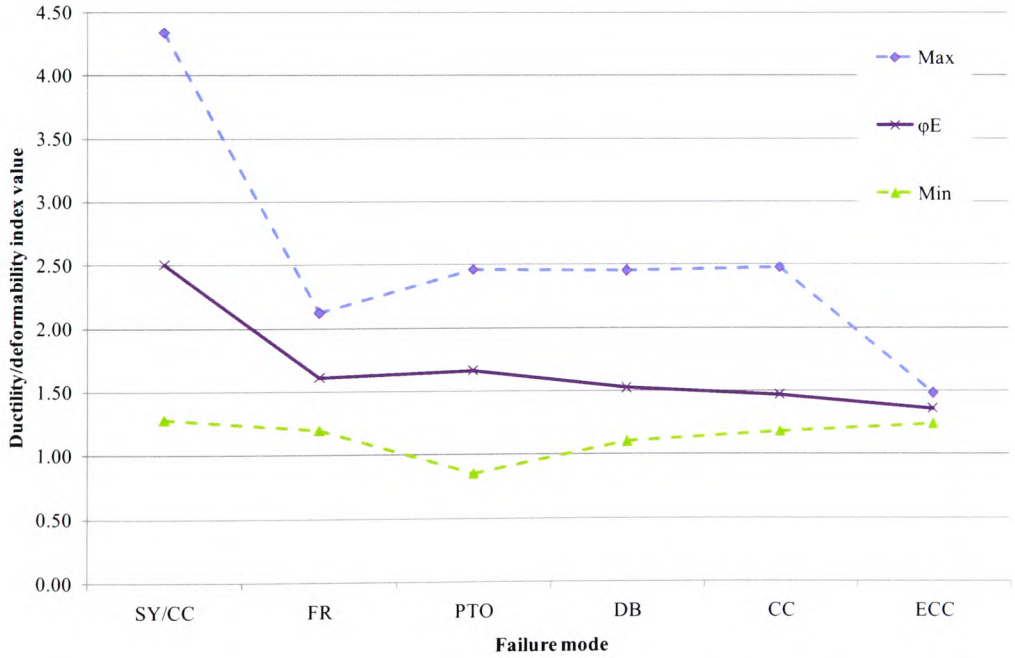

Figure 7.13 – Plot of ductility index against failure mode for φ_E (Equation 7.4) for elements from parametric study

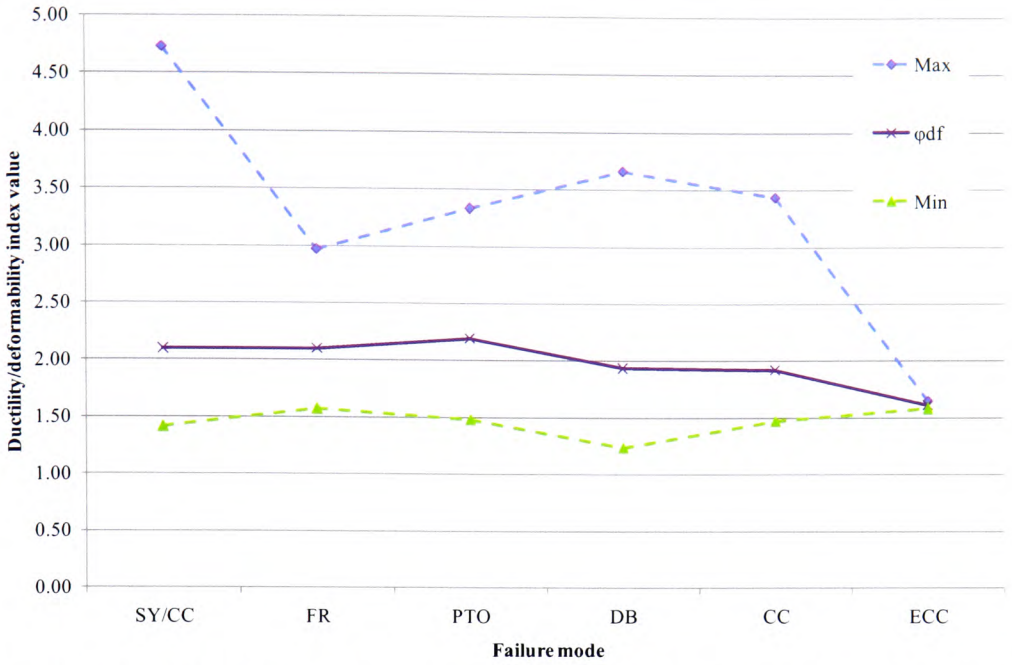

Figure 7.14 – Plot of deformability index against failure mode for φ_{df} (Equation 7.2) for elements from parametric study

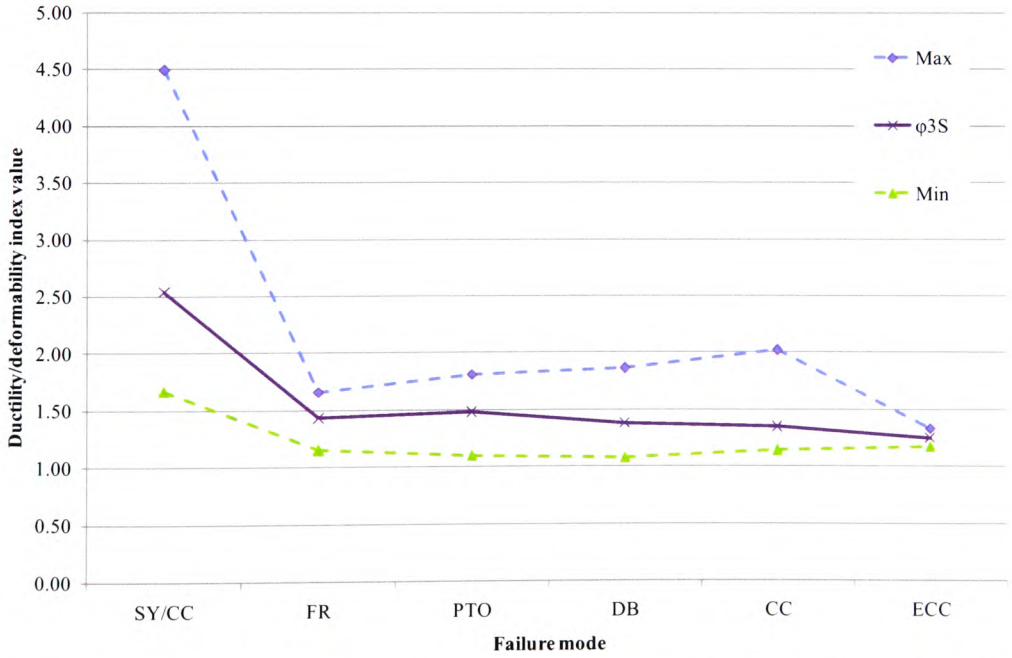

Figure 7.15 – Plot of ductility index against failure mode for φ_{3S} (Equation 7.6) for elements from parametric study

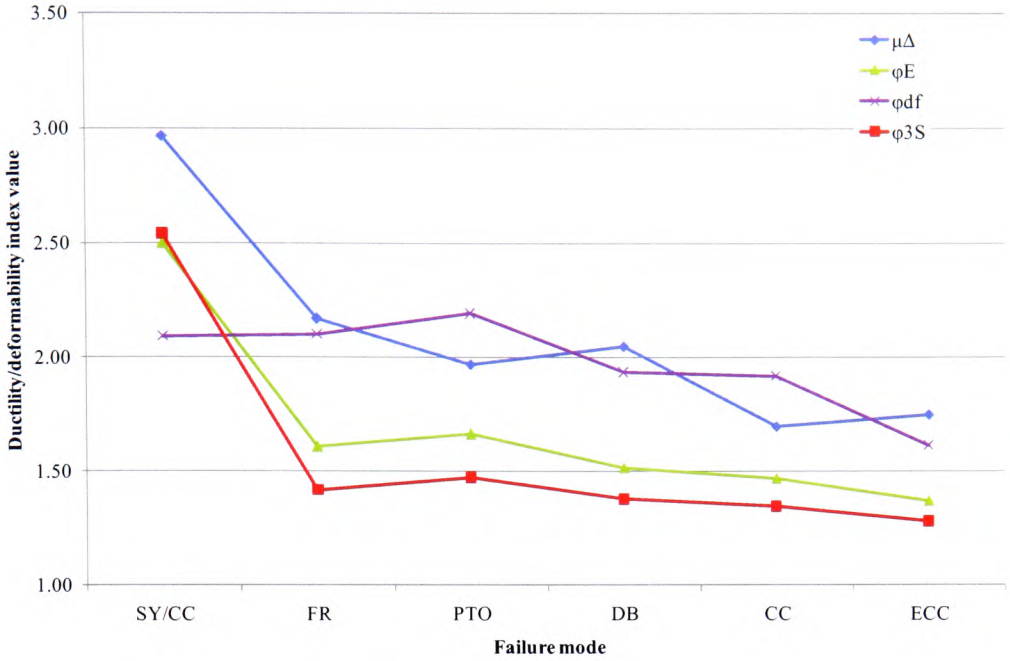

Figure 7.16 – Plot of ductility/deformability index against failure mode for all four methods for elements from parametric study

As can be seen in Figure 7.16, the values of the indices for ductile and non-ductile failure modes derived from the modified 3-slope method, vary by a larger margin than for the other methods. For the modified approach, there is a difference of 46% between the indices for the two types of failure, whereas for the other methods the difference is between 7% and 39%.

7.8 Relationship between deformability and ductility

The relationship between the deformability (φ_{df}) and ductility (φ_{3S}) can be represented by the ratio λ, where:

$$\lambda = \frac{\varphi_{df}}{\varphi_{3S}} \tag{7.7}$$

When calculated, this ratio can be seen to be closely related to the failure mode. For example, as presented in Figure 7.17, for the elements contained within the

experimental programme it can be seen that the ratio approaches unity for elements considered to have a ductile failure mode. It is also evident that as the ratio passes 1 and continues to increase, the failure mode becomes progressively more brittle.

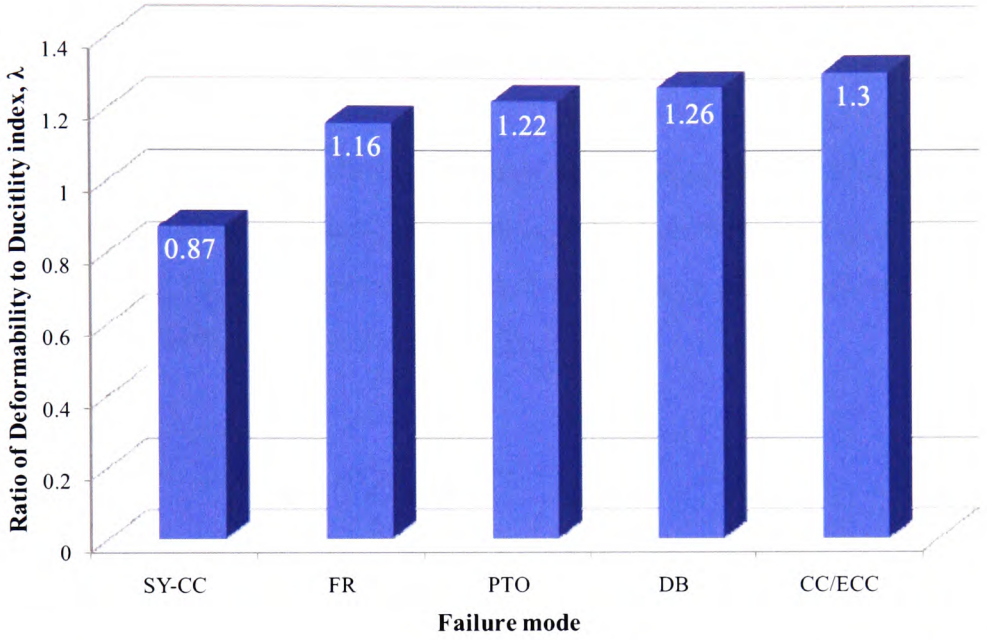

Figure 7.17 – Relationships between failure mode and deformability/ductility ratio[***]

Additionally, as can be seen in Figure 7.18, the ratio between deformability index and ductility index increases with an increase in the total equivalent steel reinforcement ratio (TESR)[†††]. This is expected, as an increase in the value of TESR is linked to a more brittle, and hence undesirable, failure mode, due to the increased stiffness in what are essentially progressively over-strengthened elements.

[***] Note: SY-CC=Steel yield followed by concrete crushing; FR=Fibre rupture; PTO=Premature tearing-off of concrete cover; DB=De-bonding of CFRP; E/CC=Explosive/Concrete crushing

[†††] See Section 7.8.1

7.8.1 Total equivalent steel-reinforcement ratio (TESR)

Due to the variable properties of different types of composite fibres, an attempt has been made to represent the total amount of cross-section tensile reinforcement (both steel and composites) with a single parametric entity called the Total Equivalent Steel-reinforcement Ratio (TESR).

7.8.1.1 Calculation of TESR

The TESR is determined by first calculating the area of composite material as an equivalent amount of steel, using the modular ratio α as shown in Eqn. (7.8), and then expressing the total equivalent amount of steel as a percentage of the total cross-sectional area, as shown in Eqn. (7.9).

$$\alpha = \frac{E_{FRP}}{E_{Steel}} \tag{7.8}$$

$$TESR = \sum \frac{100(A_S + \alpha A_F)}{bd} \tag{7.9}$$

7.8.1.2 Influences of TESR

It can be shown that increases in the RC element stiffness can be associated with high values of TESR. However, it is also true that significant increases in TESR result in a higher probability of the occurrence of an unacceptable failure mode, such as tearing-off of concrete cover or explosive concrete crushing.

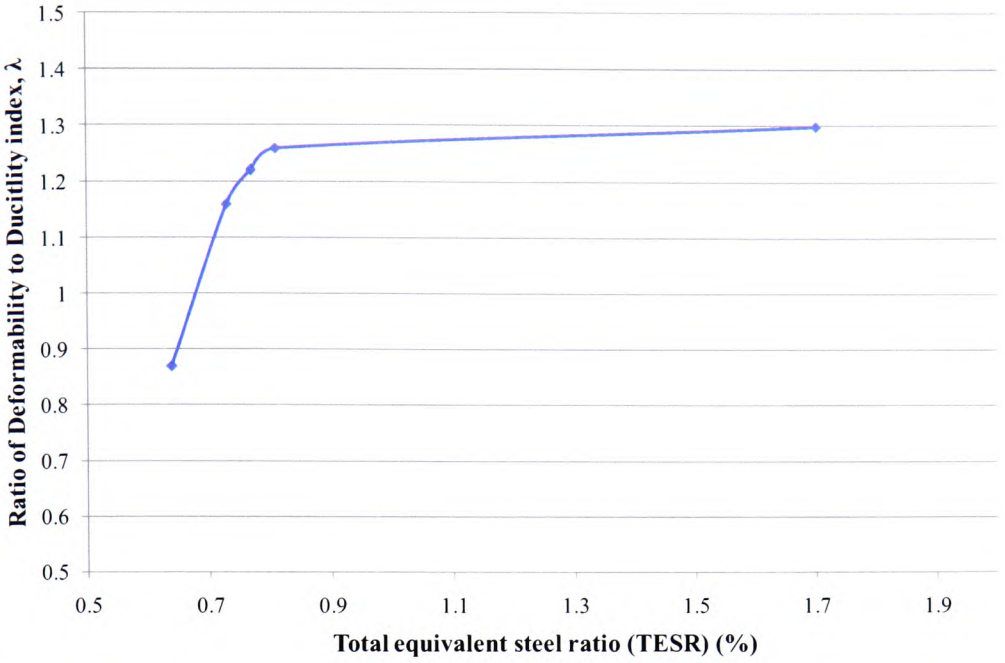

Figure 7.18 – Relationship between ratio of ductility to deformability index, λ, and Total Equivalent Steel reinforcement Ratio (TESR)

7.9 Summary

It can be seen from Section 7.5 that the proposed modified 3-slope approach yields a far more accurate prediction of the stored elastic energy within a CFRP strengthened element at ultimate limit state. The method proposed by Naaman *et al.* was originally developed to analyse elements with internal, pre-stressed FRP tendons and can significantly underestimate the stored elastic energy carried at the point of failure by those elements strengthened with FRP sheets or plates. It is therefore proposed by the candidate that the modified 3-slope method be employed when calculating the stored elastic energy in a structural element, particularly when calculating energy-based ductility indices.

Sections 7.6 and 7.7 dealt with the correlation between calculated ductility/deformability indices and failure modes. It was apparent that all methods displayed a decrease in the value of the index between preferable, ductile failure modes and those failure modes that are undesirable; i.e. non-ductile or "brittle". However, the proposed, modified 3-slope method

demonstrates a larger difference in value between the desirable and non-desirable failure modes for all elements considered, both those in the experimental programme and those in the wider study of published data; a difference of 46%, compared with an average difference of 37% for the other methods.

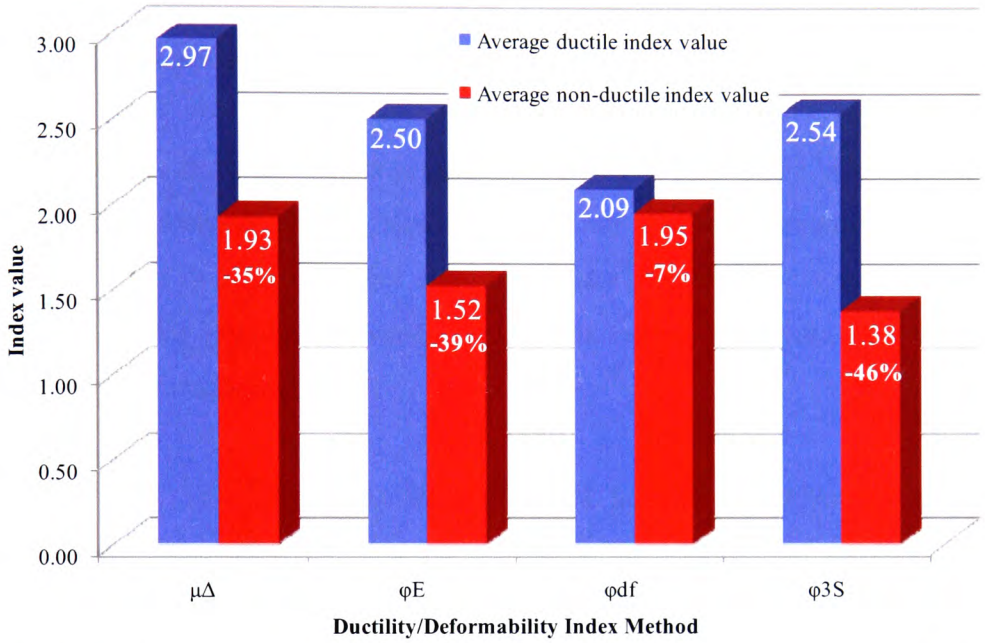

Figure 7.19 – Comparison of ductile and non-ductile index values for all methods

Consequently, it is proposed by the candidate that the modified 3-slope method for energy-based ductility is used to calculate ductility indices for strengthened elements. Moreover, the candidate would suggest that for this method an index value of 1.7 should be used as a minimum value to promote sufficiently ductile behaviour from any designed externally-FRP-strengthened structural element, with a further recommendation that a value of 1.9 is desirable to ensure ductile failure. These values are suggested as they are appreciably (and consequently more conservatively) higher than the lowest value from the additional elements analysed from published data (1.67) and also the value of 1.9 is higher than the minimum index value for suitably ductile failure from the elements contained within the experimental programme (1.89). Additionally, the value of 1.7 is higher than the largest average value for any of the undesirable failure modes for both sets of elements (1.61 and 1.47 respectively).

CHAPTER 8 CRACK PATTERNS AND PREDICTION FOR FIBRE COMPOSITES STRENGTHENED RC ELEMENTS

8.1 Crack patterns

As can be seen from the results presented in Section 4.10, crack propagation in strengthened elements differs significantly from that of normally-reinforced elements. This is to be expected as strengthened elements can be considerably stiffer than their non-strengthened counterparts, which understandably affects their behaviour under loading.

Kong *et al.* (1987) state that the failure of normally-reinforced beams is characterised by extensive concrete cracking, significant deformations and suitably ductile behaviour to warn of impending failure. The extensive cracking mentioned refers to the long and wide cracking expected in normally reinforced elements. However, the crack patterns of elements strengthened with FRP composites and/or with high levels of Total Equivalent Steel-reinforcement Ratio (TESR) differ greatly from this and have been observed on elements tested as part of the experimental programme. Initially, the load at which the first surface crack was able to be observed was seen to increase.

In addition to this, presented in Figures 8.1(a) to 8.4(c) are illustrations of the cracking patterns observed for control elements and strengthened elements from two of the experimental beam sets. It can be seen that beams with high levels of FRP composites strengthening display two further significant changes in observed surface crack patterns at later loading stages approaching element failure:

a) the number of cracks increases
b) the average crack length decreases

Figure 8.1(a) – Schematic of crack pattern for 12CON within constant moment zone at serviceability loading (67% ultimate load)

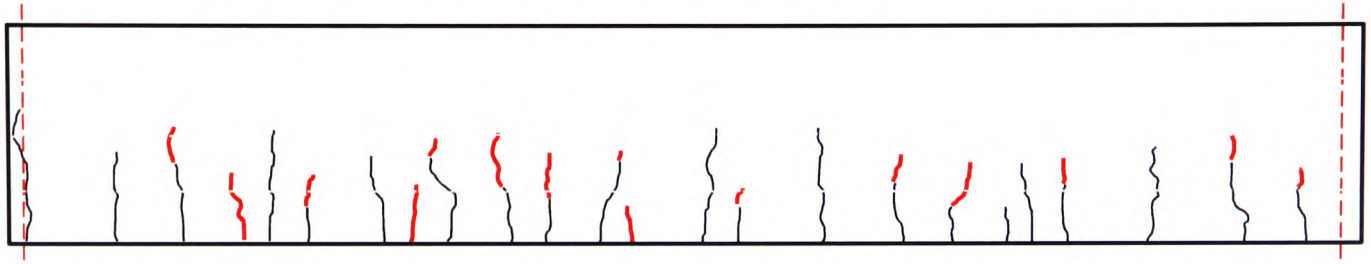

Figure 8.1(b) – Schematic of crack pattern for 12CON within constant moment zone at failure
(Note: Crack propagation/new occurrence shown in red)

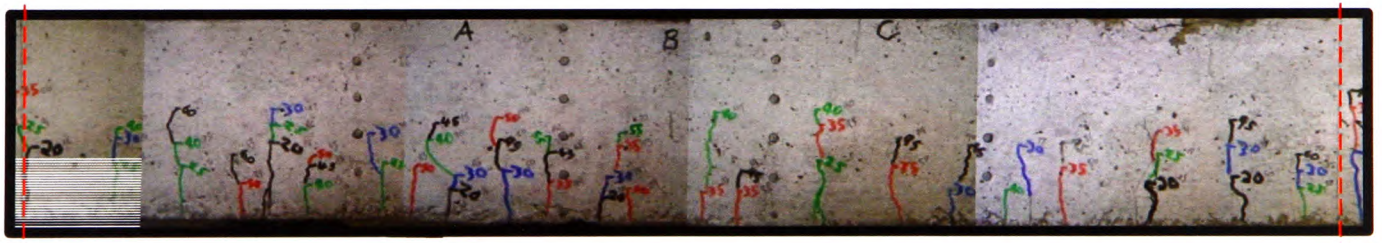

Figure 8.1(c) – Photograph of crack pattern for 12CON within constant moment zone at failure

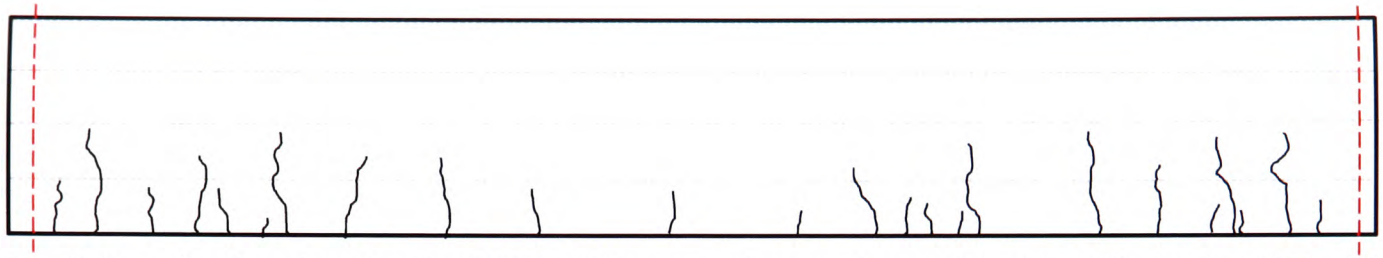

Figure 8.2(a) – Schematic of crack pattern for 12CF3 within constant moment zone at serviceability loading (67% ultimate load)

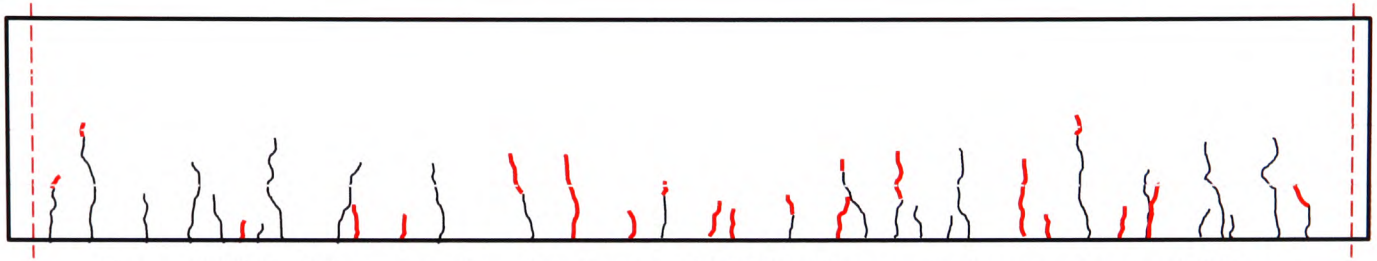

Figure 8.2(b) – Schematic of crack pattern for 12CF3 within constant moment zone at failure
(Note: Crack propagation/new occurrence shown in red)

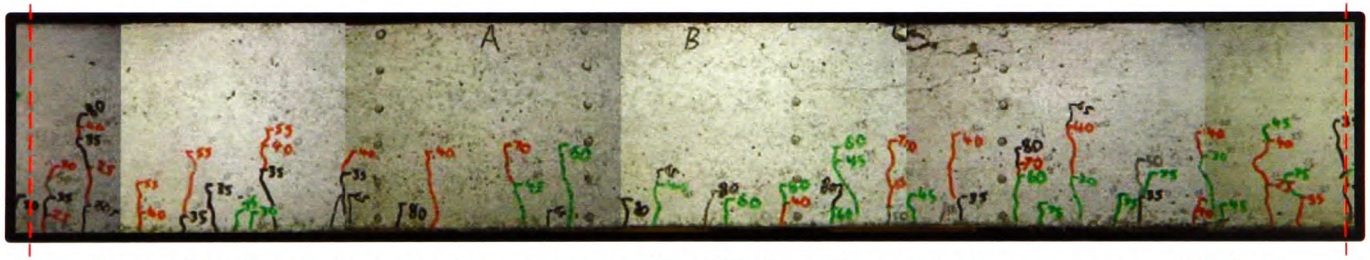

Figure 8.2(c) – Photograph of crack pattern for 12CF3 within constant moment zone at failure

Figure 8.3(a) – Schematic of crack pattern for 8CON within constant moment zone at serviceability loading (67% ultimate load)

Figure 8.3(b) – Schematic of crack pattern for 8CON within constant moment zone at failure
(Note: Crack propagation/new occurrence shown in red)

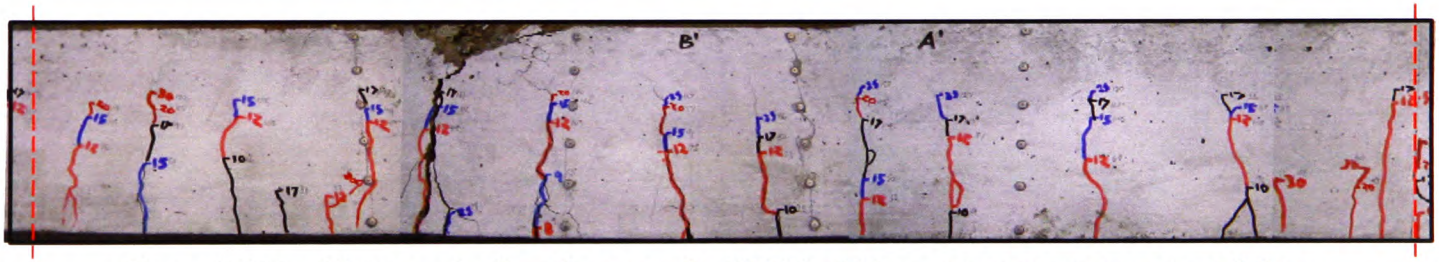

Figure 8.3(c) – Photograph of crack pattern for 8CON within constant moment zone at failure

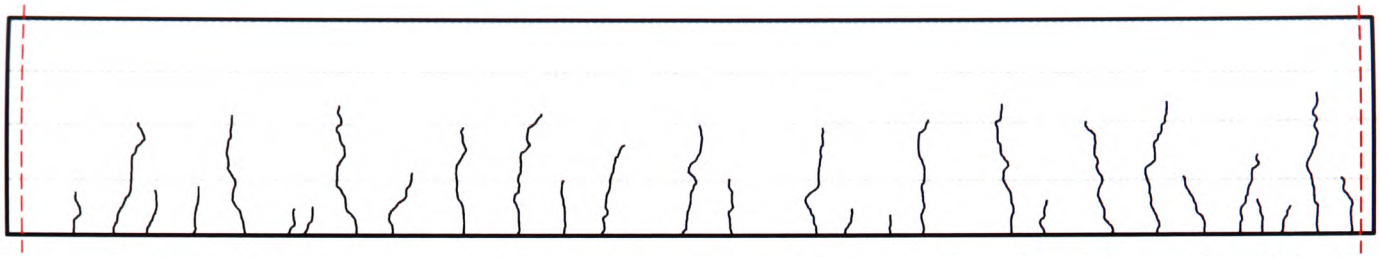

Figure 8.4(a) – Schematic of crack pattern for 8CF3 within constant moment zone at serviceability loading (67% ultimate load)

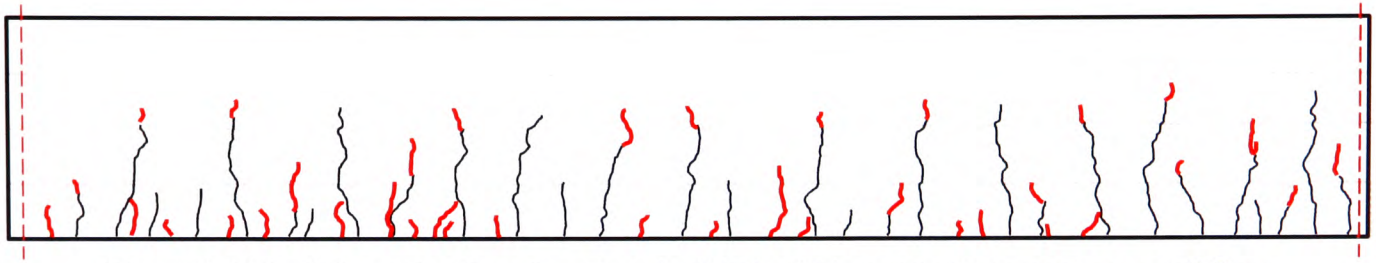

Figure 8.4(b) – Schematic of crack pattern for 8CF3 within constant moment zone at failure
(Note: Crack propagation/new occurrence shown in red)

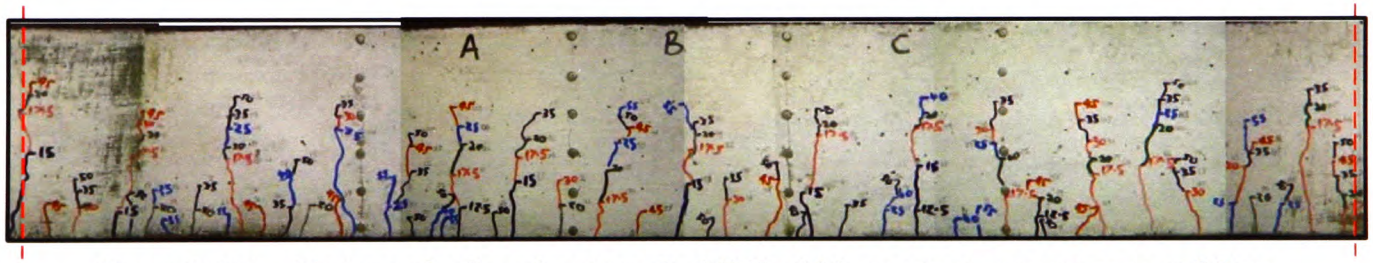

Figure 8.4(c) – Photograph of crack pattern for 8CF3 within constant moment zone at failure

The reason for this is that the presence of the fibre composites helps to better distribute the tensile forces at the soffit of the element, which results in a reduction of the width and length of cracks that would normally be expected in an un-strengthened element.

Additionally, in beams with high levels of bonded FRP composites, the amount and severity of shear cracking was increased, which in some cases resulted in the failure of the element due to tearing-off of the concrete cover, initiated at the extreme edge of the composite sheet with a shear crack. An example of this can be seen in Figure 8.5, where the failure of 10CF3, the element with two 10mm steel reinforcing bars and three layers of CFRP sheet, was initiated at the extreme end of the sheet with a shear crack, which then propagated along the level of the internal steel reinforcement. It should also be noted that in all tests of strengthened elements resulting in this type of failure, no shear cracking was observed beyond the end of the sheet.

8.2 Theoretical crack prediction

The theoretical average surface crack width for a conventionally reinforced concrete beam can be calculated from the following equation, taken from BS 8110, Part 2 (1985):

$$\text{Design surface crack width, } W_{av} = \frac{3a_{cr}\varepsilon_m}{1+2\left(\frac{a_{cr}-c_{min}}{h-x}\right)} \qquad 8.1$$

where: a_{cr} is the distance from the point considered to the surface of the nearest longitudinal bar;

ε_m is the average strain at the level where the cracking is being considered;

c_{min} is the minimum cover to the tension steel;

h is the overall depth of the member;

x is the depth of the neutral axis.

Using the above equation, it has been possible to calculate the theoretical crack width for control members at serviceability loading, which, for the purposes of this exercise, has been estimated at 67% of ultimate load ($0.67P_u$), as shown in Table 8.1.

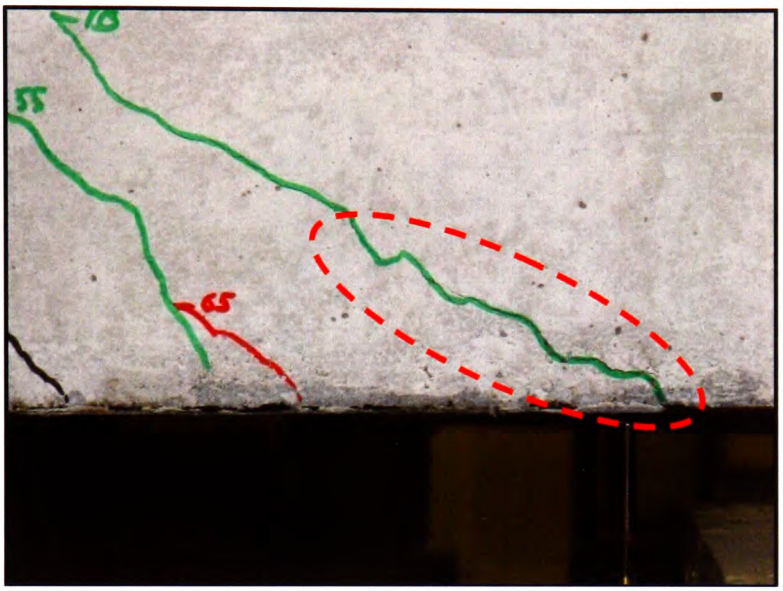

Figure 8.5(a) – Initiation of tearing-off of concrete cover at FRP composites sheet edge with shear crack, just prior to element failure

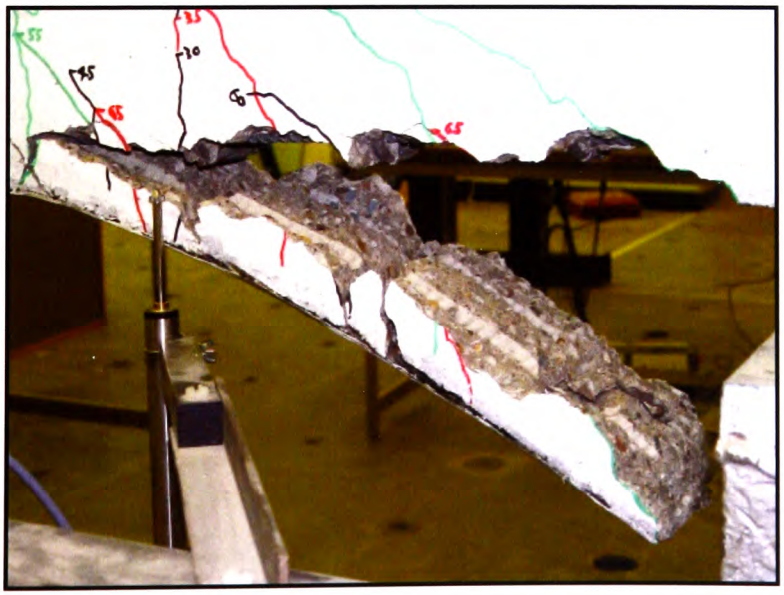

Figure 8.5(b) – Element failure due to partial tearing-off of concrete cover caused by shear cracking at end of FRP composites sheet

8.2.1 Example calculation for Ø 8mm reinforced control slab element:

Assuming it was required to determine the average crack width at the soffit of the slab,

Distance from crack location to edge of nearest reinforcement, a_{cr}=22.8 mm

ε_m can be obtained by using equation 8.2*:

$$\varepsilon_m = \varepsilon_1 - \frac{b(h-x)(a'-x)}{3E_s A_s (d-x)} \qquad 8.2$$

$$\varepsilon_1 = \frac{y}{(d-x)} \frac{f_s}{E_s} \qquad 8.3$$

Firstly, it is necessary to determine the depth of the neutral axis, 'x':

$$\frac{1}{2}bx^2 + \frac{E_s}{E_c}A_s x - \frac{E_s}{E_c}A_s d = 0 \qquad 8.4$$

$$d = 100 - 15 - \frac{8}{2} = 81mm$$

A_s =201 mm^2

From material tests:

f_{cu} = 38.1 N/mm^2; f_y=573 N/mm^2; E_s=205,000 N/mm^2; E_c=40.66 N/mm^2.

* Mosely *et al*, 1999; BS8110-2:1985

Table 8.1 – Ultimate and Serviceability loads (P_u & P_s) for tested elements

Element Ref.	Ultimate load P_u (kN)	Serviceability load P_s (=0.67P_u) (kN)	Serviceability Moment M_s (kNm)
8CON	35.1	23.5	6.8
8CF1	58.0	38.9	11.2
8CF2	62.5	41.9	12
8CF3	55.0	36.9	10.6
10CON	56.5	37.9	10.9
10CF1	62.6	41.9	12
10CF2	80.1	53.7	15.4
10CF3	70.0	46.9	13.5
12CON	65.0	43.6	12.5
12CF1	78.2	52.4	15.1
12CF2	85.0	57.0	16.4
12CF3	84.1	56.4	16.2
16CON	98.0	65.7	18.9
16CF1	96.0	64.3	18.5
16CF2	90.0	60.3	17.3
16CF3	101.2	67.8	19.5
8SCON	16.0	10.7	5.1
8SCF2	26.8	18.0	8.6
8SCP2	43.6	29.2	13.9
8SCP3	36.9	24.7	11.7
12SCON	32.0	21.4	10.2
12SCF2	68.0	45.6	21.7
12SCF4	77.0	51.6	24.5
12SCP2	75.0	50.3	23.9
12SCP3	92.5	62.0	29.5

$$\Rightarrow \frac{1}{2}(500)x^2 + \left(\frac{205}{40.66}\right)(201)x - \left(\frac{205}{40.66}\right)(201)(81) = 0$$

$$\Rightarrow 250x^2 + 1013.4x - 82085.7 = 0$$

$$\Rightarrow x = \frac{-(1013.4) \pm \sqrt{(1013.4^2) - 4(250)(-82085.7)}}{2(250)} = 16.2mm$$

Serviceability load = 10.7kN, from Table 8.1.

$$\Rightarrow M_s = 0.95\left(\frac{10.7}{2}\right) = 5.1kNm$$

$$f_s = \frac{M_s}{\left(d - \frac{x}{3}\right)A_s} = \frac{5.1x10^6}{\left(81 - \frac{16.2}{3}\right)201} = 335.62N/mm^2$$

$$\varepsilon_1 = \frac{y}{(d-x)}\frac{f_s}{E_s} = \frac{83.8}{(81-16.2)}\frac{335.62}{205x10^3} = 2.1x10^{-3}$$

$$\varepsilon_m = \varepsilon_1 - \frac{b(h-x)(a'-x)}{3E_sA_s(d-x)} = 2.1x10^{-3} - \frac{(500)(100-16.2)(100-16.2)}{3(205000)(201)(81-16.2)}$$

$$= 2.1x10^{-3} - \frac{3511220}{8010252000} = 1.66x10^{-3}$$

$$W_{av} = \frac{3a_{cr}\varepsilon_m}{1+2\left(\frac{a_{cr}-c_{min}}{h-x}\right)} = \frac{3(22.8)(1.66x10^{-3})}{1+2\left(\frac{22.8-15}{100-16.2}\right)} = \frac{0.113544}{1.186} = 0.096mm$$

From Figure 4.59(d), it can be seen that the experimental average crack width for the control slab is 0.12mm, which gives acceptable correlation with the theoretical value.

8.2.2 Example calculation for Ø 10mm reinforced control beam element:

Again, assuming it is required to determine the average crack width at the soffit of the element,

Distance from crack location to edge of nearest reinforcement, a_{cr}=23.3 mm

ε_m can be obtained by using equation 8.2[†]:

Determine the depth of the neutral axis, 'x':

$$\frac{1}{2}bx^2 + \frac{E_s}{E_c}A_s x - \frac{E_s}{E_c}A_s d = 0 \qquad (8.5)$$

$$d = 200 - 15 - 6 - \frac{10}{2} = 174mm$$

A_s =157 mm^2

From material tests:

f_{cu} = 51.5 N/mm^2; f_y=573 N/mm^2; E_s=205,000 N/mm^2; E_c=42.0 N/mm^2.

[†] Mosely et al, 1999; BS8110-2:1985

$$\Rightarrow \frac{1}{2}(100)x^2 + \left(\frac{205}{42.0}\right)(157)x - \left(\frac{205}{42.0}\right)(157)(174) = 0$$

$$\Rightarrow 50x^2 + 766.3x - 133337.9 = 0$$

$$\Rightarrow x = \frac{-(766.3) \pm \sqrt{(766.3^2) - 4(50)(-133337.9)}}{2(50)} = 44.5mm$$

Serviceability load = 37.9kN, from Table 4.2.

$$\Rightarrow M_s = 0.575\left(\frac{37.9}{2}\right) = 10.9kNm$$

$$f_s = \frac{M_s}{\left(d - \frac{x}{3}\right)A_s} = \frac{10.9x10^6}{\left(174 - \frac{44.5}{3}\right)157} = 457.5N/mm^2$$

$$\varepsilon_1 = \frac{y}{(d-x)}\frac{f_s}{E_s} = \frac{155.5}{(174-44.5)}\frac{457.5}{205x10^3} = 2.68x10^{-3}$$

$$\varepsilon_m = \varepsilon_1 - \frac{b(h-x)(a'-x)}{3E_sA_s(d-x)} = 2.68x10^{-3} - \frac{100(200-44.5)(200-44.5)}{3(205000)(157)(174-44.5)}$$

$$= 2.68x10^{-3} - \frac{2418025}{12.504x10^9} = 2.48x10^{-3}$$

$$W_{av} = \frac{3a_{cr}\varepsilon_m}{1+2\left(\frac{a_{cr}-c_{min}}{h-x}\right)} = \frac{3(23.3)(2.48x10^{-3})}{1+2\left(\frac{23.3-15}{200-44.5}\right)} = \frac{0.173352}{1.107} = 0.157mm$$

From Figure 4.54(d), we can see that the experimental average crack width for the control beam is 0.12mm, which again gives acceptable correlation with the theoretical value.

Further calculations were carried out on the remaining control elements and all the results are presented in Table 8.2, together with the concrete strain value at serviceability loading, ε_m, required to perform the calculations. It can be seen that there is very good correlation between the calculated values and those derived from the experimental results – this is demonstrated further in Figure 8.6.

However, this method of crack prediction has been developed for normally reinforced RC elements and, as such, may not be appropriate for elements strengthened with carbon fibre composites. This is further discussed in Section 8.3.

Table 8.2 – Theoretical and experimental average crack widths at serviceability loading for tested control elements

Element Ref.	Concrete strain value at serviceability loading, ε_m (mm/mm)	Calculated average crack width at serviceability loading (mm)	Actual experimental average crack width at serviceability loading (mm)
8CON	2.13×10^{-3}	0.134	0.135
10CON	2.48×10^{-3}	0.157	0.120
12CON	2.10×10^{-3}	0.129	0.105
16CON	1.42×10^{-3}	0.088	‡
8SCON	1.66×10^{-3}	0.096	0.130
12SCON	2.48×10^{-3}	0.137	0.135

8.3 Crack prediction for strengthened elements

As mentioned previously, the method detailed in 8.2.1 and 8.2.2 does not take into account the change in element behaviour due to the presence of any

‡ No experimental data available

strengthening material, such as bonded carbon fibres composites sheets and plates. It is, therefore, necessary to develop a revised method of crack width prediction for elements strengthened with carbon fibre composites.

It has been observed that the crack patterns in FRP-strengthened elements differ from those of non-strengthened elements in that the cracks are shorter, more numerous and more closely spaced. It is the consideration of the candidate that this is due to the presence of the composites (either sheets or plates), which help to distribute the stresses present during loading across the element soffit.

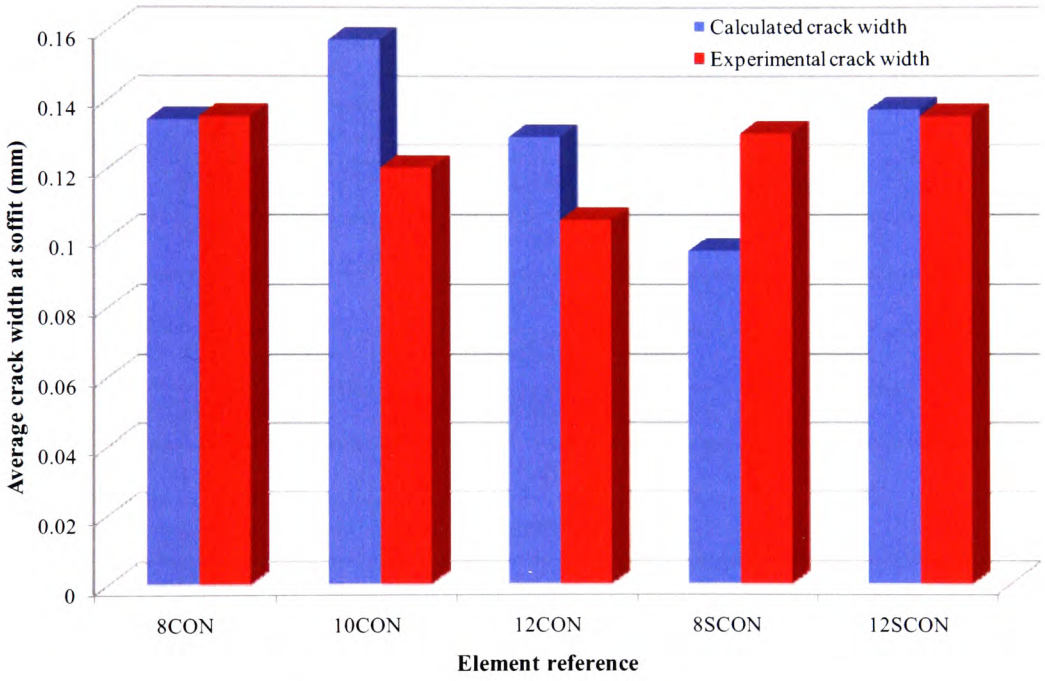

Figure 8.6 – Comparison of calculated and experimental crack widths for normally-reinforced, "control" elements

If the equations discussed in 8.2.1 and 8.2.2 are applied to the strengthened elements in the experimental programme, the calculated results are as presented in Table 8.3, together with the actual average crack widths derived from the experimental data.

Table 8.3 – Theoretical and experimental average crack widths at serviceability loading for strengthened tested elements

Element Ref.	Concrete strain value at serviceability loading, ε_m (mm/mm)	Calculated average crack width at serviceability loading W_{av} (mm)	Actual experimental average crack width at serviceability loading (mm)
8CF1	3.09×10^{-3}	0.199	0.12
8CF2	2.84×10^{-3}	0.178	0.10
8CF3	2.16×10^{-3}	0.136	0.08
10CF1	2.44×10^{-3}	0.153	0.09
10CF2	2.77×10^{-3}	0.173	0.11
10CF3	2.01×10^{-3}	0.125	0.09
12CF1	2.16×10^{-3}	0.133	0.10
12CF2	2.18×10^{-3}	0.134	0.09
12CF3	2.05×10^{-3}	0.125	0.10
16CF1	1.51×10^{-3}	0.093	0.21
16CF2	1.32×10^{-3}	0.081	0.12
16CF3	1.56×10^{-3}	0.096	0.07
8SCP2	1.61×10^{-3}	0.110	0.10
8SCP3	1.12×10^{-3}	0.090	0.08
12SCF2	2.87×10^{-3}	0.156	0.09
12SCF4	2.31×10^{-3}	0.123	0.09
12SCP2	2.33×10^{-3}	0.127	0.09
12SCP3	2.31×10^{-3}	0.123	0.05

It can be seen from Figure 8.7 that in almost every case the standard method of crack width calculation over-estimates the value of crack width. The only exception is for two of the beams reinforced with two Ø16mm steel bars and strengthened with carbon fibre composites sheets. As has been discussed previously, the amount of tensile over-strengthening in this series of elements makes their behaviour highly unpredictable and would, hence, account for their

apparent move away from the trend shown by the other elements. Consequently, these elements have been discounted in the calculation of the following revised method for average crack width for strengthened elements.

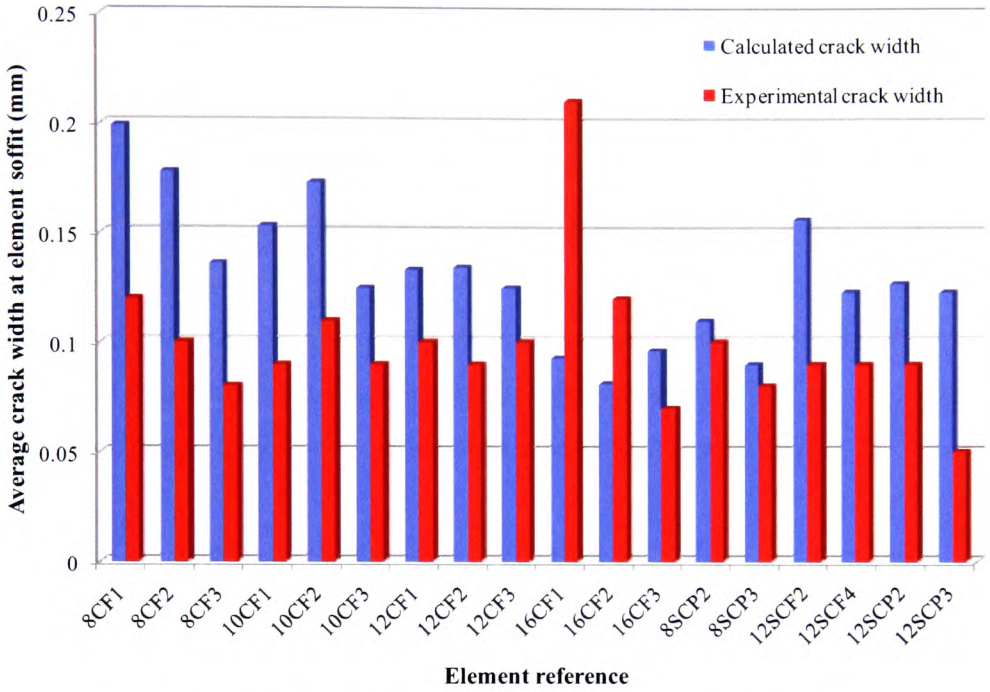

Figure 8.7 – Comparison of calculated and experimental crack widths for strengthened elements

Therefore, an analysis of the average crack widths at serviceability loading was carried out for all beam elements in the experimental programme. It was found that better correlation could be obtained if account was taken of the amount of bonded fibre composites when considered as a percentage of the total cross-sectional area. Equation 8.6 represents the revised method for average crack width calculation.

Revised design surface crack width,

$$W_{FRP} = \frac{3a_{cr}\varepsilon_m}{1 + 2\left(\frac{a_{cr} - c_{min}}{h - x}\right)} - \{0.01\psi + 0.07\} \qquad 8.6$$

where ψ is the cross-sectional area of bonded fibre composites as a percentage of the total element cross-sectional area.

This revised method yields a much closer relationship between the predicted crack width and the actual experimental values.

Following is an example crack width calculation for element 8CF3, using the revised method:

$$W_{FRP} = \frac{3a_{cr}\varepsilon_m}{1 + 2\left(\frac{a_{cr} - c_{min}}{h - x}\right)} - \{0.01\psi + 0.07\}$$

$$\Rightarrow W_{FRP} = 0.136 - \{0.01(0.247) + 0.07\}$$

Where;

0.136 has been previously calculated for the element (See Table 8.3);

ψ is calculated as the cross-sectional area of bonded fibre composites as a percentage of the total element cross-sectional area (0.247).

$$\Rightarrow W_{FRP} = 0.136 - \{0.01(0.247) + 0.07\}$$

$$\Rightarrow W_{FRP} = 0.066mm$$

As can be seen from Figure 8.8 and Table 8.4, the correlation between the predicted and actual average crack width is noticeably improved. However, it is the consideration of the candidate that further investigation is required in order to confirm the reliability of the revised method and possibly increase the accuracy.

Table 8.4 – Theoretical and experimental average crack widths at serviceability loading for strengthened tested beam elements using modified approach

Element Ref.	Calculated average crack width at serviceability loading W_{FRP}(mm)	Actual experimental average crack width at serviceability loading (mm)
8CF1	0.14	0.13
8CF2	0.12	0.11
8CF3	0.09	0.07
10CF1	0.16	0.08
10CF2	0.09	0.10
10CF3	0.12	0.06
12CF1	0.08	0.07
12CF2	0.13	0.06
12CF3	0.07	0.06
16CF1	0.08	0.01
16CF2	0.08	0.01
16CF3	0.14	0.05

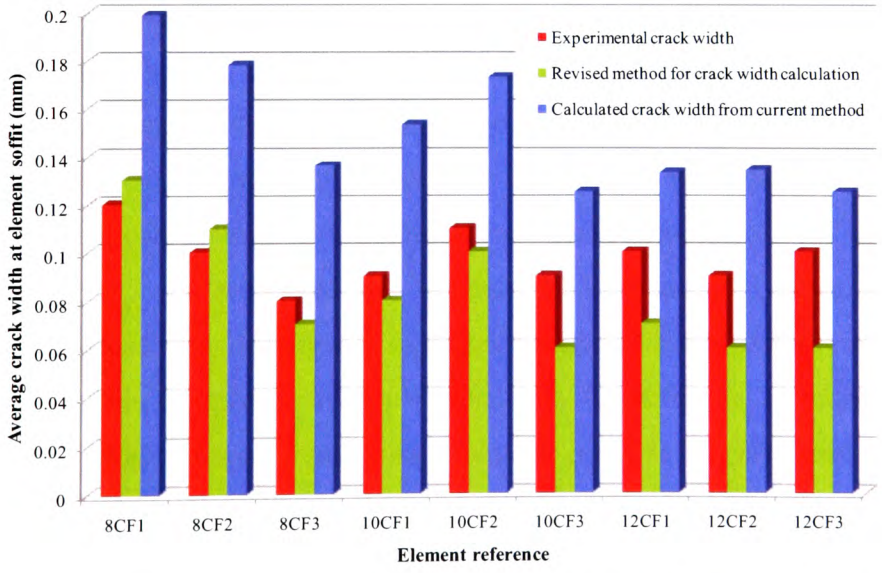

Figure 8.8 – Comparison of calculated and experimental crack widths for strengthened elements together with values from revised method

CHAPTER 9 DISCUSSIONS, CONCLUSIONS AND RECOMMENDATIONS

9.1 General discussions

A wide-ranging review of current literature on the subject of ductility and deformability found a distinct lack of specific guidelines and assistance with regards to FRP-strengthened, reinforced concrete structures, with the bulk of the published literature concentrating on concrete elements that have been reinforced with FRP bars or rods.

Consequently, a comprehensive series of experimental and numerical analytical investigations were performed, in order that the inherent ductility in FRP strengthened reinforced concrete elements could be better quantified and, hence, taken into consideration in the design process by means of a ductility or deformability index.

It was shown from the tests carried out in the experimental programme that elements strengthened with externally-bonded FRP composites display a significantly increased element stiffness together with a corresponding increase in the load-carrying capacity of the element in question, when compared to the unstrengthened counterpart. This confirms the views of other published sources[†]. Additionally, it was seen that the increase in load-carrying capacity from applying externally-bonded fibre composites is appreciably higher for elements with lower levels of internal steel reinforcement. For example, elements 8CF2 and 8SCP2, with internal steel reinforcement ratios of 0.50% and 0.40%, displayed increases in load-carrying capacity of 78% and 172% respectively. Conversely, element 16CF3, with an internal steel reinforcement ratio of 2.01%,

[†] Meier *et al.* 1992; Chajes *et al.* 1994 & 1995; Hutchinson *et al.* 1996; Shahawy *et al.* 1996; Takeda *et al.* 1996; Tumialan *et al.* 1999; Ramana *et al.* 2000; Tann *et al.* 2000; Leung 2002; Maalej *et al.* 2005; Tann 2005; Oehlers *et al.* 2006; Esfahani *et al.* 2007; Oehlers *et al.* 2008

demonstrated a strength increase of only 3%; this is in agreement with published sources[‡].

Additionally, it was seen that there is an optimum level of reinforcement, above which the benefits of strengthening are lost. This was evident with all element sets, with the exception of those with ρ=2.01% (16mm reinforced beams); this disparity with other element sets is due to the unpredictability of the behavioural characteristics of such elements with high levels of internal steel reinforcement. It was evident that for all other element sets, the increase in load-carrying capacity, over that demonstrated by the control element for the set in question, reached a peak and then dropped off at the highest levels of strengthening. As an example, the elements with an internal steel reinforcement ratio of ρ=0.79% (10mm reinforced beams) displayed increases of 11% and 42% for one layer and two layers of bonded CFRP composites respectively. However, the element with three layers of bonded CFRP displayed an increase of only 24%. This corresponds with published sources[§] and is worthy of further investigation to determine whether or not there is a generic limit to the beneficial level of strengthening for any reinforced concrete element, although this was outside the remit of the current research programme.

The load strain relationships of strengthened elements in Chapter 4 demonstrated that the surface strain for elements where debonding was the failure mode, the recorded FRP composites surface strain was consistently below 7000με. This point is important as the value is significantly lower than the current strain limit recommended in published guidance of 8000με[**]. This point obviously requires further investigation and this is a recommendation of the candidate in section 9.3.

In Chapter 5, a method of deflection prediction for fibre composites strengthened elements was considered. This can be of considerable importance when attempting to determine the ductility or deformability of such elements, as many

[‡] Hutchinson *et al.* 1996; Arduini *et al.* 1997
[§] Arduini *et al.* 1997; Andreou *et al.* 2000; Tann 2001
[**] TR55

of the main deformation-based indices rely on the load deflection behaviour of the element in question[††]. As discussed, the method developed is semi-empirical and based on an original method developed by Tann (2003). Originally, the method was developed for slab elements and, despite beam and slab elements being theoretically identical, it has been discussed previously[‡‡] that the two types of element behave in significantly different ways. Consequently, the original approach did not display a suitable level of accuracy when determining the deflection of beam elements and, subsequently, a method was developed to predict the element deflection for such elements. It was shown, by comparison to published data[§§], that the proposed method was a reliable technique that will be useful to engineers wishing to predict the load deflection relationship of fibre-composites strengthened elements.

The numerical modelling carried out, and covered in Chapter 6, was primarily successful, except for where the failure mode was premature due to tearing-off of the concrete cover, a situation it was not programmed to detect. In such cases, the model assumed that the element retained its structural integrity and, therefore, the predicted failure moment was higher than that observed in the experimental programme and the predicted failure mode was different. For example, with element 12DCF2, where the actual experimental failure mode was partial tearing-off of the concrete cover at a moment of 27.3kNm, the model recorded a higher failure moment of 28.1kNm, by which time the element was predicted to have failed by crushing of the concrete in the compressive zone. Nevertheless, for the majority of cases, the numerical model not only predicted the failure mode and moment but also accurately predicted the moment curvature, load deflection, neutral axis depth and load strain behaviour for the entire loading cycle.

The ductility and deformability of elements strengthened by externally-bonded fibre composites was covered in Chapter 7. It was discussed that the

[††] Spadea *et al.* 1998; Tann 2001; Bencardino *et al.* 2002
[‡‡] See Section 4.1
[§§] Tann 2001; Maalej *et al.* 2005; Wenwei *et al.* 2005; Esfahani *et al.* 2007

investigation of ductility issues with regard to FRP composites strengthened elements was limited, despite the consideration of structural ductility being of predominant importance to structural design. The main current methods for ductility determination were discussed and it was shown that they centre around two main categories; namely deformation-based and energy-based methods. By using a comparative study of published data to evaluate the different approaches, it was shown that the energy-based methods demonstrated a more consistent set of results. This is in keeping with previous published sources, who generally agreed that energy-based methods generate more consistent results[***].

Additionally, the energy-based methods are not reliant on the determination of the point at which the internal steel reinforcement yields; this is an area of significant concern for the deformation-based methods. Of the energy-based methods, it was shown that the one developed by Naaman *et al.* (1995) produced the most consistent results. However, this method was developed for elements internally reinforced with FRP reinforcement, rather than elements strengthened with externally-bonded composites, and relied on the estimation of the stored elastic energy in the element at failure. Consequently, a new method was developed, based on Naaman *et al.*'s approach, which enabled accurate estimation of the stored elastic energy in strengthened elements and, subsequently, a reliable ductility index based on this estimation. The method is represented by two equations, replicated here for ease of reference as equations 9.1 and 9.2:

$$S = \frac{P_1 S_1 + (P_2 - P_1)S_2 + (P_U - P_2)S_3}{P_U} \qquad 9.1$$

Where: S is the slope of the unloading line

S_1, S_2 and S_3 are the slopes of the three loading slopes

P_1, P_2 and P_3 are the corresponding loads

[***] Spadea *et al.* 1998; Naaman *et al.* 1995; Swamy *et al.* 1997; Oehlers 2006; Matthys *et al.* 2006

$$\varphi_{3S} = \frac{1}{2}\left(\frac{E_{tot}}{E'_{el}} + 1\right) \qquad 9.2$$

Where: E_{tot} is the total energy under the load deflection curve

E'_{el} is the estimated stored elastic energy

Further to the development of this new approach, a comprehensive investigation was carried out, whereby it was determined that in order for a designer to promote sufficient levels of ductility in an element strengthened with externally-bonded fibre composites, a value of 1.7 for the ductility index should be attained, with a further recommendation that to ensure ductile behaviour, a value of 1.9 is desirable. These values concur with published sources on a suitable value for the value of the ductility index in order to ensure acceptably mild failure[†††]. Additionally, these values, when applied to the developed method for ductility index calculation, will give designers a reliable means of promoting ductile behaviour in fibre composites strengthened elements.

In Chapter 8, crack propagation of crack widths for elements with externally-bonded fibre composites was investigated. It had already been shown in Chapter 4 that the occurrence of surface cracking in strengthened elements varied considerably from that of their unstrengthened counterparts. The main differences for strengthened elements can be summarised as follows and are attributable to the ability of the FRP composites to better distribute the stress in the element soffit, resulting in a more consistent crack distribution:

- There is a higher number of surface cracks
- Both the maximum and average crack lengths are shorter
- The average crack width is smaller

Subsequently, it was noted that the normal method for the determination of crack widths[‡‡‡] was inaccurate when applied to elements with externally-bonded fibre

[†††] Tann 2005; Matthys *et al.* 2006
[‡‡‡] BS 8110, Part 2 (1985)

composites and resulted in a consistent over-estimation of the crack width for such elements. This is not unexpected as the method takes no account of the presence of the FRP composites and, subsequently, the estimated crack widths are calculated as if the element is normally reinforced with no strengthening.

Consequently, a method was developed which took into account the amount of FRP composites present in any strengthened element. The method was calibrated against elements from the experimental programme and it was shown that the accuracy of the proposed approach produced a considerably improved accuracy for the crack widths of tested strengthened elements.

The candidate has addressed all the objectives of his research and feels that there is a contribution to knowledge in advancing the understanding of how fibre reinforced polymers can be used in the strengthening of reinforced concrete structures whilst maintaining a level of structural ductility that is necessary to ensure predictable and gradual modes of failure.

9.2 Summary of conclusions

The limitations of current methods of determining the ductility index of fibre reinforced composites strengthened RC elements were discussed in Chapter 2. It was noted that the most common methods for calculating ductility indices relied on the determination of the point at which the internal steel reinforcement yields, which is difficult due to the primarily elastic behaviour exhibited by fibre-composites-strengthened RC elements. The most reliable form of index determination was an approach developed by Naaman *et al.* (1995) but even this method has limitations as it depends on the establishment of the stored elastic energy in a strengthened element at ultimate limit state and was originally developed for members that have been internally reinforced with pre-stressed FRP tendons.

Consequently, it was felt that there was a need for a more reliable method of determining the ductility index of elements externally strengthened with fibre composites and, furthermore, that any developed method should be energy-based in its approach.

The main conclusions drawn from the research are presented below:

9.2.1 Failure modes

It was noted in Chapter 4 that there are a number of ways in which a reinforced concrete element that has been strengthened with fibre composites, can fail. The categories of failure mode are presented below, together with a description of the associated manner in which the element failure occurs, a diagram of the failure mode and a photograph of an example from the experimental programme.

9.2.1.1 Steel yield and concrete crushing

The internal steel reinforcement yields, which is then followed by compressive failure of the concrete at the extreme compressive fibre of the element. This type

of failure is expected for a balanced, normally-reinforced (i.e. non-strengthened) element.

9.2.1.2 Fibre rupture

Excessive deformation occurs and failure of the FRP composites takes place. It should be noted that not all fibres may reach ultimate limit state at the same time, which can result in a more gradual release of the stored elastic energy. This took place during the failure of beam 8CF1, where distinct sounds of fibres snapping were noted before ultimate failure was reached.

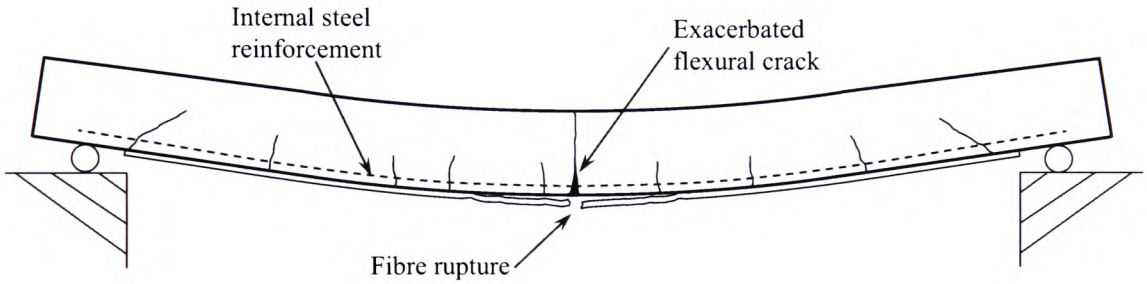

Figure 9.1 – Diagram of fibre rupture failure

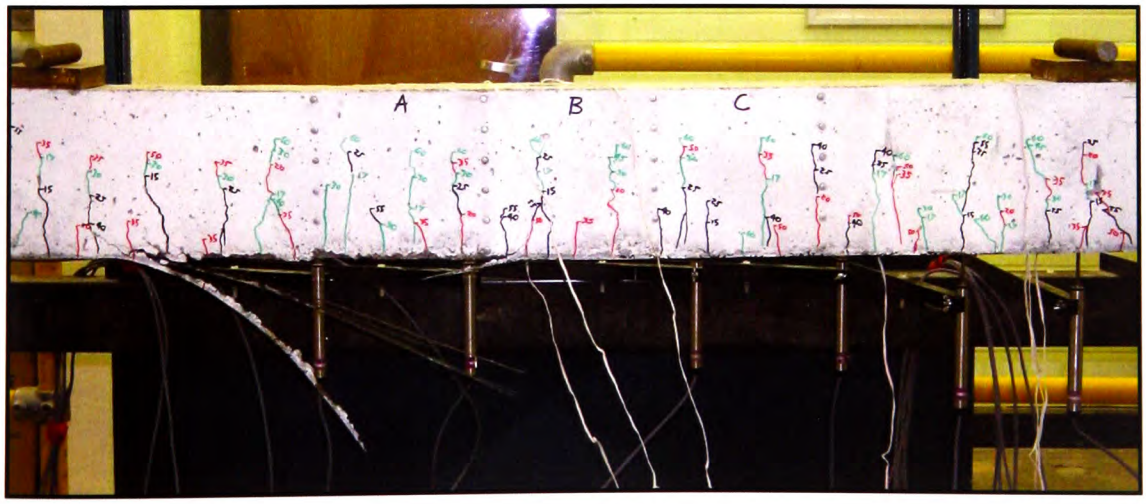

Figure 9.2 – Photograph of typical fibre rupture failure
(Experimental element 10CF1)

9.2.1.3 Fibre delamination

The adhesive bond between the fibre and the concrete substrate fails, resulting in a peeling off of the fibre composite sheet or plate along part or all of its length. This normally initiates at the end of the sheet or plate but in some cases can start elsewhere and propagate in two directions until failure occurs. Additionally, it is often the case that a delamination failure, as it propagates along the length of the beam, will become a tearing-off type failure. This occurs when the delaminating fibre composite sheet encounters a crack that is severe enough to allow the concrete cover to be torn away from the soffit of the beam, whilst remaining attached to the sheet. An example of this type of failure can be seen in Figure 9.4.

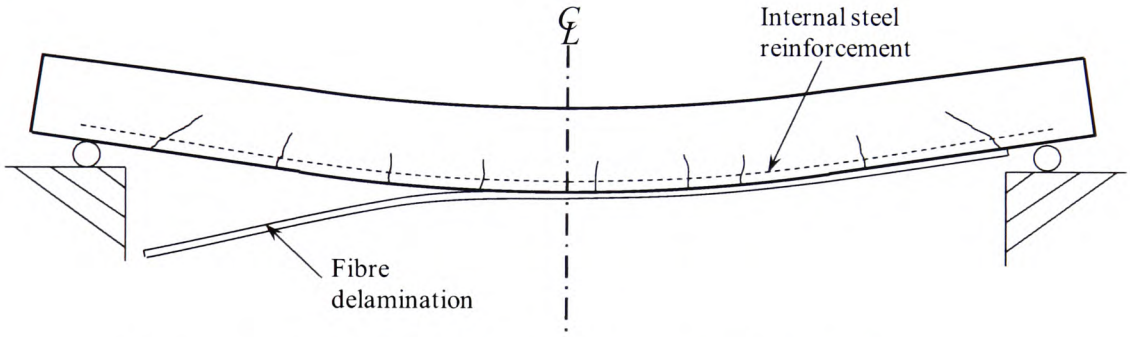

Figure 9.3 – Diagram of fibre debonding/delamination failure

Figure 9.4 – Photograph of typical debonding failure with partial tearing-off of concrete cover (Experimental element 10CF2)

9.2.1.4 Tearing-off of concrete cover

The concrete cover; i.e. that concrete between the reinforcement and the element soffit, tears away from the element. This type of failure normally occurs when there is excessive shear cracking in the element at high loads, which leads to a "joining up" of these shear cracks into a horizontal tearing-off failure.

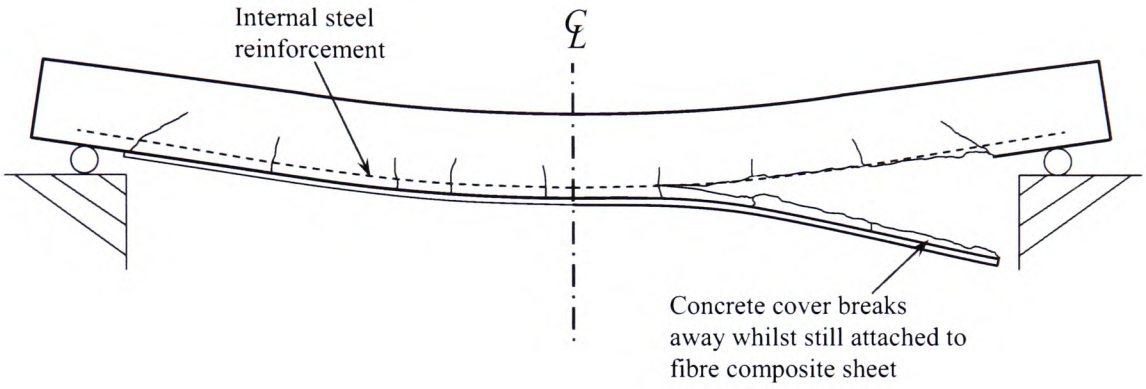

Figure 9.5 – Diagram of tearing-off of concrete cover failure

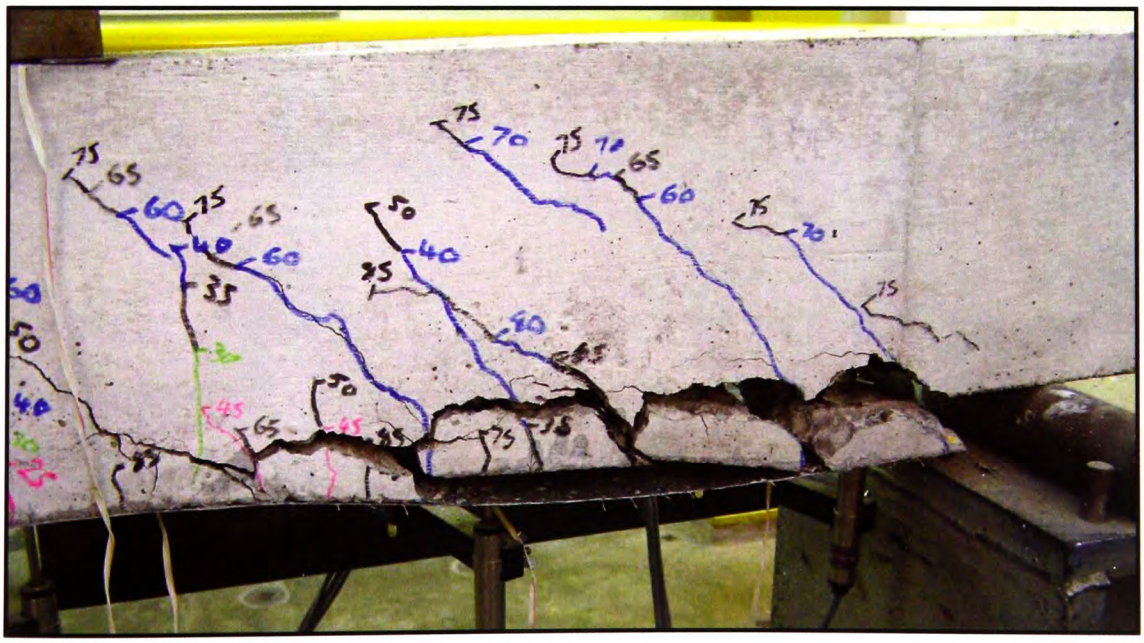

Figure 9.6 – Photograph of typical tearing-off of concrete cover failure (Experimental element 12DCF3)

9.2.1.5 Sudden concrete compressive failure

When an element is over-reinforced and/or over-strengthened in tension, the development of high compressive stresses in the compressive concrete zone results in a sudden, sometimes "explosive", compressive failure of the concrete. In this type of failure, neither the steel reinforcement nor the FRP strengthening has been fully utilised; in fact, the internal steel reinforcement has not normally even reached its yield point.

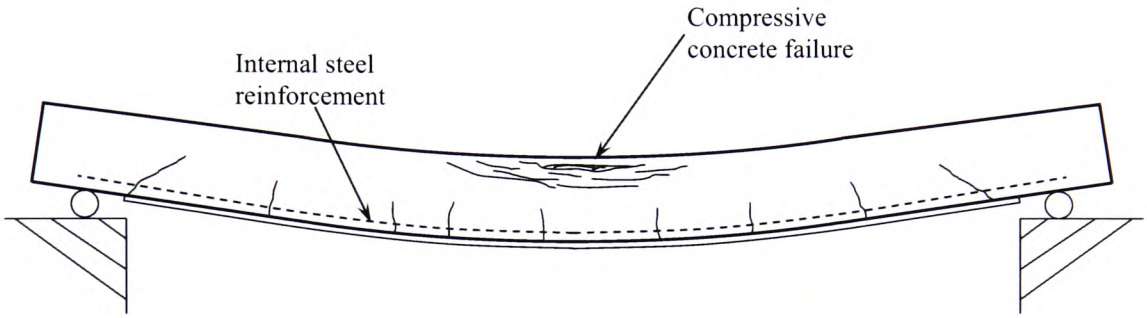

Figure 9.7 – Diagram of sudden compressive concrete failure

Figure 9.8 – Photograph of typical sudden compressive concrete failure
(Experimental element 16CF2)

9.2.2 Deflection prediction

In Chapter 5 a semi-empirical method for the prediction of deflections in fibre-composites-strengthened RC beams was discussed. A previously published method by Tann (2003) produced good results for slab elements but over-estimated the magnitude of deflections for beam elements.

Consequently, a revised method was developed, based initially on a revised method of predicting the second moment of area, I, of a strengthened beam, throughout the loading cycle. This revision amended the influence of the fibre composites and resulted in good correlation when compared with elements from the experimental programme. Subsequently, a new equation for deflection prediction was developed and checked against elements both from the experimental programme and from published data, which can reliably establish the deflection of fibre-composites-strengthened RC elements. The new method produced good quality results and will enable engineers to accurately predict the load deflection behaviour of RC beams that have been strengthened with fibre composites.

9.2.3 Ductility and deformability

Chapter 7 discussed the current methods for the calculation of ductility and deformability indices and also introduced a new, energy-based method for calculating the ductility index for a fibre-composites-strengthened RC element, based on Naaman *et al.*'s approach for elements with internal, pre-stressed FRP tendons. The new method contained an improved procedure for estimating the stored elastic energy in a fibre composites strengthened element at ultimate limit state.

A comparative study was carried out and it was found that the new method yielded values for ductility indices that were not only more consistent but also resulted in a larger difference between those indices for elements considered to

be ductile and other elements where the type of failure would be sudden or "brittle".

Subsequently, it is proposed by the candidate that the new, modified 3-slope approach is used to calculate ductility indices for fibre-composites-strengthened RC elements and, in addition, it is recommended that an index value of 1.7 is used as a minimum value to promote sufficiently ductile failure, with a further recommendation that a value of 1.9 is desirable to ensure ductile behaviour.

9.2.4 Crack patterns and prediction for fibre-composites-strengthened RC elements

A study was made of the cracking patterns of fibre-composites-strengthened RC elements and a comparison made with their normally-reinforced counterparts. It was shown that there are two main differences in the way in which cracks develop in the two types of elements. Firstly, in strengthened elements, there is a higher crack density as the loading increases; this is unlike normally reinforced elements, where the number of cracks stabilises and, subsequently, the crack widths increase. Secondly, the average length of the cracks is reduced in strengthened elements. In addition, due to both the high number of cracks at the latter loading stages and also the reduction in deformation due to the presence of the bonded fibre composites, the average crack width was seen to be markedly reduced.

Subsequently, a new method has been developed that can predict the average crack width for fibre-composites-strengthened RC elements.

9.3 Suggested further work

Despite the extensive experimental work carried out, there remain areas where there remain issues that still need to be addressed. Firstly, the non-linear model is only applicable in the constant moment zone and takes no account of the shear

stresses that occur in loaded elements. Consequently, it is desirable to develop the model to take into account these shear forces together with the bending moments.

As seen in the results from the experimental programme and further discussed in Section 9.1, there would appear to be a level of externally-bonded fibre composites above which the benefits of the strengthening are diminish. Further investigations are required to determine if there is a generic level of strengthening for any reinforced concrete element with externally-bonded fibre composites.

As discussed in Section 4.7, the FRP surface strains for the elements exhibiting a debonding mode of failure were significantly below the current design recommendation to prevent such failures; i.e. a limit of 8000με on the strain in the FRP. The results from the experimental programme suggest that debonding failure can occur at considerably lower levels of FRP surface strain and, hence, further investigation is needed to determine whether or not a revised value needs to be developed.

The deflection prediction model for strengthened beam elements, discussed in Chapter 5, has only been calibrated against the beam elements in the experimental programme and, consequently, it would be advantageous to apply the method to further strengthened elements, in order to confirm the validity and accuracy of the model.

Finally, the new method for calculating the crack widths of strengthened beam elements has again been calibrated only against the elements in the experimental programme and it is the considered view of the candidate that further comparisons are made with crack data from additional tested elements in order that the reliability of the method can be confirmed.

REFERENCES

Adhikary, Bimal Babu and Mutsuyoshi, Hiroshi (2002). "Numerical simulation of steel-plate strengthened concrete beam by a non-linear finite element method model." Construction and Building Materials **16**: 291-301.

Ahmed, O and Gemert, D Van (1999). "Behaviour of RC beams strengthened in bending by CFRP laminates." Structural Faults and Repairs.

Ahmed, Omar, Gemert, Dionys Van and Vandewalle, Lucie (2001). "Improved model for plate-end shear of CFRP strengthened RC beams." Cement and Concrete Composites **23**: 3-19.

Ahmed, S H, Xie, Y and Yu, T (1995). "Shear ductility of reinforced lightweight concrete beams of normal strength and high strength concrete." Cement and Concrete Composites **17**: 147-159.

Aiello, M A and Ombres, L (2001). "Load-deflection analysis of FRP reinforced concrete flexural members." Journal of Composites for Construction **4**(4): 164-171.

Aiello, Maria Antonietta and Ombres, Luciano (1997). Flexural behaviour of FRP reinforced concrete beams under service conditions. Non-Metallic (FRP) Reinforcement for Concrete Structures.

Almusallam, Tarek H and Al-Salloum, Yousef A (2001). "Ultimate strength prediction for RC beams externally strengthened by composite materials." Composites: Part B **32**: 609-619.

Alsayed, S H, Al-Salloum, Y A and Almusallam, T H (2000). "Fibre-reinforced polymer reapir materials - some facts." Proceedings of ICE **138**: 131-134.

Anania, Laura, Badala, Antonio and Failla, Giusy (2005). "Increasing the flexural performance of RC beams strengthened with CFRP materials." Construction and Building Materials **19**: 55-61.

Ando, T, sawada, E and Nii, K (1999). Development of new repair and maintenance technique with carbon fiber reinforced polymer composite. Fourth International Symposiuim on Fiber Reinforced Polymer Reinforcement for Reinforced Concrete Structures.

Andreou, E., Delpak, R., Pinzelli, R. and Chang, K. (2000). "The application of composite based on Kevlar for the strengthening of RC beams", Concrete Communication Conference 2000: The 10th BCA Annual Conference on Higher Education and the Concrete Industry, Birmingham. pp. 301-311

Andreou, Eftychia (2002). Performance evaluation of RC flexural elements strengthened by advanced composites, University of Glamorgan. **PhD Thesis**.

Arduini, Marco and Nanni, Antonio (1997). "Behaviour of precracked RC beams strengthened with carbon FRP sheets." Journal of Composites for Construction **1**(2): 63-70.

Arduini, Marco, Nanni, Antonio and Romagnolo, Mariano (2004). "Performance of One-Way Reinforced Concrete Slabs with Externally Bonded Fiber-Reinforced Polymer Strengthening." ACI Structural Journal **101**(2): 193-201.

Arduini, Marco, Tommaso, Angelo Di and Nanni, Antonio (1997). "Brittle failure in FRP plate and sheet bonded beams." ACI Structural Journal **94**(4): 363-370.

Arockiasamy, M, Amer, Ahmed and Shahawy, M "Concrete beams and slabs retrofitted with CFRP laminates."

Arockiasamy, M and Dutta, P K (1996). Retrofitting and structural repair with advanced polymer matrix composite materials. 6th International Offshore and Polar Engineering Conference, Los Angeles, USA.

Balendren, R V, Rana, T M and Nadeem, A (2001). "Strengthening of concrete structures with FRP sheets and plates." Structural Survey **19**(4): 185-192.

Bank, Lawrence C, Gentry, T Russell, Thompson, Benjamin P and Russell, Jeffrey S (2003). "A model specification for FRP composites for civil engineering structures." Construction and Building Materials **17**: 405-437.

Barton, Richard (1997). "Carbon fibre "plate bonding"." Structural Survey **15**(1): 11-14.

Beber, Andriei Jose and Campagnolo, Joao Luiz (1999). "Flexural strengthening of R/C beams with CFRP sheets." Structural Faults and Repairs **99**.

Beeby, A W (1997). Ductility in reinforced concrete: why is it needed and how is it achieved? The Structural Engineer. **76:** 180-183.

Belarbi, Abdeldjelil, and Hsu, Thomas T C, (1994). "Consitutive laws of concrete in tension and reinforcing bars stiffened by concrete." ACI Structural Journal **91**(4): 465-474.

Bencardino, Francesco and Spadea, Giuseppe (1997). Design to repair/upgrade structures: the key to a successful utilization of CFRP laminates. 7th International Conference on Structural Faults.

Bencardino, Francesco, Spadea, Giuseppe and Swamy, R Narayan (2002). "Strength and ductility of reinforced concrete beams externally reinforced with carbon fiber fabric." ACI Structural Journal **99**(2).

Bonacci, J F and Maalej, M (2001). "Behavioural trends of RC beams strengthened with externally bonded FRP." Journal of Composites for Construction **5**(2): 102-113.

Bridges, Design Manual for Roads and (2001). Section 3 General Design, HMSO. **1** Highway Structures: Approval Procedures and General Design.

British Standards Institution BS1881-121:1983 Testing Concrete - Part 121: Method for determination of static modulus of elasticity in compression.

British Standards Institution BS EN 1992-1-1:2004 – Eurocode 2, Design of concrete structures.

British Standards Institution BS8110:1995 - Part 1: Structural use of concrete.

Brosens, K and Gemert, D Van (1999). Anchorage design for externally bonded carbon fiber reinforced polymer laminates. Fourth International Symposiuim on Fiber Reinforced Polymer Reinforcement for Reinforced Concrete Structures.

Buyle-Bodin, Francois, David, Emmanuelle and Ragneau, Eric (2002). "Finite element modelling of flexural behaviour of externally bonded CFRP reinforced concrete structures." Engineering Structures **24**: 1423-1429.

Capozucca, R and Cerri, M Nilde (2002). "Static and dynamic behaviour of RC beam model strengthened by CFRP sheets." Construction and Building Materials **16**: 91-99.

Cha, J Y, Balaguru, P and Chung, L (1999). Experimental and analytical investigation of partially prestressed concrete beams strengthened with carbon reinforcement. Fourth International Symposiuim on Fiber Reinforced Polymer Reinforcement for Reinforced Concrete Structures.

Chajes, M J, Jr, T A Thomson and Tarantino, B (1995). Reinforcement of concrete structures using externally bonded composite materials. Non-Metallic (FRP) Reinforcement for Concrete Structures.

Chajes, Michael J, Finch, William W, Januszka, Ted F and Thomson, Theodore A (1996). "Bond and force transfer of composite material plates bonded to concrete." ACI Structural Journal **93**(2): 208-217.

Chajes, Michael J, Thomson, Theodore A and Farschman, Cory A (1995). "Durability of concrete beams externally reinforced with composite fabrics." Construction and Building Materials **9**(3): 141-148.

Chajes, Michael J, Thomson, Theodore A, Januszka, Ted F and Finch, William W (1998). "Flexural strengthening of concrete beams using externally bonded composite materials." Construction and Building Materials **8**(3): 191-201.

Chan, T K, Cheong, H K and Nguyen, D M (2001). Experimental investigation of delamination failure of CFRP strengthened beams. ICCMC/IBST 2001 International

Conference on Advanced Technologies in Design, Construction and Maintenance of Concrete Structures.

Chen, J F and Teng, J G (2003). "Shear capacity of FRP-strengthened RC beams: FRP debonding." Construction and Building Materials **17**: 27-41.

Clarke, L A and Cranston, W B "The influence of bar spacing on tension stiffening in reinforced concrete slabs." 118-128.

Concrete Society (2000). "Design guidance for strengthening concrete structures using fibre composites materials", Technical Report No. 55, The Concrete Society, Crowthorne, Berkshire, UK. 71pp.

Dall'Asta, Andrea and Zona, Alessandro (2002). "Non-linear analysis of composite beams by a displacement approach." Computers and Structures **80**: 2217-2228.

Darby, A, Ibell, T, Clarke, J, Denton, S, Farmer, N and Luke, S (2004). "Strengthening concrete structures using fibre composites." Proceedings of ICE **157**: 123-129.

David, Emmanuelle, Djelal, Chafika and Buyle-Bodin, Francois (1997). Repair and strengthening of reinforced concrete beams using composite materials. 7th International Conference on Structural Faults and Repair.

Davies, P (2003). Controlling ductility and deformability for optimal design of fibre composites strengthened concrete structures, University of Glamorgan. **MPhil Thesis**.

Dekoster, M, Buyle-Bodin, F, Maurel, O and delmas, Y (2003). "Modelling of the flexural behaviour of RC beams subjected to localised and uniform corrosion." Engineering Structures **25**: 1333-1341.

DeLorenzis, L, Galati, D and LaTegola, A (2004). "Stiffness and ductility of fibre-reinforced polymer-strengthened reinforced concrete members." Journal of Structures and Buildings **157**: 31-51.

Dristos, S, Pilakoutas, K and Kotsira, E (1995). "Effectiveness of flexural strengthening of RC members." Construction and Building Materials **9**(3): 165-171.

Duthinh, Dat and Starnes, Monica (2001). Strength and Ductility of concrete beams reinforced with Carbon FRP and steel. U. D. o. Commerce.

Ehsani, Mohammad R and Saadatmanesh, Hamid (1990). "Fiber composite plates for strengthening bridge beams." Composite Structures **15**: 343-355.

Einde, Lelli Van Den, Zhao, Lei and Seible, Frieder (2003). "Use of FRP composites in civil structural applications." Construction and Building Materials **17**: 389-403.

El-Mihilmy, Mahmoud T and Tedesco, Joseph W (2000). "Analysis of reinforced concrete beams strengthened with FRP laminates." Journal of Structural Engineering **126**(6): 684-691.

Esfahani, M R, Kianoush, M R and Tajari, A R (2007). "Flexural behaviour of reinforced concrete beams strengthened by CFRP sheets." Engineering Structures **29**: 2428-2444.

Ferreira, A J Mendes, Maques, A Torres and Sa, J Cesar de (2000). "Analysis of reinforced concrete with external composite strengthening." Composites: Part B **31**: 527-534.

Finch, William W, Chajes, Michael J, Mertz, Dennis R, Kaliakin, Victor N and Faqiri, Ahmed (1994). Bridge rehabilitation using composite materials. 3rd Materials Engineering Conference.

Fukuyama, Hiroshi, Tumialan, Gustavo and Matsuzaki, Yasuhiro (2001). Outline of the Japanese guidelines for seismic retrofitting of RC buildings using FRP materials. Non-metallic reinforcement for concrete structures FRPRCS-5, Cambridge, UK.

Garden, H N and Holloway, L C (1998). "An experimental study of the failure modes of reinforced concrete beams strengthened with prestressed carbon composite plates." Composites: Part B **29B**: 411-424.

Garden, H N and Holloway, L C (1998). "An experimental study of the influence of plate end anchorage of carbon fibre composite plates used to strengthen reinforced concrete beams." Composite Structures **42**: 175-188.

Garden, H N, Holloway, L C and Thorne, A M (1997). "A preliminary evaluation of carbon fibre reinforced polymer plates for strengthening reinforced concrete members." Proceedings of the Institution of Structral Engineers Structures and Buildings: 127-142.

Garden, H N, Holloway, L C, Thorne, A M and Parke, G A R (1996). A parameter study of the strengthening of reinforced concrete beams with bonded composites. 3rd International Conference on Bridge Management.

Grace, N F, Sayed, G A, Soliman, A K and Saleh, K R (1999). "Strengthening reinforced concrete beams using fiber reinforced polymer (FRP) laminates." ACI Structural Journal **96**(5): 865-874.

Grace, N F, Soliman, A K, Abdel-Sayed, G and Saleh, K R (1999). "Behaviour and ductility of simple and continuous FRP reinforced beams." Journal of Composites for Construction **2**(4): 186-194.

Grace, N F, Suliman, A K, Abdel-Sayed, G and Saleh, K R (1999). Strengthening of continuous beams using fiber reinforced polymer laminates. Fourth International

Symposiuim on Fiber Reinforced Polymer Reinforcement for Reinforced Concrete Structures.

Gravina, R J and Smith, S T, (2008). "Flexural behaviour of indeterminate concrete beams reinforced with FRP bars." Engineering Structures **30**: 2370-2380.

He, Jim Hong, Pilakoutas, Kypros and Waldron, Peter (1997). Analysis of externally strengthened RC beams with steel and CFRP plates. 7th International Conference on Structural Fault Analysis of Externally Strengthened RC Beams.

He, Jin Hong, Pilakoutas, Kypros and Waldron, Peter (1997). CFRP plate strengthening of RC beams. 7th International Conference of Structural Faults and Repair, Edinburgh.

Holloway, L C (2003). "The evolution of and the way forward for advanced polymer composites in the civil infrastructure." Construction and Building Materials **17**: 365-378.

Hu, C (2002). Use of infrared thermography in the assessment of structural integrity, University of Glamorgan. **PhD Thesis**.

Hulatt, J, Holloway, L and Thorne, A (2003). "The use of advanced polymer composites to form an economic structural unit." Construction and Building Materials **17**: 55-68.

Hutchinson, A R and Rahimi, H (1993). Behaviour of reinforced concrete beams with externally bonded fibre reinforced plastics. 5th International Conference of Structural Faults and Repair, Edinburgh.

Hutchinson, A R and Rahimi, H (1996). Flexural strengthening of concrete beams with externally bonded FRP reinforcement. 2nd International Conference on Advanced Composites.

Janze, Wim (1995). "Anchorage of externally bonded plates under static flexural loading." 139-148.

Joh, O, Wang, Z and Ibe, H (2003). Reinforcing effects of CFRP and AFRP sheets with respect to flexural behaviour of RC beams. 6th International Symposium on FRP Reinforcement for Concrete Structures, Singapore.

Kachlakev, D I and Barnes, W A (1999). Flexural and shear performance of concrete beams strentghened with fiber reinforced polymer laminates. Fourth International Symposiuim on Fiber Reinforced Polymer Reinforcement for Reinforced Concrete Structures.

Kaliakin, Victor N, Chajes, Michael J and Januszka, Ted F (1996). "Analysis of concrete beams reinforced with externally bonded woven composite fabrics." Composites: Part B **27B**: 235-244.

Karabinis, A I and Rousakis, T C (2002). "Concrete confined by FRP material: a plasticity approach." Engineering Structures **24**: 923-932.

Karihaloo, B L and Xiao, Q Z (2003). "Modelling of stationary and growing cracks in FE framework without remeshing: a state-of-the-art review." Computers and Structures **81**: 119-129.

Kemp, A R (1998). The achievement of ductility in reinforced concrete beams. Magazine of Concrete Research. **50:** 123-132.

Kishi, N, Mikami, H, Matsuoka, K G and Kurihashi, Y Failure behaviour of flexural strengthened RC beams with AFRP sheet. FRPRCS-5: Externally Bonded Reinforcement for Flexure.

Lau, K T, Dutta, P K, Zhou, L M and Hui, D (2001). "Mechanics of bonds in an FRP bonded concrete beam." Composites: Part B **32**: 491-502.

Leung, H Y (2002). "Strengthening of RC beams: some experimental findings." **20**(5): 173-181.

Limkatanyu, S, Thomsen, H, Spacone, E and Camata, G (2003). Parametric studies of RC beams strengthened in flexure with externally bonded FRP. 6th International Symposium on FRP Reinforcement for Concrete Structures, Singapore.

Maalej, M and Loeng, K S (2005). "Effect of beam size and FRP thickness on interfacial shear stress concentration and failure modes of FRP-strengthened beams." Composites Science and Technology **65**: 1148-1158.

Malver, L J, Warren, G E and Inaba, C (1995). Rehabilitation of navy pier beams with composite sheets. Non-metallic (FRP) Reinforcement for Concrete Structures.

Marshall, Orange S and Busel, Joh P (1996). Composite repair/upgrade of concrete structures. Proceedings of the Materials Engineering Conference.

Matthys, Stijn and Taerwe, Luc (2000). "Concrete slabs reinforced with FRP grids I: One-way bending." Journal of Composites for Construction **4**(3).

Matthys, Stijn and Tearwe, Luc (2006). "Evaluation of ductility requirements in current design guidelines for FRP strengthening." Cement and Concrete Composites **28**: 845-856.

Meier, U, Deuring, M and Kaiser, H (1992). Strengthening of structures with CFRP laminates. Glasgow, Blackie Academic and Professional.

Meier, Urs "Repair using advanced composites." 113-124.

Missihoun, M, Bazaa, I M and Labossiere, P (1997). Post-strengthening of reinforced concrete beams with carbon fiber reinforced plastic sheets. Annual Conference of the Canadian Society of Civil Engineers, Quebec.

Morton, S (1999). Externally bonded composites for strengthening concrete T-beam bridges. Fourth International Symposiuim on Fiber Reinforced Polymer Reinforcement for Reinforced Concrete Structures.

Mosallam, Ayman S and Mosalam, Khalid M (2003). "Strengthening of two-way concrete slabs with FRP composite laminates." Construction and Building Materials **17**: 43-54.

Mufti, Aftab A (2003). "FRPs and FOSs lead to innovation in Canadian civil engineering structures." Construction and Building Materials **17**: 379-387.

Naaman, A E and Jeong, S M (1995). Structural ductility of concrete beams prestressed with FRP tendons. Non-metallic (FRP) Reinforcement for Concrete Structures.

Nanni, Antonio (2003). "North American design guidelines for concrete reinforcement and strengthening using FRP: principles, applications and unresolved issues." Construction and Building Materials **17**: 439-446.

Nanni, Antonio, Bakis, Charles E and Boothby, Thomas E (1997). Externally bonded FRP composites for repair of RC structures. Non-Metallic (FRP) Reinforcement for Concrete Structures.

Oehlers, Deric John (2006). "Ductility of FRP plated flexural members." Cement and Concrete Composites **28**: 898-905.

Oehlers, D J, Griffith, M C and Mohamed Ali, M S, (2008). "Ductility components and limits of FRP-plated RC structures." Construction and Building Materials **23**: 1538-1543.

Pilakoutas, K and Haas, M (1994). Ductility design of reinforced concrete members. Earthquake Resistant Construction and Design.

Plevris, Nikolaos, Triantafillou, Thanasis C and Veneziano, Daniele (1995). "Reliability of RC members strengthened with CFRP laminates." Journal of Structural Engineering **121**(7): 1037-1044.

Quantrill, R J, Hollaway, L C, Thorne, A M and Parke, G A R (1995). Preliminary research on the strengthening of reinforced concrete beams using GFRP. Non-metallic (FRP) Reinforcement for Concrete Structures.

Quantrill, R J, Holloway, L C and Thorne, A M (1996). Experimental and analytical investigation of FRP stregthened beam response: Part 1. Magazine of Concrete Research. **48:** 331-342.

Rahimi, Hamid and Hutchinson, Allan (2001). "Concrete beams strengthened with externally bonded FRP plates." Journal of Composites for Construction **5**(1): 44-56.

Ramana, V P V, Kant, T, Morton, S E, Dutta, P K, Mukherjee, A and Desai, Y M (2000). "Behaviour of CFRPC strengthened reinforced concrete beams with varying degrees of strengthening." Composites: Part B **31**: 461-470.

Ritchie, Philip A, Thomas, David A, Lu, Le-Wu and Connelly, HGuy M (1990). External reinforcement of concrete beams using fiber reinforced plastics, Lehigh University.

Saadatmanesh, H and Ehsani, M R (1990). Fiber composite plates can strengthen beams. Concrete International**:** 65-71.

Saadatmanesh, H and Malek, A M (1998). "Design guidelines for flexural strengthening of RC beams with FRP plates." Journal of Composites for Construction **2**(4): 158-164.

Saadatmanesh, Hamid (1994). "Fiber composites for new and existing structures." ACI Structural Journal **91**(3): 346-354.

Saadatmanesh, Hamid and Ehsani, Mohammad R (1989). "Application of fiber-composites in civil engineering." 526-535.

Saadatmanesh, Hamid and Ehsani, Mohammad R (1990). Flexural strength of externally reinforced concrete beams. 1st Materials Engineering Conference.

Sato, Y, Shouji, K, Ueda, T and Kakuta, Y (1999). Uniaxial tensile behaviour of reinforced concrete elements strengthened by carbon fiber sheet. Fourth International Symposiuim on Fiber Reinforced Polymer Reinforcement for Reinforced Concrete Structures.

Shahawy, M A, Arockiasamy, M, Beitelman, T and Sowrirajan, R (1996). "Reinforced concrete rectangular beams strengthened with CFRP laminates." Composites: Part B **27B**: 225-233.

Shehata, I A E M, Cerqueira, E C, Pinto, C T M and Shehata, L C D (1995). Strengthening of RC beams in flexure and shear using CFRP laminates. Non-metallic (FRP) Reinforcement for Concrete Structures.

Sheikh, Shahim A (2002). "Performance of concrete structures retrofitted with fibre reinforced polymers." Engineering structures **24**: 869-879.

Shimomura, T, Mutsutoshi, H, Wu, Z, Kobayashi, A and Ishibashi, T (1999). Verification of safety and serviceability of concrete structures retrofitted with externally-bonded continuous fiber materials. Fourth International Symposiuim on Fiber Reinforced Polymer Reinforcement for Reinforced Concrete Structures.

Smith, S T and Teng, J G (2002). "FRP-strengthened RC beams. I: review of debonding strength models." Engineering Structures **24**: 385-395.

Smith, S T and Teng, J G (2002). "FRP-strengthened RC beams. II: assessment of debonding strength models." Engineering Structures **24**: 397-417.

Spadea, G, Bencardino, F and Swamy, R N (1998). "Structural behaviour of composite RC beams with externally bonded CFRP." Journal of Composites for Construction **2**(3): 132-137.

Spadea, G, Swamy, R N and Bencardino, F (2001). "Strength and ductility of RC beams repaired with bonded CFRP laminates." Journal of Bridge Engineering **6**(5): 349-355.

Subedi, N K and Baglin, P S (1996). "External plate reinforcement for strengthening concrete beams." Construction repair **10**(6): 24-29.

Subedi, N K and Baglin, P S (1998). "External plate reinforcement for concrete beams." Journal of Structural Engineering **124**(12): 1490-1495.

Swamy, Narayan, Mukhopadhyaya, Phalguni and Lynsdale, Cyril (1997). Ductility considerations in using GFRP sheets to strengthen and upgrade structures. 3rd International Symposium on Non-Metallic (FRP) Reinforcement for Concrete Structures.

Swamy, R N (1996). Effective strengthening with ductility: use of externally bonded plates of non-metallic composite materials. International Conference on Advanced Composite Materials in Bridges and Structures, Montreal, Canada.

Taheri, F, Shahin, K and Widiarsa, I (2002). "On the parameters influencing the performance of reinforced concrete beams strengthened with FRP plates." Composite Structures.

Takahashi, Y, Hata, C, Sato, Y, Ueda, T and Maeda, T (1999). Flexural strengthening of reinforced concrete beams with carbon fibre sheets. Fourth International Symposiuim on Fiber Reinforced Polymer Reinforcement for Reinforced Concrete Structures.

Takahashi, Y and Sato, Y (2003). Flexural behaviour of RC beams externally reinforced with carbon fibre sheets. 6th International Symposium on FRP Reinforcement for Concrete Structures, Singapore.

Takeda, Koji, Mitsui, Yoshiyuki, Murakami, Kiyoshi, Sakai, Hiromichi and Nakamura, Moriyasu (1996). "Flexural behaviour of reinforced concrete beams strengthened with carbon fibre sheets." Composites: Part A **27A**: 981-987.

Taljsten, Bjorn (1999). "Concrete beams strengthened for bending using CFRP sheets." Structural Faults and Repairs.

Taljsten, Bjorn (2003). "Strengthening concrete beams for shear with CFRP sheets." Construction and Building Materials **17**(15-26).

Tan, K Y, Tumialan, J G and Nanni, A (2003). Evaluation of externally bonded CFRP systems for the strengthening of RC slabs. 6th International Symposium on FRP Reinforcement for Concrete Structures, Singapore.

Tann, D B (2001). Retrofitting of mechanically degraded concrete structures using fibre reinforced polymer composites, University of Glamorgan. **PhD Thesis**.

Tann, D B (2003). A semi-empirical approach for the prediction of deflections of FRP strengthened RC slabs. 6th International Symposium on FRP Reinforcement for Concrete Structures, Singapore.

Tann, D B (2005). Determination of ductility and deformability indices for FRP strengthened RC slabs. 6th International Congress on Global Construction.

Tann, D B, Davies, P and Delpak, R (2003). A review of ductility determination of FRP strengthened flexural RC elements. 6th International Symposium on FRP Reinforcement for Concrete Structures, Singapore.

Tann, D B and Delpak, R (2000). Strengthening for ductility and high performance of reinforced concrete structures using externally bonded FRP composites. High Performance Concrete - Workability, Strength and Durability.

Tegola, A, Manni, O and Noviello, G (1998). Flexural reinforcement of concrete beams using FRP plates. IABSE Colloquium, Berlin.

Teng, J G, Chen, J F, Smith, S T and Lam, L (2002). FRP Strengthened RC Structures, Wiley.

Teng, J G, Smith, S T, Yao, J and Chen, J F (2003). "Intermediate crack-induced debonding in RC beams and slabs." Construction and Building Materials **17**: 447-462.

Teng, J G, Zhang, J W and Smith, S T (2002). "Interfacial stresses in reinforced concrete beams bonded with a soffit plate: a finite element study." Construction and Building Materials **16**: 1-14.

Toutanji, Houssam A and Gomez, William (1997). "Durability characteristics of concrete beams externally bonded with FRP composite sheets." Cement and Concrete Composites **19**: 351-358.

Toutanji, Houssam and Deng, Yong (2003). "Deflection and crack-width prediction of concrete beams reinforced with glass FRP rods." Construction and Building Materials **17**: 69-74.

Toutanji, Houssam and Saafi, Mahamed (1999). "Performance of concrete beams prestressed with aramid fiber-reinforced polymer tendons." Composite Structures **44**: 63-70.

Triantafillou, Thanasis C and Plevris, Nikolaos (1991). "Post-strengthening of RC beams with epoxy-bonded fiber composite materials." ASCE Advanced Composite Materials: 245-256.

Triantafillou, Thanasis and Fardis, Michael (1993). "Advanced composites for strengthening historic structures." IABSE: 541-548.

Tumialan, G, Serra, P, Nanni, A and Belarbi, A (1999). Concrete cover delamination in reinforced concrete beams strengthened with carbon fiber reinforced polymer sheets. 4th International Symposiuim on Fiber Reinforced Polymer Reinforcement for Reinforced Concrete Structures.

Tumialan, Gustavo, Fukuyama, Hiroshi and Nanni, Antonio (2001). Overview of the Japanese guidlines for seismic retrofitting of RC columns using FRP materials. Structures 2001, Washington DC, USA.

Tumialan, Gustavo, Serra, Paolo, Nanni, Antonio and Belarbi, Abdeldjelil (1999). Concrete cover delamination in RC beams strengthened with FRP sheets. 4th International Symposium on FRP for Reinforcement of Concrete Structures, Baltimore, MD, USA.

Valcuende, M, Benlloch, J and Parra, C J (2003). Ductility of reinforced concrete beams strengthened with CFRP strips and fabric. 6th International Symposium on FRP Reinforcement for Concrete Structures, Singapore.

Van Den Einde, Lelli and Seible, Frieder (2003). "Use of FRP composites in civil structural applications." Construction and Building Materials **17**: 389-403.

Vijay, P V and Gangarao, Hota V S (2001). "Bending behaviour and deformability of glass fiber-reinforced polymer reinforced concrete members." ACI Structural Journal **98**(6).

Wenwei, Wang and Guo, Li (2005). "Experimental study and analysis of RC beams strengthened with CFRP laminates under sustaining load." International Journal of Solids and Structures **43**: 1372-1387.

Whitehead, P A and Ibell, T J (2004). "Deformability and ductility in over-reinforced concrete structures." Magazine of Concrete Research **56**(3): 167-177.

Wu, Z J and Davies, J M (2003). Load capacity of concrete beams strengthened with external FRP sheets. 6th International Symposium on FRP Reinforcement for Concrete Structures, Singapore.

www.ngcc.org.uk. (2003). "Network Group for Composites in Construction website." 2003.

www.shef.ac.uk/uni/projects/tmrnet/index.html. (2003). "ConFibreCrete Network website." 2003.

Yang, Z J, Chen, J F and Proverbs, D (2003). "Finite element modelling of concrete cover separation failure in FRP plated RC beams." Construction and Building Materials **17**: 3-13.

Yoshizawa, H and Wu, Z (1999). Crack behaviour of plain concrete and reinforced concrete members strengthened with carbon fiber sheets. Fourth International Symposiuim on Fiber Reinforced Polymer Reinforcement for Reinforced Concrete Structures.

Zoghmar, A, Labossiere, P and Neale, K W (1996). Reliability of reinforced concrete beams strengthened with epoxy-bonded FRP laminates. 1st Structural Speciality Conference, Alberta, Canada.

Zupan, D and Saje, M (2003). "The three-dimensional beam theory: Finite element formulation based on curvature." Computers and Structures **81**: 1875-1888.

APPENDIX A

PUBLISHED PAPERS BY THE CANDIDATE

Appendix A-1

JOURNAL PAPER

"Ductility and deformability of fibre-reinforced polymer-strengthened reinforced concrete beams"

Journal of Structures and Buildings
Vol. 157, SB1, January 2004, pp 19-30

Proceedings of the Institution of Civil Engineers
Structures & Buildings 157
January 2004 Issue SB1
Pages 19–30

Paper 13091

Received 5/11/2002
Accepted 2/5/2003

Keywords:
composite structures/ductility
strength & testing of materials

D. B. Tann
Senior Lecturer, School of Technology, University of Glamorgan

R. Delpak
Professor, School of Technology, University of Glamorgan

P. Davies
Research Assistant, School of Technology, University of Glamorgan

Ductility and deformability of fibre-reinforced polymer-strengthened reinforced concrete beams

D. B. Tann, R. Delpak and P. Davies

This paper discusses the definition of, and the distinction between, deformability and ductility of reinforced concrete (RC) beams that are strengthened by advanced composites. The study examines the suitability of a new, design-based method for the determination of deformability, as well as an energy-based process, which is found to be suitable for quantifying the ductility levels of fibre-reinforced polymer (FRP)-strengthened RC members. Ten FRP-strengthened RC beams and four slabs have been load-tested to ultimate failure in the current study. The test results, together with the load–deflection data of an additional 26 beams from literature, form the basis of analyses and discussions. The paper concludes that high deformability does not necessarily lead to good ductility, as very brittle failure modes of such beams have been observed in the experimental studies and reported in literature. It was found that a ductility index of between 2·0 and 2·5 reflects 25–33% of elastic energy stored in the strengthened system. This level of elastic energy is considered to be the maximum acceptable in FRP-strengthened concrete flexural elements for ductile behaviour. It was also found that for ductile failure modes the deformability and ductility indices tend to converge, whereas for brittle behaviour the deformability index could be up to 33% higher. The results presented in this paper provide a rationale for the ductility considerations to be incorporated into the development of design equations for FRP strengthening.

NOTATION

A_{es} total equivalent steel reinforcement area
A_f cross-sectional area of FRP composites
A_s area of steel reinforcement
b width of beam
d effective depth
E_{el} elastic energy
E_f elastic modulus of FRP composites
E_s elastic modulus of steel
E_{tot} total energy
f_{cu} 28-day concrete cube strength
h overall depth of beam
m modular ratio $= E_p/E_s$
P_u ultimate failure load
W_s service load (defined as 0·67 P_u)
x neutral axis depth
α reinforcement position constant $= (h - x)/(d - x)$
$\Delta_{0·95}$ generic element deformation at 95% of peak load
Δ_p generic element deformation at peak load
Δ_s generic element deformation at service load
Δ_u generic element deformation at ultimate failure
$\delta_{0·95}$ deflection at 95% of peak load
δ_s deflection at service load
δ_u deflection at ultimate load
λ ratio of deformability index to ductility index $= \phi_{df}/\phi_{du}$
ρ_{es} total equivalent steel reinforcement ratio
ρ_f external FRP reinforcement ratio
ρ_s steel reinforcement ratio
ϕ_{df} deformability index
ϕ_{du} ductility index

1. INTRODUCTION

The word 'ductility' originates from the Latin *ductilis*, which means the ability of metals and alloys to retain strength and freedom from cracks when their shape is altered as a result of applied stress. Today, it is used to describe the ability of any material to sustain *inelastic* deformation before fracture. Concrete is a brittle material, but it is generally accepted that conventionally reinforced concrete (RC) members can attain suitable ductile behaviour by proper design and detailing of steel reinforcement. The yield point of steel is thus treated as an important datum beyond which inelastic deformation of the RC member takes place, thus enabling the full stress and strain capacity of concrete to be developed before ultimate failure.

Since the early 1990s, the viability of using non-metallic fibre-reinforced polymer (FRP) reinforcement instead of conventional steel reinforcing bars has been widely researched,[1] and the question of ductility for FRP-reinforced concrete elements has been a topic of debate among many researchers.[2–4] Despite these attempts to address the issue, there is, to date, still a distinct lack of general agreement as to how the ductility characteristics of such elements may be quantified and analysed. As for the ductility of FRP-strengthened RC elements, there have been relatively fewer research activities focused on this important area.[5–8] Yet consideration of structural ductility is of predominant

importance to any structural designer, as all appropriately designed structures should attain sufficiently ductile behaviour under ultimate load conditions. The reason for this is twofold: first, to ensure the redistribution of internal forces in a statically indeterminate structure, when parts of it reach the ultimate capacity, and hence to allow the formation of plastic hinges. Second, ductile structures can provide sufficient warning prior to ultimate failure, so as to prevent the structure from sudden and brittle failure at ultimate limit state (ULS).

2. TRADITIONAL METHODS FOR DUCTILITY CALCULATION

From a structural designer's viewpoint, ductility has been traditionally defined as the ability of a structure to sustain deformation before its failure under ultimate load. Kemp[9] described ductility as the 'inelastic rotations through which critically stressed regions of a beam can deform in flexure before a loss of moment capacity occurs'. It has been generally accepted that ductility can be measured by a dimensionless factor, often referred to as the *ductility index*, in several different forms within two broad categories.

2.1. Deformation-based ductility

The deformation-based ductility index, ϕ_d, of a structural element is determined as the ultimate deformation, Δ_u, divided by the corresponding value of deformation at the material yield point, Δ_y

$$\phi = \frac{\Delta_u}{\Delta_y} \quad (1)$$

The yield point, in the case of RC elements, is the point when the steel reinforcement starts yielding for under-reinforced sections. The term of deformation is a generic description of deflection, rotation, curvature or compressive strains.

2.2. Energy-based ductility

In this approach the total strain energy of a deformed element may be divided by the energy value at a reference point that is equivalent to the reinforcement yield stage. The quantity of energy may be obtained by integrating the area under the load–deflection curves of the beam considered. This approach is in fact a variant of the deformation-based method. Both depend on the clear identification of the point of reinforcement yielding for the evaluation of ductility, and should lead to exactly the same value of ductility index for an ideal elastic-plastic material.

2.3. Typical load–deformation of FRP-strengthened RC elements

For RC members strengthened by externally bonded FRP composites, the structural ductility can no longer be expected to be reasonably assessed by any of the above traditional methods. This is due to the difficulty in identifying the stage of internal steel reinforcement yielding, as the load–deflection curve of FRP-strengthened flexural members may not exhibit an apparent change of slope when the steel has yielded. The presence of the externally bonded composites can, when in full composite action and subject to high loading, contribute significantly more to the member's load resistance than that of the internal steel reinforcement. As a result, the effects of yielding of the internal steel bars on the load–deflection behaviour of the member are less apparent. The above statement is particularly applicable to heavily FRP-strengthened flexural members. Shown in Fig. 1 is a comparison of a typical load–deflection response of an under-reinforced beam with that of a similar beam strengthened by a high-strength, pultruded carbon FRP (CFRP) plate, based on laboratory test results conducted by the authors.

As is illustrated, the conventional RC beam has a clear reduction of slope at the steel yield stage (point 2 on the curve). The FRP-strengthened beam shows no such apparent behaviour, even though a numerical calculation would indicate that the internal steel has indeed yielded. Such behaviour is due to the presence of the FRP composites, which 'take over' from the internal reinforcement and sustain the level of stiffness in the strengthened system after the yielding of the steel.

2.4. Deformability of FRP-strengthened elements

An alternative terminology should be used to define the deformation characteristics of FRP-strengthened flexural members. The term *rotational capacity* can be used to distinguish the ability of a member to deform from its ductility, as was suggested by Lees.[10] However, this term could be misinterpreted as to referring only to the rotation of the beam and not to deflection or strain deformation. A more appropriate description is therefore needed for loaded FRP-strengthened elements undergoing large deformations but not necessarily displaying high ductility. The authors suggest that the term *deformability index* should be used.

The deformability index, ϕ_{df}, may be defined as the ratio of ultimate deformation to the deformation at a reference point. For FRP-strengthened flexural elements, this may be written as follows

$$\phi_{df} = \frac{\Delta_{0{\cdot}95}}{\Delta_s} \quad (2)$$

In the above equation, $\Delta_{0{\cdot}95}$ is the generic deformation at 95% of the peak load, which may comprise deflection, rotation, curvature or compressive strains. The corresponding deformation at the reference point is expressed by Δ_s. The

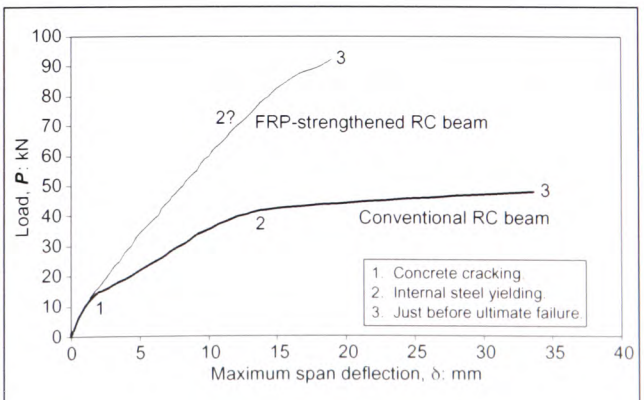

Fig. 1. Load–deflection of conventional and FRP-strengthened RC beams

figure of 95% of peak load is suggested, as it has been observed during the laboratory tests that the ultimate deflection in the beams could be greatly influenced by the loading rate and general configuration of the testing system, especially for displacement control loading regime. As a result, the ductility index at 100% of ultimate load could up to four to five times that of the same beam at 95% of peak load. With regard to the reference point, after careful consideration and comparison with other alternatives, it was found that the deformation corresponding to the service load (W_s) is best suited to be the denominator for the deformability index calculation. In the special case of equalised dead and imposed load, W_s is 67% of the design ultimate load. Consequently, for the purpose of calculating deformability index in the current study, the service load is thus assumed to be 67% of the ultimate value. This simplification of the quantity of service load is considered reasonable and unlikely to cause significant difference to the deformability analyses. For example, if the imposed load is significantly reduced, say, to 50% of the dead load, then the amount of service load is still approximately 68% of the maximum ultimate design load under the limit state design principles.

2.5. Ductility formulation for FRP-strengthened elements

An energy-based method for determining ductility was first proposed by Naaman and Jeong,[3] expressed by the following equation, where E_{tot} and E_{el} are the total and elastic energy respectively

$$\phi_{du} = \frac{1}{2}\left(\frac{E_{tot}}{E_{el}} + 1\right) \quad (3)$$

Although the equation was originally intended for RC members with internal FRP reinforcement, it is also applicable to members externally strengthened with FRPs. For an ideal elastic-plastic material, it yields exactly the same value as equation (1). For materials such as FRP composites, with linear stress–strain responses up to failure, Δ_u equals Δ_y, and the ductility index from both equations (1) and (3) becomes unity, indicating that the element possesses virtually no ductility.

Grace *et al.*[4] used an *energy ratio* method to quantify the ductility of FRP-reinforced beams, where the energy ratio is defined as the ratio of inelastic energy to total energy. The authors argued that, if the energy ratio is 75% or greater, then the beam will exhibit a ductile failure. Fundamentally, there is no difference from the Naaman and Jeong[3] procedure, as Grace's method is in effect a reversed form of this approach. If the energy ratio is 75%, then E_{tot}/E_{el} would be $1/(1 - 0{\cdot}75) = 4$, and the ductility index as determined by equation (3) would be 2·5, which is naturally an indication of acceptable ductility level.

However, the accuracy of the above method relies on the clear identification of the elastic portion of the energy, and in practice this is difficult for FRP-strengthened members as the unloading–deflection curves are not always obtainable. Naaman and Jeong[3] suggested that the elastic energy could be estimated using an equivalent triangle area under the load–deflection curve. The two initial slopes S_1 and S_2 (with the corresponding loads of P_1 and P_2) of the load–deflection curve were weighted to define a slope S for the equivalent unloading response, as shown in Fig. 2

$$S = \frac{P_1 S_1 + (P_2 - P_1) S_2}{P_2} \quad (4)$$

This empirical approach, although still somewhat arbitrary, leads to a reasonable set of results. It is therefore recommended that, before a more rigorous approach for the determination of elastic energy is developed, Naaman and Jeong's method should be used to calculate structural ductility for FRP-strengthened RC members.

3. NUMERICAL VERIFICATION

In limit state design of flexural RC members, the ductility aspects are not usually evaluated directly by designers but are incorporated in the simplified design equations. BS 8110,[11] for example, requires that all RC beams and slabs be designed as 'under-reinforced' sections by limiting the neutral axis depth to various values. This ensures that the section is sufficiently ductile for moment redistribution and will provide a warning before ultimate failure. For FRP-strengthened flexural elements, the principles of 'under-strengthening' should still apply, so that sufficient ductility may be intrinsic in the strengthened system. However, the current available design guidelines[12,13] do not make specific provisions for ductility considerations. In such cases it is more difficult to define a generic 'balanced-strengthening' scenario than for conventional RC members because of the large variation of FRP material properties. It is therefore essential to establish what constitutes an 'acceptable' value of ductility index for an FRP-strengthened member and to identify the corresponding failure mode. Subsequently, the design equations for strengthening works can be derived.

In order to test the validity of equations (2) and (3), and to establish a suitable range of ductility indices related to various failure modes, the authors compiled a comprehensive database[14] of 75 FRP-strengthened RC beams. The original data were all extracted from a series of technical reports, journal publications and theses. Of these 75 beams, however,

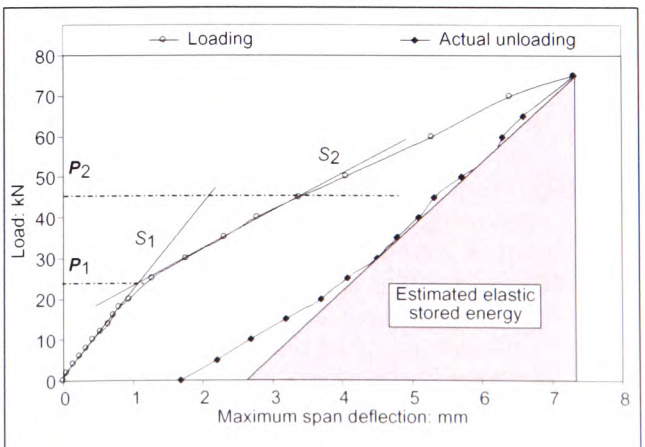

Fig. 2. Estimated elastic stored energy in FRP-strengthened RC elements

only 26 were found to contain sufficient information that could be used to process the load–deflection characteristics and the associated failure mode. These were then divided into three categories of failure mode

(a) ductile failure
(b) near-ductile failure
(c) brittle failure.

Note, however, that no photographic evidence was available, and these classifications of failure modes were based on the current authors' interpretation of the various descriptions in the original papers.

Table 1 lists the salient element data of these 26 beams. Also included in the table is the *total equivalent steel reinforcement ratio*, ρ_{es}, which is determined as follows

$$\rho_{es} = \frac{A_{es}}{bh} \quad (5)$$

where the equivalent steel area, $A_{es} = A_s + \alpha m A_f$, defined as the actual steel reinforcement area plus the cross-sectional area of the FRP composites multiplied by the modular ratio $m = E_f/E_s$, and the constant $\alpha = (h - x)/(d - x)$ compensate for the different FRP and internal reinforcement positions. For convenience of calculation, α is taken as 1·1 in the current study.

The total equivalent steel reinforcement (TESR) ratio serves only as a rough indication of the total reinforcement level, and it should be noted that material incompatibilities result in different failure mechanisms. FRP composites with large failure strains (say >1·5%) are unlikely to reach the ultimate tensile strength in a flexural strengthening system, as other forms of failure, such as (a) premature debonding, (b) concrete crushing, (c) lateral shear failure and (d) excessive cracking, would almost certainly have occurred before.[21] All FRP-strengthened beams and slabs should, ideally, be designed so that complete flexural failure is ensured at the ultimate limit state rather than the premature failure modes outlined above. However, the method of deformability and ductility analyses in the current paper is valid for all flexural members even if premature failure occurs. Once the premature failure load is estimated, the serviceability-based deformability index can always be determined using equation (2). The ductility index of such members, as calculated by equation (3), will be expected to have low values approaching unity. In the current review, only beams with typical flexural failure modes were included.

Based on the original load–deflection data and graphs, the current authors attempted to calculate the ductility indices for all beams using various traditional methods.[14] The results, as expected, appeared to be inconsistent and scattered, which confirms the invalidity of the conventional approaches. The proposed equations (2) and (3) were then used to determine the deformability and ductility indices of the above 26 beams respectively. The results, as shown in the last two columns of Table 1, illustrate a satisfyingly consistent variation between the two indices and the corresponding failure modes.

3.1. Ductile failure mode

In this case, the load–deflection variation of the six beams showed similarities with the unstrengthened RC control beam. With certain exceptions, most of the failures were initiated by steel yielding and followed by the rupture of FRP composites, which mirrored the typical failure cases with conventional under-reinforced beams. The average TESR ratio for this group was 0·93%. The average deformability and ductility indices are 2·50 and 2·59 respectively. From equation (2), the value of 2·50 can be interpreted such that a beam would be able to sustain a potential 150% of the serviceability deformation before the ultimate failure takes place. The ductility index of 2·59 from equation (3) suggests that the elastic portion of the energy is 23·9%, which is released once ultimate failure occurs. This can be regarded, clearly, as a 'reasonable' standard of ductile behaviour for FRP-strengthened flexural elements.

3.2. Near-ductile failure mode

The nine beams in this category generally exhibited relatively 'mild' behaviour at ultimate failure: no 'explosive' types of failure mode had been reported. The average TESR ratio was 1·11%: this is 19% higher than that of the ductile beams, and can be regarded as a 'balanced' section. The average deformability and ductility indices are 2·27 and 1·94 respectively, which indicates a 127% deformation extension after serviceability, and 34·7% of elastic energy release at ultimate failure.

3.3. Brittle failure mode

A sharp reduction in both deformability (1·71) and ductility (1·35) indices was evident for the eleven beams in this group. Physically, this implies that only 71% of serviceability deformation can be expected beyond the normal working load of the beams, whereas, at ultimate failure, 58·8% of the energy in the strengthened member is estimated to be elastic (to be released at the instant of beam failure), resulting in a brittle characteristic. The reported failure modes were, indeed, either of an explosive type of concrete crushing or premature tearing-off of concrete cover, which was seen to be even more sudden and brittle. The average TESR ratio for this group is 1·51%, which is indicative of 'over-strengthening'.

Figure 3 shows three distinct failure modes with the corresponding levels of deformability and ductility indices. It is clear that, for a brittle failure mechanism, the ductility index has a low value of 1·35, whereas this value increases to 2·59 for the ductile failure.

4. EXPERIMENTAL PROGRAMME

In order to further demonstrate the relationship between ductility and deformability, the authors conducted a two-phase experimental study. In Phase 1, ten FRP-strengthened RC beams, together with a control beam, were tested to ultimate failure. All beams were 2·6 m long with an effective span of 2·4 m, and the cross-section was 100 mm by 200 mm. Two high-yield, 10 mm diameter bars were used as tension reinforcement (A_s = 0·785%, f_y = 560 N/mm^2), and 6 mm diameter links at 100 mm centres were placed in the shear spans. A four-point load configuration was employed, with the space between the two point loads being 1·25 m. All FRP composite lengths were set at 2·20 m—that is, with the end of the sheet 100 mm from each support.

Failure mode	Beam No.	Original code	Reference	Cross-section: mm	A_s: mm^2 (ρ_s: %)	FRP type (ρ_f: %)	ρ_{es}: %	f_{cu}: N/mm^2	P_u: kN	ϕ_{df} (eqn 2)	ϕ_{du} (eqn 3)
Ductile failure mode	U1	DF.1	19	125 × 225	152 (0·54)	CP (0·05)	0·59	42·0*	121·1	3·11	2·78
	U2	A4	4	152 × 305	402 (0·87)	CS (0·49)	1·35	51·7	195·7	2·35	2·24
	U3	A6	4	152 × 305	402 (0·87)	CS (0·03)	0·90	51·7	143·2	2·49	2·90
	U4	A7	4	152 × 305	402 (0·87)	CS (0·06)	0·93	51·7	170·3	2·27	3·27
	U5	110	5	100 × 200	156 (0·79)	AS (0·15)	0·89	49·5	71·0	2·35	2·29
	U6	111	5	100 × 200	156 (0·79)	AS (0·15)	0·89	49·5	70·0	2·42	2·11
Near-ductile failure mode	N1	A3·4	15	140 × 300	402 (0·96)	CS (0·41)	1·19	35·4†	101·3	2·33	1·80
	N2	C1·1	15	140 × 300	402 (0·96)	CS (0·41)	1·19	21·0†	90·0	2·33	1·72
	N3	CP1-V	8	152 × 292	402 (0·91)	CP (0·45)	1·24	48·3	110·3	2·12	2·02
	N4	CP3-V	8	152 × 292	402 (0·91)	CP (1·30)	1·24	48·3	113·9	2·15	1·90
	N5	3–3	16	127 × 76·2	71 (0·73)	CS (0·46)	1·04	41·9†	21·8	2·14	1·74
	N6	4–3	16	127 × 76·2	71 (0·73)	CS (0·61)	1·19	47·6†	34·4	2·72	2·12
	N7	B2	17	152 × 305	402 (0·87)	CS (0·03)	0·90	51·7	61·74	2·06	1·83
	N8	108	18	100 × 200	156 (0·79)	AS (0·30)	1·00	45·5	86·6	2·49	2·23
	N9	109	18	100 × 200	156 (0·79)	AS (0·30)	1·00	45·5	86·0	2·09	2·10
Brittle failure mode (concrete crushing)	O1	A1·1	20	140 × 300	402 (0·96)	CP (0·23)	1·13	34·3	86·8	1·66	1·10
	O2	C1·2	15	140 × 300	402 (0·96)	CS (0·41)	1·19	22·1	102·3	1·81	1·35
	O3	8	26	76 × 127	33·3 (0·35)	CP (1·26)	1·63	44·7	37·3	1·68	1·35
	O4	4	23	100 × 200	157 (0·79)	CS (0·17)	1·14	43·0	70·0	1·70	1·27
	O5	FG4	24	150 × 200	236 (0·79)	GP (2·60)	1·18	37·5	105·9	1·71	1·48
	O6	C2	17	150 × 300	764 (1·70)	CS (0·17)	1·87	–	153·9	1·80	1·39
	O7	C3	25	200 × 150	402 (1·34)	CP (0·26)	1·52	54·0	74·9	1·51	1·20
	O8	C6	25	200 × 150	402 (1·34)	CP (0·80)	1·87	54·0	101·4	1·62	1·26
	O9	C8	25	200 × 150	402 (1·34)	GP (1·20)	2·07	54·0	86·7	1·77	1·39
	O10	B3	17	152 × 305	764 (1·70)	CS (0·11)	1·82	51·7	74·78	1·70	1·49
	O11	114	18	100 × 200	156 (0·79)	AS (0·45)	1·10	46·5	80·0	1·89	1·53

* 42-day cylinder strength.
† 28-day cylinder strength.
CP, CFRP plate; CS, CFRP sheet; AS, AFRP sheet; GP, GFRP plate.

Table 1. Failure mode, ductility and deformability indices of FRP-strengthened RC beams

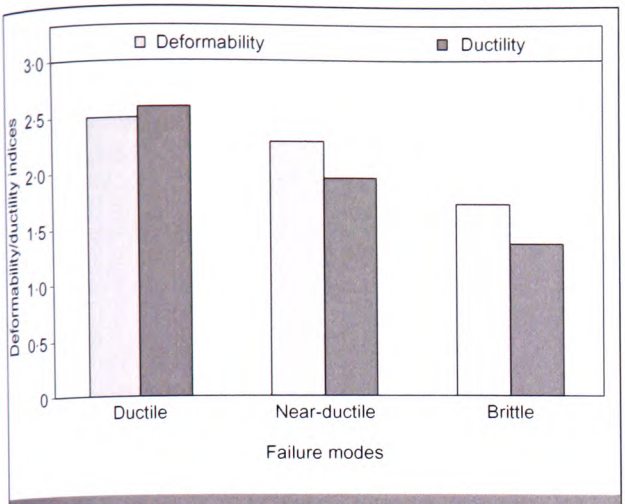

Fig. 3. Relationship between deformability/ductility indices and failure mode

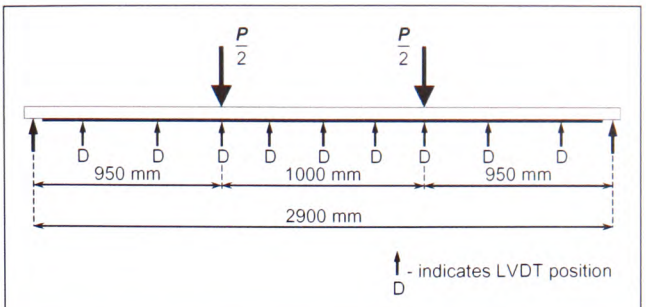

Fig. 5. Loading configuration for testing slabs

In phase 2, four simply supported RC slabs (3·0 m long by 0·5 m wide and 0·1 m overall depth) were tested. All slabs were identically reinforced with four high-yield bars of 8 mm diameter (A_s = 0·402%). One slab was used as a control (SC), one was externally bonded with three 100 mm wide CFRP fabric strips (S3), and the other two were bonded with one layer (S1) and three layers (S2) of CFRP sheets respectively, covering the full width of the slab. The load configurations of the beams and slabs are illustrated in Figs 4 and 5 respectively.

4.1. Test results of the beams

A summary of the beam test results is given in Table 2 together with the main material properties. The maximum span deflections of all beams at 95% and 67% of the ultimate load were obtained from the load–deflection curves as shown in Figs 6 and 7. Using equations (2)–(4), the deformability and ductility indices of all beams are evaluated and listed in Table 3.

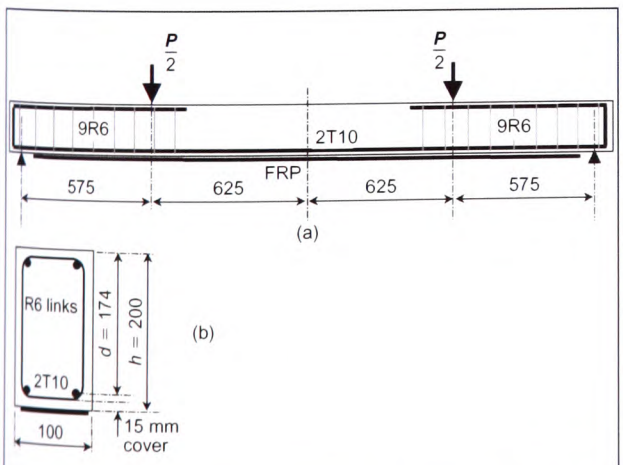

Fig. 4. Loading and reinforcement details for testing beams: (a) elevation; (b) cross-section. All dimensions in millimetres. No compression reinforcement was provided in the pure bending zone

It can be seen that, for all beams strengthened by the pultruded CFRP plates (A1–A5), the deformability index ranges from 1·57 to 1·70. This indicates that the above beams can be expected to sustain further deformation of between 57% and 70% of the corresponding values at the service load level before ultimate failure takes place. With an average deformability index of 1·65, beams A1 to A5 failed in the brittle, premature tearing-off mode. Group B beams have an average deformability index of 2·11 and failed relatively more mildly, even though concrete compression failure occurred in some of them. This reaffirms that, in order to avoid extremely brittle failure, a minimum deformability index of 2·5 is desirable (see section 3·1).

As for the state of ductility, these results clearly show that the energy-based ductility indices reflect the beam behaviour more realistically, as they take account of the unconsumed, elastic, stored strain energy at the failure stage. Upon comparison, it is apparent that the ductility index generally has a smaller value than the deformability index if the failure is of a non-ductile nature. Beams with large deformability index, such as beam B3, do not necessarily behave in a ductile manner, as the ductility index could be much lower. For all group A beams, the ductility index ranges from 1·17 to 1·32 with an average of 1·24. This relatively low figure suggests that approximately 68% of the elastic stored energy has to be released at the instant of failure, and, naturally, a brittle failure mode should be expected. It was indeed the case that all group A beams failed in an extremely brittle manner.

The single CFRP fabric layer strengthened series B beams had an average ductility index of 1·75, which was 41% higher than the group A average, and an index range of 1·32–1·97. This confirms the laboratory observations that the failures in this group of beams, as expected, had reduced brittleness compared with those of group A beams. The above characteristics can be considered as near-ductile behaviour, and the authors suggest that, for practical strengthening design purposes, a ductility index of 2·0 can be accepted as the minimum value, with 2·5 remaining as the desired value.

4.2. Test results for RC slabs

The material properties of the four test slabs are listed in Table 4, and Table 5 shows a summary of the data for the main test results. The load–deflection graphs are shown in Fig. 8.

The ultimate load-carrying capacities of the three CFRP-strengthened slabs S1, S2 and S3 increased by 165%, 458%

Beam ref.	Concrete f_{cu}: N/mm^2	Externally bonded FRP composites		Failure at ultimate limit state		
		CFRP type*	A_p: mm^2	Δ_u: mm	P_u: kN	Failure mode†
Control	43·9	n/a	n/a	31·7	48·0	SY-CC
A1‡	54·9	A	128	18·2	76·2	PTC
A2‡	44·6	A	128	18·9	73·8	PTC
A3	48·9	A	128	20·9	89·9	PTC
A4‡	49·6	A	128	19·8	74·4	PTC
A5‡	49·6	A	128	19·4	82·0	PTC
B1	36·7	D	14·5	34·8	70·0	CC
B3	44·2	D	14·5	23·0	68·4	CC
B4	31·7	C	14·5	35·4	72·5	FR-CC
B5	33·1	D	14·5	32·9	76·2	CC
B6	30·0	C	14·5	34·9	62·5	FR-CC

*CFRP type: A, 1·6 mm thick plate, UTS f_{pu} = 1500 MPa, Elastic modulus E = 125 GPa; C, 0·14 mm thick fabric sheets, f_{pu} = 1750 MPa, E = 125 GPa; D, 0·145 mm thick fabric sheets, f_{pu} = 4900 MPa, E = 230 GPa.
†Failure mode: SY-CC, steel yielding followed by concrete crushing; CC, concrete crushing; PTC, premature tearing-off of concrete cover from end of plate to centre of span; FR-CC, fibre rupture followed by concrete crushing.
‡These beams were preloaded (cracked) to service load before strengthening.

Table 2. Summary of test beams and results

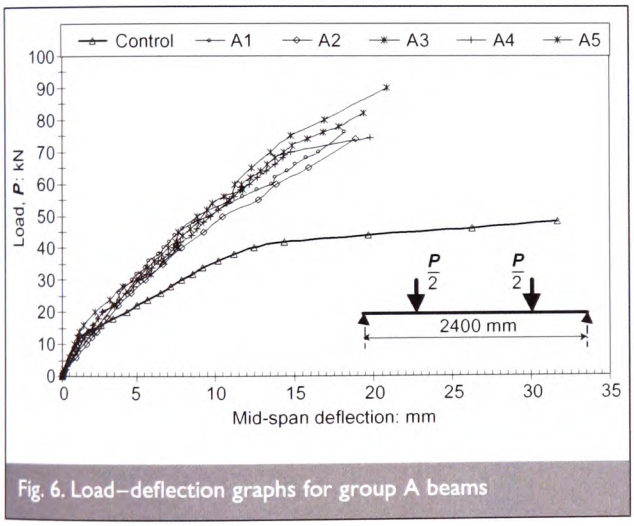

Fig. 6. Load–deflection graphs for group A beams

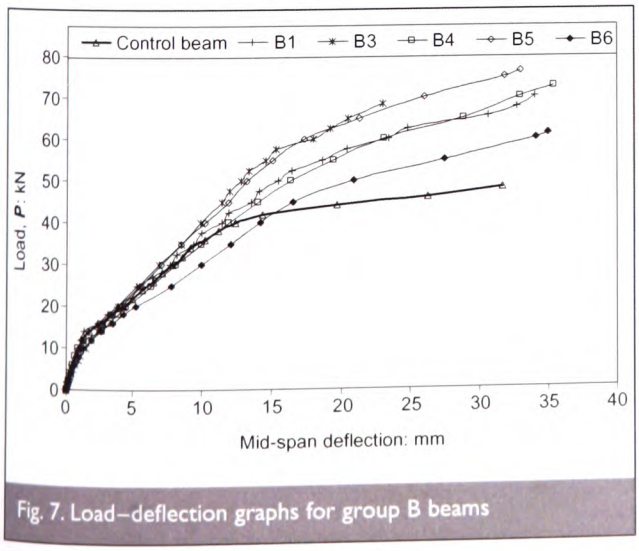

Fig. 7. Load–deflection graphs for group B beams

and 119% respectively over the control slab. It was interesting to note that, even for the over-strengthened slab S2 (ρ_{es} = 1·02%), the failure mode was much less brittle than expected. It failed by partial debonding of CFRP sheet at the slab edge, followed by gradual concrete compression failure. This was somewhat contradictory to the belief that concrete compression failure is usually sudden and brittle. Similar trends were also evident in beams B1, B3 and B5, where partial concrete compression failure took place in a near-brittle manner. Subsequent inspection of the failed slab S2 showed the development of a plastic hinge over a region of about 330 mm, or one-third the length of the constant-moment zone. This outcome was made possible by the large slab deformation (maximum central span deflection 99·8 mm) and intense cracking, which undoubtedly helped in absorbing some of the energy. The ductility index of slab S2 was found to be 1·44 (Table 7), indicating that approximately 47% of the strain energy had been dissipated in the process. The corresponding failure mode therefore, although still brittle, was less than those noted for series A beams.

Slabs S1 and S3 had a ductility index of 1·77 and 2·31 respectively. Slab S1 failed by partial rupture of CFRP sheets followed rapidly by lateral concrete shear failure. The failure mode was seen to be near-ductile. All three CFRP strips on slab S3 were fully ruptured, and the manner in which they failed was mild and ductile. A summary of the deformability and ductility indices for the beams and slabs is included in Tables 6 and 7 respectively.

5. GENERAL DISCUSSIONS

5.1. Deformability–ductility indices and failure behaviour

Table 8 shows the range of both indices related to the failure modes for the two sets of tests in the current experimental

Beam ref.	$\delta_{0.95}$: mm	δ_s: mm	ϕ_{df}	E_{tot}: kN m	E_{el}: kNm	ϕ_{du}
Control	26·3	8·6	3·10	1·129	0·249	2·77
A1	16·8	10·1	1·66	0·792	0·552	1·22
A2	17·7	10·4	1·70	0·786	0·589	1·17
A3	18·8	11·2	1·68	1·115	0·699	1·30
A4	14·9	9·5	1·57	0·910	0·557	1·32
A5	16·9	10·3	1·64	0·921	0·664	1·19
B1	31·9	13·9	2·29	1·588	0·639	1·74
B3	23·0	11·5	2·00	0·954	0·581	1·32
B4	31·2	15·3	2·04	1·778	0·619	1·93
B5	27·5	13·4	2·05	1·616	0·628	1·79
B6	32·4	15·1	2·15	1·498	0·509	1·97

Table 3. Comparison of deformability (ϕ_{df}) and ductility indices (ϕ_{du}) of all beams

Slab reference	f_{cu}: N/mm^2	Tension steel: mm^2	CFRP strength: N/mm^2	CFRP modulus, E_f: kN/mm^2	Area of CFRP: mm^2
SC – control	49·5	201	1970	235	0 (0%)
S1	45·0	201	1970	235	48 (0·096%)
S2	51·0	201	1970	235	80 (0·16%)
S3	50·0	201	1970	235	240 (0·48%)

All slabs were reinforced with 4T8 high-yield steel, with yield strength of 560 N/mm^2.

Table 4. Laboratory-evaluated material properties of RC test slabs

Slab reference	Failure load: kN	% increase over the control	Deflection at failure: mm	% reduction of the control	Failure mode
SC – control	14·40	–	120·0	–	SY*
S1	38·20	165·3	77·10	35·7	FR-CLSF
S2	80·40	458·3	99·80	16·8	PD-CC
S3	31·60	119·4	77·05	35·8	SY-FR

*The slab was deemed to have failed when maximum span deflection exceeded 120 mm, even though concrete in the compression zone had not been crushed. FR-CLSF, CFRP rupture immediately followed by concrete lateral shear failure; PD-CC, partial debonding of CFRP fabrics at slab edge followed by gradual concrete compression failure; SY-FR, steel yielding and rupture of all CFRP strips.

Table 5. Summary of main slab test results

programme, together with those of the beams reviewed in section 3. It is clear that, for a ductile failure of an FRP-strengthened member, the deformability and ductility indices tend to have similar values, ranging from 1·93 to 2·59. As the failure behaviour becomes more brittle, both sets of indices decrease, with the minimum ductility index recorded to be 1·24 in the current tests. However, the deformability index decreases more slowly, as the strengthened system retains the ability to deform, even with large areas of FRP composites present. This is due to the generally large strain capacities of the FRP composites.

5.2. Relationship between deformability and ductility

The ratio of deformability to ductility index, λ, was found to be closely related to the failure mode. For the 26 beams reviewed in section 3 it is seen to approach (but remain slightly less than) unity for a ductile failure. As the ratio λ increases, the failure mode becomes progressively more brittle. The same is valid for the beams and slabs tested in the current study. Table 9 shows a summary of failure modes relating to the λ ratio. The differences between the deformability and ductility indices become more apparent as the elastic stored energy in the strengthened system increases. This clearly shows that high deformability is a necessary but not a sufficient condition for ductile behaviour. When the value of λ reaches 1·28, and the deformability index is relatively low—say, less than 2—then a brittle failure mode can be expected.

5.3. Relationship between total amount of reinforcement and failure modes

It appears that the extent of brittle failure characteristics becomes greater with the increase in area of external FRP

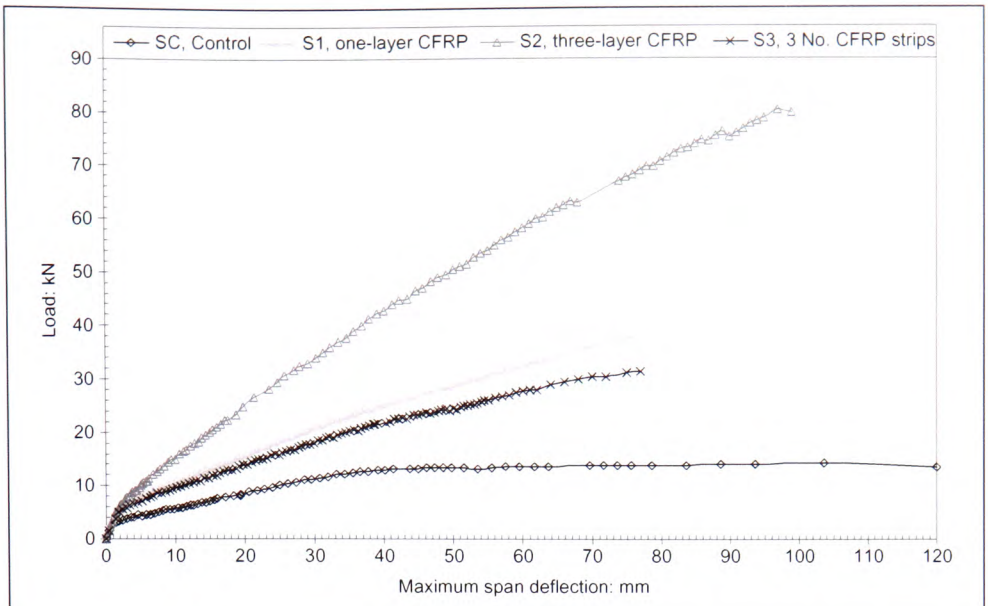

Fig. 8. Load–deflection graphs for RC slabs

Beam ref.	ϕ_{df}	ϕ_{du}	Failure characteristic
Control beam ($\rho_f = 0\%$)	3·10	2·77*	Ductile
A beams (over-strengthened, $\rho_f = 0{\cdot}64\%$)	1·65	1·24	Extremely brittle
B1, B3, B5 (under-strengthened, $\rho_f = 0{\cdot}073\%$)	2·11	1·62	Near-ductile
B4, B6 (under-strengthened, $\rho_f = 0{\cdot}073\%$)	2·09	1·95	Ductile

*The beams were tested under load-control configurations; the ductility index for the control beam could have been around four times higher if displacement control test regime had been used.

Table 6. Comparison of average deformability and ductility indices of RC beams

Slab ref.	ϕ_{df}	ϕ_{du}	Failure characteristic
SC (control slab, $\rho_f = 0\%$)	3·05	5·41*	Ductile
S1 (near balanced, $\rho_f = 0{\cdot}16\%$)	1·81	1·77	Near-ductile
S2 (over-strengthened, $\rho_f = 0{\cdot}48\%$)	1·75	1·44	Brittle
S3 (under-strengthened, $\rho_f = 0{\cdot}096\%$)	1·93	2·31	Ductile

*This value has been calculated based on 95% of the ultimate load, i.e. 13·68 kN with the corresponding deflection of 58·00 mm, which is 1/50th of the effective span. Had the full load–deflection curve been used, the ductility index of the control slab would have been 13.

Table 7. Comparison of deformability and ductility indices of RC slabs

composites. Shown in Fig. 9 is the proportion of elastic deformation of the slabs in the current study plotted against the increase of FRP ratio. The elastic (recoverable) deflections of the four slabs were recorded immediately after slab failure. It is clear that with slab S2, which has an FRP ratio of 0·48%, the elastic deformation is 78% of the total. The ductility index of 1·44 (Table 7) indicated 53% of elastic stored energy. This slab was seen to behave in the most brittle manner of the four slabs.

5.4. Summary of discussions

The review of the 26 beams, as well as the results of current tests of beams and slabs, indicates that FRP-strengthened flexural elements, whether plated or strengthened by fabric sheets, are not able to attain the ductility level of the original unstrengthened forms. However, suitably designed elements can possess acceptable ductile characteristics, as demonstrated.

It is important to distinguish between deformability and

Failure mode at ultimate limit state	Current experimental ϕ_{df}	Current experimental ϕ_{du}	Determined from review ϕ_{df} (Table 1 average)	Determined from review ϕ_{du} (Table 1 average)
Ductile	>1·93–2·09	>1·95–2·31	2·50	2·59
Near-ductile	1·81–2·11	1·62–1·77	2·27	1·94
Brittle	1·65–1·75	1·24–1·44	1·71	1·35

Table 8. Correlation between failure mode and deformability/ductility indices

Failure mode at ultimate limit state	Current experimental $\lambda = \phi_{df}/\phi_{du}$	Determined from review $\lambda = \phi_{df}/\phi_{du}$	Average $\lambda = \phi_{df}/\phi_{du}$
Ductile	0·94	0·97	0·96
Near-ductile	1·16	1·17	1·17
Brittle	1·28	1·27	1·28

Table 9. Correlation between failure mode and deformability/ductility ratio

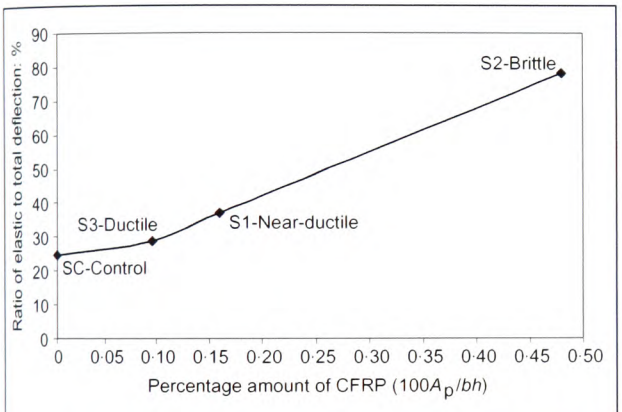

Fig. 9. Variation of elastic deformation with the increase of CFRP area

ductility indices. High deformability is a prerequisite, rather than a sufficient condition, for good ductile characteristics. Ductile elements possess high deformability, but members with high deformability alone could still fail in a very brittle manner. Nevertheless, high deformability does provide some warning, in that large elastic deformations may be observed before ultimate failure and, in order to achieve good ductility, deformability must first be ensured.

One argument against using a ductility index for an FRP-strengthened beam was presented by DiTommaso *et al.*[22] They reasoned that it should be solely the amount of inelastic energy that is used to quantify ductility, and that the proportion of elastic energy to total energy is not important. In principle this is correct, but it would be impractical to compare and determine which element is more ductile without the provision of the ductility indices for all members. It must also be emphasised that the absolute value of the deformability or ductility index is less significant than the relative comparison with that of an unstrengthened member. However, as demonstrated earlier, the deformability index gives an indication of how much further the deformation can develop after the serviceability limit, and before ultimate failure occurs. Similarly, the ductility index should give a clear indication of the proportion of elastic energy at the time of member failure: the higher the amount of elastic stored energy, the more brittle the failure will be.

The present proposed concept of a deformability index seems to be pertinent for application to FRP-strengthened RC beams. The main advantage of this method is its design-based approach and ease of use. The deformability values also clearly indicate the scope for possible additional deformation after exceeding the service load but before reaching the ultimate failure condition. Both the ductility and the deformability of FRP-strengthened members are influenced by a number of factors. Although confinement of concrete in compression does improve the ductility of FRP-strengthened RC beams, the major influencing parameters are the material properties and cross-sectional area of the strengthening FRP composites, and the properties of the elements to be strengthened.

Based on the observations from current laboratory tests, it can be concluded that RC sections under-strengthened by FRP composites possess far better deformability and ductility behaviour than over-strengthened beams. There are also strong practical reasons for not over-strengthening, owing to the risk of accidental damage to FRP materials in service. Over-strengthening should therefore be avoided whenever possible. However, it must be stressed that the present study has dealt only with simply supported flexural members. For statically indeterminate beams and slabs the level of ductility will significantly affect the amount of moment redistribution. The methods for quantifying deformability and ductility outlined in the current paper are still applicable to continuous beams, although they become more complex in estimating the values of deformation for such members. Initial test results of four large-scale continuous RC beams[21] indicate that full plastic hinges could not be developed in sections over-strengthened

with FRP composites, because the ultimate strength of the FRP composites could not be reached in these beams. It is therefore essential for designers to incorporate an appropriate level of ductility in FRP-strengthened flexural systems, whether they are simply supported or continuous members. The authors are currently undertaking further studies to correlate suitable ductility levels with the strengthening design procedures. This involves mainly the optimisation of the amount of FRP materials to be used, the material properties and the realistic levels of strength enhancement. The results of the study will be published as a continuation to this paper.

6. CONCLUSIONS

The differences between ductility and deformability characteristics of FRP-strengthened flexural elements have been examined in this paper, through the analysis of published data and the experimental results of the current study. A new method of quantifying deformability has been proposed, together with an appropriate energy-based ductility index, which was found to be the most suitable for FRP-strengthened flexural RC elements. Based on the numerical and experimental evidence, the following conclusions can be drawn.

(*a*) The three distinct failure characteristics of FRP-strengthened flexural elements—ductile, near-ductile and brittle failure modes—are inextricably linked to well-defined ductility and deformability indices.
(*b*) Over-strengthening, due to the provision of large area of FRP composites, is seen to lead to high deformability but low ductility. Consequently the strengthened members are likely to fail in a brittle manner at ultimate limit state.
(*c*) FRP-strengthened RC slabs or other elements with light internal steel reinforcement generally exhibit more ductile behaviour.
(*d*) High deformability is a necessary but not sufficient prerequisite for ductile behaviour.
(*e*) For ductile failure, the deformability and ductility indices will converge to similar values. As the ratio of deformability to ductility increases, the failure mode becomes more brittle.
(*f*) For a ductile failure mode in an FRP-strengthened flexural member, the minimum ductility index should be 2·0, whereas the desirable value is 2·5 or greater. The FRP strengthening design equations, therefore, should be derived to meet this criterion.

7. ACKNOWLEDGEMENTS

The current work forms part of an ongoing project supported by the EPSRC under grant number GR/R91397/01. All FRP materials and adhesives used in the experimental study were provided by Exchem Mining and Construction (UK) Ltd. The authors also wish to thank Dr E. Andreou for allowing parts of experimental data to be cited, and the University of Glamorgan directorate and School of Technology management for allowing maximum resources to be allocated for commencement and progression of the project.

REFERENCES

1. Clarke J. L. (ed.) *Alternative Materials for the Reinforcement and Prestressing of Concrete*, Blackie, Glasgow, 1993.
2. Saadatmanesh H. and Malek A. M. Design guidelines for flexural strengthening of RC beams with FRP plates. *ASCE Journal of Composites for Construction*, 1998, 2, No. 4, 158–164.
3. Naamam A. E. and Jeong S. M. Structural ductility of concrete beams prestressed with FRP tendons. *Proceedings of the 2nd International RILEM Symposium (FRPRCS-2), Ghent*, 1995, 379–384.
4. Grace N. F., Soliman A. K., Abdel-Sayed G. and Saleh K. R. Behaviour and ductility of simple and continuous FRP reinforced beams. *ASCE Journal of Composites for Construction*, 1998, 2, No. 4, 186–194.
5. Razaqpur G. A. and Ali M. M. Ductility and strength of concrete beams externally reinforced with CFRP sheets. *Proceedings of an International Conference on Advanced Composite Materials in Bridges and Structures*, Montreal, 1996, pp. 505–512.
6. Aridome Y., Kanakubo T., Furuta T. and Matsui, M. Ductility of T-shaped beams strengthened by CFRP sheets. *Proceedings of Japan Concrete Institute*, 1998, 20, 117–124.
7. Pisanty A. and Regan P. E. Ductility requirements for redistribution of moments in reinforced concrete elements and a possible size effect. *Materials and Structures*, 1968, 31, No. 212 530–535.
8. Grace N. F., Abdel-Sayed G., Soliman A. K. and Saleh K. R. Strengthening reinforced concrete beams using fibre reinforced polymer (FRP) laminates. *ACI Structural Journal*, 1999, 96, No. 5, 865–874.
9. Kemp A. R. The achievement of ductility in reinforced concrete beams. *Magazine of Concrete Research*, 1998, 50, No. 2, 123–132.
10. Lees J. M. *Flexure of Concrete Beams Pre-tensioned with Aramid FRPs*. PhD thesis, University of Cambridge, 1997.
11. British Standards Institution. *Structural Use of Concrete: Code of Practice for Design and Construction*. BSI, Milton Keynes, 1997, BS 8110.
12. Concrete Society. *Design Guidelines for Strengthening Concrete Structures Using Fibre Composite Materials*. Concrete Society, Crowthorne, 2000, Technical Report No. 55.
13. American Concrete Institute. *State-of-the-art Report on Fibre Reinforced Plastic (FRP) Reinforcement for Concrete Structures*. ACI, Detroit, 1996, Committee 440R-96,
14. Davies P., Delpak R. and Tann D. B. *Review of Ductility Determination of FRP Strengthened Concrete Structures*. University of Glamorgan, Pontypridd, 2002, Internal Report.
15. Bencardino F., Spadea G. and Swamy N. Strength and ductility of reinforced concrete beams externally reinforced with carbon fibre fabric. *ACI Structural Journal*, 2002, 99, No. 2, 163–171.
16. Chajes M. J., Thomson T. A. and Tarantino B. Reinforcement of concrete structures using externally bonded composite materials. *Proceedings of the 2nd International RILEM Symposium (FRPRCS-2), Ghent*, 1995, 501–508.
17. Tumialan G., Serra P., Nanni A. and Belarbi A. Concrete cover delamination in RC beams strengthened with CFRP sheets. *Proceedings of the 4th International Symposium on FRP for Reinforcement of Concrete Structures (FRPRCS-4), Baltimore*, 1999, 725–735.
18. Andreou E. *Performance Evaluation of RC Flexural*

Elements Strengthened by Advanced Composites. PhD thesis, University of Glamorgan, Pontypridd, 2002.
19. AHMED O., VAN GEMERT D. and VENDEWALLE L. Improved model for plate-end shear of CFRP strengthened RC beams. *Cement and Concrete Composites*, 2001, **23**, 3–19.
20. SPADEA G., SWAMY R. N. and BENCARDINO F. Strength and ductility of RC beams repaired with bonded CFRP laminates. *Journal of Bridge Engineering*, 2001, **6**, No. 5, 349–355.
21. TANN D. B. *Retrofitting of Mechanically Degraded Concrete Structures using Fibre Reinforced Polymer Composites*. PhD thesis, University of Glamorgan, Pontypridd, 2001.
22. DITOMMASO A., FOCACCI F. and FORABOSCHI P. Driven failure mechanisms in fibre-reinforced-plastic prestressed concrete beams for ductility requirements. *Proceedings of an International Conference on Advanced Composite Materials in Bridges and Structures*, Montreal, 1996, pp. 281–288.
23. PELHERBE E. *Repair and Strengthening of Concrete Structures*. MSc thesis, University of Glamorgan, Pontypridd, 2001.
24. ALMUSALLAM T. H. and AL-SALLOUM Y. A. Ultimate strength prediction for RC beams externally strengthened by composite materials. *Composites: Part B*, 2001, **320**, No. 7, 609–619.
25. RAHIMI H. and HUTCHINSON A. Concrete beams strengthened with externally bonded FRP plates. *Journal of Composites for Construction*, 2001, **5**, No. 1, 44–56.
26. TRIANTAFILLOU T. C. and PLEVRIS N. Strengthening of RC beams with epoxy-bonded fibre-composite materials. *Materials and Structures*, 1992, **25**, 201–211.

Please email, fax or post your discussion contributions to the secretary by 1 August 2004: email: daniela.wong@ice.org.uk; fax: +44 (0)20 7799 1325; or post to Daniela Wong, Journals Department, Institution of Civil Engineers, 1–7 Great George Street, London SW1P 3AA.

Appendix A-2

CONFERENCE PAPER

"A review of ductility determination of FRP strengthened flexural RC elements"

Proceedings of the Sixth International Symposium on FRP Reinforcement for Concrete Structures (FRPRCS-6)
Singapore, 2003

A REVIEW OF DUCTILITY DETERMINATION OF FRP STRENGTHENED FLEXURAL RC ELEMENTS

D. B. TANN, P. DAVIES and R. DELPAK

School of Technology, University of Glamorgan
Pontypridd, CF37 1DL, United Kingdom

A comparative study has been undertaken in order to determine the suitability of existing ductility evaluation methods when applied to RC elements strengthened with Fibre Reinforced Polymers. The comparison will involve considering a number of criteria such as a) consistency of prediction; b) volatility of data; c) ease of application in practical cases and d) Accuracy of prediction.

It is shown that the indices calculated for brittle members can have variations when using the existing methods. It is also seen that there is a discernible reduction in deformation based indices in comparison to energy based ones. It is therefore proposed that a revised deformability method is examined, utilising the deformations at serviceability load (P_s) and 95% of ultimate load ($P_{0.95u}$).

KEYWORDS

FRP, composites, flexure, ductility, deformability, brittleness, structural design.

INTRODUCTION

General Comments

The consideration of structural ductility is of predominant importance to all structural designers, as all appropriately designed structures must attain sufficient ductility, under ultimate loads, to provide adequate warning of failure and prevent sudden and brittle collapse.

The concept is particularly applicable to RC beams and slabs and to prestressed concrete elements. During many experiments in RC beam strengthening due to steel plate bonding, it became apparent that sudden peeling of the plates was one of the main causes of failure. This unpredictable characteristic has many similarities with RC beam strengthening using other materials such as Fibre Reinforced Polymers (FRPs).

From a practical and commercial viewpoint, there are ample cases where it may become necessary to strengthen a reinforced concrete member. Historically, this has been achieved using section enlargement or, more recently, by attaching steel plates to the tension surface. Over the past decade, FRPs have increasingly been used in place of steel plates but engineers have been hesitant in deploying this method of strengthening, mainly due to the uncertainty of sudden failure. It is recognised that FRP strengthened, reinforced concrete elements behave differently from their steel reinforced counterparts, due to the primarily linear elastic stress-strain characteristics of composites up to failure.

In this paper, the ductility or deformability indices from 55 beams (from published experimental data), which are listed in Table 1, have been calculated and studied using selected methods. All methods gave markedly different sets of results for each particular beam. Also, each method gave a wide range of indices for beams that failed in a brittle manner.

Aims

The overall aim of the study is to develop a method of determining the ductility or deformability index of any structural element strengthened with FRP. Firstly, a review will be carried out of the current methods of calculating the ductility index of structural elements. Ultimately, it is intended to develop a semi-automatic method of analysing experimental and theoretical Load/Deflection or Moment/Curvature data to determine indices.

REVIEW OF CURRENT LITERATURE

The question of ductility for FRP reinforced concrete elements has been a topic of considerable debate among researchers [1,2,3,4,5]. It has generally been accepted that ductility can be measured by a dimensionless factor, i.e. a 'ductility index', which can be calculated in several different forms from two broader categories:

Deformation Based Methods

i) Deflection ductility: $$\mu_{\Delta} = \frac{\Delta_u}{\Delta_y} \qquad (1)$$

where Δ_u is the ultimate maximum deflection of a member and Δ_y is the value where the steel reinforcement reaches its yield strength.

ii) Curvature ductility: $$\mu_{\Phi} = \frac{\Phi_u}{\Phi_y} \quad (2)$$

where Φ_u is the curvature in the constant moment region at ultimate load and Φ_y is the curvature in the constant moment region at the steel reinforcement yield point.

As can be seen for both methods, an important deformation point to ascertain is the steel reinforcement yield point. Due to the nature of FRP strengthened elements to perform in a primarily elastic manner, this cannot easily be identified, as illustrated in Fig 1. Consequently, it is apparent that the above, conventional methods of calculating ductility indices may not be considered as appropriate for FRP strengthened elements.

Energy Based Methods

i) For energy based calculations: $$\mu_{E1} = \frac{E_u}{E_y} \quad (3)$$

where E_u is the area under the Load/Deflection curve at failure and E_y is the area under the Load/Deflection curve at the steel reinforcement yield point.

ii) Another set of energy calculations are given by:

$$\mu_{E2} = \frac{1}{2}\left(\frac{E_{tot}}{E_{el}} + 1\right) \quad (4)$$

where E_{tot} is the total energy, calculated as the area under the load-deflection curve up to the failure load and E_{el} is the elastic energy.

This method was first published by Naaman and Jeong (1995) but there are practical difficulties in identifying the elastic stored energy. Consequently, Naaman and Jeong suggested that the elastic energy could be estimated using an equivalent triangle area under the load-deflection curve, with the slope of the estimated unloading line determined using the following equation (see also Fig. 2):

$$S = \frac{P_1 S_1 + (P_2 - P_1) S_2}{P_2} \quad (5)$$

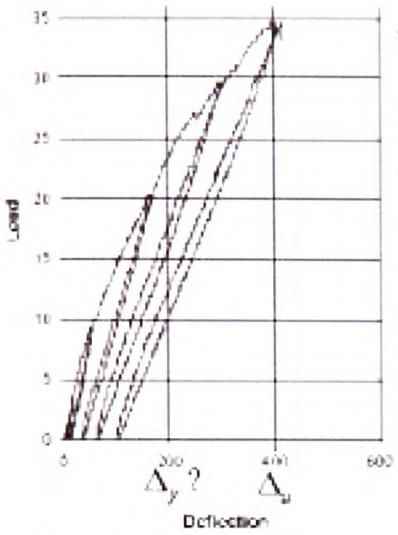

Figure 1. Diagram illustrating difficulty of ascertaining steel yield point for FRP strengthened elements[6]

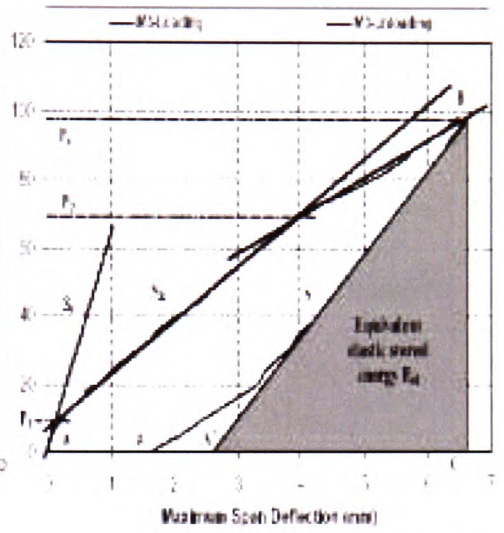

Figure 2. Example of calculation of equivalent elastic stored energy[7]

EVALUATION OF EXISTING METHODS

Experimental results from a number of published sources were used to evaluate the effectiveness of the various methods of determining ductility indices. The element data is presented in Table 1, with the calculated indices and failure modes listed in Table 2.

The values of indices from Deflection 1, Energy 1 and Energy 2 methods, for members that had exhibited a 'brittle' failure mode, were analysed to determine whether there was an apparent trend in the calculated values, together with an index based on the serviceability load[11].

This index was proposed by Tann[7], as FRP strengthened elements, when analysed using conventional methods, produce what appear to be acceptable ductility indices. However, the elements normally fail in a 'brittle' manner because the relatively large deformation is not inelastic and a large amount of elastic strain energy is stored in the strengthened beams at failure. Consequently, a more appropriate description, 'deformability index', was proposed and is defined in Eqn. (6).

Table 1. Element Data

Beam No.	Beam size (mm)	Int'l flexural reinf't	%age Int'l flex. reinf't	FRP type ★	No. of layers	FRP as %age of total x-sectional area	Concrete Strength (N/mm2)	End anch.	Loading configuration	Failure load (kN)
1A	140 x 300	2Ø16mm	0.96	C, F	2 x 200 mm wide sheets, 60mm overlap underneath and wrapped 100mm up sides	0.41	35.4 (28 day Cyl)	N	4-Point loading ↑ 1800 ↓ 1200 ↓ 1800 ↑	101.26
1B	140 x 300		0.96	C, F	4 x 200 mm wide sheets, 60mm overlap underneath and wrapped 100mm up sides	0.82	36.7 (28 day Cyl)	Y		133.09
1C	140 x 300		0.96	C, F	2 x 200 mm wide sheets, 60mm overlap underneath and wrapped 100mm up sides	0.41	21.0 (28 dayCyl)	N		90.03
1D	140 x 300		0.96	C, F	4 x 200 mm wide sheets, 60mm overlap underneath and wrapped 100mm up sides	0.82	21.9 (28 day Cyl)	Y		102.29
2A	150 x 200	3Ø10mm	0.79	G, P	1	1.52	37.5 (85 day Cyl)	N	4-Point loading ↑ 925 ↓ 200 ↓ 925 ↑	70.40
2B	150 x 200		0.79	G, P	2	3.03	37.5 (85 day Cyl)	N		82.40
2C	150 x 200		0.79	G, P	4	6.07	37.5 (85 day Cyl)	N		105.90
2D	150 x 200		0.79	C, P	1	1.17	37.5 (85 day Cyl)	N		81.90
2E	150 x 200		0.79	C, P	2	2.33	37.5 (85 day Cyl)	N		103.10
3A	100 x 100	3 x No.R6 (Ø19mm)	8.51	G, P	1 - 80mm wide	1.76	70.0 (Cube)	N	4-Point loading ↑ 300 ↓ 300 ↓ 300 ↑	47.20
3B	100 x 100		8.51	G, P	1 - 80mm wide	1.76	42.0 (Cube)	N		36.70
3C	100 x 100		8.51	G, P	1 - 30mm wide	2.56	58.0 (Cube)	N		24.60
3D	100 x 100		8.51	G, P	1 - 60mm wide	2.56	59.0 (Cube)	N		35.00
4A	152 x 292	2Ø16mm	0.91	C, P	1 (Bottom only)	0.45	48.3	N	3-Point loading ↑ 1371.5 ↓ 1371.5 ↑	110.30
4B	152 x 292		0.91	C, P	1 (Bottom + 1/4 sides)	0.81	48.3	N		105.87
4C	152 x 292		0.91	C, P	1 (Bottom + 1/2 sides)	1.30	48.3	N		113.88
5A	100 x 150	3Ø8mm	1.01	C, P	1 (Bottom and 50mm wrap on vertical sides)	0.17	35.5 (28 day Cyl)	N	3-Point loading ↑ 1125 ↓ 1125 ↑	21.00
5B	100 x 150		1.01	C, P	2 (Bottom and 50mm wrap on vertical sides)	0.33	35.5 (28 day Cyl)	N		24.50
6A	100 x 200	2T10	0.79	C, P	1	0.80	47.73 (fcu)	N	4-Point loading ↑ 575 ↓ 1250 ↓ 575 ↑	76.20
6B	100 x 200		0.79	C, P	1	0.80	42.54 (fcu)	N		90.00
6C	100 x 200		0.79	C, P	1	0.70	35.92 (fcu)	N		70.00
6D	100 x 200		0.79	C, P	1	0.70	42.61 (fcu)	N		68.30
6E	100 x 200		0.79	C, F	1	0.70	27.10 (fcu)	N		76.00
6F	100 x 200		0.79	C, F	1	0.70	29.52 (fcu)	N		61.18
6G	100 x 200		0.79	G, P	1	0.70	42.61 (fcu)	N		67.33
7A	127 x 76.2	1 x No.3 (Ø9.5mm)	0.73	A, F	1	1.37	37.8 (28 day)	Y	4-Point loading ↑ 406.4 ↓ 304.8 ↓ 406.4 ↑	16.89
7B	127 x 76.2		0.73	G, F	3	1.86	37.8 (28 day)	Y		15.38
7C	127 x 76.2		0.73	C, F	2	1.60	37.8 (28 day)	Y		14.49
8A	125 x 225	3Ø8mm	0.54	C, S	1	0.05	42.0 (42 day Cyl)	N	4-Point loading ↑ 500 ↓ 500 ↓ 500 ↑	121.10
8B	125 x 225		0.54	C, S	2	0.09	42.0 (42 day Cyl)	N		121.70
8C	125 x 225		0.54	C, S	4	0.18	40.5 (42 day Cyl)	N		126.70
9A	140 x 300	2Ø16mm	0.96	C, P	1	0.23	34.3 (Cube)	N	4-Point loading ↑ 1800 ↓ 1200 ↓ 1800 ↑	86.80
9B	140 x 300		0.96	C, P	1	0.23	29.0 (Cube)	Y		98.00
9C	140 x 300		0.96	C, P	1	0.23	29.0 (Cube)	Y		96.70
9D	140 x 300		0.96	C, P	1	0.23	37.8 (Cube)	Y		75.00
9E	140 x 300		0.96	C, P	1	0.23	33.2 (Cube)	Y		77.70
9F	140 x 300		0.96	C, P	1	0.23	35.6 (Cube)	N		74.80
9G	140 x 300		0.96	C, P	1	0.23	29.6 (Cube)	Y		98.80
9H	140 x 300		0.96	C, P	1	0.23	30.5 (Cube)	Y		98.30
10A	127 x 76.2	1 x No.3 (Ø9.5mm)	0.73	C, P	1 (Bottom only)	0.14	38.5 (28 day Cyl)	N	4-Point loading ↑ 406.4 ↓ 304.8 ↓ 406.4 ↑	21.80
10B	127 x 76.2		0.73	C, P	2 (one sheet on bottom only and second sheet 'U' wrapped)	0.46	41.9 (28 day Cyl)	Y		21.80
10C	127 x 76.2		0.73	C, P	3 (two sheets on bottom only and third sheet 'U' wrapped)	0.61	47.6 (28 day Cyl)	Y		34.40
11A	152.4 x 304.8	4 x No.5 (Ø16mm)	1.73	C, P	1 (150mm wide)	0.05	51.71	N	3-Point loading ↑ 1066.8 ↓ 1066.8 ↑	146.35
11B	152.4 x 304.8		1.73	C, P	2 (150mm wide)	0.11	51.71	N		169.03
11C	152.4 x 304.8		1.73	C, P	3 (150mm wide)	0.16	51.71	N		171.70
11D	152.4 x 304.8		1.73	C, P	3 (partially 'U' wrapped)	0.79	51.71	Y		195.72
11E	152.4 x 304.8		1.73	C, P	3 (totally 'U' wrapped)	0.79	51.71	Y		211.29
11F	152.4 x 304.8		1.73	C, P	1 (75mm wide)	0.03	51.71	N		143.23
11G	152.4 x 304.8		1.73	C, P	2 (75mm wide)	0.06	51.71	N		170.28
11H	152.4 x 304.8		1.73	C, P	6 (75mm wide)	0.16	51.71	N	3-Point loading ↑ 1981.2 ↓ 1981.2 ↑	195.99
11I	152.4 x 304.8		1.73	C, P	1 (150mm wide)	0.05	51.71	N		81.76
11J	152.4 x 304.8		1.73	C, P	1 (75mm wide)	0.03	51.71	N		61.74
11K	152.4 x 304.8		1.73	C, P	2 (75mm wide)	0.06	51.71	N		74.78
11L	152.4 x 304.8		1.73	C, P	1 (150mm wide)	0.05	51.71	N	3-Point loading (7ft span) ↑ 1066.8 ↓ 1066.8 ↑	154.35
11M	152.4 x 304.8		1.73	C, P	2 (150mm wide)	0.11	51.71	N		153.91

* FRP Type: C - Carbon, A - Aramid, G - Glass; P - Plate, F - Fabric

Table 2. Calculated Indices and Modes of Failure

Beam No.	Deflection (1) $\mu_{\Delta 1}$	Deflection (2) $\mu_{\Delta 2}$	Curvature μ_{Φ}	Energy (1) μ_{E1}	Energy (2) μ_{E2}	Failure Mode
1A	2.99 *(2.93)*	2.74	*(5.13)*	5.78 *(5.84)*	1.80	Shear cracks extended to the load points and the CF fabric peeled away from the vertical sides. Failure occurred due to yielding of the tension steel and compressive concrete crushing
1B	2.94 *(2.87)*	2.31	*(2.89)*	5.91 *(6.00)*	1.75	Rupture of the CFRP fabric where the end anchorage stopped
1C	2.99 *(3.02)*	2.72	*(3.56)*	5.92 *(6.42)*	1.72	Shear cracks extended to the load points and the CF fabric peeled away from the vertical sides. Failure occurred due to yielding of the tension steel and compressive concrete crushing
1D	2.02 *(1.99)*	2.10	*(2.31)*	3.43 *(3.42)*	1.35	As concrete in compression zone began to crush, CF fabric debonded from vertical sides
2A	3.94	2.75	-	7.81	3.09	All beams failed with crushing of concrete at top after considerable flexural cracking and yielding of the steel
2B	2.67	2.26	-	4.90	1.83	
2C	2.25	1.97	-	4.02	1.48	
2D	2.78	2.29	-	5.19	2.48	
2E	2.22	2.17	-	3.78	1.90	
3A	2.77	2.54	-	5.42	1.44	Failure at adhesive concrete interface
3B	1.80	2.22	-	2.80	0.85	Plate and concrete cover separation
3C	2.73	3.33	-	5.07	1.45	Plate separation
3D	2.00	2.27	-	3.38	1.24	Plate and concrete cover separation
4A	2.13	2.46	-	4.94	2.02	All three beams failed in tension with a horizontal shear failure in the concrete near the CFRP plates. There was no delamination or fibre rupture.
4B	1.72	2.04	-	3.34	1.68	
4C	2.15	2.43	-	4.71	1.90	
5A	-	-	4.63	-	-	Crushing of compressive concrete.
5B	-	-	2.10	-	-	Crushing of compressive concrete/detachment of CFRP sheet at ultimate load.
6A	2.43	1.86	-	4.63	1.38	Premature tearing-off
6B	1.42	1.84	-	1.83	1.31	Premature tearing-off
6C	2.11	2.37	2.10	3.19	2.02	Shear failure
6D	1.51	1.97	1.54	2.04	1.32	Concrete crushing
6E	2.17	2.39	2.17	3.47	1.79	CFRP failure followed by concrete crushing
6F	2.10	2.40	2.10	3.28	1.79	Crushing of concrete
6G	2.17	2.69	2.13	3.30	2.10	Debonding of GFRP (although the start of tearing-off was evident)
7A	2.96	3.44	-	5.13	2.48	Concrete crushing
7B	2.11	2.56	-	3.35	1.64	Fabric tensile failure
7C	2.14	2.70	-	3.33	1.89	Fabric tensile failure
8A	2.94	3.48	-	4.79	2.78	Flexure due to yielding of internal steel and rupture of CFRP laminate
8B	2.26	2.52	-	3.48	2.24	Concrete cover delamination
8C	1.78	2.00	-	2.56	1.68	Laminates end shear
9A	2.11 *(1.5)*	1.95	1.74 *(1.5)*	3.06 *(1.9)*	1.10	Explosive debonding of the CFRP plate
9B	4.34 *(4.3)*	3.66	2.75 *(2.9)*	10.14 *(9.5)*	2.45	Debonding of CFRP plate
9C	3.74 *(3.5)*	2.92	3.19 *(4.0)*	8.82 *(7.6)*	1.91	Gradual slip and debonding of the CFRP plate
9D	*(4.80)*	-	*(3.00)*	*(13.20)*	-	Gradual debonding and slippage of CFRP plate
9E	*(5.80)*	-	*(4.00)*	*(16.10)*	-	Gradual debonding and slippage of CFRP plate, concrete crushing, local damage to carbon fibers
9F	*(2.00)*	-	*(2.20)*	*(3.20)*	-	Sudden loss of capacity, explosive debonding of CFRP plate
9G	*(4.50)*	-	*(3.30)*	*(10.90)*	-	Debonding of external anchorages
9H	*(3.80)*	-	*(4.90)*	*(8.40)*	-	Gradual slip of CFRP plate
10A	2.08	2.16	-	3.15	2.15	Concrete shear failure - noted that full capacity of flexural reinforcement was not reached although strain readings just prior to failure were 0.14mm/mm, just below the ultimate strain capacity of 0.15mm/mm
10B	2.39	2.39	-	4.03	1.74	Failure of CFRP
10C	3.30	2.97	-	6.41	2.12	Failure of CFRP
11A	3.66 *(3.4)*	4.24	-	6.56	4.43	Concrete cover delamination, starting from one of the intermediate flexural cracks between the outermost crack and the maximum bending zone.
11B	2.83 *(2.1)*	3.00	-	4.77	2.70	Concrete cover delamination, starting from one of the intermediate flexural cracks between the outermost crack and the maximum bending zone.
11C	2.12 *(1.9)*	2.48	-	3.20	2.12	Concrete cover delamination starting at the ends of the CFRP sheets.
11D	2.86 *(2.2)*	2.86	-	5.20	2.24	Concrete cover delamination, starting from one of the intermediate flexural cracks between the outermost crack and the maximum bending zone.
11E	2.96 *(2.6)*	2.46	-	5.52	2.14	Concrete cover delamination
11F	2.88	3.50	-	4.83	2.90	Concrete cover delamination, starting from one of the intermediate flexural cracks between the outermost crack and the maximum bending zone.
11G	2.51	3.01	-	3.89	3.27	Concrete cover delamination, starting from one of the intermediate flexural cracks between the outermost crack and the maximum bending zone.
11H	2.99	2.50	-	5.36	2.46	Concrete cover delamination starting at the ends of the CFRP sheets.
11I	1.81	2.28	-	2.61	1.76	Concrete crushing
11J	1.59	2.28	-	2.09	1.83	CFRP rupture
11K	1.47	1.88	-	1.90	1.49	Concrete crushing
11L	2.01	2.86	-	2.89	2.22	Concrete cover delamination, starting from one of the intermediate flexural cracks between the outermost crack and the maximum bending zone.
11M	1.80	2.04	-	2.69	1.39	Concrete cover delamination starting at the ends of the CFRP sheets.

Note that figures in parentheses and italics are from the associated published paper, all other values are calculated

Table 3. Comparison of various methods of calculating ductility index

Method		*Mean*	*High*	*Low*	*Stan. dev. σ*
$\mu_{\Delta 1}$	Δ_u / Δ_y	2.45	4.32	1.42	0.65
$\mu_{\Delta 2}$	Δ_u / Δ_s	2.55	4.24	1.84	0.52
μ_{E1}	E_u / E_y	4.22	6.56	1.83	1.28
μ_{E2}	$\frac{1}{2}\left(\frac{E_{tot}}{E_{el}}+1\right)$	1.97	3.27	0.85	0.53

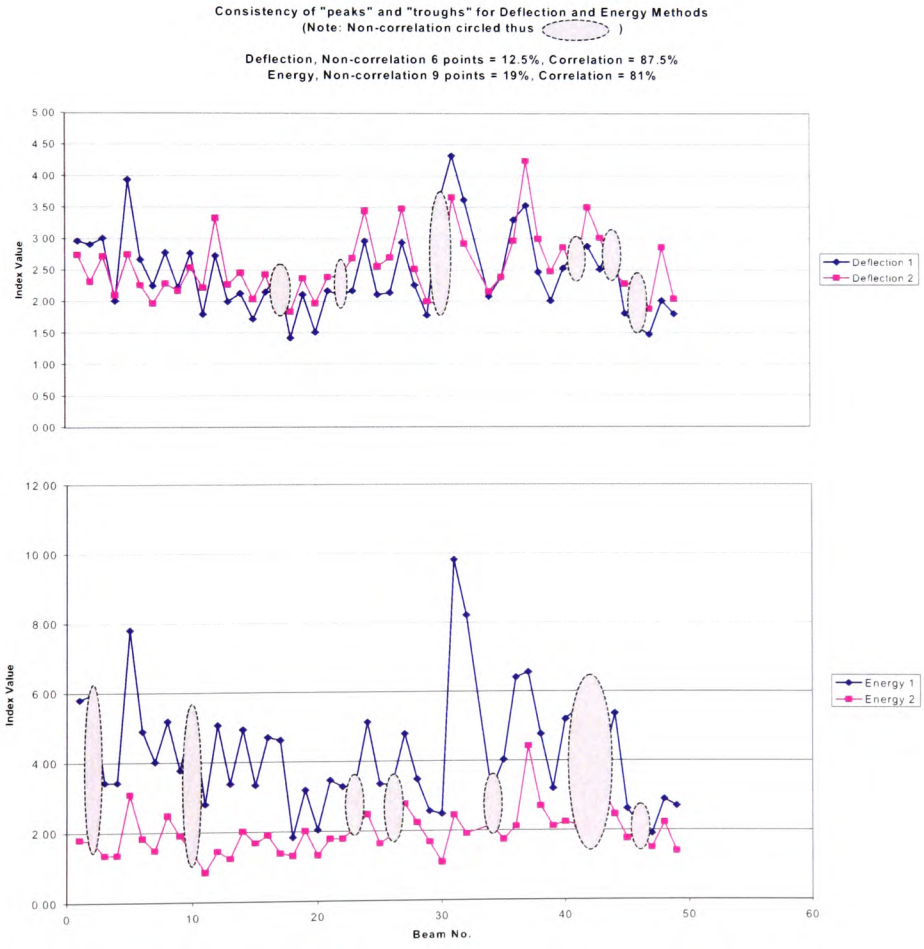

Figure 3 - Correlation of results between methods

Serviceability based deformability:

$$\mu_{\Delta 2} = \frac{\Delta_u}{\Delta_s} \qquad (6)$$

where Δ_u is the ultimate mid-span deflection and Δ_s is the mid-span deflection at the serviceability load (taken to be 67% of the ultimate load).

As can be seen in Table 2, the various methods produced widely differing results for the ductility index relating to any given member, e.g. element 2A, where the indices vary from 2.75 to 7.81, and element 9B, where the indices vary from 2.45 to 10.14.

Further analysis shows that Deflection method 2 (using serviceability limit) has a significantly lower standard deviation, therefore demonstrating a more consistent set of calculated results. The mean, high and low values, together with the standard deviation are detailed in Table 3.

As can be seen from the graphs in Fig 3, both deformation methods resulted in good correlation between data, with slightly better congruence between the deformation methods (87.5% correlation) than the energy methods (81% correlation).

The serviceability method could be further improved by the replacement of Δ_u with $\Delta_{0.95u}$, i.e. the deformation at 95% of the ultimate load, as suggested by Tann[7]. This would remove the misleading values of deformation at 100% of ultimate load, which can be up to 4 times that at 95%, and provide a more representative value for the deformability index.

Of the two energy based methods, the first (E_u / E_y) produced a larger variance in the values for ductility index. This method is particularly sensitive to sections that are over-reinforced with FRP, as the energy at yield can be relatively small compared to the total energy and give a large (and possibly misleading) value for the ductility index.

CONCLUSIONS

A study has been conducted in order to evaluate the failure characteristics of FRP strengthened RC elements. The method is focussed in having ductility indices in order to assign numerical values to various states of failure. Of the published methods, those that are exposed to maximum citation and potential engineering use were considered.

It can be seen from the data discussed earlier, that the serviceability based method produced the most consistent results as judged by the index $\mu_{\Delta 2}$ in Table 3. It is found that, for practical design purposes it would be

easier to use this method with a clear reference point, i.e. deformation at serviceability load.

It emerges that the uncertainty in forming deformation and ductility indices depends very much on the difficulties in identifying:

a) the natural yield point (due to steel yielding), and
b) the ultimate point on the Action-Deformation curve, particularly when a flat plateau obscures the actual failure point.

Hence, the authors recommend that further analysis be carried out on the deformability index, Eqn. (6), and the introduction of $\Delta_{0.95u}$ in place of Δ_u, to determine the validity of this method.

ACKNOWLEDGEMENTS

The authors wish to acknowledge the following:

- University of Glamorgan
- Engineering and Physical Sciences Research Council for the funding which enabled this work and further research to be carried out.

REFERENCES

1. Grace, N. F., Sayed, G. A., Soliman, A. K. and Saleh, K. R., "Strengthening Reinforced Concrete Beams Using Fiber Reinforced Polymer (FRP) Laminates", *ACI Structural Journal*, 96(5), p. 865-874, 1999.
2. Razaqpur, G. A. and Ali, M. M., "Ductility and strength of concrete beams externally reinforced with CFRP sheets", *Proceedings of the International Conference on Advanced Composite Materials in Bridges and Structures*, Canadian Society for Civil Engineers, Montreal, Canada, 1996.
3. Aridome, Y., Kanakubo, T., Furuta, T. and Matsui, M., "Ductility of T-shape RC beams strengthened by CFRP sheet", *Transaction of Japan Concrete Institute*, 20, p.117-124, 1998.
4. Pisanty, A. and Regan, P. E., "Ductility requirements for redistribution of moments in reinforced concrete elements and a possible size effect", *Materials and Structures*, 31, p.530-535, 1998.
5. Burgoyne, C. J., "Ductility and Deformability in Beams Prestressed with FRP Tendons", Proceedings of the International Conference on FRP Composites in Civil Engineering, Hong Kong, 12-15 December 2001, p.15-25.

6. Tumialan, G., Serra, P., Nanni, A. and Belarbi, A., "Concrete cover delamination in RC beams strengthened with CFRP sheets", *ACI Proceedings of the 4th International Symposium on FRP for Reinforcement of Concrete Structures (FRPRCS4)*, Baltimore, MD, Nov. 1999, p. 725-735.
7. Tann, D. B., "Retrofitting of Mechanically Degraded Concrete Structures Using Fibre Reinforced Polymer Composites", *PhD Thesis*, School of Technology, University of Glamorgan, Pontypridd, UK, 2001.
8. Bencardino, F, Spadea, G and Swamy N., "Strength and Ductility of Reinforced Concrete Beams Externally Reinforced with Carbon Fibre Fabric", *ACI Structural Journal*, 99(2), 2002.
9. Almusallam, T. H. and Al-Salloum, Y. A., "Ultimate strength prediction for RC beams externally strengthened by composite materials", *Composites Part B: Engineering*, 32(7), 2001.
10. Quantrill, R. J., Holloway, L. C., Thorne, A. M. and Parke, G. A. R., "Preliminary Research on the Strengthening of Reinforced Concrete Beams using GFRP", *Proceedings of the Second International RILEM Symposium (FRPRCS-2)*, Ghent, August 23-25, 1995, p.541-550.
11. Capozucca, R. and Nilde-Cerri, M, "Static and dynamic behaviour of RC beam model strengthened by CFRP-sheets", *Construction and Building Materials*, 16, 2002.
12. Chajes, M. J., Thomson, T. A., Januszka, T. F. and Finch, W., "Flexural strengthening of concrete beams using externally bonded composite materials", *Construction and Building Materials*, 8(3), 1998.
13. Ahmed, O., Van Gemert, D. and Vendewalle, L., "Improved model for plate-end shear of CFRP strengthened RC beams", *Cement and Concrete Composites*, 23(3-19), 2000.
14. Spadea, G., Swamy, R. N. and Bencardino, F., "Strength and ductility of RC beams repaired with bonded CFRP laminates", *Journal of Bridge Engineering*, 6(5), 2001.
15. Chajes, M. J., Thomson, T. A. and Tarantino, B., "Reinforcement of concrete structures using externally bonded composite materials", *Proceedings of the Second International RILEM Symposium (FRPRCS-2)*, Ghent, August 23-25, 1995, p.501-508.

Appendix A-3

CONFERENCE PAPER

"Strength and ductility of solid RC slabs strengthened by FRP composites"

4th International Conference on Advanced Composite Materials in Bridges and Structures
Calgary, Alberta, July 2004

4th International Conference on Advanced Composite Materials in Bridges and Structures
4ième Conférence Internationale sur les matériaux composites d'avant-garde pour ponts et charpentes
Calgary, Alberta, July 20 – 23, 2004 / 20 – 23 juillet 2004

STRENGTH AND DUCTILITY OF SOLID RC SLABS STRENGTHENED BY FRP COMPOSITES

D.B. Tann and P. Davies
School of Technology, University of Glamorgan
Pontypridd, CF37 1DL, Wales, UK.
dbtann@glam.ac.uk pdavies7@glam.ac.uk

ABSTRACT: An experimental study was conducted to investigate the behaviour of retrofitted reinforced concrete (RC) slabs under short term static load. Eight slabs (3.0 m x 0.5 m x 0.1 m) were load tested to ultimate failure. All slabs were cast to be identical and the internal steel reinforcement ratio was kept at 0.402%. Two slabs were used as control, while the other six were externally bonded with carbon fibre reinforced polymer (CFRP) fabric sheets or pultruted plates of varying geometry. The slabs were seen to behave significantly differently from that of typical FRP strengthened RC beams, where concrete cover tearing-off or other premature failure modes are often seen. It was found that the load carrying capacities of the CFRP strengthened slabs greatly increased over that of the control samples, by up to 458%. The maximum surface crack width of the strengthened slabs was noted to be within the normal serviceability limit until almost final failure. The average crack spacing in the constant moment zone of these members were found to be much smaller when compared with the unstrengthened control slabs. It was shown that the "over-strengthened" slabs could still exhibit reasonably ductile behaviour in comparison with similarly strengthened RC beams, even though a high proportion of elastic stored energy was evident at ultimate failure. A numerical model was used to predict the slab behaviour under the serviceability and ultimate loads, which showed excellent agreement with the experimental results. In conclusion, RC slabs are more suited for strengthening by externally bonded FRP composites than their beam counterparts. In an optimised design, the strength of FRP strengthened RC slabs can be significantly increased, while the ductility of such elements at ultimate limit state conditions can still be maintained at an acceptable level so that no catastrophic brittle failure would occur.

1. INTRODUCTION

It is well known that an appreciable number of bridges and building structures worldwide have been strengthened with externally bonded FRP composite materials over the past decade. One type of such application is the bonding of FRP fabric sheets or laminated plates to the tension face of bridge decks or floor slabs, usually to increase the flexural capacity. The design of FRP strengthened floor slabs are often treated, in a simplified approach, in exactly the same way as for the strengthening of RC beams. The design guidelines produced by the UK Concrete Society TR55 committee or the fib bulletin 14 [1-2], for example, do not specifically distinguish between slabs and beams. This is because both beams and slabs are essentially flexural elements; slabs can be regarded as a series of "shallow beams" of unit widths, which may be treated in exactly the same way as recommended in national design standards including the current British and European codes [3-4].

However, there are major characteristic and behavioural differences between RC beams and slabs. These include: (a) typical RC slabs are usually lightly reinforced when compared to beams. For example, a 175 mm solid slab with 12 mm diameter bars at 200 mm centres has a reinforcement ratio of just 0.32%, and

normal slabs are singly reinforced while beams are often doubly reinforced; (b) the ratio of neutral axis depth to the effective depth in a conventional RC slab is much smaller than that of a typical beam; and (c) shear stresses in RC slabs are much lower than in beams and shear reinforcement is not normally required.

FRP strengthened RC slabs therefore behave differently. Tann [5] used an analytical model to simulate the behaviour of RC slab and beams strengthened by various FRP composites. It was argued that doubly reinforced concrete beams should not normally be strengthened by external FRPs, if similar safety margins between the serviceability and ultimate limit states were to be maintained at the same level as that of the unstrengthened elements. It was shown that slabs are more suitable for strengthening than beams. The above conclusion was based on the criterion that FRP strengthened elements still exhibit acceptable ductility, in order to avoid catastrophic failure at ultimate limit state. Despite the large volume of research in FRP strengthening, only a few projects have specifically dealt with the design of FRP strengthened slabs. It is important for the designer of any slab strengthening scheme to be able to predict the structural behaviour at ultimate limit state from the outset. As a validation and extension procedure for the analytical model, the current study seeks to provide experimental evidence of the behaviour of FRP strengthened RC slabs.

2. EXPERIMENTAL PROGRAMME

2.1 Reinforcement arrangement and material properties

A total of eight reinforced concrete solid one-way spanning slabs were cast; the dimensions are shown in Figure 1. All elements were identically reinforced by four Ø8 mm high-yield steel bars (A_s=0.402%). The distribution bars used were Ø6 mm high-yield at 200 mm centres for group A slabs, and Ø8 mm bars in group B slabs. This slight discrepancy was not expected to have any significant influence in the experimental results, since the secondary reinforcement was only there to ensure an even distribution of applied load. The material properties of the steel and concrete were evaluated in the laboratory and are listed in Table 1.

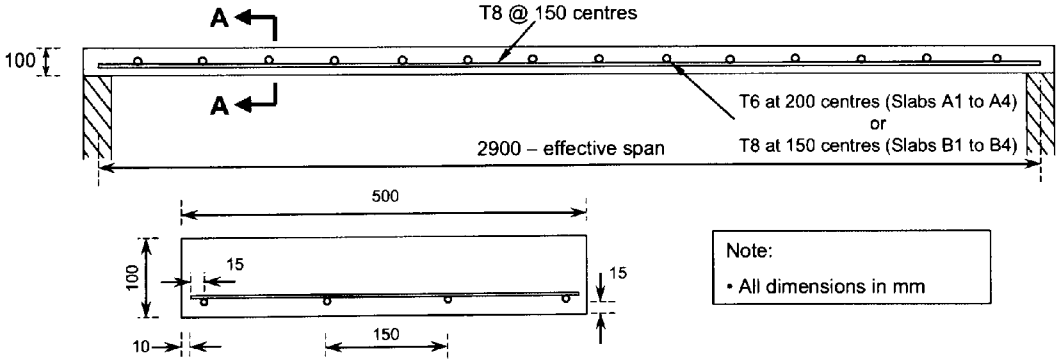

Figure 1 – Slab dimensions and reinforcement arrangement.

Table 1 – Properties of concrete and steel reinforcement.

Slab Ref.	Concrete*		Reinforcing steel**	
A1, A2, A3, A4	f_{cu} (N/mm^2)	49.5	f_y (N/mm^2)	460 (*599.0*)
	E_c (kN/mm^2)	31.2	E_s (kN/mm^2)	198.5
B1, B2, B3, B4	f_{cu} (N/mm^2)	39.3	f_y (N/mm^2)	450 (*573.1*)
	E_c (kN/mm^2)	34.8	E_s (kN/mm^2)	190.6

* For each group of slabs, at least three 100 mm cubes and one 150 mm diameter by 300 mm depth cylinder were compression tested 28 days after the slabs were cast. The average strength is quoted.
** Average yield strength of reinforcing bars was based on tensile tests carried out on four samples for each groups of slabs. Figures shown in *italics* in bracket are the ultimate tensile strength.

2.2 CFRP properties and strengthening arrangements

Two slabs were used as control samples and loaded to ultimate failure. The remaining six slabs were strengthened with CFRP sheets or CFRP pultruted plates as described in Table 2, where the FRP reinforcement ratio and the total equivalent steel ratio are also listed. The normalised thickness of the CFRP sheets was 0.14 mm (determined to be the weight per unit area divided by the density of the carbon fibre). The tensile tests were carried out on fifteen single layer laminated samples of 15 mm wide x 250 mm long, prepared at the time of lamination and the main results are shown in Table 3. The CFRP pultruted plates were 1.4 mm thick and 120 mm wide, fifteen samples of which were also cut and tested in accordance with British Standard BS 2561 [6] and the results are also detailed in Table 3. All CFRP sheets and pultruted plates were cut to a length of 2800 mm, 100 mm short of the slab at either end.

Table 2 – FRP arrangement for the strengthened slabs.

Slab Ref.	CFRP Type	CFRP Area (mm^2)	FRP ratio ρ_f (%)	Total equivalent steel ratio* ρ_{es} (%)
Slab A2	1 layer sheet, full width	70	0.14	0.567
Slab A3	3 layer sheets, full width	210	0.42	0.898
Slab A4	3 100 mm-wide strips	42	0.084	0.501
Slab B2	2 layer sheets, full-width	140	0.28	0.733
Slab B3	2 120 mm-wide plates	336	0.67	0.990
Slab B4	3 120 mm-wide plates	504	1.01	1.289

* Total equivalent steel ratio is the existing steel reinforcement ratio (ρ_s = 0.402%) plus the equivalent steel ratio of FRP composites, determined as $\rho_{es} = \rho_s + \alpha\rho_f$ where α is the modulus ratio defined as the elastic modular of FRP over the elastic modulus of the steel, $\alpha = E_f/E_s$.

Table 3 – Main elastic properties of CFRP composites.

Slab Ref.	Elastic property	Mean Value	Standard deviation
A2 A3 A4	Ultimate tensile strength (N/mm^2)	1991.6	71.2
	Elastic Modulus (kN/mm^2)	236.2	11.5
	Ultimate strain capacity (%)	0.84	0.04
B2	Ultimate tensile strength (N/mm^2)	1900	48.6
	Elastic Modulus (kN/mm^2)	222.5	10.3
	Ultimate strain capacity (%)	0.9	0.05
B3 B4	Ultimate tensile strength (N/mm^2)	1924	105.8
	Elastic Modulus (kN/mm^2)	175.6	1.9
	Ultimate strain capacity (%)	1.2	0.08

2.3 Loading and instrumentation

All slabs were loaded to ultimate failure using a four-point loading configuration, as shown in Figure 2. Nine LVDT displacement transducers were placed along the span to monitor the deflection profile at each load increment. In addition, 32 Demec strain buttons were placed within the pure bending zone and another 6 on the CFRP surface along the span.

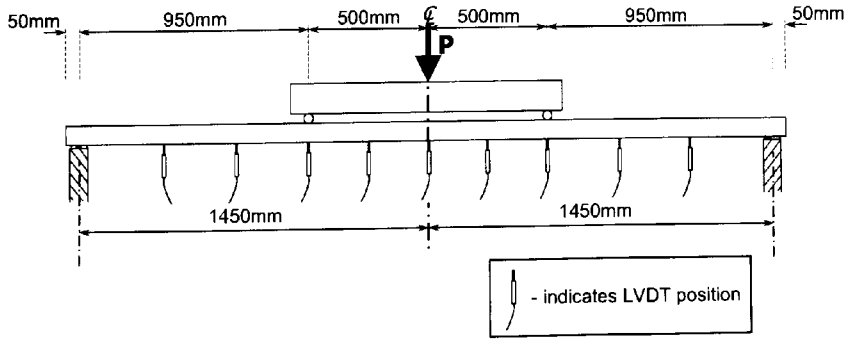

Figure 2 – Loading configuration and LVDT positions.

3. EXPERIMENTAL RESULTS

Comprehensive test data were recorded in the experimental study, which comprised the concrete and CFRP surface strains, crack propagation process and the deflection profiles at every load increment (of between 2 and 5 kN). A summary of ultimate load and maximum deflection for each slab is presented in Table 4, together with the failure mode for each slab.

Table 4 – Ultimate loads, deflections and failure modes.

Slab ref.	Ultimate load (kN)	% change	Ultimate deflection (mm)	% change	Failure mode
Ctrl*	15.8	-	111.0	-	See A1 and B1
A1	14.4	-	120.0	-	Typical ductile failure, initiated by steel yielding.
B1	17.1	-	101.0	-	Ductile failure, steel yield followed by crushing of concrete in compression.
A2	38.2	+142.5	77.10	-30.6	CFRP partial rupture, concrete lateral shear failure.
A3	80.4	+410.5	99.80	-10.1	Concrete failed in compression, partial CFRP sheet de-bonding.
A4	31.6	+100.6	77.05	-30.6	Steel yielding followed by full rupture of all three CFRP fabric sheets.
B2	57.5	+265.1	69.0	-37.8	Partial fabric rupture and slight debonding of FRP sheets at the slab edge.
B3	68.5	+334.9	55.7	-49.8	Premature sudden debonding of both CFRP plates.
B4	60.0	+280.9	44.8	-59.6	Premature sudden debonding of central plate.

* Ctrl is the average of both control slabs A1 and B1

Slab A1 was deemed to have failed at 14.4 kN, when the mid-span deflection had reached 120 mm and the maximum crack widths exceeded 3 mm. The slab displayed a typical under-reinforced failure mode, with internal steel reinforcement yield whilst the concrete in compression remained within the design strength limit. Slab A2 failed at a load of 38.2kN, with partial rupture of the CFRP sheet within the constant moment zone followed quickly by lateral concrete shear failure. Slab A3 displayed a significant increase in load-carrying capacity, 410% over the average value of the two control slabs (or 458% over control slab A1). Slab A4 was lightly strengthened, with only three 100 mm CFRP fabric strips. However, the ultimate load still increased to 31.6 kN, or about 100% increase over the control. The CFRP fabric strips all ruptured in the constant moment zone, as shown in Figure 4 (a).

Group B slabs were tested to verify the trend shown in group A results. Slab B2, which was strengthened with two layers of CFRP sheet, failed at an ultimate load of 57.5 kN, with partial CFRP sheet rupture on one side of the slab; some FRP sheet debonding was also evident near the slab edge. However, slabs B3 and B4 behaved significantly differently from the rest. Slab B3, strengthened with two 120 mm pultruted CFRP plates, failed due to premature debonding of both plates, at a load of 68.5 kN. Slab B4 failed in a similar manner, with the central plate of the three debonding at a load of 60.0 kN, as shown in Figure 4(b). Upon closer inspection of the debonded plates, it was noted that there were voids present in the adhesive, which would have contributed to the bond weakness and induced a premature shear failure at the interface between the plate and the slab.

3.1 Deflection Behaviour

Shown in Figure 3 is the load against maximum mid span deflection for all slabs. It can be seen that the deflection behaviour for the slabs is as expected, with each increase in the CFRP as a percentage of total slab cross-sectional area resulting in increased stiffness. While slabs A2, A4 and B2 had a typical reduction of between 30% and 38% in ultimate deflection, Slab A3, which has the maximum increase in strength, sees a relatively small decrease, with nearly 100 mm recorded at ultimate failure. This small 10% reduction suggests that slabs with high strength enhancement may still achieve large deformations. However, such deformation does not necessarily indicate that the slab has good ductile characteristics and this will be discussed in the following sections.

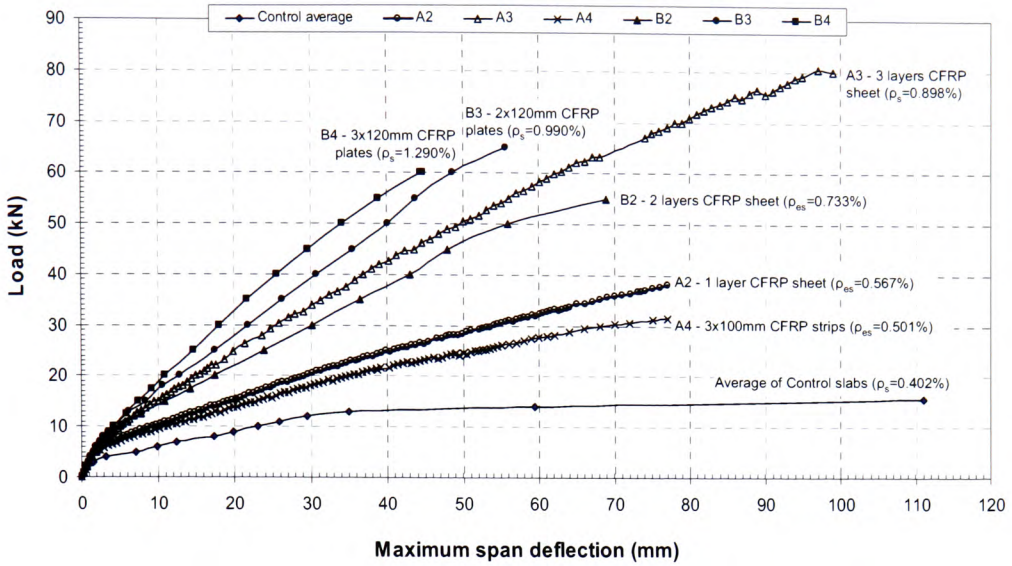

Figure 3 – Graphs of load against deflection for all slabs.

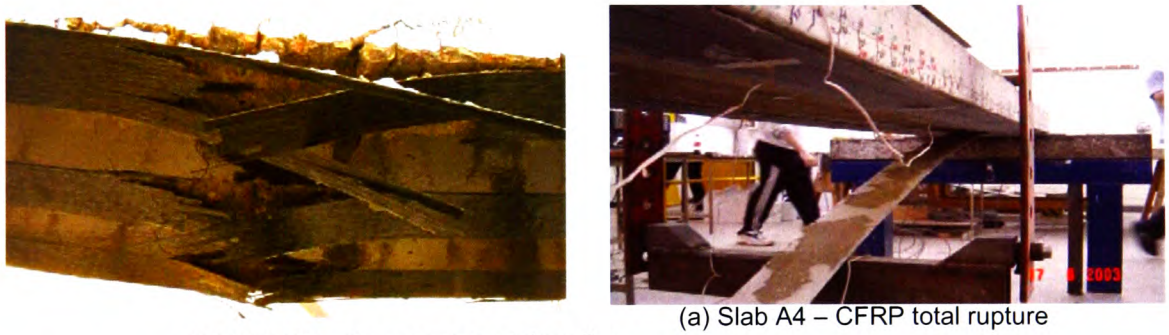

(a) Slab A4 – CFRP total rupture

(b) Slab B4 – Central plate debonding

Figure 4 – Photographs of typical failure mode of the CFRP strengthened slabs.

3.2 Strength enhancement

It is apparent that the flexural capacity of the strengthened slab is directly influenced by the amount of CFRP composites bonded to it. Shown in Figure 5 is the relationship of the increase in flexural capacity against the ratio of CFRP used. As expected, the load carrying capacity increases when the area of FRP provided is increased. However, this trend changes when the FRP ratio is greater than 0.42%, which is approximately 0.9% of total equivalent steel reinforcement (see Table 2).

Slab A3 failed by concrete crushing, while the CFRP sheets still remain intact. It may thus be assumed that any further increases in FRP area would not result in any significant increase in flexural capacity, as the concrete in the compression zone would fail first. This suggests that there should be a predefined maximum strength enhancement ratio for a given existing element. Slabs B3 and B4 partially confirmed the above assumption. These slabs had high total equivalent steel ratio and failed by premature debonding before the ultimate load reached the level of Slab A3. However, it should be noted that slabs B3 and B4 were strengthened with CFRP plates, which are expected to have a different debonding mechanism to the other slabs. This is because the bonding areas were much reduced which would result in higher interfacial bonding stress. Further tests are therefore in progress currently.

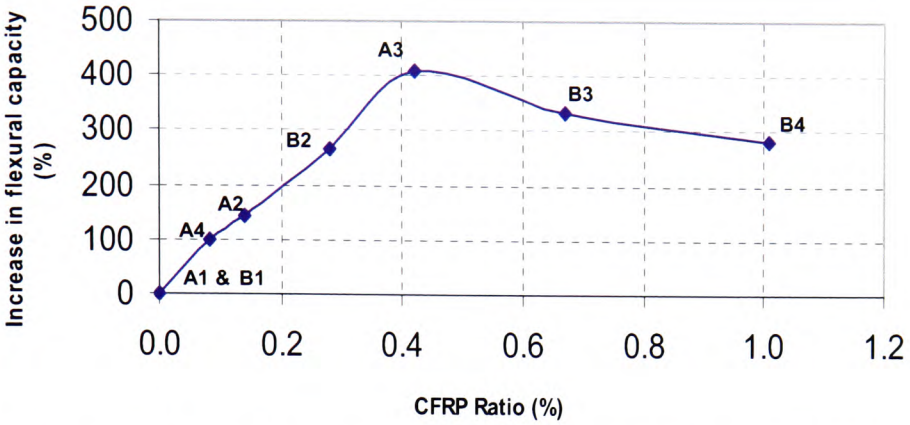

Figure 5 – Relationship between strength enhancement and CFRP ratio

3.3 Crack propagation

The crack propagation process in the constant moment zone is shown in Table 5. In general, the intensity of cracks in CFRP strengthened slabs is much higher than that of the control slabs, and the surface crack widths are considerably smaller. The number of cracks tended to stabilise after the serviceability load, and the average spacing between cracks in the CFRP strengthened slabs ranged from 22 to 25 mm, while for the control slabs, this figure is approximately between 53 and 63 mm. This phenomenon was as expected, since the bonding action between the slab surface and the CFRP composites naturally resulted in reduced crack width. As the average tensile strain in the constant moment zone increases, the number of cracks, naturally, had to increase too. It was interesting to note that for CFRP strengthened slabs, the load at which the first visible crack appeared was significantly higher than the unstrengthened controls.

Table 5 – Tensile cracks within constant moment zone at just before ultimate failure.

Slab Ref.	Load at Initial crack (kN)	Average width (mm)	Maximum width (mm)	Average length (mm)	Maximum length (mm)	Total No. of cracks
A1	3.5	0.26	0.80	49.5	75	17
A2	9.4	0.20	0.60	42.4	80	41
A3	11.4	0.12	0.20	31.5	75	48
A4	7.5	0.15	0.35	45.7	70	42
B1	5.0	0.13	0.85	39.5	80	20
B2	17.0	0.18	0.35	45.0	75	39
B3	15.0	0.15	0.15	41.0	65	27
B4	8.0	0.14	0.15	32.9	50	26

4. DUCTILITY

Ductility is an important consideration in any design scheme. In the current study, the ductility characteristics of all slabs were analysed using a number of different methods.

4.1 Calculation of ductility indices:

Traditionally, ductility may be calculated from the element deflections, as a dimensionless ductility index, defined as the maximum span deflection at failure Δ_u, over the corresponding deflection at the stage when the internal steel reinforcement yields Δ_y,

$$\mu_\delta = \frac{\Delta_u}{\Delta_y} \quad (1)$$

Tann *et al* [7] suggested another index that measures the ability of a flexural element to deform. It is termed the "deformability index," and is based on the deflection at 95% of ultimate load and at the serviceability load, as defined by Equation (2),

$$\varphi_{df} = \frac{\Delta_{0.95u}}{\Delta_s} \tag{2}$$

This overcomes the difficulty when the internal steel reinforcement yield point is often not apparent from the load-deflection curves, as is often the case with FRP strengthened elements. The deflection at 95% of ultimate load is used to remove the misleading values of deformation at Δ_u, which can be many times higher than at 95% of failure load, thus providing a more representative value for the deformability index. For the purposes of this study, the serviceability deflection has been assumed to occur at 67% of the ultimate load. A more realistic approach for the quantification of ductility was proposed by Naaman and Jeong [8], based on the total energy and the elastic stored energy at the stage of just before failure:

$$\phi_{du} = \frac{1}{2}\left\{\frac{E_u}{E_{el}} + 1\right\} \tag{3}$$

where E_u is the total energy under the load deflection curve at failure, and E_{el} is the elastic energy stored in the system at just before failure which must be released at the instance of failure. They developed a method of estimating the value of elastic stored energy E_{el}, using Equation (4) to predict the slope of the unloading curve (see Figure 6):

$$S = \frac{P_1 S_1 + (P_2 - P_1) S_2}{P_2} \tag{4}$$

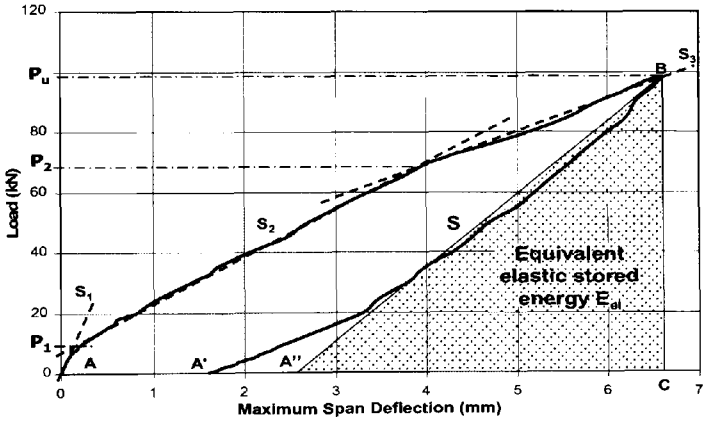

Figure 6 – Calculation of Stored Elastic Energy at failure.

4.2 Proposed Method for determination of elastic stored energy

Naaman and Jeong [8] originally developed the above Equations (4) and (5) for estimating the ductility index of prestressed concrete beams with internal FRP tendons. Although not originally intended, this method may also be applied to FRP externally strengthened flexural elements; the results are more realistic and meaningful than using equation (1) or similar methods. However, in FRP strengthened members with high FRP ratio or high total equivalent steel ratio, Naaman and Jeong's equations will lead to under estimation of the elastic stored energy, and hence overvalue the ductility index. This is because only the two initial slopes are used in Equation (4) to estimate the unloading slope.

For a typical FRP strengthened member, the load-deflection response may consist of more than two apparent initial slopes, as illustrated in Figure 6 which was from a laboratory test result of a beam by the current authors. The third slope is still linear and indeed very steep, indicating that substantially elastic behaviour of the strengthened system, after the internal steel reinforcement yielding, is evident. It is

therefore proposed in the current study that Naaman and Jeong's Equation (4) should be modified to incorporate the third slope, as expressed by Equation (5) (see also Figure 6):

$$S' = \frac{P_1 S_1 + (P_2 - P_1)S_2 + (P_3 - P_2)S_3}{P_3} \tag{5}$$

This revised slope gives a more realistic estimation of the unloading behaviour, and is especially suitable for FRP strengthened elements with a high FRP ratio. As can be seen from Figure 6, the predicted average slope matches the actual unloading curve very well. In cases where laboratory load-deflection data are unavailable, a semi-empirical method of predicting deflection until ultimate failure can be used [9]. In general, the difference between P_3 and P_u is expected to be small for FRP over strengthened members, and P_3 may thus be taken as approximately the ultimate failure load P_u. Using this modified approach, the ductility indices for all slabs have been determined as shown in Table 6, together with the deformability indices as defined from Equation (2).

It can be seen that while all CFRP strengthened slabs exhibited lower ductility than the control slab as expected, the slabs with higher total equivalent steel ratio (A3, B3 & B4) suffered the most reduction. Figure 7 shows the ductility and deformability indices determined by various methods of the six strengthened slabs.

Table 6 – Ductility and deformability indices for all slabs.

Slab reference	μ_δ (Eqn. 1)	Φ_{df} (Eqn. 2)	Φ_{du} (Eqn. 3 & 4)	Φ_{3S} (Eqn. 3 & 5)
A1	3.63	2.50	6.87	6.40
A2	1.86	1.74	2.09	1.72
A3	1.87	1.60	1.48	1.30
A4	1.95	1.87	2.23	1.86
B1	2.83	1.61	4.73	4.49
B2	1.57	1.68	1.48	1.39
B3	1.49	1.53	1.24	1.20
B4	1.68	1.57	1.25	1.16

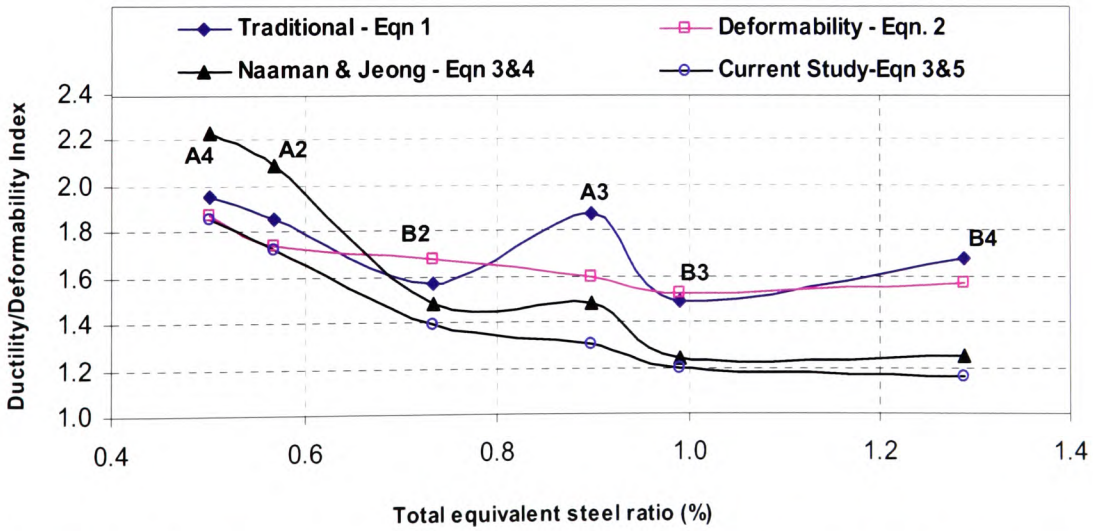

Figure 7 – Comparison of ductility and deformability indices of all strengthened slabs.

It is clear that the traditional deflection based ductility index is not reliable. The Naaman & Jeong method gives better and more consistent results but tends to be over estimating the ductility, while the current modified approach shows the best results. When the total equivalent steel ratio is low, the element

behaved in a more ductile manner, and the deformability index converged with the ductility index. As the total equivalent steel ratio increased to beyond 0.7%, the deformability index became 20% to 30% higher than the ductility values. When the ratio increased to 1.289%, a substantial amount of energy in the strengthened system was found to be unconsumed elastic energy (approximately 76%). When this energy was released at the premature failure, it resulted in a sudden and brittle collapse mechanism.

5. NUMERICAL MODELLING

A non-linear numerical model developed by Tann [5], which is based on material constitutive laws and capable of predicting the flexural strength and deformation behaviour of FRP strengthened beams and slabs from beginning of load to ultimate failure, was used in the current study to estimate the slab ultimate load capacity. A computer programme was written in Microsoft Excel for automated calculations. The results have shown excellent agreement with actual experimental values, except for slabs B3 and B4, as illustrated in Figure 8.

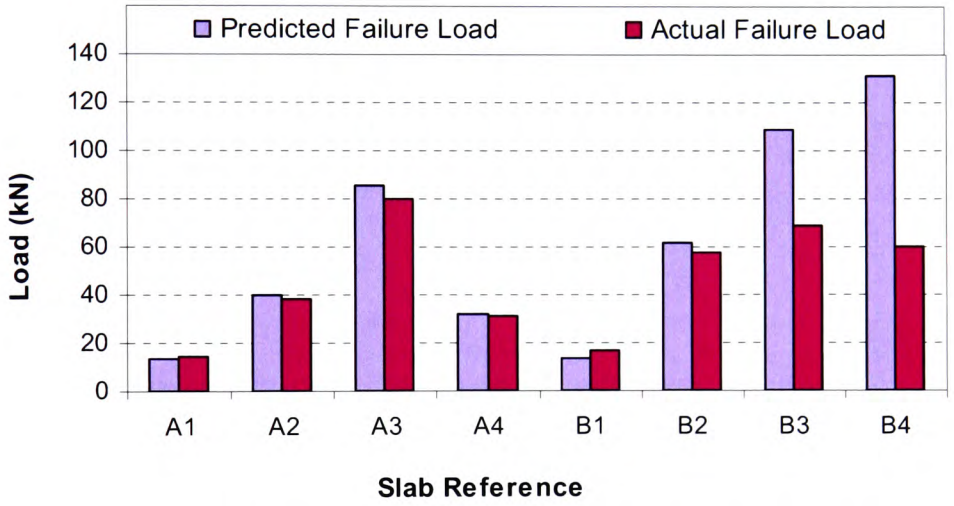

Figure 8 –Comparison of predicted and actual failure loads.

It should be noted that slabs B3 and B4 failed with premature debonding of one or more of the CFRP plates and, upon closer inspection of the failed elements, it was thought that this was due to some visible voids in the adhesive layer. Consequently, the slabs did not reach the full flexural capacity, as the concrete remained intact up to final failure.

6. DISCUSSIONS AND CONCLUSIONS

The experimental study on CFRP strengthened one-way spanning solid RC slabs has shown that premature tearing-off failures do not necessarily occur in RC slabs, and as such, the design of such members should be based on different criteria from those for beam strengthening. The FRP composite materials, when bonded to slabs, can reach higher levels of average failure strains than in beams. Based on the experimental evidence and the results of numerical modelling, the following conclusions can be drawn:

- The level of strength enhancement of CFRP strengthened RC slabs increases with the addition of extra FRP composites, until the total equivalent steel ratio reaches approximately 0.9%, at which stage the full flexural strength of the concrete can be reached

and the load carrying capacity of the strengthened slab increased to over 5 times that of the control.

- Premature debonding occurred in slabs B3 and B4, which had higher FRP ratios and total equivalent steel ratios of greater than 1%. It should be noted, however, that these two slabs were strengthened by plates rather than fabric sheets. The reduced bonding area, the plate thickness and the possible defects in the bond layer could have all contributed to the premature failure.
- The ductility of CFRP strengthened slabs can be suitably determined with an energy based method. The stored elastic energy in the CFRP strengthened system may be determined with reasonable accuracy using a modified unloading slope method.
- For all slabs with a total equivalent steel ratio of less than 0.9%, the failure mode was seen to be acceptably ductile, without any sudden or unexpected collapse at ultimate limit state.
- The deformability index and ductility index have similar values when the system is more ductile. For FRP strengthened slabs, a minimum ductility index of around 1.4 may be desirable for practical design. This is relatively low in comparison with FRP strengthened RC beams, as denser crack patterns in slabs may help release of the elastic energy at the instance of failure.
- A practical strengthening limit, based on the reinforcement ratio, loading arrangement, and geometrical and material properties of the existing structure to be strengthened, should be defined for each individual strengthening scheme. For example, for the given parameters in the current study, the suitable strengthening limit would be at slab B2, with a total equivalent steel ratio of 0.733%, the slab achieved an impressive 265% of strength enhancement, and exhibited a ductility index of 1.39.

7. ACKNOWLEDGEMENTS

The authors wish to thank the Engineering and Physical Sciences Research Council (EPSRC) of the United Kingdom for funding the research (Grant No.GR/R91397/01), and Exchem Mining and Construction Ltd. for the provision of all FRP materials and adhesives.

8. REFERENCES

[1] Concrete Society, *Design guidance for strengthening concrete structures using fibre composite materials*, Technical Report No. 55 (TR 55), Crowthorne, UK, 2000.

[2] fib Task Group 9.3, *Externally bonded FRP reinforcement for RC structures*, Technical Report Bulletin 14. July 2001.

[3] British Standards Institution, BS 8110, Part 1, *Structural use of concrete, Part 1 - code of practice for design and construction*, 1997.

[4] British Standards Institution, ENV 1992-1-1:1992, *Eurocode2: Design of concrete structures, Part 1 – general rules and rules for buildings*, 1992.

[5] Tann, D. B., *Retrofitting of mechanically degraded concrete structures using fibre reinforced polymer composites*, PhD Thesis, University of Glamorgan, Pontypridd, UK, 2001.

[6] British Standards Institution, BS EN 2561, Carbon fibre reinforced plastics – Unidirectional laminates - Tensile test parallel to the fibre direction. 1995.

[7] Tann, D.B., Delpak, R. and Davies, P., "Ductility and deformability of fibre-reinforced polymer-strengthened reinforced concrete beams," *Journal of Structures and Buildings*, Vol. 157, SB1, January 2004, pp 19-30

[8] Naaman, A. E. and Jeong, S. M. "Structural Ductility of Concrete beams Prestressed with FRP Tendons," in *Non-Metallic (FRP) Materials for the Reinforcement and Prestressing of Concrete*, Ed., Taerwe, E & FN Spon, London, pp379-384.

[9] Tann, D.B., "A semi-empirical approach for the prediction of deflections of FRP strengthened RC slabs," *Proceedings of the Sixth International Symposium on FRP Reinforcement for Concrete Structures (FRPRCS-6)*, Singapore, 1, 2003, pp 357-366.

Appendix A-4

CONFERENCE PAPER

"Relative performance of FRP strengthened RC beam sections with varying levels of initial steel reinforcement"

Proceedings of ACIC 07 - Advanced Composites in Construction
April 2007, University of Bath, Bath, UK

Proceedings of ACIC 07
Advanced Composites in Construction
2nd – 4th April 2007, University of Bath, Bath, UK

RELATIVE PERFORMANCE OF FRP STRENGTHENED RC BEAM SECTIONS WITH VARYING LEVELS OF INITIAL STEEL REINFORCEMENT

P Davies[1], R Delpak[2] and DB Tann[3]

Division of Civil and Mechanical Engineering, University of Glamorgan, United Kingdom

Abstract: This paper focuses on the determination of failure mechanisms of FRP strengthened RC beams, in relation to the ductility and deformability. It aims to establish links between the total equivalent reinforcement content and the failure mode. It involves:
(a) Database assimilation to collate failure information from 26 relevant beams tested elsewhere, and
(b) An in-house experimental programme to assess the ductility/deformability of 46 FRP strengthened RC elements with varying internal reinforcement designed to have the one of the following predetermined failure mode:

- Actual failure (rupture) of the FRP, with the bond remaining intact
- Tearing-off of the concrete cover
- De-bonding of the FRP
- Compressive failure of the concrete

No failure mode can be considered the "right" mode but the most undesirable is catastrophic failure resulting from over-reinforcing and strengthening.

The study indicates a correlation between the total level of equivalent internal reinforcement, which depends on additional FRP used for strengthening, and the corresponding failure mechanism.

Additionally, the analyses of results show that FRP strengthened RC beams exhibit significant increases in load-carrying capacity, which is achievable whilst displaying acceptable levels of deformability/ductility at all stages of loading up to ultimate limit state.

Keywords: *Ductility/deformability, Catastrophic Failure, Excessive FRP Content*

1 Introduction

The need for infrastructure rehabilitation, in contrast to demolition, is well recognised. Having accepted that FRP strengthening is a viable method of structural rehabilitation, it then becomes necessary to overcome the technical problems associated with FRP composite fibre strengthening.

Previous studies had indicated that the separation between the "FRP zone" and the RC area in close proximity of the re-bars shows dependence on the relative stiffness of the concrete element. This stiffness, in turn, depends on the level of internal steel reinforcement provided at the casting stage.

Hence, the question is posed regarding the existence of a critical level of tensile reinforcement, above which a catastrophic separation is triggered, in contrast to the type of failure where there is some pre-warning of impending failure.

Clearly, the issue is not quite as straightforward, since in addition to factors such as the percentage of tensile reinforcement there may be other considerations, e.g. concrete strength, flexural element cross-sectional geometry, etc.

2 Total Equivalent Steel Reinforcement Ratio

Due to the variable properties of different types of composite fibres, an attempt has been made to represent the total amount of cross-section tensile reinforcement (both steel and composites) with a single parametric

[1] Research student, pdavies7@glam.ac.uk
[2] Professor, rdelpak@glam.ac.uk
[3] Principal Lecturer, dbtann@glam.ac.uk

entity called the Total Equivalent Steel-reinforcement Ratio (TESR).

2.1 Calculation of TESR

The TESR is determined by first calculating the area of composite material as an equivalent amount of steel, using the modular ratio α_1, as shown in Eqns. (1a) and (1b), and then expressing the total equivalent amount of steel as a percentage of the total cross-sectional area, as shown in Eqn. (1c).

$$\alpha_1 = \frac{E_{FRP}}{E_{Steel}} \quad (1a)$$

$$\alpha_i = \frac{(E_{FRP})_i}{E_{Steel}} \quad (1b)$$

$$TESR = \sum \frac{100(A_S + \alpha_i A_{Fi})}{bd} \quad (1c)$$

2.2 Influences of TESR

It can be shown that increases in the RC element stiffness can be associated with high values of TESR. However, it is also true that significant increases in TESR result in a higher probability of the occurrence of an unacceptable failure mode, such as tearing-off of concrete cover or explosive concrete crushing.
A comparative study has been carried out, utilising experimental results from a number of published sources [1-6], to evaluate the effectiveness of the application of TESR when determining possible failure mode.

3 Experimental programme

3.1 Beam configuration and test set-up

In addition to the data gleaned from published sources, an experimental programme has been carried out.

A total of twelve beams were cast, using high-yield reinforcing steel (with a measured value of f_y=573N/mm^2), in a beam of cross-section 100x200mm. The shear reinforcement comprised Ø6mm mild steel bars (f_{yv}=250N/mm^2) spaced evenly at 100mm centres in the combined shear/moment zone; no shear reinforcement was used in the 'constant moment zone', between the loading points. The concrete cube strength, f_{cu}, was 42N/mm^2 and the concrete elastic modulus, E_c was 38kN/mm^2. The clear span for all tests was 2400mm and a four-point loading configuration, as shown in Fig.1, was used.

The beams comprised three groups with each group consisting of four beams. The variable between the groups was the internal steel reinforcement; 2 x Ø8mm bars in the first group, 2 x Ø10mm bars in the second and 2 x Ø16mm bars in the last.

Within each group there was one control beam, with the remaining three beams being strengthened with varying amounts of carbon fibre reinforced polymer (CFRP) sheet, either one, two or three layers.

3.2 FRP properties

Table 1 details the main elastic properties of the CFRP composites used in the experimental programme.

Table 1: Main elastic properties of CFRP composite

Elastic property		Mean Value
σ_{ult}	Ultimate tensile strength (N/mm^2)	1900
E_f	Elastic modulus (kN/mm^2)	222.5
ε_{ult}	Ultimate strain capacity (%)	0.9

The results in Table 1 were obtained from tensile tests carried out on fifteen single-layer samples of CFRP, which were strips 15mm wide and 250mm long.

4 Comparative study

4.1 Comparison of TESR and element failure mode

Listed in Table 2 are the beams used in this study, together with their respective TESR values and primary failure modes. The TESR values have been compiled, based on the information published by the researchers in the database.

The beams from the present experimental programme are shown at the top of the table (8CON to 16CF3) and all beams tested at the University of Glamorgan (Nos. 1 to 46) are shown in bold typeface.

It was seen that, when comparing the calculated TESR value with the observed failure mode, there is a correlation between an increase in the value of TESR and a more brittle mode of failure. Further investigations noted a trend between failure mode and TESR when plotted, as shown in Fig. 2. On the graph, the red points and their associated values represent the mean TESR value for that particular failure mode. The numbers in round brackets show the number of elements (actual tests) plotted for that particular failure mode.

It is acknowledged that all failure modes, with the exception of steel yield/concrete crushing, are brittle. However, the extent of "brittleness" in this context is to be interpreted with the deformability and ductility indices developed and referenced in this paper. This is naturally considered at the stages subsequent to steel yielding.

It is now feasible to link the distinct increase in the mean value of TESR to the mode of failure, as measured by deformability and ductility indices and it is expected that as the study progresses, with more data available for analysis, a more consistent range of values for TESR can be established for each failure mode.

Table 2: Beam details for comparative study

Beam No.	Beam Ref.	TESR (%)	Primary failure mode*
1	8CON	0.503	1
2	8CF1	0.592	1
3	8CF2	0.681	1
4	8CF3	0.771	1
5	10CON	0.785	1
6	10CF1	0.867	1
7	10CF2	0.947	3
8	10CF3	1.028	4
9	16CON	2.011	5
10	16CF1	2.091	5
11	16CF2	2.171	5
12	16CF3	2.251	5
13	A1	1.168	4
14	A3	1.168	4
15	B4	0.828	2
16	B6	0.828	2
17	B8	0.814	3
18	101	0.96	3
19	108	0.96	4
20	109	0.96	5
21	110	0.88	5
22	111	0.88	5
23	112	0.97	4
24	114	1.05	4
25	115	1.05	4
26	116	0.94	4
27	118	0.96	4
28	119	0.96	4
29	120	0.96	4
30	121	0.96	4
31	122	0.96	4
32	123	0.96	4
33	126	0.96	4
34	127	0.96	4
35	128	0.96	4
36	129	0.96	4
37	132	0.96	4
38	134	0.96	4
39	135	0.96	5
40	137	0.96	4
41	138	0.96	4
42	141	0.86	5
43	B1	0.87	5
44	B4	0.87	2
45	B5	1.18	4
46	B8	0.82	3
47	1A	1.037	1
48	1B	1.116	2
49	1C	1.037	1
50	1D	1.116	3
51	A1	1.708	4
52	A2	1.767	4
53	A3	1.826	4
54	A6	1.679	4
55	A7	1.708	4
56	A8	1.738	4
57	B3	1.708	5
58	C1	1.708	4
59	C2	1.826	4
60	FG1	0.876	5
61	FG2	0.966	5
62	FG4	1.142	5
63	FC1	0.967	5
64	FC2	1.147	5
65	B1	1.131	5
66	B2	1.256	5
67	A3	0.875	5
68	E3	0.925	2
69	G3	0.899	2
70	A1.1	1.124	3
71	A1.2	1.124	3
72	A1.3	1.124	3

* Failure modes: 1-Steel yield/concrete crushing; 2-Fibre rupture; 3-Fibre delamination; 4-Tearing-off of concrete cover; 5-Explosive concrete crushing [3]

4.2 Comparison of TESR and failure load

In addition to the above general observations for the twelve beams in the experimental programme, a comparison is made of the element failure mode in relation to the amount of TESR. The results are shown in Figs. 3 (a), (b) and (c), with the trendlines for the curves corresponding to the Ø8mm and the Ø10mm beams, in addition to the relevant equation, alongside. It can be seen that there is a definite peak for the TESR value, after which the element becomes more brittle. This leads to a reduction in the load carrying capacity.

For the beams with 2 x Ø16mm bars the failure mode led to an explosive crushing of the concrete and was highly unpredictable, even for the control beam. It is considered that an increase in the concrete strength for these beams would result in a trend comparable to that seen for the Ø8mm bars and Ø10mm bars.

5. Ductility and deformability

There are two general approaches from which a ductility or deformability index can be determined:

5.1 Deformation-based methods

$$\mu_{\Delta} = \frac{\Delta_u}{\Delta_s} \tag{2}$$

where Δ_u is the mid-span displacement at the ultimate load of the element and Δ_s is the mid-span displacement at serviceability load (taken to be 67% of the ultimate load).

However, this method has been further improved by the replacement of Δ_u with $\Delta_{0.95u}$; i.e. the mid-span displacement at 95% of the ultimate load, as suggested by Tann [3]. This would remove the misleading values for deformation at ultimate load, commonly encountered at the pre-failure stages of RC beam tests, which can be up to four times that at 95%.

$$\mu_{df} = \frac{\Delta_{0.95u}}{\Delta_s} \tag{3}$$

The authors have previously proposed calculating the energy-based index using the following equation;

$$\varphi_E = \frac{1}{2}\left[\frac{E_{tot}}{E_{el}} + 1\right] \tag{4}$$

where E_{tot} is the total energy, calculated as the total area under the Load/Deflection curve to failure, and E_{el} is the stored elastic energy.

This method was first published by Naaman and Jeong [8], who used the following equation to estimate the unloading curve, and, hence, the stored elastic energy (represented by the area under the unloading curve):

$$S = \frac{P_1 S_1 + (P_2 - P_1) S_2}{P_2} \tag{5}$$

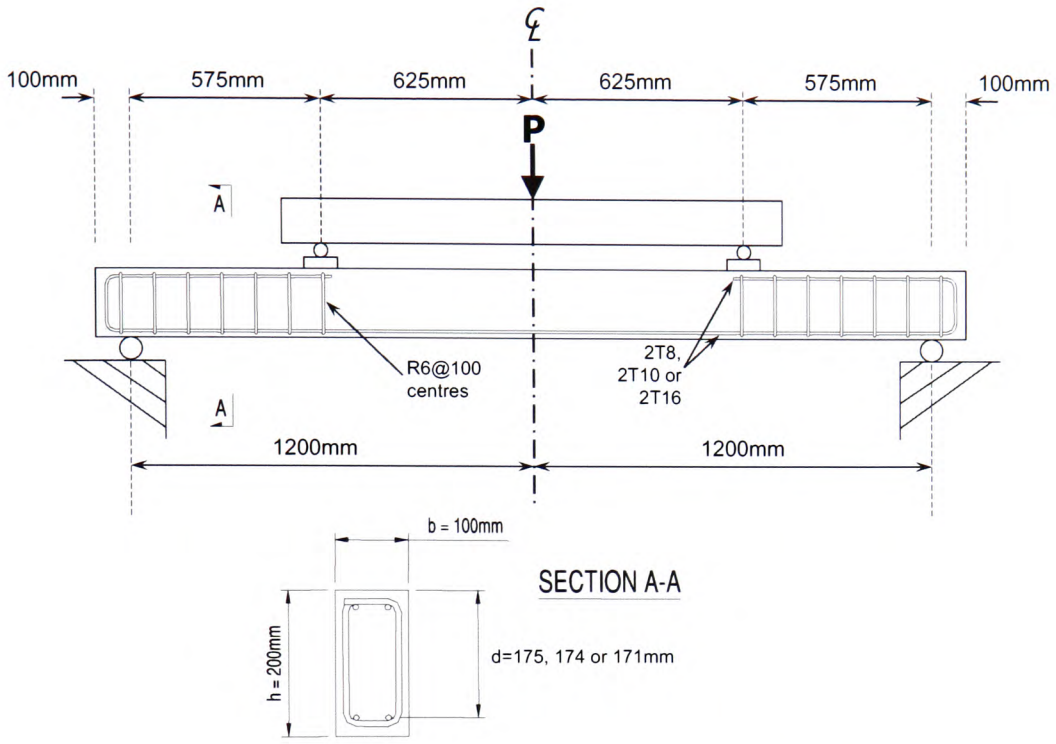

Figure 1: Beam dimensions and reinforcement details

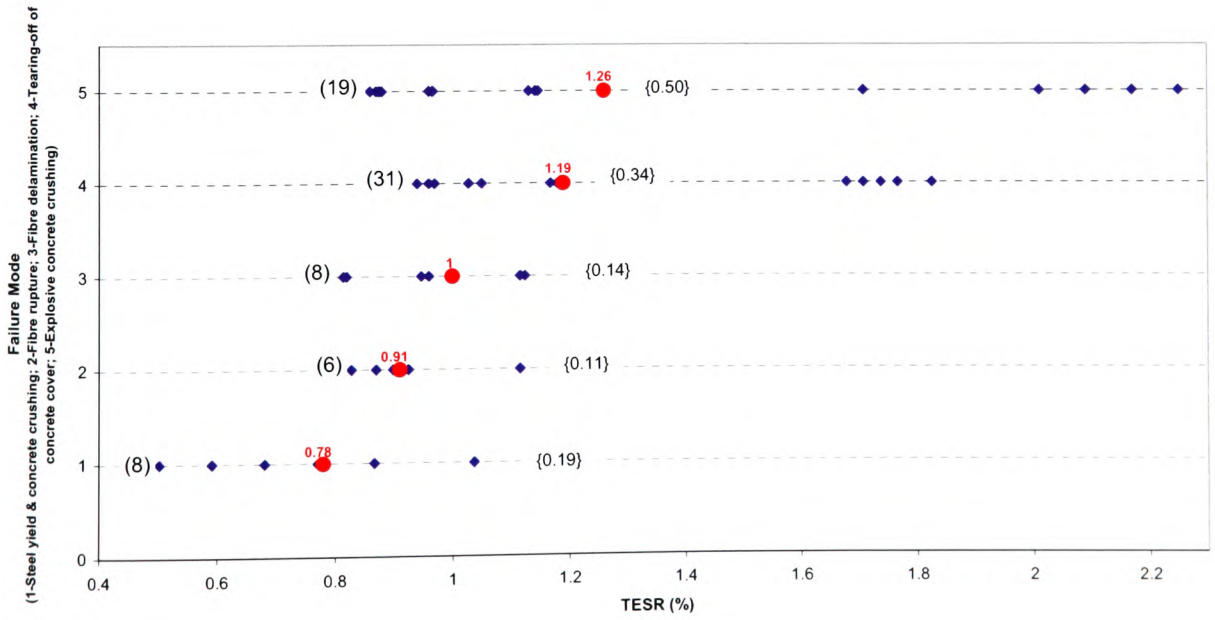

Figure 2: Graph of Failure Mode against TESR
Note that figures in ( ) represent the sample size and those in { } represent the standard deviation

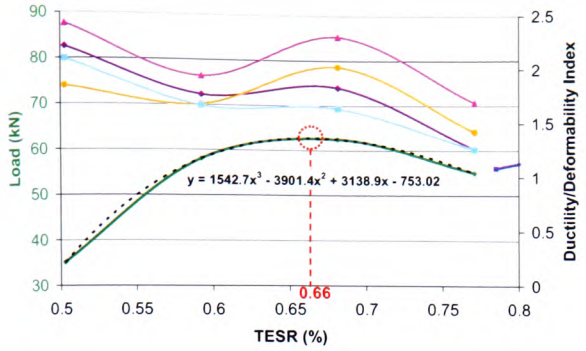

a) Graph of Failure Load vs. TESR and Ductility/deformability Index vs. TESR for beams with Ø8mm reinft.

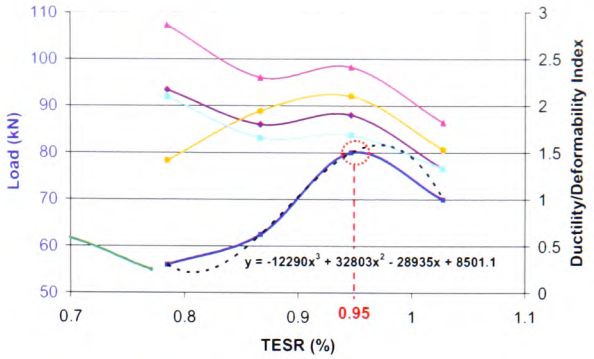

b) Graph of Failure Load vs. TESR and Ductility/deformability Index vs. TESR for beams with Ø10mm reinft.

Key:

$\mu_\Delta = \frac{\Delta_u}{\Delta_s}$ $\quad$ $\mu_{df} = \frac{\Delta_{0.95u}}{\Delta_s}$

$\varphi_E = \frac{1}{2}\left[\frac{E_{tot}}{E_{el}} + 1\right]$ $\quad$ $\varphi_{3S} = \frac{1}{2}\left(\frac{E_{tot}}{E''_{el}} + 1\right)$

Note: Circled points relate to optimum failure load and corresponding TESR value.

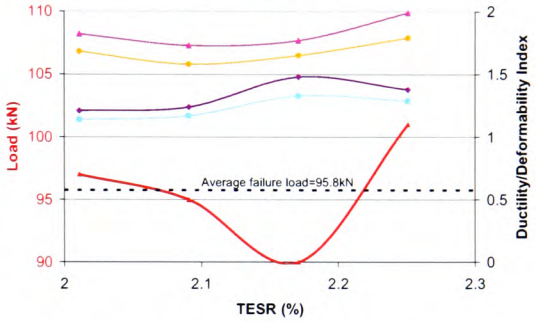

c) Graph of Failure Load vs. TESR and Ductility/deformability Index vs. TESR for beams with Ø16mm reinft.

Figure 3: Graphs of Failure Load vs. TESR and Ductility/deformability Index vs. TESR for University of Glamorgan tested elements

5.2 Energy-based methods

It has previously been proposed by the authors [9] to modify this approach in order to take into consideration the additional elastic energy developed in any FRP strengthened element during the latter stages of loading. This modified approach incorporates a third slope, S_3, when calculating the slope of the estimated unloading curve, as shown in Equation (6) {See also Fig. 4}:

$$S = \frac{P_1 S_1 + (P_2 - P_1)S_2 + (P_U - P_2)S_3}{P_U} \qquad (6)$$

This revised approach will yield an adjusted value for the estimated stored elastic energy, E''_{el}, which can then be used to calculate the modified ductility index φ_{3S} as follows:

$$\varphi_{3S} = \frac{1}{2}\left(\frac{E_{tot}}{E''_{el}} + 1\right) \qquad (7)$$

6. Relative performance of FRP strengthened beams

It has been recommended [3] that index values of more than 2.0 and 1.65 are acceptable for tolerable levels of deformability and energy-based ductility of FRP strengthened flexural elements respectively. The experimental indices shown in Table 3 are a summary of observed failure loads (and modes) listed against percentages of re-bar and TESR present.

The logical development then becomes to determine the benefit of strengthening with a maximum possible level of FRP, taking into account the initial (existing) reinforcement. Table 4 contains the percentage increase in load-carrying capacity for FRP strengthened elements from this study.

Table 3: Calculated ductility and deformability indices

Beam No.	Beam Ref.	μ_Δ	φ_E	μ_{df}	φ_{3S}
		$\frac{\Delta_u}{\Delta_S}$	$\frac{1}{2}\left(\frac{E_{tot}}{E_{el}}+1\right)$	$\frac{\Delta_{0.95u}}{\Delta_S}$	$\frac{1}{2}\left(\frac{E_{tot}}{E_{el}^{\pi}}+1\right)$
1	8CON	2.40	2.19	**1.83**	**2.08**
2	8CF1	1.93	1.76	**1.67**	**1.66**
3	8CF2	2.30	1.83	**2.02**	**1.64**
4	8CF3	1.69	1.26	**1.42**	**1.26**
5	10CON	2.86	2.17	**1.41**	**2.10**
6	10CF1	2.30	1.80	**1.94**	**1.66**
7	10CF2	2.41	1.90	**2.10**	**1.69**
8	10CF3	1.82	1.33	**1.53**	**1.33**
9	16CON	1.82	1.21	**1.68**	**1.14**
10	16CF1	1.73	1.24	**1.58**	**1.17**
11	16CF2	1.77	1.48	**1.65**	**1.33**
12	16CF3	1.99	1.38	**1.79**	**1.29**

Table 4: Estimated %age benefit through FRP strengthening of RC beams with variable levels of internal steel reinforcement

Beam number	Beam ref.	Actual reinft. %age	TESR	Failure load (kN)	Increase in capacity (%)	Comments
1	8CON	0.503	0.503	35.1	-	-
2	8CF1	0.503	0.592	58.0	+65.2	Below optimum strengthening/under performance
3	8CF2	0.503	0.681	62.5	+78.1	Optimum strengthening
4	8CF3	0.503	0.771	55.0	+56.7	Above optimum strengthening/under-performance
5	10CON	0.785	0.785	56.5	-	-
6	10CF1	0.785	0.867	62.6	+10.8	Below optimum strengthening/under performance
7	10CF2	0.785	0.947	80.1	+41.8	Optimum strengthening
8	10CF3	0.785	1.028	70.0	+23.9	Above optimum strengthening/under-performance
9	16CON	2.01	2.011	98.0	-	No perceptible benefit for the introduction of FRP strengthening
10	16CF1	2.01	2.091	96.0	-2.1	
11	16CF2	2.01	2.171	90.0	-8.2	
12	16CF3	2.01	2.251	101.0	+3.1	

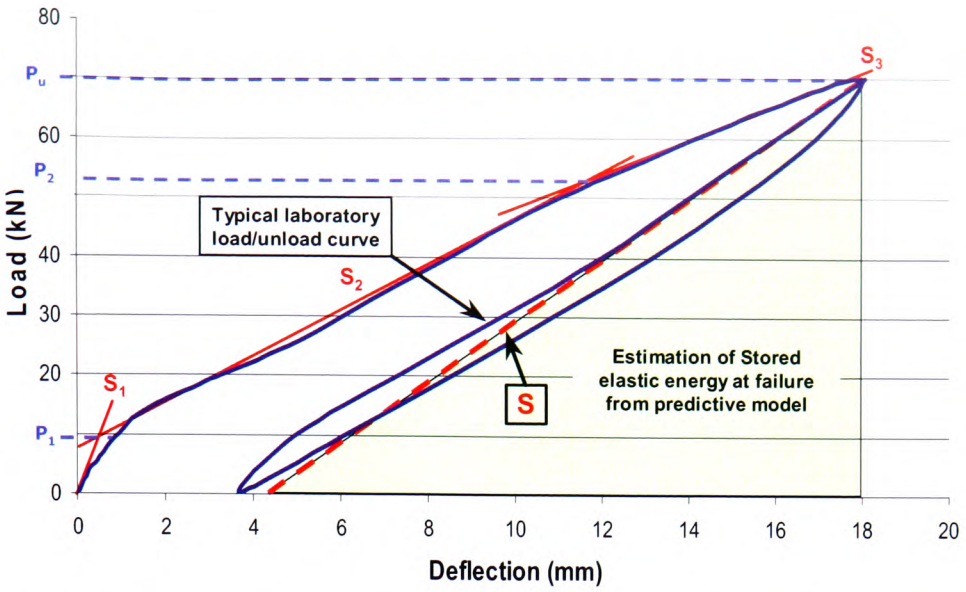

Figure 4: Typical load/deflection variation from laboratory tests and example of calculation of equivalent elastic stored energy (See text for legend of symbols)

7. Observations and conclusions

A series of investigations and laboratory-based experiments have been conducted to determine the correlation between the total level of reinforcement (both internal steel re-bar and externally-bonded FRP) and the corresponding failure mechanism. This was to verify that the FRP strengthened elements can maintain an acceptable level of ductility/deformability, whilst still benefiting from an increase in load-carrying capacity

It is acknowledged that the TESR percentage values are based on the initial elastic state of the RC element and it is further agreed that once the main reinforcement yields, the calculation mechanism requires modification. The present study is part of a more general investigation of the change in ultimate limit state behaviour of RC elements. In this work TESR was found to be a convenient parameter to relate to various states of failure as defined by deformability and ductility indices.

1. An increase in the level of bonded FRP does not always result in an increase in load-carrying capacity.
2. Any increase in FRP above the optimum level for a particular section, as seen in Fig.3, even marginal, is seen to correspond to reduced levels of load capacity.
3. Modes of failure are judged to become progressively more brittle (as calculated by deformability/ductility indices) commensurate with increased percentages of externally-bonded FRP.
4. The optimum level of strengthening, mode of failure and ductility/deformability, appear to be section specific, depending on parameters such as percentage of internal steel reinforcement, f_{cu}, etc..
5. There is a critical level of reinforcement percentage, above which the amount of FRP strengthening becomes inconsequential, where the brittle failure modes are of the most undesirable categories, leading to sudden failure with little or no visible warning.

Structural engineers are not only conscious of the load-carrying capacity of an element or structure but also consider ductility and deformability as important structural characteristics, where enhanced ductility/deformability is a good design indicator.

Examination of the graphs in Fig. 3 shows that any increase or decrease of the indices with respect to TESR is reflected accurately alongside the failure load performance. Hence, when choosing a particular design with an appropriate level of FRP present, either the ductility or deformability index can be considered against total equivalent steel reinforcement.

Therefore, the authors consider that both relative and absolute performance of these sections is fully assessed.

Acknowledgements

The current work forms part of a project that was initially supported by the EPSRC under grant GR/R91397/01. All FRP materials and adhesives used in the experimental study were provided by Exchem Mining and Construction (UK) Ltd. The authors also wish to thank the University of Glamorgan Management for allowing maximum resources to be allocated for progression of the study.

References

[1] Almusallam, T.H. and Al-Salloum, Y.A., "Ultimate strength prediction for RC beams externally strengthened by composite materials", *Composites Part B: Engineering*, 32(7), 2001.

[2] Capozucca, R. and Nilde-Cerri, M, "Static and dynamic behaviour of RC beam model

strengthened by CFRP-sheets", *Construction and Building Materials*, 16, 2002.

[3] Tann, D.B., "Retrofitting of Mechanically Degraded Concrete Structures Using Fibre Reinforced Polymer Composites", *PhD Thesis*, School of Technology, University of Glamorgan, UK, 2001.

[4] Chajes, M.J., Thomson, T. A., Januszka, T.F. and Finch, W., "Flexural strengthening of concrete beams using externally bonded composite materials", *Construction and Building Materials*, 8(3), 1998.

[5] Spadea, G., Swamy, R.N. and Bencardino, F., "Strength and ductility of RC beams repaired with bonded CFRP laminates", *Journal of Bridge Engineering*, 6(5), 2001.

[6] Tumialan, G., Serra, P., Nanni, A. and Belarbi, A., "Concrete cover delamination in RC beams strengthened with CFRP sheets", *ACI Proceedings of the 4th International Symposium on FRP Reinforcement for Concrete Structures (FRPRCS4)*, Baltimore, MD, Nov. 1999, p. 725-735.

[7] Andreou, E., "Performance Evaluation of RC Flexural Elements Strengthened by Advanced Composites", *PhD Thesis*, School of Technology, University of Glamorgan, UK, 2002.

[8] Naaman, A. E. and Jeong, S. M. "Structural Ductility of Concrete beams Prestressed with FRP Tendons," in *Non-Metallic (FRP) Materials for the Reinforcement and Prestressing of Concrete*, Ed., Taerwe, E & FN Spon, London, pp379-384, 1995.

[9] Tann, D.B., Delpak, R. and Davies, P., "Ductility and deformability of fibre-reinforced polymer-strengthened reinforced concrete beams," *Journal of Structures and Buildings*, Vol. 157, SB1, January 2004, pp 19-30

[10] Tann, D.B., Davies, P. and Delpak, R., "A review of ductility determination of FRP strengthened flexural RC elements," *Proceedings of the Sixth International Symposium on FRP Reinforcement for Concrete Structures (FRPRCS-6)*, Singapore, 1, 2003.

[11] Davies, P., Tann, D.B. and Delpak, R., Further Investigations into the Ductility and Deformability of FRP Strengthened RC Elements", *FRPRCS-8 8th International Symposium on Fiber Reinforced Polymer Reinforcement for Concrete Structures*, University of Patras, Greece, July 2007.

Appendix A-5

CONFERENCE PAPER

"Further Investigations into the Ductility and Deformability of FRP Strengthened RC Elements"

FRPRCS-8, 8th International Symposium on Fiber Reinforced Polymer Reinforcement for Concrete Structures
University of Patras, Greece, July 2007

FURTHER INVESTIGATIONS INTO THE DUCTILITY AND DEFORMABILITY OF FRP STRENGTHENED RC ELEMENTS

P. Davies, D. B. Tann and R. Delpak

Division of Civil and Mechanical Engineering, University of Glamorgan, United Kingdom.

Keywords: FRP, composites, ductility, deformability, concrete, beams.

1 INTRODUCTION

The issue of ductility is of primary concern to all structural engineers, since all appropriately designed structures should be sufficiently ductile under ultimate load to provide adequate warning of impending failure, thus preventing sudden and brittle collapse.

From a practical and commercial viewpoint, there are ample cases where it may become necessary to strengthen a reinforced concrete member. Historically, this would have been achieved by attaching steel plates to the tension surface, or through section enlargement. The difficulties of mechanical fixing of attachments, interference with internal reinforcement of through end bolting and ensuing issues such as corrosion are well documented.

However, in recent years, Fibre Reinforced Polymers (FRPs) have become more widely used in place of steel plates for strengthening of reinforced concrete (RC) structures. However, design engineers have been reluctant to use the former due to the lack of definitive data relating to the performance of FRP strengthened RC structures and, hence, the possibility of brittle failure at ultimate limit state.

It is recognised that FRP strengthened RC elements behave quite differently from the corresponding steel-only reinforced counterparts, which is primarily due to the dominant linear elastic stress-strain characteristics of the composite materials up to failure. Previously, the authors have proposed that the determination of a ductility index for FRP strengthened RC flexural elements to be based on either: a) the serviceability and ultimate loads of the element; b) the total and stored-elastic energy of the element [1].

Both these methods produced consistent results and it was proposed that further work be carried out to develop both approaches and also to evaluate the indices of elements that are considered under-reinforced.

2 REVIEW OF CURRENT METHODS

The determination of ductility for elements strengthened with FRPs has been a topic of considerable debate among researchers [2-7]. There are generally accepted to be two broad categories from which a ductility index can be determined:

2.1 Deformation-based ductility

Previously, the authors have proposed the use of the following equation to determine ductility from deformation data;

$$\mu_{\Delta 1} = \frac{\Delta_u}{\Delta_s} \tag{1}$$

where Δ_u is the mid-span displacement at the ultimate load of the element and Δ_s is the mid-span displacement at serviceability load (taken to be 67% of the ultimate load).

However, it was felt that this method could be further improved by the replacement of Δ_u with $\Delta_{0.95u}$; i.e. the mid-span displacement at 95% of the ultimate load, as suggested by Tann[8]. This would remove the misleading values for deformation at ultimate load, commonly encountered at the pre-failure stages of RC beam tests, which can be up to four times that at 95%.

$$\mu_{df} = \frac{\Delta_{0.95u}}{\Delta_s} \tag{2}$$

2.2 Energy-based ductility

The authors have previously proposed calculating the energy-based index using the following equation;

$$\varphi_E = \frac{1}{2}\left[\frac{E_{tot}}{E_{el}} + 1\right] \tag{3}$$

where E_{tot} is the total energy, calculated as the total area under the Load/Deflection curve to failure, and E_{el} is the stored elastic energy.

This method was first published by Naaman and Jeong [9], who used the following equation to estimate the unloading curve and, hence, the stored elastic energy (represented by the area under the unloading curve):

$$S = \frac{P_1 S_1 + (P_2 - P_1) S_2}{P_2} \tag{4}$$

It is proposed to modify this approach in order to take into consideration the additional elastic energy developed in any FRP strengthened element during the latter stages of loading. This modified approach incorporates a third slope, S_3, when calculating the slope of the estimated unloading curve, as shown in Equation (5):

$$S = \frac{P_1 S_1 + (P_2 - P_1) S_2 + (P_U - P_2) S_3}{P_U} \tag{5}$$

This revised approach will yield an adjusted value for the estimated stored elastic energy, E''_{el}, which can then be used to calculate the modified ductility index φ_{3S} as follows:

$$\varphi_{3S} = \frac{1}{2}\left(\frac{E_{tot}}{E''_{el}} + 1\right) \tag{6}$$

3 EXPERIMENTAL PROGRAMME

3.1 Beam geometry and loading configuration

A total of twelve beams were cast, using high-yield reinforcing steel, with a beam cross-section of 100x200mm. The tension reinforcement comprised two Ø8mm, two Ø10mm or two Ø16mm steel bars, with the shear reinforcement consisting of Ø6mm mild-steel links spaced evenly at 100mm in the

shear/moment zone. No shear reinforcement was used in the 'constant moment zone' between the loading points. The clear span for all tests was 2400mm, as shown in Figure 2.

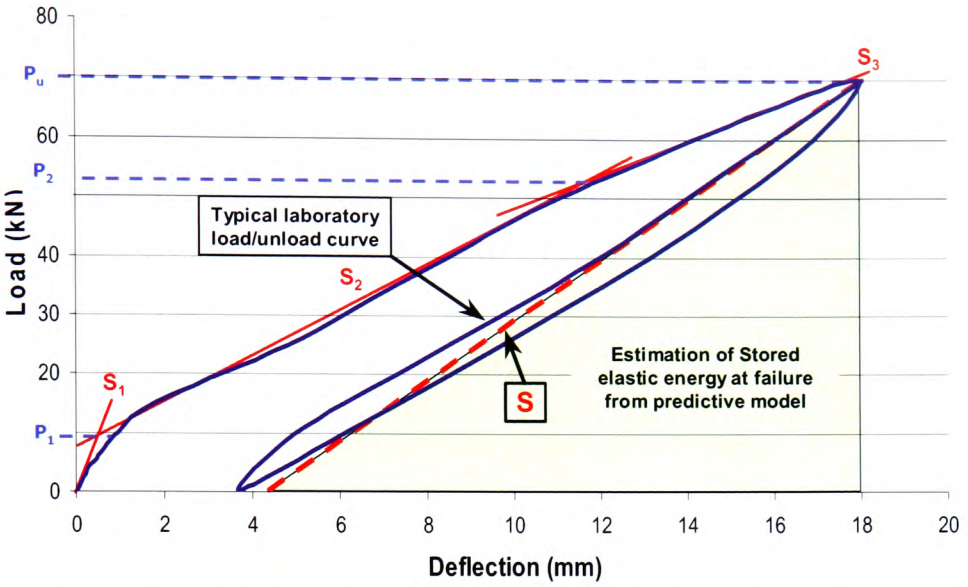

Fig. 1 Typical load/deflection variation from laboratory tests and example of calculation of equivalent elastic stored energy (See text for legend of symbols).

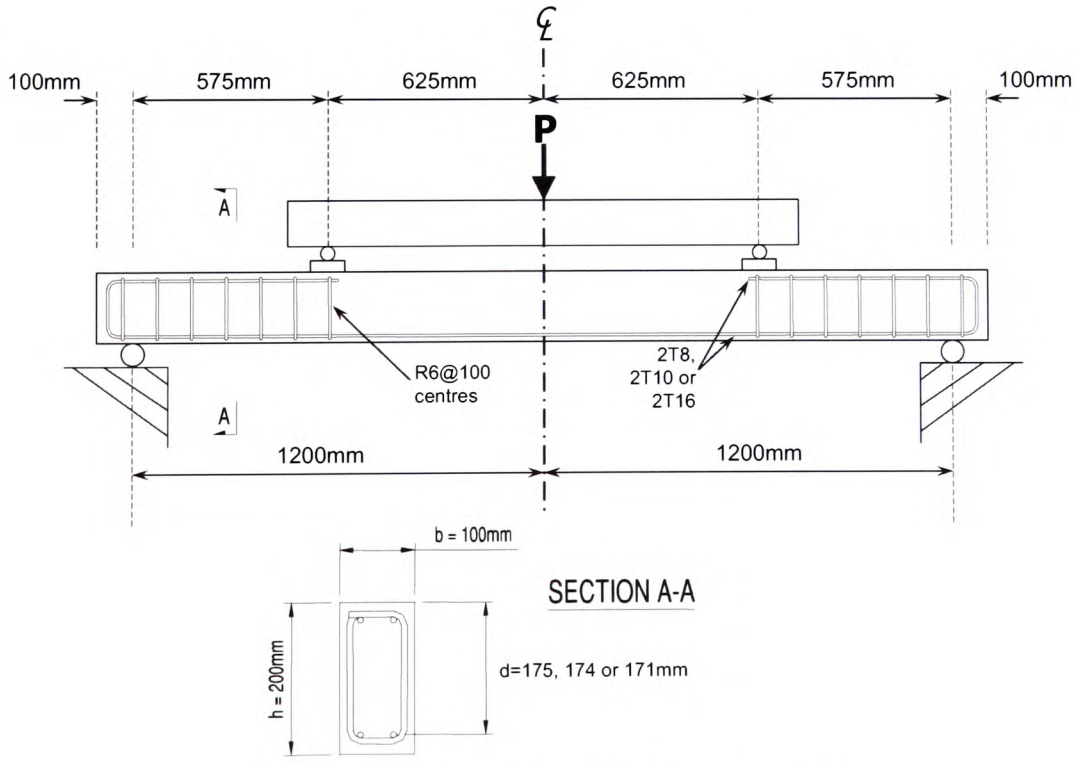

Fig. 2 Beam dimensions and reinforcement details

3.2 Testing

For all tests, a four-point loading system was used. The specimens were instrumented with electrical strain gauges bonded at the following locations:

- The finished and clean top surface of the beam, at mid-span
- The tension reinforcement, at mid-span and directly underneath the point of load application
- On the surface of the CFRP laminates

In addition, concrete surface strains were recorded using DEMEC gauges in six zones, three on either side of the beam. The deflections were recorded using calibrated Linear Variable Displacement Transducers (LVDTs).

3.3 FRP properties and strengthening arrangement

In each set of four beams, one was used as a control beam, with the remaining beams strengthened with Carbon Fibre Reinforced Polymer (CFRP) sheets, as detailed in Table 1 where the FRP ratio and total equivalent steel ratio (TESR) are also listed. The thickness of the CFRP sheets was 0.165mm. Tensile tests were carried out on fifteen single-layer samples of CFRP; the samples were 15mm wide and 250mm long. The results are presented in Table 2.

Table 1 FRP arrangement for tested beams

Beam ref.	FRP type	Sectional FRP area (mm^2)	FRP ratio ρ_f (%)	Total equivalent steel ratio (TESR)* (%)
8CON	None	-	-	0.503
8CF1	1 layer of CFRP sheet	16.5	0.083	0.592
8CF2	2 layers of CFRP sheets	33.0	0.165	0.681
8CF3	3 layers of CFRP sheets	49.5	0.248	0.771
10CON	None	-	-	0.785
10CF1	1 layer of CFRP sheet	16.5	0.083	0.864
10CF2	2 layers of CFRP sheets	33.0	0.165	0.942
10CF3	3 layers of CFRP sheets	49.5	0.248	1.02
16CON	None	-	-	2.01
16CF1	1 layer of CFRP sheet	16.5	0.083	2.09
16CF2	2 layers of CFRP sheets	33.0	0.165	2.17
16CF3	3 layers of CFRP sheets	49.5	0.248	2.24

*Total equivalent steel ratio (TESR) is the existing steel reinforcement ratio, ρ_s, plus the equivalent steel ratio of the FRP composites, determined as $\rho_{es} = \rho_s + \alpha \rho_f$, where α is the modular ratio defined as the elastic modulus of the FRP composite divided by the elastic modulus of the steel reinforcement, $\alpha = E_f/E_s$. E_s is taken to be 205,000N/mm^2.

Table 2 Main elastic properties of CFRP composites

Elastic property		Mean Value
σ_{ult}	Ultimate tensile strength (N/mm^2)	1900
E_f	Elastic modulus (kN/mm^2)	222.5
E_{ult}	Ultimate strain capacity (%)	0.9

4 RESULTS

A summary of the test results is given in Table 3, which comprise the ultimate loads and modes of failure. Table 4 presents the comparative values of the calculated ductility indices for all strengthened elements, using the index calculators of Eqns.1, 2, 3 and 6, given in Section 2.

It can be seen that each specimen provides significantly different results relating to the ductility index. However, the two proposed methods (highlighted in bold) yield much more consistent values and this is verified by comparing the calculated standard deviation (σ) for the various methods, as can be seen in Table 5.

Table 3 Ultimate loads and failure modes

Beam ref.	P_u (kN)	%age change (%)	δ_u (mm)	%age change (%)	Failure mode
8CON	35.1	-	22.1	-	SY CC
8CF1	58	+65.2	28.9	+30.8	FR
8CF2	62.5	+78.1	31.3	+41.6	DB PTO
8CF3	55	+56.7	16.5	-25.3	DB PTO
10CON	56.5	-	30.0	-	SY CC
10CF1	62.6	+10.8	26.5	-11.7	FR
10CF2	80.1	+41.8	33.8	+12.7	DB PTO
10CF3	70.0	+23.9	17.7	-41.0	CC
16CON	98.0	-	22.7	-	CC
16CF1	96.0	-2.0	20.7	-8.8	ECC
16CF2	90.0	-8.2	20.4	-10.1	ECC
16CF3	101.0	+3.1	24.9	+9.7	CC

FR=Fibre rupture; DB=Debonding of CFRP; PTO=Premature tearing-off of concrete cover; CC=Concrete crushing; ECC=Explosive concrete crushing; SY=Steel yield

Table 4 Ductility indices

Beam Ref.	μ_Δ $\frac{\Delta_u}{\Delta_S}$	φ_E $\frac{1}{2}\left(\frac{E_{tot}}{E_{el}}+1\right)$	μ_{df} $\frac{\Delta_{0.95u}}{\Delta_S}$	φ_{3S} $\frac{1}{2}\left(\frac{E_{tot}}{E'_{el}}+1\right)$
8CON	2.40	2.19	**1.83**	**2.08**
8CF1	1.93	1.76	**1.67**	**1.66**
8CF2	2.30	1.83	**2.02**	**1.64**
8CF3	1.69	1.26	**1.42**	**1.26**
10CON	2.86	2.17	**1.41**	**2.10**
10CF1	2.30	1.80	**1.94**	**1.66**
10CF2	2.41	1.90	**2.10**	**1.69**
10CF3	1.82	1.33	**1.53**	**1.33**
16CON	1.82	1.21	**1.68**	**1.14**
16CF1	1.73	1.24	**1.58**	**1.17**
16CF2	1.77	1.48	**1.65**	**1.33**
16CF3	1.99	1.38	**1.79**	**1.29**

Table 5 Comparative values of indices

Beam set	Method	Index values			
		Mean	High	Low	Std. Dev. σ
Under reinforced	μ_Δ	2.09	2.86	1.69	0.34
	φ_E	1.63	2.19	1.21	0.38
	μ_{df}	**1.72**	**2.10**	**1.41**	**0.25**
	φ_{3S}	**1.53**	**2.10**	**1.14**	**0.33**
Optimally reinforced	μ_Δ	2.09	2.86	1.69	0.43
	φ_E	1.63	2.19	1.21	0.35
	μ_{df}	**1.72**	**2.10**	**1.41**	**0.32**
	φ_{3S}	**1.53**	**2.10**	**1.14**	**0.32**
Over reinforced	μ_Δ	2.09	2.86	1.69	0.11
	φ_E	1.63	2.19	1.21	0.13
	μ_{df}	**1.72**	**2.10**	**1.41**	**0.09**
	φ_{3S}	**1.53**	**2.10**	**1.14**	**0.09**

5 NUMERICAL VERIFICATION OF PROPOSED NEW METHOD FOR ESTIMATION OF STORED ELASTIC ENERGY

During the experimental programme, it was possible to obtain an unloading curve very close to or at failure for some specimens. This enabled a comparison of the actual unloading curve with the Naaman & Jeong and proposed 3-slope estimation method. The following is a numerical comparison using the data from 10CF2, the beam reinforced with two 10mm high-yield bars and strengthened with two layers of CFRP sheet.

5.1 Case studies

5.1.1 The actual unloading curve

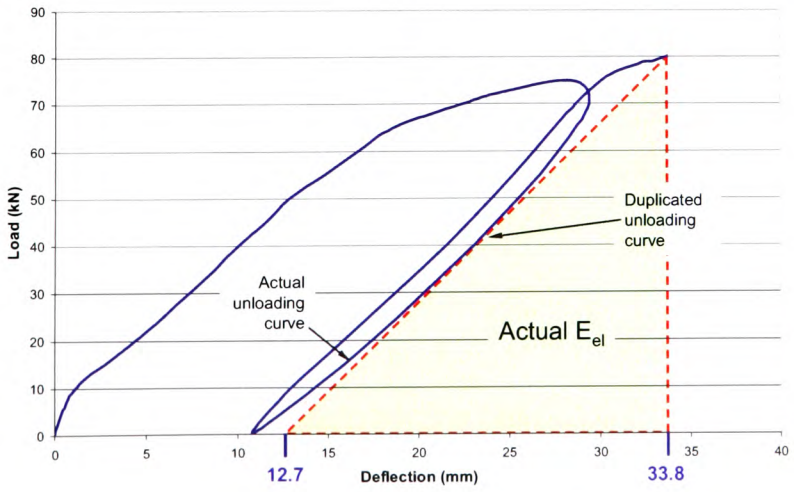

Fig. 3 Actual experimental unloading curve and Stored Elastic Energy, E_{el}, for 10CF2

From Fig. 3, the stored elastic energy is calculated from;

$$E_{el} = \frac{1}{2}(33.8 - 12.7)(80.0)$$

$$E_{el} = 844.0\,kNmm$$

5.1.2 Estimation of stored elastic energy using Naaman and Jeong's method:

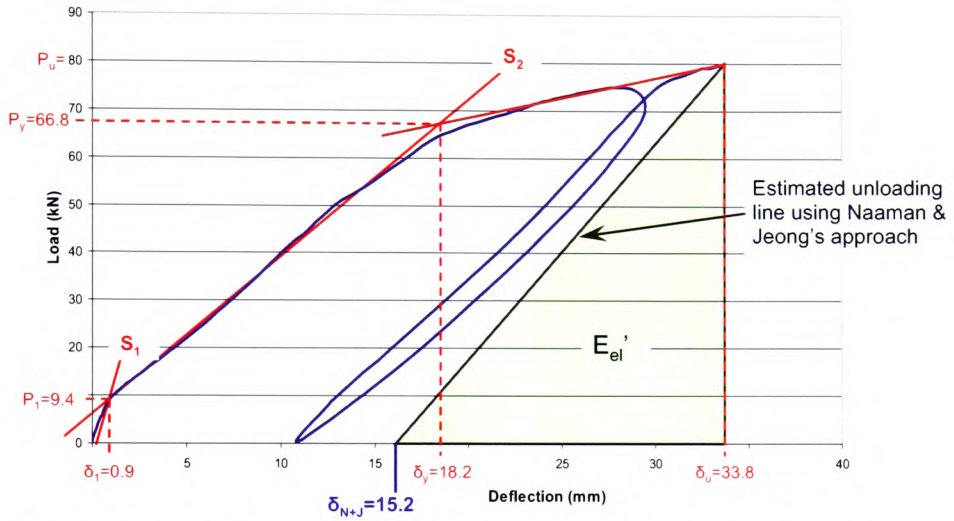

Fig. 4 Estimated unloading curve and Stored Elastic Energy, E_{el}', using Naaman and Jeong's Method

From analysis of the load/deflection graph, Fig. 4, it was possible to calculate the following:

$$S_1 = \frac{P_1}{\delta_1} = \frac{9.4}{0.9} = 10.4\,kN/mm$$

$$S_2 = \frac{(P_y - P_1)}{(\delta_y - \delta_1)} = \frac{(66.8 - 9.4)}{(18.2 - 0.9)} = 3.3\,kN/mm$$

$$S = \frac{(P_1)(S_1) + (P_y - P_1)(S_y)}{P_y} = \frac{(9.4)(10.4) + (66.8 - 9.4)(3.3)}{66.8} = 4.3\,kN/mm$$

$$\delta_{N+J} = \delta_u - \left\{\frac{P_u}{S}\right\} = 33.8 - \left\{\frac{80.0}{4.3}\right\} = 15.20\,mm$$

$$E_{el}' = \frac{1}{2}(\delta_u - \delta_{N+J})(P_u) = \frac{1}{2}(33.8 - 15.2)(80.0) = 744\,kNmm$$

5.1.3 Estimation of stored elastic energy using proposed 3-Slope method:

From analysis of the load/deflection graph, Fig. 5, the following can be calculated:

$S_1 = 10.4$, $S_2 = 3.3$ (Previously calculated)

$$S_3 = \frac{(P_u - P_y)}{\delta_u - \delta_y} = \frac{80.0 - 66.8}{33.8 - 18.2} = 0.9\,kN/mm$$

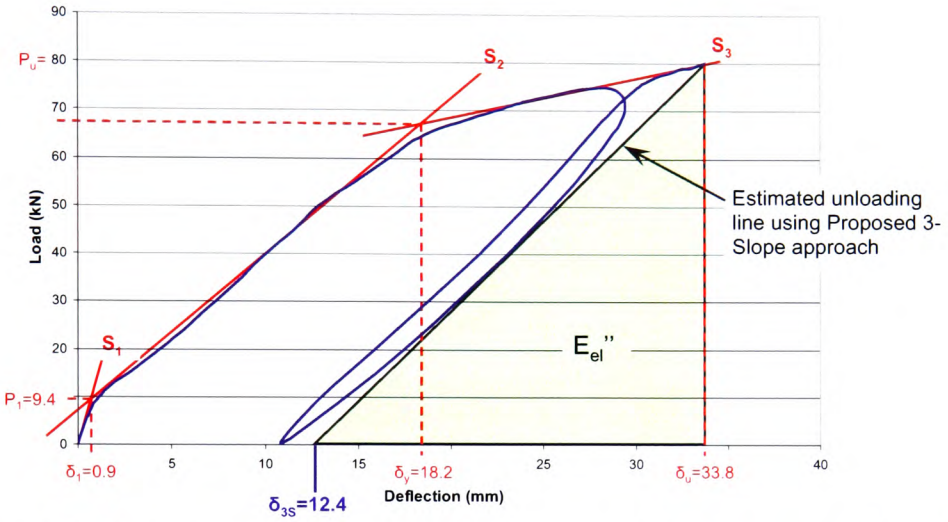

Fig. 5 Estimated unloading curve and Stored Elastic Energy, E_{el}",using Proposed 3-Slope Method

$$S' = \frac{P_1 S_1 + (P_y - P_1)S_y + (P_u - P_y)S_3}{P_u}$$

$$S' = \frac{(9.4)(10.4) + (66.8 - 9.4)(3.3) + (80.0 - 66.8)(0.9)}{80.0} = 3.74\,kN/mm$$

$$\delta_{3S} = \delta_u - \left\{\frac{P_u}{S'}\right\} = 33.8 - \left\{\frac{80.0}{3.74}\right\} = 12.4\,mm$$

$$E_{el}'' = \frac{1}{2}(\delta_u - \delta_{3S})(P_u) = \frac{1}{2}(33.8 - 12.4)(80.0) = 856\,kNmm$$

Table 6 summarises the above results.

Table 6 Summary of elastic energy

Method used	Naaman & Jeong	Proposed 3-Slope approach	Actual "E_{el}" from experimental results
Stored elastic energy (kNmm)	744	856	844

6 CONCLUSIONS

Of the different externally-strengthened beams, tested under controlled conditions, the following were confirmed:

1) Beams with a lower level of TESR displayed the typical *P/δ* characteristics normally found in under-reinforced steel-only beams, up to failure.

2) Beams with TESR regarded to be at a "balanced" level had characteristics similar to (1) but with a curtailed level of deformability, as a result of the increase in stiffness due to the increased steel reinforcement and FRP.

3) Beams with TESR considered in excess of the "balanced" state displayed trends (both observed and predicted) where it becomes difficult to identify the stage of steel-yielding.

4) It was observed that the higher the value of over-reinforcement, the more difficult it becomes to judge the point at which the internal steel yields. In these cases there was a near-linear *P/δ* relationship prior to brittle (as opposed to mild) failure.

5) In cases where the beam was unloaded as a pre-emptive (just before failure) measure it was seen that the creep portion of the P/δ curve could be identified and eliminated through the 95% method suggested by one of the authors.

6) It was possible to apply the modified Naaman and Jeong method, suggested by the first author, satisfactorily. This was successfully based on the P/δ curves during loading and un-loading.

7) The authors feel that they are close to providing structural design engineers (involved with FRP external retrofitting of RC beams) with more reliable analytical predictions for safer and more cost-effective measures in choosing FRP external strengthening systems.

ACKNOWLEDGEMENTS

The authors wish to acknowledge the Engineering and Physical Sciences Research Council for the funding which enabled this research to be conducted and also Exchem (Mining and Construction) Ltd. for the provision of materials.

REFERENCES

[1] Tann, D.B., Delpak, R. and Davies, P., "Ductility and deformability of fibre-reinforced polymer-strengthened reinforced concrete beams," *Journal of Structures and Buildings,* Vol. 157, SB1, January 2004, pp 19-30

[2] Grace, N.F., Sayed, G.A., Soliman, A.K. and Saleh, K.R., "Strengthening Reinforced Concrete Beams Using Fiber Reinforced Polymer (FRP) Laminates", *ACI Structural Journal*, 96(5), p. 865-874, 1999.

[3] Razaqpur, G.A. and Ali, M.M., "Ductility and strength of concrete beams externally reinforced with CFRP sheets", *Proceedings of the International Conference on Advanced Composite Materials in Bridges and Structures*, Canadian Society for Civil Engineers, Montreal, Canada, 1996.

[4] Aridome, Y., Kanakubo, T., Furuta, T. and Matsui, M., "Ductility of T-shape RC beams strengthened by CFRP sheet", *Transaction of Japan Concrete Institute*, 20, p.117-124, 1998.

[5] Pisanty, A. and Regan, P.E., "Ductility requirements for redistribution of moments in reinforced

concrete elements and a possible size effect", *Materials and Structures*, 31, p.530-535, 1998.

[6] Burgoyne, C.J., "Ductility and Deformability in Beams Prestressed with FRP Tendons", Proceedings of the International Conference on FRP Composites in Civil Engineering, Hong Kong, 12-15 December 2001, p.15-25.

[7] Tann, D.B., Davies, P. and Delpak, R., "A review of ductility determination of FRP strengthened flexural RC elements," *Proceedings of the Sixth International Symposium on FRP Reinforcement for Concrete Structures (FRPRCS-6),* Singapore, 1, 2003.

[8] Tann, D. B., "Retrofitting of Mechanically Degraded Concrete Structures Using Fibre Reinforced Polymer Composites", *PhD Thesis*, School of Technology, University of Glamorgan, Pontypridd, UK, 2001.

[9] Naaman, A. E. and Jeong, S. M. "Structural Ductility of Concrete beams Prestressed with FRP Tendons," in *Non-Metallic (FRP) Materials for the Reinforcement and Prestressing of Concrete*, Ed., Taerwe, E & FN Spon, London, pp379-384, 1995.

Appendix A-6

CONFERENCE PAPER

"Supplementary Investigations into the Ductility and Deformability of FRP Strengthened RC Elements"

FRPRCS9, 9th International Symposium on Fiber Reinforced Polymer Reinforcement for Concrete Structures
University of Adelaide, Australia, July 2009

SUPPLEMENTARY INVESTIGATIONS INTO THE DUCTILITY AND DEFORMABILITY OF FRP STRENGTHENED RC ELEMENTS

P.Davies [1] D.B.Tann [1] R.Delpak [1]

[1] Division of Civil and Mechanical Engineering, Faculty of Advanced Technology, University of Glamorgan, Trefforest, UK.

Keywords: FRP, composites, ductility, deformability, reinforced concrete, beams.

1 INTRODUCTION

Ductility is a chief concern to all structural design engineers, as all appropriately designed structures should be sufficiently ductile at ultimate limit state to provide adequate warning of impending failure, thereby avoiding sudden or brittle failure. In recent years, Fibre Reinforced Polymers (FRPs) have become more widely used in place of steel plates for strengthening of reinforced concrete (RC) structures. However, design engineers have been reluctant to adopt this technique due to the lack of definitive data relating to the performance of FRP strengthened RC structures and, hence, the possibility of brittle failure.

It is accepted that FRP strengthened RC elements behave quite differently from their normally-reinforced equivalents; this is primarily due to the dominant linear elastic stress-strain characteristics of composite materials up to failure. In previous papers, the authors have proposed that the determination of a ductility index for FRP strengthened RC flexural elements is to be based on either: a) the serviceability and ultimate loads of the element; b) the total and stored-elastic energy of the element [1] & [2]. Both these methods have produced consistent results and it is proposed that further work be carried out to develop both approaches.

2 OVERVIEW OF CURRENT METHODS

The determination of ductility for elements strengthened with FRPs has been a topic of considerable debate among researchers [2]. It is generally accepted that a ductility index can be determined from one of two broad categories:

2.1 Deformation-based ductility

Previously, the authors have proposed the use of the Equation (1) to determine ductility from deformation data;

$$\mu_{\Delta 1} = \frac{\Delta_u}{\Delta_s} \qquad (1)$$

where Δ_u is the mid-span displacement at ultimate load and Δ_s is the mid-span displacement at serviceability load (taken to be 67% of the ultimate load).

Tann [3] suggested replacing Δ_u with $\Delta_{0.95u}$ (i.e. the mid-span displacement at 95% of the ultimate load), which would remove the misleading values for deformation at ultimate load, which can be up to four times that at 95%.

$$\mu_{df} = \frac{\Delta_{0.95u}}{\Delta_s} \qquad (2)$$

2.2 Energy-based ductility

The authors have also previously recommended calculating the energy-based index using the Equation (3), first published by Naaman and Jeong [4];

$$\varphi_E = \frac{1}{2}\left[\frac{E_{tot}}{E_{el}} + 1\right] \qquad (3)$$

where E_{tot} is the total energy, calculated as the total area under the Load/Deflection curve up to failure, and E_{el} is the stored elastic energy.

Naaman and Jeong used the following equation to estimate the unloading curve at ultimate limit state and, hence, the stored elastic energy (represented by the area under the unloading curve – see also Figure 1):

$$S = \frac{P_1 S_1 + (P_2 - P_1) S_2}{P_2} \quad (4)$$

It has been proposed by the authors to modify this approach in order to take into consideration the additional elastic energy developed in FRP strengthened elements during the latter stages of loading. This modified approach incorporates a third slope, S_3, when calculating the slope of the estimated unloading curve, as shown in Equation (5) and Figure 1:

$$S = \frac{P_1 S_1 + (P_2 - P_1) S_2 + (P_U - P_2) S_3}{P_U} \quad (5)$$

The revised approach yields an adjusted value for the estimated stored elastic energy, E'_{el}, which can then be used to calculate a modified ductility index, φ_{3S}, as follows:

$$\varphi_{3S} = \frac{1}{2}\left(\frac{E_{tot}}{E''_{el}} + 1\right) \quad (6)$$

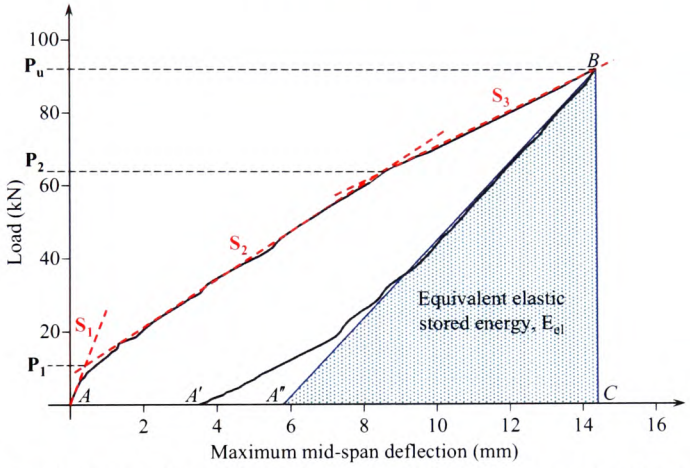

Fig. 1 Typical load/deflection variation from laboratory tests and example of calculation of equivalent elastic stored energy (See text for legend of symbols).

2 EXPERIMENTAL PROGRAMME

2.1 Beam geometry and loading configuration

An additional four beams were cast, utilising two Ø12mm steel reinforcing bars, in order to supplement the results previously obtained from twelve elements using Ø8, Ø10 and Ø16mm steel bars. The beam cross-section was 100x200mm, with the shear reinforcement consisting of Ø6mm mild-steel links spaced evenly at 100mm in the shear/moment zone. No shear reinforcement was used in the 'constant moment zone' between the loading points. The clear span for all tests was 2400mm, as shown in Figure 2.

2.2 Testing

For all tests, a four-point loading system was used. The specimens were instrumented with electrical strain gauges bonded at the various locations on the elements and, in addition, concrete surface strains were recorded using DEMEC gauges in six zones, three on either side of the beam. Deflections were recorded using calibrated Linear Variable Displacement Transducers (LVDTs).

2.3 FRP properties and strengthening arrangement

One beam was used as a control beam, with the remaining beams strengthened with Carbon Fibre Reinforced Polymer (CFRP) sheets, as detailed in Table 1 where the FRP ratio, total equivalent steel ratio (TESR), failure load and failure mode are also listed. Tensile tests were carried out on fifteen single-layer samples of CFRP; the samples were 15mm wide and 250mm long, and the material was

found to have an ultimate tensile strength of 1900N/mm^2, with an associated elastic modulus of 223kN/mm^2.

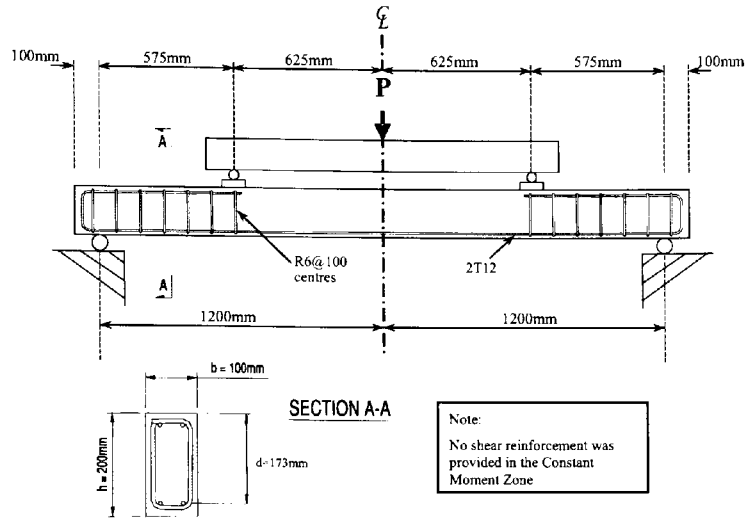

Fig. 2 Beam dimensions and reinforcement details

2.4 Results

Table 2 presents the comparative values of the calculated ductility indices for all strengthened elements, using Equations 1, 2, 3 and 6. It can be seen that each specimen provides significantly different results relating to the ductility index. However, the two proposed methods (highlighted in bold) yield much more consistent values.

2.2 Testing

For all tests, a four-point loading system was used. The specimens were instrumented with electrical strain gauges bonded at the following locations:

- The finished and clean top surface of the beam, at mid-span
- The tension reinforcement, at mid-span and directly underneath the point of load application
- On the surface of the CFRP laminates

In addition, concrete surface strains were recorded using DEMEC gauges in six zones, three on either side of the beam. The deflections were recorded using calibrated Linear Variable Displacement Transducers (LVDTs).

3 Conclusions

Of the different externally-strengthened beams, tested under controlled conditions, the following were confirmed:

1) Beams with low levels of TESR displayed the typical *P/δ* characteristics usually found in normally-reinforced beams, up to failure, whereas beams with TESR regarded to be at a "balanced" level had similar characteristics but with a curtailed level of ductility, as a result of the increased stiffness due to the higher levels of steel reinforcement and FRP.
2) Beams with TESR considered in excess of the "balanced" state displayed trends where it becomes difficult to identify the stage of steel-yielding.
3) The authors feel that they are close to providing structural design engineers with more reliable, analytical predictions for safer and more cost-effective measures in choosing FRP external strengthening systems for retrofitting projects.

REFERENCES

[1] Tann, D.B., Delpak, R. and Davies, P., "Ductility and deformability of fibre-reinforced polymer-strengthened reinforced concrete beams", *Journal of Structures and Buildings*, Vol. 157, SB1,

January 2004, pp 19-30.

[2] Davies, P., Tann, D.B. and Delpak, R., "Further investigations into the ductility and deformability of FRP strengthened RC elements", *Proceedings of the Sixth International Symposium on FRP Reinforcement for Concrete Structures (FRPRCS-8), Greece*, 1, 2007.

[3] Tann, D. B., "Retrofitting of Mechanically Degraded Concrete Structures Using Fibre Reinforced Polymer Composites", *PhD Thesis*, School of Technology, University of Glamorgan, Pontypridd, UK, 2001.

[4] Naaman, A. E. and Jeong, S. M. "Structural Ductility of Concrete beams Prestressed with FRP Tendons," in *Non-Metallic (FRP) Materials for the Reinforcement and Prestressing of Concrete*, Ed., Taerwe, E & FN Spon, London, pp379-384, 1995.

Table 1 FRP arrangement for tested beams

Beam ref.	FRP sheets	Sectional FRP area (mm^2)	FRP ratio ρ_f (%)	(TESR)* (%)	P_u (kN)	Failure mode**
8CON	None	-	-	0.50	35.1	SY CC
8CF1	1 sheet	16.5	0.08	0.59	58	FR
8CF2	2 sheets	33.0	0.17	0.68	62.5	DB PTO
8CF3	3 sheets	49.5	0.25	0.77	55	DB PTO
10CON	None	-	-	0.79	56.5	SY CC
10CF1	1 sheet	16.5	0.08	0.86	62.6	FR
10CF2	2 sheets	33.0	0.17	0.94	80.1	DB PTO
10CF3	3 sheets	49.5	0.25	1.02	70.0	CC
12CON	None	-	-	1.13	65.0	CC
12CF1	1 sheet	16.5	0.08	1.22	78.2	CC
12CF2	2 sheets	33.0	0.17	1.31	85.0	CC
12CF3	3 sheets	49.5	0.25	1.40	84.1	CC
16CON	None	-	-	2.01	98.0	CC
16CF1	1 sheet	16.5	0.08	2.09	96.0	ECC
16CF2	2 sheets	33.0	0.17	2.17	90.0	ECC
16CF3	3 sheets	49.5	0.25	2.24	101.0	CC

*Total equivalent steel ratio (TESR) is the existing steel reinforcement ratio, ρ_s, plus the equivalent steel ratio of the FRP composites, determined as $\rho_{es} = \rho_s + \alpha \rho_f$, where α is the modular ratio defined as the elastic modulus of the FRP composite divided by the elastic modulus of the steel reinforcement, $\alpha = E_f/E_s$. E_s is taken to be 205,000N/mm^2.

** FR=Fibre rupture; DB=Debonding of CFRP; PTO=Premature tearing-off of concrete cover; CC=Concrete crushing; ECC=Explosive concrete crushing; SY=Steel yield

Table 2 Ductility indices

Beam Ref.	μ_Δ $\frac{\Delta_u}{\Delta_s}$	φ_E $\frac{1}{2}\left(\frac{E_{tot}}{E_{el}}+1\right)$	μ_{df} $\frac{\Delta_{0.95u}}{\Delta_s}$	φ_{3S} $\frac{1}{2}\left(\frac{E_{tot}}{E'_{el}}+1\right)$
8CON	2.40	2.19	**1.83**	**2.08**
8CF1	1.93	1.76	**1.67**	**1.66**
8CF2	2.30	1.83	**2.02**	**1.64**
8CF3	1.69	1.26	**1.42**	**1.26**
10CON	2.86	2.17	**1.41**	**2.10**
10CF1	2.30	1.80	**1.94**	**1.66**
10CF2	2.41	1.90	**2.10**	**1.69**
10CF3	1.82	1.33	**1.53**	**1.33**
12CON	1.76	1.31	**1.63**	**1.53**
12CF1	2.00	1.53	**1.54**	**1.48**
12CF2	1.81	1.27	**1.66**	**1.20**
12CF3	1.97	1.45	**1.66**	**1.19**
16CON	1.82	1.21	**1.68**	**1.14**
16CF1	1.73	1.24	**1.58**	**1.17**
16CF2	1.77	1.48	**1.65**	**1.33**
16CF3	1.99	1.38	**1.79**	**1.29**